PHYSICS AND SEISMICITY OF ROCKS

EDITED BY: Longjun Dong, Guoyang Fu and Wei Wu
PUBLISHED IN: Frontiers in Physics

frontiers Research Topics

ISSN 1664-8714
ISBN 978-2-88971-735-4
DOI 10.3389/978-2-88971-735-4

About Frontiers

Frontiers is more than just an open-access publisher of scholarly articles: it is a pioneering approach to the world of academia, radically improving the way scholarly research is managed. The grand vision of Frontiers is a world where all people have an equal opportunity to seek, share and generate knowledge. Frontiers provides immediate and permanent online open access to all its publications, but this alone is not enough to realize our grand goals.

Frontiers Journal Series

The Frontiers Journal Series is a multi-tier and interdisciplinary set of open-access, online journals, promising a paradigm shift from the current review, selection and dissemination processes in academic publishing. All Frontiers journals are driven by researchers for researchers; therefore, they constitute a service to the scholarly community. At the same time, the Frontiers Journal Series operates on a revolutionary invention, the tiered publishing system, initially addressing specific communities of scholars, and gradually climbing up to broader public understanding, thus serving the interests of the lay society, too.

Dedication to Quality

Each Frontiers article is a landmark of the highest quality, thanks to genuinely collaborative interactions between authors and review editors, who include some of the world's best academicians. Research must be certified by peers before entering a stream of knowledge that may eventually reach the public - and shape society; therefore, Frontiers only applies the most rigorous and unbiased reviews.
Frontiers revolutionizes research publishing by freely delivering the most outstanding research, evaluated with no bias from both the academic and social point of view. By applying the most advanced information technologies, Frontiers is catapulting scholarly publishing into a new generation.

What are Frontiers Research Topics?

Frontiers Research Topics are very popular trademarks of the Frontiers Journals Series: they are collections of at least ten articles, all centered on a particular subject. With their unique mix of varied contributions from Original Research to Review Articles, Frontiers Research Topics unify the most influential researchers, the latest key findings and historical advances in a hot research area! Find out more on how to host your own Frontiers Research Topic or contribute to one as an author by contacting the Frontiers Editorial Office: frontiersin.org/about/contact

PHYSICS AND SEISMICITY OF ROCKS

Topic Editors:
Longjun Dong, Central South University, China
Guoyang Fu, Monash University, Australia
Wei Wu, Nanyang Technological University, Singapore

Citation: Dong, L., Fu, G., Wu, W., eds. (2021). Physics and Seismicity of Rocks. Lausanne: Frontiers Media SA. doi: 10.3389/978-2-88971-735-4

Table of Contents

frontiers in Physics

EDITORIAL
published: 21 October 2021
doi: 10.3389/fphy.2021.763168

Editorial: Physics and Seismicity of Rocks

Longjun Dong[1]*, *Guoyang Fu*[2] and *Wei Wu*[3]

[1]School of Resources and Safety Engineering, Central South University, Changsha, China, [2]Department of Civil Engineering, Monash University, Melbourne, VIC, Australia, [3]School of Civil and Environmental Engineering, Nanyang Technological University, Singapore, Singapore

Keywords: rock physics, seismicity, fault behavior, rock instability, fault slip, seismic nucleation processes

Editorial on the Research Topic

Physics and Seismicity of Rocks

Understanding the physical mechanisms of rock and exploring the characteristics of seismicity have attracted worldwide attention in solid earth geophysics. Due to the anthropogenic activities such as deep mining and tunneling, large-scale collapses and seismicity frequently occur leading to serious casualties and economic losses. Thus, it is extremely important to prevent the occurrence of disasters or minimize the risk and loss of accidents.

In the past, a great number of experiments have been carried out in an attempt to explain the underlying mechanisms of rocks for various geological phenomena [1, 2]. For bringing new breakthroughs of seismicity-related research, innovative experimental techniques, simulation methods, data mining, and geophysical methods are used to extract useful knowledge from the data collected in both experiments and site practices [3–7].

However, the surging demand for space and resources prompts the environment and methods we face to constantly change. The new background, new challenges, and new methods appearing in the physics and seismicity of rocks require further research. Therefore, the main goal of this issue is to fill an essential gap that is greatly missed in this field. We sincerely hope that this issue will be beneficial to the readers to present the recent findings in the field and shed some light on the physics and seismicity of rocks.

Zhao et al. selected a complex of sandstone and C40 concrete mortar to carry out the freeze-thaw cycles test and the uniaxial compression test. The sample water content, the freezing temperature, and the number of freeze-thaw cycles were analyzed based on the factorial design principle. The results showed that the freeze-thaw treatment can significantly reduce the uniaxial compressive strength (UCS) of the sample. The impact of main effects and secondary interaction on unconfined compressive strength was revealed.

Zhang et al. selected the sericite quartz schist coarse-grained soil to carry out the large-scale triaxial consolidated-drained (CD) and consolidated-undrained (CU) shear tests. In order to obtain the stress-strain, deformation, and strength of the sericite quartz schist coarse-grained soil, four different confining pressure conditions were designed in this experiment. They found the stress-strain curve of sericite quartz schist was nonlinearity, compressive hardening and elastic-plastic. Furthermore, the failure mechanism of the samples changed from shearing shrinkage at first and later dilatancy to shearing shrinkage.

Yang et al. designed a shaking table test that a bedding rock slope with weak structural plane was taken as the prototype for studying the acceleration and displacement responses at different positions of the slope. The seismic response and instability mechanism of rock bedding slope under different seismic amplitudes, frequencies and durations are analyzed by adjusting the amplitude and the type of the seismic wave in the experiment. With the increase of the amplitude of the seismic wave, the

OPEN ACCESS

Edited and reviewed by:
Alex Hansen,
Norwegian University of Science and Technology, Norway

***Correspondence:**
Longjun Dong
lj.dong@csu.edu.cn

Specialty section:
This article was submitted to Interdisciplinary Physics, a section of the journal Frontiers in Physics

Received: *23 August 2021*
Accepted: *29 September 2021*
Published: *21 October 2021*

Citation:
Dong L, Fu G and Wu W (2021) Editorial: Physics and Seismicity of Rocks. Front. Phys. 9:763168. doi: 10.3389/fphy.2021.763168

peak ground acceleration (PGA) values of the monitoring points on both sides of the sliding surface showed an opposite trend. The impact of seismic waves on the acceleration response of the bedding rock slope was closely related to its excellent frequency and the natural frequency of the slope.

Li et al. conducted the Brazilian split tests on granite, marble, sandstone, and limestone. The electron microscope system also was employed to carry out the analysis of fracture morphology. They analyzed the experiment results and found that rock characteristics such as mineral composition may have influence on the b-value and the fracture characteristics of rock. The relationship between acoustic emission signal frequency of rock fracture and the fracture scale was proposed based on the rock characteristics and the distribution characteristics of the frequency spectrum of acoustic emission signals.

Li et al. carried out three cyclic loading and unloading tests with different loading rates and initial cyclic peak stresses for researching the acoustic emission evolution characteristics of saturated limestone under different loading and unloading paths. They analyzed the distribution of signals in different frequency, the development form of the ringing count, and the law of energy evolution. The conclusion summarized in this paper advocated that the roadway should be quickly excavated in the early stage for delaying the most period of fracture behavior.

Chen et al. measured the masses and sizes of the specimens and the pH values of the acidic solution after saturating the diorite specimens in neutral water and acid solutions. They carried out the triaxial compression tests under the solutions with different pH values. The mass damage features and mechanical properties of diorite specimens saturated in solutions with different pH values were analyzed. On this basis, a damage strength model considering acidification was established.

Zhang et al. designed the shaking table experiment on the background of the rock bedding slope with a weak structural plane. The Hilbert-Huang transform (HHT) method was applied to obtain the characteristics of the seismic signal in the Frequency domain. They analyzed the distribution of the energy and the predominant frequency. Finally, the change of the peak value of the marginal spectrum was recognized as an important sign reflecting the development process of the earthquake damage inside the slope.

Li et al. proposed an analytical model to simulate the abutment pressure distribution over the coal in front of the mining face under elastic and inelastic conditions. And a new theoretical formula was derived to discuss the influences of UCS, residual strength, mining height, softening modulus, and deformation angle on the abutment pressure distribution. The field data was applied to verify the validity of the analytical model. The calculated abutment pressure distribution and the widths of the elastic and inelastic zones were compared with the monitoring data. The results showed that the proposed model have high accuracy, which can provide guidance for engineering applications.

Tu et al. proposed a two-stage constitutive model of cemented tailings backfill (CTB) under uniaxial compression based on the Weibull distribution density function, the strain equivalence principle and the damage mechanics theory. In order to verify the theoretical model, the CTB samples with different solid contents and cement-sand ratios were subjected to uniaxial compression tests. As far as the material itself is concerned, the two variables have a great influence on the sample especially prominent at the peak stress. By comparing the experiment results with the established model, it is found that the failure model of the CTB specimens was mainly tensile failure, and the constitutive model was similar to that of ordinary cement mortar M5. The above research results are helpful to improve the theory of uniaxial compression characteristics of CTB.

Wang et al. selected six parameters including the uniaxial compressive strength, the uniaxial compressive strength, elastic deformation energy index, the ratio of the maximum tangential stress to the uniaxial compressive strength, the depth of the roadway, the integrity coefficient of the rock mass indicators as indicators for rock burst propensity predictions. A finite-interval cloud model based on the CRITIC algorithm was proposed, which was applied to evaluate the relationships between indicators. By comparing the prediction results of the established model with the monitoring data, the accuracy of the model was verified.

Dong et al. analyzed the stress wave transmission in the course of a single joint and the propagation law of a reflection wave. They treated the joints as rocks in the calculation and proposed the analysis model of stress waves passing through single-joint rock. In view of the above researches, the macro-joint model of stress waves passing through a group of parallel jointed rocks was also established. Finally, the reliability of the models were verified by several tests.

Xie et al. analyzed the blast vibration waveforms from a single-deck blast test and proposed an improved method for multihole blasting seismic wave prediction. The method was applied in the practice and the results showed that it can predict the blast waveforms. The above achievement can provide a new way for design to control blast vibration.

Jing et al. established a model of the high rockfill (HRF) embankment based on the actual project. The construction and operation of the HRF embankment were simulated by a centrifuge test for obtaining the deformation laws of HRF embankment. According to the simulation results, the evolution law of the deformation value and velocity in embankment top and the slope foot during the operation was revealed.

Zhang et al. simulated the support process of tunnel excavation. And they compared simulation results and monitoring data to study the deformation behavior of the surrounding rock and the variation of the stress field in the support structure. The rock occurrence was an important factor that affected the asymmetric deformation behavior in the tunnel with large cross section passing through the soft rock of the coal seam. Several engineering treatment measures such as increasing support structure stiffness were summarized.

Su and Shen established the deep coal mine stope model containing section coal and rock pillars using the ANASYS software. The response physical characteristics of coal pillars with different widths under the roof shock disturbance

intensity and frequency from goaf were analyzed based on the dynamic structural system model. Since the model was affected by different shock disturbances, the vertical deformation and the plastic zone occupation ratio of the coal pillar were researched. The results showed that the closer the shock disturbance frequency was to the natural frequency of the model, the more unstable the coal pillar was.

Zhou et al. adopted the discrete element method (DEM) to simulate the SHPB results of acoustic emission (AE) and AE moment tensor. They found that the simulation results were feasible in analyzing the microscopic mechanism of dynamic tensile simulation in rock dynamics. The results showed that the AE simulation was consistent with the macroscopic cracking shown by HS photography. They believed that the ratio of isotropic and deviatoric components of the moment tensor can explain the evolution process of main axial crack and the shear failure zones, which will be different with the traditional method to understand the rock failure mechanism.

Liu et al. simulated the failure process in punch-through shear tests using the discrete element method. By comparing the results of the simulation and experiments, they studied the crack propagation sequence and the influence of confining stress on effective shear fracture toughness.

The analysis of the physical and mechanical characteristics of the rock requires multiple test and monitoring technology such as acoustics, displacement, and force. Especially in the research of the mechanical property of rock fracture, it is necessary to combine the methods of source location, source identification, and focal mechanism inversion for analysis. As the field of rock engineering becomes more extensive and the problems are more complicated, the research of the physics and seismicity of rocks which considers rock structures [8] and velocity variation [9] will be the trend of the future research, which can provide the assistance for disaster early warning and risk control in practical engineering.

AUTHOR CONTRIBUTIONS

LD and GF drafted the first version of the editorial. LD and WW revised the first draft and made contributions about papers they edited.

REFERENCES

1. Zhang ZZ, Gao F, and Shang XJ. Rock Burst Proneness Prediction by Acoustic Emission Test during Rock Deformation. *J Cent South Univ* (2014) 21(1): 373–80. doi:10.1007/s11771-014-1950-3
2. Zhang Y, Ma J, Sun D, Zhang L, and Chen Y. AE Characteristics of Rockburst Tendency for Granite Influenced by Water under Uniaxial Loading. *Front Earth Sci* (2020) 8:55. doi:10.3389/feart.2020.00055
3. Dong L, Hu Q, Tong X, and Liu Y. Velocity-Free MS/AE Source Location Method for Three-Dimensional Hole-Containing Structures. *Engineering* (2020) 6:827–34. doi:10.1016/j.eng.2019.12.016
4. Yang Z. Key Technology Research on the Efficient Exploitation and Comprehensive Utilization of Resources in the Deep Jinchuan Nickel Deposit. *Engineering* (2017) 3(4):559–66. doi:10.1016/j.eng.2017.04.021
5. Ma J, Dong L, Zhao G, and Li X. Focal Mechanism of Mining-Induced Seismicity in Fault Zones: A Case Study of Yongshaba Mine in China. *Rock Mech Rock Eng* (2019) 52:3341–52. doi:10.1007/s00603-019-01761-4
6. Dong LJ, Tang Z, Li XB, Chen YC, and Xue JC. Discrimination of Mining Microseismic Events and Blasts Using Convolutional Neural Networks and Original Waveform. *J Cent South Univ* (2020) 27(10):3078–89. doi:10.1007/s11771-020-4530-8
7. Zhu H, Yan J, and Liang W. Challenges and Development Prospects of Ultra-long and Ultra-deep Mountain Tunnels. *Engineering* (2019) 5(3):384–92. doi:10.1016/j.eng.2019.04.009
8. Dong L. J., Tong X. J., Hu Q. C., and Tao Q.. Empty Region Identification Method and Experimental Verification for the Two-Dimensional Complex Structure. *Int. J. Rock Mech. Min.* (2021) 147:104885. doi:10.1016/j.ijrmms.2021.104885
9. Dong L. J., Tong X. J., and Ma J.. Quantitative Investigation of Tomographic Effects in Abnormal Regions of Complex Structures. *Engineering*. doi:10.1016/j.eng.2020.06.021

Conflict of Interest: The authors declare that the research was conducted in the absence of any commercial or financial relationships that could be construed as a potential conflict of interest.

Publisher's Note: All claims expressed in this article are solely those of the authors and do not necessarily represent those of their affiliated organizations, or those of the publisher, the editors and the reviewers. Any product that may be evaluated in this article, or claim that may be made by its manufacturer, is not guaranteed or endorsed by the publisher.

frontiers in Physics

ORIGINAL RESEARCH
published: 22 July 2020
doi: 10.3389/fphy.2020.00223

Physical Characteristics of Section Coal and Rock Pillars Under Roof Shock Disturbances From Goaf

Ronghua Su and Hongshuang Shen*

School of Mechanics and Engineering, Liaoning Technical University, Fuxin, China

The stability of a rock strata structure is closely related to its response physical characteristics under external shock disturbance. The roof shock disturbance from goaf is usually one of the important factors that cause coal and rock pillar instability. It is necessary to study the dynamic physical characteristics of coal and rock pillars under roof shock disturbance from goaf. The dynamic structural system model of elastic-plastic finite element was established for the formation of surrounding rock and coal pillars in a deep stope. The response physical characteristics of coal pillars with different widths were analyzed under the roof shock disturbance intensity and frequency from goaf. The natural vibration characteristics of the stope model were calculated and the first 10-order natural frequencies were extracted. The calculations indicated that the vertical displacement and the plastic zone occupation ratio of the coal pillar increased with the increase of the shock disturbance intensity, decreased with the increase of the shock disturbance frequency, and decreased with the increase of the coal pillar width. The influence of the vertical deformation and the plastic zone occupation ratio of the coal pillar under shock disturbance frequency was more obvious compared with that of the shock disturbance intensity, especially at low frequency. The closer the shock disturbance frequency was to the natural frequency of the model, the larger the plastic zone of the coal pillars was, with the bearing capacity of the coal pillar decreasing significantly. It is significant that more attention should be paid to monitoring the frequency of roof shock disturbance signal when designing coal pillars width in the coal mine.

Keywords: rock physics, dynamic characteristics, shock disturbance intensity, shock disturbance frequency, roof goaf, coal and rock pillars

OPEN ACCESS

Edited by:
Longjun Dong,
Central South University, China

Reviewed by:
Zhigang Tao,
China University of Mining and Technology, Beijing, China
Yanlin Zhao,
Hunan University of Science and Technology, China

****Correspondence:***
Ronghua Su
suronghua@lntu.edu.cn

Specialty section:
This article was submitted to Interdisciplinary Physics, a section of the journal Frontiers in Physics

Received: *01 April 2020*
Accepted: *25 May 2020*
Published: *22 July 2020*

Citation:
Su R and Shen H (2020) Physical Characteristics of Section Coal and Rock Pillars Under Roof Shock Disturbances From Goaf. Front. Phys. 8:223. doi: 10.3389/fphy.2020.00223

INTRODUCTION

Owing to the layout of the mining operation for underground coal mining, a large number of coal and rock pillars are needed [1–4]. The coal and rock pillars have many different functions, including protecting the tunnels, isolating goafs, and avoiding surface subsidence [5–9]. The stability of coal and rock pillars will directly affect the safe production of mines and the safety of surface buildings. The stress conditions of coal and rock pillars are complex [10]. These pillars are subjected to various kinds of shock disturbances caused by mining operations, such as blast vibrations, periodic pressure disturbances, and mine earthquakes, while being subjected to gravity loads [11–14]. The periodic fault–slip burst of a roof is a common phenomenon triggered by a shock disturbance during cave mining; this phenomenon has the characteristics of a short action time and a great

shock disturbance force [15]. Shock disturbances have a great influence on the stability of coal pillars. A strong shock disturbance is one of the main factors that induce dynamic disasters of deep coal mine stopes. The determination of the section coal pillars width in a high-strength mine with a fully mechanized top-coal caving working face should consider many factors, such as repeated and intensive mining, basic roof fractures, large tunnel sections, and other shock disturbance factors [16, 17]. The rational design and the stability analysis of the coal and rock pillar size have caused a great concern in the field of mining at home and abroad and have become important research topics [18–24]. An understanding of the mechanical response characteristics of coal and rock pillars under complex loading conditions is expected and is the premise of the abovementioned analysis.

External shock disturbance must be taken into account when selecting the section coal and rock pillar widths. Thus, it has been very important to study the stability of section coal and rock pillars and determine the width of section coal and rock pillars. A mechanical model of section coal pillars with different widths during working face extraction was established by fast Lagrangian analysis of continua in three dimensions [25]. Comparing the differences in the distribution laws of the stress and deformation and plastic zones in the surrounding rock, a reasonable width of the section coal pillars was obtained. Generally, the reasonable width of a coal and rock pillar under dynamic simulation was much larger than that under static simulation [26]. The stress state of coal bodies subjected to the effect of roof strata was investigated, and the shock risk of the roof fracture vibration on coal was studied by numerical simulation [27]. The results showed that the shock risk of the coal body increases during roof shock disturbance. Crack initiation, development, and propagation in the coal were one cause of coal body instability [28]. The deformation of coal and rock pillars during excavation could be determined by on-site monitoring, and better monitoring results were obtained by using a 3D laser scanner [29]. To effectively reduce the shock disturbance on coal and rock pillars due to the dynamic pressure of mining, the stability of coal pillars in a bilateral goaf was analyzed by theoretical analyses and numerical simulations, and the stress distribution characteristics of section coal pillars were obtained [30]. Previous researches have also studied the microcrack development, structural damage, and energy transformation of coal and rock mass to the failure rules of coal and rock mass and revealed the mechanism of coal and rock dynamic disasters [31–33]. Acoustic emission technique and moment tensor analysis were used to evaluate the temporal–spatial evolution and damage of micro-cracks of schist [34]. The study of energy conversion and failure mechanism of coal mass under repeated loads was beneficial to the risk assessment of dynamic disasters [35]. It is necessary to reveal the principle of the dynamic shock disturbance effect of the roof under high-strength mining. The conditions, mechanism, and influencing factors that induced the dynamic load shock effect of the roof in high-strength mining stopes were investigated [36]. The study of the dynamic physical characteristics of coal and rock structure under shock disturbance intensity is a hot topic. The stability of the section coal and rock pillars also depends on whether the design of the coal and rock pillars is in line with the actual situation and whether the construction is in place. To investigate the reasonable size of coal and rock pillars, field monitoring and analyses [37, 38], similar simulation experiment analyses [39, 40], numerical simulations [22, 41], and other means have been applied to study the mechanism of section coal and rock pillar-induced dynamic disasters.

Roof shock disturbance from goaf, which affects mining safety, is one of the important factors to study on the dynamic physical characteristics of section coal and rock pillars. A dynamic structural system model of elastic-plastic finite element was established for the formation of surrounding rock and coal pillars in a deep stope. The physical characteristics of section coal and rock pillars in the model were investigated mainly by varying the shock disturbance frequencies and the intensities in the research. The variation characteristics of the vertical deformation and plastic zone of different section coal pillar widths, under a combination of different shock disturbance intensities and frequencies, were discussed. The vibration characteristics of the stope model were analyzed. The relationship between the physical characteristics of coal pillars under roof shock disturbance frequency and the natural vibration characteristics of the stope was discussed and analyzed. This study could provide a theoretical reference for the rational design and stability analysis of section coal and rock pillars used in deep coal mine stopes.

BASIC ASSUMPTIONS AND MODEL ESTABLISHMENT

Engineering Background and Basic Assumptions

The coal field of the underground coal mine is 850 m in depth. It belongs to the North China-type carboniferous Permian coal-bearing strata, which is located in the north margin of the syncline and is a monoclinal structure. The average thickness of the coal seam is 4 m, and the coal seam is a nearly horizontal structure. The dip angle of the maximum principal stress in the *in situ* stress field of the mining area is close to the horizontal direction. The *in situ* stress in the mining area is mainly horizontal tectonic stress. The bearing of the maximum principal stress is north by west. The roof is composed mostly of mudstone and sandy mudstone, and the floor is composed mostly of dark gray sandy mudstones. Using the method of longwall mining, the full height is immediately mined. According to the actual situation of the field, the basic hypothesis of the model is as follows: the rock stratum is regarded as a horizontal rock layer. The section coal and rock pillars (section coal pillar; hereafter sometimes referred to as the pillar) and the surrounding rock strata in the deep coal mine stope (hereafter sometimes referred to as the stope) are established by an elastoplastic model to analysis. The section coal and rock pillars, direct roof rock, and direct bottom rock of the coal seams are treated as elastic-plastic bodies, while the other layers adopt an elastic model. The Drucker–Prager (D–P) yield criterion is satisfied. The yield

condition of the D–P criterion is:

$$\alpha I_1 + (J_2)^{\frac{1}{2}} - k = 0 \tag{1}$$

where I_1 is the first invariant of the stress tensor, J_2 is the second invariant of the strain tensor, $\alpha = \frac{2\sin\phi}{\sqrt{3}(3-\sin\phi)}$, $k = \frac{2\sqrt{3}c\cos\phi}{3-\sin\phi}$, c *is* the cohesion of the material, and ϕ is the friction angle.

A schematic diagram of the section coal pillar arrangement in the profile of a fully mechanized mining face is shown in **Figure 1**. It is the profile along the strike of the vertical working face. The changes of vertical deformation and plastic zone (the region where deformation occurs under roof shock disturbance) of section coal and rock pillars are analyzed by adopting the plane strain model.

Figure 1 presents the schematic diagram of the section coal pillar arrangement. The figure shows the stratal relationships.

The width of the section coal pillars (represented by symbol B) of the stope model can be designed with different values on the working face. B refers to the solid section coal pillar width, q is the uniformly distributed vertical stress, and $Q(t)$ is the shock disturbance. The physical and the mechanical parameters of the coal and rock are obtained through laboratory experiments, and they are shown in **Table 1**. The computed strength of coal is equivalent strength, which considers the supporting conditions.

Finite Element Model

Adopting the ANSYS software, the deep coal mine stope model containing section coal and rock pillars is established, which is 628 m in length and 364.7 m in height. The Plane 82 unit (plane strain mode) is adopted. There are 27 layers of coal and rock, the thickness of each coal and rock stratum is different, and the coal is mined from the 18th layer. In this layer, the goaf is 200 m in length, the width of the section coal pillars is set as a variable quantity, and the tunnel is 4 m in length. Using the mapping grid, the key parts are processed by encrypted grids. For example, when 24 m of section coal pillars is left, 7,504 units and 7,684 nodes are divided into finite element models. To eliminate the influence of boundary effects, a 200-m boundary remains at the left and at the right ends of the model. The constraint conditions include a horizontal displacement constraint on the left and the right boundaries and a vertical displacement constraint on the lower boundary. The stress of the overlying strata, with a thickness of 750 m, is simplified as a uniformly distributed load on the top of the model. The finite element model of the deep stope with section coal pillars is shown in **Figure 2**.

According to the Ginnick hypothesis named after the Soviet scholar, the stress boundary conditions are as follows:

$$q = \gamma H \tag{2}$$

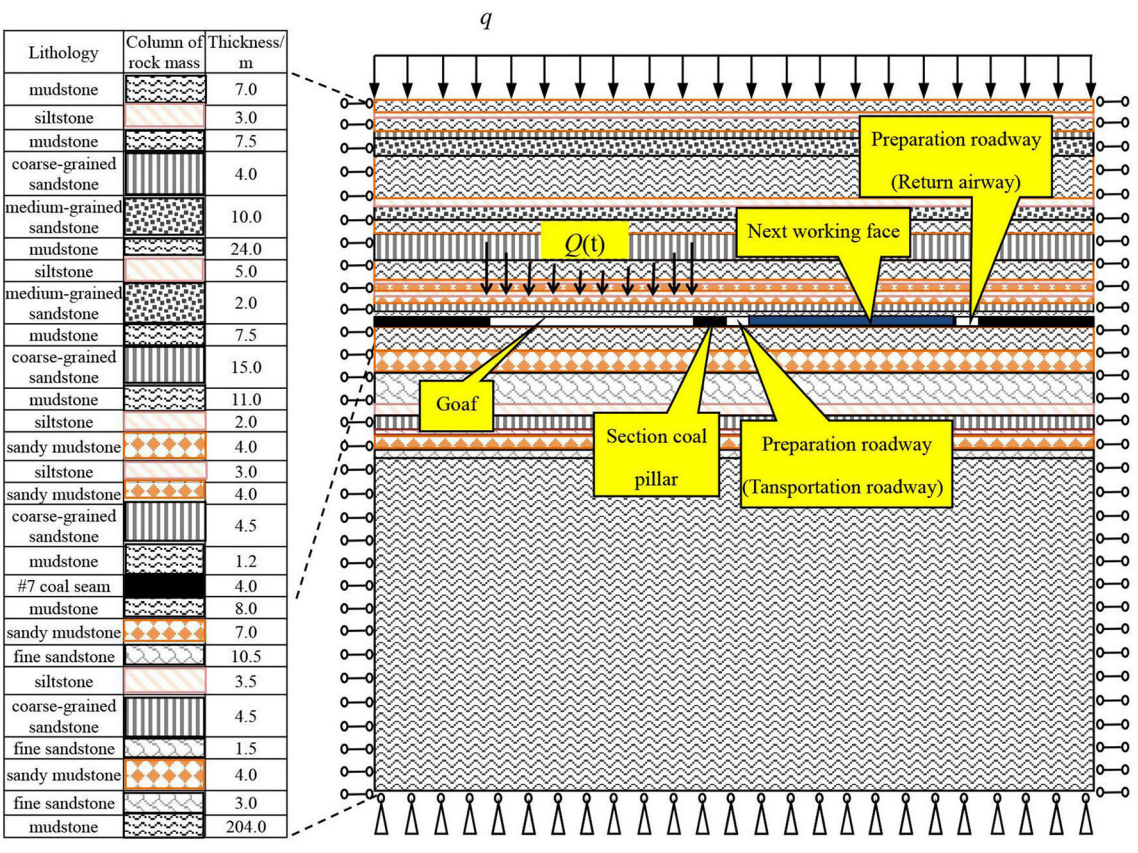

FIGURE 1 | Schematic diagram of the section coal pillar arrangement in profile of fully mechanized mining face.

TABLE 1 | The physical and the mechanical parameters of coal and rock.

Lithology	Moduli of elasticity (GPa)	Density (kg m^{-3})	Poisson's ratio	Friction angle (°)	Cohesive force (MPa)	Uniaxial compressive strength (MPa)
Mudstone	2.86	2,280	0.28	28.19	2.99	6.32
Siltstone	20.31	2,660	0.18	33.46	3.06	9.83
Mudstone	2.57	2,150	0.27	29.27	1.97	4.35
Coarse-grained sandstone	34.72	2,550	0.22	33.38	4.92	26.73
Medium-grained sandstone	27.81	2,470	0.16	38.63	6.57	16.25
Mudstone	2.78	2,250	0.25	31.52	2.89	3.97
Siltstone	18.83	2,450	0.16	32.15	2.98	8.93
Medium-grained sandstone	27.11	2,570	0.18	38.53	3.59	16.58
Mudstone	2.88	2,265	0.26	31.41	1.64	4.52
Coarse-grained sandstone	36.32	2,675	0.23	33.46	7.03	27.18
Mudstone	2.86	2,230	0.27	31.31	2.95	4.14
Siltstone	19.31	2,650	0.17	33.11	3.02	9.21
Sandy mudstone	5.75	2,470	0.26	34.63	2.07	4.20
Siltstone	20.11	2,570	0.16	33.23	2.03	9.49
Sandy mudstone	5.63	2,440	0.25	35.62	0.82	4.68
Coarse-grained sandstone	35.22	2,540	0.21	32.34	1.89	28.61
Mudstone	2.87	2,190	0.25	31.27	1.65	4.43
#7 coal seam	2.04	1,270	0.29	22.76	1.31	4.53
Mudstone	2.86	2,210	0.26	31.21	1.96	4.42
Sandy mudstone	5.73	2,470	0.25	35.22	3.15	4.76
Fine sandstone	23.41	2,570	0.15	32.57	4.97	30.64
Siltstone	19.91	2,560	0.16	32.87	2.95	9.17
Coarse-grained sandstone	35.83	2,520	0.20	30.78	5.87	27.13
Fine sandstone	23.26	2,560	0.14	32.44	3.88	30.25
Sandy mudstone	5.75	2,510	0.27	35.53	0.98	4.61
Fine sandstone	21.25	2,530	0.14	32.55	3.92	30.72
Mudstone	2.86	2,180	0.28	31.47	1.27	4.34

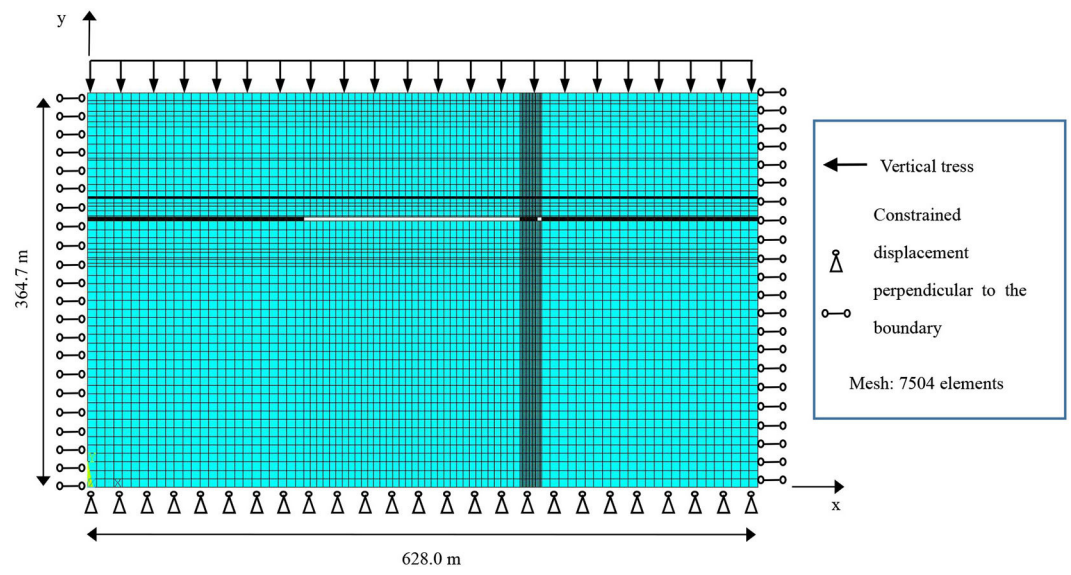

FIGURE 2 | Finite element model of the deep stope with section coal pillars.

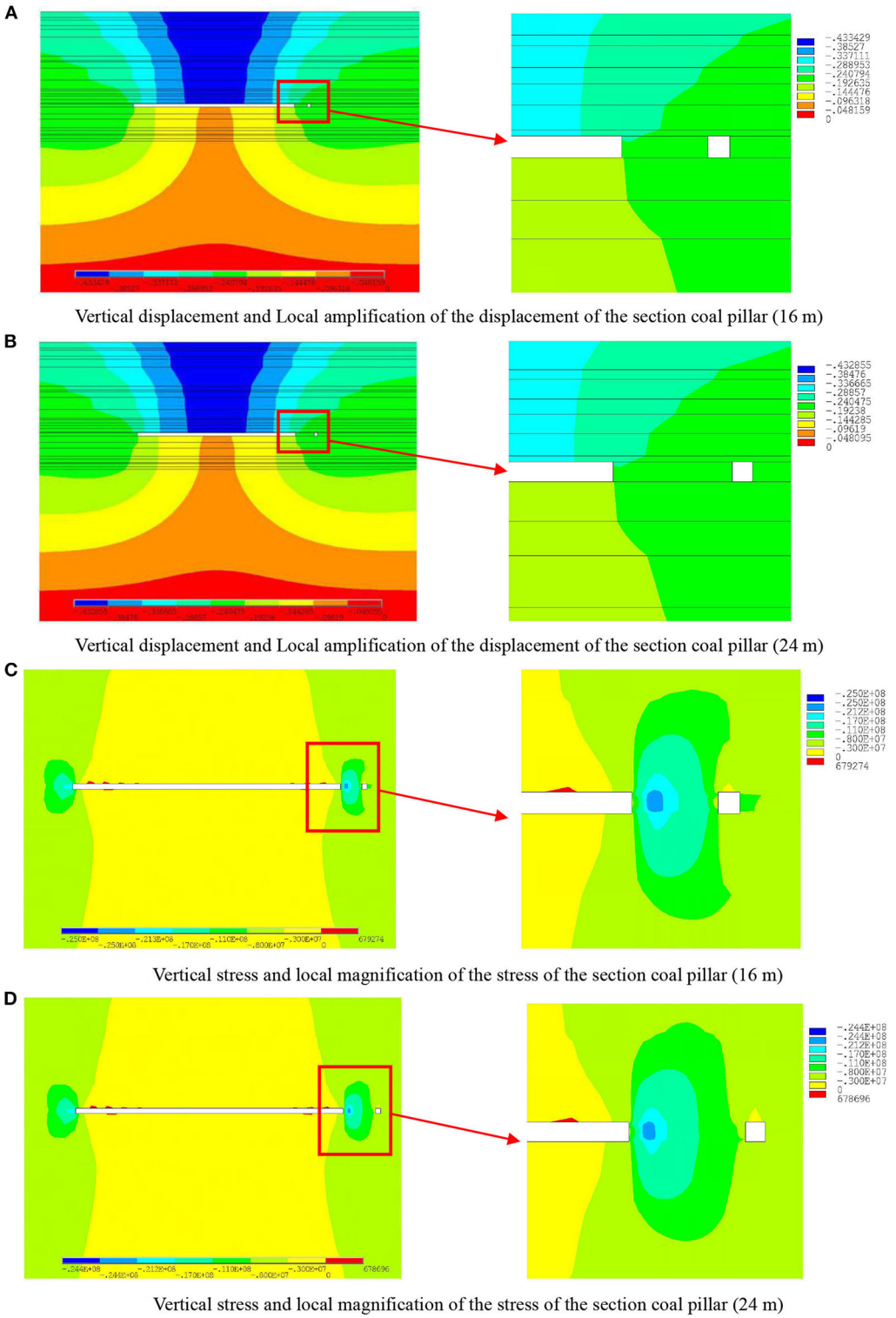

FIGURE 3 | Vertical displacement contour maps and vertical stress contour maps of the deep stope with 16 and 24 m section coal pillar width. **(A)** Vertical displacement and Local amplification of the displacement of the section coal pillar (16 m). **(B)** Vertical displacement and Local amplification of the displacement of the section coal pillar (24 m). **(C)** Vertical stress and local magnification of the stress of the section coal pillar (16 m). **(D)** Vertical stress and local magnification of the stress of the section coal pillar (24 m).

where q is the uniformly distributed vertical stress, γ is the average bulk density of the rock mass, which is set as 24.96 kN/m^3, and H is the thickness of the overlying strata of the coal seam.

In the finite element model, the thickness of the overlying strata of the coal seam is 750 m. Using formula (2), the vertical stress is calculated to be 18.75 MPa, i.e., $q = 18.75$ MPa.

The shock disturbance from the overlying strata has a significant effect on the lower rock layer or coal seam, such as the sudden breaking of the main roofs, which is much more than the effect of gravity. $Q(t)$ is the shock disturbance produced by the main roof fracture. The shock disturbance mainly propagates in the lower rock by the form of stress waves [42]. Almost all the elastic waves are superimposed by several simple harmonic waves with different amplitudes and frequencies. It is assumed that the elastic wave from the goaf roof satisfies the following relationship:

$$Q(t) = \begin{cases} \frac{1}{2}F\left(1 - \cos 2\pi ft\right) & t < t_0 \\ 0 & t \geq t_0 \end{cases} \quad (3)$$

where $Q(t)$ is the shock disturbance, F is the amplitude of the shock disturbance intensity, f is the shock disturbance frequency, and t is time; $t_0 = 1/\omega$, ω is the dynamic load frequency and t_0 is the dynamic load period.

According to the actual geological conditions and a large number of field monitoring datapoints, F is selected as 20, 30, or 40 MPa, and f is selected as 5, 8, 10, 25, or 40 Hz in this research. The physical characteristics of section coal pillars are analyzed.

RESPONSE CHARACTERISTICS OF COAL PILLARS UNDER SHOCK DISTURBANCE

Mechanical Analysis After Working Face Excavation

By simulating the coal mining process, the physical characteristics of section coal pillars are analyzed after excavation, the widths of which are $B_1 = 16$ m, $B_2 = 24$ m, $B_3 = 30$ m, or $B_4 = 40$ m. According to these four coal pillar widths, the vertical displacement and the vertical stress are obtained. **Figure 3A** shows the displacement contour map of the stope, where the 16-m section coal pillar is located, and the local enlarged displacement contour map of the section coal pillar. **Figure 3B** shows the displacement contour map of the stope, where the 24-m section coal pillar is located, and the local enlarged displacement contour map of the coal pillar. The displacement of the section coal pillar is asymmetrically distributed. The displacement of the left side of the section coal pillar next to the goaf is larger than that of the right side next to the tunnel. The maximum displacement occurs at the upper of the section coal pillar next to the goaf. With the increase of the section coal pillar width, the change tendency of the displacement on both sides of the section coal pillar decreases. The results show that the wider the section coal pillar is, the safer the section coal pillar is.

Figures 3C,D show the contour maps of the potential stress distribution in the stope. **Figure 3C** shows the stress contour map of the stope, where the 16-m section coal pillar is located, and the local enlarged stress contour map of the section coal pillar. **Figure 3D** shows the stress contour map of the stope, where the 24-m section coal pillar is located, and the local enlarged stress contour map of the coal pillar. The maximum vertical stress of the section coal pillar decreases with the increase of the section coal pillar width. When the section coal pillar width is >24 m, the stress distribution law of the section coal pillar has no obvious change with the increase of the section coal pillar width. The stress concentration of the section coal pillar decreases gradually with the increase of the coal pillar widths.

Vertical Deformation Characteristics of Pillars Under Shock Disturbance

In order to get the vertical deformation characteristics of pillars under roof shock disturbance, the shock disturbance from goaf is set to $F_1 = 20$ MPa, with $f = 25$ Hz and $t = 40$ ms. The transient nonlinear dynamic response is calculated, the analysis pillar widths selected of which are $B_1 = 16$ m, $B_2 = 24$ m, $B_3 = 30$ m, or $B_4 = 40$ m, respectively.

The displacement observation points (represented by the symbol w_i) are arranged in pairs at the top and the bottom of the pillar at 1-m intervals, that is, $B_1 = 16$ m, $i = 16$; $B_2 = 24$ m, $i = 24$; $B_3 = 30$ m, $i = 30$; and $B_4 = 40$ m, $i = 40$. The numbering of the displacement observation points of the pillar starts from the side of the goaf. The layout diagram of the measuring points is shown in **Figure 4**. The vertical displacement is represented by the symbol U_y. The vertical displacement of the different width pillars are monitored by observation points, and the deformation between each pair of observation points is calculated by:

$$U_{yi} = U_{yi,up} - U_{yi,bottom} \quad (2)$$

where U_{yi} is the vertical displacement of the i-th pair of observation points, $U_{yi,up}$ is the vertical displacement of the i-th observation point at the top of the coal pillar, and $U_{yi,bottom}$is the vertical displacement of the i-th observation point at the bottom of the coal pillar.

By using formula (2), the vertical deformation of coal pillars is obtained, and the deformation curves of the different

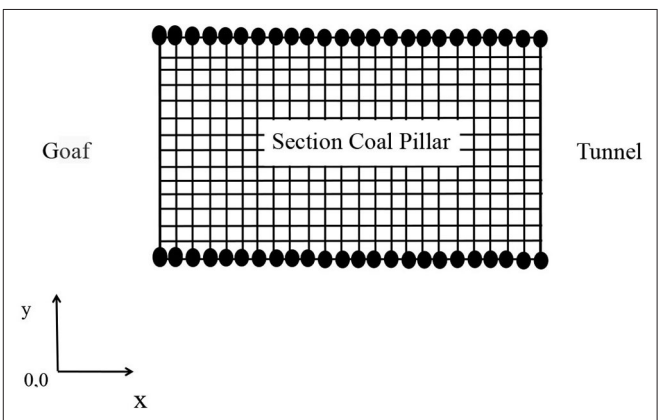

FIGURE 4 | Layout diagram of the displacement observation points of the 24 m section coal pillar.

widths coal pillar are shown in **Figure 5**. On the one hand, there is no effect of the shock disturbance intensity on the section coal pillar. On the other hand, the effect of the shock disturbance intensity and the frequency are considered. Clearly, the trends of the vertical deformation curves of the different widths coal pillar are similar, and the vertical deformation U_{yi} is related to coal pillar widths B. By comparison, the vertical deformation U_{yi} on the left side of the section coal pillar obviously increases under shock disturbance, and the vertical deformation U_{yi} on the right side of the section coal pillar changes slightly. The larger the section coal pillar width is, the smaller the deformation of the right side of the section coal pillar is. It is revealed that the deformation of the section coal pillar decreases with the increase of coal pillar widths under shock disturbance.

Development Characteristics of the Plastic Zone in the Coal Pillar

The plastic strain distribution (plastic strain is represented by the symbolε_p) in section coal pillars with different widths are analyzed under the following shock disturbances: $F_1 = 20$ MPa, $f = 25$ Hz, and $t = 40$ ms. **Figure 6** shows the distribution cloud charts of ε_p, considering the 24-m section coal pillar. As shown in **Figure 6A**, the shock disturbance is not considered, and in **Figure 6B**, the model considers the shock disturbance conditions of $F_1 = 20$ MPa, $f = 25$ Hz, and $t = 40$ ms. It was found that ε_p is related to B, and ε_p on the left of the section coal pillar, near the goaf, is more sensitively affected by the shock disturbance. Compared with the strain cloud charts of the coal pillar under shock disturbance and without shock disturbance, it shows that shock disturbance causes a sudden increase of strain

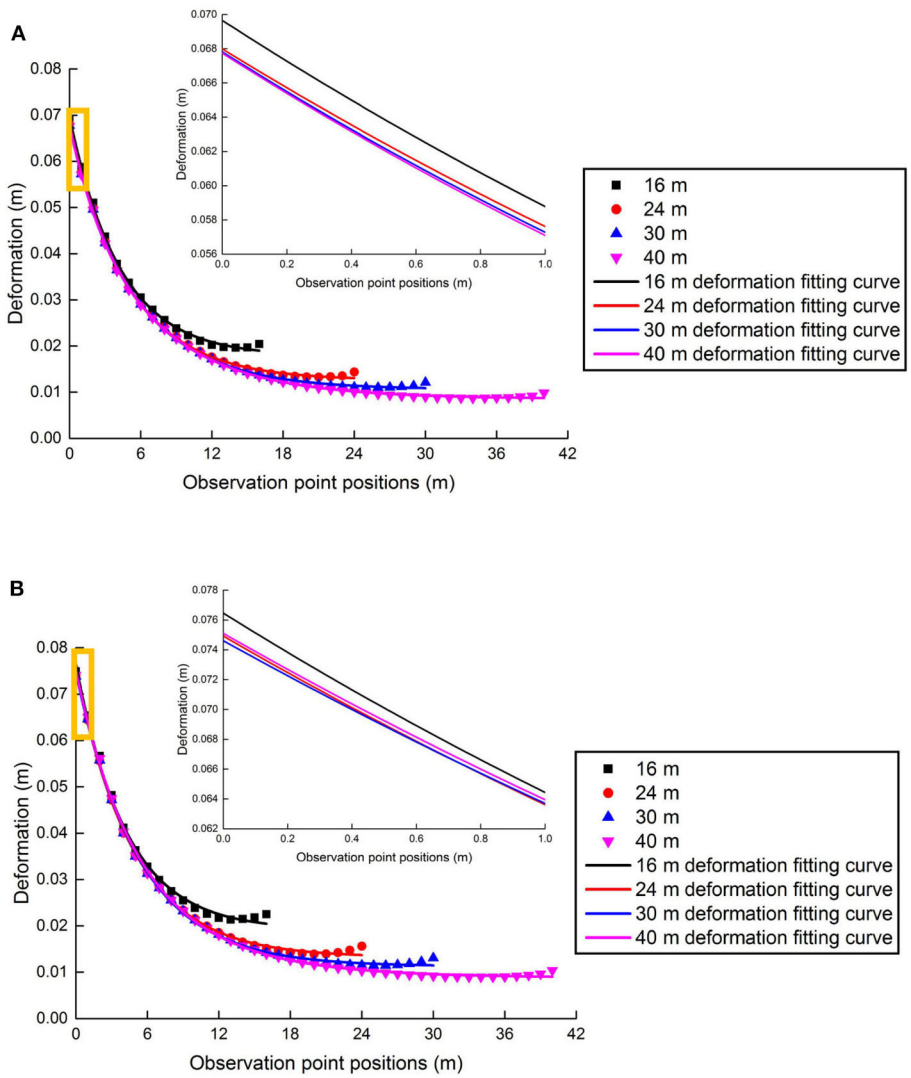

FIGURE 5 | Vertical deformation curves of the observation points of section coal pillars with different widths. **(A)** Without shock. **(B)** With shock.

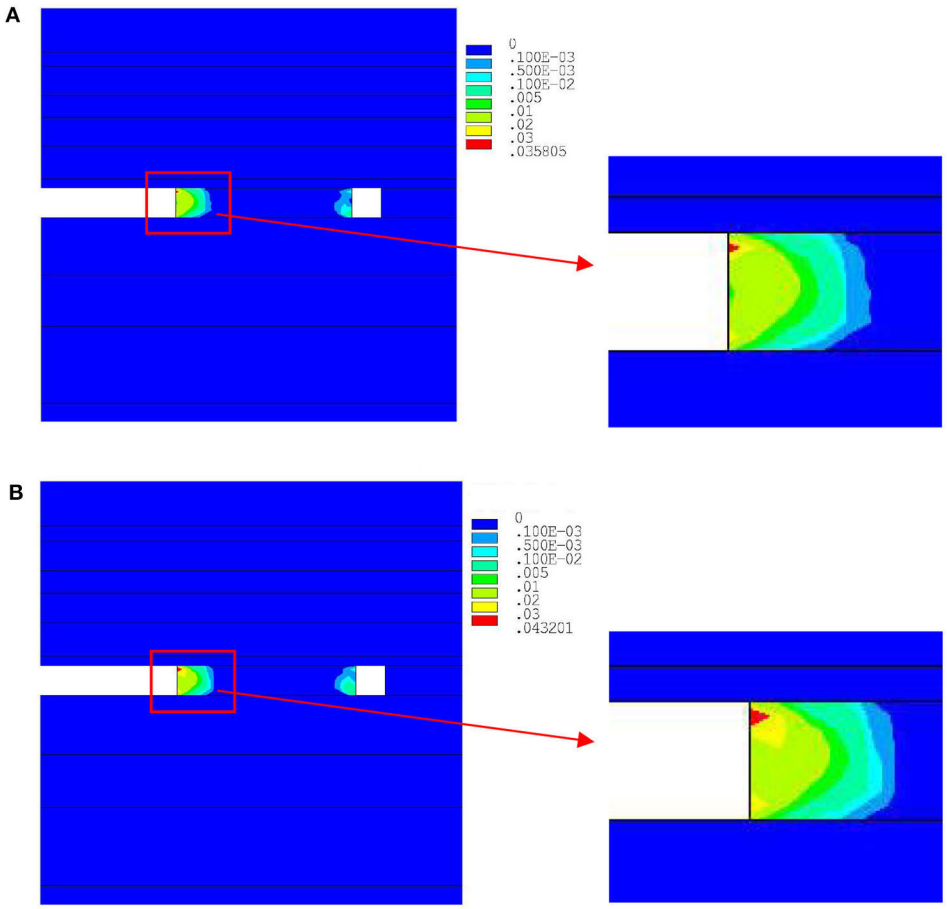

FIGURE 6 | Plastic strain distribution cloud charts of the 24 m section coal pillar. **(A)** Without shock. **(B)** With shock.

on the top of the coal pillar and an obvious increase of the plastic zone.

The percentage of plastic zone in the coal pillar is represented by the symbol Δ_R (herein referred to as the plastic zone occupation ratio), which satisfies the following relation:

$$\Delta_R = \frac{R}{A} \times 100\% \tag{3}$$

where R is the plastic zone area in the coal pillar, A is the area of the coal pillar, Δ_R is a function of F, f, and B in this research, which is $\Delta_R = \Delta_R(F, f, B)$.

Table 2 displays the data of Δ_R in coal pillars under shock disturbance or without shock disturbance. The plastic zone occupation ratio of the coal pillar under shock disturbance intensity F is represented by the symbol Δ_{R_S}, and the plastic zone occupation ratio of the coal pillar under without F is represented by the symbol Δ_{R_N}. Clearly, Δ_{R_S} is higher than Δ_{R_N} of the section coal pillars, and $\Delta_{R_S} > \Delta_{R_N}$ is true for all section coal pillar widths. Furthermore, Δ_R is related to B. Usually, Δ_R is used to evaluate the damage of the coal pillars.

TABLE 2 | Plastic zone occupation ratio with different section coal pillar widths.

Section coal pillar width	Plastic zone occupation ratio/%	
	Without shock	With shock
16 m	36.7	42.9
24 m	21.9	25.3
30 m	14.6	20.0
40 m	10.3	15.0

PHYSICAL CHARACTERISTICS OF PILLARS UNDER DIFFERENT SHOCK DISTURBANCE INTENSITIES

Vertical Deformation of Section Coal Pillars Under Different Shock Disturbance Intensities

The model is disturbed by different shock disturbance intensities. The shock disturbance intensities are $F_1 = 20$ MPa, $F_2 = 30$ MPa, or $F_3 = 40$ MPa, where the shock disturbance frequency

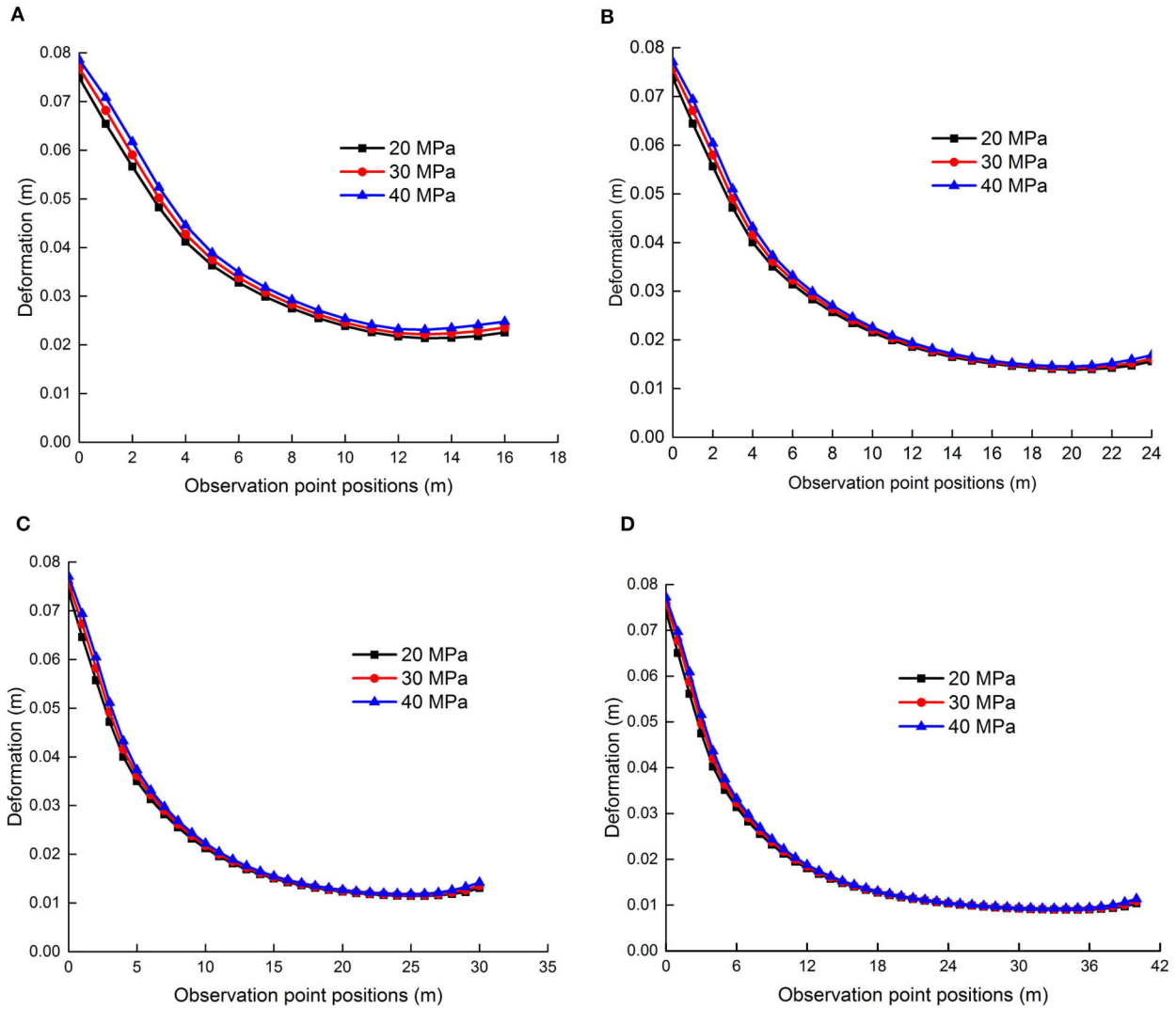

FIGURE 7 | Vertical displacement curves of the coal pillar varying with different pillar widths and shock disturbance intensities. **(A)** Vertical displacement curves of the 16 m section coal pillar. **(B)** Vertical displacement curves of the 24 m section coal pillar. **(C)** Vertical displacement curves of the 30 m section coal pillar. **(D)** Vertical displacement curves of the 40 m section coal pillar.

is $f = 25$ Hz and the coal pillar widths are $B_1 = 16$ m, $B_2 = 24$ m, $B_3 = 30$ m, or $B_4 = 40$ m. The vertical deformation $U_y(F, f, B)$ ($F \in [F_1, F_2, F_3]$, and $B \in [B_1, B_2, B_3, B_4]$) of coal pillars is obtained. **Figure 7** shows the vertical deformation curves varying with the observation points position w_i in the coal pillar. In **Figure 7**, the vertical deformation increases with the shock disturbance intensity, which creates a greater deformation at the goaf side (the left side of the coal pillar). On the left side of the coal pillar, the vertical deformation $U_y\left(F, f, B\right)\big|_{F=F_3}$ of the observation point under shock disturbance intensity F_3 is obviously greater than that of $U_y\left(F, f, B\right)\big|_{F=F_1}$ under shock disturbance intensity F_2. With the increase of the coal pillar width, the middle position of the coal pillar is formed, the deformation invariable area (where no plastic strain occurs in the section coal pillar), and the external shock disturbance intensity is not obviously affected on the deformation of coal pillar. The deformation of both sides of the coal pillar is changed under the shock disturbance intensity, of which there is always

$$U_y\left(F, f, B\right)\big|_{F=F_1} < U_y\left(F, f, B\right)\big|_{F=F_2} < U_y\left(F, f, B\right)\big|_{F=F_3},$$

at f = 25 Hz with the same coal pillar width.

Plastic Deformation Characteristics of Pillars Under Different Shock Disturbance Intensities

The maximum plastic strain $\varepsilon_{p\max}$ of the section coal pillars under different shock disturbance intensities are shown in **Table 3**, considering that $F_1 = 20$ MPa, $F_2 = 30$ MPa, or

TABLE 3 | Maximum plastic strain of section coal pillars varying with different widths.

Section coal pillar width	Maximum plastic strain		
	20 MPa	30 MPa	40 MPa
16 m	0.04459	0.04758	0.05158
24 m	0.04320	0.04612	0.04993
30 m	0.04295	0.04582	0.04960
40 m	0.04274	0.04560	0.04934

$F_3 = 40$ MPa and $f = 25$ Hz, that is, $F \in [F_1, F_2, F_3]$ and $B \in [B_1, B_2, B_3, B_4]$. The maximum plastic strain $\varepsilon_{p\max}(F, f, B)$ of the coal pillar increases with the increase of shock disturbance intensity F, when the coal pillar width is fixed, that is:

$$\varepsilon_{p\max}(F, f, B)|_{F=F_1} < \varepsilon_{p\max}(F, f, B)|_{F=F_2} < \varepsilon_{p\max}(F, f, B)|_{F=F_3},$$

under shock disturbance frequency f = 25 Hz.

The more serious the plastic deformation of the coal pillar is, the more serious the damage of the coal pillar is.

The plastic zone occupation ratio $\Delta_R(F, f, B)$ of the coal pillar is calculated under different shock disturbance intensities, where, and $f = 25$ Hz. The corresponding histogram of the plastic zone occupation ratio is shown in **Figure 8**. The plastic zone occupation ratio $\Delta_R(F, f, B)$ of the coal pillar increases and the damage probability of the coal pillar increases with the increase of shock disturbance intensity under the same shock disturbance frequency, that is,

$$\Delta_R(F, f, B)|_{F=F_1} < \Delta_R(F, f, B)|_{F=F_2} < \Delta_R(F, f, B)|_{F=F_3},$$

while the coal pillar width is fixed.

The plastic zone occupation ratio $\Delta_R(F, f, B)$ of the coal pillar decreases with the increase of coal pillar widths when the shock disturbance intensity of the coal pillar is fixed; thus:

$$\Delta_R(F, f, B)|_{B=B_1} > \Delta_R(F, f, B)|_{B=B_2} > \Delta_R(F, f, B)|_{B=B_3} > \Delta_R(F, f, B)|_{B=B_4} \text{ at } f = 25 \text{ Hz}.$$

The dynamic physical characteristics of the section coal pillars under the shock disturbance intensity do not change significantly when the coal pillar width is >24 m.

PHYSICAL CHARACTERISTICS OF PILLARS UNDER DIFFERENT SHOCK DISTURBANCE FREQUENCIES

Vertical Deformation of Pillars Under Various Shock Disturbance Frequencies

The vertical deformation of the section coal pillars is obtained under different shock disturbance frequencies. The shock disturbance frequency is $f_1 = 5$ Hz, $f_2 = 8$ Hz, $f_3 = 10$ Hz, $f_4 = 25$ Hz, or $f_5 = 40$ Hz applied to the model, while the shock disturbance intensity is $F_1 = 20$ MPa, and the coal pillar width is set to $B_1 = 16$ m, $B_2 = 24$ m, $B_3 = 30$ m, or $B_4 = 40$ m, that is, $f \in [f_1, f_2, f_3, f_4, f_5], B \in [B_1, B_2, B_3, B_4]$. The vertical deformation $U_y(F, f, B)$ of section coal pillars changed with displacement observation points w_i, as shown in **Figure 9**. **Figure 9** shows that the larger the shock disturbance frequency is, the smaller the vertical deformation $U_y(F, f, B)$, while the shock disturbance intensity is constant. The change of the vertical deformation $U_y(F, f, B)$ of the section coal pillars is more significant under shock disturbance frequency compared with that of shock disturbance intensity. The low shock disturbance frequency causes a large vertical deformation $U_y(F, f, B)$ to the coal pillar. Specifically, the deformation $U_y(F, f, B)$ of both sides of the 16-m section coal pillar is more obvious under a condition of $f = 5$ Hz shock disturbance, where the $U_y(F, f, B)$ of the coal pillar is obviously affected by the shock disturbance frequency f.

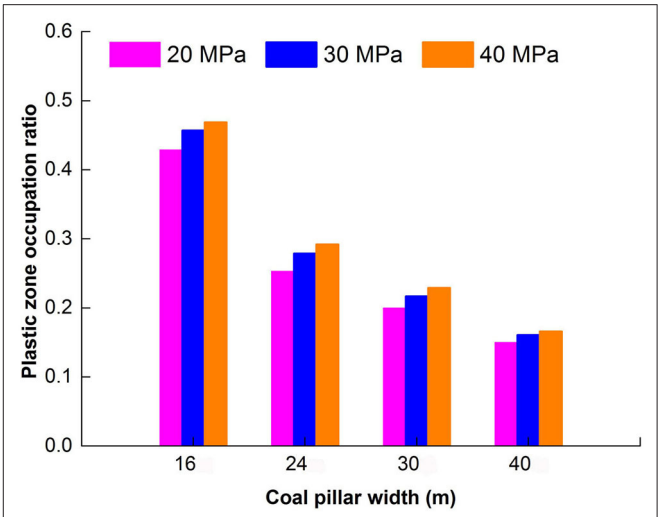

FIGURE 8 | Plastic zone occupation ratio chart of section coal pillars varying with different widths and shock disturbance intensities.

Plastic Deformation Characteristics of Section Coal Pillars Under Various Shock Disturbance Frequencies

Figure 10 shows a histogram of the plastic zone occupation ratio $\Delta_R(F, f, B)$ in the section coal pillars with different coal pillar widths, where$f \in [f_1, f_2, f_3, f_4, f_5]$, $B \in [B_1, B_2, B_3, B_4]$, and F is a constant.

It can be seen from **Figure 10** that the plastic zone occupation ratio $\Delta_R(F, f, B)$ decreases with an increase in the shock disturbance frequency f for the same shock disturbance intensity F, while the coal pillar width is a constant. When the shock disturbance frequency is $f = 5$ Hz, the plastic zone occupation ratio of $B_1 = 16$ m accounts for more than 50%, that is, $\Delta_R(F, f, B)|_{f=f_1, B=B_1} > 50.0\%$, and there is a potential safety

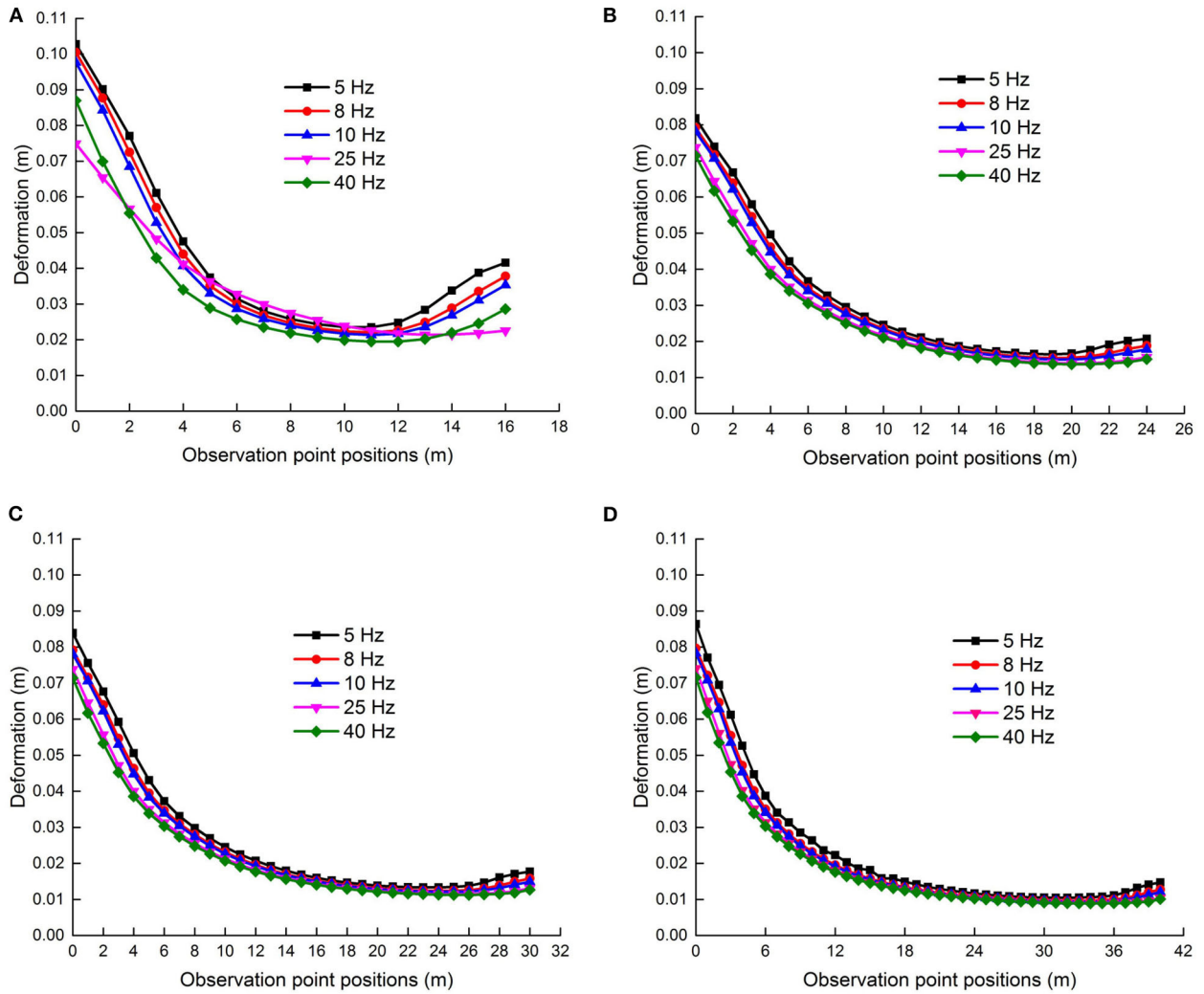

FIGURE 9 | Vertical displacement curves of the section coal pillar varying with different widths and shock disturbance frequencies. **(A)** Vertical displacement curves of the 16 m section coal pillar. **(B)** Vertical displacement curves of the 24 m section coal pillar. **(C)** Vertical displacement curves of the 30 m section coal pillar. **(D)** Vertical displacement curves of the 40 m section coal pillar.

hazard, which is if the coal pillar loses its carrying capacity. When the width of the coal pillar is $B_2 = 24$ m, $\Delta_R\left(F,f,B\right)\big|_{f=f_1,B=B_2} =$ 39.0%. When the coal pillar width is $B_3 = 30$ m or $B_4 = 40$ m and the plastic zone occupation ratio $\Delta_R\left(F,f,B\right)\big|_{f=f_1,B=B_3}$ or $\Delta_R\left(F,f,B\right)\big|_{f=f_1,B=B_4}$ is <35.0%, then the coal pillar has a better bearing capacity. It turns out that the smaller the frequency f is, the larger the plastic zone occupation ratio Δ_R of the coal pillar is.

Under different shock disturbance intensities and frequencies, in the case of the same section coal pillar width, it turns out that the plastic zone occupation ratio increases with increasing shock disturbance intensity, that is:

$$\Delta_R\left(F,f,B\right)\big|_{F=F_1} < \Delta_R\left(F,f,B\right)\big|_{F=F_2} < \Delta_R\left(F,f,B\right)\big|_{F=F_3},$$

and decreases with the increase of the shock disturbance frequency, that is:

$$\Delta_R\left(F,f,B\right)\big|_{f=f_1} > \Delta_R\left(F,f,B\right)\big|_{f=f_2} > \Delta_R\left(F,f,B\right)\big|_{f=f_3} > \Delta_R\left(F,f,B\right)\big|_{f=f_4} > \Delta_R\left(F,f,B\right)\big|_{f=f_5}.$$

The change of the dynamic physical characteristics of coal pillars is more obvious under shock disturbance frequency than that of shock disturbance intensity. Especially the plastic zone proportion ratio of the section coal pillars is changed obviously under shock disturbance frequency. When the shock disturbance frequency is

$$f_1 < f_2 < f_3 < f_4 < f_5,$$

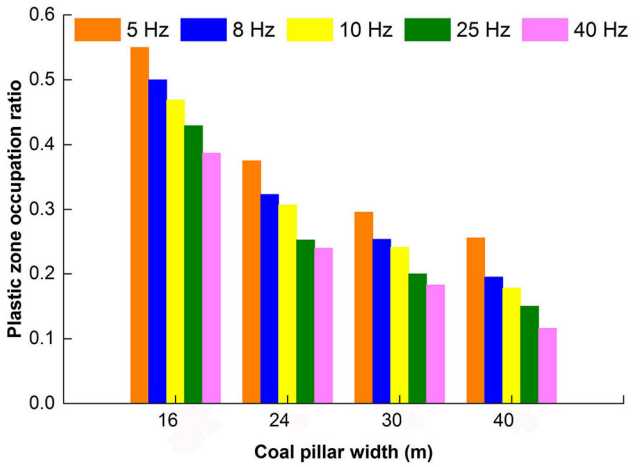

FIGURE 10 | Plastic zone proportion ratio chart of section coal pillars varying with different widths and shock disturbance frequencies.

TABLE 4 | Natural frequency of the stope of section coal pillars varying with different widths.

Order	16 m/Hz	24 m/Hz	30 m/Hz	40 m/Hz
1	2.537	1.601	1.600	1.597
2	2.672	1.670	1.663	1.652
3	2.970	2.054	2.050	2.044
4	3.249	2.374	2.363	2.346
5	3.416	2.613	2.598	2.573
6	3.534	2.623	2.612	2.594
7	4.271	2.879	2.863	2.839
8	4.458	3.183	3.171	3.150
9	4.489	3.249	3.237	3.216
10	4.593	3.296	3.287	3.274

there are always

$$\Delta_R\left(F,f,B\right)\big|_{f=f_1} > \Delta_R\left(F,f,B\right)\big|_{f=f_2} > \Delta_R\left(F,f,B\right)\big|_{f=f_3} > \Delta_R\left(F,f,B\right)\big|_{f=f_4} > \Delta_R\left(F,f,B\right)\big|_{f=f_5},$$

regardless of the coal pillar width.

NATURAL VIBRATION CHARACTERISTICS OF THE STOPE

The natural vibration characteristics of the deep coal mine stope are simulated, and the natural vibration frequencies and modal shapes are obtained. The natural frequencies of the stope model with different section coal pillars widths are listed in **Table 4**. The first three-order modes of the stope with a 16-m section coal pillar and a 24-m section coal pillar are shown in **Figure 11**.

In **Table 4**, the natural vibration frequencies of the first 10-order modes of the stope model are <5 Hz. The natural vibration frequencies decrease with the increase of the section coal pillar width, the magnitude of the decrease of which varies.

The above analysis reveals that the effect of the shock disturbance frequency is more sensitive than that of the shock disturbance intensity under the given calculation conditions. According to the analysis of the natural vibration characteristics of the coal pillars of the stope, the deformation of the roof or the floor in the goaf is remarkable, and the deformation of the adjacent sides of the coal pillar and goaf is also significant. The first 10 natural frequencies of the stope are all low frequency. If the shock disturbance frequency is lower than 5 Hz, the development of the plastic zone of the section coal pillars is inevitably accelerated. The mechanical response of the section coal pillars under a shock disturbance is closely related to the natural vibration characteristics of the stope with pillars.

The 24-m coal pillar was used to the mine. The deformation of the coal pillar had been monitored. The results were consistent with the numerical calculation results. The model and the results obtained are credible and meaningful. In conclusion, the 24-m section coal pillar retained can meet the design requirements on the working face of the deep coal mine stope with section coal pillars.

CONCLUSION AND DISCUSSION

A dynamic structural system model of elastic-plastic finite element is established for the formation of surrounding rock and coal pillars in a deep stope. Based on the model, the dynamic physical characteristics of coal pillars are analyzed under the roof shock disturbance from goaf. The results show that under certain conditions, the roof shock disturbance from goaf has a significant effect on the dynamic physical characteristics of coal pillars, which increases the risk of instability of coal pillars:

(1) When the roof shock disturbance intensity from goaf increases, the vertical deformation of coal pillar increases. The plastic zone occupation ratio of the section coal pillar increases with increasing shock disturbance intensity and decreases with increasing coal pillar widths.
(2) The roof shock disturbance frequency from goaf has an obvious different effect on the physical characteristics of coal pillars compared with that of shock disturbance intensity. When the roof shock disturbance frequency from goaf increases, the vertical deformation and the plastic zone of coal pillars decrease. The plastic zone of the coal pillar increases with decreasing coal pillar widths.
(3) Throughout the comparison of the dynamic physical characteristics of coal pillars under shock disturbance frequency and intensity, when the shock disturbance frequency is closer to the natural frequency of the stope, the shock disturbance frequency has a significant influence on the dynamic physical characteristics of coal pillars. The dynamic physical characteristics of coal pillars are more sensitive to shock disturbance frequency.

The dynamic physical characteristics of coal and rock pillars should be paid close attention relative to the natural vibration characteristics of the stope. In the design of coal and rock pillars, the natural vibration characteristics of the stope structure

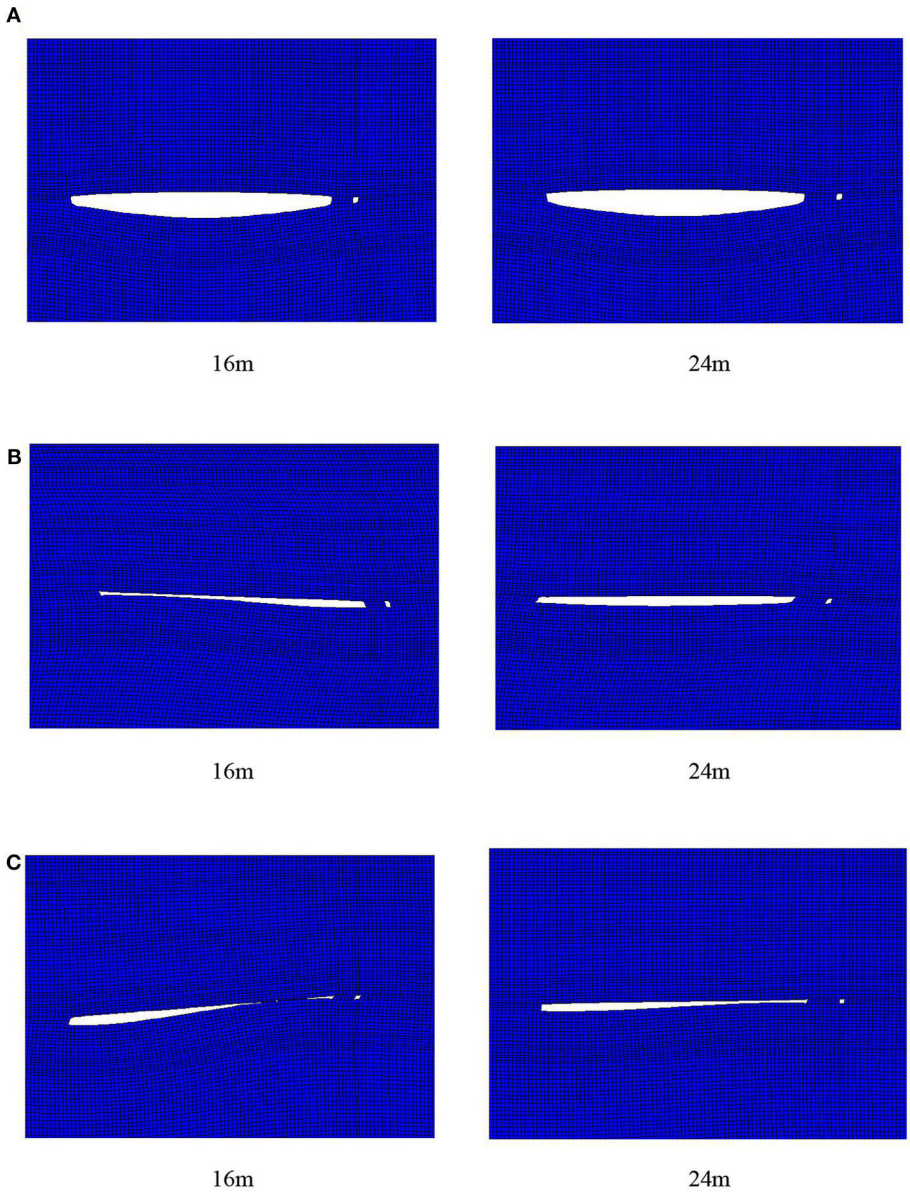

FIGURE 11 | Cloud charts of the stope vibration mode of the 16 m section coal pillar and the 24 m section coal pillar. **(A)** First-order mode. **(B)** Second-order mode. **(C)** Third-order mode.

system are adequately considered. The frequency of the shock disturbance signal monitored should be paid attention.

DATA AVAILABILITY STATEMENT

The raw data supporting the conclusions of this article will be made available by the authors, without undue reservation.

AUTHOR CONTRIBUTIONS

RS puts forward the research ideas, designs the research plan, and revises the final version. HS was responsible for numerical calculation, data collection and analysis, and drafting the paper. All authors contributed to the article and approved the submitted version.

FUNDING

This study was supported by the National Natural Science Foundation of China (Grant Nos. 51474120 and 51704142).

ACKNOWLEDGMENTS

The authors would like to thank the editors and the peer reviewers for their valuable comments on this paper.

REFERENCES

1. Kang HP. Support technologies for deep and complex roadways in underground coal mines: a review. *Int J Coal Sci Technol.* (2014) **1**:261–77. doi: 10.1007/s40789-014-0043-0
2. Wang JH, Shao MX, Shang YF, Cao SW, Zhang X, Hu CM. Determination of rational coal and rock pillars height of coal mining under the loose aquifer. *Adv Eng Res.* (2014) 306–11. doi: 10.2991/mining-14.2014.44
3. Mohammad J, Rabindra KS. Design of rhombus coal pillars and support for roadway stability and mechanizing loading of face coal using SDLs in a steeply inclined thin coal seam-a technical feasibility study. *Arab J Geosci.* (2018) **11**:415. doi: 10.1007/s12517-018-3747-4
4. Wang CX, Shen BT, Chen JT, Tong WX, Jiang Z, Liu Y, et al. Compression characteristics of filling gangue and simulation of mining with gangue backfilling: An experimental investigation. *Geomechanics Eng.* (2020) **20**:485–95.
5. Zhang HW, Wan ZJ, Ma ZY, Zhang Y. Stability control of narrow coal pillars in gob-side entry driving for the LTCC with unstable overlying strata: a case study. *Arab J Geosci.* (2018) **11**:665. doi: 10.1007/s12517-018-3994-4
6. Wang Q, Gao HK, Jiang B, Li SC, He MC, Wang DC, et al. Research on reasonable coal pillar width of roadway driven along goaf in deep mine. *Arab J Geosci.* (2017) **10**:466. doi: 10.1007/s12517-017-3252-1
7. Gao W, Ge MM. Stability of a coal pillar for strip mining based on an elastic-plastic analysis. *Int J Rock Mech Min Sci.* (2016) **87**:23–8. doi: 10.1016/j.ijrmms.2016.05.009
8. Philippe M. *A Ground Support Design Strategy for Deep Underground Mines Subjected to Dynamic-Loading Conditions.* University of Toronto (2015). Available online at: http://hdl.handle.net/1807/71525
9. Guo WJ, Wang HL, Chen SJ. Coal pillar safety and surface deformation characteristics of wide strip pillar mining in deep mine. *Arab J Geosci.* (2016) **9**:137. doi: 10.1007/s12517-015-2233-5
10. Satyabadi KJ, Ritesh DL, Manoj P, Nirmal K. Development of a model to estimate strata behavior during bord and pillar extraction in underground coal mining. *Arab J Geosci.* (2019) **12**. doi: 10.1007/s12517-019-4381-5
11. Brady BHG, Brown ET. *Rock Mechanics for Underground Mining*. George Allen Unwin (1985) 527.
12. Yang YJ, Duan HQ, Xing LY. Fatigue deformation and energy evolution of coal under uniaxial cyclic loading. *J Basic Eng.* (2018) **26**:154–67. doi: 10.16058/j.issn.1005-0930.2018.01.014
13. Chen SJ, Yin DW, Jiang N, Wang F, Zhao Z. Mechanical properties of oil shale-coal composite samples. *Int J Rock Mech Min Sci.* (2019) **123**:104120. doi: 10.1016/j.ijrmms.2019.104120
14. Ma J, Zhao GY, Dong LJ, Chen GH, Zhang CX. A comparison of mine seismic discriminators based on features of source parameters to waveform characteristics. *Shock Vibr.* (2015) **2015**:919143. doi: 10.1155/2015/919143
15. Liu JX, Liu YL, Li WX, Zhang XG, Xin CR. Measures to deal roof-shock during tunneling at deep and extra-thick coal. *Arab J Geosci.* (2019) **12**:189. doi: 10.1007/s12517-019-4340-1
16. Zhu WB, Chen L, Zhou ZL, Shen BT, Xu Y. Failure Propagation of pillars and roof in a room and pillar mine induced by longwall mining in the lower seam. *Rock Mech Rock Eng.* (2019) **52**:1193–209. doi: 10.1007/s00603-018-1630-y
17. Kumar A, Waclawik P, Singh R, Ram S, Korbel J. Performance of a coal pillar at deeper cover: Field and simulation studies. *Int J Rock Mech Min Sci.* (2019) **113**:322–32. doi: 10.1016/j.ijrmms.2018.10.006
18. Li XW, Chai YJ. Determination of pillar width to improve mining safety in a deep burst-prone coal mine. *Safety Sci.* (2019) **113**:244–56. doi: 10.1016/j.ssci.2018.12.003
19. Kong DZ, Pu SJ, Zheng SS, Wang CH, Lou YH. Roof broken characteristics and overburden migration law of upper seam in upward mining of close seam group. *Geotech Geol Eng.* (2019) **37**:3193–203. doi: 10.1007/s10706-019-00836-x
20. Robert B, Kurt D, Garry M. An Approach to model the strength of coal pillars. *Int J Rock Mech Min Sci.* (2016) **89**:165–75. doi: 10.1016/j.ijrmms.2016.09.003
21. Feng G, Wang XC, Wang M, Kang Y. Experimental investigation of thermal cycling effect on fracture characteristics of granite in a geothermal-energy reservoir. *Eng. Fract Mech.* (2020) 107180. doi: 10.1016/j.engfracmech.2020.107180
22. Zhu HZ, Liu P, Tong ZY. Numerical simulation research and application on protected layer pressure relief affection under different coal pillar width. *Proc Eng.* (2014) **84**:818–25. doi: 10.1016/j.proeng.2014.10.501
23. Ren DZ, Zhou DS, Liu DK, et al. Formation mechanism of the Upper Triassic Yanchang Formation tight sandstone reservoir in Ordos Basin-Take Chang 6 reservoir in Jiyuan oil field as an example. *J Petroleum Sci Eng.* (2019) **178**:497–505. doi: 10.1016/j.petrol.2019.03.021
24. Jiang N, Wang CX, Pan HY, et al. Modeling study on the influence of the strip filling mining sequence on mining-induced failure. *Energy Sci Eng.* (2020). **8**:2239–55. doi: 10.1002/ese3.660
25. Gao W. Study on the width of the non-elastic zone in inclined coal pillar for strip mining. *Int J Rock Mech Min Sci.* (2014) **72**:304–10. doi: 10.1016/j.ijrmms.2014.09.013
26. Yu YX, Huang RB, Wang BQ. Analysis on limit equilibrium zone of coal pillar in mining roadway based on mechanical model of elastic foundation beam. *J Eng Mech.* (2016) **142**:04016009. doi: 10.1061/(ASCE)EM.1943-7889.0001032
27. Sinha RK, Jawed M, Sengupta S. Influence of rock mass rating and in situ stress on stability of roof rock in bord and pillar development panels. *Int J Min Min Eng.* (2015) **6**:258–75. doi: 10.1504/IJMME.2015.071175
28. Lv JK, Yang YJ, Ning S, Duan HQ. The fatigue strength and failure mode of coal sample subjected to cyclic loading. *Geotech Geol Eng.* (2019) **37**:2255–66. doi: 10.1007/s10706-018-0725-2
29. Vlastimil K, Radovan K, Petr W, Jan N. Innovative approach to monitoring coal pillar deformation and roof movement using 3D laser technology. *Procedia Eng.* (2017) **191**:873–9. doi: 10.1016/j.proeng.2017.05.256
30. Sun W, Zhang Q, Luan YZ, Zhang XP. A study of surface subsidence and coal pillar safety for strip mining in a deep mine. *Environ Earth Sci.* (2018) **77**:1–16. doi: 10.1007/s12665-018-7810-y
31. Feng G, Kang Y, Wang XC, Hu YQ, Li XH. Investigation on the failure characteristics and fracture classification of shale under brazilian test conditions. *Rock Mech Rock Eng.* (2020) **53**:3325–40. doi: 10.1007/s00603-020-02110-6
32. Huang H, Babadagli T, Chen X, Li HZ, Zhang YM. Performance comparison of novel chemical agents for mitigating water-blocking problem in tight gas sandstones. *SPE Reservoir Eval Eng.* (2020) **2020**:1–9. doi: 10.2118/199282-PA
33. Zhang Y, Cao SG, Zhang N, Zhao CZ. The application of short-wall block backfill mining to preserve surface water resources in northwest China. *J Cleaner Prod.* (2020) **261**:121232. doi: 10.1016/j.jclepro.2020.121232
34. Ren FQ, Zhu C, He MC. Moment tensor analysis of acoustic emissions for cracking mechanisms during schist strain burst. *Rock Mech Rock Eng.* (2020) **53**:153–70. doi: 10.1007/s00603-019-01897-3
35. Shan PF, Lai XP. An associated evaluation methodology of initial stress level of coal-rock masses in steeply inclined coal seams, Urumchi coal field, China. *Eng Comput.* (2020) *37*:2177–92. doi: 10.1108/EC-07-2019-0325
36. Li HL, Bai HB. Simulation research on the mechanism of water inrush from fractured floor under the dynamic load induced by roof caving: taking the Xinji Second Coal Mine as an example. *Arab J Geosci.* (2019) **12**:1–24. doi: 10.1007/s12517-019-4621-8
37. He WR, He FL, Zhao YQ. Field and simulation study of the rational coal pillar width in extra-thick coal seams. *Energy Eng.* (2020) **8**:627–46. doi: 10.1002/ese3.538
38. Dong LJ, Li XB, Xie GN. Nonlinear methodologies for identifying seismic event and nuclear explosion using random forest, support vector machine, and naive bayes classification. *Abstract Appl Anal.* (2014) **2014**:1–8. doi: 10.1155/2014/459137

39. Zhao YX, Wang H, Liu SM, Mu ZL, Lu ZG. Dynamic failure risk of coal pillar formed by irregular shape longwall face: a case study. *Int J Min Sci Technol.* (2018) **28**:775–81. doi: 10.1016/j.ijmst.2018.08.006
40. Li XB, Cao WZ, Tao M, Zhou ZL, Chen ZH. Influence of unloading disturbance on adjacent tunnels. *Int J Rock Mech Min Sci.* (2016) **84**:10–24. doi: 10.1016/j.ijrmms.2016.01.014
41. Wang SL, Hao SP, Chen Y, Bai JB, Wang XY, Xu Y. Numerical investigation of coal pillar failure under simultaneous static and dynamic loading. *Int J Rock Mech Min Sci.* (2016) **84**:59–68. doi: 10.1016/j.ijrmms.2016.01.017
42. Lu CP, Dou LM, Zhang N, Xue JH, Wang XN, Liu H, et al. Microseismic frequency-spectrum evolutionary rule of rockburst triggered by roof fall. *Int J Rock Mech Min Sci.* (2013) **64**:6–16. doi: 10.1016/j.ijrmms.2013.08.022

Conflict of Interest: The authors declare that the research was conducted in the absence of any commercial or financial relationships that could be construed as a potential conflict of interest.

frontiers in Physics

ORIGINAL RESEARCH
published: 23 July 2020
doi: 10.3389/fphy.2020.00173

A Constitutive Model for Cemented Tailings Backfill Under Uniaxial Compression

Bingbing Tu[1,2], Lang Liu[3,4], Kangli Cheng[3], Bo Zhang[3], Yujiao Zhao[3], Qixing Yang[3] and Kiil Song[5]*

[1] College of Science, Xi'an University of Science and Technology, Xi'an, China, [2] State Key Laboratory of Green Building in Western China, Xi'an University of Architecture and Technology, Xi'an, China, [3] Energy School, Xi'an University of Science and Technology, Xi'an, China, [4] Key Laboratory of Western Mines and Hazards Prevention, Ministry of Education of China, Xi'an, China, [5] Department of Civil Engineering, Inha University, Incheon, South Korea

Constitutive model is the foundation describing the mechanical properties of materials. Cemented tailings backfill (CTB) plays an important role in goaf filling. However, a universally applicable constitutive model for CTB has not been proposed yet. In this paper, a two-stage constitutive model of CTB under uniaxial compression was established, based on the Weibull distribution density function, the strain equivalence principle and the damage mechanics theory. Eight groups of CTB samples with a diameter of 50 mm and a height of 100 mm prepared with different solid contents (70–78 wt%) and cement-sand ratios (1/4–1/10) were subjected to uniaxial compression tests to verify the validity of the theoretical model. The compared results showed that the predictions of the proposed constitutive model agreed well with the experimental results. The following conclusions were also obtained: (i) Solid content and cement-sand ratio had a significant effect on the basic mechanical parameters of the CTB samples, especially at the peak stress; (ii) The constitutive model of CTB was similar to that of the ordinary cement mortar M5, but with obvious residual stress; (iii) The failure mode of the CTB specimens under uniaxial compression was mainly tensile failure. The results presented in this paper contribute to a better understanding of the uniaxial compression characteristics of CTB and lay an important foundation for future research.

Keywords: cemented tailings backfill, constitutive model, strain equivalence principle, Weibull distribution, uniaxial compression strength

OPEN ACCESS

Edited by:
Longjun Dong,
Central South University, China

Reviewed by:
Jordan Yankov Hristov,
University of Chemical Technology and Metallurgy, Bulgaria
Laurent Olivier Louis,
New England Research, United States

***Correspondence:**
Lang Liu
liulang@xust.edu.cn

Specialty section:
This article was submitted to Interdisciplinary Physics, a section of the journal Frontiers in Physics

Received: *03 March 2020*
Accepted: *24 April 2020*
Published: *23 July 2020*

Citation:
Tu B, Liu L, Cheng K, Zhang B, Zhao Y, Yang Q and Song K (2020) A Constitutive Model for Cemented Tailings Backfill Under Uniaxial Compression. Front. Phys. 8:173. doi: 10.3389/fphy.2020.00173

HIGHLIGHTS

- A constitutive model for CTB under uniaxial compression was established.
- Influences of solid content and cement-sand ratio were analyzed.
- The failure mode of CTB specimens under uniaxial compression was mainly tensile failure.

INTRODUCTION

As one of the most commonly used filling aggregates for goaf filling, cemented tailings backfill (CTB) plays an important role in the safe, green, and efficient mining of metals [1]. CTB can effectively solve the problems related to deep rock pressure control and surface subsidence above the goaf, and can also avoid the environmental pollution caused by the accumulation of tailings

[2–4]. Typically, CTB consists of dewatered tailings, a hydraulic binder and mixing water [5, 6]. Since its first use for the Bad Ground Mine (Germany) in the late 1970s, CTB has been widely used in many metal mines worldwide [7–12].

Many factors affect the mechanical properties of CTB samples, such as the filling parameters (filling times, filling interval times, and filling surface angles) [13–15], curing conditions [16–19], binding materials, admixtures (superplasticizers, organosilanes, and limestone powders) [20–23], solid contents, and cement-sand ratios [24–26], which have been considered in previous studies. Meanwhile, the strength properties of CTB under a frozen state and with different fiber reinforcements [27–31] have been analyzed. Moreover, numerous experimental studies have been carried out, especially uniaxial compression tests, which provide the most important parameters for underground mine backfill design [32–35].

The abovementioned research mainly focused on the strength properties of CTB. However, the constitutive model of CTB, which is very important for assessing and predicting its mechanical properties, has not been adequately addressed.

Only a few studies have been performed to investigate the constitutive relation of CTB in the literature. For example, several multiphysics models have been presented to describe and predict the temperature-time behavior [36] and the thermo-hydro-mechanical-chemical behavior of CTB [37, 38]. Evolutive elasto-plastic models based on the D–P yield criterion [39] have been developed to capture the mechanical behavior of CTB. Moreover, intelligent constitutive models have been proposed, based on boosted regression trees (BRT), particle swarm optimization (PSO), random forest (RF), firefly algorithm (FA), machine learning (ML) algorithm, genetic algorithm (GA), and genetic programming (GP), to predict the uniaxial compressive strength of CTB [40–42].

However, the existing studies on constitutive models have mainly focused on experimental data and give stress-strain relationships for a specific situation, but no universally applicable constitutive model has been proposed.

When the tailing cement filling method is used to mine underground mineral resources, before the end of ore mining at the middle level, CTB often acts as a pillar to support the surrounding rocks. At this point, the CTB pillar is under uniaxial compression and its stability plays an important role in stope safety [43, 44]. Therefore, the study on the mechanical properties of CTB under uniaxial compression has a great significance to ensure construction safety of ore mining used the tailing cement filling method.

In this paper, we propose a universally applicable constitutive model to accurately describe and predict the mechanical behavior of CTB under uniaxial loading conditions. Meanwhile, the influences of solid content and cement-sand ratio are analyzed.

DAMAGE VARIABLE

It is assumed that the correlated variables of the CTB element follow the Weibull distribution [45, 46], and the probability density function can be expressed as [47]:

$$P(F) = \frac{m}{F_0}\left(\frac{F}{F_0}\right)^{m-1} \exp\left[-\left(\frac{F}{F_0}\right)^{m}\right], \tag{1}$$

where F is a random variable, and $m>0$ and $F_0>0$ are the shape parameter and the scaling parameter, respectively.

The damage variable D under a certain load is defined as follows [48]:

$$D = \frac{N_t}{N}, \tag{2}$$

where N_t is the number of broken elements, and N is the total number of elements.

In an interval of $[F, F+dF]$, the number of broken elements is $NP(F)dF$. When the external force is equal to F, the number of broken elements can be described as:

$$N_t(F) = \int_0^F NP(F)dF = N\left\{1 - \exp\left[-\left(\frac{F}{F_0}\right)^{m}\right]\right\}. \tag{3}$$

Substituting Equation (3) into Equation (2) gives:

$$D = \frac{N_t}{N} = 1 - \exp\left[-\left(\frac{F}{F_0}\right)^{m}\right]. \tag{4}$$

Equation (4) is established using the general theory of continuous damage and statistics. The random variable F can be replaced by other physical quantities to establish different damage models. The axial linear strain ε is defined as the random variable in this paper. Then, Equation (4) can be rewritten as:

$$D = 1 - \exp\left[-\left(\frac{\varepsilon}{F_0}\right)^{m}\right]. \tag{5}$$

CONSTITUTIVE MODEL

According to the strain equivalence principle proposed by Lemaitre [49], the constitutive relation of damaged materials can be derived from undamaged materials, but the nominal stress is replaced by the effective stress of the damaged materials under uniaxial stress. Then, the constitutive relation can be defined [50]:

$$\sigma = E\varepsilon(1 - D). \tag{6}$$

Substituting Equation (5) into Equation (6) gives:

$$\sigma = E\varepsilon \exp\left[-\left(\frac{\varepsilon}{F_0}\right)^{m}\right]. \tag{7}$$

Considering the effect of the residual stress, Equation (7) is redefined as a two-stage function:

$$\sigma = \begin{cases} E\varepsilon \exp\left[-\left(\frac{\varepsilon}{F_0}\right)^{m}\right], \varepsilon < \varepsilon_m \\ E\varepsilon_m \exp\left[-\left(\frac{\varepsilon_m}{F_0}\right)^{m}\right], \varepsilon \geq \varepsilon_m \end{cases}. \tag{8}$$

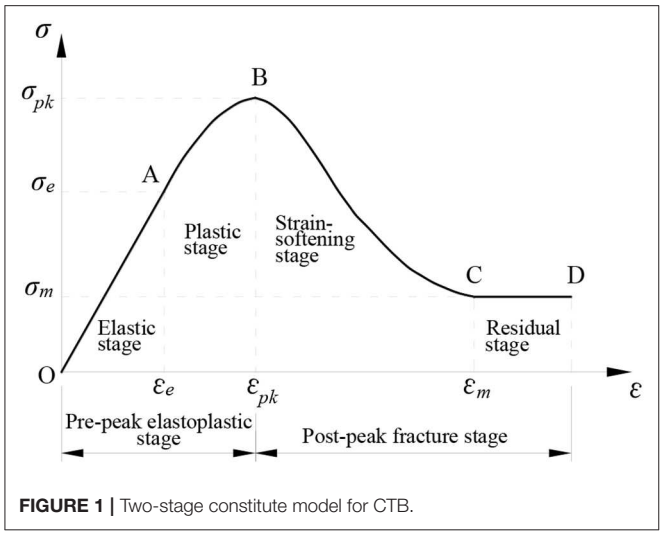

FIGURE 1 | Two-stage constitute model for CTB.

In this paper, the elastic modulus E of the CTB is defined as follows, considering the influence of solid content and cement-sand ratio.

$$E = E(x_1, x_2), \tag{9}$$

where x_1 is the solid content, and x_2 is the cement-sand ratio.

Then, Equation (8) can be rewritten as:

$$\sigma = \begin{cases} E(x_1,x_2)\varepsilon \exp[-(\frac{\varepsilon}{F_0})^m], \varepsilon < \varepsilon_m \\ E(x_1,x_2)\varepsilon_m \exp[-(\frac{\varepsilon_m}{F_0})^m], \varepsilon \geq \varepsilon_m \end{cases}. \tag{10}$$

The corresponding constitutive model is shown in **Figure 1**, where σ_e, σ_{pk}, and σ_m represent the elastic stress, the peak stress, and the residual stress, and the corresponding strains ε_e, ε_{pk}, and ε_m are the elastic strain, the peak strain, and the starting strain of the residual stage, respectively.

DETERMINATION OF MODEL PARAMETERS

To determine the unknown parameters m and F_0 in the first formula of Equation (10), the following boundary conditions are given:

(i) $\sigma = \sigma_{pk}, \varepsilon = \varepsilon_{pk}$, (ii) $\varepsilon = \varepsilon_{pk}, d\sigma/d\varepsilon = 0$.

Based on the given boundary conditions (i), the following equation can be obtained:

$$E(x_1,x_2)\varepsilon_{pk} \exp[-(\frac{\varepsilon_{pk}}{F_0})^m] = \sigma_{pk}. \tag{11}$$

Then, according to the boundary conditions (ii), the following equation can be obtained:

$$\frac{d\sigma}{d\varepsilon} = E(x_1,x_2)[1 - m(\frac{\varepsilon}{F_0})^m] \exp[-(\frac{\varepsilon}{F_0})^m], \tag{12}$$

$$E(x_1,x_2)[1 - m(\frac{\varepsilon_{pk}}{F_0})^m] \exp[-(\frac{\varepsilon_{pk}}{F_0})^m] = 0, \tag{13}$$

where $E(x_1, x_2)$ and $\exp[-(\frac{\varepsilon_{pk}}{F_0})^m]$ cannot be equal to zero, then Equation (13) can be simplified as:

$$1 - m(\frac{\varepsilon_{pk}}{F_0})^m = 0. \tag{14}$$

Equation (11) and Equation (14) are solved simultaneously, and then the unknown parameters m and F_0 can be obtained:

$$m = -\frac{1}{\ln\left\{\sigma_{pk} / [E(x_1,x_2)\varepsilon_{pk}]\right\}}, \tag{15}$$

$$F_0 = \frac{\varepsilon_{pk}}{\sqrt[m]{1/m}}. \tag{16}$$

Substituting Equation (15) and Equation (16) into Equation (10) gives:

$$\sigma = \begin{cases} E(x_1,x_2)\varepsilon \exp[-(\frac{\varepsilon \sqrt[m]{1/m}}{\varepsilon_{pk}})^m], \varepsilon < \varepsilon_m \\ E(x_1,x_2)\varepsilon_m \exp[-(\frac{\varepsilon_m \sqrt[m]{1/m}}{\varepsilon_{pk}})^m], \varepsilon \geq \varepsilon_m \end{cases} \tag{17}$$

UNIAXIAL COMPRESSION TESTS

Characteristics of the Tailings

The tailings used in this paper are from a copper mine located in northwest China, and the particle size distribution is shown in **Figure 2**. The average particle size d_{50} is 80.41 μm, the uniformity coefficient C_u is 8.57, and the curvature coefficient C_c is 1.71. As shown in **Figure 2**, the particle grading curve is smooth and continuous, and Fits grade is mild. Therefore, the tailings selected here have good gradation, compaction, and mechanical properties.

The chemical compositions of the tailings used in this paper are shown in **Figure 3**, which indicates that the main chemical compositions of the tailings are Fe_2O_3 and S_iO_2, accounting for 79% of the total solid weight. The content of CaO is less than 10%, which shows that the used tailings are low-calcium tailings.

Specimen Preparation and Experimental Equipment

CTB is composed of gelling agents, aggregates and water. The gelling agent used in this experiment is ordinary Portland cement P.O42.5, the aggregates are the tailings mentioned above and the water is ordinary city tap water from Xi'an in China's Shaanxi Province. Eight groups of CTB cylinder specimens with dimensions of 50 and 100 mm in diameter and height, respectively, were made to perform uniaxial compression tests. Three specimens were in each group, and a total of 24 specimens, contained five groups with a constant cement-sand ratio of 1/4 and solid contents of 70, 72, 74, 76, and 78 wt% and three groups with a constant solid content of 76 wt% and cement-sand ratios of 1/6, 1/8, and 1/10. The curing environment was set at a constant temperature of 20°C with a relative humidity of 95%, and the curing period was 28 days. Then, the average value of each group was taken as the final result for the relevant quantities.

The experimental equipment is LRT-300 electric-fluid servo triaxial compression machine (see **Figure 4**) and the sample is loaded as **Figure 5**. The loading process was controlled by displacement at the rate of 1×10^{-5} m/s.

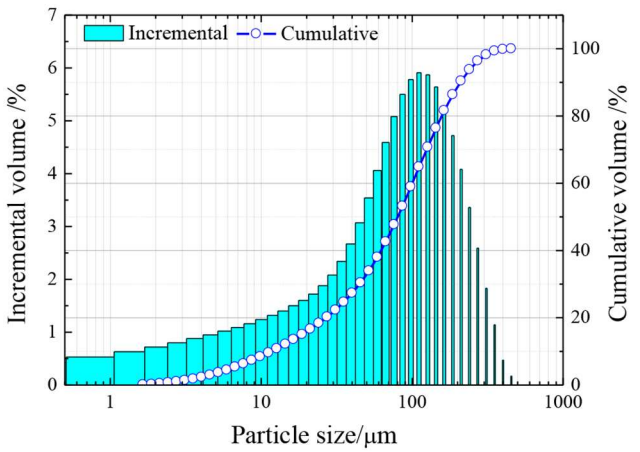

FIGURE 2 | Particle size distribution of the used tailings.

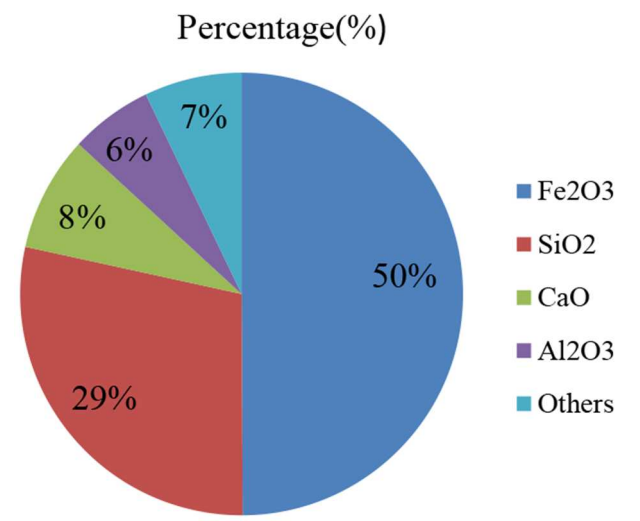

FIGURE 3 | Chemical components of the used tailings.

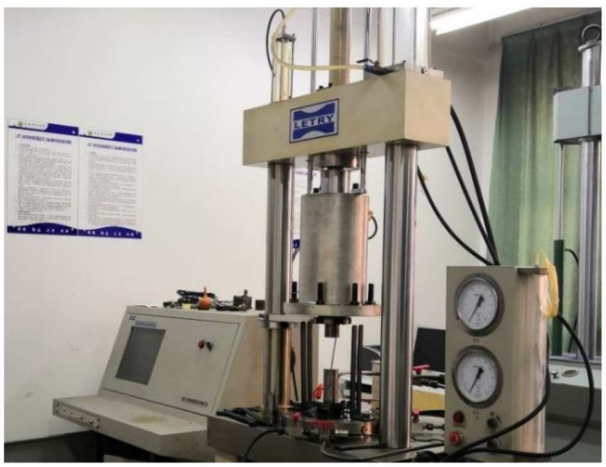

FIGURE 4 | LRT-300 electric-fluid servo triaxial compr-ession machine.

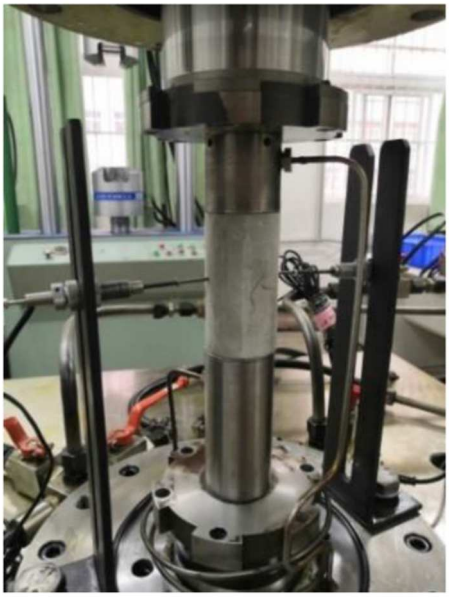

FIGURE 5 | Experimental process.

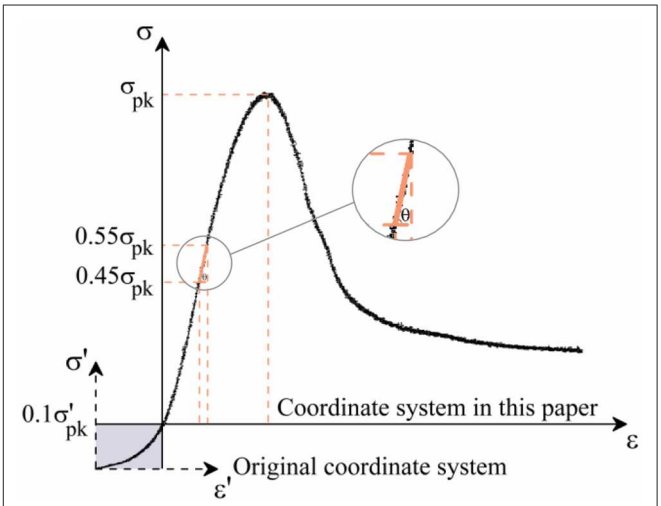

FIGURE 6 | Initial compaction stage and value of elastic modulus defined in this paper.

Model Parameters

Through experimental investigation, it is found that at the initial stage of loading, when the stress is less than 10% of the peak value, the CTB has a compaction phase, especially for the low strength specimens [51]. At this stage, the stress-strain curve is concave, and the initial cracks are closed under axial pressure. For convenience in application, the constitutive model is simplified into two stages in the theoretical part of this paper, without considering the initial compaction stage. Therefore, the initial compaction stage of the material is ignored in this paper, assuming that the material starts directly from the elastic stage after loading, as shown in **Figure 6**. σ'-ε' and σ'_{pk} represent the original coordinate system and the true peak stress, and σ-ε and

TABLE 1 | Model parameters and constitutive models.

Group number	Solid content /wt%	Cement-sand ratio	E /GPa	σ_{pk} /MPa	ε_{pk} /%	m	ε_m /%	Constitutive model ($\varepsilon < \varepsilon_m$)
1	70	1:4	0.74	3.80	0.74	2.74	1.60	$740\varepsilon \exp[-(93.54\varepsilon)^{2.74}]$
2	72	1:4	1.32	5.59	0.61	2.74	1.39	$1320\varepsilon \exp[-(113.48\varepsilon)^{2.74}]$
3	74	1:4	1.53	6.59	0.6	3.02	1.15	$1530\varepsilon \exp[-(115.58\varepsilon)^{3.02}]$
4	76	1:4	1.98	7.2	0.49	3.35	0.89	$1980\varepsilon \exp[-(142.26\varepsilon)^{3.35}]$
5	78	1:4	2.26	7.51	0.47	2.88	0.95	$2260\varepsilon \exp[-(147.37\varepsilon)^{2.88}]$
6	76	1:6	1.11	3.88	0.5	2.79	0.93	$1110\varepsilon \exp[-(138.46\varepsilon)^{2.79}]$
7	76	1:8	0.49	2.04	0.64	2.33	1.57	$490\varepsilon \exp[-(108.70\varepsilon)^{2.33}]$
8	76	1:10	0.21	1.37	0.78	5.60	1.33	$210\varepsilon \exp[-(94.25\varepsilon)^{5.60}]$

The parameters of each group in the table are the average values.

σ_{pk} represent the coordinate system selected in this paper and the corresponding peak stress, respectively.

The elastic modulus E is defined as the tangent of the secants corresponding to 45–55% of the peak stress [52]. The average stress-strain curve of the specimens with a cement-sand ratio of 1/4 and a solid content of 76 wt% was taken as an example to show the value of the elastic modulus E defined in this paper (see **Figure 6**).

Table 1 lists the values of σ_{pk} and the model parameters involved in the constitutive model of Equation (17). Meanwhile, the first stages of the corresponding constitutive models are given. The average stress-strain curve of the three CTB cylinder specimens for each group was obtained. Then, the variables of E, σ_{pk}, ε_{pk}, and ε_m in **Table 1** were gained from the average stress-strain curves. The value of E was defined as **Figure 6**, σ_{pk} and ε_{pk} are the peak stress and strain of the average curves, ε_m is the starting strain of the residual stage, and m was calculated according to Equation (15).

RESULTS AND DISCUSSION

Effects of Solid Content and Cement-Sand Ratio

Different solid contents (70, 72, 74, 76, and 78 wt%) and cement-sand ratios (1/4, 1/6, 1/8, and 1/10) were considered in the tests to analyze the effects of solid content and cement-sand ratio on the mechanical properties of CTB. The change in the mean stress-strain curves and the basic mechanical variables with solid contents and cement-sand ratios are shown in **Figures 7**, **8**. The values of all the relevant variables in each group are the mean values of the three specimens.

It can be seen from **Figure 7** that the solid content gradually increases from 70 to 78 wt% or the cement-sand ratio gradually increases from 1/10 to 1/4, the peak points of the stress-strain curves rise and shift to the left relative to the axis, which indicates that the strength (σ_{pk} and σ_m), the elastic modulus E and the energy dissipation capacity of the CTB specimens increases, while ε_{pk} decreases. Meanwhile, with the increase of the solid content or the cement-sand ratio, the descending part of the curves gradually steepens, which indicates that the ductility decreases and the friability increases.

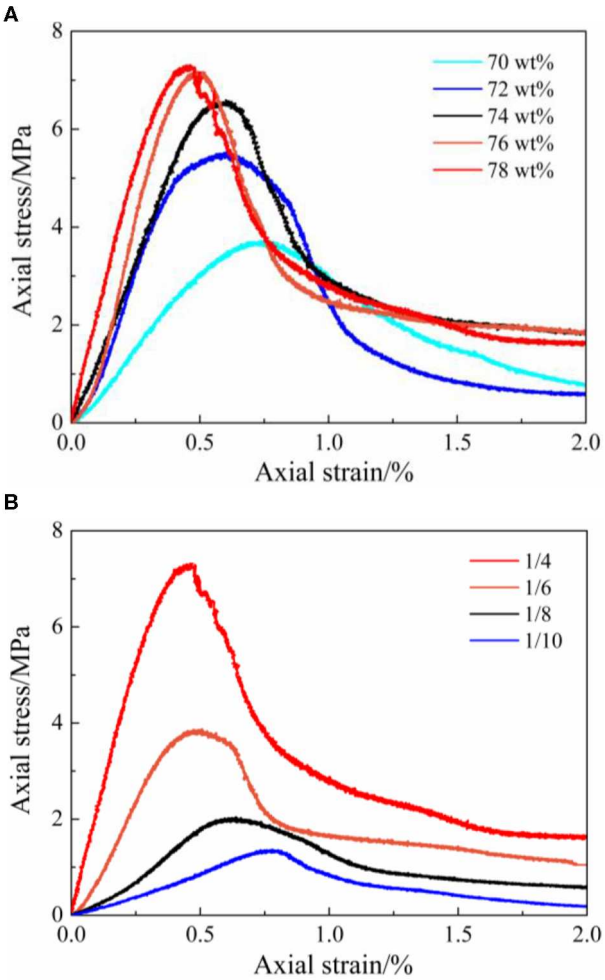

FIGURE 7 | Stress-strain curves for different solid contents and cement-sand ratios: **(A)** solid contents, **(B)** cement-sand ratios.

From **Figure 8A**, it can be observed that when the solid content ranges from 70 to 78 wt%, the corresponding value of E varies between 0.5 and 2.0 GPa, σ_{pk} varies between 4.0 and 7.5

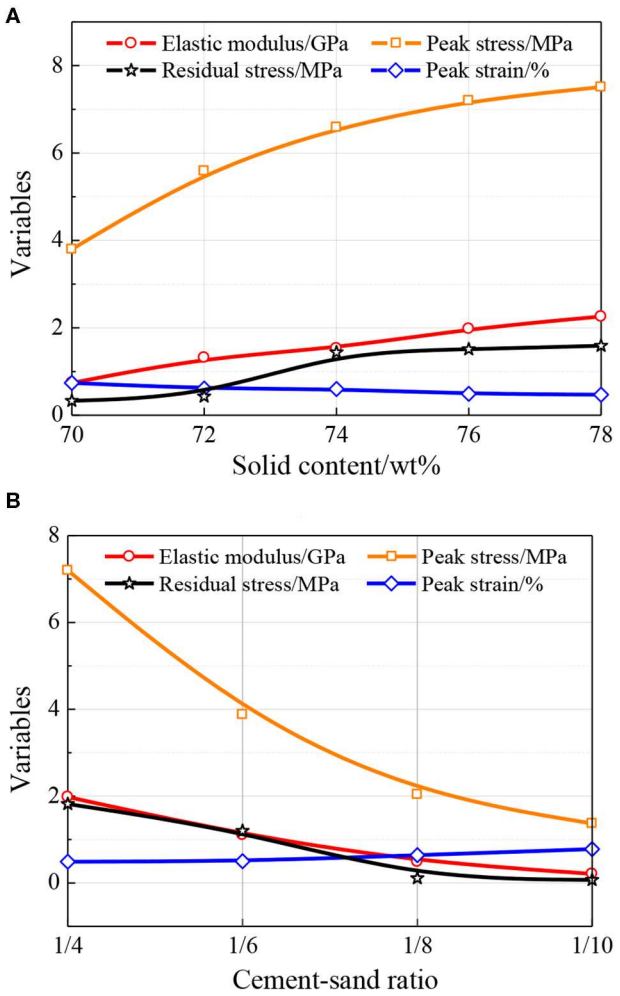

FIGURE 8 | Basic mechanical variables for different solid contents and cement-sand ratios: **(A)** solid contents, **(B)** cement-sand ratios.

MPa, ε_{pk} varies between 0.5 and 0.8% and σ_m varies between 0.5 and 1.5 MPa. Then, if the initial compaction stage is considered, the value range of σ_{pk} is from 4.5 to 8.5 MPa and the value range of σ_m is from 1.0 to 2.5 MPa.

From **Figure 8B**, it can be observed that when the cement-sand ratio ranges from 1/4 to 1/10, the corresponding value of E varies between 0.5 and 2.0 GPa, σ_{pk} varies between 1.5 and 7.5 MPa, ε_{pk} varies between 0.5 and 0.8% and σ_m varies between 1.0 and 2.0 MPa. Then, if the initial compaction stage is considered, the value range of σ_{pk} is from 2.0 to 8.5 MPa, and the value range of σ_m is form 0.3 to 3.0 MPa.

As shown in **Figure 8**, the influence of the solid content and cement-sand ratio on σ_{pk} is more obvious than that of the other quantities (E, ε_{pk} and σ_m), and the variation gradients of E and σ_m increase with the increase of solid content and cement-sand ratio are approximately equal. From **Figures 7**, **8**, it can be seen that the increasing gradient of σ_{pk} gradually decreases with the increase of solid content but increases with the increase of cement-sand ratio.

Verification and Comparison of the Constitutive Model

To verify the validity of the constitutive model of CTB established in this paper, the experimental results are compared with those calculated using the theoretical model. The calculated and experimental results are in good agreement, especially in the pre-peak region (see **Figure 9**). Therefore, the proposed constitutive model can be used to describe the mechanical properties of CTB under uniaxial compression.

Ordinary cement mortar is also composed of gelling agents, aggregates and water, which is similar to the composition of CTB except that the aggregates are river sand and not tailings. To compare and illustrate the performance difference between the two materials under uniaxial compression, the peak point of the stress-strain curves for ordinary cement mortar M5 in reference [53] was scaled by the average peak value of each group of specimens in this paper. Then, the uniaxial compression stress-strain curves of the CTB and ordinary cement mortar M5 are compared in **Figure 9**. It can be seen that before the residual stress, the curves of the two materials are similar in shape. However, the CTB exhibits obvious residual stress, but the ordinary cement mortar M5 does not. Furthermore, the ordinary cement mortar M5 is slightly stronger than CTB at the pre-failure stage, but slightly weaker at the post-failure stage.

Meanwhile, it can also be seen from **Figure 9** that under uniaxial compression, the CTB cylinder specimens are subjected to axial compression and transverse tension. The major failure mode is columnar splitting failure caused by tensile stress.

Limitations and Future Work

The results of the two-stage constitutive model for CTB proposed in this paper is in good agreement with the experimental results and can be used to predict the constitutive relation of CTB under uniaxial compression. The constitute model provided here is generally applicable, but the model parameters need to be specifically determined by testing the tailings from different sources.

Meanwhile, the long-term stress state of the CTB is constrained in three directions rather than in one direction. Therefore, our future work will investigate the mechanical properties of CTB under triaxial compression by triaxial compression tests and provide a simple and universally applicable triaxial compression constitutive model.

CONCLUSIONS

In this paper, the constitutive model for low-calcium copper mine tailings under uniaxial compression has been studied. The validity of the proposed two-stage constitutive model for CTB was verified by a comparison with the test results. Meanwhile, the effects of solid content and cement-sand ratio on the mechanical properties of CTB were also analyzed. The results are described as follows:

i) With the increase of solid content or cement-sand ratio, the strength (σ_{pk} and σ_m), E and energy dissipation capacity of

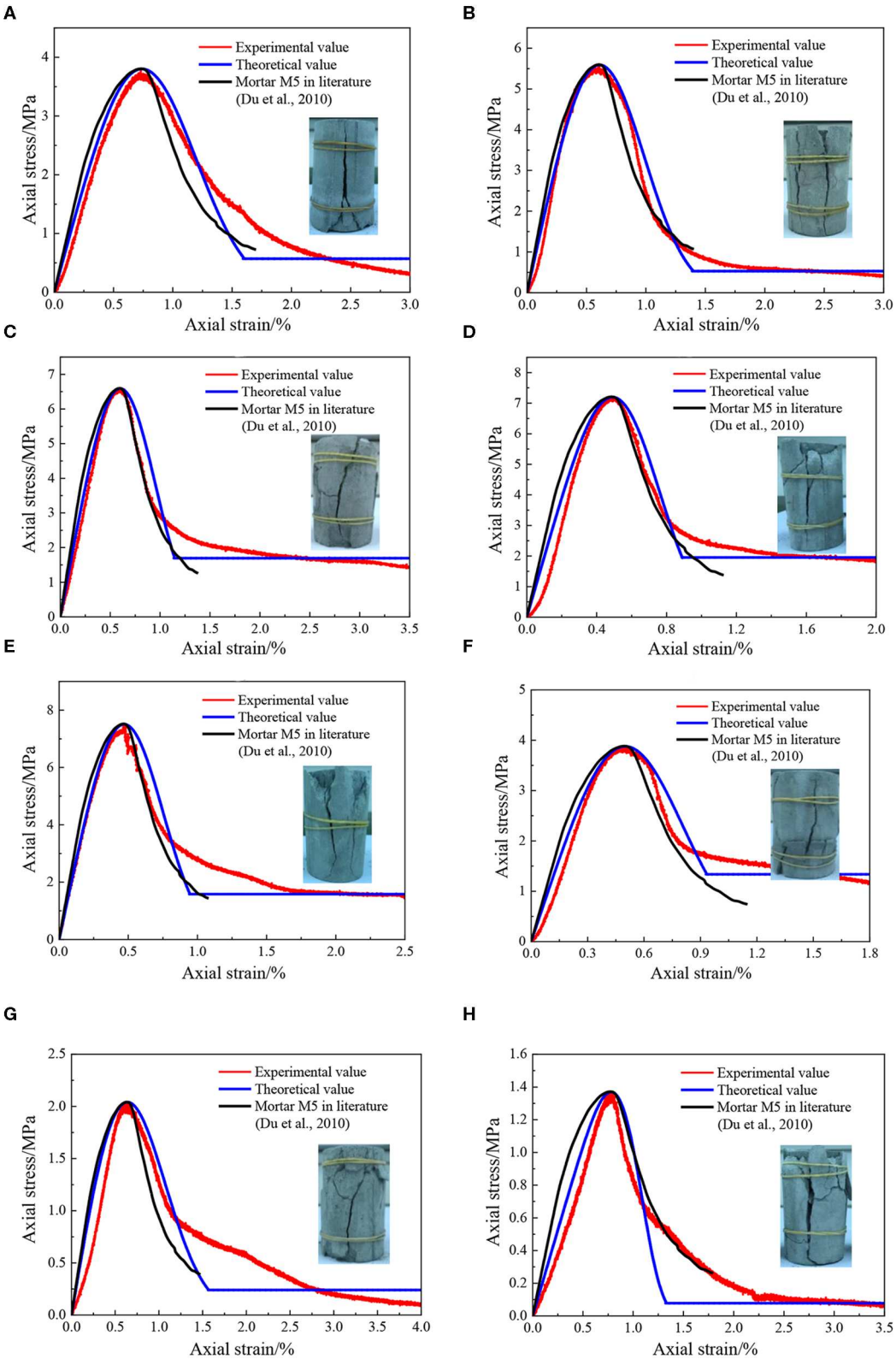

FIGURE 9 | Comparison of theoretical and experimental results for stress-strain curves (cement-sand ratio = C/S, solid content = SC): **(A)** C/S = 1/4 and SC = 70 wt%, **(B)** C/S = 1/4 and SC = 72 wt%, **(C)** C/S = 1/4 and SC = 74 wt%, (**D**) C/S = 1/4 and SC = 76 wt%, **(E)** C/S = 1/4 and SC = 78 wt%, **(F)** C/S = 1/6 and SC = 76 wt%, **(G)** C/S = 1/8 and SC = 76 wt%, **(H)** C/S = 1/10 and SC = 76 wt%.

the CTB increased, but ε_{pk} and the ductility decreased. The influence on σ_{pk} is more obvious than that on the other quantities (E, ε_{pk} and σ_m).

ii) Regardless of the initial compaction stage, for CTB specimens with solid contents of 70–78 wt% and cement-sand ratios of 1/4–1/10, the corresponding value of E remained between 0.5 and 2.0 GPa, σ_{pk} remained between 1.5 and 7.5 MPa, ε_{pk} remained between 0.5 and 0.8% and σ_m remained between 0.5 and 2.0 MPa. Then, if the initial compaction stage was considered, σ_{pk} ranged from 2.0 to 8.5 MPa and σ_m ranged from 0.3 to 3.0 MPa.

iii) The stress-strain curve of CTB is similar to that of ordinary cement mortar M5 but exhibits obvious residual stress. The failure mode of the CTB samples under uniaxial compression is mainly columnar splitting failure caused by tensile stress.

DATA AVAILABILITY STATEMENT

The raw data supporting the conclusions of this article will be made available by the authors, without undue reservation, to any qualified researcher.

AUTHOR CONTRIBUTIONS

BT and KC: writing-original draft preparation. LL: conceptualization. BZ: methodology. YZ: data curation. KS: validation. QY: supervision. All authors have read and agreed to the published version of the manuscript.

FUNDING

This research was supported by the National Natural Science Foundation of China (Nos. 51674188, 51874229, 51504182, 51974225, 51904224, 51904225, and 51704229), Shaanxi Innovative Talents Cultivate Program-New-star Plan of Science and Technology (No. 2018KJXX-083), Natural Science Basic Research Plan of Shaanxi Province of China (Nos. 2018JM5161, 2018JQ5183, 2015JQ5187, and 2019JM-074), Scientific Research Program funded by the Shaanxi Provincial Education Department (Nos. 2019JQ-354, 15JK1466, and 19JK0543), China Postdoctoral Science Foundation (No. 2015M582685), Open Project of State Key Laboratory of Green Building in Western China (No. LSKF201915), and Outstanding Youth Science Fund of Xi'an University of Science and Technology (No. 2018YQ2-01).

ACKNOWLEDGMENTS

The authors are grateful for the support provided by College of Science and Energy School, Xi'an University of Science and Technology, Xi'an, 710054, China.

REFERENCES

1. Dong L, Sun D, Shu W, Li X. Exploration: safe and clean mining on Earth and asteroids. *J Clean Prod.* (2020) **257**:120899. doi: 10.1016/j.jclepro.2020.120899
2. Sun X, Wang W. Theoretical research on high water material replacement mining the strip coal pillar above confined aquifer. *J China Coal Soc.* (2011) **36**:909–13. doi: 10.13225/j.cnki.jccs.2011.06.018
3. Zhang Q, Zhang J, Huang Y, Ju F. Backfilling technology and strata behaviors in fully mechanized coal mining working face. *Int J Mining Sci. Technol.* (2012) **22**:151–7. doi: 10.1016/j.ijmst.2011.08.003
4. Yilmaz E, Belem T, Bussiere B, Mbonimpa M, Benzaazoua M. Curing time effect on consolidation behaviour of cemented paste backfill containing different cement types and contents. *Constr Build Mater.* (2015) **75**:99–111. doi: 10.1016/j.conbuildmat.2014.11.008
5. Belem T, Benzaazoua M. Design and application of underground mine paste backfill technology. *Geotech Geol Eng.* (2007) **26**:147–74. doi: 10.1007/s10706-007-9154-3
6. Qi C, Chen Q, Fourie A, Zhang Q. An intelligent modelling framework for mechanical properties of cemented paste backfill. *Miner Eng.* (2018) **123**:16–27. doi: 10.1016/j.mineng.2018.04.010
7. Kesimal A, Yilmaz E, Ercikdi B, Alp I, Deveci H. Effect of properties of tailings and binder on the short-and long-term strength and stability of cemented paste backfill. *Mater Lett.* (2005) **59**:3703–9. doi: 10.1016/j.matlet.2005.06.042
8. Ercikdi B, Cihangir F, Kesimal A, Deveci H, Alp I. Utilization of water-reducing admixtures in cemented paste backfill of sulphide-rich mill tailings. *J Hazard Mater.* (2010) **179**:940–6. doi: 10.1016/j.jhazmat.2010.03.096
9. Cihangir F, Ercikdi B, Kesimal A, Deveci H, Erdemir F. Paste backfill of high-sulphide mill tailings using alkali-activated blast furnace slag: effect of activator nature, concentration and slag properties. *Miner Eng.* (2015) **83**:117–27. doi: 10.1016/j.mineng.2015.08.022
10. Chen Q, Zhang Q, Qi C, Fourie A, Xiao C. Recycling phosphogypsum and construction demolition waste for cemented paste backfill and its environmental impact. *J Clean Prod.* (2018) **186**:418–29. doi: 10.1016/j.jclepro.2018.03.131
11. Liu L, Fang Z, Qi C, Zhang B, Guo L, Song K. Experimental investigation on the relationship between pore characteristics and unconfined compressive strength of cemented paste backfill. *Constr Build Mater.* (2018) **179**:254–64. doi: 10.1016/j.conbuildmat.2018.05.224
12. Lu H, Qi C, Chen Q, Chen Q, Gan D, Xue Z, et al. A new procedure for recycling waste tailings as cemented paste backfill to underground stopes and open pits. *J Clean Prod.* (2018) **188**:601–12. doi: 10.1016/j.jclepro.2018.04.041
13. Cao S, Song W. Effect of filling interval time on long-term mechanical strength of layered cemented tailing backfill. *Adv Mater Sci Eng.* (2016) **2016**:1–7. doi: 10.1155/2016/9507852
14. Cao S, Song W. Effect of filling interval time on the mechanical strength and ultrasonic properties of cemented coarse tailing backfill. *Int J Miner Process.* (2017) **166**:62–8. doi: 10.1016/j.minpro.2017.07.005
15. Cao S, Song W, Yilmaz E. Influence of structural factors on uniaxial compressive strength of cemented tailings backfill. *Constr Build Mater.* (2018) **174**:190–201. doi: 10.1016/j.conbuildmat.2018.04.126
16. Jiang H, Fall M. Yield stress and strength of saline cemented tailings in sub-zero environments: Portland cement paste backfill. *Int J Min Process.* (2017) **160**:68–75. doi: 10.1016/j.minpro.2017.01.010
17. Yin S, Shao Y, Wu A, Wang Y, Chen X. Expansion and strength properties of cemented backfill using sulphidic mill tailings. *Constr Build Mater.* (2018) **165**:138–48. doi: 10.1016/j.conbuildmat.2018.01.005
18. Zheng J, Guo L, Sun X, Li W, Jia Q. Study on the strength development of cemented backfill body from lead-zinc mine tailings with sulphide. *Adv Mater Sci Eng.* (2018) **2018**:1–8. doi: 10.1155/2018/7278014
19. Xu W, Li Q, Zhang Y. Influence of temperature on compressive strength, microstructure properties and failure pattern of fiber-reinforced cemented tailings backfill. *Constr Build Mater.* (2019) **222**:776–85. doi: 10.1016/j.conbuildmat.2019.06.203
20. Zheng J, Zhu Y, Zhao Z. Utilization of limestone powder and water-reducing admixture in cemented paste backfill of coarse copper mine tailings.

Constr Build Mater. (2016) **124**:31–6. doi: 10.1016/j.conbuildmat.2016.07.055
21. Hou C, Zhu W, Yan B, Guan K, Du J. Influence of binder content on temperature and internal strain evolution of early age cemented tailings backfill. *Constr Build Mater.* (2018) **189**:585–93. doi: 10.1016/j.conbuildmat.2018.09.032
22. Mangane M, Argane R, Trauchessec R, Lecomte A, Benzaazoua M. Influence of superplasticizers on mechanical properties and workability of cemented paste backfill. *Miner Eng.* (2018) **116**:3–14. doi: 10.1016/j.mineng.2017.11.006
23. Zheng J, Sun X, Guo L, Zhang S, Chen J. Strength and hydration products of cemented paste backfill from sulphide-rich tailings using reactive MgO-activated slag as a binder. *Constr Build Mater.* (2019) **203**:111–9. doi: 10.1016/j.conbuildmat.2019.01.047
24. Xu W, Cao P, Tian M. Strength development and microstructure evolution of cemented tailings backfill containing different binder types and contents. *Minerals.* **8**:167. doi: 10.3390/min8040167
25. Liu L, Xin J, Feng Y, Zhang B, Song K. Effect of the cement-tailing ratio on the hydration products and microstructure characteristics of cemented paste backfill. *Arab J Sci Eng.* (2019) **44**:6547–56. doi: 10.1007/s13369-019-03954-z
26. Xu W, Cao Y, Liu B. Strength efficiency evaluation of cemented tailings backfill with different stratified structures. *Eng Struct.* (2019) **180**:18–28. doi: 10.1016/j.engstruct.2018.11.030
27. Jiang H, Fall M, Cui L. Freezing behaviour of cemented paste backfill material in column experiments. *Constr Build Mater.* (2017) **147**:837–46. doi: 10.1016/j.conbuildmat.2017.05.002
28. Yi X, Ma G, Fourie A. Compressive behaviour of fibre-reinforced cemented paste backfill. *Geotext Geomembr.* (2015) **43**:207–15. doi: 10.1016/j.geotexmem.2015.03.003
29. Chen X, Shi X, Zhou J, Chen Q, Li E, Du X. Compressive behavior and microstructural properties of tailings polypropylene fibre-reinforced cemented paste backfill. *Constr Build Mater.* (2018) **190**:211–21. doi: 10.1016/j.conbuildmat.2018.09.092
30. Cao S, Yilmaz E, Song W. Fiber type effect on strength, toughness and microstructure of early age cemented tailings backfill. *Constr Build Mater.* (2019) **223**:44–54. doi: 10.1016/j.conbuildmat.2019.06.221
31. Xue G, Yilmaz E, Song W, Yilmaz E. Influence of fiber reinforcement on mechanical behavior and microstructural properties of cemented tailings backfill. *Constr Build Mater.* (2019) **213**:275–85. doi: 10.1016/j.conbuildmat.2019.04.080
32. Wang M, Liu L, Wang S, Lv B, Zhang B, Zhang X, et al. Numerical investigation of heat transfer and phase change characteristics of cold load and storage functional CPB in deep mine. *Front Earth Sci.* (2020) **8**:31. doi: 10.3389/feart.2020.00031
33. Hu J, Ren Q, Jiang Q, Gao R, Zhang L, Luo Z. Strength characteristics and the reaction mechanism of stone powder cement tailings backfill. *Adv Mater Sci Eng.* (2018) **2018**:1–14. doi: 10.1155/2018/8651239
34. Cao S, Yilmaz E, Song W, Yilmaz E, Xue G. Loading rate effect on uniaxial compressive strength behavior and acoustic emission properties of cemented tailings backfill. *Constr Build Mater.* (2019) **213**:313–24. doi: 10.1016/j.conbuildmat.2019.04.082
35. Sun Q, Cai C, Zhang S, Tian S, Li B, Xia Y, et al. Study of localized deformation in geopolymer cemented coal gangue-fly ash backfill based on the digital speckle correlation method. *Constr Build Mater.* (2019) **215**:321–31. doi: 10.1016/j.conbuildmat.2019.04.208
36. Wang Y, Wu A, Wang H, Wang Y, Cui L, Jin F, et al. Damage constitutive model of cemented tailing paste under initial temperature effect. *Chinese J Eng.* (2017) **39**:31–8. doi: 10.13374/j.issn2095-9389.2017.01.004
37. Cui L, Fall M. A coupled thermo–hydro-mechanical–chemical model for underground cemented tailings backfill. *Tunnel Undergr Space Technol.* (2015) **50**:396–414. doi: 10.1016/j.tust.2015.08.014
38. Wu D, Deng T, Zhao R. A coupled THMC modeling application of cemented coal gangue-fly ash backfill. *Constr Build Mater.* (2018) **158**:326–36. doi: 10.1016/j.conbuildmat.2017.10.009
39. Cui L, Fall M. An evolutive elasto-plastic model for cemented paste backfill. *Comput Geotech.* (2016) **71**:19–29. doi: 10.1016/j.compgeo.2015.08.013
40. Qi C, Fourie A, Chen Q, Zhang Q. A strength prediction model using artificial intelligence for recycling waste tailings as cemented paste backfill. *J Clean Prod.* (2018) **183**:566–78. doi: 10.1016/j.jclepro.2018.02.154
41. Qi C, Chen Q, Fourie A, Tang X, Zhang Q, Dong X, et al. Constitutive modelling of cemented paste backfill: a data-mining approach. *Constr Build Mater.* (2019) **197**:262–70. doi: 10.1016/j.conbuildmat.2018.11.142
42. Qi C, Tang X, Dong X, Chen Q, Fourie A, Liu E. Towards Intelligent Mining for Backfill: a genetic programming-based method for strength forecasting of cemented paste backfill. *Miner Eng.* (2019) **133**:69–79. doi: 10.1016/j.mineng.2019.01.004
43. Wu E. *Specific energy characteristics of cemented tailings backfill of damage and fracture under uniaxial compression* (Master). Wuhan: Wuhan University of Science and Technology (2018).
44. Dong L, Tong X, Li X, Zhou J, Wang S, Liu B. Some developments and new insights of environmental problems and deep mining strategy for cleaner production in mines. *J Clean Prod.* (2019) **210**:1562–78. doi: 10.1016/j.jclepro.2018.10.291
45. Wang J, Song W, Tan Y, Fu J, Cao S. Damage constitutive model and strength criterion of horizontal stratified cemented backfill. *Rock Soil Mech.* (2019) **40**:1731–9. doi: 10.16285/j.rsm.2018.0017
46. Ahmad A, Ghazal M. Exponentiated additive Weibull distribution. *Reliabil Eng Syst Saf.* (2020) **193**:106663. doi: 10.1016/j.ress.2019.106663
47. Zhang H, Yuan C, Yang G, Wu LY, Peng C, Ye W, Shen Y, Moayedi H. A novel constitutive modelling approach measured under simulated freeze–thaw cycles for the rock failure. *Eng. Comput.* (2019) 35:1–14. doi: 10.1007/s00366-019-00856-4
48. Dong L, Sun D, Li X, Ma J, Zhang L, Tong X. Interval non-probabilistic reliability of surrounding jointed rockmass considering microseismic loads in mining tunnels. *Tunnel Undergr Space Technol.* (2018) **81**:326–35. doi: 10.1016/j.tust.2018.06.034
49. Lemaitre J. A continuous damage mechanics model for ductile fracture. *J Eng Mater Technol.* (1985) **107**:83–9. doi: 10.1115/1.3225775
50. Dong L, Shu W, Li X, Zhang J. Quantitative evaluation and case studies of cleaner mining with multiple indexes considering uncertainty factors for phosphorus mines. *J Clean Prod.* (2018) **183**:319–34. doi: 10.1016/j.jclepro.2018.02.105
51. Cheng A, Zhang Y, Dai S, Dong F, Zeng W, Li D. Space-time evolution of acoustic emission parameters of cemented backfill and its fracture prediction under uniaxial compression. *Rock Soil Mech.* (2019) **40**:2965–74. doi: 10.16285/j.rsm.2018.1940
52. Wang X, Kang H, Gao F, Zhao K. DEM simulation of mechanical behavior of jointed coal in large scale under uniaxial compression. *J China Coal Soc.* (2018) **43**:3088–97. doi: 10.13225/j.cnki.jccs.2018.0834
53. Du X, Wang Y, Lu D. Study on static and dynamic stress strain relationship of cement mortar material. *China Civil Eng J.* (2010) **43S**:119–26. doi: 10.15951/j.tmgcxb.2010.s2.033

Conflict of Interest: The authors declare that the research was conducted in the absence of any commercial or financial relationships that could be construed as a potential conflict of interest.

frontiers in Physics

ORIGINAL RESEARCH
published: 11 August 2020
doi: 10.3389/fphy.2020.00263

Coal Mine Abutment Pressure Distribution Based on a Strain-Softening Model

Ang Li[1,2]*, *Qiang Ma*[1,3], *Li Ma*[2], *Li Kang*[4], *Qian Mu*[1] and *Jianbo Chen*[1]

[1] School of Architecture and Civil Engineering, Xi'an University of Science and Technology, Xi'an, China, [2] Key Laboratory of Coal Resources Exploration and Comprehensive Utilization, Ministry of Land and Resources, Xi'an, China, [3] Drilling Technology and Engineering Research Institute, China Coal Technology & Engineering Group Xi'an Research Institute, Xi'an, China, [4] Key Laboratory of Coal Resources Exploration and Comprehensive Utilization, Ministry of Land and Resources, Shaanxi Coalfield Geophysical Prospecting and Surveying Group Co. Ltd., Xi'an, China

The coal in front of the mining face presents strain softening deformation characteristics. An analytical model is proposed to simulate the abutment pressure distribution over the coal in front of the mining face under elastic and inelastic conditions. A new theoretical formula is derived from calculating the abutment pressure distribution and its width in elastic and inelastic regions of the coal under the limit equilibrium condition. The influences of UCS, residual strength, mining height, softening modulus, and deformation angle on the abutment pressure distribution are discussed. The study results show that (1) the stress gradient in the plastic area is larger than that in the crushed zone; (2) the width of the plastic region is independent of the peak abutment pressure, but it is dependent on UCS, residual strength, mining height, softening modulus, and deformation angle; (3) the width of the crushed zone in the inelastic area is closely related to the peak abutment pressure, coal-floor interface cohesion, and friction coefficient; (4) the width of the elastic zone is dependent on the mining height, coefficient of horizontal pressure, coal-floor interface friction coefficient, and peak abutment pressure, where the coefficient of horizontal pressure has the highest impact, in that the width of the elastic zone undergoes logarithmic decrease with the increase in the coefficient of horizontal pressure. A case study was carried out at longwall panel 07 of No. 5 coal seam in Dongjiahe Coal Mine to verify the analytical model. The abutment pressure distribution and the widths of the elastic and inelastic zones under the limit equilibrium condition are calculated based on the relevant parameters. The theoretical results are compared with the field monitoring data and show a very good fit. It is proved that the proposed analytical model has high accuracy, and the feasibility of the model is verified. The study results can provide guidance for similar engineering applications.

Keywords: abutment pressure distribution, elastic-plastic strain-softening model, coal limit equilibrium zone, influencing factor, case verification

OPEN ACCESS

Edited by:
Guoyang Fu,
Monash University, Australia

Reviewed by:
Muktish Acharyya,
Presidency University, India
Allbens Picardi Faria Atman,
Federal Center for Technological Education of Minas Gerais, Brazil

***Correspondence:**
Ang Li
angli@xust.edu.cn

Specialty section:
This article was submitted to Interdisciplinary Physics, a section of the journal Frontiers in Physics

Received: *30 March 2020*
Accepted: *11 June 2020*
Published: *11 August 2020*

Citation:
Li A, Ma Q, Ma L, Kang L, Mu Q and Chen J (2020) Coal Mine Abutment Pressure Distribution Based on a Strain-Softening Model. Front. Phys. 8:263. doi: 10.3389/fphy.2020.00263

INTRODUCTION

As mining goes deeper and deeper, the engineering and geological conditions of mining entries become more and more complicated. Low coal strength and high deformation at ribs are the key points of difficulty for the control of the surrounding rock mass at mining entries. Much in-depth research has been done on the deformation and failure of the rock surrounding mining entries.

Yuan and Chen analyzed the mechanical behavior at the plastic and crushed zones of mining entries based on the rock strain-softening characteristics and elastic-plastic softening model [1, 2]. Hou and Ma determined the coal interface stress and the depth critical stress equilibrium zone of mining entries with loose medium stress equilibrium theory [3, 4]. Ma calculated the plastic zone radius and stress of mining entries with a mechanic model based on the full strain-stress curve [5, 6]. Zheng and Yang calculated the width of the coal rib damaged zone with a simplified rib stress distribution [7, 8]. Li, Pan, and Wang studied the influence of the support zone on the plastic zone of the coal with grouting-bolting combined support on coal ribs [9–11]. In addition, the coal rib stress and displacement distribution have been discussed by many researchers [12–18]. However, the impacts of the abutment pressure in the elastic zone on the limit equilibrium zone have been neglected. It is hard to determine the relevant mechanical parameters for use in practical engineering applications. Actually, rib coal is a special rock mass that exists deep underground and is rich in cracks. Its mechanical characteristics under abutment pressure are different from those of shallow rocks [19–31]. In this study, the elastic foundation beam theory is adopted to study the load distribution and width of the limit equilibrium zone of mining entries. A case study was conducted for the verification of the model, which provides a theoretical basis for the design of rib support.

ELASTIC-PLASTIC STRAIN-SOFTENING MODEL

Coal Deformation and Failure Characteristics

Coal is a rock mineral that forms during the sedimentary evolution of surface plants from the ancient past. The deformation and ring breaking process of the coal body is manifested by the compaction, generation, and development of fissures. **Figure 1** shows the stress–strain relation of coal under different confining pressures. Under different confining pressures, the failure process and residual strength of coal

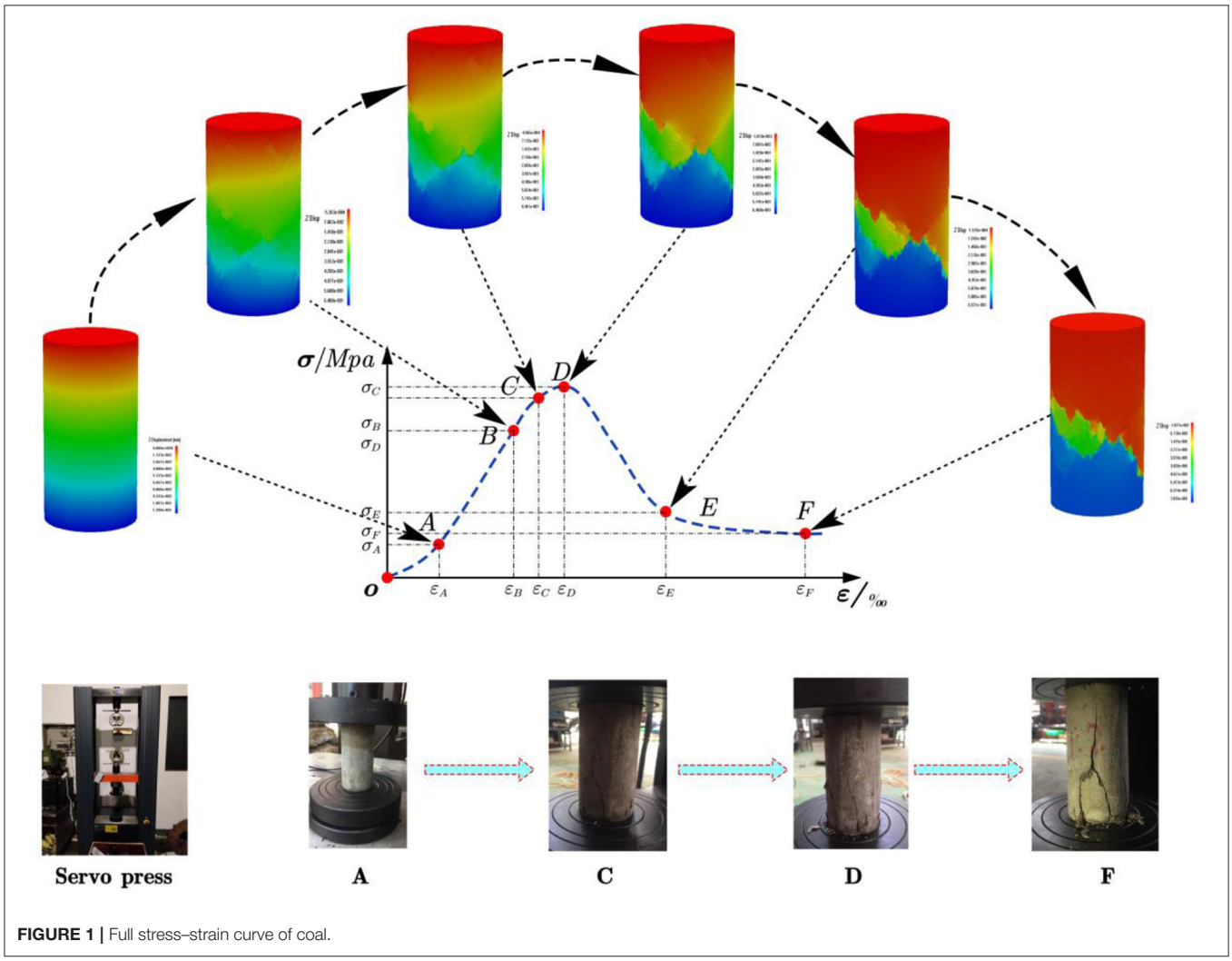

FIGURE 1 | Full stress–strain curve of coal.

show remarkable differentiation, normally showing elastic–plastic softening characteristics.

The coal failure process with an elastic–plastic softening characteristic can be represented by five sections of the stress–strain curve, as shown in **Figure 1**.

The OA section is the compaction phase that occurs during the initial loading stage of the coal sample; the strain rate is larger than the stress rate, the *in-situ* cracks are compacted, and the curve trends upward.

The AB section is the stage of linear elastic deformation; the stress–strain relationship of the coal body is linear. B is the elastic limit point, and new cracks form after point B.

The BD section is the strain-hardening section. Due to the generation, expansion, and transfixion of the new cracks in coal, the strain rate increases, which is represented by remarkable dilatation. Before the stress achieves critical strength, cracks are expanding relatively slowly in the BC section. After point C, cracks develop very rapidly in the CD section, the coal volume is expanded, and many vertical cracks occur, and at point D, the critical strength is reached.

The DE section is the plastic softening section, in which stress decreases rapidly along with crack development. The deformation increases, cracks connect and cut through the coal, and the coal sample is crushed by compression. The deformation characteristics of the coal sample are closely related to the internal crack compaction, expansion, and evolution.

The EF section is the flow deformation section, in which coal still has certain residual strength after failure due to lateral stress and internal friction.

Constitutive Model and Yield Criterion

A simplified perfect linear elastic-plastic softening model shown in **Figure 2A** is proposed based on the coal stress-strain curve discussed in the above section. The deformation process is divided into elastic deformation before critical strength, plastic softening after critical strength, and flow deformation. The degree of plastic softening can be represented by α (α ≠ 0).

Elastic Deformation

Coal deformation in this section is in accordance with Hooke's Law, and the yield condition satisfies the Mohr-Coulomb criterion.

$$\sigma_1 = k_p \sigma_3 + \sigma_c \tag{1}$$

where $k_p = \frac{1+\sin\varphi}{1-\sin\varphi}$, σ_c is the critical uniaxial compression strength of coal (MPa), $\sigma_c = \frac{2C\cos\varphi}{1-\sin\varphi}$, and C and φ are the cohesion (Mpa) and friction angle (°) of coal, respectively.

Plastic Deformation

In this section, the cohesion C decreases remarkably while the cohesion angle φ has insignificant change. Assuming that the cohesion angle is constant, coal strength decreases with the deformation. Coal strength under plastic softening is derived in Equation (2).

$$\sigma_1 = k_p \sigma_3 + \sigma_c^p \tag{2}$$

where σ_c^p is the plastic softening coal strength (Mpa), which can be derived from Equation (3).

$$\sigma_c^p = \sigma_c - M_0\left(\varepsilon_1 - \varepsilon_1^e\right) \tag{3}$$

M_0 is the slope of the strain softening section, i.e., the softening modulus (MPa), $M_0 = \tan\alpha$, and ε_c^e is the major principal strain when coal achieves critical strength, i.e., the major principal strain at the junction between elastic and plastic deformation.

Flow Deformation

In this section, the coal strength decreases to the residual value and the yield condition during flow deformation satisfies the

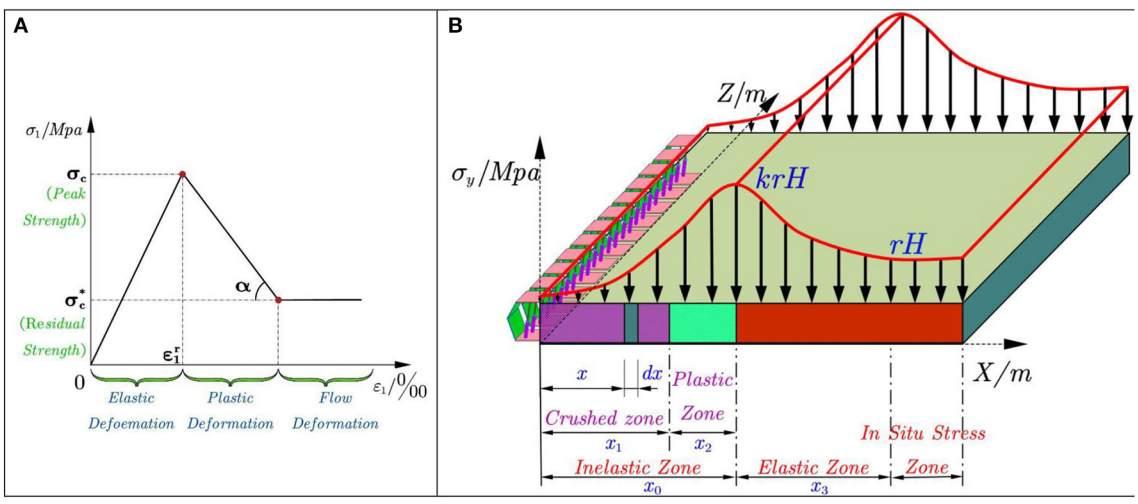

FIGURE 2 | Elastic-plastic strain-softening model and abutment pressure distributions. **(A)** Elastic-plastic strain-softening model. **(B)** Distribution law of advance bearing pressure on the working face.

Mohr-Coulomb criterion.

$$\sigma_1 = k_p^* \sigma_3 + \sigma_c^* \tag{4}$$

where $k_p^* = \frac{1+\sin\varphi^*}{1-\sin\varphi^*}$, σ_c^* is the residual strength (MPa) with uniaxial compression, $\sigma_c^* = \frac{2C^*\cos\varphi^*}{1-\sin\varphi^*}$, and C* and φ^* are the residual cohesion (Mpa) and friction angle (°) of coal. It is assumed that the internal friction angle is constant during the flow deformation section, i.e., $\varphi^* = \varphi$, $k_p^* = k_p$.

ABUTMENT PRESSURE DISTRIBUTIONS

The elastic deformation stage, plastic strain softening, and flow deformation stage of the elastic-plastic strain-softening model correspond to the elastic zone, plastic zone, and crushed zone of the coal rib, respectively. The strain-softening rules can be adopted here to study the abutment pressure distribution, as shown in **Figure 2B**. The z-axis in this figure represents the inclined length of the working face.

Inelastic Mechanics Model

In the inelastic zone, based on the ground control theory and the practical conditions of floor deformation, the roof stratum in the inelastic zone deforms linearly. **Figure 3A** shows the mechanics model in the inelastic condition. The abutment pressure in the inelastic zone under limit equilibrium condition can be derived.

In **Figure 3A**, taking differential unit dx, the normal stress, lateral stress, and the coal-roof and coal-floor interface friction resistance acting on the differential unit satisfy the stress limit equilibrium condition. Neglecting gravity, the equilibrium equations of the differential unit are as follows.

$$\sum F_X = 0 \tag{5}$$

$$\sum F_Y = 0 \tag{6}$$

$$T_1 = C_1 + f_1 \sigma_y \tag{7}$$

$$T_2 = C_1 + f_1 \sigma_{yg} \tag{8}$$

The equilibrium equation in lateral direction is (see **Appendix**),

$$\sigma_x\left(h_2 + x\tan\theta\right) - \left(\sigma_x + d\sigma_x\right)\left[h_2 + \left(x + dx\right)\tan\theta\right] + T_1\cos\theta\frac{dx}{\cos\theta} + \sigma_y\sin\theta\frac{dx}{\cos\theta} + T_2 dx = 0 \tag{9}$$

where σ_y is the normal stress from the roof (MPa), C_1 is the cohesion between coal and roof, floor (MPa), f_1 is the friction coefficient between coal and roof, floor (°), H is the height of the coal seam (m), $H = h_1 + h_2$, h_1 is the coal deformation at the rib (m), and h_2 is the height of the coal seam at the rib (m).

The equilibrium equation in the vertical direction is,

$$\sigma_{yg}dx + T_1\sin\theta\frac{dx}{\cos\theta} - \sigma_y\cos\theta\frac{dx}{\cos\theta} = 0 \tag{10}$$

where σ_{yg} is the normal stress from the floor (MPa).

Crushed Zone

The deformation angle θ of the real coal seam is pretty small. The stress condition of the differential unit is similar to in the coal sample experiment. Therefore, σ_1 and σ_3 in Equations (1), (2), and (4) can be substituted by σ_{yg} and σ_x in the inelastic stress limit equilibrium condition. The coal failure critical condition is

$$\sigma_{yg} = k_p^*\sigma_x + \sigma_c^* \tag{11}$$

The boundary condition is

$$\sigma_x|_{x=0} = 0 \tag{12}$$

With Equations (7)–(11), the following equations can be derived,

$$\sigma_y = \frac{k_p^*\sigma_x + \sigma_c^* + C_1\tan\theta}{1 - f_1\tan\theta} \tag{13}$$

$$\frac{d\sigma_x}{dx} + \frac{\sigma_x}{h_2 + x\tan\theta}\left[\tan\theta - k_p^* f_1 - \frac{k_p^*\left(f_1 + \tan\theta\right)}{1 - f_1\tan\theta}\right] - \frac{1}{h_2 + x\tan\theta}\left[2C_1 + f_1\sigma_c^* + \frac{\left(\sigma_c^* + C_1\tan\theta\right)\left(f_1 + \tan\theta\right)}{1 - f_1\tan\theta}\right] = 0 \tag{14}$$

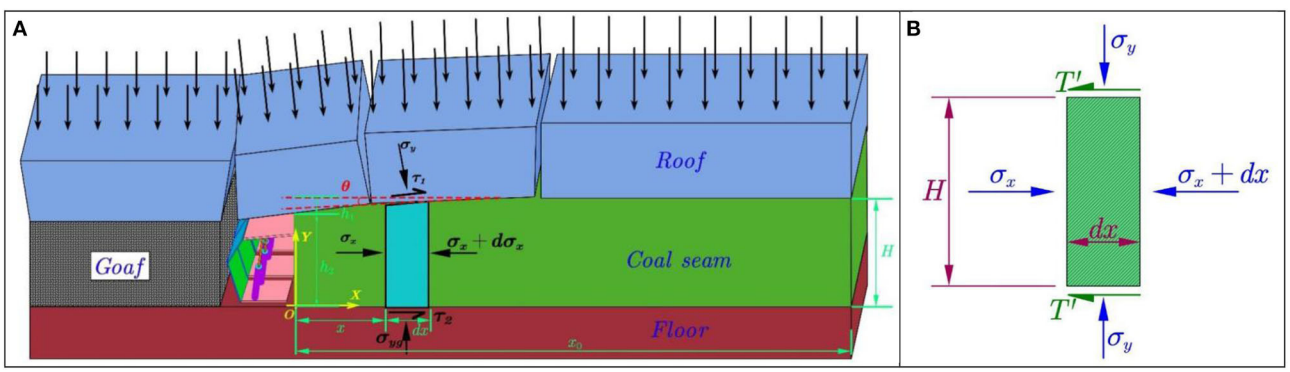

FIGURE 3 | Coal mechanics model in inelastic and elastic condition. **(A)** Inelastic mechanics model. **(B)** Elastic mechanics model.

Assuming

$$A = \tan\theta - k_p^* f_1 - \frac{k_p^*\left(f_1 + \tan\theta\right)}{1 - f_1\tan\theta}$$
$$B = 2C_1 + f_1\sigma_c^* + \frac{\left(\sigma_c^* + C_1\tan\theta\right)\left(f_1 + \tan\theta\right)}{1 - f_1\tan\theta}$$

Equation (14) can be simplified,

$$\frac{d\sigma_x}{dx} + \frac{A}{h_2 + x\tan\theta}\sigma_x = \frac{B}{h_2 + x\tan\theta} \tag{15}$$

Equation (15) is a linear first-order differential equation. By substituting the boundary condition in Equation (12), the lateral stress σ_x, vertical stress σ_{yg}, and abutment pressure σ_y can be calculated as follows.

$$\sigma_x = \frac{B}{A} - \frac{B}{A}\left(\frac{h_2}{x\tan\theta + h_2}\right)^{\frac{A}{\tan\theta}} \tag{16}$$

$$\sigma_{yg} = \frac{Bk_p^*}{A} - \frac{Bk_p^*}{A}\left(\frac{h_2}{x\tan\theta + h_2}\right)^{\frac{A}{\tan\theta}} + \sigma_c^* \tag{17}$$

$$\sigma_y = \frac{BC}{A} - \frac{BC}{A}\left(\frac{h_2}{x\tan\theta + h_2}\right)^{\frac{A}{\tan\theta}} + D \tag{18}$$

where $C = \frac{k_p^*}{1 - f_1\tan\theta}$, $D = \frac{\sigma_c^* + C_1\tan\theta}{1 - f_1\tan\theta}$.

As coal seam deformation h_1 at the rib is very small comparing to the width of the inelastic zone, i.e., the deformation angle θ of the coal seam is very small, the coefficients A, B, C, and D in Equations (16)–(18) can be expanded in a Taylor Series on deformation angle θ as follows.

$$A = \left[1 - k_p^*\left(1 + f_1^2\right)\right]\theta - 2k_p^* f_1$$
$$B = 2C_1 + 2f_1\sigma_c^* + \theta\left(C_1 f_1 + \sigma_c^* + \sigma_c^* f_1^2\right)$$
$$C = k_p^*\left(1 + f_1\theta\right)$$
$$D = \sigma_c^* + \left(C_1 + \sigma_c^* f_1\right)\theta$$

Substituting the above coefficients into Equations (16)–(18), the equations for calculating lateral stress σ_x, vertical stress σ_{yg}, and abutment pressure σ_y can be simplified as follows.

$$\sigma_x = \frac{C_1 + f_1\sigma_c^*}{k_p^* f_1}\left[\left(1 + \frac{\theta}{h_2}x\right)^{\frac{2k_p^* f_1}{\theta}} - 1\right] \tag{19}$$

$$\sigma_{yg} = \sigma_y = \frac{C_1 + f_1\sigma_c^*}{f_1}\left(1 + \frac{\theta}{h_2}x\right)^{\frac{2k_p^* f_1}{\theta}} - \frac{C_1}{f_1} \tag{20}$$

Plastic Zone

The plastic zone in the plastic strain-softening stage of the elastic-plastic strain-softening model is very small. The roof also has very little compression deformation in the plastic zone. The stress analysis can be conducted under the inelastic condition, and the plastic strain ε_1 can be derived in the following equation.

$$\varepsilon_1 = \varepsilon_1^p + \varepsilon_1^e = \frac{x_0 - x}{H}\tan\theta + \varepsilon_1^e \tag{21}$$

where ε_1^p is plastic strain; ε_1^e is elastic strain; x_0 is the width of the inelastic zone; x is the width of the crushed zone.

In the plastic softening stage, σ_1 and σ_3 in Equations (1) and (2) can be substituted by σ_{yg} and σ_x in the inelastic stress limit equilibrium condition. The critical condition for coal failure is

$$\sigma_{yg} = k_p\sigma_x + \sigma_c^p \tag{22}$$

Substituting Equations (3) and (21) into Equation (22),

$$\sigma_{yg} = k_p\sigma_x + \sigma_c - M_0\frac{x_0 - x}{H}\tan\theta \tag{23}$$

As the plastic zone and the crushed zone are continuous, when $x = x_1$, the width of the plastic zone is,

$$x_2 = \frac{\sigma_c - \sigma_c^*}{M_0 tan\theta}H \approx \frac{\sigma_c - \sigma_c^*}{M_0\theta}H \tag{24}$$

where $\varphi^* = \varphi$, $k_p^* = k_p$.

With the stress continuous condition, the lateral stresses at $x = x_1$ for the plastic zone and crushed zone are equal. The boundary condition is

$$\sigma_x|_{x=1} = \frac{C_1 + f_1\sigma_c^*}{k_p^* f_1}\left[\left(1 + \frac{\theta}{h_2}x_1\right)^{\frac{2k_p^* f_1}{\theta}} - 1\right] \tag{25}$$

Substituting Equation (25) at boundary condition ($x = x_1$) into the differential equation derived from Equations (9), (10), and (23), the lateral stress σ_x, vertical stress σ_{yg}, and abutment pressure σ_y can be calculated as follows.

$$\sigma_x = \frac{\sigma_c - \sigma_c^*}{k_p}\left(\frac{\theta x + h_2}{\theta x_1 + h_2}\right)^{\frac{2k_p f_1}{\theta}} + \frac{C_1 + f_1\sigma_c^*}{k_p f_1}\left(\frac{\theta x}{h_2} + 1\right)^{\frac{2k_p f_1}{\theta}} - \frac{C_1 + f_1\sigma_c}{k_p f_1} \tag{26}$$

$$\sigma_{yg} = \sigma_y = \left(\sigma_c - \sigma_c^*\right)\left(\frac{\theta x + h_2}{\theta x_1 + h_2}\right)^{\frac{2k_p f_1}{\theta}} + \left(\frac{C_1}{f_1} + \sigma_c^*\right)\left(\frac{\theta x}{h_2} + 1\right)^{\frac{2k_p f_1}{\theta}} - \frac{M_0\theta}{H}(x_0 - x) - \frac{C_1}{f_1} \tag{27}$$

Since the deformation angle θ is small, it is two orders of magnitude different from h_2, and it is reasonable to assume that $\frac{\theta x + h_2}{\theta x_1 + h_2} \approx 1$, Equations (26) and (27) can be simplified to

$$\sigma_x = \frac{C_1 + f_1\sigma_c^*}{k_p f_1}\left(\frac{\theta x}{h_2} + 1\right)^{\frac{2k_p f_1}{\theta}} + \frac{\sigma_c - \sigma_c^*}{k_p} - \frac{C_1 + f_1\sigma_c}{k_p f_1} \tag{28}$$

$$\sigma_{yg} = \sigma_y = \left(\frac{C_1}{f_1} + \sigma_c^*\right)\left(\frac{\theta x}{h_2} + 1\right)^{\frac{2kpf_1}{\theta}} + \sigma_c - \sigma_c^* - \frac{M_0\theta}{H}(x_0 - x) - \frac{C_1}{f_1} \quad (29)$$

To find the width of the inelastic zone (x_0), we assume that the peak abutment pressure P at the elastic and plastic interface ($x = x_0$) is

$$P = K\gamma H_1 \quad (30)$$

where K is the peak abutment pressure coefficient, γ is the average overburden density (N/m^3), and H_1 is the coal seam depth (m).

Based on the stress continuous condition, the abutment pressures at the elastic and plastic interface ($x = x_0$) are equal; substituting Equation (30) into Equation (29), the width of the inelastic zone can be derived as follows.

$$x_0 = \frac{H}{\theta}\left\{\left[\left(K\gamma H_1 + \frac{C_1}{f_1} - \sigma_c + \sigma_c^*\right)\left(\frac{f_1}{C_1 + f_1\sigma_c^*}\right)\right]^{\frac{\theta}{2kpf_1}} - 1\right\} \quad (31)$$

The width of the crushed zone (x_1) is,

$$x_1 = \frac{H}{\theta}\left\{\left[\left(K\gamma H_1 + \frac{C_1}{f_1} - \sigma_c + \sigma_c^*\right)\left(\frac{f_1}{C_1 + f_1\sigma_c^*}\right)\right]^{\frac{\theta}{2kpf_1}} - 1\right\} - \frac{\sigma_c - \sigma_c^*}{M_0\theta}H \quad (32)$$

Elastic Mechanics Model

Coal in the elastic zone has a single elastic stress distribution that shows high peak stress at the peak abutment pressure location. The ratio of lateral stress to abutment pressure is constant. In the whole elastic zone, coal is under an elastic compression condition. Therefore, as shown in **Figure 3B**, the stress equilibrium condition with $\sum F_X = 0$ and shearing stress $T' = f\sigma_y$ of a differential unit in the elastic zone of coal is

$$\left(\sigma_x + d\sigma_x\right)H + 2\left(f\sigma_y\right)dx - \sigma_x H = 0 \quad (33)$$

The lateral stress and vertical stress in the elastic zone have the following relationship

$$\sigma_y = \beta\sigma_x \quad (34)$$

where β is the lateral stress coefficient.

For consideration of the friction resistance, $T'\big|_{x=x_0} = K\gamma H_1$ and $T'\big|_{x=x_0+x_3} = 0$, it is reasonable to assume that

$$f = \frac{(x_0 + x_3 - x)f_1}{x_3} \quad (35)$$

where x_3 is the width of the elastic zone (m).

Substituting Equations (34) and (35) into Equation (33) and substituting the boundary condition $\sigma_x|_{x=x_0} = \frac{K\gamma H_1}{\beta}$, the abutment pressure in the elastic zone can be derived by the following equation.

$$\sigma_y = K\gamma H_1 e^{\frac{\beta f_1}{Hx_3}(x_0 - x)(2x_3 + x_0 - x)} \quad (36)$$

When $x = x_0 + x_3$, substituting $\sigma_y\big|_{x=x_0+x_3} = \gamma H_1$ into Equation (36), the width of the elastic zone can be calculated by the following equation.

$$x_3 = \frac{H}{\beta f_1}\ln K \quad (37)$$

PARAMETRIC ANALYSIS OF ABUTMENT PRESSURE

Underground coal ribs at a certain depth present remarkable strain-softening characteristics. Coal in front of the mining face will have an inelastic zone (crushed zone and plastic zone) and an elastic zone. The discussions in section Elastic-Plastic Strain-Softening Model show that the stress change gradient in the plastic zone is larger than in the crushed zone. The width of the plastic zone has nothing to do with the peak abutment pressure and only relates to the uniaxial compression strength, residual strength, mining depth, softening modulus, and deformation angle. However, the width of the crushed zone relates to the peak abutment pressure, the cohesion between coal and the roof and floor, and the friction coefficient. Discussions are made in this study on the impacts of the parameters on the abutment pressure. Taking the longwall panel at No. 5 coal of Dongjiahe Coal Mine in Chenghe mine field as an example, **Table 1** shows the basic mechanical parameters. Parametric analysis will be conducted on these parameters.

Mining Depth

Substituting the parameters listed in **Table 1** into Equations (20), (29), (31), (32), (36), and (37) with four mining depths of 200, 300, 400, and 500 m, the abutment pressure and the widths of different zones can be calculated. **Figure 4** shows the abutment pressure curves vs. mining face location at various mining depths.

It can be discovered from **Figure 4** that the widths of the crushed zone and inelastic zone increase by a logarithmic law with the increase in mining depth, and the mining depth has no impacts on the widths of the plastic zone and elastic zone. And at the same time, the abutment pressure changes at the crushed zone are identical. However, the peak abutment pressure increases with the increase in mining depth.

TABLE 1 | Basic mechanical parameters.

θ (°)	K	γ (KN/m^3)	f_1	σ_c (MPa)	σ_c^* (Mpa)	k_p	C_1 (MPa)	H (m)	β
2	3	22	0.2	10	$\sigma_c/8$	3	0.25	3.5	0.8

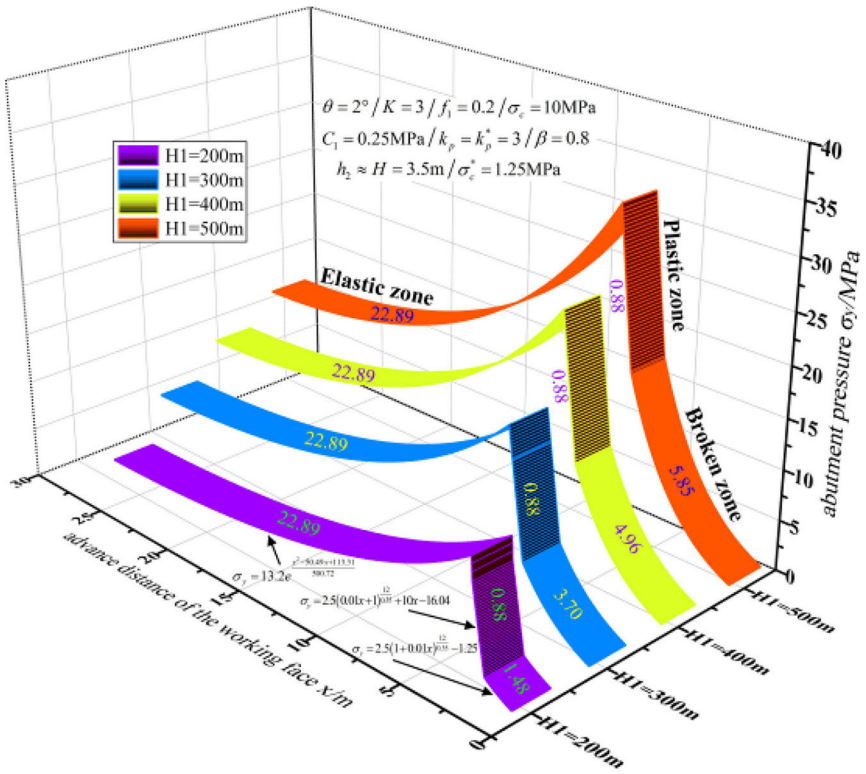

FIGURE 4 | Impacts of mining depth on abutment pressure.

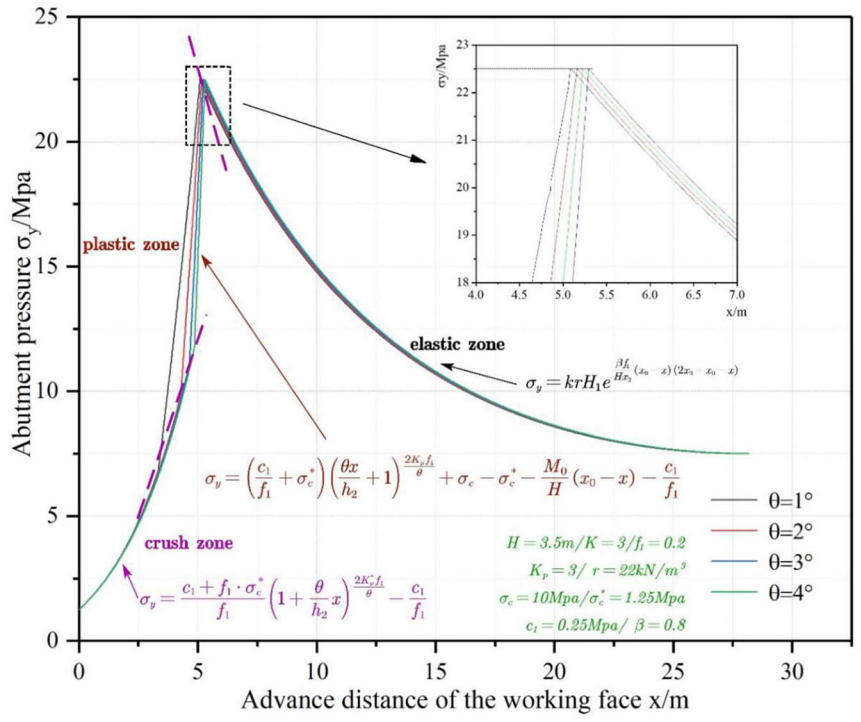

FIGURE 5 | Impacts of deformation angle on abutment pressure.

Deformation Angle

Four different deformation angles, i.e., 1°, 2°, 3°, and 4°, are substituted into the model to study the impacts on the abutment pressure. **Figure 5** shows the abutment pressure curves vs. mining face location at various deformation angles.

It can be discovered from **Figure 5** that the deformation angle has no impact on the widths of the elastic and inelastic zones. By substituting the deformation angle into the theoretical formula, it can be seen that when the deformation angle $\theta = 1°$, the width of the crushed zone is 3.34 m, and the width of the plastic zone is 1.76 m; when the deformation angle $\theta = 2°$, the width of the crushed zone is 4.28 m, and the width of the plastic zone is 0.88 m; when the deformation angle $\theta = 3°$, the width of the crushed zone is 4.64 m, and the width of the plastic zone is 0.59 m; when the deformation angle $\theta = 4°$, the width of the crushed zone is 4.85 m, and the width of the plastic zone is 0.44 m. The width of the crushed zone increases logarithmically with increase in the mining depth, and the width of the plastic zone decreases following a power law with increase in the mining depth. The abutment pressure curves at different deformation angles are similar, and the abutment pressure curves at the crushed zone and elastic zone almost overlap each other, which indicates that the deformation angle has no impact on abutment pressure.

Peak Abutment Pressure Coefficient

To study the impacts of the peak abutment pressure coefficient on the abutment pressure, four different peak abutment pressure coefficients, i.e., K = 2, 3, 4, and 5, are discussed. **Figure 6** shows the abutment pressure curves vs. mining face location at various peak abutment pressure coefficients.

It can be discovered from **Figure 6** that the widths of the crushed zone and inelastic zone increase following a logarithmic law with the increase in peak abutment pressure coefficient, and the width of the elastic zone increases following a parabolic law with the increase in peak abutment pressure coefficient. The peak abutment pressure coefficient has no impact on the width of plastic zone. At the same time, the abutment pressure increases remarkably with the increase in the peak abutment pressure coefficient.

Friction Coefficient

The impacts of the friction coefficient on the abutment pressure are discussed for four different friction coefficients, i.e., $f_1 = 0.1$, 0.2, 0.3, and 0.4. **Figure 7** shows the abutment pressure curves vs. mining face location at various friction coefficients.

It can be discovered from **Figure 7** that the widths of the crushed zone and inelastic zone decrease following a logarithmic

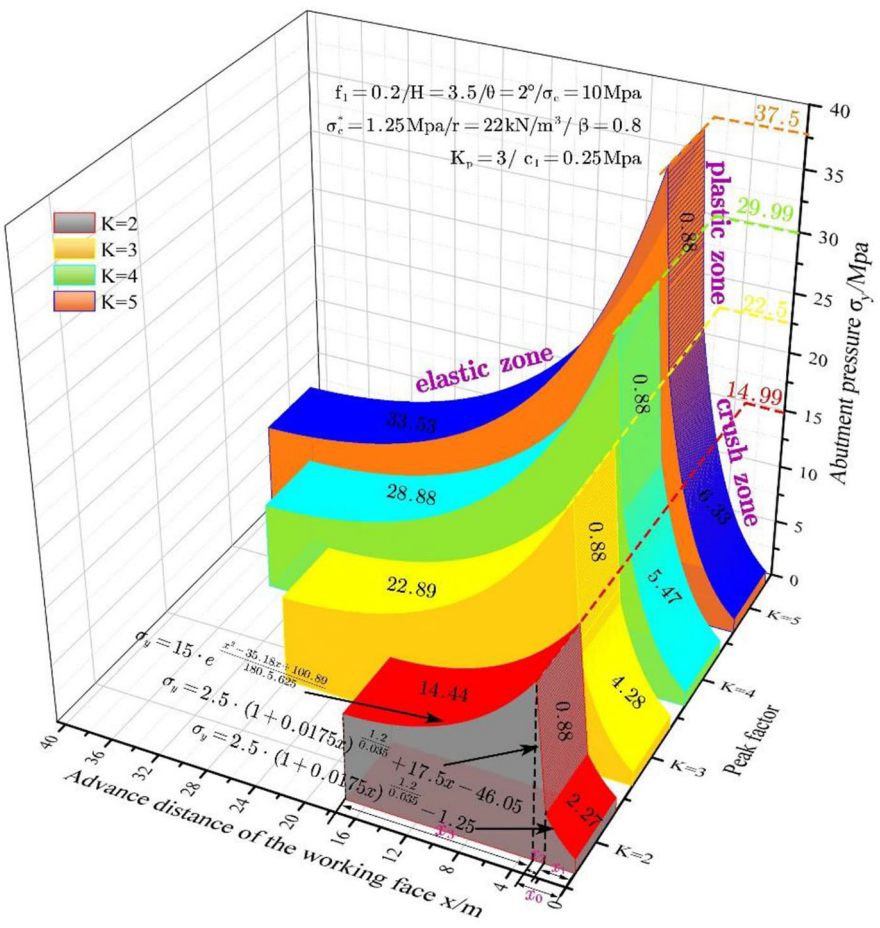

FIGURE 6 | Impacts of peak abutment pressure coefficient on abutment pressure.

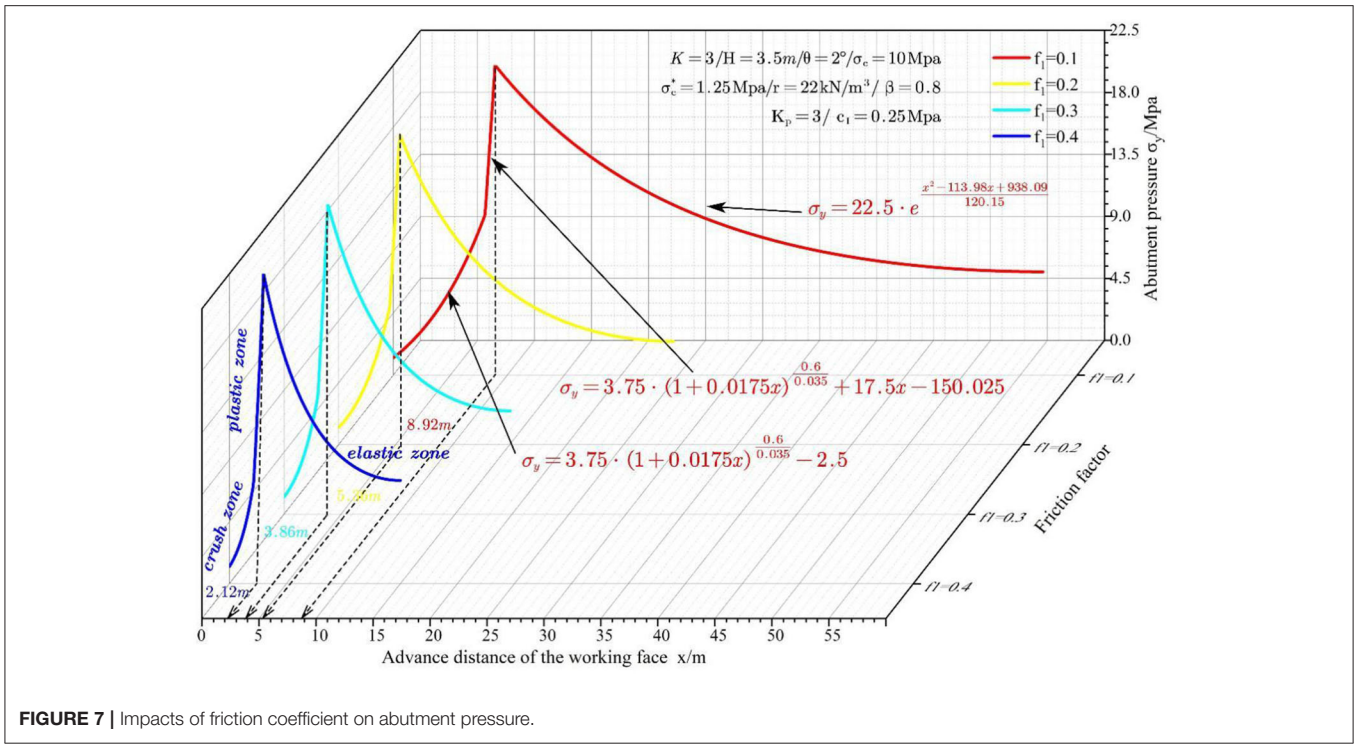

FIGURE 7 | Impacts of friction coefficient on abutment pressure.

law with the increase in friction coefficient. The friction coefficient has no significant impact on the width of the plastic zone, while it has a remarkable impact on the width of the elastic zone. At the same time, the abutment pressure curve shifts to the left as the friction angle increases. The friction coefficient is only related to the lithology of the coal, roof, and floor, and the roughness of the interface. The deformation of coal has a very small influence on friction angle.

Cohesion

Four different cohesions, i.e., 0.24, 0.48, 0.72, and 0.96 MPa, are substituted into the model to study the impacts on the abutment pressure. **Figure 8** shows the abutment pressure curves vs. mining face location at various cohesions.

It can be discovered from **Figure 8** that the widths of the crushed zone and the inelastic zone decrease following a logarithmic law with the increase in cohesion. The cohesion has no significant impact on the width of the plastic zone and elastic zone. At the same time, the abutment pressure curve shifts to the left as the cohesion increases. The cohesion relates to the bonding condition between coal and the roof/floor and the relative slippage at the interface.

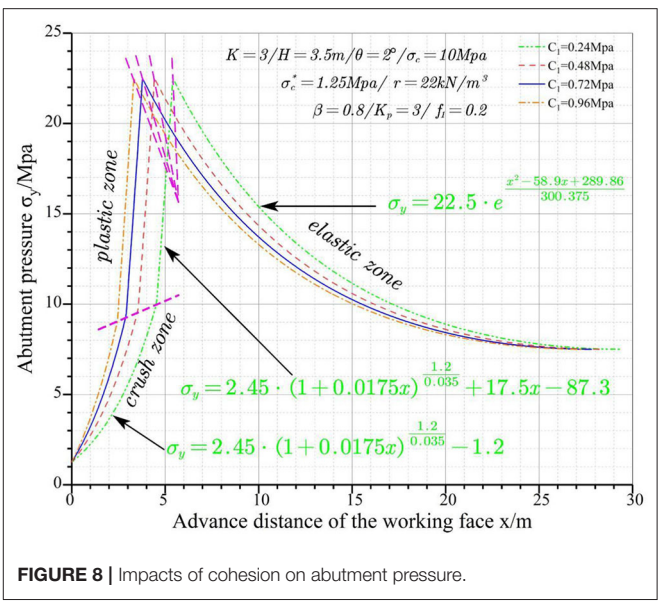

FIGURE 8 | Impacts of cohesion on abutment pressure.

Uniaxial Compression Strength

To study the impacts of the UCS on the abutment pressure, four different UCS values, i.e., $\sigma_c = 6, 9, 12$, and 15 MPa, are discussed. **Figure 9** shows the abutment pressure curves vs. mining face location at various UCS values.

It can be discovered from **Figure 9** that the widths of the crushed zone and inelastic zone decrease almost linearly with the increase in UCS. The width of the plastic zone increases almost linearly with the increase in UCS. The UCS has no significant impact on the width of the elastic zone. At the same time, the abutment pressure curve shifts to the left as the UCS increases.

Mining Height

Four mining heights, i.e., 2, 3, 4, and 5 m, are substituted into the model to study the impacts on the abutment pressure. **Figure 10** shows the abutment pressure curves vs. mining face location at various mining heights.

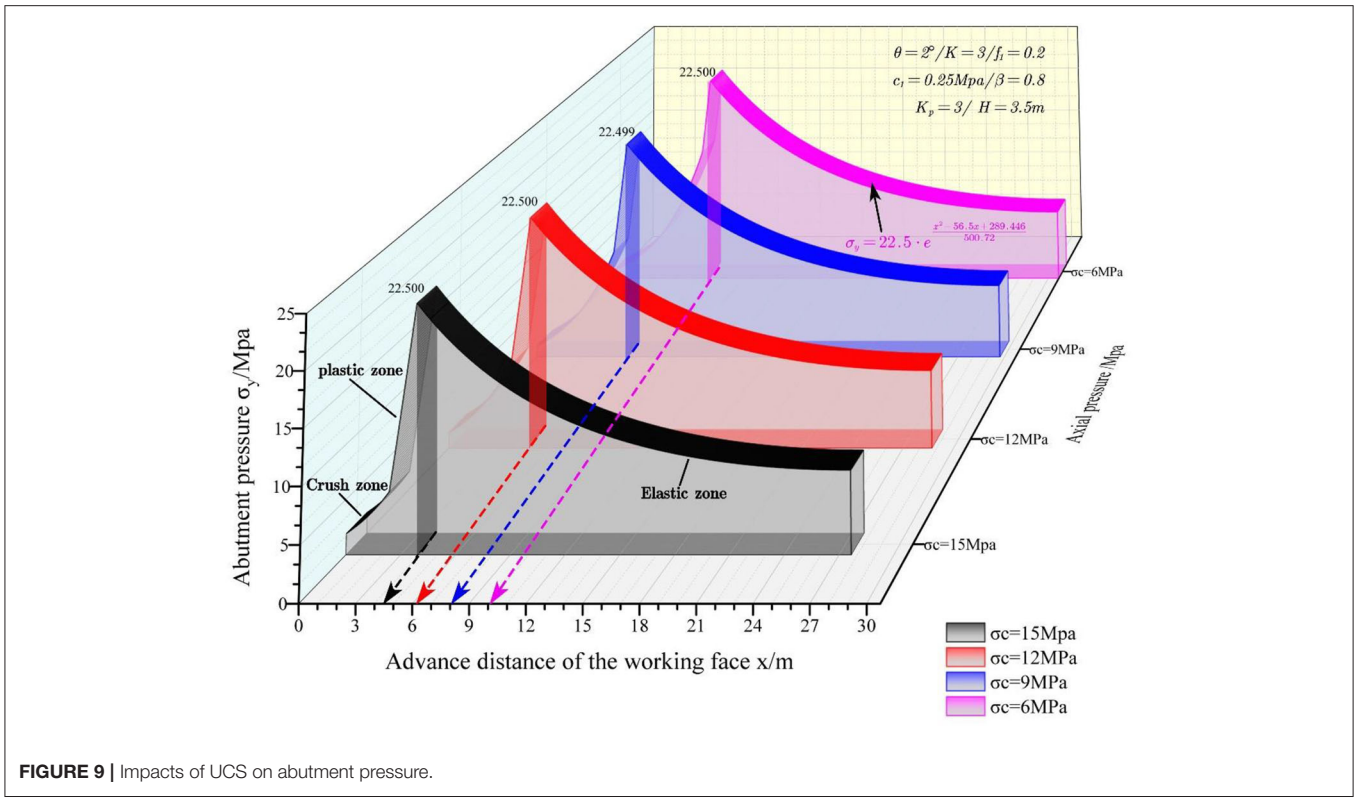

FIGURE 9 | Impacts of UCS on abutment pressure.

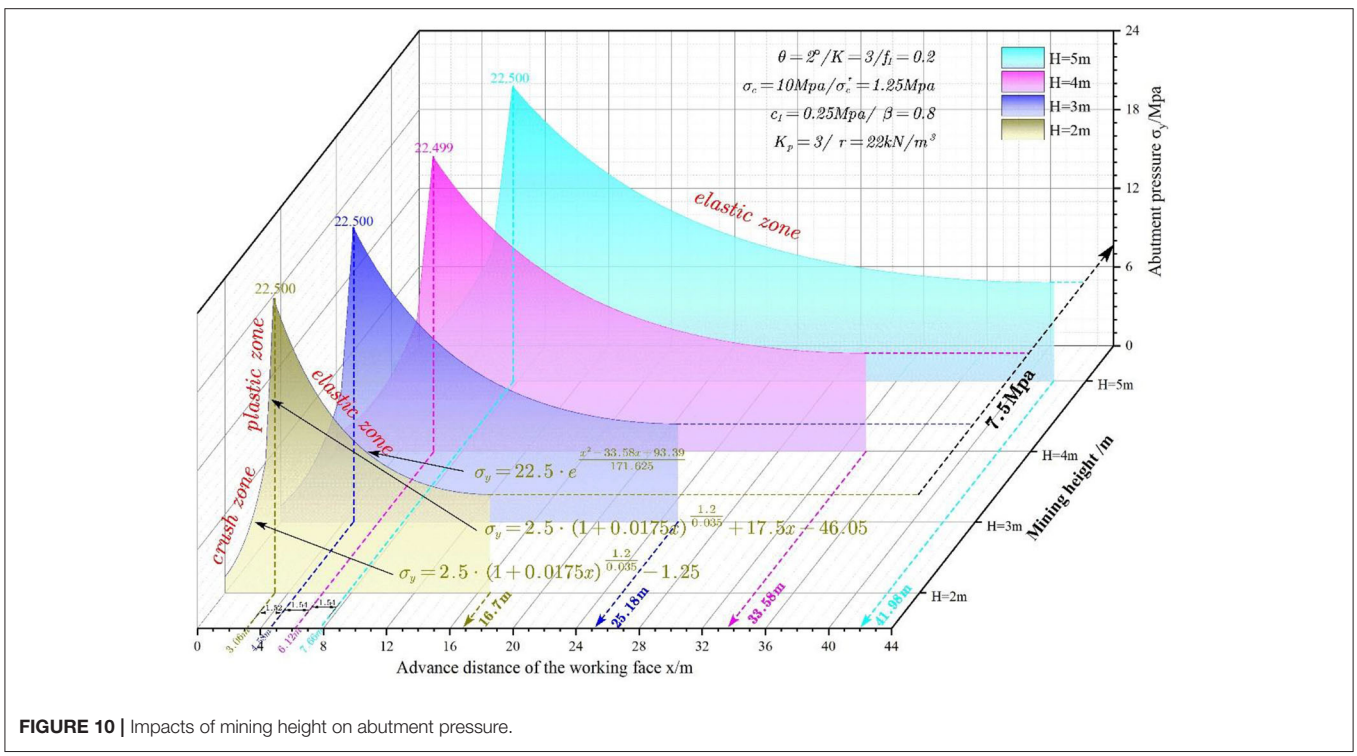

FIGURE 10 | Impacts of mining height on abutment pressure.

It can be discovered from **Figure 10** that the widths of the crushed zone, plastic zone, inelastic zone, and elastic zone increase linearly with the increase in mining height. The width increase rate of the elastic zone is higher than those of the other three zones. The mining height has significant impacts on abutment pressure curves. The abutment

pressure curve shifts to the right rapidly as the mining height increases.

VERIFICATION

A case study has been conducted at No. 5 coal seam (denoted "No. 5 Coal") of Dongjiahe Coal Mine with field observations and measurements to verify the analytical model proposed in this study.

Longwall Panel Location and Mining Conditions

Dongjiahe Coal Mine is one of the major producing coal mines in Chenghe Coalfield in Shaanxi province. It was constructed and started to produce in December of 1980 and has a 40-year mining history. The coal seam is in the Taiyuan Group of the Upper Carboniferous system and the Shanxi Group of the Lower Permian system. Currently, the minable seams are No. 5 Coal and No. 10 Coal. No. 5 Coal is buried at a depth of about 173.64–420.04 m, and it is the major minable coal seam. No. 10 Coal is buried at a depth of about 190.5–452.5 m, and it is an unstable coal seam in which most of the seam can be mined. The coal mine utilizes slope access, with multiple mining elevations and uphill/downhill developments. The major mining seam now is No. 5 Coal, and its average thickness is 3.71 m.

Longwall panel 07 is at No. 5 Coal at Dongjiahe Coal Mine, is separated by a 30-m barrier pillar from panel 06 in the south, and is surrounded by solid coal in the north. Coal in this panel is completely developed with an average thickness of about 3.0 m. The surface elevations are about +644.2∼+680.7 m, while the panel elevations are about +255∼+273 m. The longwall panel is 910 m in strike direction and 114 m in dip direction. The coal seam is high in the south and low in the north, with coal seam being inclined by about 0°-15°. No. 5 Coal is at the upper section of the Taiyuan Group. The immediate roof is hard gray K4 medium sandstone with a thickness of 10.9–18.15 m and major components of quartz and silicon sludge cementing and with fairly developed cracks. The immediate floor is hard dark gray coarse sandstone with a thickness of 0.2–3.21 m and contains many mica plates and localized sandstone stripes. The main floor is K3 fine quartz sandstone or siltstone with a thickness of about 3.4–7.8 m.

The sizes of the headgate and tailgate are 3.4 × 2.8 m, and they are supported by bolt, mesh, anchor, and beam. The open cut excavates along the roof with a length of 114 m. Its cross-section is 6.6 × 3.0 m, and it is supported by bolt, mesh, anchor, and beam. This panel utilizes longwall retreat mining on the No. 5 Coal floor. ZY4600/18/42 shields are adopted for roof support. The roof above the gob area caves as mining advances.

Selection of Experiment Location

In order to obtain the stress distribution of the tailgate during retreat mining, an experiment was conducted at 80 m in front of the mining face in the tailgate of panel 07 at Dongjiahe Coal Mine. **Figure 11** shows a layout diagram of the actual measurement of coal pillar advance bearing pressure.

Vibration wire borehole stress gauges (XL-YSYLJ) (as shown in **Figure 11**) and data loggers were installed in the tailgate perpendicular to the gate road direction for monitoring the abutment pressure distribution during retreat mining. Three boreholes were prepared, with one vibration wire borehole stress gauge (XL-YSYLJ) for each borehole, which were located at 60, 80, and 100 m from the open cut. The depths of the boreholes were 10 m to avoid the influence of stress concentration around the tailgate. The spacing between each group of survey lines was 20 m, and the borehole was about 1.6 m above the floor.

The data were recorded once per cut (0.6 m) when the longwall face was <15 m from the survey station, once per two cuts (1.2 m) when the distance from the survey station to the longwall face was about 15–30 m, and once per four cuts (2.4 m) when the longwall face was more than 30 m from the survey station.

Abutment Pressure Measurements

Monitoring of the abutment pressure was conducted at the tailgate of the longwall panel. The data are processed to obtain

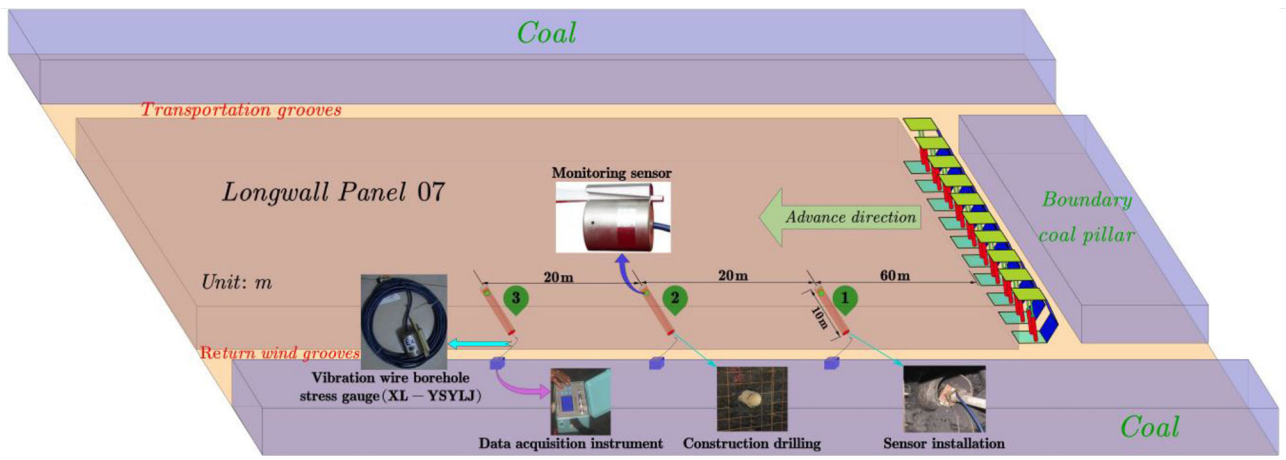

FIGURE 11 | Layout diagram of actual measurement of coal pillar advance bearing pressure.

the abutment pressure curves vs. distance of the working face and survey station. **Figure 12** shows the abutment pressure distribution curves.

According to **Figure 12A**, the borehole stress gauge readings decrease after installation. This is because the coal surrounding the borehole deforms and becomes loose when subject to the initial pressure of the borehole stress gauge. As the deformation of the borehole continues, the stress will achieve a stable condition; this stress is the initial stress of the borehole. For borehole stress gauge 1, the peak abutment pressure is 22.73 MPa, occurring at about 5.8 m from the longwall face (inelastic zone width), the stress concentration coefficient is 3.12, the abutment pressure influence zone is 27.8 m (width of the inelastic zone and elastic zone), and the apparent influence distance is 4.2 m (crushed zone). For borehole stress gauge 2, the peak abutment pressure is 19.72 MPa, occurring at about 5.4 m from the longwall face (inelastic zone width), the stress concentration coefficient is 2.92, the abutment pressure influence zone is 30.2 m (width of the inelastic zone and elastic zone), and the apparent influence distance is 4.8 m (crushed zone). For borehole stress gauge 3, the peak abutment pressure is 23.84 MPa, occurring at about 6.2 m from the longwall face (inelastic zone width), the stress concentration coefficient is 2.90, the abutment pressure influence zone is 28.6 m (width of the inelastic zone and elastic zone), and the apparent influence distance is 4.2 m (crushed zone). **Table 2** lists the data from the three stress gauges.

Comparison

Table 3 shows a comparison of the theoretical calculations and the field measurements. The theoretical fitting curve of the bearing pressure distribution of the working face can be drawn using the figures in **Table 3**, as shown in **Figure 12B**.

Relative error analysis was applied to compare the theoretical calculations and field measurements. The lower the relative error, the higher the precision. It is shown in **Table 3** that the abutment pressure distribution and the widths of the inelastic zone and the elastic zone coincide with the field measurements very well, which indicates that the theoretical model has very high accuracy.

CONCLUSIONS

Coal near the mining face presents remarkable strain-softening characteristics. The coal in front of the mining face has a crushed zone, a plastic zone, and an elastic zone when subjected to overburden stress.

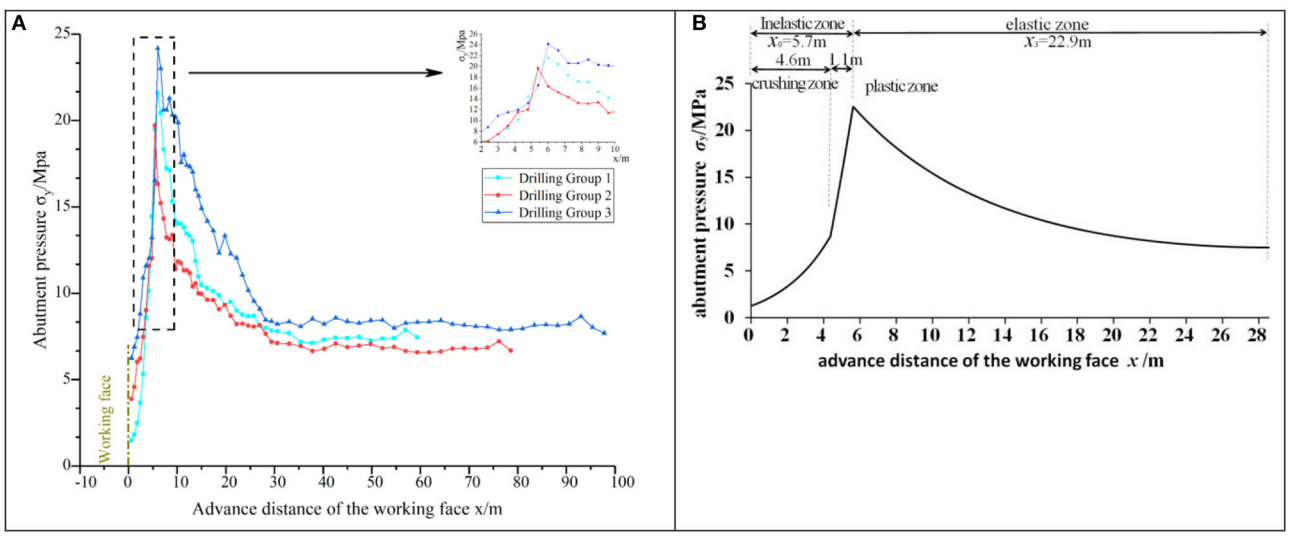

FIGURE 12 | Abutment pressure distribution curve. **(A)** Field monitoring of abutment pressure distribution. **(B)** Theoretical fit curve of the abutment pressure distribution.

TABLE 2 | Abutment pressure at different survey stations.

Hole No.	Distance between survey station and open cut L/m	Apparent influence distance x_1/m	Peak abutment pressure location x_0/m	Abutment pressure influence range ($x_0 + x_3$)/m	Initial stress P_0/MPa	Peak abutment pressure P/MPa	Abutment pressure coefficient K/MPa
1	60	4.2	5.8	27.8	7.28	22.73	3.12
2	80	4.8	5.4	30.2	6.75	19.72	2.92
3	100	4.2	6.2	28.6	8.22	23.84	2.90
Avg.	–	4.4	5.8	28.9	7.42	22.10	2.98

TABLE 3 | Comparison of theoretical calculations and field measurements.

	Crushed zone x_1/m	Plastic zone x_2/m	Inelastic zone x_0/m	Elastic zone x_3/m	Initial stress P_0/MPa	Peak abutment pressure P/MPa	Abutment pressure coefficient K/MPa
Theoretical	4.6	1.1	5.7	22.9	7.50	22.5	3.00
Measured	4.4	1.4	5.8	23.1	7.42	22.1	2.98
Error/%	4.55	21.43	1.72	0.87	1.08	1.81	0.67

The elastic deformation stage, plastic strain-softening stage, and flow deformation stage of the elastic–plastic strain-softening model correspond to the elastic zone, plastic zone, and crushed zone of the coal rib, respectively. Our abutment pressure model was built based on the strain-softening characteristics of coal. The equations calculating abutment pressure and the widths of the elastic zone and inelastic zone (crushed zone and plastic zone) were derived.

Parametric analysis was conducted on the abutment pressure model. The strain change rate in the plastic zone is larger than in the crushed zone. The width of the plastic region is independent of the peak abutment pressure, but it is dependent on the UCS, residual strength, mining height, softening modulus, and deformation angle.

A case study was carried out at longwall panel 07 of No. 5 coal seam in Dongjiahe Coal Mine to verify the analytical model. The abutment pressure distribution and the widths of the elastic and inelastic zones under the limit equilibrium condition were calculated based on the relevant parameters. The theoretical results were compared with the field monitoring data and showed a very good fit. It is thus proven that the proposed analytical model has high accuracy, and the feasibility of the model is verified. The study results can provide guidance for similar engineering applications.

PATENTS

This manuscript has produced five invention patents.

Firstly, the invention patent "Monitoring and Measuring Device and Installation and Measuring Method for Multi-point Separation of Roadway Surrounding Rock Mass" (patent number: ZL 2013 10614482.5) is used to monitor the deformation of the plastic zone of a coal and rock mass. Secondly, according to the theory of the manuscript, theoretical calculation is carried out. Then, based on the theoretical calculation results, the width of the artificial or natural coal pillar in the retaining roadway is used to select the length of the bolt and cable used. Four patents have been granted as follows: "A Supporting Method for Setting up Double Roadways in One-time Driving with U-type Ventilation" (ZL 2016 10459175.8); "A Production Line for Double Roadway Excavation in One-time Excavation" (ZL 2016 10459072.1); "A Reinforcement Method of Narrow Coal Pillar in Gob-side Driving Roadway" (ZL 2016 10536888.X); "Anchorage Structure and Reinforcement Method of Narrow Coal Pillar in Gob-side Retaining Roadway" (ZL 2016 10537791.0).

DATA AVAILABILITY STATEMENT

The raw data supporting the conclusions of this article will be made available by the authors, without undue reservation.

AUTHOR CONTRIBUTIONS

AL and QMa: conceptualization, writing—original draft preparation, and writing—review and editing. AL: methodology, project administration, and funding acquisition. QMa: software. AL, LM, and LK: validation. AL and QMu: data curation. AL and JC: supervision. All authors: contributed to the article and approved the submitted version.

FUNDING

This research was funded by the Natural Science Basic Research Program of Shaanxi (2020JZ-52); Key Laboratory of Coal Resources Exploration and Comprehensive Utilization, Ministry of Land and Resources (KF2018-2); the Basic Science Research Project of Shaanxi Province (2014JM2-5064); the National Natural Science Foundation of China (41402265); the Basic Research Project of Shaanxi Natural Science Foundation of China (2016JM4014); and the China Postdoctoral Science Foundation (2016M590961).

ACKNOWLEDGMENTS

The authors heartily thank the above fund projects, without support of which the data and field test equipment needed to complete this study could not have been obtained.

REFERENCES

1. Yuan WB, Chen J. Analysis of plastic zone and loose zone around opening in softening rock mass. *J China Coal Soc.* (1986) **11**:77–85.

2. Fellgett MW, Kingdon A, Waters CN, Field L, Ougier-Simonin A. Lithological constraints on borehole wall failure; a study on the pennine coal measures of the United Kingdom. *Front Earth Sci.* (2019) **7**:163. doi: 10.3389/feart.2019.00163

3. Hou CJ, Ma NJ. Stress in in-seam roadway sides and limit equilibrium zone. *J China Coal Soc*. (1989) **14**:21–9.
4. Islavath SR, Deb D, Kumar H. Development of a roof-to-floor convergence index for longwall face using combined finite element modelling and statistical approach. *Int J Rock Mech Min Sci.* (2020) **127**:104221. doi: 10.1016/j.ijrmms.2020.104221
5. Ma NJ. A study of plastic zone around openings in the softening rock mass. *J Fuxin Min Inst: Nat Sci*. (1995) **14**:18–21.
6. Yadav A, Behera B, Sahoo SK, Singh GSP, Sharma S. An approach for numerical modeling of gob compaction process in longwall mining. *Min Metall Exp*. (2020) **37**:631–49. doi: 10.1007/s42461-020-00182-0
7. Zheng GR, Yang WB. A calculation method of the failure zone width of the coal-wall of roadway in seams. *J China Coal Soc*. (2003) **28**:37–40. doi: 10.1007/s11769-003-0003-x
8. Yang XJ, Wang EY, Ma XG, Zhang GF, Huang RF, Lou HP. A case study on optimization and control techniques for entry stability in non-pillar longwall mining. *Energies*. (2019) **12**:391. doi: 10.3390/en12030391
9. Li SQ, Pan CL, Wang WJ. Analysis of plastic region of sidewalls in coal drifts reinforced by association of rock bolt and grouting. *J Hunan Univ Nat Sci Ed*. (2007) **22**:5–8.
10. Huang QX, Cao J. Research on coal pillar malposition distance based on coupling control of three-field in shallow buried closely spaced multi-seam mining, China. *Energies*. (2019) **12**:462. doi: 10.3390/en12030462
11. Yao QL, Zheng CK, Tang CJ, Xu Q, Li XH. Experimental investigation of the mechanical failure behavior of coal specimens with water intrusion. *Front Earth Sci.* (2020) **7**:348. doi: 10.3389/feart.2019.00348
12. Xu GA, Jing HW, Ding SX, Niu SJ, Ma B. Evolution rules of stress and displacement for narrow coal pillars between double gob- side entries. *J Min Saf Eng*. (2010) **27**:160–5. doi: 10.1145/1806596.1806616
13. Xie GX, Yang K, Liu QM. Study on distribution laws of stress in inclined coal pillar for fully-mechanized top-coal caving face. *China J Rock Mech Eng*. (2006) **25**:545–9. doi: 10.3321/j.issn:1000-6915.2006.03.017
14. Li A, Liu Y, Mou L. Impact of the panel width and overburden depth on floor damage depth in no. 5 coal seam of Taiyuan Group in Chenghe mining area. *Electron J Geotech Eng*. (2015) **20**:1603–17.
15. Jayanthu S, Singh TN, Singh DP. Stress distribution during extraction of pillars in a thick coal seam. *Rock Mech Rock Eng*. (2004) **37**:171–92. doi: 10.1007/s00603-003-0003-2
16. Gong SC (editor). Study on the plastic displacement solution in the coal-side. In: *Theory and Practice of Western Mine Construction Projects Proceedings*. Xuzhou: China University of Mining and Technology Press (2009). p. 264–8.
17. Qu Q. Study on distressing technology for a roadway driven along goaf in a fully mechanized top coal caving face. *J Coal Sci. Techno.* (2003) **9**:33–7.
18. Wang Z, Yin L, Chen J, Ma K. Research on distribution law of advanced abutment pressure in deep soft rock working face. *Grotech Geol Eng.* (2019) **37**:4089–97. doi: 10.1007/s10706-019-00895-0
19. Fairhurst C. General report: deformation, yield, rupture and stability of excavations at depth in rock. *Int Soc Rock Mech Rock Eng.* (1989) 98:1103–14.
20. Xue Y, Dang FN, Gao ZZ, Du F, Ren J, Chang X, et al. Deformation, permeability and acoustic emission characteristics of coal masses under mining-induced stress paths. *Energies.* (2018) **11**:2233. doi: 10.3390/en11092233
21. Zhang JW. Stability of split-level gob-side entry in ultra-thick coal seams: a case study at xiegou mine. *Energies.* (2019) **12**:628. doi: 10.3390/en12040628
22. Zhou XP, Wang FH, Qian QH, Zhang BH. Zonal fracturing mechanism in deep crack-weakened rock masses. *Theor Appl Fract Mech*. (2008) **50**:57–65. doi: 10.1016/j.tafmec.2008.04.001
23. Ma XG, He MC, Wang J, Gao YB, Zhu DY, Liu YX. Mine strata pressure characteristics and mechanisms in gob-side entry retention by roof cutting under medium-thick coal seam and compound roof conditions. *Energies.* (2018) **11**:2539. doi: 10.3390/en11102539
24. Sellers EJ, Klerck P. Modeling of the effect of discontinuities on the extent of the fracture zone surrounding deep tunnels. *Tunn Undergr Sp Tech*. (2000) **15**:463–9. doi: 10.1016/S0886-7798(01)00015-3
25. Ren L, Xie HP, Xie LZ, Ai T. Preliminary study on strength of cracked rock specimen based on fracture mechanics. *Eng. Mech.* (2013) **30**:156–62. doi: 10.6052/j.issn.1000-4750.2011.07.0464
26. Xu SP, Mao XB, Zhang DS. Study on pillar's plastic zone based on elastic visco-plastic theory. *J Liaoning Tech Univ*. (2006) **25**:194–6.
27. Huang BX, Liu CY, Zhen BS, Cheng QY. Distribution abutment pressures on laneway pillars for super-wide isolated fully mechanized top coal caving face. *China J Rock Mech Eng.* (2007) **29**:932–7. doi: 10.1016/S1872-2067(07)60020-5
28. Li SQ, Wang WJ, Pan CL, Peng B. Stability analysis of sidewalls of horizontal coal drifts. *J Hunan Univ Nat Sci Ed*. (2008) **23**:1–4.
29. Zhou XP, Qian QH, Zhang BH, Zhang YX. The mechanism of the zonal disintegration phenomenon around deep spherical tunnels. *Eng Mech*. (2010) **27**:69–75. doi: 10.3724/SP.J.1011.2010.01138
30. Zhang JW, Li YL. Coal strength development with the increase of lateral confinement. *Energies.* (2019) **12**:405. doi: 10.3390/en12030405
31. Yu YX, Hong X, Chen FF, Chen F. Study on load transmission mechanism and limit equilibrium zone of coal wall in extraction opening. *J China Coal Soc*. (2012) **37**:1630–5. doi: 10.1007/s11783-011-0280-z

Conflict of Interest: LK was employed by Shaanxi Coalfield Geophysical Prospecting and Surveying Group Co. Ltd.

The remaining authors declare that the research was conducted in the absence of any commercial or financial relationships that could be construed as a potential conflict of interest.

APPENDIX

The proof process of Equation (9):

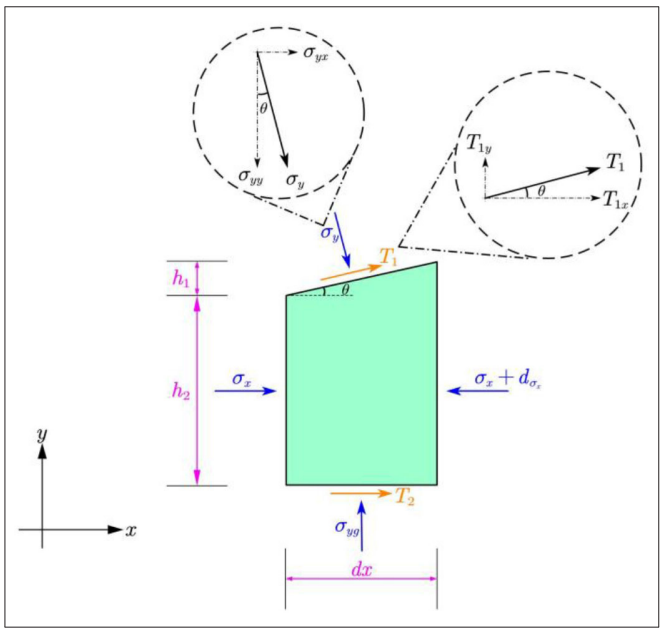

As shown in the figure above, the mechanical analysis of σ_y, T_1 and B is carried out:

$$T_{1x} = T_1 . \cos\theta$$
$$\sigma_{yx} = \sigma_y . \sin\theta$$

According to equation (5), the equilibrium equation can be listed:

$$\sigma_x.(h_2 + x.\tan\theta) + \sigma_y.\sin\theta.\frac{dx}{\cos\theta} + T_1\cos\theta.\frac{dx}{\cos\theta} + T_2.dx = (\sigma_x + d_\sigma).[h_2 + (x + dx).\tan\theta])$$

The formula (9) is obtained by simplifying the above formula.

frontiers in Physics

ORIGINAL RESEARCH
published: 26 August 2020
doi: 10.3389/fphy.2020.00327

Stress Evolution in Punch-Through Shear Tests: A Numerical Study Based on Discrete Element Method

Jie Liu[1]*, *Wen Wan*[2], *Yanlin Zhao*[2] and *Xiang Fan*[3]

[1] Department of Building Engineering, Hunan Institute of Engineering, Xiangtan, China, [2] School of Resource, Environment and Safety Engineering, Hunan University of Science and Technology, Xiangtan, China, [3] School of Highway, Chang'an University, Xi'an, China

The discrete element method is adopted to investigate the failure process in punch-through shear tests. The numerical tests agree well with the laboratory tests on crack propagation sequence and the influence of confining stress on effective shear fracture toughness. More importantly, the numerical tests indicate that the increase in axial force first causes stress concentrations. When the stresses reach critical values, cracks initiate and the concentrated stresses dissipate. With further increase in axial displacement, the axial force may fluctuate, accompanied with crack development. In addition, the increase in confining stress promotes the critical values of the concentrated stresses before crack propagation. Thus, the numerical tests show that the increase in confining stress promotes the effective shear fracture toughness and restrains the propagation of tensile cracks.

Keywords: effective shear fracture toughness, failure process, confining stress, crack propagation, fluctuation

OPEN ACCESS

Edited by:
Longjun Dong,
Central South University, China

Reviewed by:
Allbens Picardi Faria Atman,
Federal Center for Technological Education of Minas Gerais, Brazil
Davy Dalmas,
UMR5513 Laboratoire de Tribologie et Dynamique des Systèmes (LTDS), France

***Correspondence:**
Jie Liu
ljydslj@163.com

Specialty section:
This article was submitted to Interdisciplinary Physics, a section of the journal Frontiers in Physics

Received: *19 April 2020*
Accepted: *15 July 2020*
Published: *26 August 2020*

Citation:
Liu J, Wan W, Zhao Y and Fan X (2020) Stress Evolution in Punch-Through Shear Tests: A Numerical Study Based on Discrete Element Method. Front. Phys. 8:327. doi: 10.3389/fphy.2020.00327

INTRODUCTION

Rock masses containing many initial defects may be in complex geological conditions and subjected to various external loads [1–3]. Then, loads frequently cause stress concentrations and may further result in the opening (Mode I) and sliding (Mode II) displacements of the crack surfaces. In rock engineering, sliding (Mode II) is the commonest mode of failure [4]. Thus, many researchers have performed laboratory and numerical studies to investigate the shear fracture toughness (K_{IIC}), a critical index for shear (sliding) failure. For example, Rao et al. [4] conducted shear-box tests to determine the Mode II crack toughness and proposed that effective K_{IIC} decreases with the increase of both the specimen thickness. Timothy and Don [5] applied double-edge notched compression specimens to determine the Mode II fracture toughness and found that the ratio of K_{IIC} to K_{IC} (tensile fracture toughness) is ∼1.6. In addition, their study showed that shear force fluctuates near the peak points, and residual shear occurs. Similar fluctuations and residual shear were observed in the laboratory study, by applying punch-through shear tests [6]. Based on the calculation model by Watkins [7] and Golewski and Sadowski [8] proposed that the content of the fly-ash influences the K_{IIC} by performing electronic scanning tests and shear tests on concrete specimens. They further proposed an equation describing the critical force (corresponding to the shear crack initiation) and the shear fracture toughness. By performing compression tests on the cracked chevron-notched Brazilian Disc specimens, Ghanbari et al. [9] stated that the effective shear fracture toughness first increases and then decreases with the increase in temperature. Dehestani et al. [10, 11] applied crack Brazilian disc specimens to investigate the influence of wetting–drying cycles on the effective shear fracture toughness in neutral and acidic environments. They found that the increase in the

wetting–drying cycles decreases the effective shear fracture toughness. By conducting numerical and laboratory tests on the fine-grained marble specimens, Xu et al. [12] proposed that the optimal height–diameter ratio is 2. The above studies clearly show that many methods can measure the shear fracture tests. In addition, many factors, including confinement, geometric sizes, and test temperature, can influence the measured results. Besides the above methods, the punch-through shear test is the suggested method of the ISRM (International Society for Rock Mechanics) [13, 14]. By performing extensive laboratory tests, Backers et al. [6] and Backers and Stephansson [13] found that tensile crack may first form, and then shear planes initiate from the bottom tip of the notches. In addition, they proposed that the shear crack propagates in a stable way, and the effective shear fracture toughness closely relates to the peak axial compression force and the confinement. The conclusion on shear crack propagation agrees well with the laboratory tests by Golewski and Sadowski [8] and Wu et al. [15].

Roux et al. [16] and Patinet et al. [17] stated that the effective toughness is the average of the local toughness in the weak pinning regime, characterized by regular propagation. However, in the strong pinning regime, a much higher effective toughness, accompanied with unstable propagation, is observed. The shear fracture in the specimen gradually propagates [6, 13]. However, the stress evolution in the rock bridge, remaining unclear, may successfully explain the above phenomena. However, the stress measurement in the laboratory test is approximately impossible [6]. The numerical method may shed some light on how to correlate fractures to stress evolution. For example, Liu et al. [18] measured the shear fracture toughness using the rock failure process analysis. Moon et al. [19] and Moon and Oh [20] successfully applied discrete element method to measure the tensile fracture toughness. Recent, by applying finite element method, Aminzadeh [21] et al. and Ma et al. [22] investigated the shear behavior of the rock specimens. Especially, among these methods, the discrete element method can record the crack development [23–25]. Thus, with the recent studies, using the measure circle logic to study stress evolution characteristics [15, 26–28], we applied Particle Flow Code 2D (PFC 2D) to relate the stress evolution to crack development in the punch-through tests.

NUMERICAL PREPARATION

Calibration

In the present article, the laboratory dates reported by Backers were referred [29] (**Table 1**). The uniaxial compression strength (UCS)/tensile strength (TS) ratio is higher than 14. To obtain this realistic ratio, the flat-joint model instead of the parallel bond model was adopted [30, 31]. This model mainly consists of particles and the flat-joint contacts. In this model, two groups of springs can provide the normal and the shear stiffness. The first group includes the normal stiffness of the particles (K_n) and the flat-joint contact (K_n'), respectively (**Figure 1A**). Correspondingly, the other group consists of the shear stiffness, K_s and K_s' (**Figure 1B**). When the normal stress between particles exceeds the TS, σ_b, the bond breaks in a tensile manner, and the bond fails (**Figure 1C**). The shear strength first follows the Coulomb criterion when the shear stress is relatively low:

$$\tau_c = c_b - \bar{\sigma} \tan \phi_b \tag{1}$$

where c_b and ϕ_b are the bond cohesion and the local friction angle.

When the shear stress increases to a critical value, the bond fails in a shear manner. However, residual shear stress remains because of the friction:

$$\tau_r = -\bar{\sigma} \tan \phi_r \tag{2}$$

where τ_r and ϕ_r are the residual friction strength and the residual friction angle. Thus, the flat-joint model can successfully simulate the post-peak behavior.

UCS and TS are two important parameters for rock fracture [30, 31]. Thus, by modifying bond cohesion, particle contact modulus, and bond modulus (**Table 2**), the elastic modulus and UCS were first calibrated according to the disciplines of trial and error tests [31]. Then, the TS was subsequently calibrated by modifying bond normal strength (**Table 2**). **Figure 2** shows the calibration results, using the uniaxial compression tests and the Brazil tensile tests. Clearly, a shear failure plane and a tensile plane form in the uniaxial compression test and Brazil tension test, respectively. The UCS and the TS are close to the laboratory results (**Table 1**).

TABLE 1 | Mechanical parameters.

	Elastic modulus (GPa)	UCS	TS	Effective KIIC (confining stress is 5 MPa)
Carrara marble	49	95–107 MPa	7 MPa	3.8–4.1 (MPa * $m^{1/2}$)
Simulated results	48.5	106.7 MPa	6.7 MPa	4.37 (MPa * $m^{1/2}$)
Error (%)	−1	−0.2 to 12.3	4.2	6.5–15

Numerical Model and Test Scheme

According to the suggested sizes of ISRM and the previous studies [13, 15, 32], the numerical model containing 16,865 particles and 45,632 flat-joint bonds was established (**Figure 3A**). Before loading, the lateral walls were servo-controlled to ensure the specified confinement. Then, the middle-upper wall was displacement-controlled to compress the specimen with a constant rate of 0.05 m/s. The studies by Goldhirsch and Goldenberg [33] and Goldenberg et al. [34] indicated that force chains appear in granular materials, and continuum theories may be valid for granular materials. In the PFC model (consisting of particles), contact forces that can form force chains can be computed. However, they cannot be directly transferred to a continuum model. Averaging procedures are necessary to make the step from the microscale to a continuum [35]. Thus, PFC 2D calculates the average stress in a measurement region using the following equation:

$$\overline{\sigma} = -\frac{1}{V} \sum_{N_c} F^{(c)} \otimes L^{(c)} \tag{3}$$

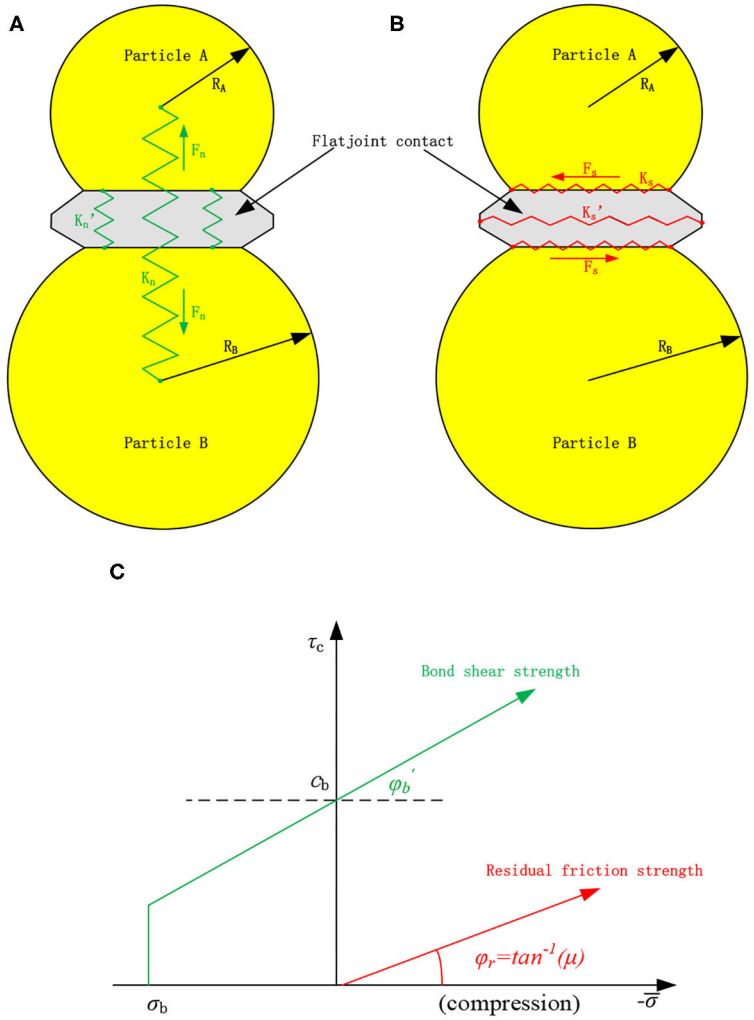

FIGURE 1 | Deformability and strength of a flat-joint contact. **(A)** normal stiffness, **(B)** shear stiffness, and **(C)** strength criterion.

TABLE 2 | Microparameters.

	Particle radius (mm)	Particle contact modulus (GPa)	Particle normal/shear stiffness	Bond modulus (GPa)	Bond normal/shear stiffness	Bond normal strength (MPa)	Bond cohesion (MPa)
Value	0.14–0.24	41	1.8	41	1.8	44	43

where $\bar{\sigma}$, V, N_c, $F^{(c)}$, $\otimes$, and $L^{(c)}$ are the average stress, the volume in 3D (area in 2D), the number of contacts in the measurement region or on its boundary, the contact force vector in the circle region, the outer product, and the branch vector joining the centroids of the two bodies in contact, respectively. In the loading process, overlapping measure circles with a radius of 1 mm (**Figure 3B**), covering more than six particles, were installed to record the horizontal (σ_h), vertical (σ_v), and shear stresses (τ_{xy}) in the specimen. Thus, the shear stress and the maximum principal stress, being equal to $\frac{\sigma_v+\sigma_h}{2}+\sqrt{(\frac{\sigma_v-\sigma_h}{2})^2+\tau^2}$, can be recorded in the loading process.

NUMERICAL RESULTS AND DISCUSSIONS

Comparison Between Numerical and Laboratory Results

Figure 4 shows the axial force–displacement curves in the laboratory tests [6] and the present numerical study with the confining stress of 5 MPa. In PFC 2D, the default thickness of the specimen is 1 m. Thus, the shear area in the model was 0.03 m^2. In the laboratory tests by Backers [32], the shear area was 0.00118 m^2. Thus, according to Equation 4 obtained by fitting the laboratory results [13, 32], for the same shear area, the

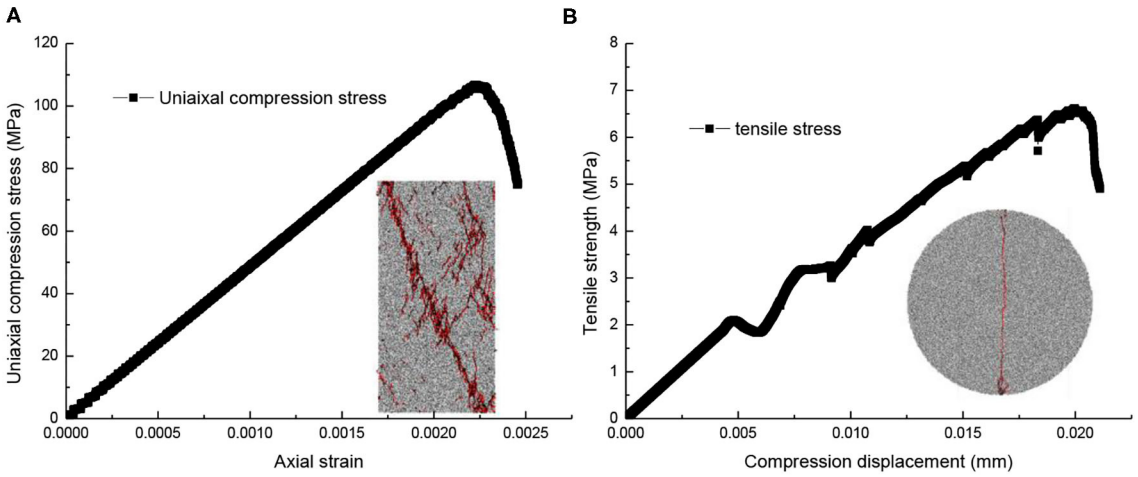

FIGURE 2 | Calibration results: **(A)** and **(B)** correspond to UCS and TS, respectively.

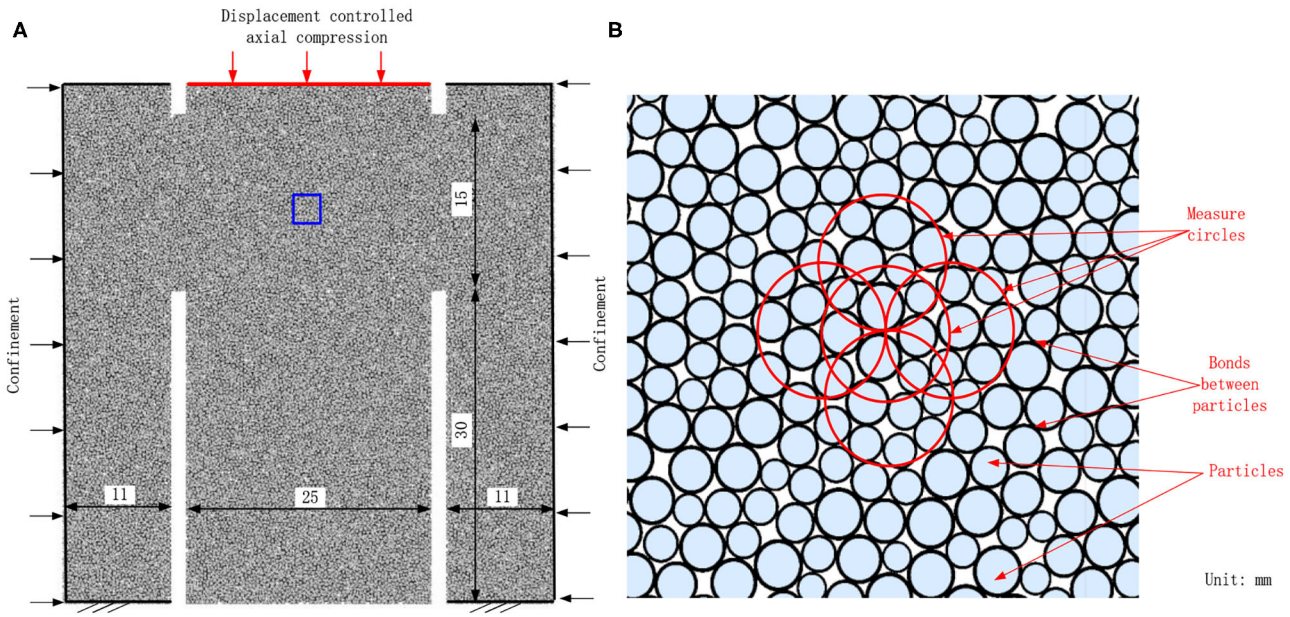

FIGURE 3 | Details of the numerical model: **(A)** is the geometry and the loading schematic of numerical model, and **(B)** is the magnified picture of the blue rectangle.

calculated effective shear fracture toughness is 4.37 MPa * $m^{1/2}$. This simulated effective shear fracture toughness is close to the laboratory results (**Table 1**). The above descriptions indicate that the laboratory axial force–displacement curve agrees well with the numerical axial force–displacement curve in the peak value. However, the axial force–displacement curve for the laboratory test is concave, which is different from the numerical curve. In the laboratory tests, the micropores are responsible for the concave curve in the early compression process of rock materials. However, in the PFC simulation, the intact bonds between particles before cracking may prevent the pore compaction [24]. Interestingly, similar to the previous studies [5, 6, 15], the axial compression force fluctuates near the peak. These fluctuations may relate to the shear crack propagation and the stress evolution in the shear process and deserve further investigation.

$$K_{IIC} = 0.0774F_{\max} - 0.0018P_c \quad (4)$$

where $F_{\max}$ and P_c are the peak axial force (kN) and the confinement (MPa), respectively.

The laboratory tests indicate that two tensile cracks, denoted in red lines in **Figure 5A**, first initiated from the inner tips of the lower notches. Subsequently, shear cracks, numbered 1 and denoted in pink lines, initiated from the outer tips of the

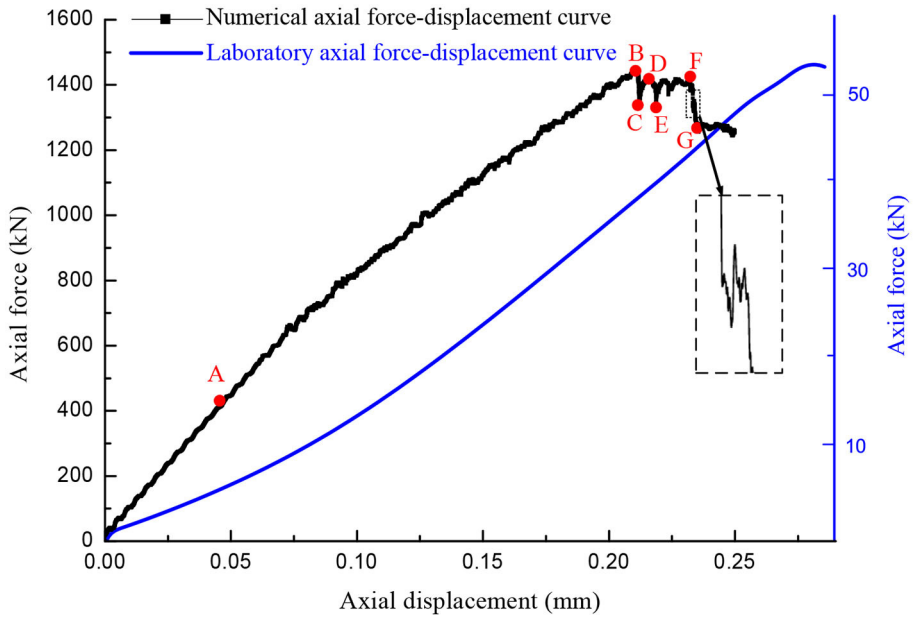

FIGURE 4 | Numerical and laboratory [6] axial compression forces and the monitor points on the numerical curve.

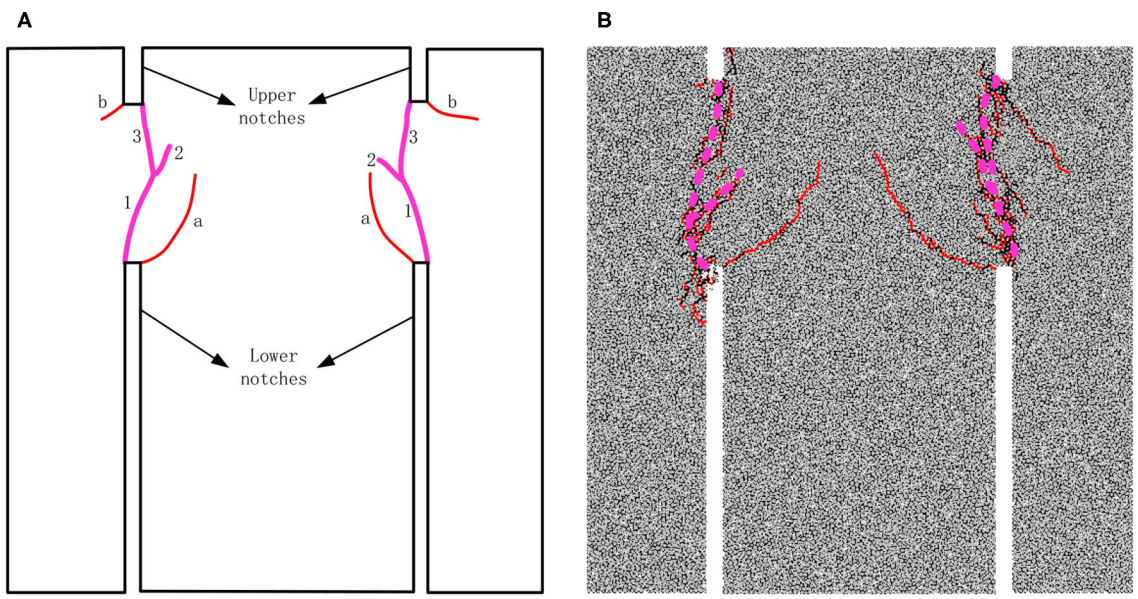

FIGURE 5 | Fractures in punch-through tests: **(A)** and **(B)** are the laboratory [29] and numerical fractures, respectively.

lower notches. In addition, Backers [32] stated that these shear crack show some opening from this junction to the notch. In other words, these cracks may be shear–tensile cracks. With the increase in axial displacement, shear cracks, numbered 2 and 3, sequentially connected the rock bridges between the upper and the lower notches [29]. Interestingly, at Mode II loading conditions, the macroscopic fracture follows the direction of Mode II. Besides, tensile cracks appear in the specimen. This phenomenon may be reasonable because fracturing in rock material always involves a mixed mode on the microscale [13]. Clearly, the numerical failure pattern is similar to the laboratory result (**Figure 5B**). However, the crack propagation sequence is still unclear. The previous studies [26–28] show that the stress evolution relates to the crack development. According to the comparisons on the axial compression force and the fracture pattern between laboratory and numerical results, we may infer

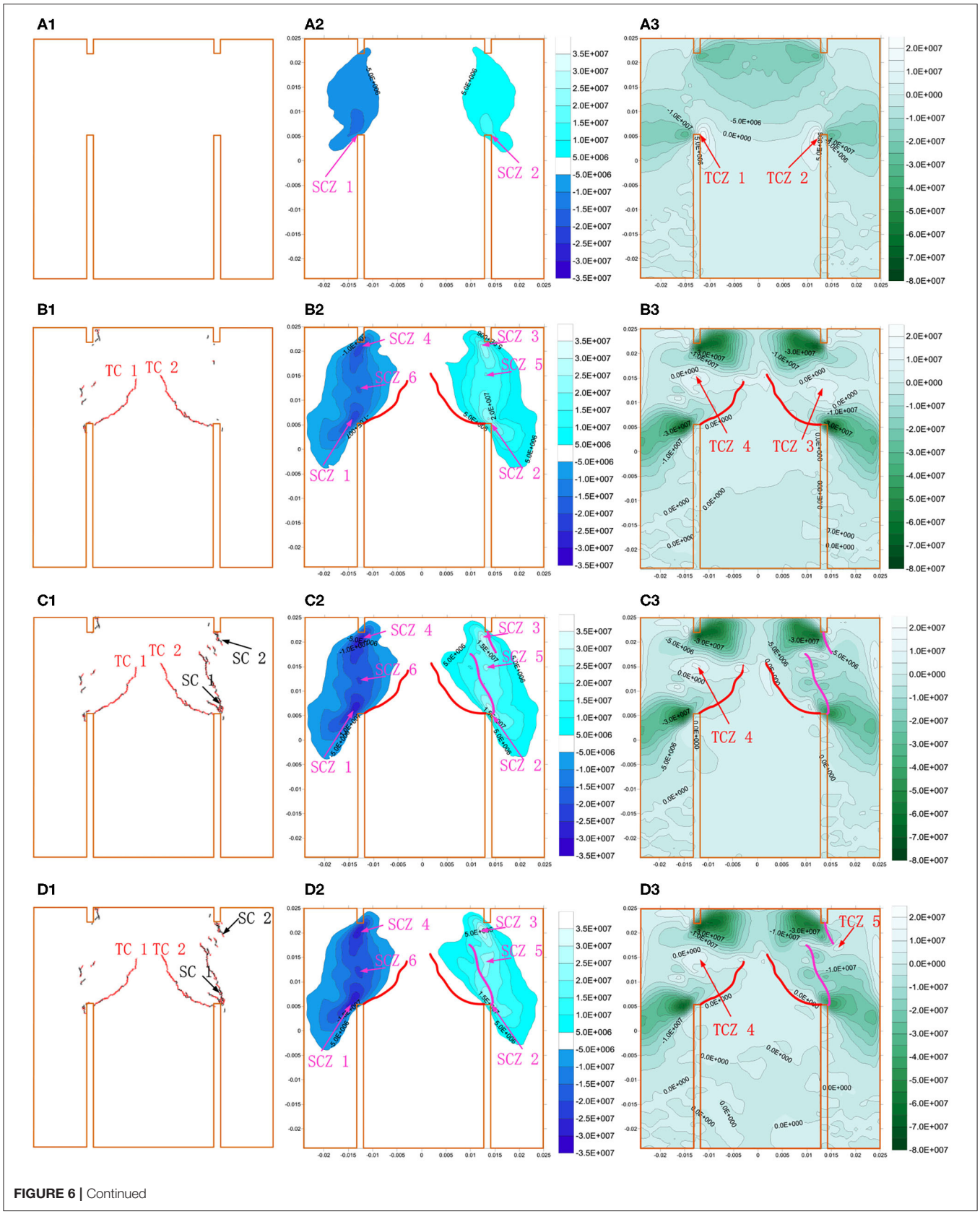

FIGURE 6 | Continued

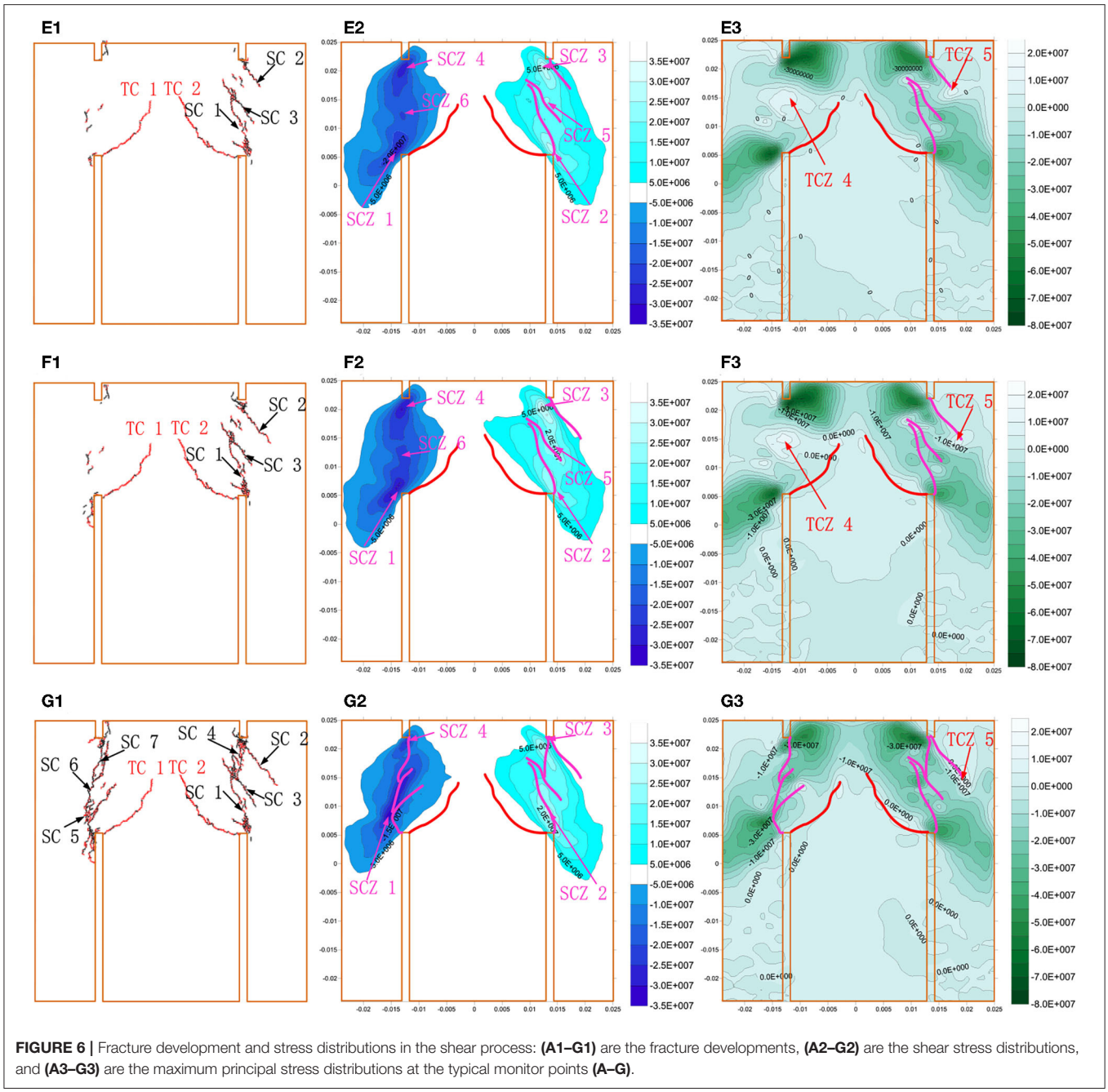

FIGURE 6 | Fracture development and stress distributions in the shear process: **(A1–G1)** are the fracture developments, **(A2–G2)** are the shear stress distributions, and **(A3–G3)** are the maximum principal stress distributions at the typical monitor points **(A–G)**.

that the stress evolution may relate to the crack development and the fluctuations in axial compression force. Thus, in the following section, we are trying to investigate the stress evolution in the shear process.

Stress Evolution in the Shear Process

The concentrated stresses may be responsible for the crack development. Thus, to investigate the typical crack (shear and tensile cracks) developments, **Figure 6** shows the numerical crack propagation and stress evolution in the shear process at typical monitor points (A–G) on the axial force–displacement curve in **Figure 4**. At Point A, two shear concentration zones (SCZ), named SCZ 1 and SCZ 2, form at the outer tips of the bottom notches (**Figure 6A2**). Simultaneously, in PFC 2D, tensile stress is positive; thus, **Figure 6A3** clearly shows that two tensile concentration zones (TCZs) form at the inner tips of the bottom notches. However, shear and tensile cracks fail to form (**Figure 6A1**). When the axial displacement increases to 0.21 mm, the first peak axial force at point B appears (**Figure 4**). Two tensile cracks, accompanied with minor fluctuations on the axial compression force, TC 1 and TC 2, form during this loading period (**Figure 6B1**). These tensile cracks also formed at previous

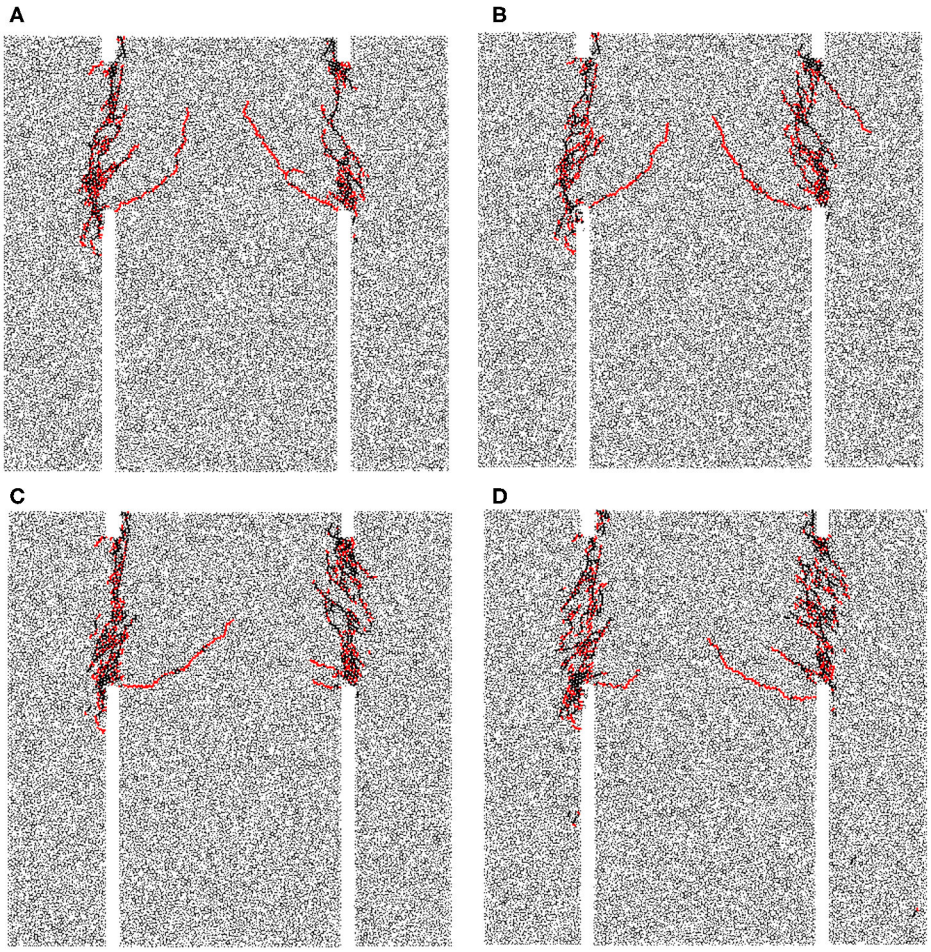

FIGURE 7 | Numerical fractures: **(A–D)** are the fractures when the confining stresses are 0, 5, 10, and 15 MPa, respectively.

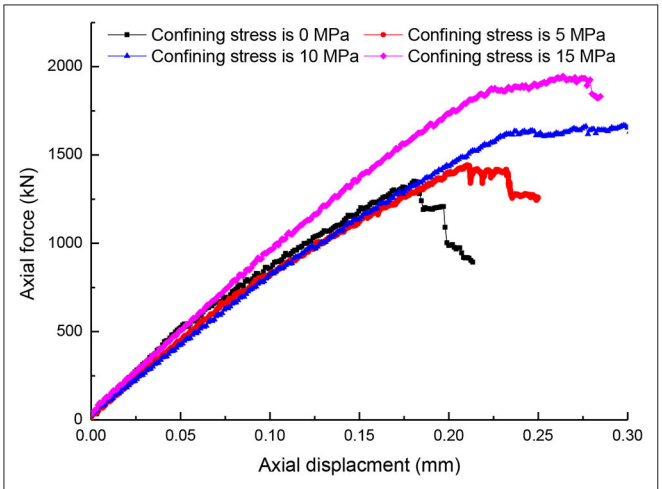

FIGURE 8 | The axial force–displacement curves for various confinements.

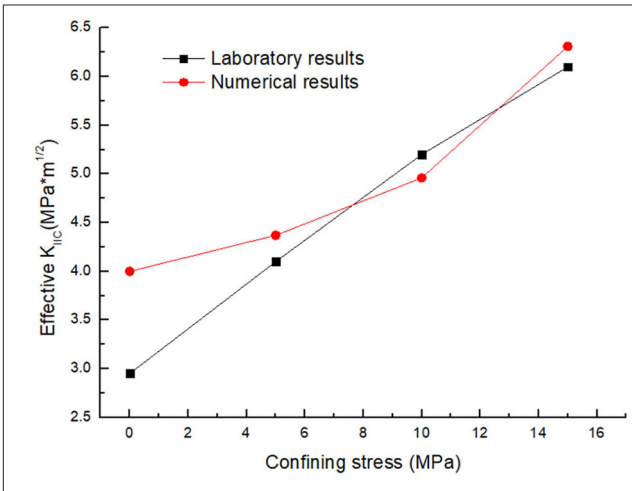

FIGURE 9 | The numerical and laboratory effective shear fracture toughness for various confinements.

laboratory tests [6, 32]. Interestingly, the initiation points locate at the TCZ 1 and TCZ 2, and the tensile stress concentrations at these crack tips significantly dissipate (**Figure 6B3**). Thus, we can infer that the concentrated tensile stresses at the inner tips of the bottom notches first form tensile cracks. In addition, TCZ 3 and TCZ 4 form at the rock bridges between the upper and the bottom notches (**Figure 6B3**). At the peak point, the shear stresses at SCZ 1 and SCZ 2 highly concentrate, and four shear concentration zones (SCZ 3–SCZ 6) form at the inner tips of the upper notches and the rock bridges (**Figure 6B2**). With further increase in axial displacement, the axial force sharply drops. At the first bottom point C, a shear crack (SC 1) initiates from the outer tip of the right-bottom notch, and the initiation point overlaps with the SCZ 2 (**Figures 6C1,C2**). The shear stress concentration at SCZ 2 dissipates, and the tensile stress concentration at TCZ 3 significantly dissipates. Thus, we can infer that the shear and tensile concentration at SCZ 2 and TCZ 3 are responsible for SC 1. This inference can properly verify the referred laboratory results that the shear crack shows some opening from this junction to the notch [32]. In addition, another shear crack (SC 2) initiates from the right-upper notch. With further increase in axial displacement, the axial force reaches the second peak at Point D. Clearly, the cracks fail to further generate (**Figures 6C1,D1**). However, the shear stresses at SCZ 5 and SCZ 6 further concentrate. Additionally, TCZ 5 forms at the tip of SC 2 (**Figure 6D1**). Subsequently, the second drop at Point E appears, accompanied with the formation of SC 3 (**Figures 4**, **6E1**). After the formation of SC 3, the area of SCZ 5 slightly decreases; however, the compression at the right rock bridge greatly concentrates. In addition, the tensile stress further concentrates at TCZ 5. Then, when the axial displacement further increases to 0.23 mm, the third peak appears at point F (**Figure 4**). The development of the cracks is minor. However, the shear stresses further concentrate at the shear concentration zones (except SCZ 2), and the tensile stress simultaneously concentrates at TZ 4. Finally, with further increase in axial displacement, the axial force significantly drops, and the third bottom point (G) forms. Between Points F and G, similar fluctuations generate (shown

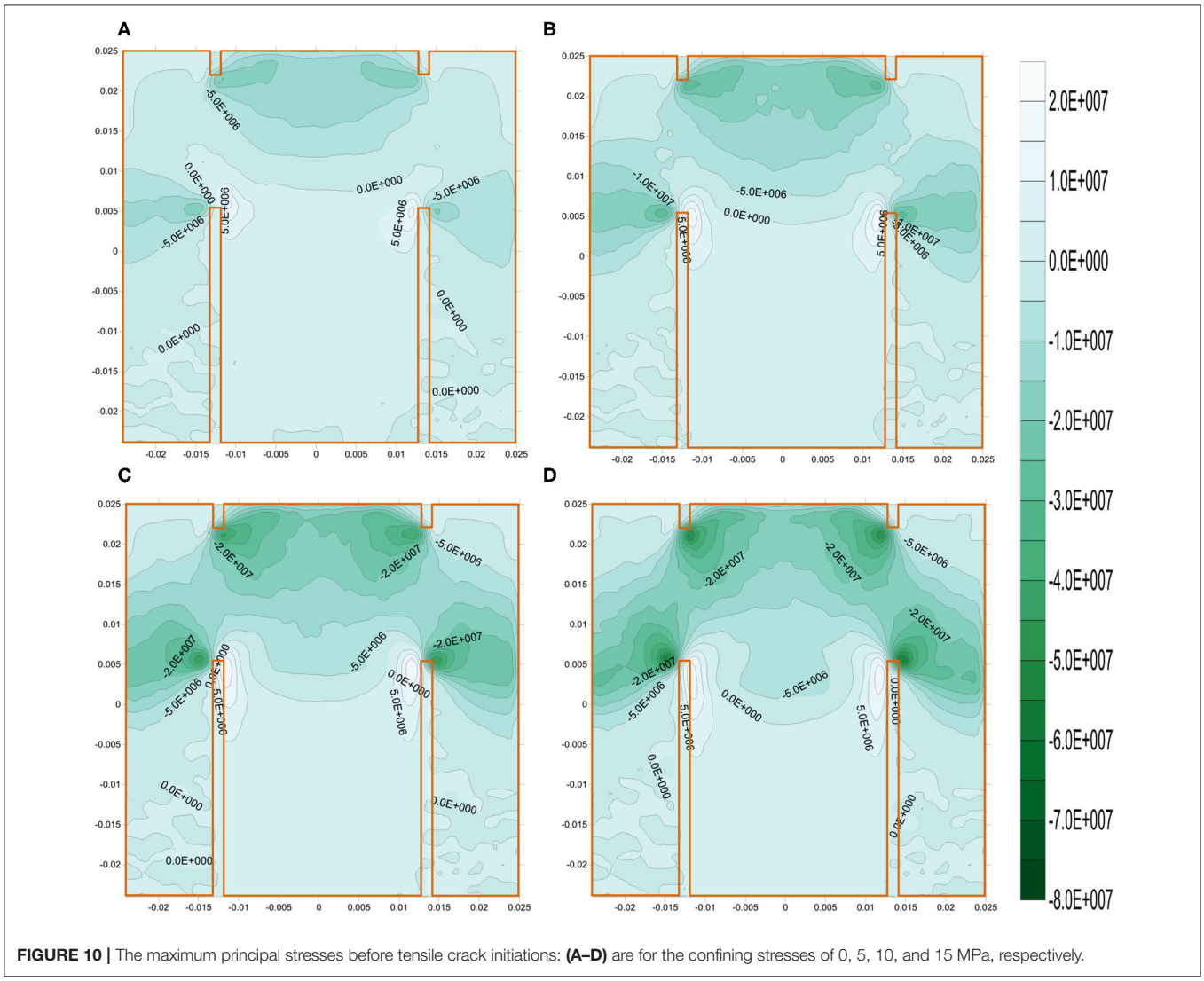

FIGURE 10 | The maximum principal stresses before tensile crack initiations: **(A–D)** are for the confining stresses of 0, 5, 10, and 15 MPa, respectively.

by the magnified area in **Figure 4**). In addition, SC 5, SC 6, and SC 7 sequentially connected the bottom and upper notches (**Figure 6G1**). Interestingly, the shear concentrations at SCZ 1 and SCZ 2 slightly move upward (**Figure 6G2**) and the tensile stress at TCZ 4 dissipates.

The above descriptions indicate that the tensile concentrations at TCZ 1 and TCZ 2 are responsible for the TC 1 and TC 2, reported in previous studies [6, 32]. In addition, shear stress concentrations at the outer tips of the bottom tips first form shear cracks, and then, with the tensile concentration at the rock bridge, shear–tensile cracks form. With further increase in axial displacement, the shear cracks, driven by the shear concentrations at the inner tip of the upper notches, finally coalesce the rock bridge. The reported laboratory tests and the numerical simulation agree well on crack propagation sequence. More interestingly, we find that the drop of the axial force frequently accompanies crack propagation and stress dissipation, whereas the increase in the axial displacement usually causes stress concentrations instead of obvious crack propagation.

The Influence of Confining Stress on the Failure Characteristics

The laboratory tests by Backers et al. [6] and Backers [32] indicated that the increase in confining stress frequently promotes the tested effective shear fracture toughness and restrains the development of tensile cracks. Thus, to verify the above conclusions, three simulations with the confining stresses of 0, 10, and 15 MPa were performed.

Similar to the laboratory tests [6, 32], the increase in confining stress restrains the tensile crack propagation (**Figure 7**). In addition, the width of the shear band between the upper and bottom notches increases with the increase in confining stress. Moreover, for the relatively low confining stresses, the axial force significantly fluctuates after the peak points (**Figure 8**). However, with the increase in confining stress, the fluctuations of the axial force are minor. This phenomenon agrees well with the laboratory results [6, 32]. More importantly, the increase in confining stress promotes the peak axial force. Thus, according to Equation 4 proposed by Backers and Stephansson [13] and

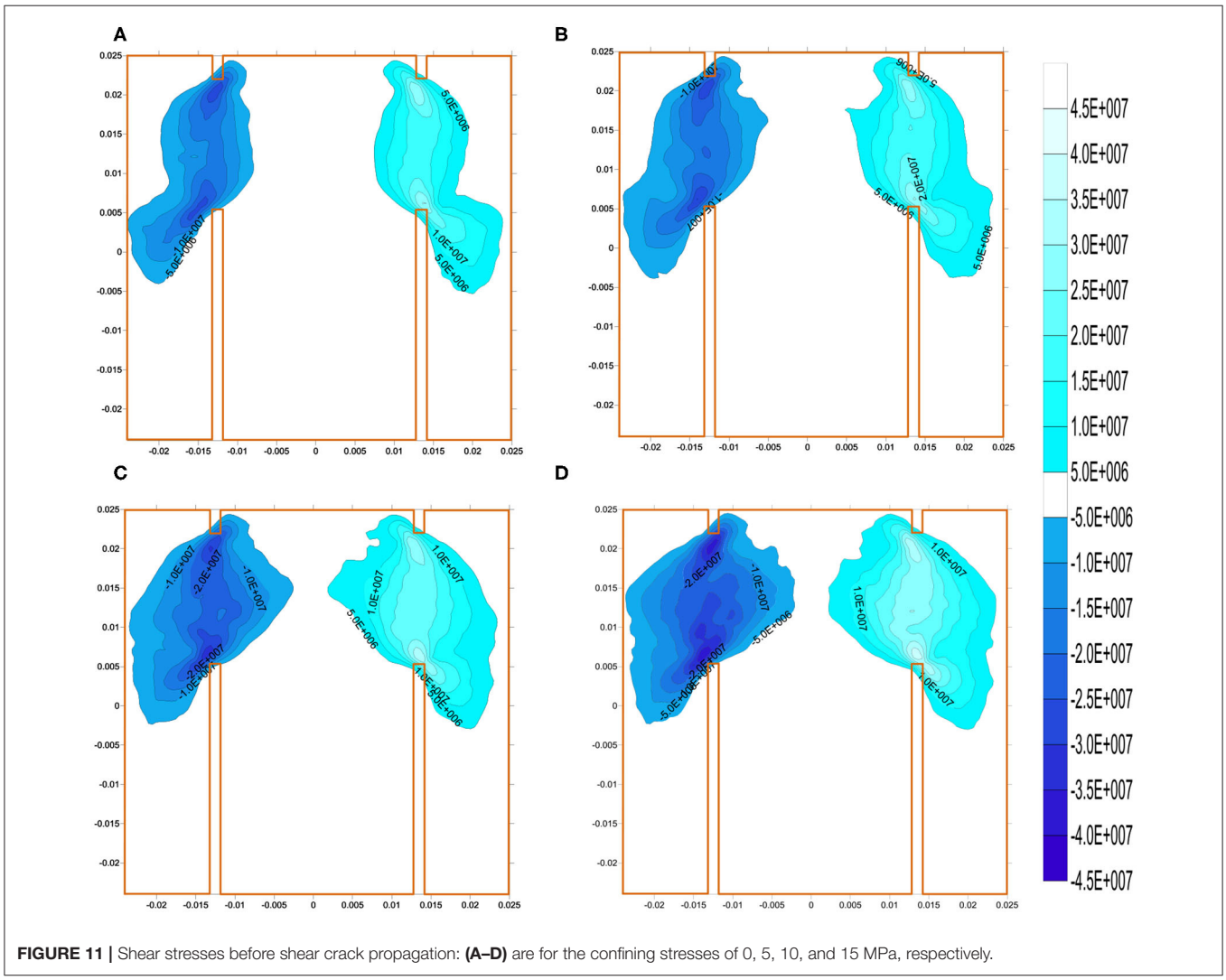

FIGURE 11 | Shear stresses before shear crack propagation: **(A–D)** are for the confining stresses of 0, 5, 10, and 15 MPa, respectively.

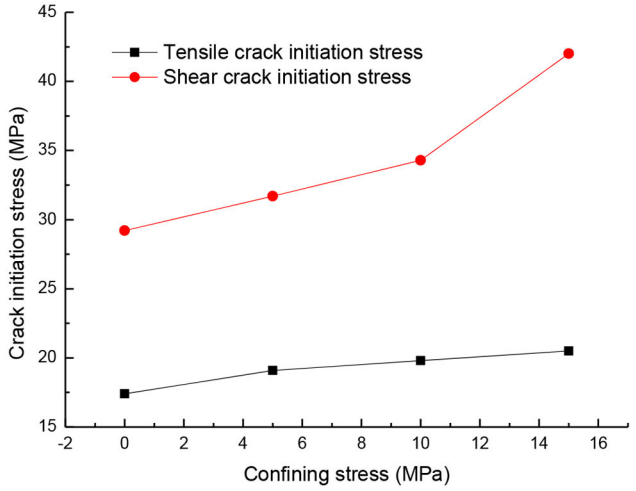

FIGURE 12 | The tensile and shear crack initiation stresses.

Backers [32], the calculated effective shear fracture toughness simultaneously increases (**Figure 9**), and the numerical values of the effective shear fracture toughness are close to the laboratory ones.

The above descriptions indicate that the numerical results agree well with the laboratory results on the effects of confining stress on fracture development and effective shear fracture toughness. To explain the above phenomena, we will further discuss the stress evolution for various confining stresses.

Figure 10 shows the maximum principal stresses before tensile crack initiation. Clearly, tensile stress concentration zones form at the inner tips of the bottom notches. These concentrated tensile stresses are responsible for the tensile crack propagation in **Figure 7**. Interestingly, the increase in confining stress elevates the corresponding maximum principal stresses (**Figure 12**). Thus, we can infer that the increase in confining stress may increase the effective tensile fracture toughness. Simultaneously, the absolute value of the maximum principal stress (negative) significantly increases between the upper and bottom notches. In other words, the compression at the rock between the upper and bottom notches intensifies with the increase in confining stress. The increased compression will restrain the tensile crack propagation between the upper and bottom notches. Thus, according to the above description, we may infer that the promoted effective tensile fracture toughness and the compression between the upper and bottom are responsible for the restrained tensile crack propagation when the confining stress increases.

The peak axial force, usually corresponding to the shear crack initiation from the outer tip of the bottom notches, can be used to calculate the effective shear fracture toughness. Thus, **Figure 11** depicts the shear stress contours at the first peak point of the axial force. With the initiation shear stresses in **Figure 12**, we can obtain that the increase in confining stress promotes the shear initiation stresses. The geometries of the notches are the same; thus, these promoted shear initiation stresses can properly verify that the increase in confining stress promotes the effective shear fracture toughness [6, 32].

CONCLUSIONS

The numerical simulation agrees well with the previous laboratory result that tensile cracks first initiate from the inner tips of the bottom notches. Then, shear–tensile cracks initiate from the outer tips of the bottom notches. Subsequently, the cracks at the middle of the rock bridge and the shear cracks initiating from the upper notches connect the rock bridge. More importantly, near the peak point of the axial compression force curve, the numerical tests indicate that the drops of the axial compression force frequently accompany with crack propagation and stress dissipation, whereas the increases in the axial force concentrate the stresses with hardly crack propagation. Then, the numerical tests indicate the increase in confining stress promotes the effective tensile fracture toughness and the compression between the upper and bottom notches. Thus, the increasing confining stress restrains tensile crack propagation and promotes the effective shear fracture toughness.

DATA AVAILABILITY STATEMENT

The raw data supporting the conclusions of this article will be made available by the authors, without undue reservation.

AUTHOR CONTRIBUTIONS

All authors performed the simulation, provided financial support, provided theoretical guidance, and provided numerical guidance, respectively.

FUNDING

The authors would like to acknowledge these financial supports: Projects (51804110) supported by the National Natural Science Foundation of China; Projects (2020JJ5101) supported by the Natural Science Foundation of Hunan Province; Scientific Research Foundation of Hunan Province Education Department (18B391, 18A345).

REFERENCES

1. Zhao YL, Wang YX, Wang WJ, Tang LM, Liu Q. Modeling of rheological fracture behavior of rock cracks subjected to hydraulic pressure and far field stresses. *Theor Appl Fract Mech.* (2019) **101**:59–66. doi: 10.1016/j.tafmec.2019.01.026
2. Dong LJ, Zou W, Li XB, Shu WW, Wang ZW. Collaborative localization method using analytical and iterative solutions for microseismic/acoustic emission sources in the rockmass structure for underground mining. *Eng Fract Mech.* (2019) **210**:95–112. doi: 10.1016/j.engfracmech.2018.01.032
3. Zhao YL, Zhang LY, Wang WJ, Pu CZ, Wan W, Tang JZ. Cracking and stress-strain behavior of rock-like material containing two flaws

under uniaxial compression. *Rock Mech Rock Eng.* (2016) **49**:2665–87. doi: 10.1007/s00603-016-0932-1
4. Rao QH, Sun ZQ, Stephansson O, Li CL, Stillborg B. Shear fracture (Mode II) of brittle rock. *Int J Rock Mech Min Sci.* (2003) **40:**355–75. doi: 10.1016/S1365-1609(03)00003-0
5. Timothy DB, Don E III. The shear fracture toughness, KIIc, of graphite. *Carbon*. (2016) **98**:267–79. doi: 10.1016/j.carbon.2015.10.084
6. Backers T, Stephansson O, Rybacki E. Rock fracture toughness testing in Mode II punch-through shear test. *Int J Rock Mech Min Sci.* (2002) **39**:755–69. doi: 10.1016/S1365-1609(02)00066-7
7. Watkins J. Fracture toughness test for soil-cement samples in mode II. *Int J Fract.* (1983) **23**:RI35–8. doi: 10.1007/BF00020700
8. Golewski GL, Sadowski T. An analysis of shear fracture toughness KIIc and microstructure in concretes containing fly-ash. *Constr Build Mater.* (2014) **51**:207–14. doi: 10.1016/j.conbuildmat.2013.10.044
9. Ghanbaria N, Hosseinia M, Saghafiyazdia M. Effects of temperature and confining pressure on the mode I and mode II fracture toughness of cement mortar. *Theor Appl Fract Mech.* (2019) **104**:102361. doi: 10.1016/j.tafmec.2019.102361
10. Dehestani A, Hosseini M, Beydokhti AT. Effect of wetting-drying cycles on mode I and mode II fracture toughness of cement mortar and concrete. *Theor Appl Fract Mech.* (2020) **106**:102448. doi: 10.1016/j.tafmec.2019.102448
11. Dehestani A, Hosseini M, Beydokhti AT. Effect of wetting-drying cycles on mode I and mode II fracture toughness of sandstone in natural (pH = 7) and acidic (pH = 3) environments. *Theor Appl Fract Mech.* (2020) **107**:102512. doi: 10.1016/j.tafmec.2020.102512
12. Xu Y, Yao W, Zhao GL, Xia KW. Evaluation of the short core in compression (SCC) method for measuring mode II fracture toughness of rocks. *Eng Fract Mech.* (2020) **224**:106747. doi: 10.1016/j.engfracmech.2019.106747
13. Backers T, Stephansson O. ISRM suggested method for the determination of mode II fracture toughness. *Rock Mech Rock Eng.* (2012) **45**:45–56. doi: 10.1007/s00603-012-0271-9
14. Yao W, Xu Y, Yu CY, Xia KW. A dynamic punch-through shear method for determining dynamic Mode II fracture toughness of rocks. *Eng Fract Mech.* (2017) **176**:161–77. doi: 10.1016/j.engfracmech.2017.03.012
15. Wu HY, Kemeny J, Wu SC. Experimental and numerical investigation of the punch-through shear test for mode II fracture toughness determination in rock. *Eng Fract Mech.* (2017) **184**:59–74. doi: 10.1016/j.engfracmech.2017.08.006
16. Roux S, Vandembroucq D, Hild F. Effective toughness of heterogeneous brittle materials. *Eur J Mech A Solids.* (2003) **22**:743–49. doi: 10.1016/S0997-7538(03)00078-0
17. Patinet S, Vandembroucq D, Roux S. Quantitative prediction of effective toughness at random heterogeneous interfaces. *Phys Rev Lett.* (2006) **110**:165507. doi: 10.1103/PhysRevLett.110.165507
18. Liu HY, Kou SQ, Lindqvist PA, Tang CA. Numerical simulation of shear fracture (Mode II) in heterogeneous brittle rock. *Int J Rock Mech Min Sci.* (2004) **41**:355. doi: 10.1016/j.ijrmms.2003.12.148
19. Moon T, Nakagawa M, Berger J. Measurement of fracture toughness using the distinct element method. *Int J Rock Mech Min Sci.* (2007) **44**:449–56. doi: 10.1016/j.ijrmms.2006.07.015
20. Moon T, Oh J. A Study of optimal rock-cutting conditions for hard rock TBM using the discrete element method. *Rock Mech Rock Eng.* (2012) **45**:837–49. doi: 10.1007/s00603-011-0180-3
21. Aminzadeha A, Fahimifara A, Nejatib M. On Brazilian disk test for I/II mixed-mode fracture toughness experiments of anisotropic rocks. *Theor Appl Fract Mech.* (2019) **102**:222–38. doi: 10.1016/j.tafmec.2019.04.010
22. Ma LF, Yari N, Wiercigroch M. Shear stress triggering brittle shear fracturing of rock-like materials. *Int J Mech Sci.* (2018) **146–7**:295–302. doi: 10.1016/j.ijmecsci.2018.07.008
23. Fan X, Li KH, Lai HP, Xie YL, Cao RH, Zheng J. Internal stress distribution and cracking around flaws and openings of rock block under uniaxial compression: a particle mechanics approach. *Comput Geotech.* (2018) **102**:28–38. doi: 10.1016/j.compgeo.2018.06.002
24. Cao Rh, Cao P, Lin H, Pu CZ, Ou K. Mechanical behavior of brittle rock-like specimens with pre-existing fissures under uniaxial loading: experimental studies and particle mechanics approach. *Rock Mech Rock Eng.* (2015) **49**:763–83. doi: 10.1007/s00603-015-0779-x
25. Dong LJ, Deng SJ, Wang FY. Some developments and new insights for environmental sustainability and disaster control of tailings dam. *J Clean Prod.* (2020) **269**:122270. doi: 10.1016/j.jclepro.2020.122270
26. Liu J, Wang J, Wan W. Numerical study of crack propagation in an indented rock specimen. *Comput Geotech.* (2018) **96**:1–11. doi: 10.1016/j.compgeo.2017.10.014
27. Liu J, Wang J. The effect of indentation sequence on rock breakages: a study based on laboratory and numerical tests. *C R Mecanique.* (2018) **346**:26–38. doi: 10.1016/j.crme.2017.11.004
28. Liu J, Wan W, Chen Y, Wang J. Dynamic indentation characteristics for various spacings and indentation depths: a study based on laboratory and numerical tests. *Adv Civil Eng.* (2018) **2018**:1–12. doi: 10.1155/2018/8412165
29. Backers T, Dresen G, Rybacki E, Stephansson O. New data on mode II fracture toughness of rock from the punch-through shear test. *Int J Rock Mech Min Sci.* (2004) **41**:349–546. doi: 10.1016/j.ijrmms.2003.12.059
30. Wu SC, Xu XL. A study of three intrinsic problems of the classic discrete element method using flat-joint model. *Rock Mech Rock Eng.* (2016) **49**:1813–30. doi: 10.1007/s00603-015-0890-z
31. Yang XX, Qiao WG. Numerical investigation of the shear behavior of granite materials containing discontinuous joints by utilizing the flat-joint model. *Comput Geotech.* (2018) **104**:69–80. doi: 10.1016/j.compgeo.2018.08.014
32. Backers T. *Fracture Toughness Determination and Micromechanics of Rock Under Mode I and Mode II Loading*. Potsdam: University of Potsdam (2004).
33. Goldhirsch I, Goldenberg C. On the microscopic foundations of elasticity. *Eur Phys J E.* (2002) **9**:245–51. doi: 10.1140/epje/i2002-10073-5
34. Goldenberg C, Atman APF, Claudin P, Combe G, Goldhirsch I. Scale separation in granular packings: stress plateaus and fluctuations. *Phys Rev Lett.* (2006) **96**:168001. doi: 10.1103/PhysRevLett.96.168001
35. Itasca Consulting Group Inc. *PFC3D Manual, Version 4.0*. Minneapolis, MN (2008).

Conflict of Interest: The authors declare that the research was conducted in the absence of any commercial or financial relationships that could be construed as a potential conflict of interest.

frontiers in Physics

ORIGINAL RESEARCH
published: 25 September 2020
doi: 10.3389/fphy.2020.00322

Factorial Experiment Study on the Mechanical Properties of Sandstone–Concrete Specimens Under Different Freeze–Thaw Conditions

Tao Zhao[1]*, *Gengshe Yang*[1], *Jiami Xi*[1], *Yanjun Shen*[1] and *Ki-iL Song*[2]

[1] College of Civil and Architectural Engineering, Xi'an University of Science and Technology, Xi'an, China, [2] Department of Civil Engineering, Inha University, Incheon, South Korea

The contact part between shaft wall and rock is affected by many factors, such as temperature and formation pressure, in the commonly used freezing method in coal mine development through quicksand and water-rich strata. To confine the relationships between these factors and the compressive strength of the contact surface, the sandstone which contacts with the outer well wall was selected in this study to prepare a complex of sandstone and C40 concrete mortar. The factorial design of the multi-factors affecting the uniaxial compressive strength of the complex specimens based on the freeze–thaw cycles test, the uniaxial compression test, and the statistical principle was used to study the interactive effect of various factors. Significant analysis was performed via analyzing the sample water content, the freezing temperature, and the number of freeze–thaw cycles based on the factorial design principle. The results show that the uniaxial compressive strength (UCS) of the dry sandstone–concrete complex specimens is significantly higher than that of the water-saturated sandstone–concrete complex specimens. After freeze–thaw cycles, the UCS of both the dry sandstone–concrete complex specimens and water-saturated sandstone–concrete complex specimens decrease significantly. In addition, the significant effects of main effect and primary and secondary interaction on unconfined compressive strength were obtained, and the major interaction among the factors was synergistic interaction, and the minor interaction among the factors is non-interactive interaction and antagonism.

Keywords: sandstone–concrete complex, freeze–thaw cycles, uniaxial compressive strength (UCS), factorial design, interaction

OPEN ACCESS

Edited by:
Longjun Dong,
Central South University, China

Reviewed by:
Hang Lin,
Central South University, China
Srutarshi Pradhan,
Norwegian University of Science and Technology, Norway

***Correspondence:**
Tao Zhao
zhaotao@xust.edu.cn

Specialty section:
This article was submitted to Interdisciplinary Physics, a section of the journal Frontiers in Physics

Received: *21 February 2020*
Accepted: *13 July 2020*
Published: *25 September 2020*

Citation:
Zhao T, Yang G, Xi J, Shen Y and Song K (2020) Factorial Experiment Study on the Mechanical Properties of Sandstone–Concrete Specimens Under Different Freeze–Thaw Conditions. Front. Phys. 8:322. doi: 10.3389/fphy.2020.00322

HIGHLIGHTS

- The mechanical properties of sandstone–concrete complex specimen under different freeze–thaw conditions were obtained.
- UCS of the dry sandstone–concrete specimens is higher than that of the water-saturated specimens.
- The UCS of both the dry and water-saturated sandstone–concrete specimens decrease significantly after freeze–thaw cycles.

INTRODUCTION

With the rapid development of national economy, the energy demand has been further enhanced. Also, the raising of strategic conception of "Belt and Road" creates great potential for coal and the development of other energy sources in the western China region [1]. According to incomplete statistics, no <50 mine shafts in water-abundant bedrock were built with a depth of over 400 m since 2000 AD. Most of these mine shafts crossed the water-abundant rocks with characteristics such as low strength, weak cementation, and softening after contact with water which were formed during the Cretaceous and the Jurassic. Thus, freezing shaft sinking method is the most commonly used method in these mine shaft excavations [2–4]. However, shaft lining, horsehead water inrush, and even flooded shaft need to be solved urgently in the process of freezing shaft sinking [5].

A possible solution to overcome the aforementioned problems is to study the mechanical characteristics of well-bore and surrounding medium (rock and concrete) at a low-temperature environment. Therefore, researchers all across the world show much interest in the physical and mechanical properties of frozen rocks in recent decades. Matsuoka et al. studied the mechanism of freezing and thawing failure of rock and the influence of freezing and thawing cycle number on rock strength [6, 7]. Yambae tested the thermal expansion strain of sandstone after one freeze–thaw cycle and its unconfined compressive strength (UCS) at different temperatures; they found that the axial deformation of dry rock samples remained elastically deformed whereas the axial deformation of the water-saturated rock sample became plastically deformed; moreover, UCS increased with the decrease of temperature after one freeze–thaw cycle [8]. Yang et al. studied the water-saturated rocks at different freezing temperatures by CT imaging technology; they analyzed the relationship between the rock damage and the freezing temperature and relationship between the rock damage and the freezing speed [9, 10]. Yang et al. performed the single-axis and tri-axial compression tests at different confining pressure and different temperature conditions using hydraulic servo rock pressure tester; they analyzed the influences of confining pressure and low temperature on the strength characteristics of different rocks, and deduced the non-linear failure criterion of frozen rock considering temperature [4, 11]. Xi et al. studied the effects of freezing temperature on submit strength, adhesion force, internal friction angle, and residual strength of sandy mudstone, and analyzed the relationship between the confining pressure and the submit strength and the relationship between the confining pressure and the residual strength [12]. Yang et al. studied the design theory of shaft freezing method at home and abroad, especially the design theory of shaft freezing method at home, and carried a prospect analysis on the design theory of shaft freezing method in coal mine [13]. Wang et al. conducted the uniaxial compression test of five different strain rates and different water cuts (dry, saturated) in the Hokkaido Nobile frozen tuff using MTS 312.21 electro-hydraulic servo test machine. Also, the empirical formula of the uniaxial compressive strength considering the strain rate of the saturated frozen rock sample was established after analyzing the reason and effect caused by the strain rate [14]. Xie et al. developed a statistical damage constitutive model considering whole joint shear deformation and Wang et al. studied the fracture behavior of rock [15, 16]. Xu et al. conducted uniaxial and tri-axial compression tests on dry and water-saturated red sandstone and shale at the temperature range of −20 to 20°C; they found that UCS and elastic modulus of the two investigated rocks increase with the decrease of temperature. Moreover, the strength of red sandstone is influenced by temperature more profoundly. They also come out with the conclusion that the influence of water content on the strength of frozen rock is significant [17]. There are many reports that focused on the influence of low-temperature environment in the concrete strength as well. Shi et al. conducted the freeze–thaw cycle test on concrete specimens [18] and Zou et al. performed scanning electron microscopy on concrete specimens to compare the relationship between the internal structure of concrete and the number of freeze–thaw cycles before and after freezing and thawing [19]. Shang et al. established the correlative mathematical expressions to clarify the relationship between the freeze–thaw cycles and the uniaxial compressive strength and the relationship between freeze–thaw cycles and the tensile strength of concrete [20].

All the aforementioned reports studied the UCS of rock or concrete materials separately, and there are few studies on the mechanics of rock and concrete complexes. Xiang et al. established the damage softening statistical constitutive model of the complex sample before and after freezing and thawing by freeze–thaw cycle test and uniaxial compression test and micro-scanning test [21]. Yi et al. established a two-media and two-body two-mechanical model to study the mechanical properties of the interface between the two media by relative experimental tests [22]. Shen et al. studied on meso-debonding process of the sandstone–concrete interface induced by freeze–thaw cycles using NMR technology [23]. Tian et al. investigated the durability of engineered cementitious composites-to-concrete interface under salt freeze–thaw cycles [24]. These studies mainly use rock, concrete separately, and a combination of them as the research object to carry out the low-temperature mechanical test, including freeze–thaw cycle number, freezing temperature, surrounding rock pressure, and water content. Also, all these reported studies only focused on the influence of a single factor, which is far from the actual project.

The aim of the present work is to study the influence of the interaction between drying state, saturation zone, freezing and thawing cycle number, and freezing temperature on the non-lateral compressive strength of the Cretaceous sandstone–concrete composite. The factorial design method was used to analyze the significance of different factors and their interaction effects.

EXPERIMENTAL PROGRAM AND PROCEDURE

Factorial Experiment

Factorial experiment design is a kind of multi-factor cross-grouping design, which can not only check whether there is

a difference between two factors or among even more factors at different levels but can also check whether there is an interaction between/among the investigated factors. The factorial experimental design of three factors can not only study whether there are differences among different levels of factors *A*, *B*, and *C* but can also study whether there are first-order interactions ($A \times B$, $A \times C$, $B \times C$) or second-order interactions ($A \times B \times C$) among the three factors. Interactive interaction refers to the fact that the single effect of one factor varies with the change of another factor. In this circumstance, we deem that there is an interactive interaction between the two factors. As for the circumstance that there exist three factors *A*, *B*, and *C*, factor A has r levels: *A1*, *A2*, *A3*, …, *Ar*; factor *B* has s levels: *B1*, *B2*, *B3*, …, *Bs*; factor *C* has t levels: *C1*, *C2*, *C3*, …, *Ct*; the freedom degree of factor *A* is r−1, the freedom degree of factor *B* is s−1, and the freedom degree of factor *C* is t−1; and factors *A*, *B*, and *C* are independent compared with each other in the horizontal combination (*Ar*, *Bs*, *Ct*) [25].

Denoting that $rstm = n$, then

$$\overline{X} = \frac{1}{n}\sum_{i=1}^{r}\sum_{j=1}^{s}\sum_{k=1}^{t}\sum_{l=1}^{m} X_{ijkl} = \frac{1}{n}X \tag{1}$$

$$\overline{X}_i = \frac{r}{n}\sum_{i=1}^{r}\sum_{j=1}^{s}\sum_{k=1}^{t}\sum_{l=1}^{m} X_{ijkl} = \frac{r}{n}X_i \tag{2}$$

$$\overline{X}_j = \frac{s}{n}\sum_{i=1}^{r}\sum_{j=1}^{s}\sum_{k=1}^{t}\sum_{l=1}^{m} X_{ijkl} = \frac{s}{n}X_j \tag{3}$$

$$\overline{X}_k = \frac{t}{n}\sum_{i=1}^{r}\sum_{j=1}^{s}\sum_{k=1}^{t}\sum_{l=1}^{m} X_{ijkl} = \frac{t}{n}X_k \tag{4}$$

$$\overline{X}_{ij} = \frac{1}{tm}\sum_{i=1}^{r}\sum_{j=1}^{s}\sum_{k=1}^{t}\sum_{l=1}^{m} X_{ijkl} = \frac{1}{tm}X_{ij} \tag{5}$$

$$\overline{X}_{ik} = \frac{1}{sm}\sum_{i=1}^{r}\sum_{j=1}^{s}\sum_{k=1}^{t}\sum_{l=1}^{m} X_{ijkl} = \frac{1}{sm}X_{ik} \tag{6}$$

$$\overline{X}_{jk} = \frac{1}{rm}\sum_{i=1}^{r}\sum_{j=1}^{s}\sum_{k=1}^{t}\sum_{l=1}^{m} X_{ijkl} = \frac{1}{rm}X_{jk} \tag{7}$$

$$\overline{X}_{ijk} = \frac{1}{m}\sum_{l=1}^{m} X_{ijkl} = \frac{1}{m}X_{ijk} \tag{8}$$

$$\begin{aligned} S_{ABC} &= m\sum_{i=1}^{r}\sum_{j=1}^{s}\sum_{k=1}^{t}\sum_{l=1}^{m}(\overline{X}_{ijk} - \overline{X}_{ij} - \overline{X}_{ik} - \overline{X}_{jk} \\ &+ \overline{X}_i + \overline{X}_j + \overline{X}_k - \overline{X})^2 \\ &= \frac{1}{m}\sum_{i=1}^{r}\sum_{j=1}^{s}\sum_{k=1}^{t}\sum_{l=1}^{m} X^2{}_{ijk} - S_{AB} - S_{AC} \\ &- S_{BC} - S_A - S_B - S_C - T^2 \end{aligned} \tag{9}$$

It can be verified by Equation (9) that the sum of the intersection terms in the S_T decomposition formula is 0. If $T^2 = nX^2$, the following equations can be obtained:

$$S_T = \sum_{i=1}^{r}\sum_{j=1}^{s}\sum_{k=1}^{t}\sum_{l=1}^{m} X_{ijkl}^{\ 2} - T^2 \tag{10}$$

$$S_A = stm\sum_{i=1}^{r}(\overline{X}_i - \overline{X})^2 = \frac{r}{n}\sum_{i=1}^{r}\overline{X}^2{}_i - T^2 \tag{11}$$

$$S_B = rtm\sum_{i=1}^{r}(\overline{X}_j - \overline{X})^2 = \frac{s}{n}\sum_{i=1}^{r}\overline{X}^2{}_j - T^2 \tag{12}$$

$$S_C = rsm\sum_{i=1}^{r}(\overline{X}_k - \overline{X})^2 = \frac{t}{n}\sum_{i=1}^{r}\overline{X}^2{}_k - T^2 \tag{13}$$

$$\begin{aligned} S_{AB} &= tm\sum_{i=1}^{r}\sum_{j=1}^{s}(\overline{X}_{ij} - \overline{X}_i - \overline{X}_j + \overline{X})^2 = \\ &\frac{1}{tm}\sum_{i=1}^{r}\sum_{j=1}^{s}X_{ij}^{\ 2} - T^2 - S_A - S_B \end{aligned} \tag{14}$$

$$\begin{aligned} S_{AC} &= sm\sum_{i=1}^{r}\sum_{j=1}^{s}(\overline{X}_{ik} - \overline{X}_i - \overline{X}_k + \overline{X})^2 = \\ &\frac{1}{sm}\sum_{i=1}^{r}\sum_{j=1}^{s}X_{ik}^{\ 2} - T^2 - S_A - S_C \end{aligned} \tag{15}$$

$$\begin{aligned} S_{BC} &= rm\sum_{i=1}^{r}\sum_{j=1}^{s}(\overline{X}_{jk} - \overline{X}_j - \overline{X}_k + \overline{X})^2 = \\ &\frac{1}{rm}\sum_{i=1}^{r}\sum_{j=1}^{s}X_{jk}^{\ 2} - T^2 - S_B - S_C \end{aligned} \tag{16}$$

$$\begin{aligned} S_{ABC} &= m\sum_{i=1}^{r}\sum_{j=1}^{s}\sum_{k=1}^{t}\sum_{l=1}^{m}(\overline{X}_{ijk} - \overline{X}_{ij} - \overline{X}_{ik} - \overline{X}_{jk} + \\ &\overline{X}_i + \overline{X}_j + \overline{X}_k - \overline{X})^2 = \frac{1}{m}\sum_{i=1}^{r}\sum_{j=1}^{s}\sum_{k=1}^{t}\sum_{l=1}^{m}X^2{}_{ijk} \\ &- S_{AB} - S_{AC} - S_{BC} - S_A - S_B - S_C - T^2 \end{aligned} \tag{17}$$

$$\begin{aligned} S_E &= \sum_{i=1}^{r}\sum_{j=1}^{s}\sum_{k=1}^{t}\sum_{l=1}^{m}(X_{ijkl} - \overline{X}_{ijk})^2 \\ &= S_T - S_A - S_B - S_C - S_{AB} - S_{AC} - S_{BC} - S_{ABC} \end{aligned} \tag{18}$$

Therefore, the following equations can be deduced:

$$\frac{S_T}{\sigma^2} \sim \chi^2(n-1), \frac{S_A}{\sigma^2} \sim \chi^2(r-1) \tag{19}$$

$$\frac{S_B}{\sigma^2} \sim \chi^2(s-1), \frac{S_C}{\sigma^2} \sim \chi^2(t-1) \tag{20}$$

$$\frac{S_{AB}}{\sigma^2} \sim \chi^2((r-1)(s-1)) \tag{21}$$

$$\frac{S_{AC}}{\sigma^2} \sim \chi^2((r-1)(t-1)) \tag{22}$$

TABLE 1 | Three-factor analysis of variance of interaction effects.

Source	Sum of squares	Degree of freedom	Mean square	*F*-value
A	S_A	$r-1$	$MS_A = \frac{S_A}{(r-1)}$	$F_A \rangle F_{1-\alpha}$ $(r-1, rst(m-1))$
B	S_B	$s-1$	$MS_B = \frac{S_B}{(s-1)}$	$F_B = \frac{MS_B}{MS_E}$
C	S_C	$t-1$	$MS_B = \frac{S_B}{(s-1)}$	$F_C = \frac{MS_C}{MS_E}$
AB	S_{AB}	$(r-1)(s-1)$	$MS_{AB} = \frac{S_{AB}}{(r-1)(s-1)}$	$F_{AB} = \frac{MS_{AB}}{MS_E}$
AC	S_{AC}	$(r-1)(t-1)$	$MS_{AC} = \frac{S_{AC}}{(r-1)(t-1)}$	$F_{AC} = \frac{MS_{AC}}{MS_E}$
BC	S_{BC}	$(s-1)(t-1)$	$MS_{BC} = \frac{S_{BC}}{(t-1)(s-1)}$	$F_{ABC} = \frac{MS_{ABC}}{MS_E}$
ABC	S_{ABC}	$(r-1)(s-1)(t-1)$	$MS_{ABC} = \frac{S_{ABC}}{(r-1)(t-1)(s-1)}$	
E	S_E	$rst(m-1)$	$MS_E = \frac{S_E}{rst(m-1)}$	
T	S_T	$n-1$		

$$\frac{S_{BC}}{\sigma^2} \sim \chi^2((t-1)(s-1)) \tag{23}$$

$$\frac{S_{ABC}}{\sigma^2} \sim \chi^2((r-1)(s-1)(t-1)) \tag{24}$$

$$\frac{S_E}{\sigma^2} \sim \chi^2(rst(m-1)) \tag{25}$$

Table 1 shows the critical value of the F test. It can be easily found that the significance analysis is the same as the single factor analysis.

If $F_B \rangle F_{1-\alpha}(s-1, rst(m-1))$, H_{02} is rejected and factor B is considered to have a significant influence on the index value.

If $F_C \rangle F_{1-\alpha}(t-1, rst(m-1))$, H_{03} is rejected and factor C is considered to have a significant influence on the index value.

If $F_{AB} \rangle F_{1-\alpha}((r-1)(s-1), rst(m-1))$, H_{04} is rejected and the interaction of factors A and B has a significant influence on the index value.

If $F_{AC} \rangle F_{1-\alpha}((r-1)(t-1), rst(m-1))$, H_{05} is rejected and the interaction between factors A and C is considered to have a significant impact on the index value.

If $F_{BC} \rangle F_{1-\alpha}((t-1)(s-1), rst(m-1))$, H_{06} is rejected and the interaction between factors B and C is considered to have a significant impact on the index value.

If $F_{ABC} \rangle F_{1-\alpha}((r-1)(t-1)(s-1), rst(m-1))$, H_{07} is rejected and the interaction between factors A and B and C is considered to have a significant influence on the index value.

The size of the significant effect is defined as follows:

If, its significance is defined as I;

If, its significance is defined as II;

If, its significance is defined as III;

If $\alpha \geq 0.1$, its significance is defined as IV.

There are two or more independent variables in the experiment. When the effect of one independent variable is different at each level of another independent variable, it indicates that there is interactive interaction between/among these independent variables. When there exists interactive interaction, it is of little significance to study the effect of one single factor but it is necessary to study the effect of the factor at different levels of another factor. The interaction in the experimental design method indicates that the effect of the simultaneous action of two or more factors can be strengthened or weakened compared with the effect of the single level factor and interactive interaction is a factor that must be considered in the study. The three common interactions are mainly non-interactive interaction, synergistic interaction, and antagonism, as shown in **Figure 1** [26].

In the design of factorial experiments, if changing the level of one factor causes a change in the response difference between the other levels, there is an interaction between these factors. As shown in **Figures 1B,C**, the straight line *A1* intersects with the straight line *A2*. For the factors at the same level, the factors take different levels, and the results are different. That is, the effect of the factor depends on the level chosen by the factor. Therefore, there is an interactive interaction between factors and factors, and interactions include synergy and antagonism. As shown in **Figure 1A**, the straight line *A1* and the straight line *A2* are almost parallel, indicating that there is no interactive interaction between the factors. If there is an interactive interaction between the two factors, the individual effects of each factor must be analyzed one by one in the statistical analysis; if there is no interactive interaction between the two factors, the main effects of each factor can be analyzed one by one.

Experimental Programs

Experimental Model of Factorial Design

The $2 \times 4 \times 4$ factorial design refers to that there are 3 factors, including 2 levels, 4 levels, and 4 levels, respectively. There are 32 combinations, as shown in **Table 2**. Three factors were selected in this experiment: moisture content, the number of freeze–thaw cycles, and freezing temperature. Moisture content (A) takes 2 levels: saturated state and unsaturated state. The number of freeze–thaw cycles (B) was set at four levels: one time, five times, eight times, and 12 times; freezing temperature (C) takes 4 levels: -5, -10, -20, and -30°C.

Specimen Preparation and Test Process

The rocks in Cretaceous strata have characteristics such as low strength, easy softening in water, and well-developed pores (fractures). Fresh and complete cretaceous sandstone samples were taken from a coal mine freezing construction site in Gansu province and sealed, boxed, and transported with polyethylene material to ensure the rock moisture content is basically unchanged and the integrity of the overall structure remains. According to the specification of rock test regulations for water conservancy and hydropower projects (DL/T5368-2007), cylindrical specimens with a diameter of 50 mm and a length of 100 mm were sampled by water drilling.

According to C40 concrete and the principle of similar proportion in construction site, the C40 concrete mortar required for the test were prepared. Also, the uniaxial compressive strength of concrete mortar specimens was carried out. The ratio of concrete mortar determined according to the UCS of concrete mortar specimens is the same as the UCS of specimens in Cretaceous strata. The rock cutter is used to cut along the central axis of the round section of the sandstone specimen, and

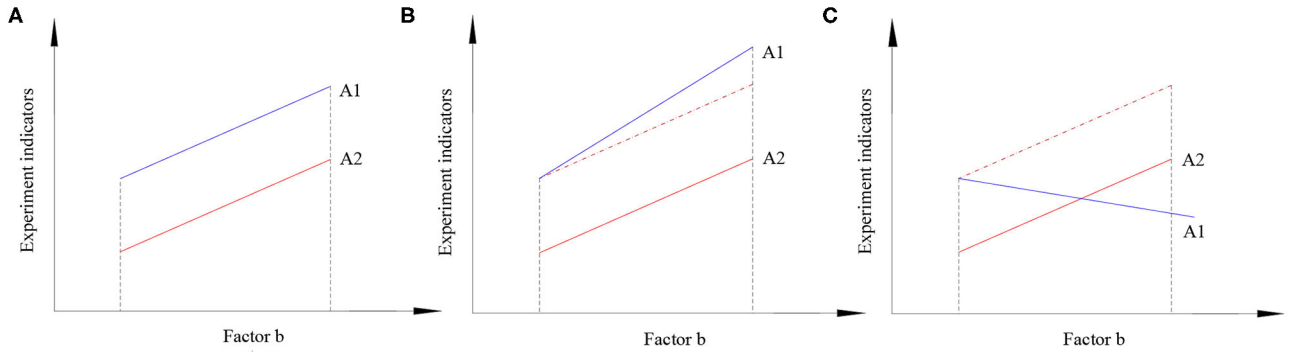

FIGURE 1 | The working period of CLS backfill applied in upward sublevel filling method. **(A)** Before filling; **(B)** cold releasing; **(C)** cold fully released.

TABLE 2 | 2 × 4 × 4 factorial experimental design model.

		A_1				A_2		
	C_1	C_2	C_3	C_4	C_1	C_2	C_3	C_4
B_1	$A_1B_1C_1$	$A_1B_1C_2$	$A_1B_1C_3$	$A_1B_1C_4$	$A_2B_1C_1$	$A_2B_1C_2$	$A_2B_1C_3$	$A_2B_1C_4$
B_2	$A_1B_2C_1$	$A_1B_2C_2$	$A_1B_2C_3$	$A_1B_2C_4$	$A_2B_2C_1$	$A_2B_2C_2$	$A_2B_2C_3$	$A_2B_2C_4$
B_3	$A_1B_3C_1$	$A_1B_3C_2$	$A_1B_3C_3$	$A_1B_3C_4$	$A_2B_3C_1$	$A_2B_3C_2$	$A_2B_3C_3$	$A_2B_3C_4$
B_4	$A_1B_4C_1$	$A_1B_4C_2$	$A_1B_4C_3$	$A_1B_4C_4$	$A_2B_4C_1$	$A_2B_4C_2$	$A_2B_4C_3$	$A_2B_4C_4$

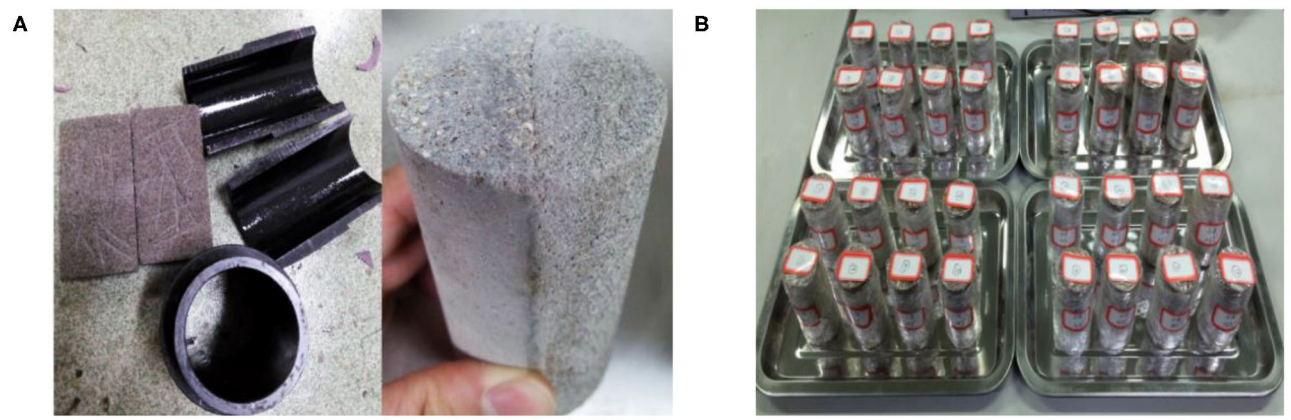

FIGURE 2 | Sandstone–concrete samples used in the experiments. **(A)** Combination test piece and mold; **(B)** compression test assembly test piece.

the cutting surface is roughened with a steel chisel. The semi-cylindrical rock specimen will be placed in the mold with inner diameter of 50 mm and length of 100 mm, and then the mold was filled with concrete mortar. After 28-days standard maintenance, the product of ϕ 50 × 100 mm standard sandstone–concrete complexes as shown in **Figure 2** was obtained.

The complex specimens were screened preliminarily after preparation and processing, and the ones with obvious defects on the interface and large surface porosity were removed. Half of the test piece was placed in vacuuming equipment for 24 h to prepare the non-saturated combination specimens.

The number of freeze–thaw cycles of the designed complex specimens is 1 time, 5 times, 8 times, and 12 times. As shown in **Figure 2B**, the prepared unsaturated and water-saturated combination test pieces were placed in the DWX-30 cryogenic chamber for testing. The pieces were frozen at −30°C for 4 h and then thawed into a freeze–thaw cycle for 12 h at 25°C (**Figure 3A**). The designed combination specimens were subjected to a freeze–thaw cycle test at freezing temperatures of −5, −10, −20, and −30°C, respectively. Also, a mechanical test was performed on a RE-TES uniaxial compression tester. The designed testing scheme is illustrated in **Figure 3B**.

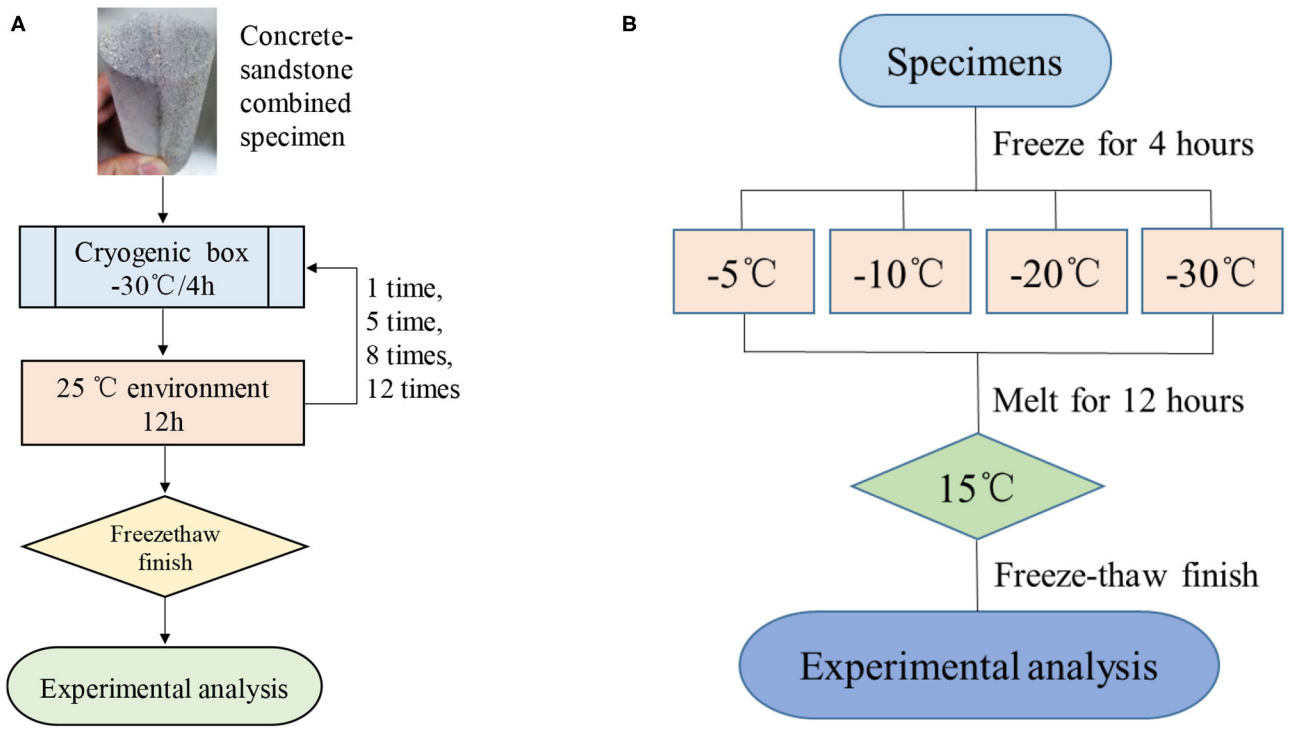

FIGURE 3 | Experimental design of different freeze–thaw methods. **(A)** Different freeze–thaw cycles; **(B)** different freezing temperatures.

RESULTS AND DISCUSSION

The Influence of Different Freezing and Thawing Environment on UCS

Figure 4 shows the stress–strain curves of sandstone–concrete complex specimens without lateral limit single-axis compression under various freezing and thawing conditions, and some typical experimental results are given here. Generally speaking, the stress–strain relationship of sandstone–concrete composite specimens can be roughly divided into: compaction stage, elastic stage, yield stage, and failure stage.

Figure 4A shows the stress–strain curves with only one freeze–thaw cycle for the complex specimens with different moisture contents (factor *A*) under freezing temperature of −10°C. Before the damage, the compressive strength of the unsaturated specimen was significantly higher than that of the water-saturated specimen; however, the plasticity stage of the feeding specimen was advanced and significant. The reason is that water has little effect on the compressive strength of concrete, mainly because the sandstone part of the complex specimen is softened by water and thus the strength is lowered, which leads to the decrease of the compressive strength of the specimen.

Figures 4C,D shows stress–strain curves with only one freeze–thaw cycle for unsaturated specimens (**Figure 4C**) and water-saturated (**Figure 4D**) complex specimens at different freezing temperatures (factor *C*). As the freezing temperature continues to decrease, the compressive strength of the test piece also decreases. The reason is that the lower the freezing temperature, the more sufficient the water freezing degree in the complex specimen, the greater the frost heaving force generated, and the more serious the damage to the specimen.

Figure 4B shows the stress–strain curve shape of the sandstone–concrete composite specimen, which is obviously changed by the number of freeze–thaw cycles. With the increasing number of freeze–thaw cycles, the compaction stage increases, the elastic stage decreases, the elastic modulus decreases, and the compressive strength also decreases. The reason is that with the increase of the number of freeze–thaw cycles, the number of pores and cracks in the specimen also increased, which leads to the deterioration of the internal degradation damage and the decrease of strength of the composite specimen.

The Influence of the Interaction of Different Factors on UCS

The factorial design results of UCS of the sand–concrete complex specimens with different water contents, different freeze–thaw cycle times, and different freezing temperatures are shown in **Table 3**. **Table 3** shows the degrees of freedom and mean sum of square of each main effect and interaction effect affecting UCS of the complex specimens according to the distribution characteristics of UCS and the factorial experiment principle in Experimental programs section. Therefore, through joint hypotheses test (*F* test), all the aforementioned influencing factors have different degrees of influence on UCS. According to

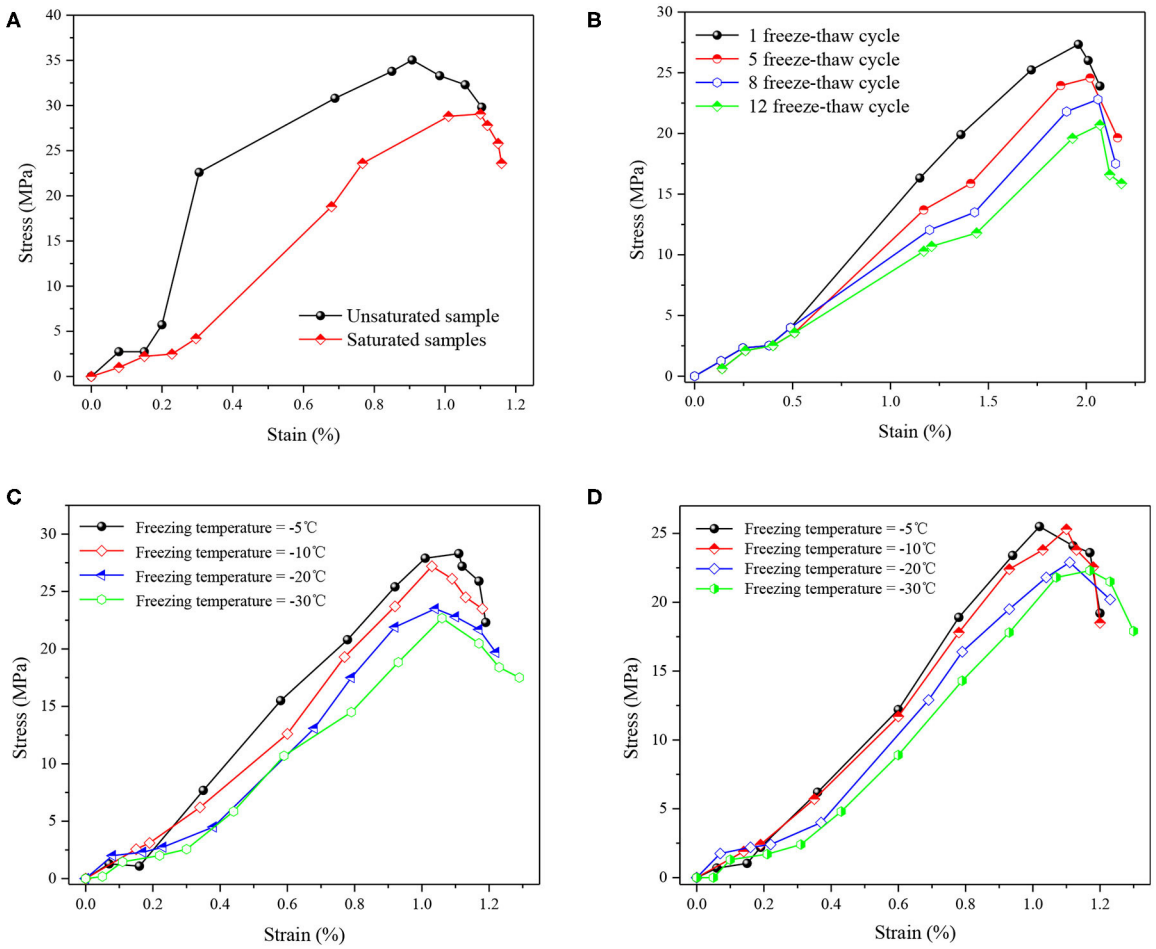

FIGURE 4 | Stress–strain curves of sandstone–concrete composite under different freeze–thaw conditions: **(A)** freezing temperature = −10°C, freeze–thaw cycle = 1; **(B)** water-saturated specimen, freezing temperature = −10°C; **(C)** unsaturated specimen, freeze–thaw cycle = 1; **(D)** water-saturated specimen, freeze–thaw cycle = 1.

TABLE 3 | Analysis of unconfined compressive strength of sandstone–concrete samples.

Source of variance	Degree of freedom	Mean square	*F* -value	*P* -value	Significant
Moisture content	2	84.718	140.52	0.000	I
Freeze–thaw cycles	3	123.514	204.86	0.000	I
Freezing temperature	1	62.714	104.02	0.000	I
$A \times B$	6	11.133	18.47	0.000	I
$B \times C$	3	0.024	0.04	0.844	III
$A \times C$	2	2.031	3.37	0.079	III
$A \times B \times C$	6	1.699	2.82	0.106	II
Error	24	14.470	–	–	–
Sum	31	307.473	–	–	–

the calculation, it can be concluded that factor *A*, factor *B*, factor *C*, and interaction $A \times B$ have a more prominent effect on UCS.

Figure 5 shows the Pareto diagram of the standardized effect. The Pareto diagram can determine the magnitude and importance of the effect. The magnitude corresponding to the reference line in this figure is 2.06. It can be seen from **Figure 5** that the significance of the main effect and the interaction of the first and second order on the UCS of the complex specimen

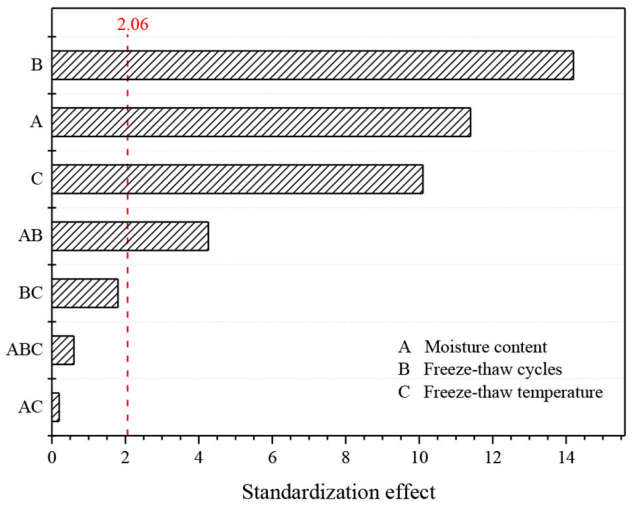

FIGURE 5 | Pareto diagram of standardization effect.

is decreased in the order of freeze–thaw cycle number (factor *B*), moisture content (factor *A*), freezing temperature (factor *C*), first-order interaction $A \times B$, first-order interaction $B \times C$, second-order interaction $A \times B \times C$, and first-order interaction $A \times C$. According to the standardization effect, the main factors affecting UCS are the main effect *B*, *A*, *C* and interaction $A \times B$. The standardization effect for effect *B* is about 1.3 times that for main effect *A*, and about four times of those for main effect *C* and interaction $A \times B$; the standardization effect for main effect *A* is about three times as large as those for main effect *C* and interaction $A \times B$; the standardized effects of main effect *C* and interaction $A \times B$ is almost the same (∼2.2).

Through the six interaction diagrams of factors *A*, *B*, and *C* displayed in **Figure 6**, it can be concluded that synergistic interaction is the main interactive interaction among these three investigated factors, whereas non-interactive interaction and antagonistic effect are the auxiliary. The synergistic interaction is evident in the freeze–thaw cycle one time and five times, freezing temperature from −5 to −10°C.

As **Figure 7** shows, one of the three investigated factors *A*, *B*, and *C* was kept unchanged and contour maps were drawn of the other two factors and UCS. **Figure 7A** shows that the UCS value is >19.5 kPa when the moisture content of the complex specimen is between 14.00 and 16.35% and the number of freeze–thaw cycles is between 1 and 3. When the moisture content is between 16.35 and 18.45%, the number of freeze–thaw cycles is between 3 and 5, and the UCS value is in the range of 18–19.5 kPa. When the moisture content increases by about 2.00% and the number of freeze–thaw cycles increases by about 2 times, the UCS value will enter the next level. **Figure 7B** shows that when the freeze–thaw cycle number of the complex specimen at freeze temperature of −15°C was 1.6 and the freeze–thaw cycle number of the complex specimen at freeze temperature of −5°C was 3.5, the UCS values are higher than 16.8 kPa; when the freeze–thaw cycle number of the complex specimen at freeze temperature of −15°C was 3.8 and the freeze–thaw cycle number of the complex specimen at freeze temperature of −5°C was 5.7, the UCS values are in the range of 15.6–16.8 kPa. The aforementioned results show that the decrease of freeze temperature and the increase of freeze–thaw cycle have an interactive effect on the UCS of the complex specimen. The relationship revealed by **Figure 7C** is basically the same as that revealed in **Figure 7B**, indicating that there is an interactive effect between moisture content and freezing temperature on the UCS of the complex specimen.

According to the experimental results, the main effect value of each factor and the interaction effect value among factors *A*, *B*, and *C* were obtained, and the following regression equation was fitted by using the Design Expert software:

$$k = 31.12 - 70.4 \times A - 0.519 \times B + 0.2712 \times C - 0.01841 \times B \times C + 0.298 A \times B \times C \quad (26)$$

where *k* is the UCS of the sand–concrete complexes. Considering the three factors *A*, *B*, and *C*, the effects of moisture content (factor *A*) and freeze–thaw cycle (factor *B*) can only be positive, whereas the effect of freezing temperature (factor *C*) is negative. Therefore, it can be obtained from Equation (26) that factors *B*, *C*, and $A \times B \times C$ have negative regression coefficients, and their weighted coefficients are 1.836, 0.311, and 0.276, respectively. The regression coefficient of factor *B* is the largest, indicating that *B* has the most apparent impact on the UCS of the complex specimen. With the increase of the number of freeze–thaw cycles, the UCS of the complex specimen significantly decreases, and the synergistic effect in the system also decreases, whereas the antagonistic effect increases. The regression coefficients of factors *A*, $A \times B$, $A \times C$, and $B \times C$ are positive, indicating that the main effect and the interaction have a positive contribution to the UCS of the complex specimen. When the degree of factors *A*, $A \times B$, $A \times C$, and $B \times C$ increases, the UCS of the complex specimen will slightly decrease, and the synergistic effect of the factors increases and antagonistic effect of the factors decreases.

Based on the aforementioned analysis, it can be seen that not only the moisture content, freeze–thaw cycle times, and freezing temperature have impacts on the mechanical properties of the sand–concrete complex specimen but the interactions between various factors are also significant. Therefore, the independent effect of each factor cannot be simply considered separately, but the influence of each factor and their interaction should be considered comprehensively.

CONCLUSION

Based on the experimental study on the UCS of sandstone–concrete complex specimen under different freeze–thaw conditions and the interactive interaction among different factors, the main understandings and achievements are as follows:

(1) The UCS of the sandstone–concrete dry complex specimen is significantly higher than that of the water-saturated complex

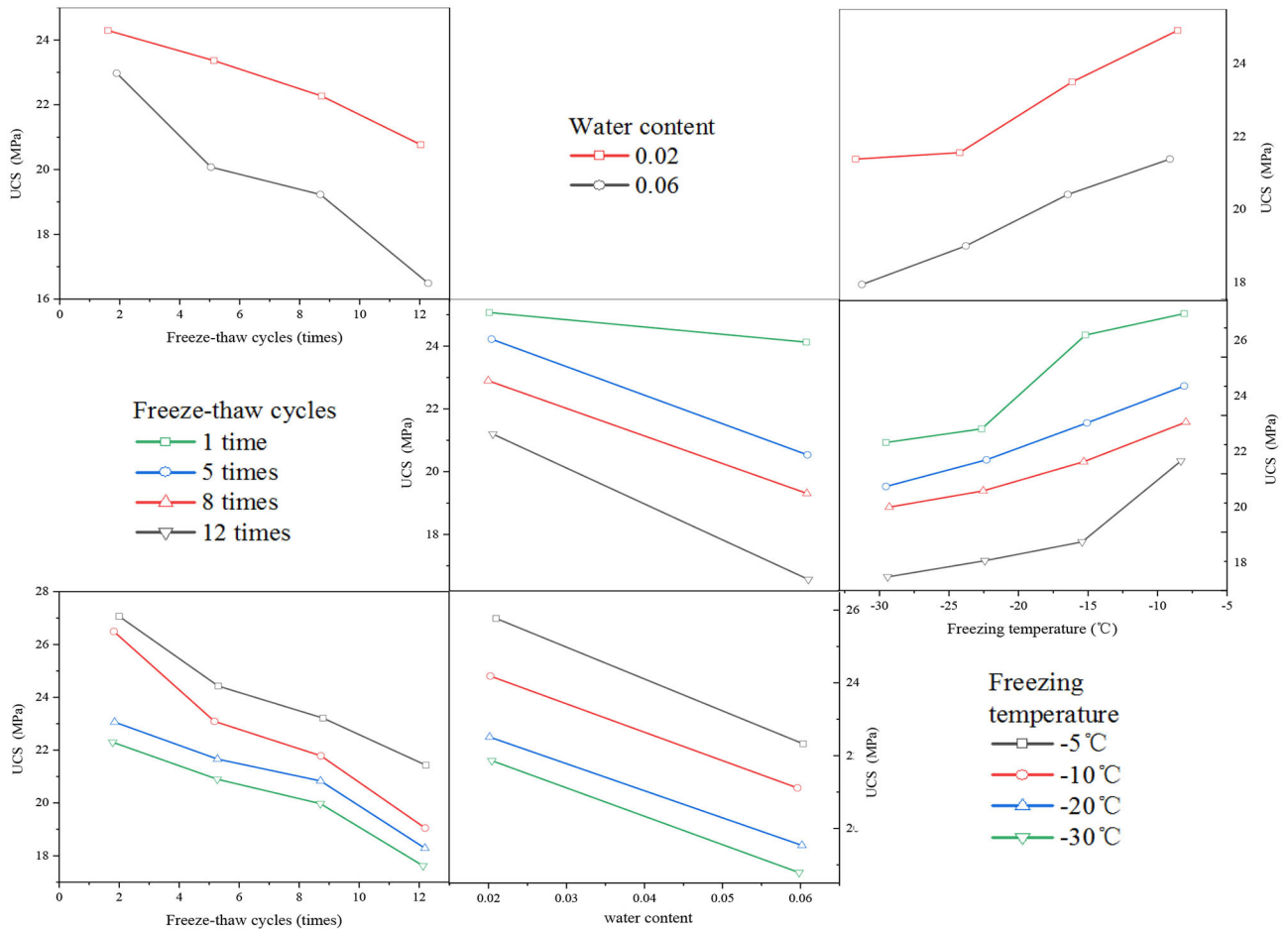

FIGURE 6 | Pareto diagram of standardization effect.

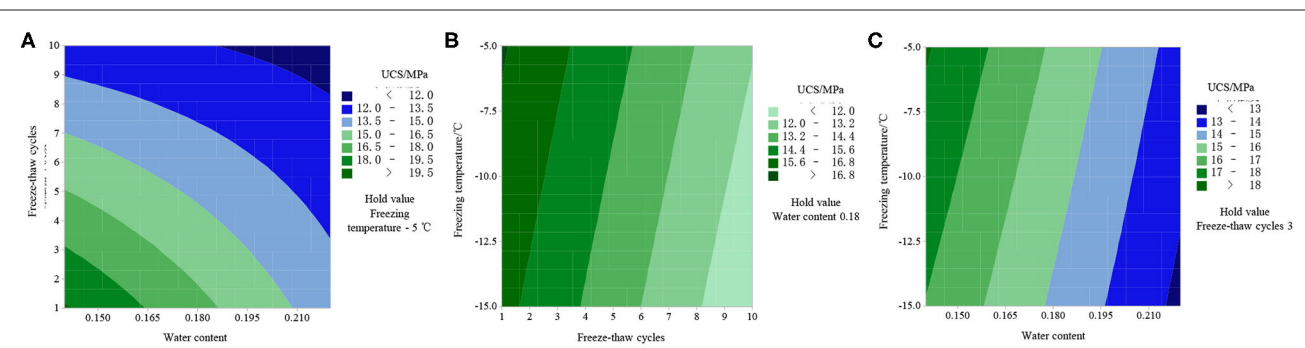

FIGURE 7 | Isoline between UCS of sandstone–concrete complex and factors *A*, *B*, and *C*. **(A)** Isoline between UCS and factors *A*, *B*; **(B)** isoline between UCS and factors *B*, C; **(C)** isoline between UCS and factors *A*, *C*.

specimen and the plastic phase of the water-saturated specimen shifts to an earlier time and is more significant. It can be explained that pore pressure increases with water content and therefore the effective stress on the sample gets reduced, and that makes the UCS lower (according to Mohr–Coulomb failure criterion). The stress–strain curves of the composite specimens under different freezing temperatures were significantly changed under the action of one freeze–thaw cycle, and the UCS of composite specimens decreased with the freezing temperature.

(2) After 0, 1, 5, 8, and 12 freeze–thaw cycles, the UCS of both the dry complex specimen and water-saturated complex specimen decreased significantly. After 12 freeze–thaw cycles, the strength was only between 50 and 70% compared with that of the unfrozen samples.
(3) The main effects and the interactions of the first and second order on the UCS of the complex specimen are as follows: freeze–thaw cycle number (factor A), water content (factor B), freezing temperature (factor C), first-order interaction $A \times B$, the second-level interaction $A \times B \times C$, the first-level interaction $A \times C$, and the first-level interaction $B \times C$.
(4) The interaction among the factors is mainly the synergistic interaction, supplemented by non-interactive interaction and antagonism. The synergistic effect is profoundly observed when the freeze–thaw cycle number is in the range of 5–8, the moisture content is in the range of 14–18%, and the freezing temperature decreases from −5 to −15°C. The significance of the freeze–thaw cycle 0 times and 1 time was significantly higher than eight times and 12 times, and the freeze–thaw damage of the complex specimens showed cumulative effect with freeze–thaw number.

In the future study, non-destructive testing technology (nuclear magnetic resonance) will be used to study the micropore characteristics of sandstone–concrete composite under the action of freeze–thaw cycle and the relationship between the micropore characteristics and macromechanical properties.

DATA AVAILABILITY STATEMENT

All datasets generated for this study are included in the article/supplementary material.

AUTHOR CONTRIBUTIONS

TZ: writing—original draft preparation. JX: methodology. YS: software. K-iS: validation. GY: supervision. All authors have read and agreed to the published version of the article.

FUNDING

This research was supported by the National Natural Science Foundation of China (no. 51772341), Key R&D Projects in Shaanxi Province (no. 2019SF-264) and the National Research Foundation of Korea (NRF) funded by the Ministry of Science, ICT & Future Planning (no. 2017R1E1A1A01075118).

ACKNOWLEDGMENTS

We are grateful for the support provided by the College of Civil and Architectural Engineering, Xi'an University of Science and Technology, Xi'an 710054, China.

REFERENCES

1. Wang L. Development and utilization of coal resources in west china to regional contribution and typical demo reference. *Coal Econ Res.* (2017) **37**:28–33. doi: 10.13202/j.cnki.cer.2017.01.005
2. Li Y, Jing H, Zhang L. Construction technology of freezing method for low temperature large section shaft. *Mod Mining.* (2014) **30**:182–4. doi: 10.3969/j.issn.1674-6082.2014.07.066
3. Cheng H, Cai H. Safety situation and thinking about deep shaft construction with freezing method in china. *J Anhui Univ Sci Tech.* (2013) **33**:1–6. doi: 10.3969/j.issn.1672-1098.2013.02.001
4. Yang G, Xi J, Li H, Cheng L. Experimental study of rock mechanical properties under triaxial compressive and frozen conditions. *Chin J Rock Mech Eng.* (2010) **29**:459–64.
5. Cheng H, Yao Z, Rong C. The key technical problems of freeing methods of sinking shaft in the western region of china. In: *New Progress in Mine Construction Engineering Technology, Xiamen, 2009 National Academic Conference on Mine Construction* (Vol I) (2009).
6. Matsuoka N. Mechanisms of rock breakdown by frost action: an experimental approach. *Cold Regions Sci Technol.* (1990) **17**:253–70. doi: 10.1016/S0165-232X(05)80005-9
7. Hroi M. Micromechanical analysis on deterioration due to freezing and thawing in porous brittle materials. *Int J Eng Sci.* (1998) **36**:511–22. doi: 10.1016/S0020-7225(97)00080-3
8. Yamabe T, Neaupane KM. Determination of some thermo-mechanical properties of Sirahama sandstone under subzero temperature conditions. *Int J Rock Mech Mining Sci.* (2001) **38**:1029–34. doi: 10.1016/S1365-1609(01)00067-3
9. Yang G, Zhang Q, Pu Y. CT scanning test of meso-damage propagation of rock under different freezing temperature. *J Chang'an Univ.* (2004) **24**:40–6. doi: 10.3321/j.issn:1671-8879.2004.06.010
10. Yang G, Zhang Q, Ren J, Pu Y. Study on the effect of freezing rate on the damage ct values of tongchuan sandstone. *Chin J Rock Mech Eng.* (2004) **23**:4099–104. doi: 10.3321/j.issn:1000-6915.2004.24.001
11. Yang G, Lv X. Experimental study on the sandy mudstone mechanical properties of shaft sidewalls under the frozen conditions. *J Mining Saf Eng.* (2012) **29**:492–6.
12. Xi J, Yang G, Dong X. Effect of freezing temperature on mechanical properties of sandy mudstone. *J Chang'an Univer.* (2014) **34**:92–6. doi: 10.19721/j.cnki.1671-8879.2014.04.014
13. Yang E, Xi J. Review and prospects of research on freezing design theory of coal mine shaft. *Chin J Undergr Space Eng.* (2010) 6:627–35. doi: 10.3969/j.issn.1673-0836.2010.03.034
14. Wang K. Test study on the mechanical property of tuff at different strain rates in freezing condition. In: *New Process of Mine Construction Engineering-Proceedings of 2006 National Conference on Mine Construction* (Vol II), Yunnan, (2006). p. 330–4.
15. Xie S, Lin H, Wang Y, Chen Y, Xiong W, Zhao Y, et al. A statistical damage constitutive model considering whole joint shear deformation. *Int J Damage Mech.* (2020) **29**:1056789519900778. doi: 10.1177/1056789519900778
16. Wang Y, Zhang H, Lin H, Zhao Y, Liu Y. Fracture behaviour of central-flawed rock plate under uniaxial compression. *Theoret Appl Fracture Mech.* (2020) **106**:102503. doi: 10.1016/j.tafmec.2020.102503
17. Xu G, Liu Q, Peng W, Chang X. Experimental study on basic mechanical behaviors of rocks under low temperatures. *Chin J Rock Mech Eng.* (2006) 25:2502–8. doi: 10.1016/S1872-1508(06)60035-1
18. Shi S. Effect of freezing-thawing cycles on mechanical properties of concrete. *J China Civil Eng.* (1997) **04**:35–42.
19. Zou C, Zhao J, Lang F, Ba H. Experimental study on stress strain relationship of concrete in freeze thaw environment. *J Harbin Inst Technol.* (2007) **39**:229–231. doi: 10.3321/j.issn:0367-6234.2007.02.014
20. Shang H, Song Y, Tan L. Experimental study on the performance of ordinary concrete after freeze-thaw cycle. *China Concrete Cement Prod.* (2005) 9–11.

21. Xiang W, Liu X. Experimental study of mechanical properties of complex specimen with rock and shotcrete under freezing-thawing cycles. *Chin J Rock Mech Eng.* (2010) **29**:2510–21.
22. Yi C, Liu J, Wang C, Li Z. Photo elastic method and numerical simulation of the interface between bi-material specimen. *Chin J Rock Mech Engin.* (2008) **37**:450–5. doi: 10.3724/SP.J.1011.2008.00367
23. Shen Y, Wang Y, Wei X, Jia H, Yan R. Investigation on meso-debonding process of the sandstone–concrete interface induced by freeze–thaw cycles using NMR technology. *Constr Build Mater*. (2020) **252**:118962. doi: 10.1016/j.conbuildmat.2020.118962
24. Tian J, Wu X, Zheng Y, Hu S, Ren W, Du Y, et al. Investigation of damage behaviors of ECC-to-concrete interface and damage prediction model under salt freeze-thaw cycles. *Constr Build Mater*. (2019) **226**:238–49. doi: 10.1016/j.conbuildmat.2019.07.237
25. Guo P. Principle and application of three factors analysis of variance. *J Shenyang Univ*. (2015) **27**:40–3.
26. Lu S, Wang L, Zhuang W, Shen C, Wang S. Influence of processing parameters and their interaction on shrinkage of injection molded parts. *Die & Mould Industry*. (2006) **32**:59–63. doi: 10.16787/j.cnki.1001-2168.dmi.2006.10.018

Conflict of Interest: The authors declare that the research was conducted in the absence of any commercial or financial relationships that could be construed as a potential conflict of interest.

frontiers in Physics

ORIGINAL RESEARCH
published: 07 October 2020
doi: 10.3389/fphy.2020.553643

Aging Features and Strength Model of Diorite's Damage Considering Acidization

Wei Chen[1]*, *Wen Wan*[1]*, *Yanlin Zhao*[1], *Senlin Xie*[1], *Bing Jiao*[1], *Zhenming Dong*[1], *Xianqing Wang*[1] and *Shuailong Lian*[2]

[1]School of Resource, Environment and Safety Engineering, Hunan University of Science and Technology, Xiangtan, China, [2]School of Civil Engineering, Guizhou University, Guizhou, China

Acidic fluids will cause rock erosion and further endanger the safety of rock engineering. To explore the aging characteristics of the mechanical damage under acid condition, diorite specimens were saturated in neutral water and acid solutions with pH values of 3 and 5 for 49 days. The masses and sizes of the specimens and the pH values of the acidic solution were tracked and measured. Besides, the specimens before and after saturations were observed by an electron microscope scanner. Meanwhile, triaxial compression tests were carried out under neutral water, pH = 5 and pH = 3 hydrochloric acid solutions, respectively. The mass damage features and mechanical properties of diorite specimens saturated in solutions with different pH values were analyzed. The results show: 1) after acidic saturation, the original lamellar structures and crystal forms were spongy or flocculent. The structure loosened and the boundary between layers became fuzzy. Meanwhile, the number of micro-cracks and micro-pores increased, which weakened the macro-mechanical performances of diorite; 2) the acid condition with pH value of 3 could be used to simulate the long-term effect of the weakly acidic environment in nature; 3) internal friction angle of diorite was more sensitive to acidic solutions than its cohesion; 4) at the initial stage of saturation, diorite broke rapidly. With increasing saturation time, the damage rate slowed down and finally stabilized. The established damage strength model considering acidification could properly describe the test results.

Keywords: rock mechanics, acidification erosion, mechanics damage, aging characteristics, strength model

OPEN ACCESS

Edited by:
Longjun Dong,
Central South University, China

Reviewed by:
Eric Josef Ribeiro Parteli,
University of Cologne, Germany
Niravkumar J. Joshi,
University of California, Berkeley, United States

***Correspondence:**
Wei Chen
180101020001@mail.hnust.edu.cn
Wen Wan
wanwenhunst@163.com

Specialty section:
This article was submitted to Interdisciplinary Physics, a section of the journal Frontiers in Physics

Received: *19 April 2020*
Accepted: *14 September 2020*
Published: *07 October 2020*

Citation:
Chen W, Wan W, Zhao Y, Xie S, Jiao B, Dong Z, Wang X and Lian S (2020) Aging Features and Strength Model of Diorite's Damage Considering Acidization. Front. Phys. 8:553643. doi: 10.3389/fphy.2020.553643

INTRODUCTION

The mechanical properties of rock masses could be affected by water erosion [1–3]. Moreover, the differences in water fluid chemicals significantly affect their mechanical properties and chemical composition [4–7]. Compared with distilled water, water chemical fluids produce more intense latent erosion and molten corrosion, resulting in the overall deterioration and the destruction of the micro-mechanical structure of the rock mass [8–10]. Subsurface rock mass is subject to groundwater erosion and thawing. Therefore, the mechanical properties of rock mass are easily influenced by the external conditions [11–15]. Meanwhile, in various water-related rock engineering constructions, such as dam foundation, slope, tunnel, and underground mining, it is important to understand the influence of water erosion on the characteristics of the bearing capacity and deformation of the structure [11, 12, 16, 17].

Atkinson et al. [12] and Dunning et al. [14] used distilled water, inorganic water chemical solution, and organic solution to research the effects of different water chemical solutions on the fracture development of single-crystal quartz and glass. Rebinder et al. [15] analyzed the influence of the water chemical environment on the mechanical properties of rock mass based on the Griffith strength theory. Karfakis et al. [18] performed tensile tests on rocks saturated in different water chemical solutions and analyzed the influence of different chemical solutions on the fracture toughness. Feucht et al. [19] conducted triaxial compression tests on prefabricated sandstone specimens in NaCl, $CaCl_2$, and Na_2SO_4 solutions. They further discussed the effects of different water chemical solutions on the friction factors of the sandstone crack surfaces. Hutchinson et al. [20] and Heggheim et al. [21] used HCl, H_2SO_4 and other diluted solutions to simulate acid rain. Then, they measured the effect on the determination of the mechanical parameters of limestone and the damage mechanism. Moreover, the corrosion resistance and corrosion mechanism of different types of cement mortar were studied comprehensively. It is found that the deterioration of samples of cementing materials under acid rain erosion is mainly due to the coupling effect of H^+ and SO_4^{2-}. Meanwhile, it leads to the increase of porosity and the loss of weight and strength of cementing materials [22, 23]. Brzesowsky et al. [24] investigated the coupling effect of the hydrochemical environment and the stress state on the creep characteristics of sandstone under compression. Moreover, by changing particle sizes in the rock sample, the time-dependent effect of water chemical environment on rock particle destruction was proposed. Liu et al. [25] studied the effects of hydrochemical solutions on the mechanical parameters of sandstone. In the works of Tang et al. [26–29], the mechanism and quantification method of rock hydrochemical damage were systematically discussed. Ding et al. [30, 31] analyzed the damaging effect of the water chemical solution on the macro and microstructures of limestone. Furthermore, they quantified the law of water chemical damage on its mechanical properties. Chen et al. [32–34] performed uniaxial and triaxial compression tests on sandstone, granite, and limestone specimens in various solutions. As a consequence, the dynamic parameters of rocks affected by corrosion were obtained by applying computed tomography scanning. According to the fracture characteristics and evolution law, a chemical damage constitutive model was established. Using various flow rates and pH values, Miao et al. [35, 36] performed uniaxial compression, triaxial compression and splitting tests on the dry granite specimens and corroded ones. They further analyzed the strength evolution, deformation characteristics and response mechanism of mechanical parameters in acidic environment. Besides, they observed the characteristics of mass damage and pH changes of acidic solution during the process, and then examined the ion chromatographic detection of chemical components and concentrations of the solution after saturation. By using scanning electron microscopy (SEM) and electronic energy spectroscopy, they also discussed the aging features of acidic chemical solution on the macrophysical properties [12, 18, 37].

The previous researches mainly focus on the hydrophysical and hydrochemical effects on the macro-mechanical properties of rocks. Nonetheless, the researches on the mechanism of rock chemical damage based on the effects of water and rock microscopic effect are still relatively scarce [38–41]. Water-rock chemical action has a great influence on the deterioration of rock micro-mechanical structure, and also affects the macro-mechanical properties [42–44]. Besides, quantitative studies on the hydrochemical damage of rocks have emerged. But researches on the damage effects of water-rock chemistry on the mechanical properties of rock mass have been rarely reported [45, 46]. Therefore, the researches on damage, strength and failure modes of rocks in acidic environments are urgent. Based on the above-mentioned tests, the hydrogeological survey of Copper-Iron mine in Qianchang County, Anhui Province was carried out. Through investigation, weak acid groundwater was found to be in this mine area, where the surrounding rocks of diorite are damaged by the groundwater erosion for a long time. Therefore, this paper intends to take the diorite rock in this mine area as the research object, simulate the groundwater erosion environment, conduct immersion on the diorite rock, SEM observations and triaxial compressive strength (TCS) tests were performed on diorite specimens before and after saturations with pH values of 3, 5, and 7 for 49 days. Furthermore, the effect of natural long-term acidity condition on the time-dependent characteristics of rock damage was studied and a damage strength model was established.

LABORATORY TESTS

Preparation of Rock Specimens

Diorite was taken from Line 10 in the middle -300 section of Qianchang Copper–Iron Mine in Anhui Province, China. Following the standards of the International Society for Rock Mechanics [47, 48], the specimens were first processed into a cylinder with a diameter of 50 mm and a height of 100 mm for TCS tests. Meanwhile, due to the size of the SEM observation platform, the standard specimen was further processed into three small specimens with a diameter of 50 mm and a height of 25 mm. Three different pH values of 3, 5, and 7 were used to simulate the different subsurface acidic environments, respectively.

Test pieces were inserted into the preservation boxes containing the hydrochloric acid solution. During saturation process, the pH value of the solution in each box was measured and recorded.

Experiment Content and Test Method

To observe the mechanical properties of diorite before and after the acidification treatment, SEM observations and TCS tests were performed (see **Supplementary Figure S1**).

Scanning Electron Microscopy Observation

The SEM observations were performed four times. DJ-1 was scanned before and after saturation in distilled water for 49 days. DJ-2 and DJ-3 were scanned after saturation in acid solutions

with pH values of 3 and 5 for the same time, respectively (**Figure 1A**). The sample surfaces were scanned with a magnification coefficient of 400–450 (**Figure 1B**).

Triaxial Compressive Strength Experiment

The TCS tests were performed on RMT-150C with confining stresses (σ_3) of 10, 20, and 30 MPa. The axial and lateral loading rates were 0.1 KN/s and 0.2 MPa/s, respectively. The stress-strain curves were recorded during the test. Besides, the damaged specimen was photographed for later reference (see **Supplementary Figure S2**).

CHEMICAL DAMAGE ANALYSIS

The main component of diorite in the Qianchang copper-iron area is oxidized minerals (**Figure 2**). Under acidic solution, the oxidized mineral components in diorite will react with H^+ as follows:

$$Al_2O_3 + 6H^+ == 2Al^{3+} + 3H_2O \quad (1)$$

$$Na_2O + 2H^+ == 2Na^+ + H_2O \quad (2)$$

$$CaO + 2H^+ == Ca^{2+} + H_2O \quad (3)$$

$$K_2O + 2H^+ == 2K^+ + H_2O \quad (4)$$

$$MgO + 2H^+ == Mg^{2+} + H_2O \quad (5)$$

$$Fe_2O_3 + 6H^+ == 2Fe^{3+} + 3H_2O \quad (6)$$

Rock Surface Characteristics After Acidification

The main changes of the specimen surface after saturation in a hydrochemical solution are reflected in macro and micro aspects [8, 49–51].

Diorite samples were smooth after coring, cutting, and grinding. Macroscopic viewing also suggests that the samples were uniformly dense and flat before acid saturation (**Figure 3A**). After saturation for 49 days in acidic solutions with pH = 3 and pH = 5, powders were stripped from the surface of the rock samples. While the powders were rinsed, the outer surface became rough and some micro-cracks appear (**Figure 3C**). After long-term saturation, the outer surface was dissolved, and the color turned slightly gray. There were severe unevennesses on the surface under acid solution of pH = 3 (**Figure 3D**). However, after saturation in distilled water, no obvious macro changes were observed, except for a lighter surface (**Figure 3B**). It suggests that the chemical damage negatively relates to the pH value. The macro comparison of the representative test specimens after saturation for 49 days is shown in **Figure 3**.

Microscopically, according to the scanning electron micrographs in **Figure 4A**, the rock sample showed a clear layered structure or flaky crystal form before saturation, with superior homogeneity, tight internal structure, small interlayer

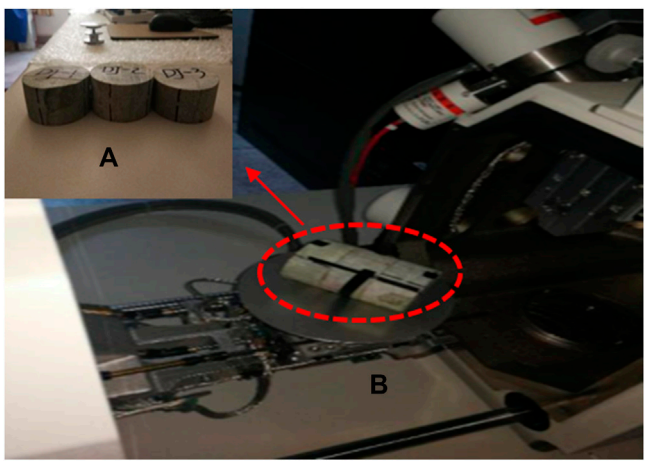

FIGURE 1 | Scanning electron microscopy observation: **(A)** specimens, and **(B)** testing platform.

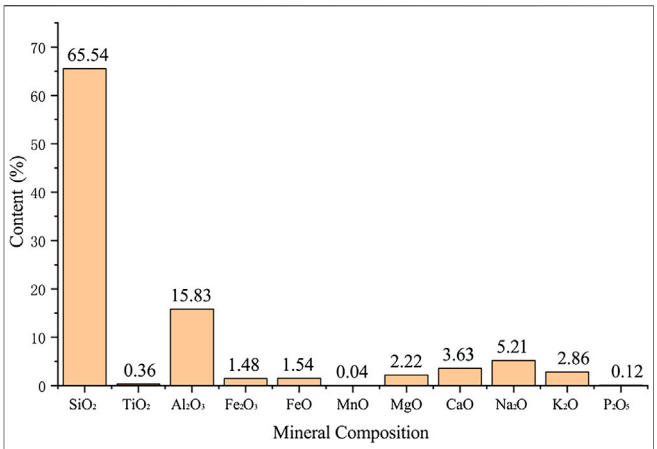

FIGURE 2 | Main chemical constituents of diorite before saturation.

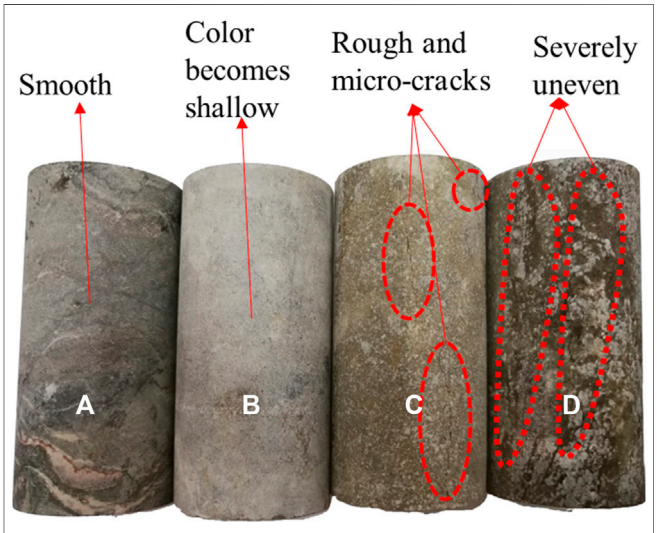

FIGURE 3 | Macro comparison of sample surfaces after different saturations: **(A)** naturally dry condition, **(B)** pH = 7, **(C)** pH = 5, and **(D)** pH = 3.

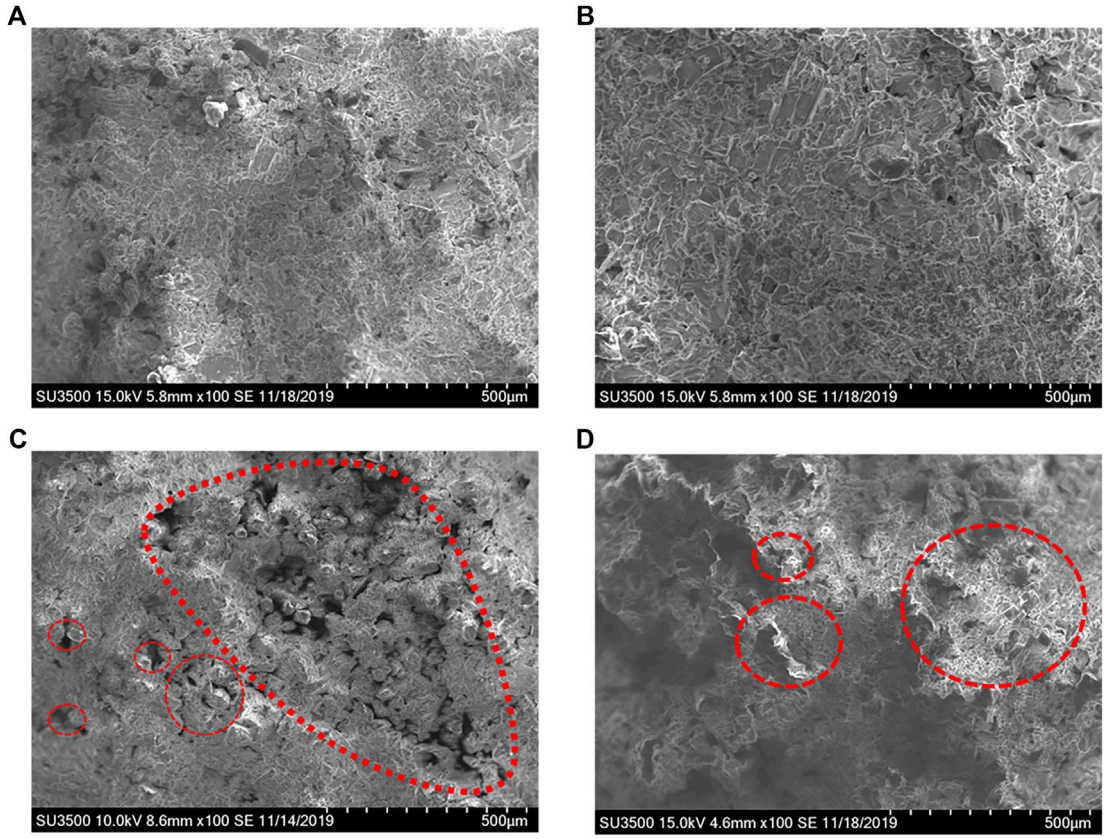

FIGURE 4 | Scanning electron microscopy of diorite surfaces after different saturations: **(A)** naturally dry condition, **(B)** pH = 7, **(C)** pH = 5, and **(D)** pH = 3.

distance, and micro-cracks. The micropore was small and dispersed. The microstructure consisted of homogeneous and dense particles, fine and sparse pores, indicating the positive macro mechanical properties before acidification and erosion.

However, the specimens saturated in acidic solutions exhibited a spongy or flocculent structure. The structure was loosened, and the boundary between layers became blurred (**Figures 4C, D**). The number of micro-fissures and micro-pores increased, and some independent small-sized micro-pores were dispersively interconnected with each other to form a larger "gully" (**Figure 4C**). In comparison, more powders were shed and the edges were the more distinct at pH = 3 (**Figure 4D**). After saturation in distilled water, the microscopic morphology did not change obviously (**Figure 4B**). Clearly, the decrease in pH value accelerated the chemical damage.

Mass Damage After Acidification

After saturation for 49 days, the surfaces of the rock samples were rinsed with distilled water, dried, and measured. Compared with the rock sample mass before saturation, the mass decreased by various degrees with different pH values. However, the masses after dipping in distilled water were basically the same as the ones before saturations. Five samples were randomly selected from the three groups. Comparisons between the mass before and after saturations with different pH values are shown in **Figure 5**.

The stronger and faster reaction was caused by the higher concentration of H^+ in the solution [52, 53]. It can be further concluded that stronger acidity led to the destruction of more micro-structures. As shown in **Figure 5**, the mass was slightly diminished after saturated in distilled water. It proves the existence of water-soluble mineral components. To quantitatively characterize the degree of mass damage after saturation, a time-dependent mass damage factor $D_{(t)}$ is defined:

$$D_{(t)} = \frac{M_0 - M_{(t)}}{M_0} \times 100\% \tag{7}$$

Where M_0 is the mass of the rock sample before saturation, and $M_{(t)}$ is the mass at t days during saturation.

The mass damage factors of the samples saturated for 49 days at pH = 3 and pH = 5 are presented in **Figure 6**. Relatively speaking, the change in distilled water is not obvious. Thus, the factors are not provided here.

Figure 6A shows that the mass damage factors at pH = 3 are higher than pH = 5. The average value of the factors at pH = 3 is 2.30%, while which at pH = 5 is 1.21% (see **Figure 6B**). Obviously, the latter is almost half of the former. Under the two actions, the standard deviations are almost the same. The standard deviation is 0.25 at pH = 3 and 0.24 at pH = 5. Hence, the comparison between the two is reliable. In conclusion, during the same time of

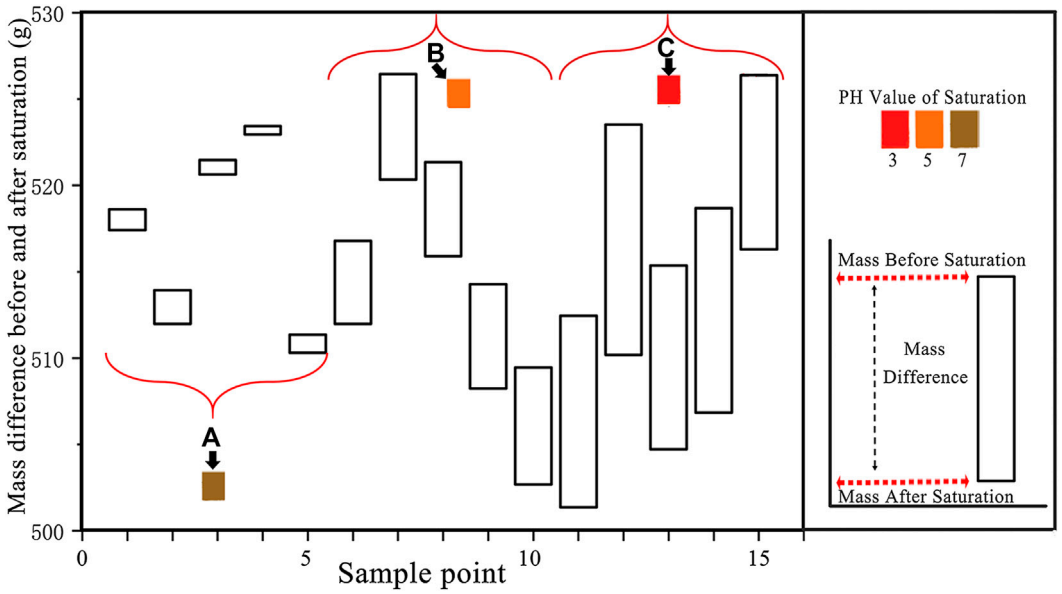

FIGURE 5 | Comparison of mass differences before and after different saturations: **(A)** rock samples soaked with distilled water, **(B)** rock samples under pH = 5 acidic saturation, and **(C)** rock samples under pH = 3 acidic saturation.

saturation, lower pH value will strengthen the reaction, leading to larger mass damage and corrosion.

LABORATORY RESULTS AND DISCUSSION

Calculation of Time Scale

The time scale refers to the ratio of the amount of H^+ substances consumed per unit time for two solutions with different initial pH values [52, 54]. Assuming that under a strongly acidic solution, the amount of H^+ substances consumed per unit time is Δn_1, and that in weak acid is Δn_2, the time scale $\eta(t)$ of two different acidic solutions can be defined as:

$$\eta(t) = \frac{\Delta n_1}{\Delta n_2} \tag{8}$$

Theoretically, the time scale $\eta(t)$ is a variable with the selected period. Due to the limitations of the laboratory, it is impossible to accurately determine the amount of H^+ substances at any time during saturation process. In this paper, the unit time is set as 12 h to calculate the time scale. **Table 1** lists the changes in the amount

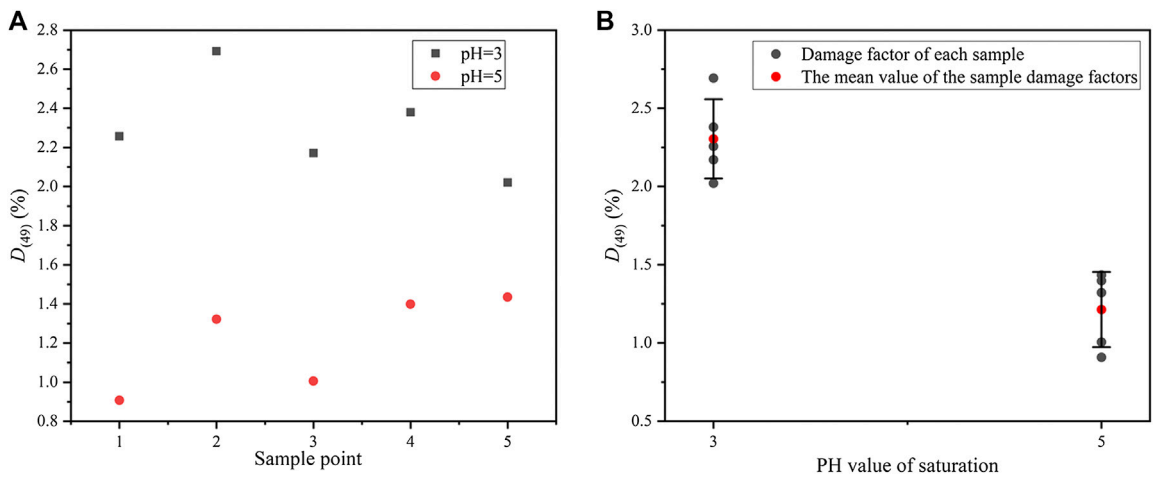

FIGURE 6 | Mass damage factors of rock samples after different acidic saturations for 49 days: **(A)** damage factor of each sample, and **(B)** error bars of damage factors.

TABLE 1 | Change in the amount of H^+ and time scale conversion.

Initial pH	Change in the amount of H^+ substance per unit volume/mol			
	12 h	24 h	36 h	48 h
3	-9.998×10^{-4}	-9.975×10^{-4}	-9.737×10^{-4}	-8.341×10^{-4}
5	-9.661×10^{-6}	-9.088×10^{-6}	-7.709×10^{-6}	-4.872×10^{-6}
Initial pH	**Time scale $\eta(t)$**			
	12 h	**24 h**	**36 h**	**48 h**
3	1.00	1.00	1.00	1.00
5	103.49	109.76	126.31	171.20

of H^+ substances under the two acidic solutions. Thus, the calculated results are provided in **Table 1**.

According to **Table 1**, the consumption of H^+ shows a decreasing trend, indicating that the reaction gradually slows down. In the first 12 h, the consumption of H^+ in the acidic solution with initial pH = 3 is 103.49 times as much as the initial pH = 5 (see **Table 1**). The time scale reflects the chemical damage caused by the two acidic solutions. Thus, in the first 12 h, the solution of pH = 3 causes 103.49 times the damage compared to that of pH = 5. Similarly, based on the change of H^+ per unit time, the time scale of chemical damage caused by two different acidic solutions can be calculated at any period. The characteristics of the solution with pH = 5 is close to the natural environment. Through the conversion of the time scale, saturation under pH = 3 could be tried to simulate the long-term effect caused by natural environment in a short time, which may shed some lights on predicting the durability of rock masses in nature.

Characteristics of pH Change During Acidification

As mentioned above, the pH value of the acidic solution plays an important role in the corrosion of diorite. The change of pH value can directly reflect the reaction rate and degree. In the tests, the pH value was measured every 12 h. To maintain the initial concentrations (pH = 3 and 5), concentrated hydrochloric acid was added dropwise *via* plastic dropper. The rock sample and the acidic solution reacts violently at the beginning (see **Figures 7A, C**). Meanwhile, the pH value increases significantly, which is close to neutral. Hence, it shows that the H^+ ions in the two solutions have almost been consumed. As saturation time increases, the pH values gradually decrease. Besides, the two decline rates continuously decrease, while the decline rate with pH = 3 is faster than that with pH = 5. Lastly, the pH of the initial solution with pH = 3 starts to stabilize slowly on the 29th day (the 58th measurement) (see **Figure 7D**), and the pH is slightly higher than 3. Thus, the reaction proceeds slowly after the 29th day, but it does not indicate the end. When the minerals on the outer surface have been dissolved, the internal structure may fail to display signs of reaction due to the tight structure arrangement. In contrast, the pH of the initial solution of pH = 5 gradually stabilizes on the 32nd day (64th measurement) (see **Figure 7B**). However, the corresponding pH is greater than 5, indicating that the reaction has changed from the 32nd day. Change of the pH value in distilled water is minimal. It indicates that no obvious chemical reaction has occurred. Therefore, its curve over time is not provided.

According to **Figure 7**, the time-dependent pH value at initial pH = 3 is:

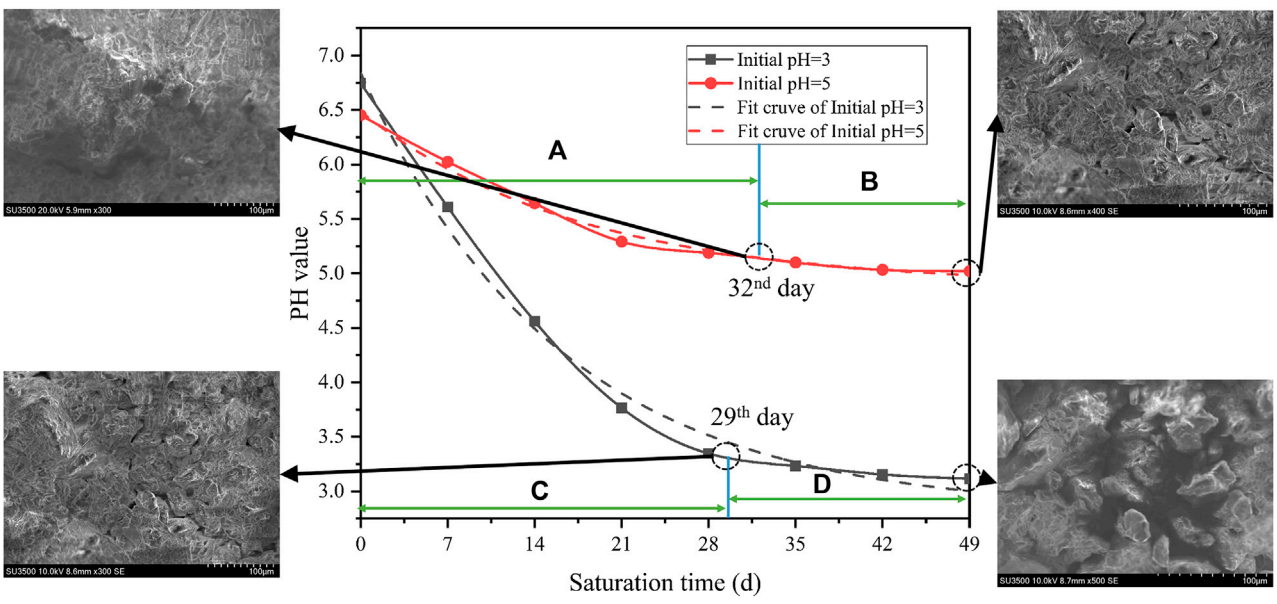

FIGURE 7 | Aging characteristics of pH values of acidic solution during saturations: **(A)** violent stage during acidification reaction under saturation (pH = 5), **(B)** stable stage during acidification reaction under saturation (pH = 5), **(C)** violent stage during acidification reaction under saturation (pH = 3), and **(D)** stable stage during acidification reaction under saturation (pH = 3).

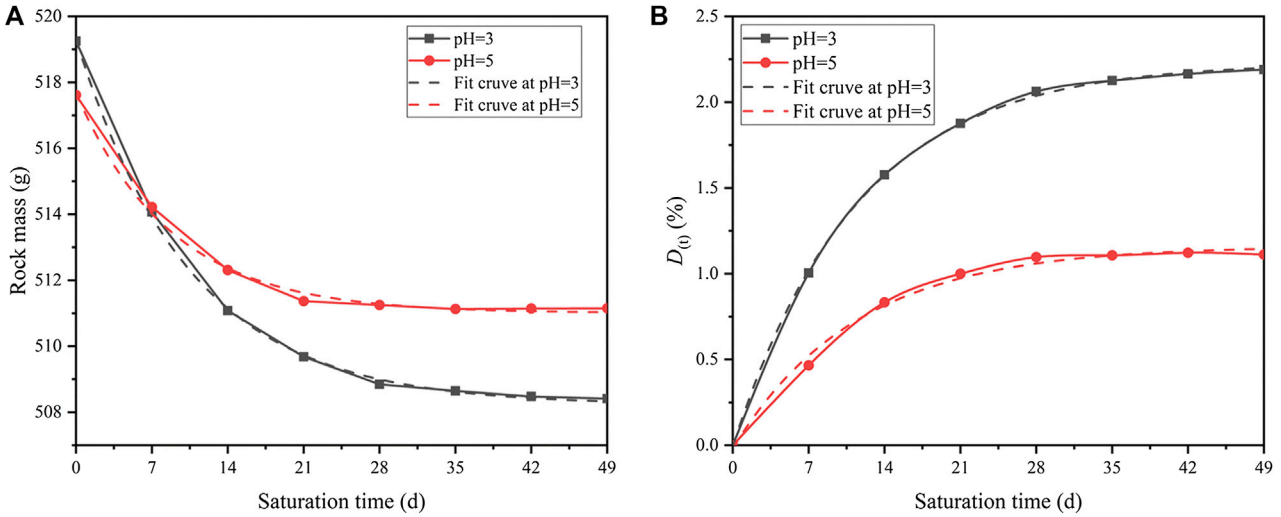

FIGURE 8 | Aging curves of mass damage during different saturations: **(A)** rock mass, and **(B)** rock mass damage factor.

$$P(t) = 2.81 + 4.02e^{\frac{-t}{16}} \tag{9}$$

The time-dependent pH value at initial pH = 5 is:

$$P(t) = 4.88 + 1.6e^{\frac{-t}{17}} \tag{10}$$

The time-varying characteristics indicate that lower pH value leads to faster corrosion. Thus, severer corrosion is caused by a lower pH value. This further verifies the time scale principle that the reaction speed can be accelerated by increasing the reactant concentration.

Aging Characteristics of Mass Damage During Acidification

The test pieces were taken out from the solution and placed in an indoor ventilation environment for 24 h. Then, the mass measurement was performed after the test pieces were completely dried. Samples were randomly selected from the acidic solutions of pH = 3 and pH = 5. The results show that after different acidic saturations, the masses of the samples decreases to various degrees. Besides, the decreasing rate gradually slows down. To characterize the relationship between mass damage and saturation time, the time-dependent characteristic curves of mass damage are calculated and plotted (see **Figure 8A**).

Where the time-dependent mass $M(t)$ is defined. According to **Figure 8A**, the fitted curve of $M(t)$ at condition of pH = 3 is:

$$M(t) = 508.23 + 11.07e^{\frac{-t}{10.5}} \tag{11}$$

The fitted curve of $M(t)$ under solution of pH = 5 is:

$$M(t) = 511.01 + 6.66e^{\frac{-t}{8.8}} \tag{12}$$

According to **Figure 8B**, the fitted curve of $D(t)$ at condition of pH = 3 is:

$$D(t) = 2.23 - 2.23e^{\frac{-t}{11}} \tag{13}$$

The fitted curve of $D(t)$ under solution of pH = 5 is:

$$D(t) = 1.17 - 1.17e^{\frac{-t}{11}} \tag{14}$$

Thus, the decreasing rate of $D(t)$ at condition of pH = 3 is:

$$D(t)' = \frac{2.23}{11}e^{\frac{-t}{11}} \tag{15}$$

The decreasing rate of $D(t)$ under solution of pH = 5 is:

$$D(t)' = \frac{1.17}{11}e^{\frac{-t}{11}} \tag{16}$$

With increasing saturation time, the cumulative damage of the mass gradually increases and finally stabilizes (see **Figure 8B**). According to **Eqs 13** and **14**, the mass damage factors will gradually decrease and eventually reach zero. Comparing the characteristics of the damage caused by two acidic solutions, lower pH will produce larger mass damage during the same saturation time (see **Eqs 15** and **16**). This trend is similar to the change of pH values and agrees well with the results from the perspective of chemical kinetic principles.

Mechanical Damage Characteristics During Acidification

Effect of Acidification Time on the Strength and Deformation

To simulate the long-term corrosion induced by weakly acidic groundwater and the actual confining pressure, test results for rock samples at pH = 3 and σ_3 = 10 MPa are further provided.

According to **Figure 9**, the stress–strain curves of pH = 3 under triaxial compression (σ_3 = 10 MPa) have obvious stepwise trends. Four obvious stages can be observed: (A) initial crack compaction stage (**Figure 9A**), (B) elastic deformation to stable micro-elastic crack development stage (**Figure 9B**), (C) unstable

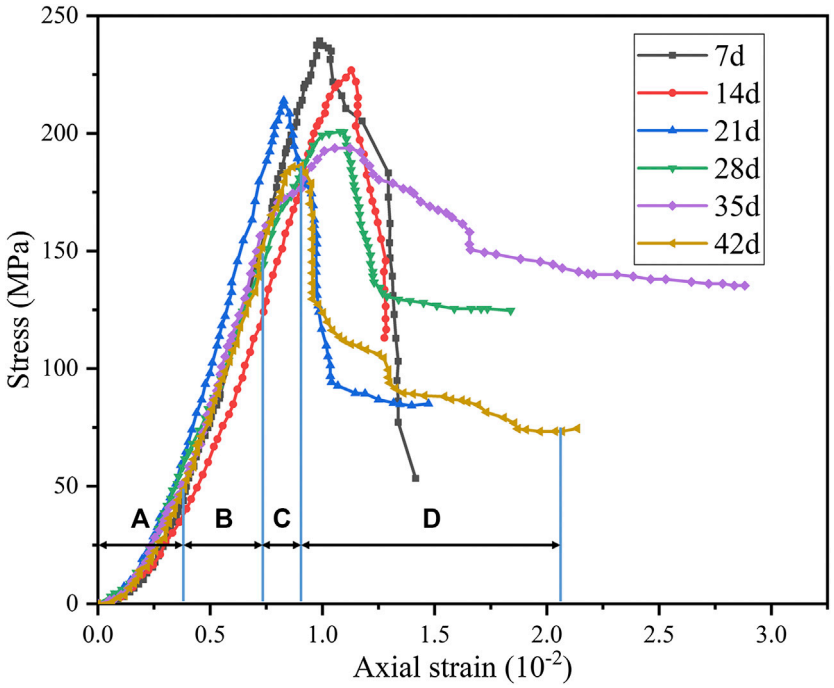

FIGURE 9 | Stress–strain curves for different saturated periods under triaxial compression (σ_3 = 10 MPa, pH = 3): **(A)** initial crack compaction stage, **(B)** elastic deformation to stable micro-elastic crack development stage, **(C)** unstable crack development stage, and **(D)** post-fracture stage.

crack development stage (**Figure 9C**), and (D) post-fracture stage (**Figure 9D**). However, as saturation time increases, stress-strain curves exhibit different characteristics.

At the initial crack compaction stage, the degree of concavity on the curve gradually increases, indicating that samples will produce more micro-fissures. At the elastic deformation to stable micro-elastic crack development stage, the slope of the curve gradually decreases, indicating that the elastic modulus will also gradually decrease. In the unstable crack development stage, the peak stress drops significantly with time. Besides, in the post-fracture stage, the deformation after peak stress gradually increases with time. This shows that diorite has a tendency to change from brittle to ductile after acid saturation. Besides, this tendency will become more obvious with longer saturation time.

To quantify the damage aging characteristics of compressive strength during saturation, the compressive strength damage $Q(t)$ [55–57] is introduced as:

$$Q(t) = 1 - \frac{\sigma_t}{\sigma_0} \tag{17}$$

where σ_t is the TCS of diorite samples after saturation (pH = 3 and σ_3 = 10 Mpa) for t days. σ_0 represents the TCS of diorite in the natural dry state (σ_3 = 10 Mpa). The TCS damage is shown in **Figure 10**.

The equation of fitted curve is:

$$Q(t) = 0.34 - 0.33e^{\frac{-t}{20}} \tag{18}$$

Hence, the damage rate $q(t)$ can be defined as:

$$q(t) = Q(t)' = \frac{0.33}{20}e^{\frac{-t}{20}} \tag{19}$$

The TCS gradually decreases with time. Besides, the rate also gradually decreases. The maximum rate (4.18 MPa/d) occurs in the first 7 days. When saturation reaches 35 days, the TCS tends to be stable, which is consistent with the damage characteristics and the changes of the pH values. As the soluble matter on the surface dissolves, the reaction gradually slows down. So the mechanical damage weakens.

The TCS damage reflects time-dependent characteristics. As saturation time increases, the TCS damage of diorite gradually increases. However, the damage rate decrease slowly. After reaching a certain time (35 days), the damage gradually stabilizes. As shown in **Eq. 18** the strength damage of diorite will reach 0.34 instead of developing continuously. This suggests that the mechanical damage mainly occurs at the fierce physical-chemical reaction. For rocks that are hard to be completely dissolved, the mechanical properties will not be affected at certain reaction point. This is of great significance for predicting the residual strength of rocks in acidic environments. After immersing granite samples with different pH values, Liu et al. [52] reached a similar conclusion through the uniaxial compression tests.

Parameter Damage Characteristics During Acidification

The cohesion (c) and internal friction angle (φ) values of rocks are two important physical and mechanical rock parameters [58–60].

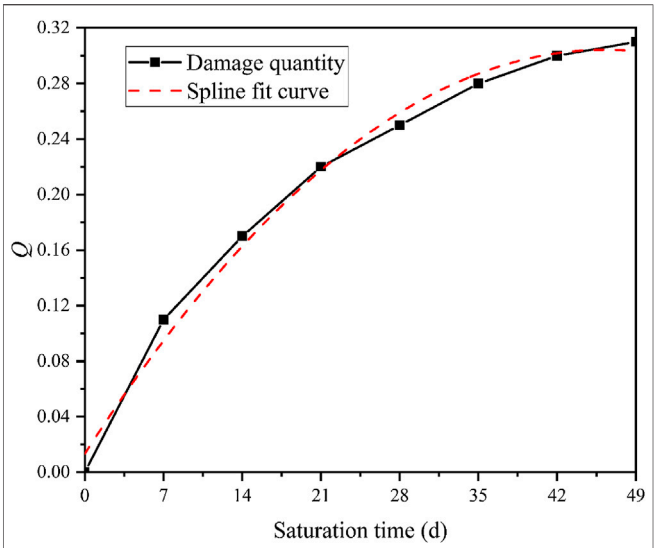

FIGURE 10 | Variation curve of triaxial compressive strength damage of diorite with saturation time (σ_3 = 10 MPa, pH = 3).

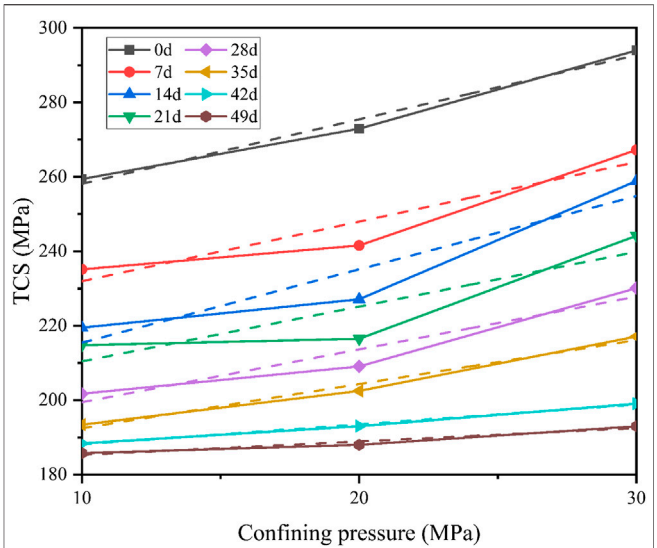

FIGURE 11 | The fitting curves of triaxial compressive strength (TCS) and confining pressure.

Therefore, it is necessary to study the damage aging characteristics of the c and φ values during saturation process. The fitted curves of the TCS and confining pressure obtained at different saturation times are shown in **Figure 11**.

The c and φ values are calculated as:

$$\sigma_1 = \frac{P_{\mathrm{MAX}}}{A} \tag{20}$$

where σ_1 represents the TCS, P_{MAX} is the axial load when the rock fails, and A represents the cross-sectional area of the specimen.

$$\sigma_1 = \sigma_0 + k\sigma_3 \tag{21}$$

where σ_3 is confining pressure, σ_0 represents the intercept in the relationship between σ_1 and σ_3, and k represents the slope.

$$c = \frac{\sigma_0(1-\sin\varphi)}{2\cos\varphi} \tag{22}$$

$$\varphi = \sin^{-1}\frac{k-1}{k+1} \tag{23}$$

The calculation results are shown in **Figure 12**.

According to **Figure 12**, the c and φ values decrease with time. The φ values decrease significantly in the first 21 days after saturation, from the initial 29.4° to around 22.9°. The reduction rate reaches the maximum value of 2.17°/7 days. Then the φ values keep decreasing with a lower rate at around 0.875°/7 days. The c and φ values decrease by 41.9 and 59.7% in the first 21 days. The c values decrease first and then increase steadily. The average rate of c reduction is about 1 MPa/7 days. During the reaction, a stepwise trend could be observed for the development of φ. It is consistent with the trends of rock mass damage and pH value. The trend of φ can be seen as the cumulative effect of time, which suggests that the φ of diorite is more sensitive to acidic solutions than its c.

Mechanical Damage Model During Acidification

Calculation of Corrosion Depth of Diorite During Acidification

The sizes of the rock samples are measured after acidification with pH = 3. The average change of five random diameters with saturation time is shown in **Figure 13A**.

It can be seen that a dramatic decline in diameter occurs in the first 7 days. It is from 50.8 mm to around 50.1 mm. Then the trend immediately slows down with a minimal 0.2 mm reduction during the rest of acidification. This indicates that the rock sample reacts violently with the acidic solution at the initial

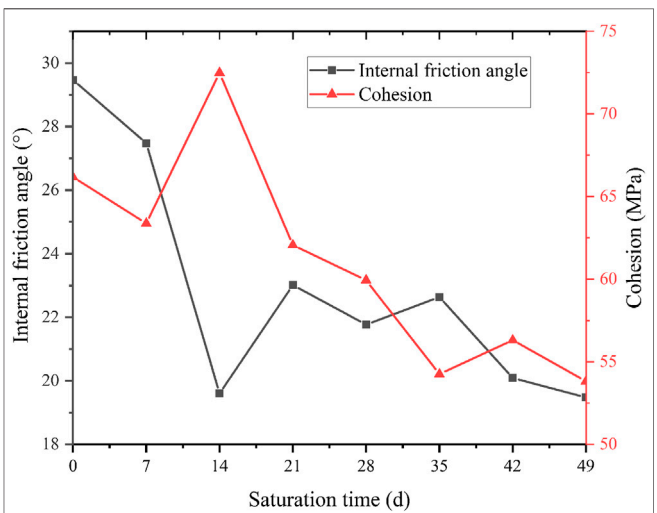

FIGURE 12 | Curves of the c and φ value changing with saturation time (pH = 3).

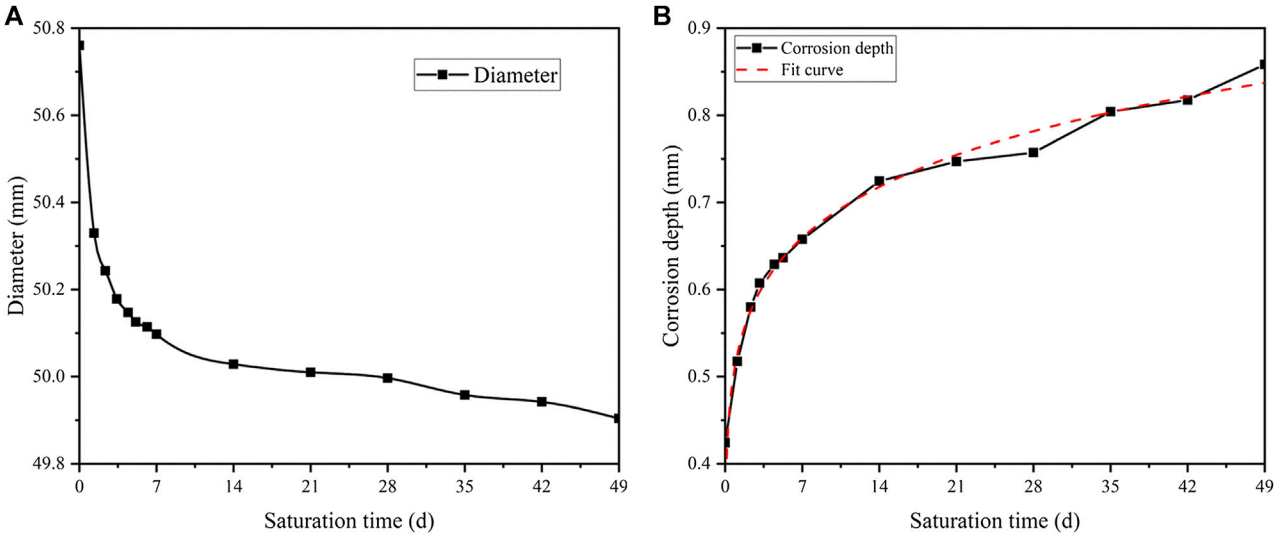

FIGURE 13 | The average size change during saturation (pH = 3): **(A)** the changing curve of diameter of rock samples, and **(B)** the fitting curve of corrosion depth.

stage. Besides, the intensity of the reaction slows down quickly with time.

To quantify the loss of diameter, a corrosion depth parameter is proposed as follows:

$$\Delta d(t) = d_0 - d_{(t)} \tag{24}$$

where $d_{(t)}$ refers to the diameter at t days, and d_0 is the initial diameter. Therefore, the radius change is:

$$\nabla r(t) = \frac{\Delta d(t)}{2} \tag{25}$$

where $\nabla r(t)$ is the corrosion depth.

Based on the development of diameter, the development of corrosion depth is presented in **Figure 13B**. The function of the fitting curve is shown in **Eq. 26**.

$$\nabla r(t) = 0.48t^{0.15} \tag{26}$$

Strength Damage Model of Diorite During Acidification

Before establishing the strength damage model of diorite during acidification, four hypotheses are given:

(1) Diorite specimen is a two-phase material consisting of rock matrix and pores.
(2) The strength of diorite specimen is proportional to its matrix bearing area and inversely proportional to its porosity.
(3) Diorite specimens can reduce matrix bearing area and increase porosity during acidification.
(4) The matrix bearing area could decrease and the porosity could increase during acidification.

The percentage of residual strength of diorite sample during acidification is:

$$\lambda = \frac{\sigma_{(t)}}{\sigma_0} \tag{27}$$

where $\sigma_{(t)}$ is the compressive strength after saturation for t time and σ_0 is the compressive strength in the natural dry state. Based on the hypothesis and theoretical derivation, Huo [61] obtained the relationship between residual strength percentage and porosity as follows:

$$\lambda = \mu\left(1 - 1.40\omega_p^{\frac{2}{3}}\right) \tag{28}$$

where μ is the coefficient to be determined and ω_p is the porosity. The increase in the corrosion depth by the acidic solution is the main reason for the growth of porosity [62]. The test piece has a height of 100 mm and a diameter of 50 mm. The corrosion depth of the test piece is $\nabla r(t)$. Therefore, the load-bearing area $A(t)$ of the test piece is:

$$A(t) = \pi\left(\frac{50}{2}\right)^2 - \pi\left(\frac{50}{2} - \nabla r(t)\right)^2 \tag{29}$$

From Hypothesis (4), **Eq. 29** could be produced as:

$$\begin{aligned} \omega_\rho &= \gamma A(t)h \\ &= \pi\gamma h\left[25^2 - (25 - \nabla r(t))^2\right] \\ &= \pi\gamma h\nabla r(t)(50 - \nabla r(t)) \end{aligned} \tag{30}$$

Where γ is the scale constant. Substituting **Eq. 30** into **Eq. 28** gives:

$$\lambda = \mu\left\{1 - 1.40\left[\pi\lambda h\nabla r(t)(50 - \nabla r(t))\right]^{\frac{2}{3}}\right\} \tag{31}$$

Substituting **Eq. 26** into **Eq. 31** gives:

$$\lambda = \mu\left[1 - \left(\alpha_1 t^{0.15} - \alpha_2 t^{0.3}\right)^{\frac{2}{3}}\right] \tag{32}$$

In **Eq. 32**, α_1 and α_2 are test constants, which are larger than 0. When t is equal to 0, $\lambda = 1$. Hence, $\mu = 1$. **Equation 32** can be presented as:

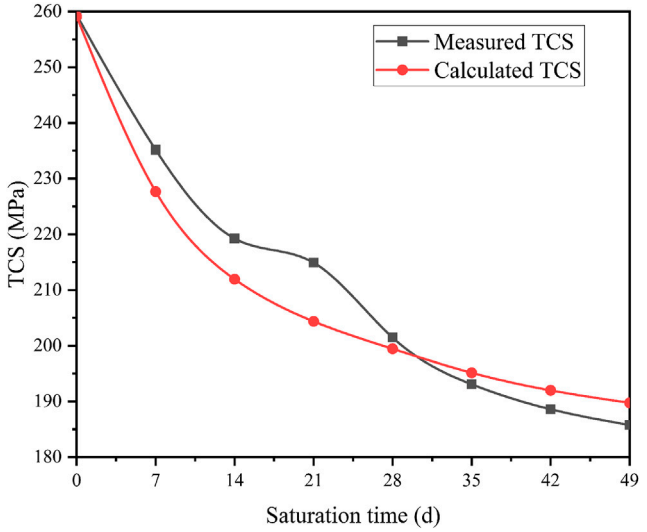

FIGURE 14 | Measured and calculated values of triaxial compressive strength triaxial compressive strength (TCS) of diorite (σ_3 = 10 MPa, pH = 3).

$$\lambda = 1 - \left(\alpha_1 t^{0.15} - \alpha_2 t^{0.3}\right)^{\frac{2}{3}} \tag{33}$$

Substituting **Eq. 23** into **Eq. 27**, the formula of the rock's strength over time during saturation in an acidic solution of pH = 3 is:

$$\sigma_{(t)} = \sigma_0 \left[1 - \left(\alpha_1 t^{0.15} - \alpha_2 t^{0.3}\right)^{\frac{2}{3}}\right] \tag{34}$$

To verify the reliability of the established strength damage model (see **Eq. 34**), two groups of experimental data (σ_3 = 10 MPa, pH = 3) are randomly selected to produce α_1 = 0.124 and α_2 = 0.032. **Figure 14** shows the measured and calculated compressive strength of diorite specimen.

As can be seen from **Figure 14**, when σ_3 = 10 MPa and pH = 3, the trends of the measured and calculated values of diorite's compressive strength with time are roughly the same. In the initial stage of saturation, the strength damage range of diorite is relatively large and the damage rate is high. With the increase of saturation time, the intensity of the damage rate gradually slows down. By comparing the measured and calculated values of compressive strength, the aging model of diorite strength damage established based on the corrosion depth agrees well with the aging characteristics. Thus, the proposed model can be used to simulate residual triaxial compression strength of diorite in acidic environment.

CONCLUSIONS

In light of the above work, the main conclusions of this paper can be drawn as follows:

(1) Under the action of acidic chemical solutions, the microstructure of the amorphous particles changes, which causes damage to the physical properties and weakens the macro mechanical performances of diorite.

(2) Through the conversion of the time scale, saturation of pH = 3 can be used to simulate the long-term effect of the weakly acidic environment in a short period.

(3) As saturation time passes, the pH value of the two acidic solutions gradually decreases with decreasing rates. After reaching a certain time (29, 32 days), the pH values stabilize at higher values than the initial.

(4) When saturation time reaches 35 days (pH = 3), the TCS gradually levels. The cohesion (c) and internal friction angle (φ) tend to decrease with time. The change of φ shows a clear decreasing trend. The magnitude of change in c values is relatively gentle throughout saturation process. Therefore, the φ of diorite is more sensitive to acidic solutions than its c.

(5) The established model of diorite during saturation (σ_3 = 10MPa, pH = 3) shows that in the initial stage, diorite experiences strong strength damage at a high rate. With the increase of saturation time, the intensity damage rate gradually decreases, which agrees well with the test results and provides guidance for practical calculation.

DATA AVAILABILITY STATEMENT

The raw data supporting the conclusions of this article will be made available by the authors, without undue reservation.

AUTHOR CONTRIBUTIONS

WC, WW, and YZ, methodology and funding acquisition; SX, software; ZD and XW, data curation and formal analysis; BJ, visualization; and SL, supervision. All authors have read and agreed to the published version of the manuscript.

FUNDING

This research was funded by the National Natural Science Foundation of China (Grant nos 51774132, 51774131, 51974118, and 51904101) and the Natural Science Foundation of Hunan Province (Grant no. 2020JJ5188).

ACKNOWLEDGMENTS

We thank Longjun Dong, Xiaofan Wu, Jie Liu, Wenhao Li, Wenbing Peng, and Qiuhong Wu for useful discussions and early contributions to the project as well as the reviewers for very helpful and inspiring comments.

SUPPLEMENTARY MATERIAL

The Supplementary Material for this article can be found online at: https://www.frontiersin.org/articles/10.3389/fphy.2020.553643/full#supplementary-material

REFERENCES

1. Wu Q, Weng L, Zhao Y, Zhao F, Peng W, Zhang S. Deformation and cracking characteristics of ring-shaped granite with inclusion under diametrical compression. *Arab. J. Geosci* (2020) **13**(14):681. doi:10.1007.s12517-020-05718-8
2. Dong L, Sun D, Shu W, Li X. Exploration: safe and clean mining on earth and asteroids. *J Clean Prod* (2020) **257**:120899. doi:10.1016/j.jclepro.2020.120899
3. Zhao Y, Wang Y, Wang W, Tang L, Liu Q, Cheng G. Modeling of rheological fracture behavior of rock cracks subjected to hydraulic pressure and far field stresses. *Theor Appl Fract Mech* (2019) **101**:59–66. doi:10.1016/j.tafmec.2019.01.026
4. Dong L, Zou W, Li X, Shu W, Wang Z. Collaborative localization method using analytical and iterative solutions for microseismic/acoustic emission sources in the rockmass structure for underground mining. *Eng Fract Mech* (2018) **210**:95–112. doi:10.1016/j.engfracmech.2018.01.032
5. Wang ZH, Li L, Zhang YX, Wang W-T. Bond-slip model considering freeze-thaw damage effect of concrete and its application. *Eng Struct* (2019) **201**:109831. doi:10.1016/j.engstruct.2019.109831
6. Chen W, Wan W, Zhao Y, Peng W. Experimental study of the crack predominance of rock-like material containing parallel double fissures under uniaxial compression. *Sustainability* (2020) **12**:5188. doi:10.3390/su12125188
7. Zhou XP, Zhang YX, Ha QL, Zhu KS. Micromechanical modelling of the complete stress-strain relationship for crack weakened rock subjected to compressive loading. *Rock Mech Rock Eng* (2008) **41**:747–69. doi:10.1007/s00603-007-0130-2
8. Wang Y, Niu D, Song Z. Effect of acid rain erosion on steel fiber reinforced concrete. *J Wuhan Univ Technol -Materials Sci Ed* (2017) **32**:121–8. doi:10.1007/s11595-017-1569-y
9. Carmona-Quiroga PM, Blanco-Varela MT. Use of barium carbonate to inhibit sulfate attack in cements. *Cement Concr Res* (2015) **69**:96–104. doi:10.1016/j.cemconres.2014.12.006
10. Zhao Y, Zhang L, Wang W, Wan W, Ma W. Separation of elastoviscoplastic strains of rock and a nonlinear creep model. *Int J GeoMech* (2018) **18**:04017129. doi:10.1061/(asce)gm.1943-5622.0001033
11. Chen R, Yang K, Qiu X, Zheng X, Wang P, Xu J, et al. Degradation mechanism of CA mortar in CRTS I slab ballastless railway track in the Southwest acid rain region of China - materials analysis. *Construct Build Mater* (2017) **149**:921–33. doi:10.1016/j.conbuildmat.2017.04.017
12. Kean A, Meredith P. Stress corrosion cracking of quartz: a note on the influence of chemical environment. *Tectonophysics* (1981) **77**:1–11. doi:10.1016/0040-1951(81)90157-8
13. Han T, Shi J, Chen Y, Dang S, Peng S. Salt solution attack induced mechanical property degradation and quantitative analysis method for evolution of meso-structure damages of mortar. *Chin J Mater Res* (2015) **29**:921–30. doi:10.11901/1005.3093.2015.12.921
14. Dunning J, Douglas B, Miller M, McDonald S. The role of the chemical environment in frictional deformation: stress corrosion cracking and comminution. *Pageoph* (1994) **143**:151–78. doi:10.1007/bf00874327
15. Rebinder P, Shreiner L, Zhigach K. *Hardness reducers in drilling: a physico-chemical method of facilitating the mechanical destruction of rocks during drilling*. Council for Scientific and Industrial Research, Melbourne (1948)
16. Wu Q, Li X, Weng L, Li Q, Zhu Y, Luo R. Experimental investigation of the dynamic response of prestressed rockbolt by using an SHPB-based rockbolt test system. *Tunn Undergr Space Technol* (2019) **93**:103088. doi:10.1016/j.tust.2019.103088
17. Zhou XP. Localization of deformation and stress-strain relation for mesoscopic heterogeneous brittle rock materials under unloading. *Theor Appl Fract Mech* (2005) **44**(1):27–43. doi:10.1016/j.tafmec.2005.05.003
18. Karfakis MG, Akram M. Effects of chemical solutions on rock fracturing. *Int J Rock Mech Min Sci Geomech Abstr* (1993) **30**:1253–9. doi:10.1016/0148-9062(93)90104-l
19. Feucht LJ, Logan JM. Effects of chemically active solutions on shearing behavior of a sandstone. *Tectonophysics* (1990) **175**:159–76. doi:10.1016/0040-1951(90)90136-v
20. Hutchinson AJ, Johnson JB, Thompson GE, Wood GC, Sage PW, Cooke MJ. Stone degradation due to wet deposition of pollutants. *Corrosion Sci* (1993) **34**:1881–98. doi:10.1016/0010-938x(93)90025-c
21. Heggheim T, Madland MV, Risnes R, Austad T. A chemical induced enhanced weakening of chalk by seawater. *J Petrol Sci Eng* (2005) **46**:171–84. doi:10.1016/j.petrol.2004.12.001
22. Fan YF, Wang DW, Luan H. Study on the load carrying capacity of reinforced concrete beams under acid precipitation. *Eng Mech* (2014) **31**:147–54. doi:10.6052/j.issn.1000-4750.2012.11.0845
23. Chen MC, Wang K, Xie L. Deterioration mechanism of cementitious materials under acid rain attack. *Eng Fail Anal* (2013) **27**:272–85. doi:10.1016/j.engfailanal.2012.08.007
24. Brzesowsky RH, Hangx SJT, Brantut N, Spiers CJ. Compaction creep of sands due to time-dependent grain failure: effects of chemical environment, applied stress, and grain size. *J. Geophys. Res. Solid Earth* (2014) **119**:7521–41. doi:10.1002/2014jb011277
25. Spiers J, Li P, Qiao L, Zhu J. Experimental research on creep behavior and mechanism of sandstones with hydro-physico-chemical effects. *Chin J Rock Mech Eng* (2008) **27**:2540–50. doi:10.3321/j.issn:1000-6915.2008.12.022
26. Tang L, Zhang P, Wang S. Testing study of effects of chemical action of aqueous solution on crack propagation in rock. *Chin J Rock Mech Eng* (2002) **21**:822–27. doi:10.3321/j.issn:1000-6915.2002.06.012
27. Tang L, Wang S. Analysis on mechanism and quantitative methods of chemical damage in water-rock interaction. *Chin J Rock Mech Eng* (2002) **21**:314–9. doi:10.3321/j.issn:1000-6915.2002.03.004
28. Tang L, Wang S. Testing study on macroscopic mechanics effect of chemical action of water on rocks. *Chin J Rock Mech Eng* (2002) **21**:523–6. doi:10.3321/j.issn:1000-6915.2002.04.015
29. Tang L, Wang S. Progress in the study on mechanical effect of the chemical action of water-rock on deformation and failure of rocks. *Adv Earth Sci* (1999) **14**:433–9. doi:10.11867/j.issn.1001-8166.1999.05.0433
30. Ding W, Feng X. Study of chemical damage effect and quantitative analysis method of meso-structure of limestone. *Chin J Rock Mech Eng* (2005) **24**:1283–8. doi:10.3321/j.issn:1000-6915.2005.08.002
31. Ding W, Feng X. Testing study on mechanical effect for limestone under chemical erosion. *Chin J Rock Mech Eng* (2004) **23**:3571–6. doi:10.3321/j.issn:1000-6915.2004.21.002
32. Chen S, Feng X, Zhou H. Study on triaxial meso-failure mechanism and damage variables of sandstone under chemical erosion. *Rock Soil Mech* (2004) **25**:1363–7. doi:10.3969/j.issn.1000-7598.2004.09.004
33. Chen S, Feng X, Zhou H, Li S. Effects of chemical erosion on uniaxial compressive strength and meso-fracturing behaviors of rock. *Chin J Rock Mech Eng* (2003) **22**:547–51. doi:10.3321/j.issn:1000-6915.2003.04.007
34. Chen S, Feng X, Zhou H. Experiments on the mechanical effects of sandstone with chemical erosion under the triaxial compression. *J Northeast Univ (Nat Sci)* (2003) **24**:292–5. doi:10.3321/j.issn:1005-3026.2003.03.023
35. Miao S, Cai M, Ji D. Damage effect of granite's mechanical properties and parameters under the action of acidic solutions. *J China Coal Soc* (2016) **41**:829–35. doi:10.13225/j.cnki.jccs.2015.0845
36. Miao S, Cai M, Ji D, Guo Q, Bai Y. Aging features and mechanism of Granite's damage under the action of acidic chemical solutions. *J China Coal Soc* (2016) **41**:1137–44. doi:10.13225/j.cnki.jccs.2015.1263
37. Zhang C, Wang Y, Jiang T. The propagation mechanism of an oblique straight crack in a rock sample and the effect of osmotic pressure under in-plane biaxial compression. *Arab J Geosci* (2020) **13**:736. doi:10.1007/s12517-020-05682-3
38. Zhang Y, Zhang Z, Xue S, Wang R, Xiao M. Stability analysis of a typical landslide mass in the Three Gorges Reservoir under varying reservoir water levels. *Environmental Earth Sciences* (2020) **79**:1–14. doi:10.1007/s12665-019-8779-x
39. Wang ZH, Li L, Zhang YX, Zheng SS. Reinforcement model considering slip effect. *Eng Struct* (2019) **198**:109493. doi:10.1016/j.engstruct.2019.109493
40. Zhou W, Shi X, Lu X, Qi C, Luan B, Liu F. The mechanical and microstructural properties of refuse mudstone-GGBS-red mud based geopolymer composites made with sand. *Construct Build Mater* (2020) **253**:119193. doi:10.1016/j.conbuildmat.2020.119193
41. Zhou XP, Yang HQ. Dynamic damage localization in crack-weakened rock mass: strain energy density factor approach. *Theor Appl Fract Mech* (2018) **97**:289–302. doi:10.1016/j.tafmec.2017.05.006
42. Wu Q, Chen L, Shen B., Dlamini B., Li S., Zhu Y. Experimental investigation on rockbolt performance under the tension load. *Rock Mech Rock Eng* (2019) **52**:4605–18. doi:10.1007/s00603-019-01845-1

43. Zhao Y, Zhang L, Wang W, Tang J, Lin H, Wan W. Transient pulse test and morphological analysis of single rock fractures. *Int J Rock Mech Min Sci* (2017) **91**:139–54. doi:10.1016/j.ijrmms.2016.11.016
44. Zhao Y, Zhang L, Wang W, Pu C, Wan W, Tang J. Cracking and stress-strain behavior of rock-like material containing two flaws under uniaxial compression. *Rock Mech Rock Eng* (2016) **49**:2665–87. doi:10.1007/s00603-016-0932-1
45. Lin Z, Yang L, Jian L, Wei J, Qiang L, Li M. Experimental study of fracture toughness and subcritical crack growth of three rocks under different environments. *Int J GeoMech* (2020) **20**:04020128. doi:10.1061/(ASCE)GM.1943-5622.0001779
46. Zhou XP, Yang HQ. Micromechanical modeling of dynamic compressive responses of mesoscopic heterogenous brittle rock. *Theor Appl Fract Mech* (2007) **48**:1–20. doi:10.1016/j.tafmec.2007.04.008
47. Ulusay R. *The isrm suggested methods for rock characterization, testing and monitoring: 2007-2014*. **Vol. 15**. New York, NY: Springer International Publishing. (2014) p. 47–8.
48. Kahraman S. Evaluation of simple methods for assessing the uniaxial compressive strength of rock. *Int J Rock Mech Min Sci* (2001) **38**:981–94. doi:10.1016/s1365-1609(01)00039-9
49. Dong L, Tong X, Li X, Zhou J, Wang S, Liu B. Some developments and new insights of environmental problems and deep mining strategy for cleaner production in mines. *J Clean Prod* (2019) **210**:1562–78. doi:10.1016/j.jclepro.2018.10.291
50. Wang M, Wan W. A new empirical formula for evaluating uniaxial compressive strength using the Schmidt hammer test. *Int J Rock Mech Min Sci* (2019) **123**:104094. doi:10.1016/j.ijrmms.2019.104094
51. Zhang C, Zou P, Wang Y, Jiang T, Lin H, Cao P. An elasto-visco-plastic model based on stress functions for deformation and damage of water-saturated rocks during the freeze-thaw process. *Construct Build Mater* (2020) **250**:118862. doi:10.1016/j.conbuildmat.2020.118862
52. Liu J, Wan W, Zhao Y, Fan X. Stress evolution in punch-through shear tests: a numerical study based on discrete element method. *Front Phys.* (2020) **8**:327. doi:10.3389/fphy.2020.00327
53. Zhao Y, Zhang L, Wang W, Liu Q, Tang L, Cheng G. Experimental study on shear behavior and a revised shear strength model for infilled rock joints. *Int J GeoMech* (2020) **20**:04020141. doi:10.1061/(asce)gm.1943-5622.0001781
54. Zhao Y, Wang Y, Wang W, Wan W, Tang J. Modeling of non-linear rheological behavior of hard rock using triaxial rheological experiment. *Int J Rock Mech Min Sci.* (2017) **93**:66–75. doi:10.1016/j.ijrmms.2017.01.004
55. Sammis CG, Ashby MF. The failure of brittle porous solids under compressive stress states. *Acta Metall* (1986) **34**:511–26. doi:10.1016/0001-6160(86)90087-8
56. Ashby MF, Hallam SD. The failure of brittle solids containing small cracks under compressive stress states. *Acta Metall* (1986) **34**:497–510. doi:10.1016/0001-6160(86)90086-6
57. Wu Q, Weng L, Zhao Y, Guo B, Luo T. On the tensile mechanical characteristics of fine-grained granite after heating/cooling treatments with different cooling rates. *Eng Geol* (2019) **253**:94–110. doi:10.1016/j.enggeo.2019.03.014
58. Parteli E, Schmidt J, Blumel C, Wirth K, Peukert W, Poschel T. Attractive particle interaction forces and packing density of fine glass powders. *Sci Rep* (2015) **4**:6227. doi:10.1038/srep06227
59. Zhang C, Lin H, Qiu C, Jiang T, Zhang J. The effect of cross-section shape on deformation, damage and failure of rock-like materials under uniaxial compression from both a macro and micro viewpoint. *Int J Damage Mech* (2020) **29**:1076–99. doi:10.1177/1056789520904119
60. Dong L, Sun D, Li X, Ma J, Zhang L, Tong X. Interval non-probabilistic reliability of surrounding jointed rockmass considering microseismic loads in mining tunnels. *Tunn Undergr Space Technol* (2018) **81**:326–35. doi:10.1016/j.tust.2018.06.034
61. Huo R. Experimental research on progressive and deteriorative characteristics of sandstone and mortar subjected to hydrochloric acid corrosion. *Chin J Rock Mech Eng* (2007) **26**:647–51. doi:10.3321/j.issn:1000-6915.2007.03.031
62. Chen W, Wan W, Xie S, Kuang W, Peng W, Wu Q. Features and Constitutive Model of Gypsum's Uniaxial Creep Damage considering Acidization. *Geofluids.* (2020) **2020**:8874403. doi:https://doi.org/10.1155/2020/8874403

Conflict of Interest: The authors declare that the research was conducted in the absence of any commercial or financial relationships that could be construed as a potential conflict of interest.

frontiers in Physics

ORIGINAL RESEARCH
published: 08 October 2020
doi: 10.3389/fphy.2020.577787

Three-Dimensional Finite Element Modeling of Soft Rock Tunnel With Large Section: A Case Study

Junyun Zhang, Zhuoling He and Xu Yu*

School of Civil Engineering, Southwest Jiaotong University, Chengdu, China

With deep-buried depth, large span, high geo-stress, complex geological conditions, and its large sections, the deformation behavior of the Gaopo Tunnel is a complex three-dimensional problem. To reveal the deformation behavior of the tunnel and evaluate the current support scheme, this paper establishes a three-dimensional model by benching tunneling method, and compares the monitoring data to analyze the deformation behavior of the surrounding rock and the variation of the stress field in the support structure. The results demonstrate that the rock inclination angle is 4° to 10°, the micro-dip layered structure, which is the main factor for the asymmetric deformation behavior of soft rock tunnel with large section passing through coal seams. The maximum displacement of surrounding rock and the maximum stress of the supporting structure are within the safe range in current scheme. Furthermore, some measures are summarized, which may provide some reference for similar engineering in the future.

Keywords: numerical simulation, deep-buried tunnel, large section, large deformation, asymmetric deformation, coal seam

OPEN ACCESS

Edited by:
Wei Wu,
Nanyang Technological University, Singapore

Reviewed by:
Mingfeng Lei,
Central South University, China
Yong Li,
Chongqing University, China

****Correspondence:***
Junyun Zhang
zjywxfbb@swjtu.edu.cn

Specialty section:
This article was submitted to Interdisciplinary Physics, a section of the journal Frontiers in Physics

Received: *29 June 2020*
Accepted: *03 September 2020*
Published: *08 October 2020*

Citation:
Zhang J, He Z and Yu X (2020) Three-Dimensional Finite Element Modeling of Soft Rock Tunnel With Large Section: A Case Study. Front. Phys. 8:577787. doi: 10.3389/fphy.2020.577787

INTRODUCTION

Tunnels excavated in deep-buried and layered soft surrounding rock often encounter large deformation, accompanied by lining cracking and serious deformation of steel arch, such as Gushan Tunnel and Muzhailing Tunnel [1–3]. Unlike shallow tunnel, the deformation mechanism and stability of surrounding rock are difficult to control due to deep burial, high geo-stress, large span, and complex rock characteristics [4–10]. When excavating a tunnel in soft rock under squeezing stress, the ground slowly enters the opening without obvious cracks or loss of continuity. Continuous inward deformation of rock may occur due to the separation of rock debris or blocks from the excavated vault and wall [11]. Because of the damage of large deformation in the construction of soft rock tunnel, its deformation mechanism and control has attracted the attention of many scholars from the view of mechanics or geology for a long time [12–19].

With the development of computer technology, numerical simulation analysis of tunnel surrounding rock deformation is used widely. Especially after Mroueh and Shahrour [20] put forward the three-dimensional numerical simulation modeling and analysis, the numerical simulation has been recognized widely. Han et al. [21] used the step-by-step approaches modeling, combined with ANSYS, and carried out a full three-dimensional finite element analysis of the wall movement and damage caused by the excavation of the Hobart Tunnel. Liu et al. [22] used the monitoring data combined with ANSYS and FLAC3D to analyze the deformation behavior of the surrounding rock mass between the adit and the major tunnel of Wangdeng Tunnel.

In this paper, to reveal the large-deformation phenomena and evaluate the safety during tunneling in Gaopo Tunnel, comprehensive investigations have been undertaken by combining monitoring data and numerical simulation. The main reason of the large asymmetric deformation in Gaopo Tunnel is analyzed. And the feasibility of new support scheme is analyzed.

SITE DETAILS

Engineering Geology Condition

The large deformation section D3K342+750∼D3K343+169 of Gaopo Tunnel is located at the southeast wing of Gaopo 1# anticline core.

The surrounding rock is mainly soft rock in the V class and the geological conditions are complex. The stratum at the construction site of the Gaopo Tunnel is mainly composed of sandstone, mudstone, carbonaceous shale, sandy mudstone, and coal seam. Located at the upper part of the formation, Longtan Group (P_2l) has 5 to 31 coal seams, including 2 minable coal seams, with a total thickness of 120–180 m. P_2l in the tunnel area contains poor coal quality, and pyrite nodule is well developed, and sulfur content is high. The vault and floor are mostly mudstone and bauxite mudstone, and the structure of coal seam is relatively simple.

Located in the fold belt of the East Yunnan Platform of Yangzi Quasi Platform in the north of Yungui Plateau, the geological structure of this tunnel is complex. The faults and folds are developed, mainly in the East-West structure, and the rock mass is broken. The representative occurrence of the corresponding proof stratum in this section is N40°-60°W/9°-12°SW. The route of the tunnel is about N46°W, approximately parallel to the stratum trend.

Geological exploration shows that surface water mainly consists of gully water and stream water. The rainfall is abundant. The branch gully is mostly seasonal running water. Replenished by atmospheric rainfall, the flow is greatly affected by seasonal changes, and the flow is discharged in the form of evaporation, infiltration, and runoff. Groundwater is mainly composed of pore water and bedrock fissure water. The pore water is localized in the partial gullies and the loose accumulation layer, and the bedrock fissure water exists and migrates in various structural surfaces of the bedrock and in the fault fracture zone. The two mainly receive atmospheric precipitation and surface water replenishment.

Geo-Stress Test

In this paper, the *in-situ* stress was measured by hydraulic fracturing method [23–26].

As shown in **Table 1**, within the depth range of geo-stress measurement, the maximum horizontal principal stress (σ_H) at the section was 14.37 MPa. The results indicated that the maximum principal stress and the minimum principal stress were both horizontal stresses and that only the second principal stress was in the vertical direction. The lateral pressure coefficient, the ratio of the σ_H and the vertical principal stress (σ_v), reached nearly 1.4. Generally, within the test depth of the tunnel, the minimum horizontal stress (σ_h) was the minimum principal stress, and the difference between the σ_v and σ_H was not significant. The effect of tectonic stress was not strong, and it was above the intermediate level. The directions of the maximum σ_H from shallow depth to deep depth were N50°W, N42°W, and N54°W respectively, indicating that the direction of the maximum principal stress near the measuring point was N49°W. The direction of route was about N46°W, and it was approximately parallel to the direction of the σ_H.

TABLE 1 | Geo-stress test in the large deformation section at Gaopo Tunnel.

Depth (m)	Maximum horizontal stress (σ_H[MPa])	Minimum horizontal stress(σ_h[MPa])	Vertical stress (σ_v[MPa])	Direction of maximum horizontal principal stress
278.8	7.19	4.73	7.37	/
295.3	10.45	6.69	7.81	/
358.8	14.37	9.31	10.2	NW50°
388.1	12.26	7.8	10.26	NW42°
425.7	12.13	7.77	11.26	/
448.6	12.56	8.4	11.87	NW54°

Deformation and Failure Characteristics

According to the in-site observation and monitoring data, the large deformation characteristics of coal seam section of Gaopo Tunnel are summarized as follows:

1) Large and uneven deformation. The main deformation in the tunnel was vault subsidence, floor heaven and sides shrinkage. And its development direction was perpendicular to the gentle dip direction of the stratum.
2) Large initial deformation and long-term deformation. The buried depth of the railway was 350–445 m, and the strength of the surrounding rock was low. The phenomena of floor heave, vault subsidence and side shrinkage lasted for a long period after 2018. Monitoring data indicated the deformation velocity of surrounding rock in this tunnel could reach 16 mm/d, and the deformation duration was usually 10 months.
3) Support failure. The Gaopo Tunnel was supported by original support scheme in December 2016. In January 2018, the whole tunnel was penetrated. Before the penetration, the surrounding rock was strengthened, and no obvious large deformations occurred. In March 2018, intense deformation and serious failure happened in the D3K34+750∼D3K343+169 section of the main tunnel and the corresponding adit. The deformation sign of the initial support and lining is shown in **Figures 1**, **2**. The maximum deformation of side near the main tunnel was about 1 m. The longitudinal influence range was wide. There were long longitudinal cracks on the vault and floor of main tunnel, and the longitudinal crack on the filling surface of floor was up to 50 mm (**Figure 3**).

FIGURE 1 | Initial support failure.

FIGURE 2 | Deformation of major tunnel lining.

Original Support Scheme and Current Support Scheme

Original Support Scheme

Gaopo Tunnel was constructed by scheme of "two cross passageways, main and auxiliary inclined shaft and one ventilation shaft." The horseshoe excavation section of the main tunnel reached 155 m^2, belonging to super-large section tunnel. The original support scheme of deformation section was determined by relevant mechanical tests in the test section and the geological conditions. In the design scheme, the floor is removed, and inverted arch with I-shaped steel is added. And the support scheme for the main tunnel is:

1) Severely deformed section: Increase the curvature of the inverted arch, and deepen the center of the inverted arch by 50 cm. Add anchors to the inverted arch, and increase the reserved deformation by 30 cm. Reinforced concrete is used for the initial support, and type III composite lining is used for the secondary lining. The support parameters are shown in **Table 2** and the section structure parameters are shown in **Figure 4A**.
2) Moderately large deformation section: The reserved deformation is 25 cm, and the initial support is reinforced with full-ring I20b steel. The secondary lining is reinforced concrete, type A composite lining. The supporting parameters are specified in **Table 3**.

FIGURE 3 | Deformation sign of support.

TABLE 2 | Parameters of type III composite lining.

Setting part	Severed deformation (cm)	Air-tight shotcrete		Φ8 reinforcement mesh	
		Setting part	Thickness	Setting part	Space (m)
Arch wall	30	Arch wall	27	Full-ring	0.2 × 0.2
		Inverted arch	27		

Setting part	Anchor rod			Steel arch	
	Type	Length (m)	Space (m)	Setting part	Space (m)
Arch	Φ22 combined hollow anchor	4.0	0.8 m × 0.8 m (tangential × radial)	I20b steel full ring	0.6
Sidewall	Φ32 self-feeding anchor	4.0			
Inverted arch	Φ22 combined hollow anchor	5.0			

Current Support Scheme

The Gaopo Tunnel is a deep-buried tunnel, and the buried depth is more than 400 m. The excavation section is large, the horseshoe section is nearly 155 m^2. It was difficult to achieve sufficient accuracy in the preliminary geological survey. Although the original support scheme of the section D3K342+750∼D3K343+169 was determined by the mechanical test in the test section, the influence of the core part of the Gaopo 1# anticline was not fully considering. From the deformation of the supporting structure, the structural stiffness of the type III composite lining was still insufficient, and the length of the anchor rod was not enough. And the radius of the loose circle of the surrounding rock was large. Therefore, type IV composite lining was adopted. Specific engineering measures are as follows:

1) Grouting with aperture of 50 mm is adopted for the range of arch wall in deformed section, with 5 m length per hole and 1.2 ×1.2 m (tangential × radial) spacing to improve surrounding rock conditions at arch wall.
2) Removal and expansion of original support structure are carried out in turn with trolley, with the length of each expansion about 6–10 m. The previous horseshoe section is expanded to circle section. Open-fire operation is forbidden in the whole process. Tunnel ventilation is strengthened to ensure that gas concentration in air flow is not more than 0.4%.
3) New support structure consists of two layers of initial support and one layer of secondary lining with design thickness. HW200 I-steel is used for the first layer of initial support steel arch, and HW175 I-steel is used for the second layer of initial support steel arch. The spacing of the steel arch is 0.6 m. The construction time of the secondary initial support depends on the deformation of the surrounding rock and monitoring data after the first initial support is installed. The secondary lining should be installed after the surrounding rock is basically stable after the construction of primary support.
4) Anchors with 12 and 10 m long are designed to strengthen the whole ring in the tunnel arch wall and the inverted arch. The actual length of anchor rod during construction is optimized according to the monitoring data of test section and actual construction situation in site, and reinforced concrete is applied in the full ring.
5) The form of tunnel track depends on the field deformation and monitoring data at later stage, and ballasted track is recommended. Specific parameters of type IV composite lining of Gaopo Tunnel are shown in **Table 4** and structural parameters of section are shown in **Figure 4B**.

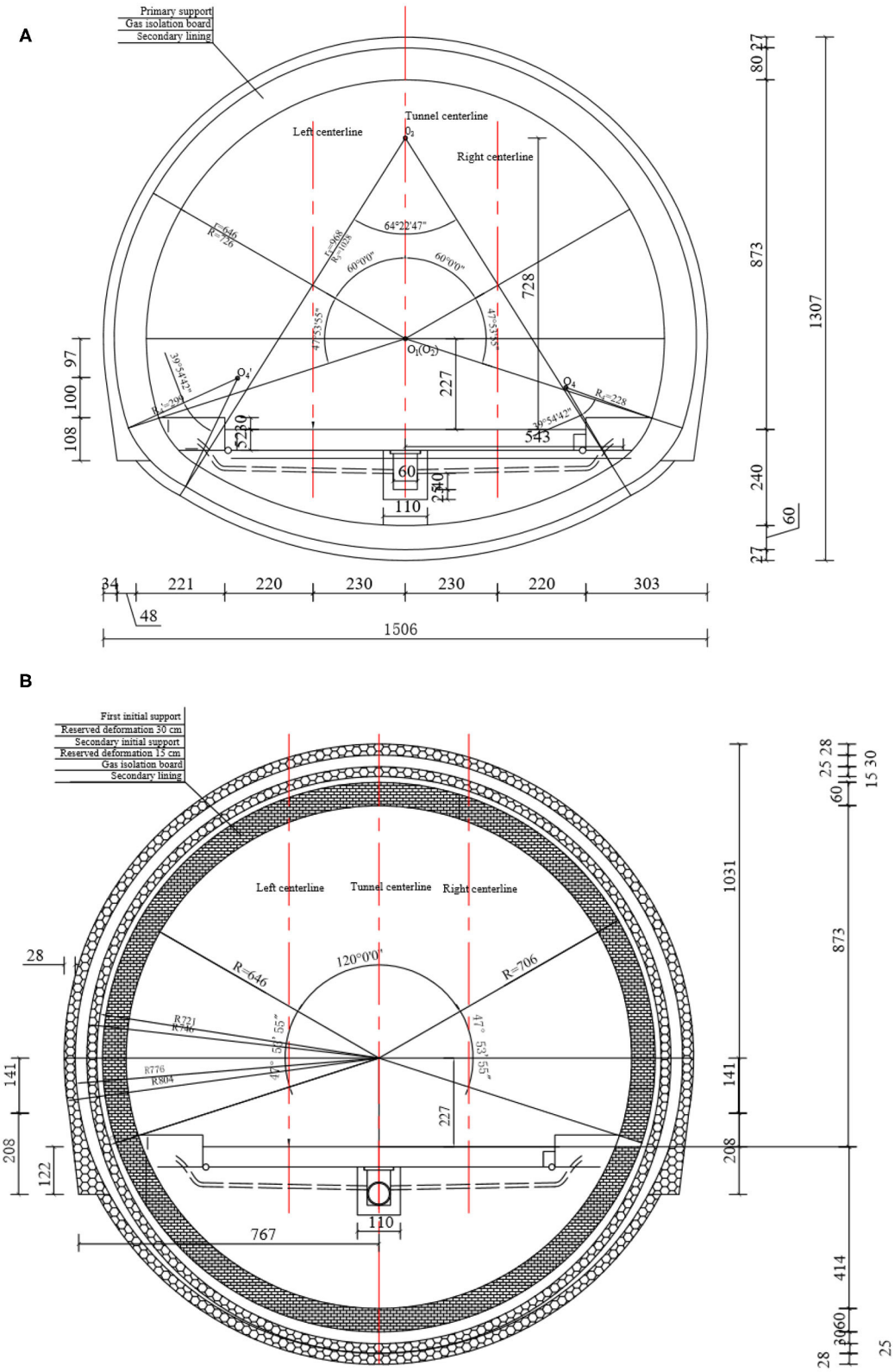

FIGURE 4 | Section structure parameters: **(A)** Type III composite lining section. **(B)** Type IV composite lining.

THREE-DIMENSIONAL NUMERICAL ANALYSIS

Model and Material Parameters

In this paper, the geometric dimension of the model is defined as width X × Y × Z = 170 m × 170 m × 50 m. The model is defined as three parts: upper, middle and lower parts, corresponding to the general stratum, coal seam and general stratum respectively, as shown in **Figure 5**. The coal seam is the surrounding rock of inclined layered coal measure stratum that the tunnel passes through, and the dip angle of stratum is set as 9°.

According to the new support scheme, the maximum excavation span of circular tunnel section is 16.08 m. To simplify the calculation, the influence of the reserved deformation is not considered in the support structure. The reinforcement, steel mesh and shotcrete in the two layers of initial support are simplified as one layer of support, and the thickness of initial support is 53 cm, regarded as solid element, and its material parameters are determined according to the weight ratio of each component. The diameter of anchor is 32 mm, realized by wire element. The steel arch frame is HW200 I-beam steel, realized by wire element. Both of them bear the load by embedding into the soil. The length of arch wall is 12 m, and the range of inverted arch is 10 m, realized by solid element. The thickness of secondary lining is 60 cm, ignoring the existence of reinforcement, regarded as solid element. After the model assembly, there are 25,433 units and 27,635 nodes in total. C3D8R (8-node linear brick, reduced integration with hourglass control) element was used for surrounding rock simulation.

In the design model, the horizontal direction of displacement is fixed in X direction. The bottom surface is fixed in X direction, Y direction and Z direction. The excavation direction is fixed by Z direction, and the top is free.

The Drucker-Prager model is adopted in this numerical analysis, and the required parameters are sorted out as **Table 5** according to the geological exploration data.

TABLE 3 | Parameters of type A composite lining.

Setting part	Severed deformation (cm)	Air-tight shotcrete		Φ8 reinforcement mesh	
		Setting part	Thickness	Setting part	Space (m)
Arch wall	25	Arch wall	27	Full-ring	0.2 × 0.2
		Inverted arch	27		

	Anchor rod			Steel arch	
Setting part	Type	Length (m)	Space (m)	Setting part	Space (m)
Arch	Φ22 combined hollow anchor	4.0	1.0 m × 1.0 m (tangential × radial)	I20b steel full ring	0.6
Sidewall	Φ32 self-feeding anchor	4.0			
Inverted arch	Φ22 combined hollow anchor	5.0			

Numerical Model Establishment

In the process of numerical simulation, 19 construction steps are set to simulate the support process of tunnel excavation. In the field, the support is excavated by benching tunneling method. The length of each excavation step is set at 3 m and excavation is set at 7 steps, which are divided into two steps. The initial support is lagged behind one construction step of excavation and the lining is lagged behind four construction steps of excavation. And keyword "Model Change" is used to rock mass excavation and support structure installment. Load conditions are as follows:

1) Calculation of initial geo-stress field.
2) Balance of geo-stress.
3) First step excavation of upper bench.

TABLE 4 | Parameters of type IV composite lining.

Initial support	Setting part	Reserved deformation (cm)	Air-tight shotcrete		Φ8 reinforcement mesh	
			Setting part	Thickness (cm)	Setting part	Space (m)
First initial support	Arch wall	30	Full-ring	28	Full-ring	0.2 × 0.2
	Inverted arch	0				
Secondary initial support	Arch wall	15	Full-ring	25	Full-ring	0.2 × 0.2
	Inverted support	30				

	Anchor rod				Steel arch	
Setting part	Type	Length (m)	Space (m)	Setting part	Type	Space (m)
Arch	Φ32 self-feeding anchor	12	1.2 m × 1.2 m (tangential × radial)	Full-ring	HW200	0.6
Sidewall	Φ32 self-feeding anchor	12				
Inverted arch	Φ32 self-feeding anchor	10				
				Full-ring	HW175	0.6

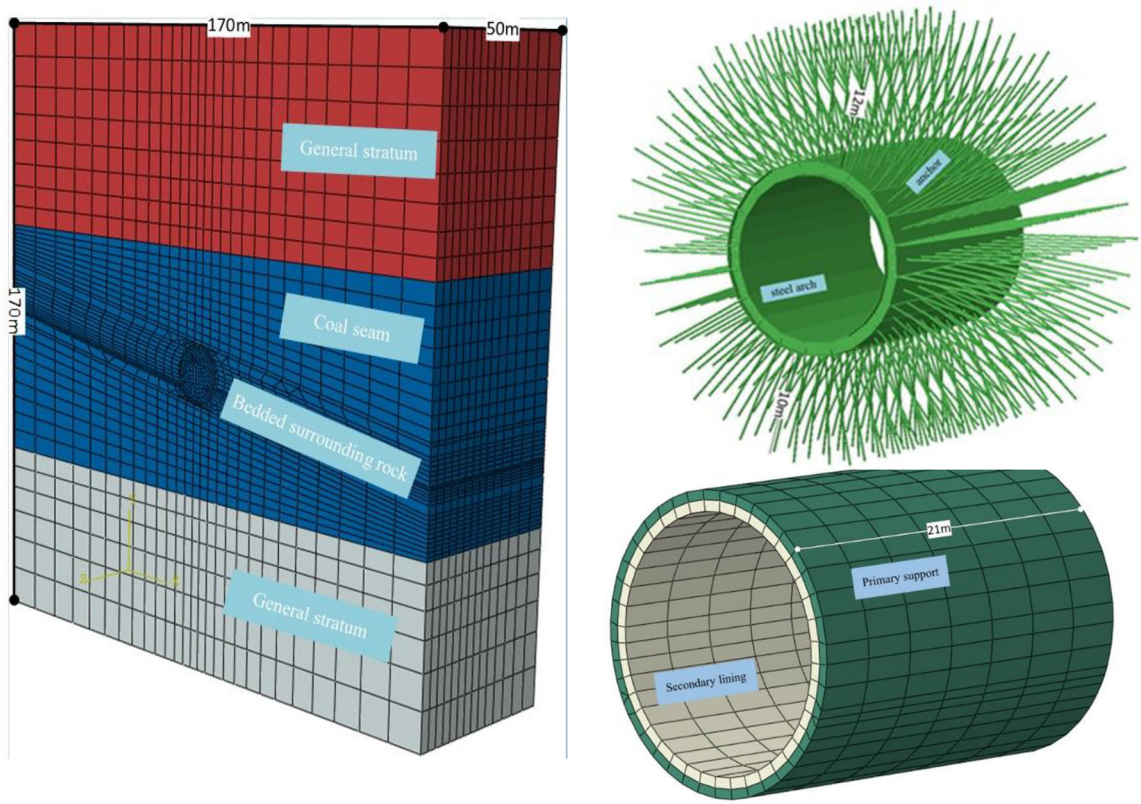

FIGURE 5 | The numerical model and the element mesh.

TABLE 5 | Physical-mechanical properties of the material at site.

Material	Density (kg/m^3)	Elastic modulus (GPa)	Poisson's ratio	Cohesion (kPa)	Friction angle (°)	Yield strength (MPa)
General stratum	2100	2.50	0.39	300	32	31.1
Coal seam	2000	1.80	0.35	200	27	24.6
Initial support	2300	29.57	0.20	/	/	/
Secondary support	2500	33.5	0.20	/	/	/
Anchor	7800	200	0.20	/	/	/

4) Second step excavation of upper bench and initial support installation of the previous step.
5) Excavation of upper bench to 12 m, installment of initial support to 9 m and installment of the first step lining, and start of excavation of lower bench.
6) Excavation of upper bench to 15 m, excavation of lower bench to 6 m, and installment of initial support to the lower bench of 3 m. The second step lining installment and start of the third excavation of the lower bench.
7) In turn, analogy is carried out until the scheduled excavation of surrounding rock and support structure are installed.

Typical working conditions of 3-D numerical simulation of Gaopo Tunnel are shown as **Figures 6–8**.

RESULTS

Based on the in-site monitoring data of D3K342+940 section of Gaopo Tunnel, the simulation results are compared with the corresponding monitoring data to discuss the deformation of surrounding rock and stress of support structure in Gaopo Tunnel. The main items for comparison and analysis are surrounding rock deformation, initial support stress, steel arch stress, anchor axial force and secondary lining reinforcement stress. According to the ABAQUS stress symbol, the compression is negative and the tension is positive.

It should be pointed out, that, due to construction and other reasons, part of the anchor hole grouting is not compact, which cannot ensure that the monitoring data can perfectly reflect the tension stress of the anchor rod. And other measuring points

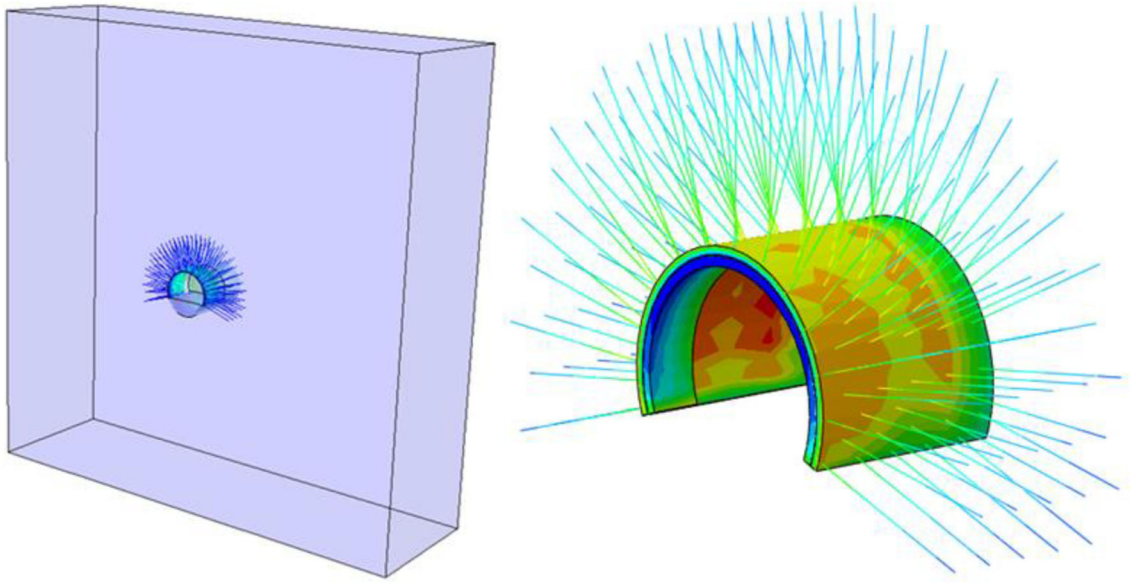

FIGURE 6 | The fifth construction step: excavation up to 12 m, initial support construction up to 9 m, and lining installation.

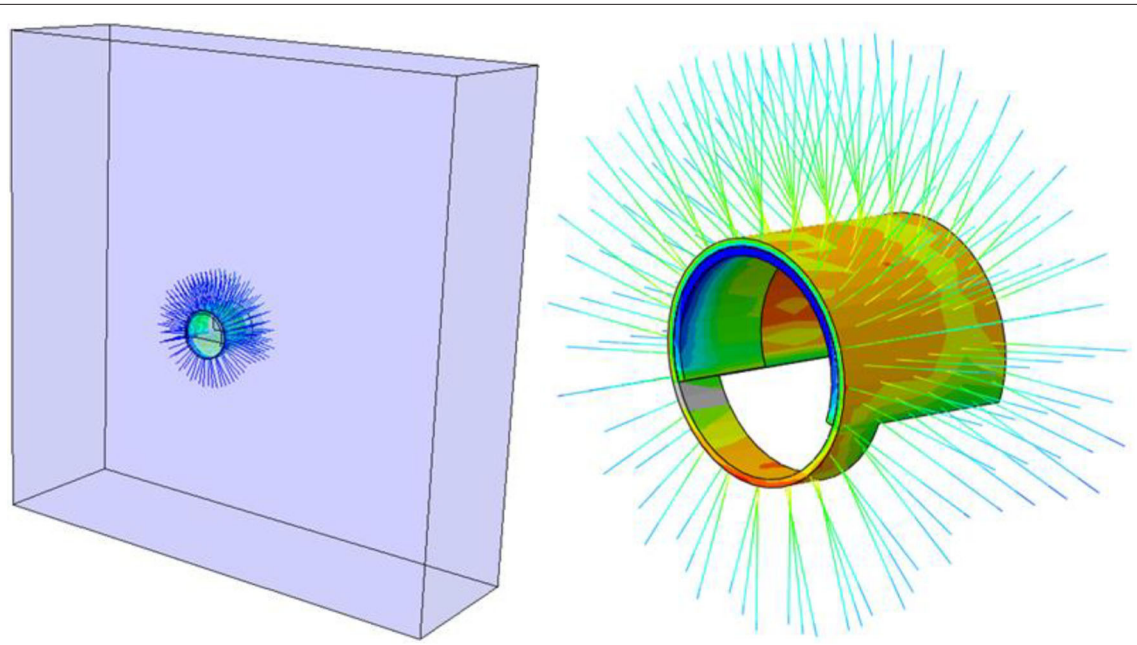

FIGURE 7 | The sixth construction step: excavation up to 15 m, excavation down to 6 m, and initial support down to the lining.

cause data distortion due to component wire breakage caused by construction.

Displacement Analysis

After the tunnel excavation and support structure installment by benching tunneling method, the nephogram of horizontal and vertical displacements of surrounding rocks is shown in **Figure 9**. Vault subsidence, inverted arch floor heaven, left or right sidewall convergences corresponding joints of target section are extracted, and the displacements with the construction steps are shown in **Figure 10**. The displacements of the section D3K342+940 are shown in **Figure 11**.

From **Figures 9**, **11**, the overall deformation of surrounding rock after tunnel stabilization is in centimeter level, consistent with the magnitude of monitoring data. The horizontal convergence of surrounding rock is slightly larger than the

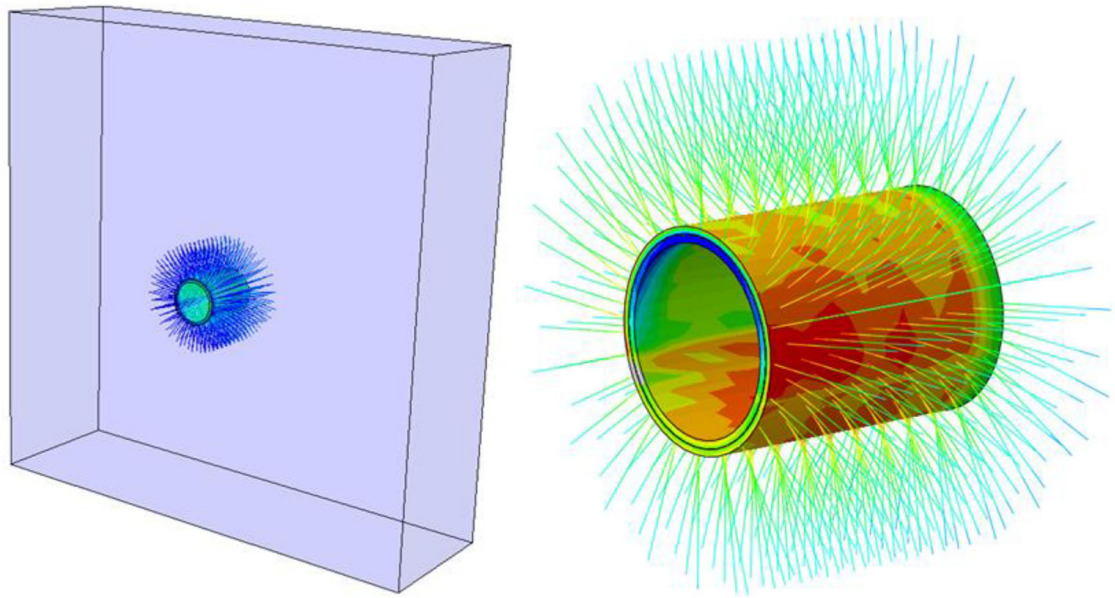

FIGURE 8 | The seventh construction step: the planned surrounding rock excavation completion and support structure construction.

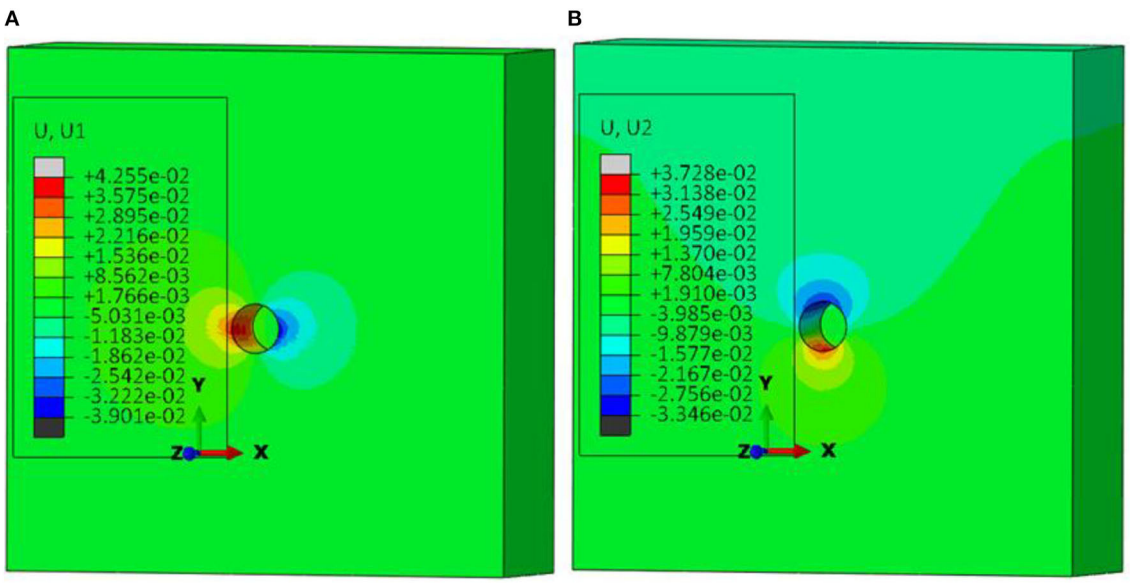

FIGURE 9 | Displacement nebulogram after excavation and support: **(A)** Horizontal displacement after stabilization **(B)** Vertical displacement after stabilization (Unit: m).

vertical displacement, which is consistent with the law that the horizontal stress is greater than the vertical stress in field stress test. In addition, in the horizontal displacement, the convergence value of the left is larger than that of the right.

From **Figure 10**, the deformation of surrounding rock presents a "S" shape with tunnel excavation. Before the tunnel face reaches the target section, vault subsidence, inverted arch floor heaven, left or right sidewall convergences are 9.43, 10.97, 8.44, and 6.13 cm, accounting for 28.7, 31.2, 21.2, and 16.5% of the total amount, respectively. After the tunnel face reaches the target section, vault subsidence, floor heaven, left or right sidewall convergence are 32.68, 19.19, 23.47, and 18.7 cm, respectively. They account for 99.4, 54.8, 58.9, and 50.4% of the total amount, respectively. With the continuous advancement of the tunnel face and the disturbance near the target section of the construction team, the deformation of surrounding rock is further expanded. After that, with the construction of initial support and lining on the target section, the deformation of surrounding

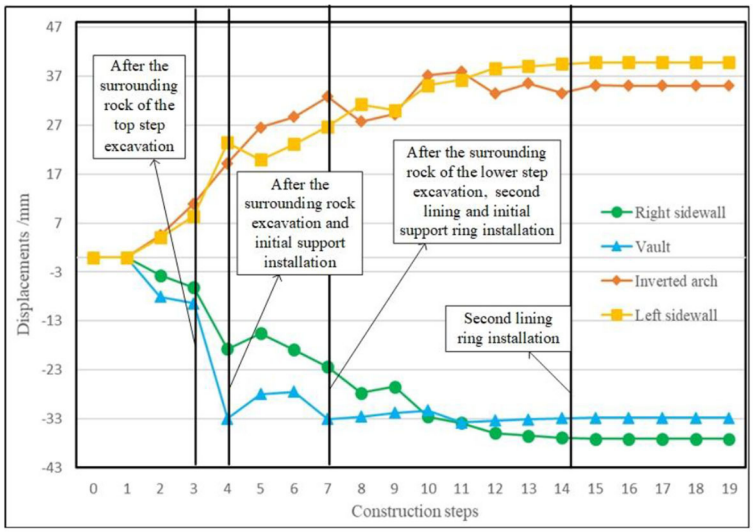

FIGURE 10 | Curves of displacements and construction steps of surrounding rock.

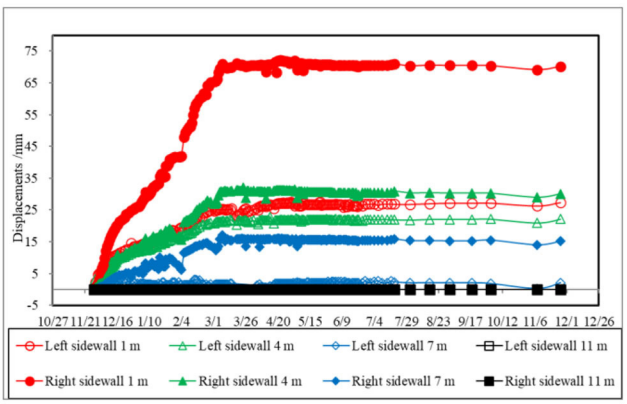

FIGURE 11 | Displacements curves of the monitoring section D3K342+940.

rock on the target surface is restrained and finally tends to stabilize.

Stress Analysis

The stress nephogram after stabilization is shown in **Figure 12**. And the in-site monitoring data is shown in **Figure 13**. Because of the difficulty of construction in site, in the large deformation test section of Gaopo Tunnel, only anchor element, embedded at sidewalls and inverted arch, is measured the axial force of anchor rods. Therefore, only the tensile stress of sidewalls and joint at inverted arch is extracted.

In **Figure 12**, the compressive stress in initial support mainly concentrates on about 23 MPa, with the maximum value of 52.3 MPa. The compressive stress in steel arch mainly concentrates on between 200 and 450 MPa. The maximum tensile stress in anchor is 570 MPa. Within the limit tensile strength of the anchor, the tensile stress groups are mainly located near the clearance part of the anchor. The tensile stress of anchor rod gradually decreases with the extension of deep-buried surrounding rock, and the variation is consistent with monitoring data.

From **Figures 12**, **13**, the compression stress of arch wall is greater than that of inverted arch. The maximum compressive stress is concentrated in the right part. The tensile stress of anchor rod at sidewalls is much higher than that at inverted arch, and the value of tension stress of anchor rod is not different from that of monitoring significantly. In addition, the tension stress of anchor rod at left side and left elevation arch is higher than that at right side and right elevation arch, which agrees with monitoring data.

The compressive stress of secondary lining in numerical simulation is generally smaller than that of in-site monitoring data. This is because the in-site monitoring value is the compressive stress of secondary lining force on steel bar, and the joint fissures are developed in large deformation section of Gaopo Tunnel, which is affected by Gaopo1# anticline core. The surrounding rock is mainly soft rock, such as argillaceous sandstone. In addition, during the excavation of the tunnel, plastic deformation is not considered in numerical simulation, for simplifying calculation.

In general, the compressive stress of the secondary lining steel bar monitored in site or analyzed by numerical simulation is small, about 10–25 MPa, only 7.4% of the compressive strength of the steel bar. Therefore, under the current support scheme, the secondary lining bears less compressive stress in fact. It is more to deal with the plastic deformation of surrounding rock softening after tunnel operation, and it exists as a safety reserve.

Gaopo Tunnel Deformation Control Technology

Considering that surrounding rock of this deformation section is coal seam, the risk of gas leakage existences if reinforcement

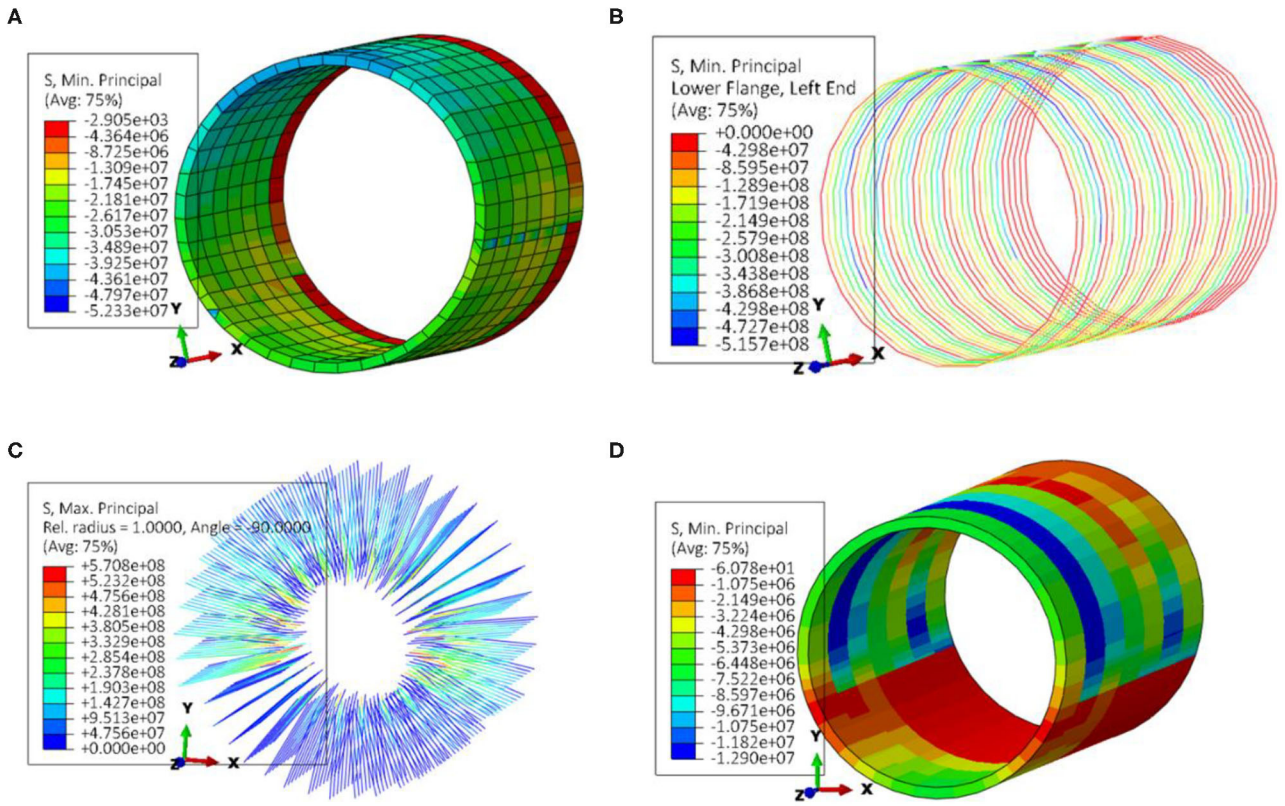

FIGURE 12 | Simulated results: **(A)** Initial support **(B)** Steel arch **(C)** Anchor rod **(D)** Secondary lining (Unit: Pa).

is carried out based on original support structure. In order to control large deformation of tunnel, the original support structure of the deformation section is determined to be removed and a new support scheme is implemented. Now the engineering measures for large deformation treatment of Gaopo Tunnel are introduced as follows, which may provide some reference for similar projects in the future.

Increase Support Structure Stiffness

Compared with the original support scheme with one layer of initial support, the new support scheme uses two layers of initial support. In the new support scheme, the thickness of shotcrete has been increased from 27 to 53 cm, the type of steel arch has changed from I20b to HW200 with higher strength and two-layer support. And the anchor has changed from Φ22 combined hollow anchor to Φ32 self-feeding anchor, and the length has increased from 4 m to 12 m.

Improve Tunnel Section Shape

In order to make full use of the potential of support structure and reduce stress concentration, the horseshoe tunnel section is changed to a circular section. The circular section can make the stress distribution of support structure more uniform and it is more convenient to the construction of two-layer steel arch. After the support structure is installed, the circular section is beneficial to the slow geo-stress release.

Layered Support to Control Deformation

In order to reduce the disturbance to surrounding rock, flexible supporting structure is often used. After fully releasing the stress of surrounding rock, the rigid support is used to support in time. So that the surrounding rock and the supporting structure form a whole and bear the stress together. The new support scheme of Gaopo Tunnel adopts two-layer primary support. After the deformation of the first layer of initial support is stable, the second layer of primary support is installed in time. After the deformation of the initial support tends to be stable, the secondary lining should be installed in time. With enough reserved deformation, the stress of surrounding rock can be fully released, and then flexible supporting structure is applied to make the surrounding rock and supporting structure reach a new equilibrium.

Intensify Inverted Arch and Restrain Uplift

In the large deformation section of Gaopo Tunnel, the stress of support is asymmetric, and the stress of the upper structure is generally greater than that of the lower structure. Therefore, the inverted arch is expanded into a circle, and two layers of initial support and two layers of steel arch are carried. In addition, 10 m long Φ32 self-feeding anchor rod is installed. Therefore, the support strength at the bottom of the tunnel is sufficient.

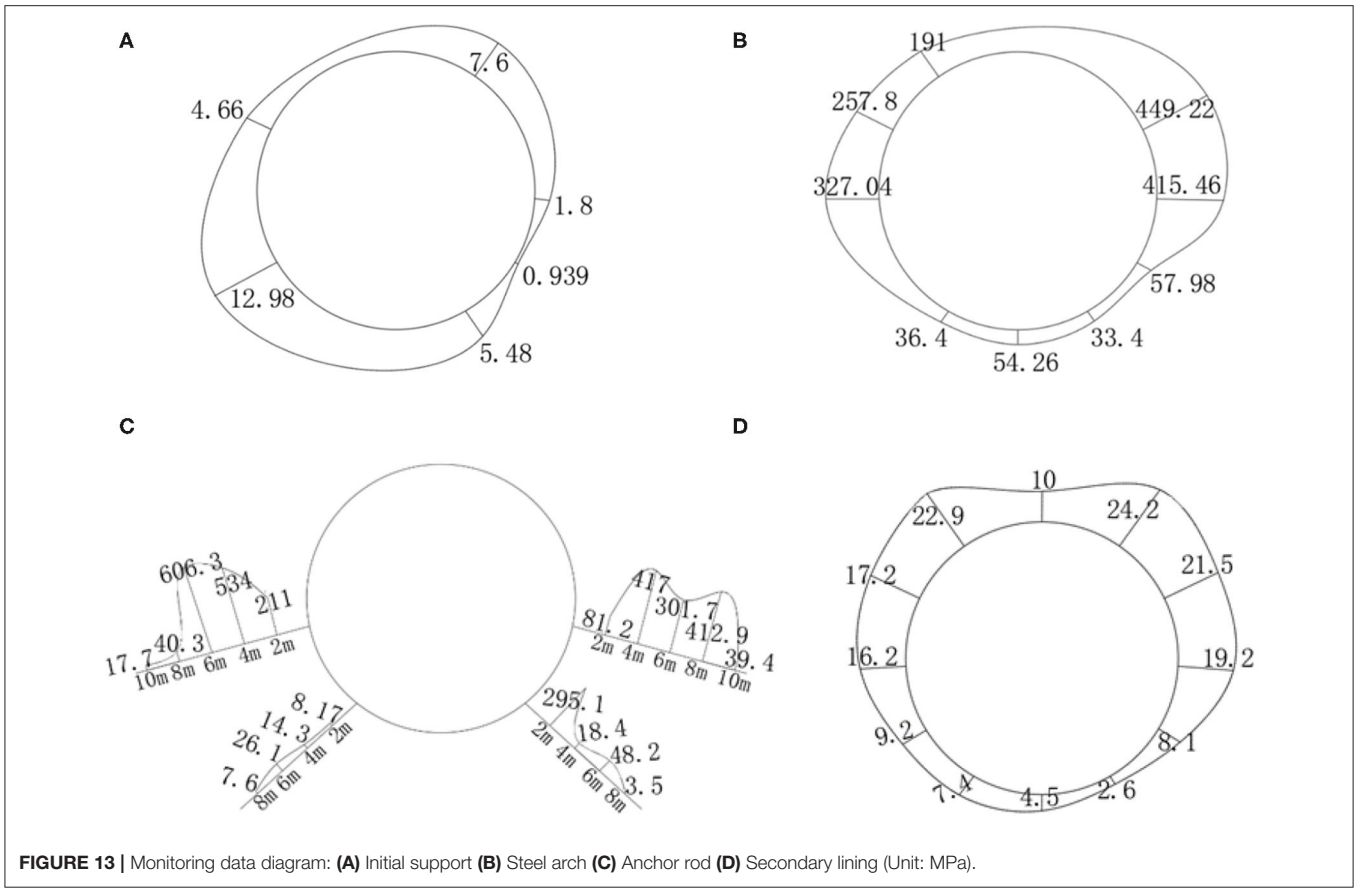

FIGURE 13 | Monitoring data diagram: **(A)** Initial support **(B)** Steel arch **(C)** Anchor rod **(D)** Secondary lining (Unit: MPa).

CONCLUSION

The tunnel is a typical coal seam tunnel with deep-buried depth, large section. Based on monitoring data and numerical simulation, the deformation behavior is analyzed. Some measures have been taken to restrain the large deformation. The main conclusions are as follows:

1) Softening expansion exists in surrounding rocks. The surrounding rock in the deformation section is mainly composed of mudstone and carbonaceous shale, which has weak expansion, even medium expansion in partial region. The site revealed that linear and strand-shaped groundwater flowed near the tunnel. Inadequate management, coupled with the release of stress after the tunnel construction, the rock fissures gradually expanded, and a favorable water channel was formed, causing the surrounding rock softened, which increased the stress on the supporting structure, resulting its deformation.
2) The surrounding rocks are mainly weak weathered mudstone, carbon shale with sandy mudstone, etc. Soft and hard rocks alternate each other, and the rock mass is relatively fractured. The dip angle of stratum is 4°-10° and it belongs to gentle dip layered structure. The deformation of surrounding rock and support stress are controlled by the layered structure with gentle dip obviously. Horizontal convergence of surrounding rocks is slightly larger than vertical displacement, in addition, convergence value of left sidewall is larger than right sidewall in horizontal displacement. Compressive stress of arch wall is greater than that of inverted arch floor, and overall compressive stress of right part of steel arch is greater than that of left part. Tensile stress of anchor rod at sidewall is much greater than that at inverted arch floor, and tensile stress of anchor rod at left sidewall and left inverted arch floor is greater than that at the right.
3) After the installment of the support structure, the maximum displacement of surrounding rock and the maximum stress of the supporting structure are within the safe range. And their changes during the tunnel excavation are basically stable after the completion of the secondary lining construction. The stress of the secondary lining is similar to the field monitoring data, and the overall stress is very small. The secondary lining is mainly used to resist the surrounding rock plastic deformation after the tunnel operation, which is the same as the idea of NATM. In the process of tunnel excavation, the broken-rock pressure and deformation pressure of surrounding rock are mainly produced by surrounding rock and initial support. Compared with field monitoring data, it can be concluded that Gaopo Tunnel is safe under the current support scheme.
4) The engineering treatment measures for large deformation section of Gaopo Tunnel are analyzed and summarized, including increasing support structure stiffness, improving

tunnel section shape, deformation controlling by layered support, and strengthening inverted arch and restraining uplift.

DATA AVAILABILITY STATEMENT

All datasets generated for this study are included in the article/supplementary material.

AUTHOR CONTRIBUTIONS

JZ conceived and designed the research and contributed to funding supports. XY performed the data monitoring. XY and ZH analyzed the data. XY wrote the manuscript. ZH revised the English language of the manuscript.

FUNDING

This research was supported by the National Nature Science Foundation of China (Grant No. 51678494).

ACKNOWLEDGMENTS

This work was also carried out under the tunnel engineering research and development project of the Southwest Jiaotong University. We appreciate any institutions and individuals that have provided support for this paper.

REFERENCES

1. Gioda G, Cividini A. Numerical methods for the analysis of tunnel performance in squeezing rocks. *Rock Mech Rock Eng.* (1996) **29**:4. doi: 10.1007/BF01042531
2. Li SC, Hu C, Li LP, Song SG, Zhou Y, Shi SS. Bidirectional construction process mechanics for tunnels in dipping layered formation. *Tunnel Underground Space Technol.* (2013) **36**:57–65. doi: 10.1016/j.tust.2013.01.009
3. Yang SQ, Chen M, Jing HW, Chen KF, Meng B. A case study on large deformation failure mechanism of deep soft rock roadway in Xi'an coal mine, China. *Engineer Geol.* (2017) **217**:89–101. doi: 10.1016/j.enggeo.2016.12.012
4. Barla G, Bonini M, Semeraro M. Analysis of the behaviour of a yield-control support system in squeezing rock. *Tunn Undergr Space Technol.* (2011) **26**:146–54. doi: 10.1016/j.tust.2010.08.001
5. Cao CY, Shi CH, Lei MF, Yang W, Liu J, et al. Squeezing failure of tunnels: a case study. *Tunn Undergr Space Technol.* (2018) **77**:188–203. doi: 10.1016/j.tust.2018.04.007
6. Schubert W. Dealing with squeezing conditions in alpine tunnels. *Rock Mech Rock Eng.* (1996) **29**:145–53. doi: 10.1007/BF01032651
7. Xu F, Li SC, Zhang QQ, Li L, Shi S, Zhang Q. A new type support structure introduction and its contrast study with traditional support structure used in tunnel construction. *Tunn Undergr Space Technol.* (2017) **63**:171–82. doi: 10.1016/j.tust.2016.11.012
8. Indraratna B, Haque A, Aziz N. Shear behavior of idealized filled joints under constant normal stiffness. *Geotechnique.* (1999) **49**:331–55. doi: 10.1680/geot.1999.49.3.331
9. Indraratna B, Jayanathan M, Brown ET. Shear strength model for over consolidated clay-filled idealised rock joints. *Geotechnique.* (2008) **58**:55–65. doi: 10.1680/geot.2008.58.1.55
10. Indraratna B, Oliveira DAF, Brown ET. A shear-displacement criterion for soil-filled rock discontinuities. *Geotechnique.* (2010) **60**:623–33. doi: 10.1680/geot.8.P.094
11. Bian K, Liu J, Liu ZP, Liu SG, Ai F, Zheng XQ, et al. Mechanisms of large deformation in soft rock tunnels: A case study of Huangjiazhai Tunnel. *Bull Eng Geol Environ.* (2019) **78**:431–44. doi: 10.1007/s10064-017-1155-8
12. Brox D, Hagedorn H. Extreme deformation and damage during the construction of large tunnels. *Tunn Undergr Space Technol.* (1999) **14**:23–8. doi: 10.1016/S0886-7798(99)00010-3
13. Dalgic S. Tunneling in squeezing rock, the Bolu tunnel, Anatolian motorway, Turkey. *Eng Geol.* (2002) **67**:73–96. doi: 10.1016/S0013-7952(02)00146-1
14. Bizjak KF, Petkovsek B. Displacement analysis of tunnel support in soft rock around a shallow highway tunnel at Golovec. *Eng Geol.* (2004) **75**:89–106. doi: 10.1016/j.enggeo.2004.05.003
15. Zhou X, Qian Q. Zonal fracturing mechanism in deep tunnel. *Chin J Rock Mech Eng.* (2007) **26**:877–85. doi: 10.1016/S1872-2067(07)60020-5
16. Khanlari G, Meybodi RG, Mokhtari E. Engineering geological study of the second part of water supply Karaj to Tehran tunnel with emphasis on squeezing problems. *Engineer Geol.* (2012) **145–146**:9–17. doi: 10.1016/j.enggeo.2012.06.001
17. Wang MY, Zhang N, Li J, Ma LJ, Fan PX. Computational method of large deformation and its application in deep mining tunnel. *Tunn Undergr Space Technol.* (2015) **50**:47–53. doi: 10.1016/j.tust.2015.06.006
18. Shou YD, Zhou XP, Qian QH. A critical condition of the zonal disintegration in deep rock masses: Strain energy density approach. *Theoret Appl Fract Mech.* (2018) **97**:322–32. doi: 10.1016/j.tafmec.2017.05.024
19. Kalamaris GS, Bieniawski ZT. A rock mass strength concept for coal incorporating the effect of time. In: *Proceedings of the Eighth International Congress on Rock Mechanics*. Rotterdam: Balkema. (1995). p. 295–302.
20. Mroueh H, Shahrour I. A full 3-D finite element analysis of tunneling–adjacent structures interaction. *Comput Geotech.* (2003) **30**:245–53. doi: 10.1016/s0266-352x(02)00047-2
21. Han HY, Liu HY, Chan A, Mcmanus T. Three-dimensional finite element modelling of excavation-induced tunnel wall movement and damage: a case study. *Sādhanā.* (2019) **44**:185. doi: 10.1007/s12046-019-1167-0
22. Liu H-L, Li S-C, Li L-P, Zhang QQ. Study on deformation behavior at intersection of adit and major tunnel in railway. *J Civil Engin.* (2017) **21**:2459–66. doi: 10.1007/s12205-017-2128-y
23. Matsunaga I, Kuriyagawa M, Sasaki S. In situ stress measurements by the hydraulic fracturing method at Imaichi pumped storage power plant, Tochigi, Japan. *Int J Rock Mech Min Sci Geomech Abstr.* (1989) **26**:203–9. doi: 10.1016/0148-9062(89)91970-0
24. Hayashi K, Ito T. In situ stress measurement by hydraulic fracturing at the Kamaishimine. *In t J Rock Mech Min Sci Geomech Abstr.* (1993) **30**:951–7. doi: 10.1016/0148-9062(93)90051-E
25. Haimson BC, Cornet FH. ISRM suggested methods for rock stress estimation-part 3: hydraulic fracturing (HF) and/or hydraulic testing of pre-existing fractures (HTPF). *Int J Rock Mech Min Sci.* (2003) **40**:1011–20. doi: 10.1016/j.ijrmms.2003.08.002
26. Kuriyagawa M, Kobayashi H, Matsunaga I, Yamaguchi T, Hibiya K. Application of hydraulic fracturing to three-dimensional *in situ* stress measurement. *Int J Rock Mech Min Sci Geomech Abstr.* (1989) **26**:587–93. doi: 10.1016/0148-9062(90)90706-8

Conflict of Interest: The authors declare that the research was conducted in the absence of any commercial or financial relationships that could be construed as a potential conflict of interest.

frontiers in Physics

ORIGINAL RESEARCH
published: 23 October 2020
doi: 10.3389/fphy.2020.558547

Seismic Response Time-Frequency Analysis of Bedding Rock Slope

Liang Zhang[1], *Changwei Yang*[1]*, *SuJian Ma*[1], *Xueyan Guo*[1], *Mao Yue*[1] *and Yang Liu*[2]

[1] *Department of Civil Engineering, Southwest Jiaotong University, Chengdu, China,* [2] *Zhongke (Hunan) Advanced Rail Transit Research Institute, Zhuzhou, China*

According to the potential disaster points of the rock bedding slope with a weak structural plane along the Sichuan Tibet railway, the shaking table test of earthquake simulation was designed and carried out. The acceleration response and displacement response of the slope under different input earthquake conditions were monitored, and the HHT method was mainly used to analyze the seismic response of the slope. The results show that the rock bedding slope shows obvious "elevation effect" and "surface effect" under the action of seismic waves of different intensities. With the increase of the amplitude value of the input earthquake, the elevation effect and the surface effect gradually weakened. When the amplitude of the seismic wave reached 0.9 g, the movement inconsistency of the slope on both sides increased, and the slope gradually separated from the main body of the slope, resulting in slope instability. The characteristics of the seismic signal in the time–frequency domain can be better described by the Hilbert-Huang transform. In the time domain, the energy is mainly concentrated in 2–6 and 12–15 s, and the predominant frequency is concentrated between 5 and 40 hz. With the increase of elevation, the former increases and the latter decreases. In addition, the change of the peak value of the marginal spectrum can clearly show the development process of the earthquake damage inside the slope. At the height of 100 cm, the inflection point can be seen obviously in the slope. It shows that the damage occurs at the height of 100 cm, and the degree of earthquake damage near the slope is stronger than that inside the slope. The recognition results of marginal spectrum are in good agreement with the experimental results.

Keywords: bedding rock slopes, shaking table test, seismic response, peak acceleration, time-frequency analysis, Hilbert-Huang transform

OPEN ACCESS

Edited by:
Longjun Dong,
Central South University, China

Reviewed by:
Eric Josef Ribeiro Parteli,
University of Cologne, Germany
Reinaldo Roberto Rosa,
National Institute of Space Research (INPE), Brazil

***Correspondence:**
Changwei Yang
yangchangwei56@163.com

Specialty section:
This article was submitted to Interdisciplinary Physics, a section of the journal Frontiers in Physics

Received: *03 May 2020*
Accepted: *21 August 2020*
Published: *23 October 2020*

Citation:
Zhang L, Yang C, Ma S, Guo X, Yue M and Liu Y (2020) Seismic Response Time-Frequency Analysis of Bedding Rock Slope. Front. Phys. 8:558547. doi: 10.3389/fphy.2020.558547

INTRODUCTION

The Sichuan-Tibet railway starts from Chengdu, passes through Ya'an, Kangding, Changdu, and Linzhi to Lhasa, with a total length of 1,800 km. Influenced by the collision and compression of the Indian plate on the Eurasian plate, the terrain along the Sichuan-Tibet railway is characterized by high mountains, deep valleys, and crisscross gullies. There are many active fault zones in the transition zone between the plateau and the basin, which are the root cause of earthquakes. Frequent seismic activity and a fragile geological environment are factors that easily induce large-scale landslides. The Wenchuan Ms 8.0 earthquake, Lushan Ms 7.0 earthquake, and Ludian Ms 6.5 earthquake have all caused a large number of slope collapses [1–4]. The bedding rock slope is a very common type of slope distributed in the Sichuan-Tibet railway construction area [5, 6]. Due to the influence of internal structural characteristics, the stability of this type of slope is poor, and it

is very prone to collapse in the event of an earthquake [7, 8]. This seriously affects the safety of the Sichuan-Tibet railway during the construction and operation period.

Seismic stability of bedding rock slopes has always been a hot issue in geological disaster research. In general, the most commonly used method in stability analysis is the quasi-static method. In this method, the influence of peak ground motion parameters on slope stability is considered, and the instantaneous action of earthquake is equivalent to load acting on the center of gravity of sliding mass [9–12]. Earthquake modeling in the laboratory scale is one of the most powerful methods to reveal the dynamic response and failure process of slopes in the event of strong earthquakes [13–15]. Li L Q [16] studied the seismic response of bedding and toppling rock slope through large-scale shaking table tests. According to the acceleration and earth pressure of different parts of the slope, it was found that the acceleration amplifying factor was larger than the earth pressure amplifying factor at the slope surface. The earth pressure amplifying factor at the top surface for a toppling rock slope was close to that of a bedding rock slope. Fan G [17] also used a shaking table test to study the bedding slope with a weak interlayer. The results show that the dynamic failure mode of the slope mainly included the horizontal and vertical staggered cracks, the extrusion of the weak interlayer, and the fracture of the slope top. Salmi and Hosseinzadeh [18] used the Universal Distinct Element Code software package to evaluate the stability of rock slope and identify the critical failure mode. The study found that bedding sliding was the main failure mode of the slope, and the nature of discontinuities plays a key role in the slope instability. Liu et al. [19] used the programming language FISH in FLAC (3D) to realize the process of slope vibration degradation, and used the numerical calculation method to analyze the stability of the slope in the event of an earthquake and the long-term stability of the slope under frequent microseisms. The above study only considers the acceleration and earth pressure parameters of the seismic wave, and ignores the influence of the frequency and duration of the seismic wave on the slope stability.

In the whole process of earthquake motion, the seismic wave is very complex, and the slope will show obvious non-linear characteristics [20, 21]. Hilbert-Huang transform (HHT) is a self-adaptive time-frequency analysis method suitable for non-linear and unstable signal processing proposed by Huang et al. [22]. This method has high time-frequency resolution for seismic signals, and can more accurately describe the energy distribution of seismic signals in time-frequency. Moreover, the Hilbert marginal spectrum obtained by integrating the Hilbert spectrum represents the distribution of the signal energy amplitude in the frequency domain. Therefore, HHT has been widely used in the seismic response analysis of non-linear non-stationary dynamic systems in the field of civil engineering [23–25].

In this paper, the potential rock bedding slope disaster points in the Sichuan-Tibet railway construction area are selected, and the similar system of the model is designed. The shaking table test of the rock bedding slope with a weak structural plane is carried out to study the seismic dynamic response characteristics and failure process of this kind of slope. On this basis, the HHT method is used to analyze the characteristics of seismic waves in time and frequency domains. The results can provide reference for the formulation of slope disaster prevention and mitigation measures.

OVERVIEW OF SHAKING TABLE TEST

A shaking table physical simulation test is one of the most powerful means of revealing the strong vibration response and failure process of slopes [26, 27]. An earthquake simulation shaking table test was carried out in the laboratory of the School of Architecture and Civil Engineering, Xinyang Normal University. The shaking table is a large-scale one-way seismic simulation shaking table with a table size of 3 × 3 m. The table structure is a steel welded single-layer grid. The maximum load capacity of the table is 10 t and the maximum speed is 0.7 m/s. The frequency of this shaking table is 0.1–50 Hz, the displacement range is ±125 mm, and the maximum acceleration is 15 m/s^2, which can meet the requirements of this shaking table test. This test uses a 64-channel BBM data acquisition system, the maximum reference error ≤0.5%. The signal adaptor is connected to the charge converter to convert the voltage signal, the maximum reference error is ≤1 %. Data acquisition, monitoring signal, and online analysis are carried out synchronously, as shown in **Figure 1**.

Design and Manufacture of Slope Model

The model box used in this model test is a rigid model box welded by angle steel, channel steel, and steel plate. The model box is 2.0 m long, 2.0 m wide and 1.5 m high, as shown in **Figure 2**. A polyethylene foam with a thickness of 10 cm is placed between the steel plate and the model as a shock-absorbing layer to reduce the influence of the model box boundary effect [26]. The slope prototype is the bedding rock slope at the exit of a tunnel on the Sichuan-Tibet railway. In this test, the density (ρ), elastic modulus (E), and geometric size (L) are used as control parameters, and a similar system of the model is designed through the "π theorem" [28, 29]. The scale ratio of the model is 1:10, and the time similarity ratio is 1:3.16. Simplifying the slope to facilitate model establishment. After simplification, the slope angle of the rock layer is 35° and the slope foot angle is 60°. The thickness of the rock layer is 6 cm and the thickness of the weak interlayer is 1 cm, as shown in **Figure 3**. In addition, the raw materials of the simulation materials used in the experiment are gypsum, clay, river sand, and water [30]. Through repeated material ratio tests, it is determined that the ratio of the simulated rock material is gypsum:clay:river sand:water = 1:5.38:1.52:0.27, and the ratio of the weak structure plane simulated material is clay:river sand:water = 1:6.89:0.25. Through density tests, direct shear tests, and triaxial compression tests, the density of the rock material is 1.908 g/cm^3, the cohesion is 15.5 kPa, the internal friction angle is 37.9°, the density of the structural surface material is 1.72 g/cm^3. The cohesion force is 2.7 kPa and the internal friction angle is 41.7°.

FIGURE 1 | Data acquisition system for shaking table test.

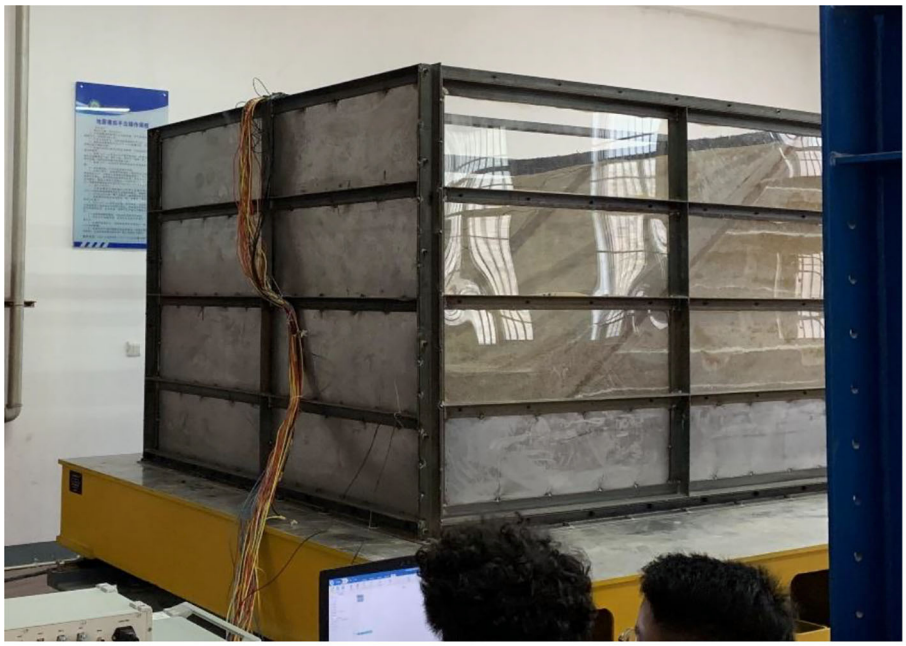

FIGURE 2 | Test model box.

Measuring Point Layout

In this test, one-way acceleration sensors, three-way acceleration sensors, and cable displacement sensors are arranged at different positions in the slope model to obtain the seismic response of the bedding rock slope. The acceleration sensor adopts the three-way acceleration sensor (Type: 1C101) and one-way acceleration sensor (Type: 1C301) produced by the Donghua Testing Company. One-way acceleration sensors are mainly used to test the distribution of the acceleration field in the bedrock, and three-way acceleration sensors are used to monitor the

FIGURE 3 | Test model.

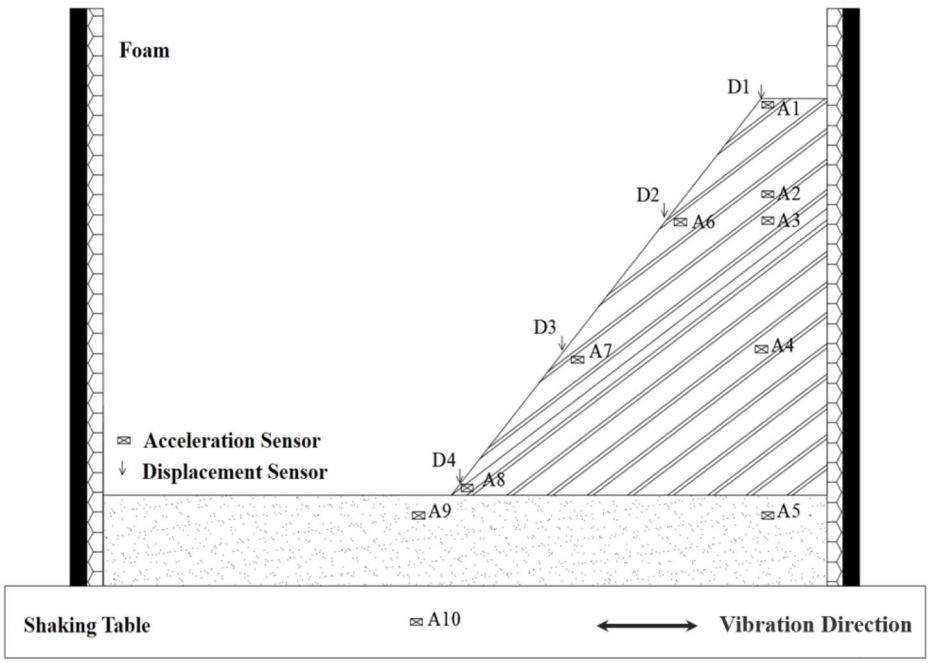

FIGURE 4 | Arrangement of measuring points of the shaking table.

acceleration field in the slope. The cable displacement sensors are also produced by the Donghua Testing Company and its type is 5G203. It is used to monitor the displacement change of the slope during the earthquake. In addition, in order to more accurately describe the response of the entire model during the earthquake, this test used an independently developed high-frequency digital camera system to record it. The layout of the measuring points is shown in **Figure 4**.

Loading Mode

According to the results of field investigation and seismic risk assessment, the Wenchuan Wolong wave and El Centro wave are selected for loading in this test. The acceleration peak value of the input seismic wave is normalized, and the duration is adjusted according to a similar relationship. **Figure 5** shows the two kinds of adjusted seismic wave acceleration time-history curves. The acceleration peaks of the two seismic waves are 0.1, 0.2, 0.4, 0.7, and 0.9 g, respectively, and load in order from small to large. Before each peak earthquake wave is loaded, the model is scanned for white noise with an amplitude of 0.05 g. The loading conditions are shown in **Table 1**.

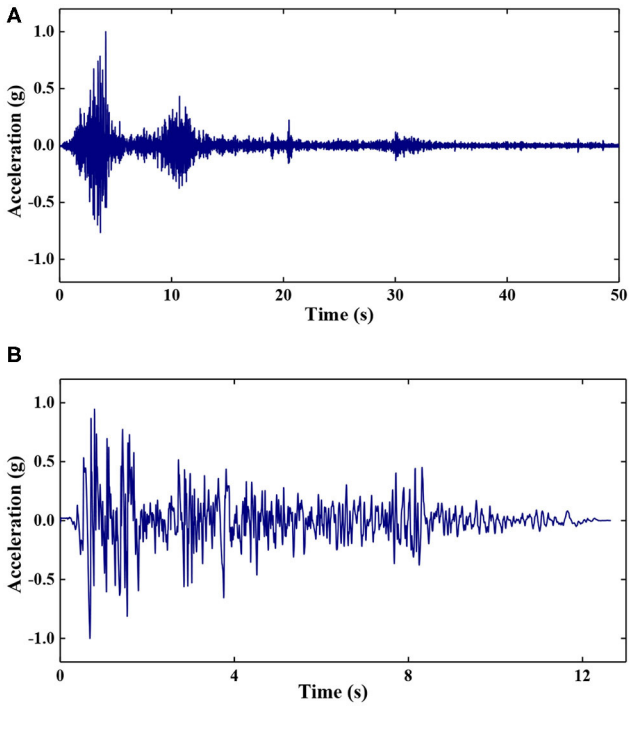

FIGURE 5 | Horizontal seismic wave acceleration curve after adjustment of test input. **(A)** Acceleration time-history curve of the Wenchuan Wolong wave and **(B)** Acceleration time-history curve of the El Centro wave.

SEISMIC RESPONSE OF THE BEDDING ROCK SLOPE

Acceleration Amplification Effect of the Slope

Under the action of an earthquake, the acceleration response of different parts of the slope often present different changing laws [31, 32]. In this test, the Y-direction acceleration of measuring points A1, A2, A3, A4, and A5 is taken as the basis of the acceleration response of the slope surface, and the Y-direction acceleration of measuring points A1, A6, A7, A8, and A9 is taken as the basis of the acceleration response of the slope body. The acceleration peak amplification factor (PGA) is defined as the ratio of the y-direction acceleration peak value of each measuring point above to the y-direction acceleration peak value of the A10 measuring point, which is arranged on the vibration table top. Taking the El Centro earthquake wave as an example, the variation law of the slope and PGA with different heights under different seismic amplitudes is described.

Figures 6A,B show the variation of PGA with elevation at each measurement point in the slope and at the slope surface at different seismic amplitudes. The GPA on the slope surface gradually increased along the height direction, while the GPA of the slope body showed a trend of decreasing first and then increasing. The bedding rock slope has an obvious "elevation effect" under earthquake action. With the increase of seismic amplitude, the dynamic shear strength and modulus of slope materials decrease gradually, while the damping ratio increases, which enhances the isolation and damping capabilities of the slope. In the process of seismic wave propagation from bottom to top, the loss of energy increases, the PGA amplification coefficient of each measuring point decreases gradually, and the elevation effect decreases. When the amplitude of the seismic wave reaches 0.9 g, the GPA amplification coefficient of the slope and each measuring point of the slope decreases significantly, especially at the height of 100 cm.

The reason for the above phenomenon is that the internal structure of the slope is damaged. Under the action of a 0.9 g earthquake, the middle and upper part of the slope gradually slide down along the interlayer structure, and the rear edge of the slope begins to separate from the model box. Due to the block

TABLE 1 | Loading condition of shaking table test.

Load sequence	Loaded wave and its amplitude		Load sequence	Loaded wave and its amplitude	
1	White noise	0.05 g	10	White noise	0.05 g
2	Wenchuan Wolong wave	0.10 g	11	Wenchuan Wolong wave	0.70 g
3	El Centro wave		12	El Centro wave	
4	White noise	0.05 g	13	White noise	0.05 g
5	Wenchuan Wolong wave	0.20 g	14	Wenchuan Wolong wave	0.90 g
6	El Centro wave		15	El Centro wave	
7	White noise	0.05 g			
8	Wenchuan Wolong wave	0.40 g			
9	El Centro wave				

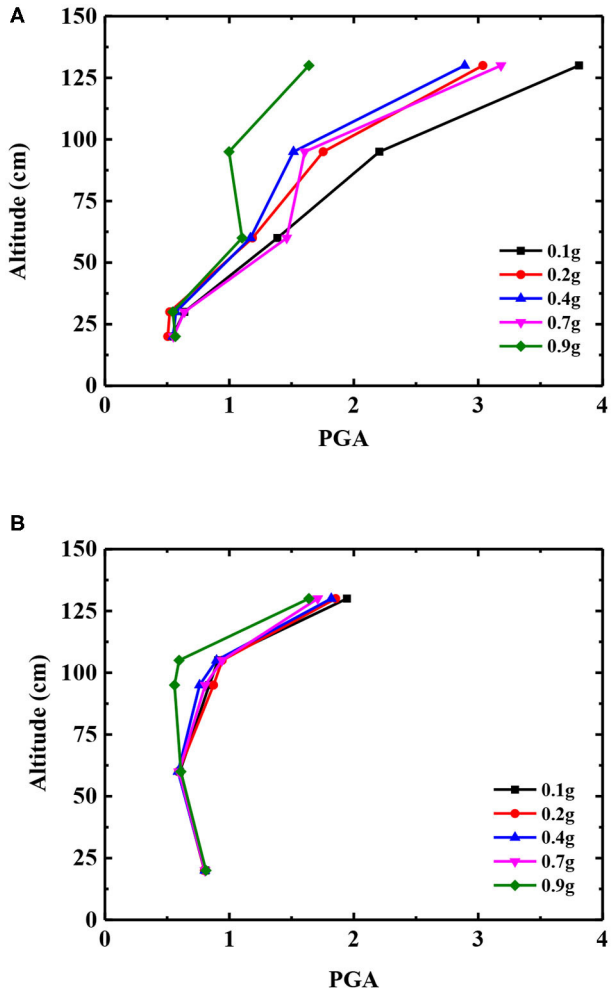

FIGURE 6 | PGA of slope surface and body under different seismic amplitudes. **(A)** Slope surface and **(B)** Slope body.

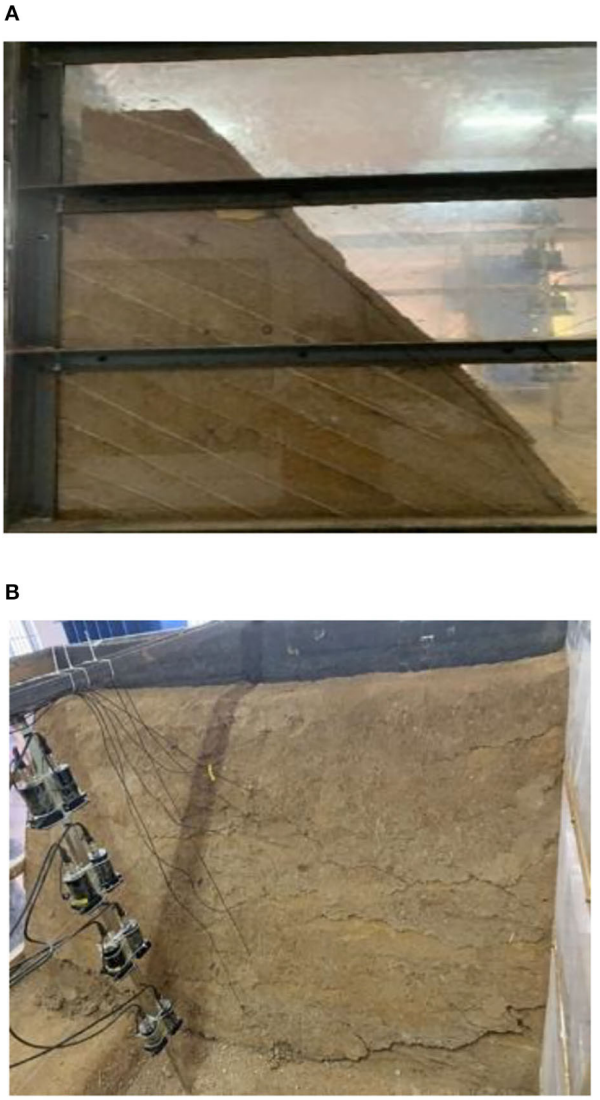

FIGURE 7 | Failure phenomenon of the bedding rock slope. **(A)** Left view and **(B)** Front view.

of the middle and lower "locking section" of the slope body, there are tensile cracks perpendicular to the rock layer at the height of 100 cm on the slope surface, as shown in **Figure 7**. The top of the slope is gradually separated from the slope body, and the inconsistency of the movement of the slope on both sides of the structural plane increases, so the GPA magnification coefficient decreases. In addition, the internal friction and friction energy consumption of the block increase, which further reduces the amplification coefficient of GPA.

Acceleration Response Spectrum of Slope

The shape of the acceleration response spectrum of the bedding rock slope under earthquake action has important reference value for understanding the dynamic response characteristics of the slope. In this section, the Y-acceleration time history of each measuring point of the slope and the slope under the action of an El Centro seismic wave with a peak acceleration of 0.2 g is selected for analysis. It is worth noting that this acceleration response spectrum calculation uses the damping ratio commonly used in engineering 5% [33].

It can be seen from **Figure 8** that the peak of the acceleration response spectrum gradually increases along the elevation under the action of the 0.2 g El Centro seismic wave. The shape of the acceleration response spectrum of the slope has a double peak in the lower part of the slope (height below 60 cm), and single peak in the upper part (height above 60 cm). The excellent period is concentrated around $T = 0.6$ s, and the amplitude of the response spectrum corresponding to the short period ($T = 0.0$–1.2 s) has a certain amplification along the elevation. The shape of the acceleration response spectrum of the slope along elevation is basically the same, the predominant period is approximately $T = 0.4$ s, and the amplitude of the response

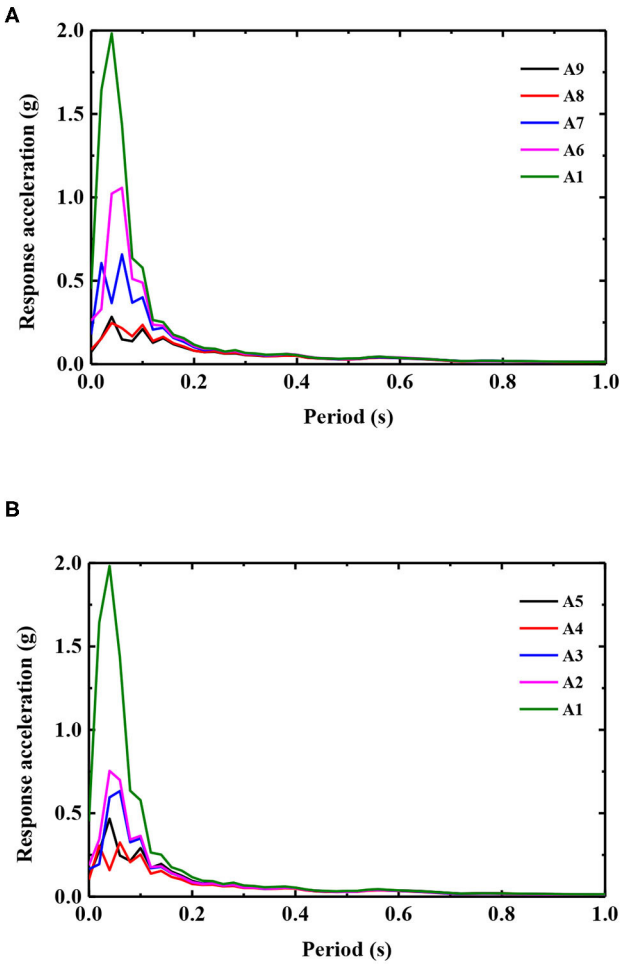

FIGURE 8 | Acceleration response spectrum of the slope surface and body under 0.2 g seismic amplitude. **(A)** Slope surface and **(B)** Slope body.

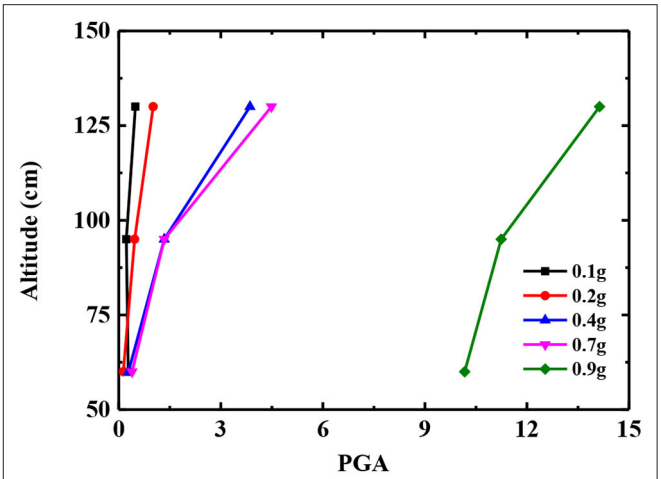

FIGURE 9 | Displacement of the slope surface with different seismic amplitudes.

spectrum corresponding to the short period part ($T = 0.0$–1.2 s) also has a certain amplification effect along elevation. Compared with the amplitude of the acceleration response spectrum of the slope surface and slope body, the peak value of the acceleration response spectrum of the slope surface above 25 cm is obviously larger than that of the slope body. The difference value gradually increases with the elevation, showing the "trend effect."

Displacement Response of the Slope

Figure 9 shows the displacement of the slope surface under different earthquake amplitudes. Under the peak earthquake of 0.1, 0.2, 0.4, and 0.7 g, the displacement response of the slope surface is smaller, and the displacement of each measuring point is <5 mm. When the amplitude of the seismic wave reaches 0.9 g, the displacement of the slope increases significantly, and the slope begins to be damaged. In addition, due to the existence of an interlayer structure surface, the movement of different parts of the slope is not consistent, and the displacement of the slope increases with the increase of elevation. With the increase of seismic amplitude, the non-uniform movement between the rock layers further increases. As a result, the shear slip of the top of the slope relative to the main body, the separation of the back edge of the slope and the model box, and the tension crack gradually extend to the structural plane in the slope locking section, which causes the whole slope to fail.

SEISMIC RESPONSE TIME-FREQUENCY ANALYSIS

Hilbert-Huang Transform

A Hilbert-Huang transform includes two parts: EMD empirical mode decomposition and Hilbert spectrum analysis. EMD empirical mode decomposition assumes that any signal is a composite signal composed of different intrinsic modal functions (IMFs), and each IMF component must meet two conditions: (1) the number of extreme points and zero crossing points were the same or have at most one difference, (2) the mean of the upper and lower envelope of the signal was zero. In this way, any signal can be decomposed into multiple IMFs. Then, the Hilbert spectrum and marginal spectrum are obtained by Hilbert transformation for each eigenmode function [34, 35].

For the seismic signal *F(t)*, which was decomposed into multiple IMFs, its Hilbert transformation is as follows:

$$G(t) = \frac{1}{\pi} K \int_{-\infty}^{\infty} \frac{F(\delta)}{t-\delta} d\delta \tag{1}$$

where K is a Cauchy principal value. Established analytic signal *P(t)*:

$$P(t) = F(t) + jG(t) = a(t)e^{j\Phi(t)} \tag{2}$$

where a(t) is the amplitude function; and Φ(t) is the phase function.

$$a(t) = \sqrt{F^2(t) + G^2(t)} \tag{3}$$

$$\Phi(t) = arctan\frac{G(t)}{F(t)} \tag{4}$$

The instantaneous frequency of the signal could be obtained by differentiating the phase. Therefore, the Hilbert transform of the decomposed IMF component can obtain the distribution law of the signal on the time-frequency-energy scale, which is the form of the Hilbert spectrum:

$$H(\omega, t) = Re\sum_{i=1}^{n+1} a_i(t) \cdot e^{j\int \omega_i(t)dt} \tag{5}$$

By integrating the time in the expression formula of the Hilbert spectrum, the distribution law of the signal on the frequency-amplitude scale can be obtained, which is the form of the corresponding marginal spectrum:

$$h(\omega, t) = \int_{-\infty}^{\infty} H(\omega, t)dt \tag{6}$$

Hilbert Spectrum Analysis

According to the above method, the acceleration time history of each measuring point on the slope under the action of 0.1, 0.2, 0.4, 0.7, and 0.8 g Wenchuan Wolong seismic waves is transformed by HHT. The Hilbert spectrum of each measuring point under the action of different amplitude seismic waves is obtained. The characteristics of the seismic signal energy in the time-frequency domain are represented by a two-dimensional plane contour

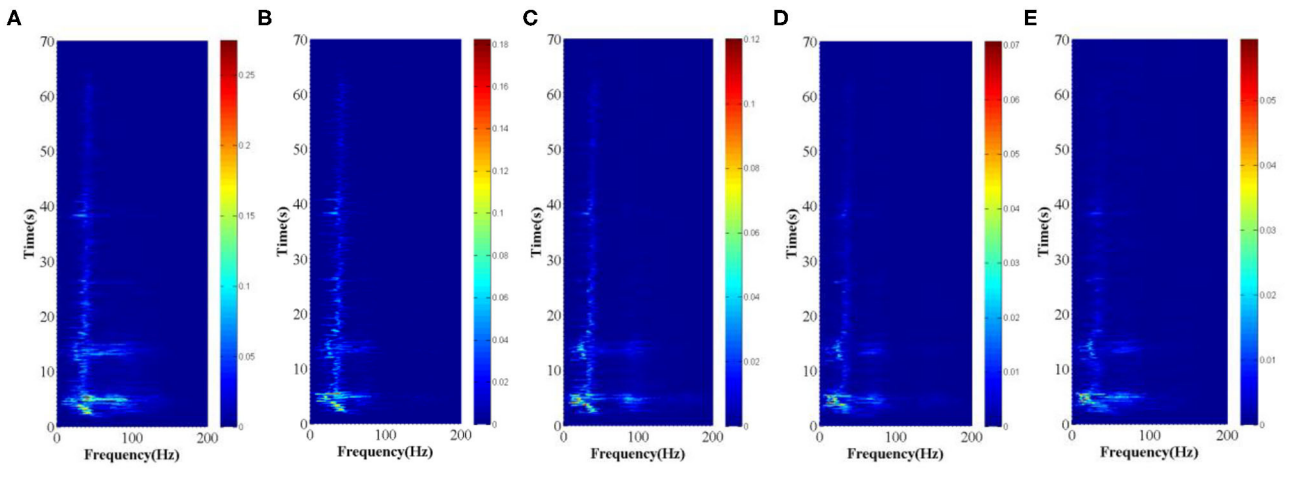

FIGURE 10 | Hilbert spectrum of the slope surface. **(A)** A1, **(B)** A6, **(C)** A7, **(D)** A8, and **(E)** A9.

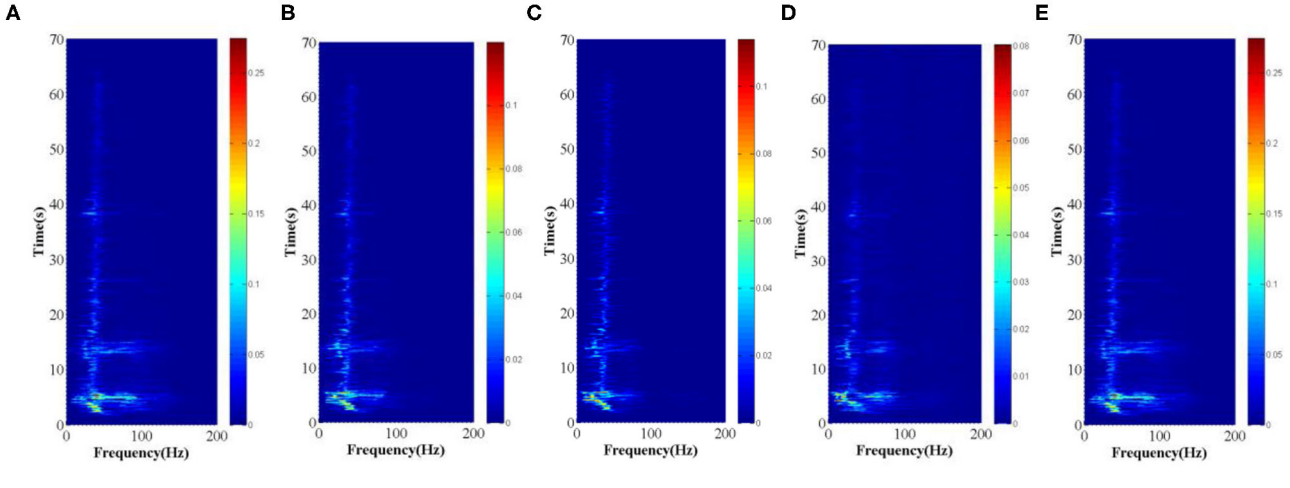

FIGURE 11 | Hilbert spectrum of the slope body. **(A)** A1, **(B)** A2, **(C)** A3, **(D)** A4, and **(E)** A5.

map, and the Hilbert spectrum under the action of a 0.2 g Wenchuan Wolong seismic wave is shown in **Figures 10**, **11**.

According to the comprehensive analysis of **Figures 10**, **11**, it can be found that the Hilbert Huang transform can accurately describe the time-frequency characteristics of the seismic signal. From **Figures 10**, **11**, it can be seen that the energy of the Wenchuan Wolong earthquake wave gradually increases from bottom to top. In the time domain, the energy is mainly concentrated in 2–6 and 12–15 s, corresponding to the time node when the compression wave of the Wolong earthquake reaches the double peak value. The predominant frequency is concentrated between 5 and 40 hz. With the increase of elevation, the former increases and the latter decreases. The above phenomenon may be related to the first natural frequency of the slope test model, which causes the amplification of the surrounding frequency components. This is consistent with the conclusion that the slope soil has a filtering effect on the high frequency component of the seismic wave and an amplifying effect on the low frequency component [36, 37]. For the bedding rock slope soil, the natural frequency is relatively small, which can enlarge the frequency band around the natural frequency of the seismic wave, and filter the frequency band in other ranges.

Hilbert Marginal Spectrum Analysis

The Hilbert energy spectrum of each measuring point on the slope under the action of 0.1, 0.2, 0.3, 0.4, and 0.6 g Wenchuan Wolong seismic waves is integrated in time, and the Hilbert marginal spectrum of each measuring point under the action of different amplitude seismic waves is obtained. The marginal spectrum of the slope under the action of 0.2 and 0.9 g Wenchuan Wolong seismic waves is shown in **Figures 12**, **13**.

It can be seen from **Figures 12**, **13** that under the action of a 0.2 g seismic wave, the shape of the marginal spectrum of each measuring point on the slope and in the slope is basically the same, all of which are single peaks. The distribution of the marginal spectrum frequency is relatively pure, and the predominant frequency is about 18 Hz. The peak value of the marginal spectrum increases with the increase of elevation. Under the action of a 0.6 g seismic wave, the shape of the marginal spectrum changes from a single peak to a double peak. The predominant frequency of A1, A2, and A3 measuring points has changed, which is concentrated around 12 Hz. That is to say, with the increase of the peak value of the input ground motion, the high frequency component of the site is weakened and the low frequency component is increased. The A6 and A7 measuring points of the slope surface have a similar marginal spectral peak, while the A3, A4, and A5 measuring points of the slope body have a similar marginal spectral peak. The difference of the peak value of the marginal spectrum indicates that earthquake damage has occurred in the slope [23, 25]. In order to further reveal the damage development process of the slope, the peak value of the marginal spectrum of each measuring point under the action of different amplitude seismic waves is extracted for analysis, as shown in **Figures 14**, **15**.

Figures 14, **15** show the energy change characteristics in the frequency domain during the bottom-up propagation of the seismic wave in the slope. Under the action of 0.1, 0.2, 0.4, and 0.7 g seismic waves, the peak value of the marginal spectrum increases linearly with the height, and there is no obvious inflection point for the peak value of the marginal spectrum. It shows that the continuity of each part of the slope is good, and that the energy of the seismic wave can be transferred upward smoothly. When the seismic amplitude reaches 0.9 g, the change rule of the peak value of the marginal spectrum under the height of 100 cm on the slope does not change. The turning point can be seen at the height of 100 cm on the slope surface, and the same phenomenon also occurs in the slope body. The peak value of the marginal spectrum above 100 cm on the slope is basically consistent with that under a 0.7 g seismic wave. It shows that there is damage and a tension crack at the height of 100 cm, which affects the upward propagation of the seismic wave. The degree of earthquake damage near the slope is stronger than that inside the slope. However, the slope has good continuity at other positions without damage. This is basically consistent with the failure phenomenon observed in the test.

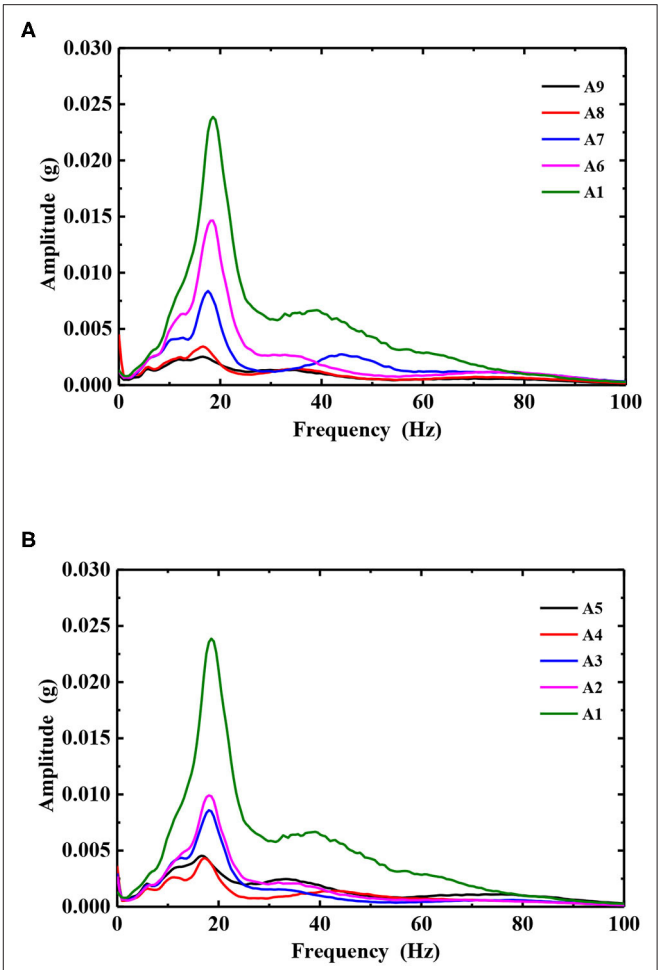

FIGURE 12 | The Hilbert marginal spectrum of the slope surface and body under 0.2 g of seismic amplitude. **(A)** Slope surface and **(B)** Slope body.

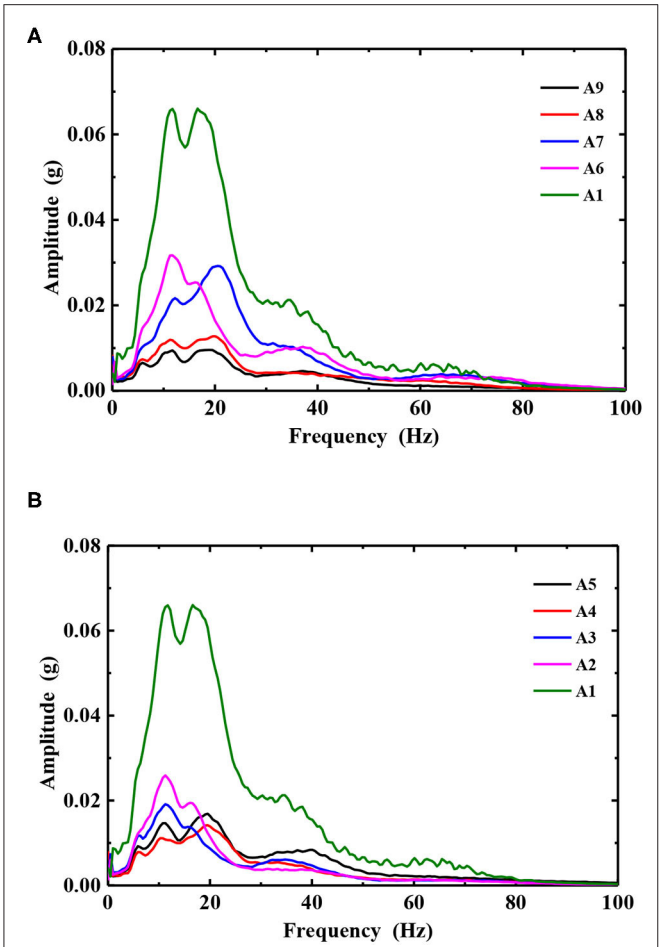

FIGURE 13 | The Hilbert marginal spectrum of slope surface and body under 0.9 g of seismic amplitude. **(A)** Slope surface and **(B)** Slope body.

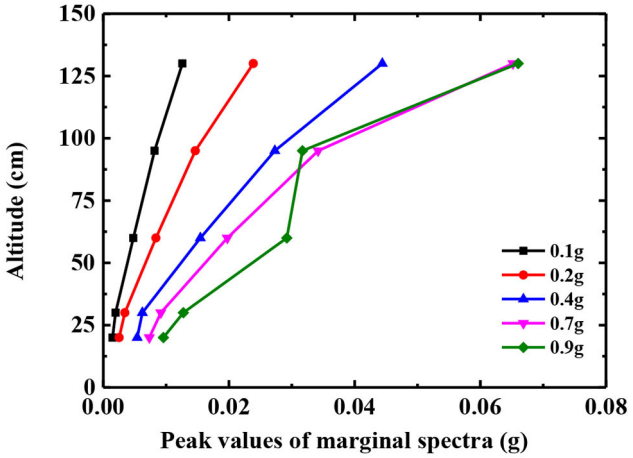

FIGURE 14 | PGA of the slope surface under different amplitudes.

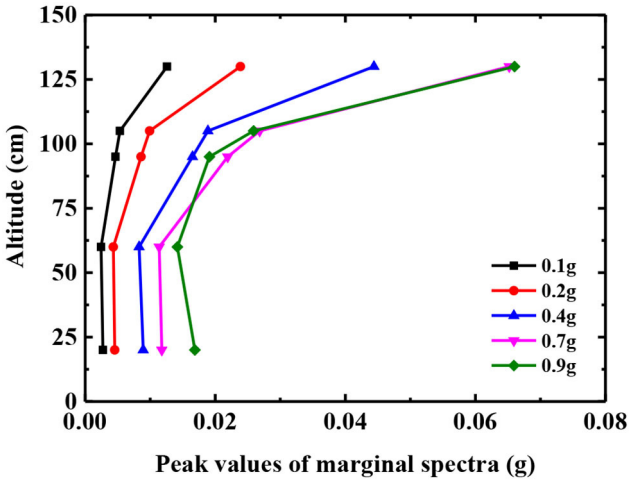

FIGURE 15 | PGA of the slope body under different amplitudes.

CONCLUSION

In this paper, based on the large-scale shaking table experiment of similar materials and the HHT method, the seismic dynamic response and instability mechanism of the bedding rock slope under different seismic amplitude values are systematically studied, and the following conclusions are drawn:

Firstly, the bedding rock slope has an obvious elevation effect under earthquake action. With the increase of the seismic amplitude value, the energy loss of the seismic wave in the process of bottom-up propagation increases, the PGA amplification coefficient of the slope body and each measuring point of the slope decreases gradually, and the elevation effect weakens. When the amplitude of the seismic wave reaches 0.9 g, the GPA amplification coefficient of the slope and each measuring point of the slope decreases significantly, especially at the height of 100 cm.

Secondly, under the action of an earthquake, the peak value of the acceleration response spectrum of the slope gradually increases along the elevation. The shape of the acceleration response spectrum of the slope has a double peak value in the lower part (height below 60 cm) and a single peak value in the upper part (height above 60 cm). The predominant period is about $t = 0.6$ s. The acceleration response spectrum of the slope body is basically the same along the elevation, and the predominant period is about $t = 0.4$ s. Compared with the amplitude of the acceleration response spectrum of the slope surface and the slope body, the peak value of the acceleration response spectrum of the slope surface above 25 cm is significantly higher than that of the slope body, showing a trend effect.

Thirdly, due to the existence of an interlayer structural plane, the movement of different parts of the slope is not consistent, and the displacement of the slope increases with the increase of elevation. The failure mechanism of the bedding rock slope is mainly divided into two stages. The first stage: under the action of gravity and seismic force, the top rock of the slope

starts to slide along the structural plane, the trailing edge of the slope is separated from the model box, and a tensile crack that gradually expands into the structural plane is generated in the locking section of the slope. The second stage: as the ground motion continues, the inconsistent motion between the rock layers increases further, the tensile cracks penetrate the structural plane, the top slope body slides out along the shear slip surface, and the entire slope becomes unstable and is destroyed.

Fourthly, the characteristics of the seismic signal in time–frequency domain can be better described by the Hilbert Huang transform. In the time domain, the energy is mainly concentrated in 2–6 and 12–15 s, corresponding to the time node when the compression wave of the Wolong earthquake reaches the double peak value. The predominant frequency is concentrated between 5 and 40 hz. With the increase of elevation, the former increases and the latter decreases.

Fifthly, the change of the peak value of the marginal spectrum clearly shows the development process of the earthquake damage inside the slope. The change rule of the peak value of the marginal spectrum under the height of 100 cm of the slope has not changed. At the height of 100 cm, the inflection point can be seen obviously, and the same phenomenon also occurs in the slope. It shows that the damage occurs at the height of 100 cm, and the degree of earthquake damage near the slope is stronger than that inside the slope. The recognition results of the marginal spectrum are in good agreement with the experimental results.

DATA AVAILABILITY STATEMENT

The raw data supporting the conclusions of this article will be made available by the authors, without undue reservation.

ETHICS STATEMENT

Written informed consent was obtained from the individual(s) for the publication of any potentially identifiable images or data included in this article.

AUTHOR CONTRIBUTIONS

LZ was the site representative of the field tests. CY was the project administrator and the person responsible for model tests, they proposed the research ideas. SM finished the first version of the manuscript. XG and MY finished the data process work. YL helped LZ finish the field tests. All authors contributed to the article and approved the submitted version.

FUNDING

This study was supported in part by the National Key Research and Development Plan (No. 2018YFE0207100); the Natural Science Foundation of China (Contract No. 41731288); the Sichuan Provincial Science and Technology Support Project (Nos. 18MZGC0186, 18MZGC0247, 2018JY0549); the China National Railway Group Co. Ltd Scientific Research Project (Nos. SY2016G003, N2019G002; P2019T001); the China Academy of Railway Sciences Corporation Limited Research and Development Fund (No. 2019YJ026); the 2017–2019 Young Elite Scientist Sponsorship Program by CAST. 2019 Young Top Talents Sponsorship Program of China Ten Thousand People Plan (No. 2019YJ300); the 2018 Sichuan Province Ten Thousand People Plan; the Nanchang Railway Bureau Scientific Research Project (No. 20171106), and the China Railway Eryuan Engineering Group Co. Ltd Scientific Research Project [No. KYY2019145(19-20)].

REFERENCES

1. Huang R, Fan X. The landslide story. *Nat Geosci*. (2013) **6**:325–6. doi: 10.1038/ngeo1806
2. Tang C, Ma G, Chang M, Li WL, Zhang DD, Jia T. Landslides triggered by the 20 April 2013 Lushan earthquake, Sichuan province, China. *Eng Geol*. (2015) **187**:45–55. doi: 10.1016/j.enggeo.2014.12.004
3. Wang WP, Yin YP, Yang LW, Zhang N, Wei YJ. Investigation and dynamic analysis of the catastrophic rockslide avalanche at Xinmo, Maoxian, after the Wenchuan Ms 8.0 earthquake. *Bull Eng Geol Environ*. (2020) **79**:495–512. doi: 10.1007/s10064-019-01557-4
4. Yingying T, Chong X, Jian C. Spatial distribution and susceptibility analyses of pre-earthquake and coseismic landslides related to the Ms 6.5 earthquake of 2014 in Ludian, Yunan, China. *Geocarto Int*. (2016) **32**:978–89. doi: 10.1080/10106049.2016.1232316
5. Zhang S, Guang-Ze Z, Liang-Wen J, Guang WU. Analysis of the characteristics of major geological disasters and geological alignment of Sichuan-Tibet railway. *Railway Stand Des*. (2016) **1**:14–9. doi: 10.13238/j.issn.1004-2954.2016.01.003
6. Huang R, Li W. Research on development and distribution rules of Geohazards induced by Wenchuan earthquake on 12th May. *Chin J Rock Mech Eng*. (2008) **27**:2585–92. doi: 10.3321/j.issn:1000-6915.2008.12.028
7. Chigira M, Wu X, Inokuchi T, Wang G. Landslides induced by the 2008 Wenchuan earthquake, Sichuan, china. *Geomorphology*. (2010) **118**:225–38. doi: 10.1016/j.geomorph.2010.01.003
8. Zhen-Lin C, Xiao HU, Qiang XU. Experimental study of motion characteristics of rock slopes with weak intercalation under seismic excitation. *J Mt Sci*. (2016) **13**:178–88. doi: 10.1007/s11629-014-3212-0
9. Yin Y, Sun P, Zhang M, Li B. Mechanism on apparent dip sliding of oblique inclined bedding rockslide at Jiweishan, Chongqing, China. *Landslides*. (2011) **8**:49–65. doi: 10.1007/s10346-010-0237-5
10. Yu-Chuan Y, Hui-Ge X, Xing-Guo Y, Ming-Liang C, Jia-Wen Z. Experimental study on the dynamic response and stability of bedding rock slopes with weak interlayers under heavy rainfall. *Environ Earth Sci*. (2018) **77**:433. doi: 10.1007/s12665-018-7624-y
11. Danqing S, Ailan C, Zhu C, Xiurun G. Seismic stability of a rock slope with discontinuities under rapid water drawdown and earthquakes in large-scale shaking table tests. *Eng Geol*. (2018) **245**:153–68. doi: 10.1016/j.enggeo.2018.08.011
12. Gischig VS, Eberhardt E, Moore JR, Hungr O. On the seismic response of deep-seated rock slope instabilities–insights from numerical modeling. *Eng Geol*. (2015) **193**:1–18. doi: 10.1016/j.enggeo.2015.04.003
13. Brito VP, Costa RF, Gomes MAF, Parteli EJR. Sliding susceptibility of a rough cylinder on a rough inclined perturbed surface. *Physica A*. (2003) **335**:47–58. doi: 10.1016/j.physa.2003.11.012
14. Parteli EJR, Gomes MAF, Brito VP. Nontrivial temporal scaling in a Galilean stick-slip dynamics. *Phys Rev E Stat Nonlin Soft Matter Phys*. (2005) **71**(3 Pt 2A):036137. doi: 10.1103/PhysRevE.71.036137

15. Parteli EJR, Gomes MAF, Montarroyos E, Brito VP. Omori law for sliding of blocks on inclined rough surfaces. *Physica A*. (2001) **292**:536–44. doi: 10.1016/S0378-4371(00)00629-4
16. Long-qi L, Neng-pan J, Zhang S, Deng XX. Shaking table test to assess seismic response differences between steep bedding and toppling rock slopes. *Bull Eng Geol Environ*. (2017) **78**:1–13. doi: 10.1007/s10064-017-1186-1
17. Fan G, Zhang J, Wu J, Yan K. Dynamic response and dynamic failure mode of a weak intercalated rock slope using a shaking table. *Rock Mech Rock Eng*. (2016) **49**:1–14. doi: 10.1007/s00603-016-0971-7
18. Salmi EF, Hosseinzadeh S. Slope stability assessment using both empirical and numerical methods: a case study. *Bull Eng Geol Environ*. (2015) **74**:13–25. doi: 10.1007/s10064-013-0565-5
19. Liu X, Liu Y, He C, Li X. Dynamic stability analysis of the bedding rock slope considering the vibration deterioration effect of the structural plane. *Bull Eng Geol Environ*. (2018) **77**:87–103. doi: 10.1007/s10064-016-0945-8
20. Yang C, Zhang J, Zhang M. A prediction model for horizontal run-out distance of landslides triggered by Wenchuan earthquake. *Earthquake Eng Eng Vibr*. (2013) **12**:201–8. doi: 10.1007/s11803-013-0163-3
21. Dong LJ, Wesseloo J, Potvin Y. Discriminant models of blasts and seismic events in mine seismology. *Int J Rock Mech Min Sci*. (2016) **86**:282–91. doi: 10.1016/j.ijrmms.2016.04.021
22. Huang NE, Shen Z, Long SR, Wu MC, Shih HH, Zheng Q. et al. The empirical mode decomposition and the Hilbert spectrum for non-linear and non-stationary time series analysis. *Proceedings A*. (1998) **454**:903–95. doi: 10.1098/rspa.1998.0193
23. Fan G, Zhang JJ, Fu X, Zhou LR. Dynamic failure mode and energy-based identification method for a counter-bedding rock slope with weak intercalated layers. *J Mt Sci*. (2016) **13**:2111–23. doi: 10.1007/s11629-015-3662-z
24. Fan G, Zhang LM, Zhang JJ, Yang CW. Time-frequency analysis of instantaneous seismic safety of bedding rock slopes. *Soil Dyn Earthquake Eng*. (2017) **94**:92–101. doi: 10.1016/j.soildyn.2017.01.008
25. Yan K, Liu F, Zhu C, Wang Z, Zhang J. Dynamic responses of slopes with intercalated soft layers under seismic excitations. *Chin J Rock Mech Eng*. (2017) **36**:2686–98. doi: 10.13722/j.cnki.jrme.2017.0440
26. Huang R, Li G, Ju N. Shaking table test on strong earthquake response of stratified rock slopes. *Chin J Rock Mech Eng*. (2013) **32**:865–75. doi: 10.3969/j.issn.1000-6915.2013.05.003
27. Xu Q, Liu H, Zou W, Fan X, Chen J. Large-scale shaking table test study of acceleration dynamic responses characteristics of slopes. *Chin J Rock Mech Eng*. (2010) **29**:2420–8. doi: 10.1016/S1876-3804(11)60004-9
28. Yuan W. *Simulation Theory and Static Model Test*. Chengdu: Southwest Jiaotong University Press (1998).
29. Zhang M. Study of similitude laws for shaking table tests. *Earthquake Eng Eng Vibr*. (1997) **17**:52–8. doi: CNKI:SUN:DGGC.0.1997-02-006
30. Changwei Y, Xinmin L, Jianjing Z, Zhiwei C, Cong S, Hongbo G. Analysis on mechanism of landslides under ground shaking: a typical landslide in the Wenchuan earthquake. *Environ Earth Sci*. (2014) **72**:3457–66. doi: 10.1007/s12665-014-3251-4
31. Chen XL, Gao RX, Gong W. Random seismic response and dynamic fuzzy reliability analysis of bedding rock slopes based on pseudoexcitation method. *Int J Geomech*. (2018) **18:**04017165. doi: 10.1061/(ASCE)GM.1943-5622.0001084
32. Dong L, Wesseloo J, Potvin Y, Li X. Discrimination of mine seismic events and blasts using the fisher classifier, naive Bayesian classifier and logistic regression. *Rock Mech Rock Eng*. (2016) **49**:183–211. doi: 10.1007/s00603-015-0733-y
33. Yang-Chang W. *Research on the Ground Motion Characteristics of Rock Slope and the Landslide Genesis Mechanism, Stability Identification and Damage Scope Evaluation System of Base-Covered Slope*. Chengdu: Southwest Jiaotong University (2013).
34. Huang NE. Introduction to the Hilbert-Huang transform and its related mathematical problems. *Interdiscip Math*. (2005) 1–26. doi: 10.1142/9789812703347_0001
35. Huang NE, Wu Z. A review on Hilbert-Huang transform: method and its applications to geophysical studies. *Rev Geophys*. (2008) **46**:1–23. doi: 10.1029/2007RG000228
36. Changwei Y, Ning F, Jianjing Z, Junwei B, Jun Z. Research on time-frequency analysis method of seismic stability of covering-layer type slope subjected to complex wave. *Environ Earth Sci*. (2015) **74**:5295–306. doi: 10.1007/s12665-015-4540-2
37. Dong L, Zou W, Li X, Shu W, Wang Z. Collaborative localization method using analytical and iterative solutions for microseismic/acoustic emission sources in the rockmass structure for underground mining. *Eng Fract Mech*. (2018) **210**:95–112. doi: 10.1016/j.engfracmech.2018.01.032

Conflict of Interest: The authors declare that this study received funding from China National Railway Group Co. Ltd, China Academy of Railway Sciences Corporation Limited, and China Railway Eryuan Engineering Group Co. Ltd. The funder was not involved in the study design, collection, analysis, interpretation of data, the writing of this article or the decision to submit it for publication.

frontiers in Physics

ORIGINAL RESEARCH
published: 12 November 2020
doi: 10.3389/fphy.2020.551232

Study of Sericite Quartz Schist Coarse-Grained Soil by Large-Scale Triaxial Shear Tests

Hui-qing Zhang[1], Feng Zhao[1], Shi-qiang Cheng[1], Yan-qing Zhang[2], Ming-jie Gou[2], Hong-jun Jing[2] and Hong-feng Zhi[3]*

[1]Ankang Highway Bureau of Shaanxi Province, Ankang, China, [2]School of Architecture and Civil Engineering, Xi'an University of Science and Technology, Xi'an, China, [3]Safety Technology Department, Shaanxi Future Energy and Chemical Co. LTD, Yulin, China

The large-scale triaxial consolidated-drained (CD) and consolidated-undrained (CU) shear tests were carried out to investigate performances of the sericite quartz schist coarse-grained soil on stress-strain, deformation, and strength under four different confining pressure conditions. The test results indicated that the stress-strain curve of sericite quartz schist was nonlinearity, compressive hardening and elastic-plastic. The shear strength envelope curve was better. In the triaxial CD shear test, the sericite quartz schist exhibited weak strain softening under different confining pressures. The sample showed shearing shrinkage at first and later dilatancy under confining pressures of 200, 400, and 600 kPa. When the confining pressure was 800 kPa, the sample showed a trend of shearing shrinkage. In the triaxial CU shear test, the sericite quartz schist exhibited strain hardening, presenting a tendency of shearing shrinkage at first and later dilatancy. It is more reasonable to take account of the cohesion of sericite quartz schist in practical engineering design by linear-regression analysis.

Keywords: soil mechanics, coarse-grained soil, dilatancy effect, characteristics of deformation and strength, large-scale triaxial shear test

OPEN ACCESS

Edited by:
Alex Hansen, Norwegian University of Science and Technology, Norway

Reviewed by:
Eric Josef Ribeiro Parteli, University of Cologne, Germany
Allbens Picardi Faria Atman, Federal Center for Technological Education of Minas Gerais, Brazil

****Correspondence:***
Yan-qing Zhang
zhangyq@xust.edu.cn

Specialty section:
This article was submitted to Interdisciplinary Physics, a section of the journal Frontiers in Physics

Received: *12 April 2020*
Accepted: *02 October 2020*
Published: *12 November 2020*

Citation:
Zhang HQ, Zhao F, Cheng SQ, Zhang YQ, Gou MJ, Jing HJ, Zhi HF (2020) Study of Sericite Quartz Schist Coarse-Grained Soil by Large-Scale Triaxial Shear Tests. Front. Phys. 8:551232. doi: 10.3389/fphy.2020.551232

HIGHLIGHTS

(1) Large-scale triaxial consolidated-drained and consolidated-undrained shear tests were conducted.
(2) Explored feasibility of coarse aggregates of sericite quartz schist as embankment filler.
(3) Basic engineering mechanical properties of argillaceous limestone were analyzed.

INTRODUCTION

Coarse-grained soil is generally regarded as an earth-rock material with a particle size greater than 0.075 mm and a particle content exceeding 50% of the total mass. Coarse-grained soil is widely distributed in nature. Recently, it was found that coarse sand particles reaching 1 mm size occur on the surface of sand dunes (which have mean particle size 100–300 microns), thereby affecting their shape and dynamics rich in reserves [1]. Coarse-grained soil has excellent engineering performances such as good compaction property, strong water permeability, high shear

strength, and high liquefaction resistance under seismic load. It has been widely used in engineering construction [2]. As the main filler of the roadbed, the performances of the coarse-grained soil have significantly effects on the stability of the construction and the operation of the project. The large-scale triaxial shear tester is an ideal experimental equipment to evaluate the engineering properties of coarse-grained soil. Although it cannot reflect the intermediate principal stress, and the measured value is lower than that of the plane strain gauge and the true triaxial instrument, it is partial to the safety of the engineering application, and it is widely adopted due to the simple principle and operation [3].

Many scholars have conducted in-depth research on the performances of coarse-grained soil. Four groups of large-scale triaxial tests were conducted to investigate the influence of dilatancy on strength and deformation behaviors of coarse-grained soils at different initial densities [4]. Based on large-scale triaxial shearing apparatus, Meng et al. [5] conducted consolidated-drained shear tests on the saturated coarse-grained soil, and put forward a function for fitting the axial strain and lateral strain in the triaxial test, by which the volumetric strain of the soil-sample in the test could be predicted. The triaxial consolidated-drained (CD) shear tests were carried out to examine the stress-strain relationship, strength and deformation property of coarse-grained soil. The influence factors of shear dilatancy coefficient that reflects the degree of dilatancy were explored and the feasibility of the current empirical formulas was verified [6]. Wei et al. [7] experimentally investigated the wetting deformation of a coarse-grained soil at various stress levels, and obtained the relation curve between stress, axial strain, and volume strain. The triaxial tests were carried out to study the development of permeability of crustal rock to help to understand fault mechanics and constrain larger-scale models that predict bulk fluid flow within the crust [8]. In order to study the dilatancy effect of granular soil and its effect on dilatancy tendency under different confining pressure conditions, a series of red stone granular soils tests were executed by the large scale triaxial shearing apparatus [9]. For over coarse -grained soils, the stress-strain relationship, shear strength behavior and the influence of water on strength and deformation under low confining pressures were detailedly analyzed via large-scale triaxial test [10]. Large-scale triaxial shear tests and finite element analysis were carried out to study the deformation properties of coarse-grained soil under static loads [11]. Zhou et al. [12] studied the stress-strain relationship and strength characteristics of the coarse-grained soil in the earthquake area, in which the confining pressure, shear rates, and consolidation time were considered as test variables. The CD triaxial tests were conducted for coarse-grained soil, by means of experiments and particle-based numerical simulations. The numerical model of triaxial test for graded coarse-grained soil was established by programming PFC3D (particle flow code of three dimension) from the view of microscopic scale. Stress-strain relationship from particle flow model and triaxial test were compared under different confining pressures, and the influence of micro-properties on coarse-grained soil strength was analyzed [13]. A series of large-scale triaxial compression tests was conducted to investigate the effect of stress path on critical state and particle breakage–induced grading evolution of rockfill material [14]. Based on cellular automata method, the HHC-CA model was developed by combining the laboratory triaxial tests of coarse-grained soil, which generated the coarse-grained soil samples of different initial grain fabrics to illustrate the heterogeneous and random distribution of coarse-grained soil grain group. By means of the fast Lagrangian analysis of continua in three dimensions (FLAC3D), triaxial numerical simulation of coarse-grained soil was conducted and the relationship between the gravel content and internal friction angle of sample shear band was discussed [15].

In this paper, the mechanical properties of sericite quartz schist coarse-grained soil under different stress states were investigated. Large size soil samples were adopted to eliminate the size effect of coarse-grained soil and ensure the authenticity of the test results. Large-scale triaxial consolidated-drained (CD) and consolidated-undrained

FIGURE 1 | Large-scale static triaxial apparatus.

TABLE 1 | Indexes of basic properties of samples.

Test material	Specific gravity	Porosity (%)	Water content (%)	Dry density (g/cm^3)
Sericite quartz schist	2.65	18.9	4.6	2.15

(CU) shear tests of coarse-grained soil were carried out at four different confining pressures to evaluate the mechanical properties of coarse-grained soil.

EXPERIMENTAL

Experiment Equipment and Materials

The experiment was conducted on the large-scale static triaxial apparatus (**Figure 1**) of the Nanjing Hydraulic Research Institute (NHRI). The sample size is 300 mm × 700 mm, and the maximum particle size is not exceeding 60 mm.

The test material was the roadbed filler of section K21 + 350-K21 + 541.751 of the second-class road reconstruction project from Xunyang to Ankang, which is part of the national road 316 in shaanxi, China. The lithology of the test material is sericite quartz schist. The indexes of basic properties of samples were listed in **Table 1**, and the gradation curve was shown in **Figure 2**.

Experimental Design

The sample was designed according to the dry density, size and gradation curve of the test. In light of the particle size range, the sample was divided into five equal parts: 60–40 mm, 40–20 mm, 20–10 mm, 10–5 mm, and 5–0 mm. A water permeable plate was placed on the pedestal of the sample, where a rubber membrane was attached on. The forming barrel was installed and the rubber membrane was turned on, then the gas was pumped outside the forming barrel so that the rubber membrane could be attached tightly to the inner wall of the forming barrel. The first layer of sample was placed, and the surface was flattened evenly. The vibrator was used to make the sample become dense according to the dry bulk density required by each sample. The static pressure of the vibrator plate was 14 kPa, and the vibration frequency was 40 Hz. Then, added the water permeable plate and sample cap on the sample, tightening the rubber membrane, and removed the forming barrel (the triaxial sample after removing the forming barrel was shown in **Figure 3**). Finally, installed the pressure chamber with opened kicker port, and closed the kicker port after filling water into the pressure chamber. The sample was saturated by drip saturation method, and the confining pressure was applied to the saturated sample according to the requirements. The tests could be carried out once the consolidation of the sample was completed.

During the tests, the axial load, axial deformation, displacement and pore water pressure of the sample were

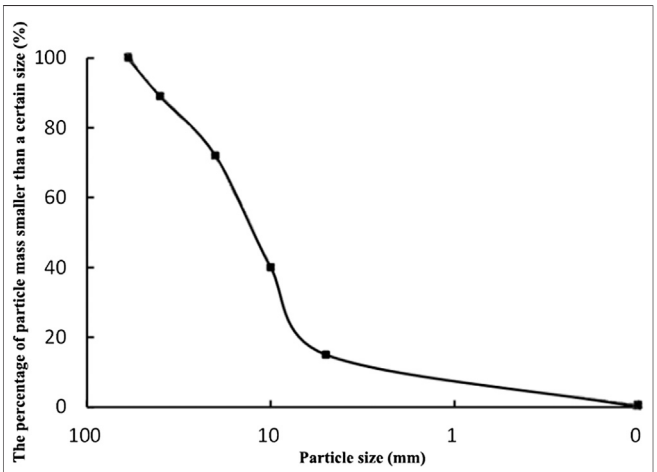

FIGURE 2 | Gradation curve of sericite quartz schist.

FIGURE 3 | Finished sample.

FIGURE 4 | Sample after test.

collected automatically by the computer, and the stress-strain curve was drawn simultaneously until the specimen was broken or the axial strain of the specimen up to 15%.

If there was a failure point, a peak would appear on the stress-strain curve, the value of which represented the principal stress difference ($\sigma_1 - \sigma_3$), corresponding to the failure strength of the rockfill. Otherwise, the point corresponding to 15% of the axial strain could represent the failure point and the principal stress difference ($\sigma_1 - \sigma_3$) was the failure strength of the rockfill. The above process was repeatedly executed under the confining pressure conditions of 200, 400, 600, and 800 kPa, respectively. The whole test process was carried out according to the Geotechnical Test Procedure (SL237-1999). The sample after the test was shown in **Figure 4**.

RESULTS AND DISCUSSION

Stress-Strain Relationship

The stress-strain relationship curves of CD and CU shear test of samples under different confining pressure conditions were demonstrated in **Figure 5**.

In **Figure 5**, it can be seen that the stress-strain curve of sericite quartz schist exhibited characteristics of nonlinearity, compressive hardening and elastic-plastic. The confining pressure had a significant influence on the stress-strain relationship curve of coarse-grained soil, which was the main effect factor for the strength of the sample. In the initial stage, the initial tangential modulus increased with the increase of confining pressure. When the test condition is constant, the deviatoric stress increased with the increase of confining pressure under the same axial strain condition.

Related researches [16, 17] indicated that grain breakage is smaller under low confining pressure, and increase of grain breakage will significantly degrade material strength. With the increase of particle breakage, the position of the particles is rearranged, and the fine particles fill the voids continuously, so that the sample becomes dense.

For the triaxial CD shear test (**Figure 5A**), the pore water pressure of the sample dissipated rapidly, and under the action of confining pressure, the stress peak occurred when the axial strain is small. However, as the confining pressure increased, the particles were crushed, causing the stress-strain curve of the sample to decrease slightly after reaching the peak stress, and eventually to be residual stress, which was characterized by weak

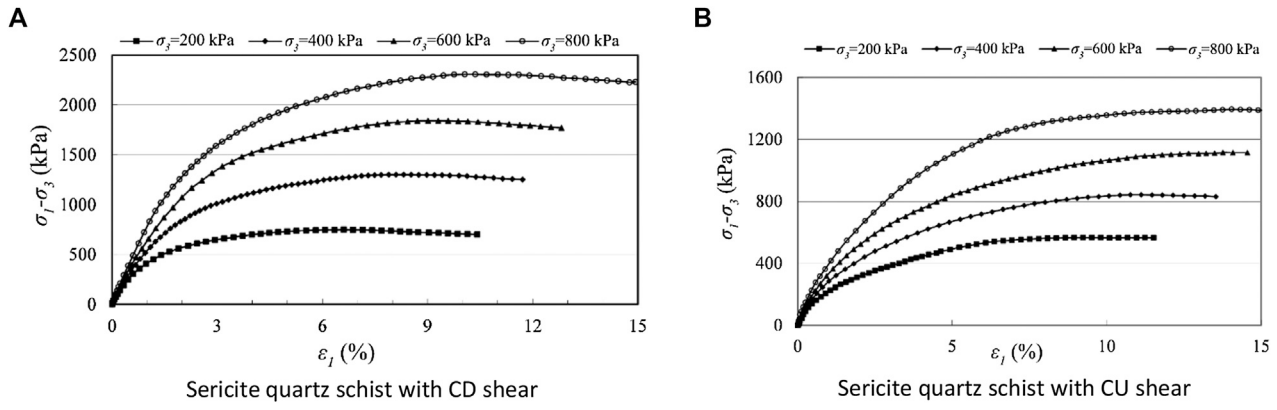

FIGURE 5 | Stress-strain curves of saturated samples under different confining pressures.

strain softening and mainly due to volume reduction and density increase of the sample.

For the triaxial CU shear test, the volume is constant, and the stress-strain curve had no obvious peak strength, which was characterized by strain hardening. The main reason was attributed to the fracture of coarse particles in the sample, making the sample more dense and not easy to break, so the curve showed a gentle trend.

Deformation Characteristics

Figures 6 and **7** showed the curves of ($\varepsilon_1 \sim \varepsilon_v$) and ($\varepsilon_1 \sim u_w$) of saturated samples under drained and undrained conditions. In this CU shear test, the pore water pressure was measured by the pore pressure sensor at the top of the specimen and was collected automatically by computer.

For the triaxial CD shear test, the volumetric strain of the sample was obtained by measuring the amount of water discharged from the inside of the sample. Under undrained conditions, the sample volume was generally considered to be unchanged. However, for samples with high stone content, due to the sliding extrusion, crushing and filling voids between the stones during the shearing process, the samples also exhibited characteristics of dilatancy and shearing shrinkage [18]. Since the pore water cannot be discharged, the dilatancy and shearing shrinkage tendency of the sample was converted into a constant change of pore water pressure. When the sample showed the dilatancy tendency, the inner pore increased, and the volumetric strain as well as the pore water pressure decreased. When the sample was shearing shrinkage, the inner pore decreased while the volumetric strain and the pore water pressure increased [19].

From **Figures 6** and **7**, it can be found that under drainage condition, when the confining pressures were 200, 400, and 600 kPa, respectively, the volumetric strain increased first and then decreased with the increase of the axial strain, which indicated that the sample was shearing shrinkage at first, then dilatancy later, appearing that the amount of shearing shrinkage increased with the increase of the confining pressure, then reached the peak, and then the volumetric strain decreased gradually. When the confining pressure was 800 kPa, the sample showed the tendency of shearing shrinkage. The main reason was that the coarse particles in the sample was not be broken under the lower confining pressure, and was easy to turn and roll under the action of shearing force, which was characterized by dilatancy or dilatancy at first, then shearing shrinkage later. According to the discussion in "*Stress-Strain Relationship*" section, the coarse particles in the sample were easily broken under a relatively high confining pressure, and might also be squeezed to fill the pores, rarely flipped and rolled, which was represented as shearing shrinkage macroscopically. For undrained conditions, under the four confining pressure conditions, the overall trend of pore water pressure of the sample was firstly increased and then decreased, indicating that the volumetric strain of the sample increased first and then decreased, showing the tendency of shearing shrinkage at first, then dilatancy later for the sample. When the confining pressure was 200 kPa, the change of pore water pressure of the sample was small and the increase was less than the decrease, indicating that the sample mainly exhibited the dilatancy trend; when the confining pressure is 400, 600, and 800 kPa, the pore water pressure of the sample was larger and the increase is greater than the decrease, indicating that the sample was shearing shrinkage at first, then dilatancy later, and the shearing shrinkage tendency was obvious. In the initial stage, the pore water pressure at a confining pressure of 200 kPa was slightly larger than that under the other three confining pressures, which was related to the compactness of the sample. When the initial pressure was applied, the particles in the sample were mutually displaced and rearranged, resulting in a larger variation of pore volume in the sample, so that the pore water pressure was abrupt. Then the sample was gradually compacted, as the confining pressure increased, the pore water pressure was no longer abrupt, and the curve of pore water pressure became smooth.

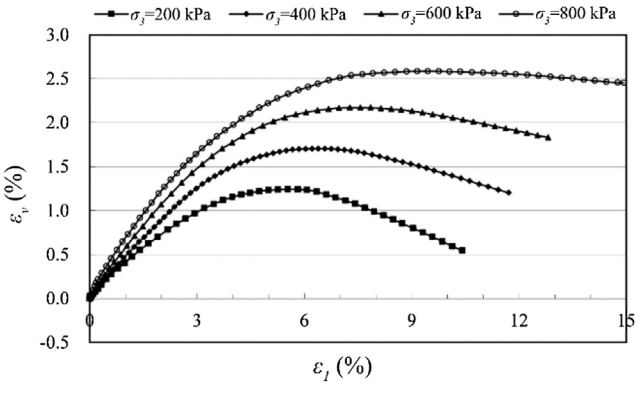

FIGURE 6 | Curves of ($\varepsilon_1 \sim \varepsilon_v$) of saturated sample under different confining pressures (CD).

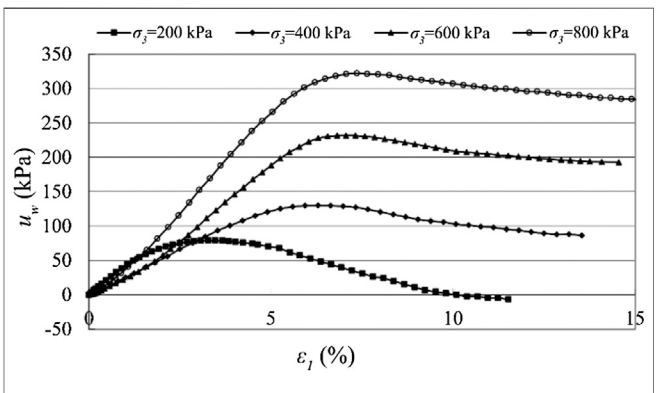

FIGURE 7 | Curves of ($\varepsilon_1 \sim u_w$) of saturated sample under different confining pressures (CU).

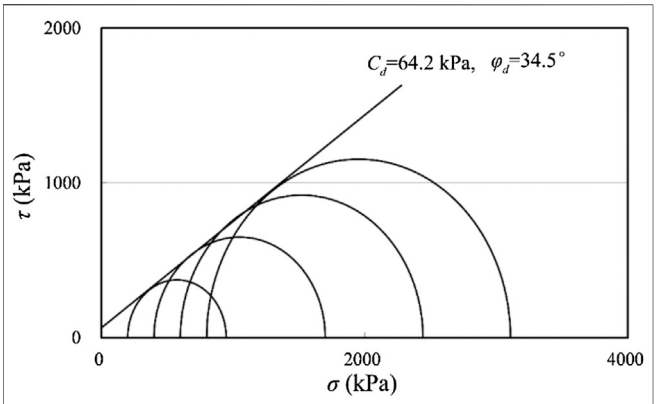

FIGURE 8 | Mohr circle and strength envelope of sericite quartz schist (CD).

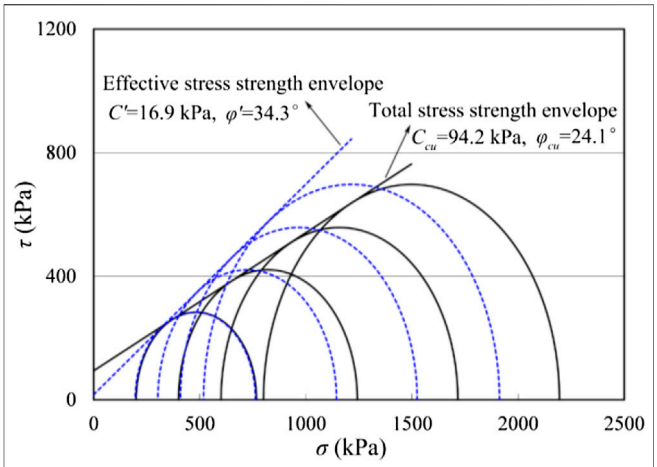

FIGURE 9 | Total stress strength envelope and effective stress strength envelope of sericite quartz schist (CU).

Strength Characteristics

The shear strength of non-cohesive soils mainly comes from the friction and bite force between the soil particles. It is generally recognized that the factors affecting the shear strength of coarse-grained soil include density, coarse particle content, fine particle content, particle geometry, strength of the particles, water content, diameter ratio, sample size and shear speed [20]. For non-cohesive soils, it is generally supposed that the cohesion need not to be considered. However, in the triaxial test, when the Mohr circle strength envelope was fitted by a straight line, there was generally an intercept. The intercept of the non-cohesive soil was related to the bite force between the soil particles, and it is fundamentally different from the cohesion of the cohesive soil. Related tests had shown that the intercept was related to the mineral composition, particle shape, gradation of the soil sample, which was a component of the strength of the granular soil.

There are many different experimental approaches to assess the cohesive properties of polydisperse particle systems, the packing fraction measurement is relatively simple. Parteli et al. [21] applied experiments and numerical simulations to measure the packing fraction of strongly polydisperse powders.

Figures 8 and **9** showed the Mohr circle and the strength envelope of the saturated sample under both drained and undrained conditions.

It can be found that in CD shear test, the internal friction angle (φ) of the saturated sericite quartz schist was 34.5° (**Figure 8**), while in CU shear test, the effective internal friction angle (φ') was 34.3° and the index (φ_{cu}) of total stress strength was 24.1°. The Mohr circle strength envelope was fitted by a straight line, and the cohesion of the roadbed filler was considered in the engineering design. Related research [22] indicated that when the Mohr circle strength envelope was fitted by a straight line, if the cohesion was neglected in the low dam design, the dam was generally conservative; However, if the cohesion was neglected in the high dam design, it was very unreasonable to draw a conclusion that the damage area was obviously larger in the stress-strain calculation.

CONCLUSION

In this study, the CD and CU shear tests of the sericite quartz schist were conducted by using the large-scale triaxial shear apparatus. During the triaxial shearing process, the changes of deviatoric stress, body strain and pore water pressure with the axial strain were monitored comprehensively. The main conclusions are as follows:

1) The large sample well eliminated the size effect of the coarse-grained soil and ensures the reliability of the experimental results. The stress-strain curve of the sericite quartz schist exhibited performances of nonlinearity, compressive hardening and elastic-plastic. Under four confining pressure conditions, the sericite quartz schist showed weak strain softening characteristics in CD shear test and strain hardening characteristics in CU shear test. This was closely related to the volume of the sample and the pore water pressure.

2) The sericite quartz schist presented different dilatancy trends under different confining pressures. For the drained conditions, the samples showed shearing shrinkage at first and dilatancy later under confining pressures of 200, 400, and 600 kPa respectively, while that under 800 kPa just showed shearing shrinkage. For the undrained conditions, the samples showed shearing shrinkage at first and dilatancy later under all the confining pressures.

3) In the CD shear test, the internal friction angle (φ) of the saturated sericite quartz schist was 34.5°; In the CU shear test, the effective internal friction angle (φ') was 34.3° and the index (φ_{cu}) of total stress strength was 24.1°. The Mohr circle strength envelope was fitted by a straight line, and the cohesion of the sericite quartz schist was considered in the engineering design to ensure the rationality of the design.

The study results can provide a certain test basis for understanding the engineering characteristics of sericite quartz schist and the stability analysis of rock fill embankment.

DATA AVAILABILITY STATEMENT

All datasets presented in this study are included in the article/ supplementary material.

AUTHOR CONTRIBUTIONS

Y-QZ and M-JG, writing-original draft preparation; H-QZ and FZ, methodology; H-JJ and H-FZ, validation; S-QC, supervision. All authors have read and agreed to the published version of the manuscript.

FUNDING

This research was supported by the National Natural Science Foundation of China (Grant No. 51378090).

ACKNOWLEDGMENTS

The authors are grateful for the support provided by School of Architecture and Civil Engineering, Xi'an University of Science and Technology, Xi'an, 710054, China.

REFERENCES

1. Zhang ZC, Dong ZB, Hu GY, Parteli EJR. Migration and morphology of asymmetric barchans in the central hexi corridor of northwest China. *Geosciences*. (2018). **8**:204. doi:10.3390/geosciences8060204.
2. Guo QG. *Research and application of the engineering properties of coarse-grained soil*. Zhengzhou, China: Yellow River Water Conservancy Press (1998). 12 p.
3. Liu MC, Gao YF, Liu HL, Fei K. Development of study on a large scale triaxial test of coarse-grained materials. *Rock Soil Mech.* (2002). **23**: 217–21. doi:10.1007/s11769-002-0073-1.
4. Jiang JS, Cheng ZL, Zuo YZ, Ding HS. Dilatancy of coarse-grained soil in large-scale triaxial tests study. *Rock Soil Mech.* (2014). **35**:3129–38. doi:10.16285/j.rsm.2014.11.010.
5. Meng F, Zhang JS, Hu QF, Chen XB, Wang QY. Large-scale triaxial test study on volumetric strain law of coarse-grained soil. *Water Resour Hydropower Eng.* (2013). **44**:139–43. doi:10.13928/j.cnki.wrahe.2013.06.034.
6. Chu FY, Zhu JG, Wang GQ, Liu HL. Large scale triaxial test study on deformation and strength characteristics of coarse-grained material. *J Shandong Agric Univ.* (2011). **42**:572–8. doi:10.3969/j.issn.1000-2324.2011.04.021.
7. Wei S, Zhu JG. Study on wetting behavior of coarse grained soil in triaxial test. *Rock Soil Mech.* (2007). **28**:1609–14. doi:10.16285/j.rsm.2007.08.017.
8. Mitchell TM, Faulkner DR. Experimental measurements of permeability evolution during triaxial compression of initially intact crystalline rocks and implications for fluid flow in fault zones. *J Geophys Res.* (2008). **113**:B11412. doi:10.1029/2008jb005588.
9. Chen XB. Study of dilatancy effect of red stone coarse grained soil by large scale triaxial tests. *Chin J Rock Mech Eng.* (2010). **29**:3145–9. doi:CNKI:SUN:YSLX.0.2010-S1-081.
10. Qin SL, Chen SX, Han Z, Xu XC. Large-scale triaxial test study of behavior of over coarse -grained soils. *Rock Soil Mech.* (2010). **31**:189–193. doi:10.16285j.rsm.2010.s2.068.
11. Leng WM, Mei HH, Nie RS, Yang Q, Zhao CY. Static characteristic research on coarse grained soil filling in heavy haul railway subgrade bed. *J Railw Eng Soc.* (2016). **11**:23–9. doi:10.3969/j.issn.1006-2106.2016.11.005.
12. Zhou XJ, Zou Q, Xiang LZ. Mechanical study on the coarse-grained soil using laboratory triaxial shear test. *J Southwest Univ Sci Tech.* (2012). **27**:40–3. doi:10.3969/j.issn.1671-8755.2012.04.009.
13. Geng L, Huang ZQ, Miao Y. Meso-mechanics simulation triaxial test of coarse-grained soil. *J Civ Eng Manag.* (2011). **28**:24–9. doi:10.3969/j.issn.2095-0985.2011.04.006.
14. Ning F, Liu J, Kong X, Zou D. Critical state and grading evolution of rockfill material under different triaxial compression tests. *Int J GeoMech.* (2020). **20**: 04019154. doi:10.1061/(asce)gm.1943-5622.0001550.
15. Wang GJ, Yang CH, Zhang C, Ma HL, Mao HJ, Hou KP. Numerical simulation triaxial tests for coarse-grained soil and preliminary study of initial fabric of sample grain. *Rock Soil Mech.* (2011). **32**:585–90. doi:10.16285/j.rsm.2011.02.047.
16. Hidalgo RC, Herrmann HJ, Partelli EJR. Force chains in granular packings. *Proc Int Sch Phys Enrico Fermi.* (2004). **155**:153–72.
17. Zhang JM, Jiang GS, Wang R. Research on influences of grain breakage and dilatancy on shear strength of calcareous sands. *Rock Soil Mech.* (2009). **30**:2043–8. doi:10.16285/j.rsm.2009.07.056.
18. Chi MJ, Zhao CG, Li XJ. Stress-dilation mechanism of sands. *China Civ Eng J.* (2009). **42**:99–104. doi:CNKI:SUN:TMGC.0.2009-03-022.
19. Xia JG, Hu RL, Qi SW, Gao W, Sui HY. Large-scale triaxial shear testing of soil rock mixtures containing oversized particles. *Chin J Rock Mech Eng.* (2017). **36**:2031–9. doi:10.13722/j.cnki.jrme.2016.1638.
20. Zhang QY, Si HY. Strength and stress-strain properties of the coarse-grained soils by large triaxial shear test. *J Hydraul Eng.* (1982). 22–31.
21. Parteli EJR, Schmidt J, Blümel C, Wirth KE, Peukert W, Pöschel T. Attractive particle interaction forces and packing density of fine glass powders. *Sci Rep.* (2014). **4**:6227. doi:10.1038/srep06227.
22. Gan L, Yuan GG. High pressure large triaxial tests and strength characteristics of coarse-grained soil. *Dam Obs Geotech Tests.* (1997). **21**:9–12. doi:CNKI:SUN:DBGC.0.1997-03-002.

Conflict of Interest: Author H-FZ was employed by Shaanxi Future Energy and Chemical Co. LTD.

The remaining authors declare that the research was conducted in the absence of any commercial or financial relationships that could be construed as a potential conflict of interest.

frontiers in Physics

ORIGINAL RESEARCH
published: 01 December 2020
doi: 10.3389/fphy.2020.556714

Shaking Table Test on Dynamic Response of Bedding Rock Slopes With Weak Structural Plane Under Earthquake

Changwei Yang[1], Liang Zhang[1], Yang Liu[1], Denghang Tian[1], Xueyan Guo[1] and Yang Liu[2]*

[1]Department of Civil Engineering, Southwest Jiaotong University, Chengdu, China, [2]Zhongke (Hunan) Advanced Rail Transit Research Institute, Zhuzhou, China

Taking a bedding rock slope with weak structural plane as the prototype, a shaking table test with a similarity ratio of 1:10 is designed and carried out. By analyzing the acceleration and displacement responses at different positions of the slope, the seismic response and instability mechanism of rock bedding slope under different seismic amplitudes, frequencies, and durations are studied. Before the failure of the slope, the rock bedding slope shows an obvious "elevation effect" and "surface effect" under the action of Wenchuan Wolong earthquake wave with different amplitudes. With the increase of the amplitude of the input seismic wave, the elevation effect and the surface effect gradually weaken. When the amplitude of the seismic wave reaches 0.9 g, the rock bedding slope begins to show damage, which demonstrates that the difference of PGA amplification coefficients on both sides of the weak structural plane increases significantly. Compared with the Kobe seismic wave and Wenchuan Wolong seismic wave, the excellent frequency of EL Centro seismic wave is closer to the first-order natural frequency of slope model and produces resonance phenomenon, which leads to the elevation effect of PGA amplification coefficient more significantly. Through the analysis of the instability process of rock bedding slope, it can be found that the failure mechanism of the slope can be divided into two stages: the formation of sliding shear plane and the overall instability of the slope.

Keywords: shaking table test, bedding rock slopes, dynamic response, peak acceleration amplification coefficient, failure mechanism

OPEN ACCESS

Edited by:
Alex Hansen,
Norwegian University of Science and Technology, Norway

Reviewed by:
Haroldo V. Ribeiro,
State University of Maringá, Brazil
Feifei Wang,
Chongqing Jiaotong University, China

****Correspondence:***
Liang Zhang
zhangliangdpme@my.swjtu.edu.cn

Specialty section:
This article was submitted to Interdisciplinary Physics, a section of the journal Frontiers in Physics

Received: *28 April 2020*
Accepted: *02 October 2020*
Published: *01 December 2020*

Citation:
Yang C, Zhang L, Liu Y, Tian D, Guo X and Liu Y (2020) Shaking Table Test on Dynamic Response of Bedding Rock Slopes With Weak Structural Plane Under Earthquake. Front. Phys. 8:556714. doi: 10.3389/fphy.2020.556714

1 INTRODUCTION

Due to the influence of collision and compression between the Indian Ocean plate and the Eurasian plate, the neotectonic movement in the mountainous area of Southwest China is extremely strong. There are a lot of active fault zones in this area, which means high-intensity earthquakes occur frequently [1, 2]. When high-intensity earthquakes occur, strong ground vibrations may induce large-scale landslides [3, 4]. For example [5–7], the Wenchuan Ms 8.0 earthquake triggered about 60,000 landslides, which caused the injuries and deaths of more than 20,000 people. Five years later, the magnitude 7.0 earthquake in Lushan also triggered more than 3,800 landslides. Debris flow from the slope collapse destroyed a lot of infrastructure and tens of thousands of people lost their homes. It can be seen that earthquakes are a significant threat to the stability of a slope.

A bedding rock slope with a weak structural plane is one of the most common slope types in Southwest China [8]. Compared with stacked slopes, this type of slope is more prone to instability and failure under seismic force. Due to the existence of weak structural planes, the instability mechanism of bedding rock slopes is extremely complex. During strong earthquakes, the increase of dynamic load and horizontal seismic force reduces the normal pressure on the weak structural plane of the slope. The overall sliding force of the slope also increases due to the earthquake inertia force [9, 10]. These reasons reduce the safety factor of the slope and make the slope unstable.

A considerable amount of research has been conducted on the seismic stability of bedding rock slopes using shaking table model tests and numerical simulation [11–14]. For example, Huang R Q [15] established a conceptual model of the failure mechanism of the layered rock mass slope through actual geological observation work on site, and studied the seismic dynamic response characteristics and failure processes of different structural types of slopes through large-scale shaking table experiments; Liu X R et al. [16, 17] used the shaking table test and numerical simulations to study the stability of bedding rock slopes under the action of the high frequency micro earthquake induced by the Three Gorges reservoir, and considered the influence of different dynamic load amplitudes, dynamic load frequencies, and slope heights on slope cumulative failure; Fan G. [18–20] carried out the shaking table test to obtain the dynamic failure mode of bedding rock slope, and used the energy identification method to characterize the development process of earthquake damage inside slope; Chen X L et al. [21, 22] proposed a method for calculating the dynamic fuzzy reliability of bedding rock slopes under random earthquake excitation based on the Newmark-beta method, and analyzed the influence of ground motion parameters and uncertainty on the reliability of bedding rock slopes. These research results have a certain guiding significance for understanding the seismic response characteristics of bedding rock slopes.

However, the existing research results are based on simple layered bedding and do not consider the influence of weak structural planes between layers on the seismic response of bedding rock slopes. Moreover, due to the randomness of seismic force and the different mechanical parameters of slopes, the slope often has different dynamic response and failure mechanisms [23], and it is necessary to study it more deeply and systematically. The large-scale shaking table physical simulation test is one of the most effective methods to reveal the seismic response and failure process of slopes. Therefore, this method is used to study the dynamic response of bedding rock slopes with weak structural planes under a strong seismic force.

In this paper, a bedding rock slope which may collapse in the southwest mountain area is selected, and the 1:10 scale shaking table physical simulation test of this slope is designed and carried out. By analyzing the acceleration and displacement responses at different measuring points of bedding rock slope in the shaking table test, the seismic dynamic response characteristics and failure processes of this slope are obtained. On this basis, the influence of seismic wave frequency, amplitude, and duration on slope dynamic response is analyzed by loading different types of seismic waves. The research results can provide a reference for the prevention and treatment of bedding rock slopes.

2 OVERVIEW OF THE SHAKING TABLE TEST

The Parameters of the Shaking Table

Based on the bedding rock slope at the exit of a tunnel in the mountainous area of Southwest China, the shaking table test is designed and carried out. The test site is the earthquake simulation shaking table laboratory at the School of Architecture and Civil Engineering, Xinyang Normal University. The shaking table is a large-scale one-way seismic simulation shaking table with a table size of 3 m × 3 m. The table structure is a steel-welded single-layer grid. The maximum load capacity of the table is 10 t and the maximum speed is 0.7 m/s. The frequency of this shaking table is 0.1–50 Hz, the displacement range is ±125 mm, and the maximum acceleration is 15 m/s^2, which can meet the requirements of this shaking table test.

Design of Similar Systems and Similar Materials

In the shaking table simulation test, keeping the model similar to the prototype is a prerequisite to ensure the accuracy of the test results. According to the similarity theory [24], the density (ρ), elastic modulus (E), and geometric dimension (L) are taken as control parameters to design a similar system to the model test. Considering the size of the prototype slope and the condition of test equipment, the similarity constants of geometric dimensions are set to 10. The other similarity constants are shown in **Table 1**. The geological survey report shows that the lithology of the prototype slope is mainly quartz sandstone splint. Referring to the types of raw materials commonly used in model test and their mechanical properties [25, 26], gypsum, clay, river sand, and water are used as raw materials of similar materials in this test. Through repeated material ratio test, it is determined that the ratio of the simulated rock material is gypsum: clay: river sand: water = 1: 5.38: 1.52: 0.27, and the ratio of the weak structure plane simulated material is clay: river Sand: water = 1: 6.89: 0.25. Through a density test, direct shear test, and triaxial compression test, the density of the rock material is 1.908 g/cm^3, the cohesion is 15.5 kPa, the internal friction angle is 37.9°, and the density of the structural surface material is 1.72 g/cm^3. The cohesion force is 2.7 kPa and the internal friction angle is 41.7°.

The Process of Making the Slope Model

The model box used in this model test is a rigid model box welded by angle steel, channel steel, and steel plate, and its size is 2.0 m × 2.0 m × 1.5 m (length × width × height), as shown in **Figure 1**. In order to observe and record the deformation and failure of the slope model during the test, 12 mm thick plexiglass is used for visualization on both sides of the model box. Vaseline was evenly applied on the inside of the plexiglass to reduce the friction between the model and the plexiglass. A polyethylene foam with a thickness of 10 cm is placed between the steel plate and the model as a shock-absorbing layer to reduce the influence of the model box boundary effect [27].

According to previous geological exploration, the prototype slope is a rock slope with many weak structural planes. These weak structural planes are approximately equally spaced. In order to facilitate the establishment of the test model, the prototype

TABLE 1 | Similar constants of shaking table test.

No	Physical quantity	Similarity	Similar constants	Remarks
1	Geometric dimensions L	C_l	10	Control parameter
2	Soil weight γ	C_γ	1	Control parameter
3	Duration T_d	$C_{Td} = C_l^{0.5}$	3.16	—
4	Cohesion c	$C_c = C_l$	10	—
5	Internal friction angle φ	$C_\varphi = 1$	1	—
6	Elastic modulus E	$C_E = C_l$	10	—
7	Poisson's ratio μ	$C_\mu = 1$	1	—
8	Shear wave velocity v_s	$Cv_s = C_l^{0.5}$	3.16	—
9	Acceleration of gravity g	$C_g = 1$	1	Control parameter
10	Input acceleration A	$C_A = 1$	1	—
11	Input vibration frequency ω	$C_\omega = C_l^{-0.5}$	0.316	—
12	Response linear displacement s	$C_S = C_l$	10	—
13	Response angular displacement θ	$C_\theta = 1$	1	—
14	Response strain ε	$C_\varepsilon = 1$	1	—
15	Response speed V	$C_V = C_l^{0.5}$	3.162	—
16	Response stress σ	$C_\sigma = C_l$	10	—
17	Response acceleration a	$C_a = 1$	1	—

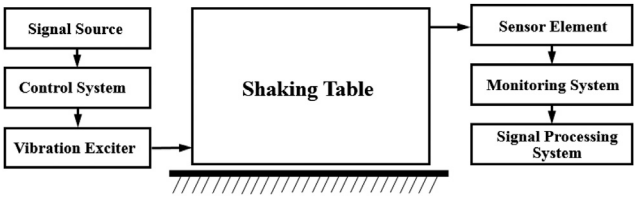

FIGURE 1 | Principle of shaking table test.

FIGURE 2 | The model box used in the test.

slope is simplified as a slope with parallel rock layers, the inclination angle of rock stratum is 35°, and the angle of slope foot is 60°. The thickness of the rock layer is 6 cm and the thickness of the weak structural planes is 1 cm for layered filling and compaction. In this process, the three-way acceleration sensor is arranged inside the slope body and on

FIGURE 3 | The slope model in the test.

the slope body surface, and the acceleration sensors is also arranged on the vibrating table as a reference point for calculating the peak ground acceleration (PGA) amplification coefficient. In addition, pull-wire displacement sensors are used to measure the displacement at different heights of the slope. The test model is shown in **Figure 3**, and the measuring point layout is shown in **Figure 4**.

The Loading Conditions of the Test

In order to study the dynamic response of bedding rock slopes under seismic waves of different frequencies, amplitudes, and durations, this test applied three seismic waves in the horizontal direction: Wenchuan Wolong seismic wave, Kobe seismic wave, and EL Centro seismic wave. The acceleration peak values of the three seismic waves are normalized, and the duration is adjusted according to the similarity relationship. The adjusted acceleration

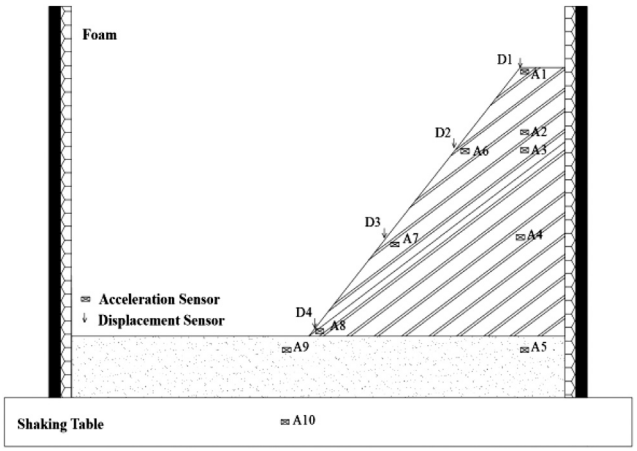

FIGURE 4 | Acceleration and displacement point arrangement in the test.

time history curves of the three seismic waves are shown in **Figure 5**. The shaking table test started with an amplitude of 0.1 g, and the amplitude of each seismic wave (0.1–1.2 g) was gradually increased in the order of the Wenchuan Wolong seismic wave, Kobe seismic wave, and EL Centro seismic wave until the model failed. Before each peak seismic wave loading, the model was swept by white noise with an amplitude of 0.05 g. The specific loading conditions are shown in **Table 2**.

3 ACCELERATION RESPONSE OF BEDDING ROCK SLOPE

Acceleration Response of Slope Under Different Seismic Wave Amplitudes

Under the action of seismic force, the slope surface and slope body of the bedding rock slope generally show different acceleration responses [28, 29]. In this test, the Y-direction acceleration of A1, A2, A3, A4, and A5 measuring points is taken as the acceleration response of slope surface, and the Y-direction acceleration of A1, A6, a7, a8, and A9 is taken as the acceleration response of the slope surface. The PGA amplification coefficient is defined as the ratio of the peak acceleration of each measuring point to the peak acceleration of A10 measuring point; A10 is the peak acceleration of the shaking table. Taking the Wenchuan seismic wave as an example, the variation law of the PGA amplification coefficient of the slope surface and slope body with elevation under different seismic amplitude values is analyzed.

Figures 6 and **7** show the variation law of the PGA amplification coefficient of the slope and slope body with elevation. Before the slope failure (input seismic wave amplitude is 0.1–0.8 g), the slope has an obvious elevation amplification effect on the input seismic wave. In particular, the PGA amplification coefficient at the top of the slope increases significantly, which is about 2–3 times that at the slope shoulder

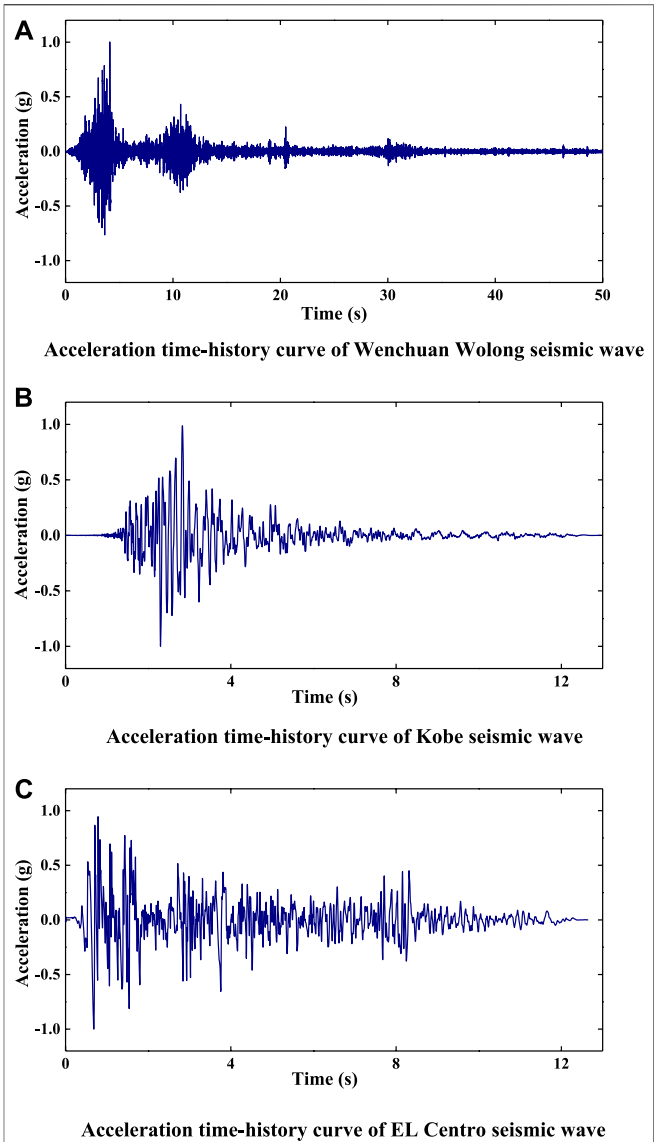

FIGURE 5 | The horizontal seismic waves used in the test. **(A)** Acceleration time-history curve of Wenchuan Wolong seismic wave. **(B)** Acceleration time-history curve of Kobe seismic wave. **(C)** Acceleration time-history curve of EL Centro seismic wave.

(2/3 height of the slope). With the increase of seismic wave amplitude, the PGA amplification coefficient of the slope body and slope surface decreases gradually, and the elevation amplification effect weakens. The reason for this phenomenon is that the dynamic shear strength and dynamic shear modulus of slope materials decrease gradually with the increase of input seismic amplitude, and the damping ratio of slope increases, the nonlinear characteristics gradually strengthen. The slope has better isolation and damping effects, and more energy is consumed in the process of seismic wave propagation from bottom to top, which leads to the weakening of the elevation effect of the PGA amplification coefficient.

TABLE 2 | Loading conditions of shaking table test.

Serial number	The type of seismic wave and its amplitude		Serial number	The type of seismic wave and its amplitude	
1	0.05 g	White noise	25	0.7 g	White noise
2	0.1 g	Wenchuan wave	26	0.7 g	Wenchuan wave
3		Kobe wave	27		Kobe wave
4		EL Centro wave	28		EL Centro wave
5	0.05 g	White noise	29	0.05 g	White noise
6	0.2 g	Wenchuan wave	30	0.8 g	Wenchuan wave
7		Kobe wave	31		Kobe wave
8		EL Centro wave	32		EL Centro wave
9	0.05 g	White noise	33	0.05 g	White noise
10	0.3 g	Wenchuan wave	34	0.9 g	Wenchuan wave
11		Kobe wave	35		Kobe wave
12		EL Centro wave	36		EL Centro wave
13	0.05 g	White noise	37	0.05 g	White noise
14	0.4 g	Wenchuan wave	38	1.0 g	Wenchuan wave
15		Kobe wave	39		Kobe wave
16		EL Centro wave	40		EL Centro wave
17	0.05 g	White noise	41	0.05 g	White noise
18	0.5 g	Wenchuan wave	42	1.2 g	Wenchuan wave
19		Kobe wave	43		Kobe w ave
20		EL Centro wave	44		EL Centro wave
21	0.05 g	White noise	—	—	—
22	0.6 g	Wenchuan wave	—	—	—
23		Kobe wave	—	—	—
24		EL Centro wave	—	—	—

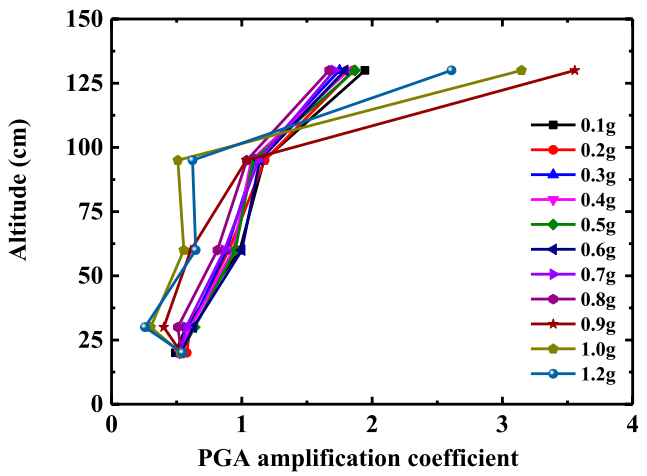

FIGURE 6 | PGA amplification coefficient of slope surface under different seismic wave amplitudes.

When the seismic wave amplitude reaches 0.9 g, the slope begins to show damage. Taking the slope shoulder as the boundary point, the GPA amplification coefficient of the measuring points below the slope shoulder decreases

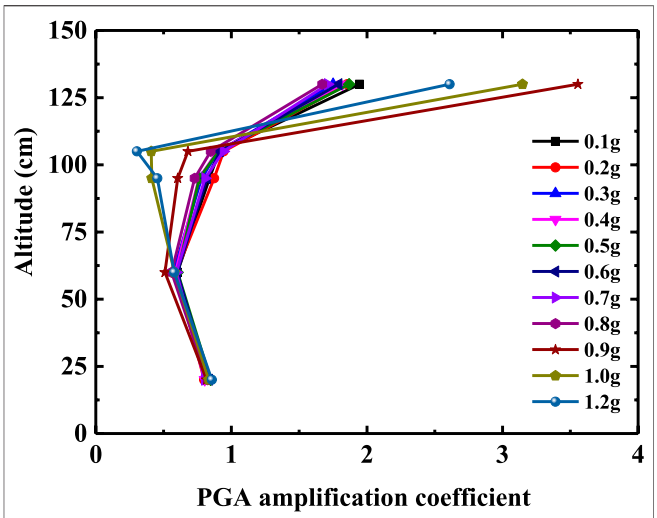

FIGURE 7 | PGA amplification coefficient of slope body under different seismic wave amplitudes.

significantly. The GPA amplification coefficient of the measuring point above the slope shoulder suddenly increases, and the GPA amplification coefficient of the slope top measuring point is about 6 times that of the slope shoulder measuring point. Continuing to increase the input seismic wave amplitude, the PGA amplification coefficient of the slope top measuring point begins to decrease, but the difference between it and the slope shoulder does not change. The main reason for the above phenomenon may be that the internal structure of the slope is damaged, and there are a large number of micro-cracks in the rock mass, which divide the slope into loose blocks and enhance the filtering effect of the slope material. At the same time, the internal friction and frictional energy consumption between the slope layers increase [30], which further leads to a significant decrease in the GPA amplification coefficient of each measuring point below the slope shoulder. The slope body above the slope shoulder produces relative slip through the structural plane, and gradually separates from the main slope body. The inconsistency of slope movement on both sides of the structural plane increases, so the difference of GPA amplification coefficient increases.

Acceleration Response of Slope Under Different Seismic Waves

In order to clearly explain the variation law of slope acceleration response with elevation under different types of seismic waves, the acceleration responses of rock bedding slopes under the action of 0.1 g Wolong seismic wave, El Centro earthquake wave, and Kobe seismic wave are selected for comparative analysis, as shown in **Figures 8** and **9**.

It can be seen from **Figures 8** and **9** that the Y-direction PGA amplification coefficient of the slope body and slope surface shows an obvious elevation amplification effect, which is independent of the seismic wave type. Comparing the PGA amplification coefficient of the slope surface and slope body under different seismic waves, El Centro seismic wave has the

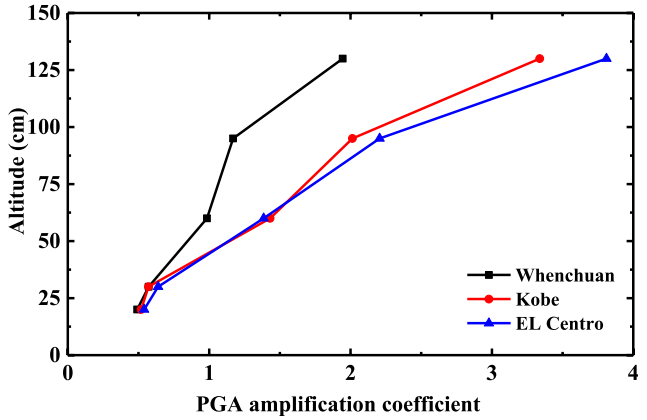

FIGURE 8 | PGA amplification coefficient of slope surface under different seismic wave.

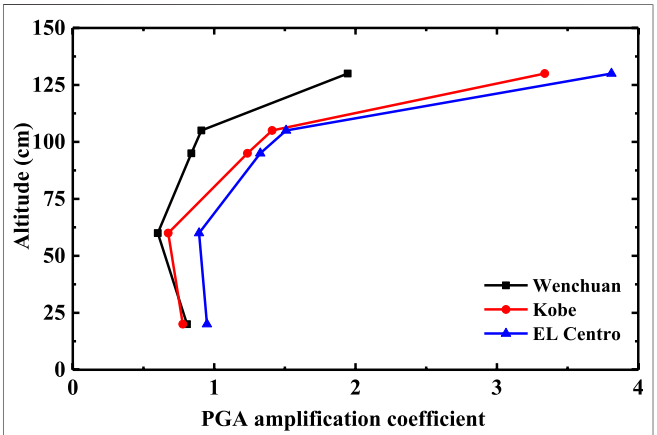

FIGURE 9 | PGA amplification coefficient of slope body under different seismic wave.

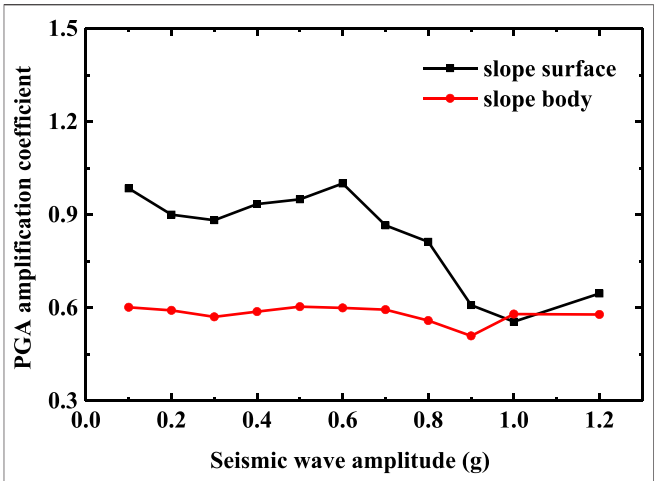

FIGURE 10 | Difference of PGA amplification coefficient between slope surface and slope body (the slope waist).

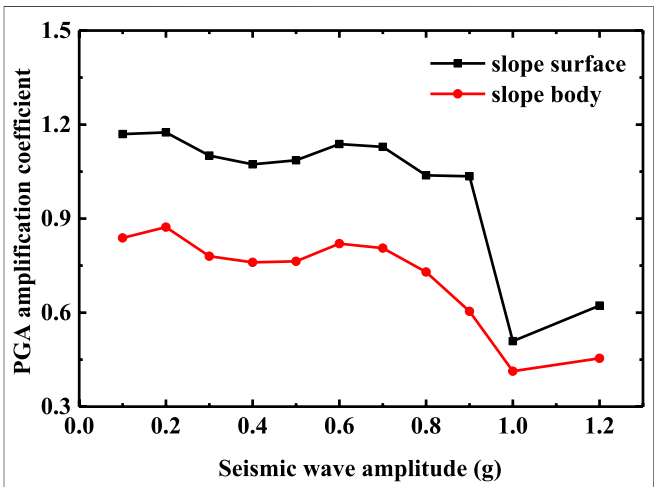

FIGURE 11 | Difference of PGA amplification coefficient between slope surface and slope body (the slope shoulder).

greatest impact on the slope, Kobe seismic wave takes the second place, and Wolong Wenchuan seismic wave is the smallest. According to the frequency spectrum analysis of acceleration time history curve, compared with Kobe seismic wave and Wenchuan Wolong seismic wave, the predominant frequency of El Centro seismic wave is closer to the first-order natural frequency of the slope model, so it is easier to produce resonance phenomenon. The acceleration time history curve of the measurement point is analyzed by FFT spectrum. Therefore, the influence of different seismic waves on the acceleration response of bedding rock slope is mainly reflected in the difference between the predominant frequency of seismic waves and the natural frequency of the slope.

Difference of Acceleration Response Between Slope Surface and Slope Body

The Y-direction PGA amplification coefficient of measuring points at the slope waist (A2 and A7) and slope shoulder (A3 and A8) under the action of Wenchuan seismic wave are selected. The difference of acceleration response between slope surface and slope body is analyzed, as shown in **Figures 10** and **11**.

It can be seen from **Figures 10** and **11**, whether at the slope waist or the slope shoulder, the PGA amplification coefficient of the slope body is always smaller than that of the slope surface. This phenomenon indicates that the seismic wave is refracted and projected on the free surface of the slope surface, which makes the acceleration response of the slope more intense, and the acceleration response of the bedding rock slope has an obvious "surface effect" [32] in the horizontal direction. With the increase of seismic amplitude, the slope begins to show damage, the cracks in the slope are gradually connected, which leads to the further strengthening of the filtering effect of the slope, and the "surface effect" is gradually reduced. Especially when the seismic amplitude reaches 1.0 g, the tensile cracks at the slope

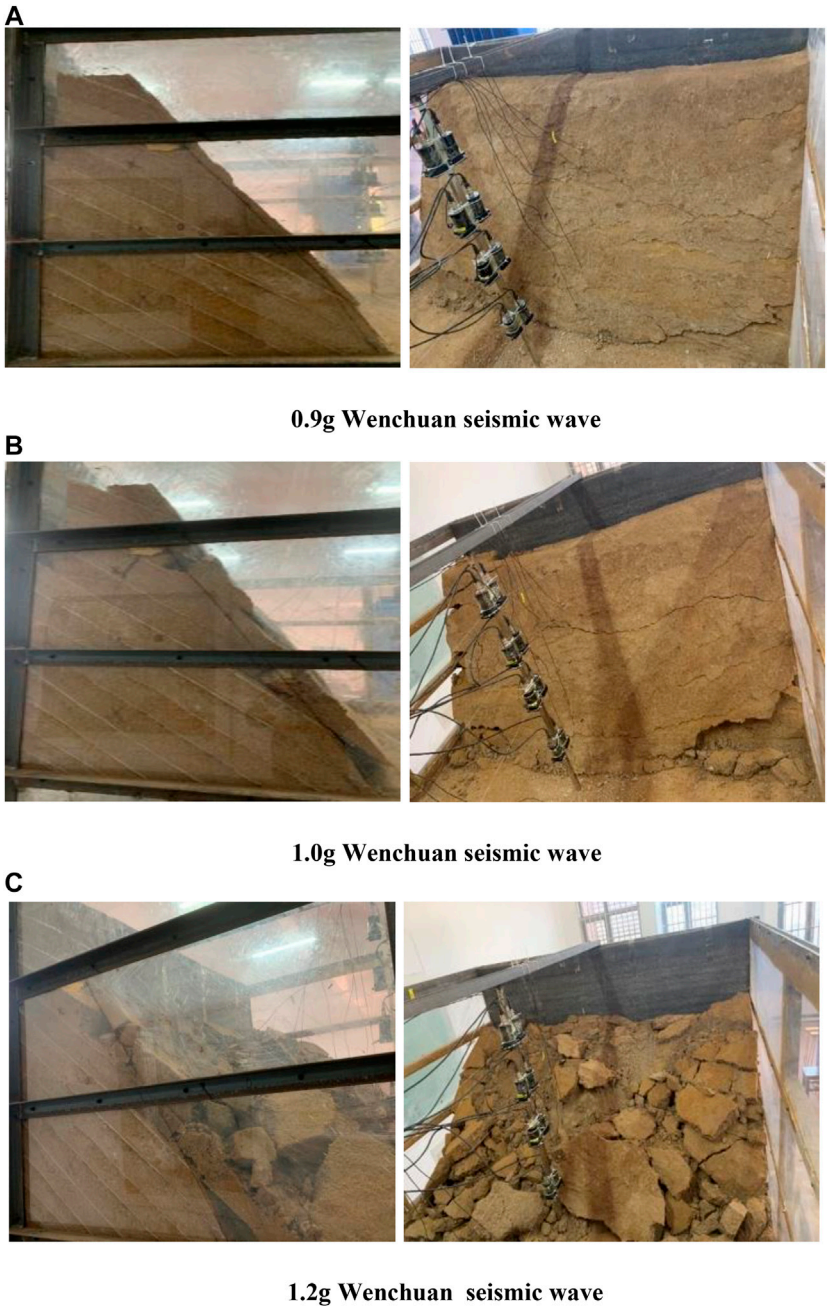

FIGURE 12 | The instability process of bedding rock slope. **(A)** 0.9 g Wenchuan seismic wave. **(B)** 1.0 g Wenchuan seismic wave. **(C)** 1.2 g Wenchuan seismic wave.

shoulder and slope waist expand and open, which further affect the horizontal acceleration response of the bedding rock slope.

4 FAILURE MECHANISM OF BEDDING ROCK SLOPE

In this test, the high-speed camera system was used to record the instability process of the slope model. The bedding rock slope began to damage in the process of the Wenchuan earthquake wave with 0.9 g amplitude, and collapsed in the process of the Wenchuan earthquake wave with 1.2 g amplitude. The whole instability process of the slope is shown in **Figure 12**.

Based on the comprehensive analysis of **Figure 12**, the whole instability process of bedding rock slopes can be obtained. Under the action of 0.8 g and less than 0.8 g seismic wave, the bedding rock slope does not take damage. When the input seismic wave amplitude reaches 0.9 g, the middle and upper parts of the slope

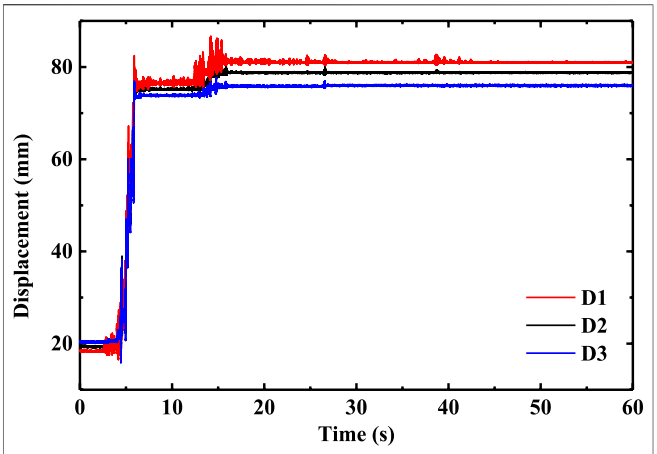

FIGURE 13 | displacement time history curves of slope surface measuring points D1, D2 and D3 under the action of 0.9 g Wenchuan seismic wave.

gradually slide down along the weak structural plane, and the trailing edge of the slope begins to separate from the model box. The middle and upper part of the slope are blocked by the "locked section" of the slope body, which fails to slide out along the weak structural plane, and two tensile cracks perpendicular to the rock layer are generated at the shoulder and waist of the slope surface, as shown in **Figure 12A**. When the amplitude of the seismic wave is increased to 0.9 g, the sliding behavior of the slope is more intense, and the two tensile fissures expand and open to the weak structural plane. At the same time, there are many through cracks on the slope surface, and some rock blocks at the foot of the slope are spalling, as shown in **Figure12B**. When the input seismic amplitude reaches 1.2 g, the tensile fracture and the sliding structural plane connect and form a shear slip surface, which leads to the separation of the upper rock layer and lower rock layer, and the upper rock layer collapses in the form of blocks. The slope loses its stability and damages, as shown in **Figure 12C**.

Taking the displacement time history curves of slope surface measuring points D1, D2, and D3 under the action of 0.9 g Wenchuan seismic wave as an example, the failure mechanism of the slope is further analyzed. It can be seen from **Figure 13** that the displacement of the slope surface gradually increases with the increase of elevation. This phenomenon shows that, due to the existence of a weak structural plane, the movement of different parts of the slope is not consistent, which leads to the shear slip of the top of the slope relative to the main body. In addition, the time of displacement mutation is about 5 and 14 s respectively, which corresponds to the time node when the input seismic wave reaches the double peak value.

Considering the acceleration response and displacement response of the slope, the instability mechanism of bedding rock slopes can be divided into two stages. Due to the existence of a weak structural plane, the first stage involves the inconsistent movement of different parts of the slope. Under the action of gravity and seismic force, the top of the slope slides down along the structural plane, the back edge of the slope is separated from the model box, and the tension cracks gradually expand to the structural plane in the locked section of the slope. With the continuous ground motion, the second stage sees inconsistent movement between the rock layers further increases, and the tensile fracture connects with the structural plane and forms a shear slip surface. The top slope slides out along the shear slip surface, and the slope loses its stability and damages.

5 CONCLUSION

In this paper, a similarity ratio of 1:10 shaking table test is designed and carried out to systematically study the seismic dynamic response and instability mechanism of rock bedding slopes under different seismic amplitudes, frequencies, and durations. The conclusion is as follows:

Firstly, the slope has an obvious elevation effect and surface effect on the input seismic wave before the slope failure. The PGA amplification coefficient at the top of slope specifically increases significantly. With the increase of seismic wave amplitude, the nonlinear and damping characteristics of slope materials change gradually. The PGA amplification coefficient of slope body and slope surface increases, while the elevation effect and surface effect decrease.

Secondly, when the seismic wave amplitude reaches 0.9 g, tension cracks occur in the slope structure and damage occurs. The GPA amplification coefficient of the slope measuring points below the sliding surface decreases significantly while that of the slope measuring points above the sliding surface increases significantly. Continuing to increase the input seismic wave amplitude, the upper area slips along the sliding surface, and gradually separates from the main body of the slope, resulting in slope destabilization and destruction.

Thirdly, the influence of different seismic waves on the acceleration response of bedding rock slopes is mainly reflected in the difference between the excellent frequency of seismic waves and the natural frequency of the slope. Compared with Kobe seismic wave and Wenchuan Wolong seismic wave, the excellent frequency of EL Centro seismic wave is closer to the first-order natural frequency of the slope model and produces resonance phenomenon, which leads to the elevation effect of the PGA amplification coefficient more significantly.

Fourthly, the instability mechanism of bedding rock slopes is mainly divided into two stages: penetration of sliding shear plane and integral instability of slope. Under the action of gravity and seismic force, rock at the top of the slope begins to slide along the structural plane, the rear edge of the slope is separated from the model box, and tension cracks gradually extend to the structural plane at the slope locking section. With the continuous seismic motion, the inconsistent movement between rock layers increases further, tension cracks run through the structural plane, the top slope slides along the shear sliding surface, and the slope loses its stability and damages.

6 DISCUSSION

This paper selected a typical bedding rock slope in the southwest mountainous area to study its seismic response and failure mechanism. The results are basically consistent with the

instability process of other similar slopes. In addition, some of the research results in this article have been applied to practical projects, such as the reinforcement of vulnerable parts of a slope. However, the seismic response of bedding rock slope is a very complex nonlinear dynamic process, which needs further improvement.

DATA AVAILABILITY STATEMENT

The raw data supporting the conclusions of this article will be made available by the authors, without undue reservation.

ETHICS STATEMENT

Written informed consent was obtained from the individual(s) AND/OR minor(s)' legal guardian/next of kin for the publication of any potentially identifiable images or data included in this article.

AUTHOR CONTRIBUTIONS

CY is the project administrator, was responsible for field tests, and proposed the research ideas. LZ is the site representative of field tests and helped CY to finish the modification of the revised article. YL (3rd author) finished the data process work. DT finished the data process work. XG finished the first version of the article. LY (6th author) helped Zhang Liang to finish the field tests.

FUNDING

This study is supported in part by Natural Science Foundation of China (Contract NO. 51408510), Sichuan Provincial Science and Technology support project (NO.2016GZ0338), The Fundamental Research Funds for the Central Universities (NO. 2682016CX023), 2016–2018 Young Elite Scientist Sponsorship Program by CAST/CSRME (YESS), Nanchang Railway Bureau scientific research project (NO. 20171106), and the Education department of Sichuan Province scientific research project (NO. 16ZB0012). The authors declare that this study received funding from China National Railway Group Co. Ltd., China Academy of RAILWAY Sciences Corporation Limited and China Railway Eryuan Engineering Group Co. Ltd. The funder was not involved in the study design, collection, analysis, interpretation of data, the writing of this article, or the decision to submit it for publication.

REFERENCES

1. Royden LH, King RW, Chen Z, Liu Y. Surface deformation and lower crustal flow in eastern Tibet. *Science* (1997) 276(5313):788–90. doi:10.1126/science.276.5313.788
2. Judith H, John HS. Uplift of the Longmen Shan and Tibetan plateau, and the 2008 Wenchuan (m = 7.9) earthquake. *Nature* (2009) 458(7235):194–7. 10.1038/nature07837
3. Jongmans D, Stéphane Garambois S. Geophysical investigation of landslides: a review. *Bull Soc Geol Fr* (2007) 178(2):101–12. doi:10.2113/gssgfbull.178.2.101
4. Guo CB, David RM, Zhang YS, Wang K, Yang ZH. Quantitative assessment of landslide susceptibility along the Xianshuihe fault zone, Tibetan Plateau, China. *Geomorphology* (2015) 248:93–110. doi:10.1016/j.geomorph.2015.07.012
5. Huang R, Fan X. The landslide story. *Nat Geosci* (2013) 6(5):325–6. doi:10.1038/ngeo1806
6. Zhou Z, Ma G, Chang M, Li WL, Zhang DD, Jia T. Landslides triggered by the 20 April 2013 Lushan earthquake, Sichuan province, China. *Eng Geol* (2015) 187:45–55. doi:10.1016/j.enggeo.2014.12.004
7. Wang WP, Yin YP, Yang LW, Zhang N, Wei YJ. Investigation and dynamic analysis of the catastrophic rockslide avalanche at Xinmo, Maoxian, after the Wenchuan Ms 8.0 earthquake. *Bull Eng Geol Environ* (2020) 79(1):495–512. doi:10.1007/s10064-019-01557-4
8. Zhang S, Guang-Ze Z, Liang-Wen J, Guang WU. Analysis of the characteristics of major geological disasters and geological alignment of sichuan-tibet railway. *Railway Std Design* (2016) 1:14–9. doi:10.13238/j.issn.1004-2954.2016.01.003
9. Xiao KQ, Li HB, Liu YQ, Xia X, Zhang LQ. Study on deformation characteristics of bedding slopes under earthquake. *Rock Soil Mech* (2007) 28(8):1557–64. doi:10.1016/S1874-8651(08)60066-6
10. Gong W, Li Y, Zhao X, Chen X. Dynamic reliability analysis of bedding slope under non-stationary earthquake. *J Huazhong Univ Sci Technol (Nat Sci Edn)* (2018) 46(10):1–6. doi:10.13245/j.hust.181001
11. Xiangning J, Qiangbing H, Tao W, Ning Z, Zikan J. Shaking table test of dynamic responses of loess-mudstone slopes with a steep dip bedding fault zone. *Chin J Rock Mech Eng* (2018) 37(12):85–96. doi:10.13722/j.cnki.jrme.2018.0719-en
12. Yu-Chuan Y, Hui-Ge X, Xing-Guo Y, Ming-Liang C, Jia-Wen Z. Experimental study on the dynamic response and stability of bedding rock slopes with weak interlayers under heavy rainfall. *Environ Earth Sci* (2018) 77(12):433. 10.1007/s12665-018-7624-y
13. Che A, Yang H, Wang B, Ge X. Wave propagations through jointed rock masses and their effects on the stability of slopes. *Eng Geol* (2016) 201:45–56. doi:10.1016/j.enggeo.2015.12.018
14. Dong L, Sun D, Li X, Zhou Z. Interval non-probabilistic reliability of a surrounding jointed rockmass in underground engineering: a case study. *IEEE Access* (2017) 5:18804–17. doi:10.1109/access.2017.2745705
15. Huang R, Li G, Ju N. Shaking table test on strong earthquake response of stratified rock slopes. *Chinese J Rock Mech Eng* (2013) 32(5):865–75. doi:10.3969/j.issn.1000-6915.2013.05.003
16. Liu XR, Xu B, Liu YQ, Wang JW, Lin GY. Cumulative damage and stability analysis of bedding rock slope under frequent microseisms. *Chin J Geotech Eng* (2020) 42(4):631–41. doi:10.1007/s12517-020-05299-6
17. Liu SL, Yang ZP, Liu XR, Liu YQ, Hu YN, Wu ZS. Shaking table model test and numerical analysis of the bedding rock slopes under frequent micro-seismic actions. *J Rock Mech Eng* (2018) 037(010):2264–76. doi:10.1007/s10706-018-0679-4
18. Fan G, Zhang J, Wu J, Yan K. Dynamic response and dynamic failure mode of a weak intercalated rock slope using a shaking table. *Rock Mech Rock Eng* (2016) 49(8):3243–56. doi:10.1007/s00603-016-0971-7
19. Fan G, Zhang LM, Zhang JJ, Yang CW. Time-frequency analysis of instantaneous seismic safety of bedding rock slopes. *Soil Dynam Earthq Eng* (2017) 94:92–101. doi:10.1016/j.soildyn.2017.01.008
20. Fan G, Zhang JJ, Fu X, Zhou LR. Dynamic failure mode and energy-based identification method for a counter-bedding rock slope with weak intercalated layers. *J Mt Sci* (2016) 13(12):2111–23. doi:10.1007/s11629-015-3662-z
21. Chen XL, Gao RX, Gong W. Random seismic response and dynamic fuzzy reliability analysis of bedding rock slopes based on pseudoexcitation method. *Int J Geomech* (2018) 8(3):04017165. doi:10.1061/(ASCE)GM.1943-5622.0001084
22. Chen X, Gong W, Zhong X, Qiu J, Li Y. Dynamic reliability analysis of bedding rock slopes under horizontal and vertical earthquake actions. *China Civ Eng J* (2017) 50(10):91–8. doi:CNKI:SUN:TMGC.0.2017-10-012

23. Gu DZ. *Similar materials and similar models*. Beijing, China: China Mining Press (1995).
24. Zuo-Bao C, Chen-Cong X, Liu-Cai H, Shen Q, Xiao-Guo F, Liu Xiao W. Research on similar material of slope simulation experiment. *Rock Soil Mech* (2014) 5(11):125–8. doi:10.1007/BF02911033
25. Liu-Han X. *Research on seismic dynamic response of rock slope based on shaking table test*. Chengdu, China: Chengdu University of Technology (2014).
26. Dong JY, Yang GX, Wu FQ. The large-scale shaking table test study of dynamic response and failure mode of bedding rock slope under earthquake. *Rock Soil Mech* (2011) 10:2977–82. doi:10.1177/0883073810379913
27. Yang-Chang W. *Research on the ground motion characteristics of rock slope and the landslide genesis mechanism, stability identification and damage scope evaluation system of base-covered slope*. Chengdu, China: Southwest Jiaotong University (2013).
28. Dong L, Wesseloo J, Potvin Y, Li X. Discriminant models of blasts and seismic events in mine seismology. *Int J Rock Mech Min Sci* (2016) 86:282–91. doi:10.1016/j.ijrmms.2016.04.021
29. Fan G, Zhang JJ, Fu X. Dynamic response differences between bedding and count-tilt rock slopes with siltized intercalation. *Chinese J Geotech Eng* (2015) 37(4):692–9. doi:10.11779/CJGE201504015
30. Changwei Y, Ning F, Jianjing Z, Junwei B, Jun Z. Research on time-frequency analysis method of seismic stability of covering-layer type slope subjected to complex wave. *Environmental earth ences* (2015) 74(6):5295–306. doi:10.1007/s12665-015-4540-2
31. Dong L, Zou W, Li X, Shu W, Wang Z. Collaborative localization method using analytical and iterative solutions for microseismic/acoustic emission sources in the rockmass structure for underground mining. *Eng Fract Mech* (2018) 210:95–112. doi:10.1016/j.engfracmech.2018.01.032
32. Dong L, Wesseloo J, Potvin Y, Li X. Discrimination of mine seismic events and blasts using the Fisher classifier, naive bayesian classifier and logistic regression. *Rock Mech Rock Eng* (2016) 49(1):183–211. doi:10.1007/s00603-015-0733-y
33. Wang KL, Lin ML. Initiation and displacement of landslide induced by earthquake — a study of shaking table model slope test. *Eng Geol* (2011) 122(1–2):106–14. doi:10.1016/j.enggeo.2011.04.008

Conflict of Interest: The authors declare that the research was conducted in the absence of any commercial or financial relationships that could be construed as a potential conflict of interest.

frontiers in Physics

ORIGINAL RESEARCH
published: 04 December 2020
doi: 10.3389/fphy.2020.590710

Limestone Acoustic Emission Evolution Characteristics Under Different Experimental Loading and Unloading Conditions

Jielin Li[1,2]*, *Liu Hong*[1], *Keping Zhou*[1], *Caichu Xia*[2,3]* and *Longyin Zhu*[1]

[1]School of Resources and Safety Engineering, Central South University, Changsha, China, [2]Key Laboratory of Rock Mechanics and Geohazards of Zhejiang Province, Shaoxing, China, [3]College of Civil Engineering, Tongji University, Shanghai, China

To study the acoustic emission evolution characteristics of saturated limestone under different loading and unloading paths, three cyclic loading and unloading tests were conducted with different loading rates and initial cyclic peak stresses, and acoustic emission monitoring was performed simultaneously. The results indicate that, during loading and unloading, the intermediate-frequency signals of saturated rock exhibit a variation trend of sparse–dense–sparse signals, whereas the low-frequency signals are continuously and massively produced. With the increase in the loading rate, the development trends of cumulative hits and energy become closer, and the development form of ringing count changes from N-type to U-type and then to N-type. The slight increase period and attenuation period are extended, whereas the intense growth period and postpeak calm period are shortened. With an increase in the initial cyclic peak stress, the change in cumulative energy is more obvious than that in cumulative hits near the rock failure. The development form of the ringing count changes from U-type to W-type and then to N-type, and each period is first shortened and then extended. With the increase in loading rate, the increase in the slow-change period tends to change from gradually increasing to increasing and then decreasing. By contrast, the increase in the step tends to change to a gradual increase. With the increase in the initial cyclic peak stress, the duration of and increase in the energy in the step and the slow-change period tend to decrease and then increase.

Keywords: cyclic loading and unloading, loading rate, initial stress, acoustic emission characteristics, step characteristics, localization, frequency and amplitude

OPEN ACCESS

Edited by:
Wei Wu,
Nanyang Technological University, Singapore

Reviewed by:
Jiangfeng Liu,
China University of Mining and Technology, China
Srutarshi Pradhan,
Norwegian University of Science and Technology, Norway

***Correspondence:**
Caichu Xia
xiacaichu@tongji.edu.cn
Jielin Li
lijielin@163.com

Specialty section:
This article was submitted to Interdisciplinary Physics, a section of the journal Frontiers in Physics

Received: *02 August 2020*
Accepted: *04 November 2020*
Published: *04 December 2020*

Citation:
Li J, Hong L, Zhou K, Xia C and Zhu L (2020) Limestone Acoustic Emission Evolution Characteristics Under Different Experimental Loading and Unloading Conditions. Front. Phys. 8:590710. doi: 10.3389/fphy.2020.590710

INTRODUCTION

With the gradual depletion and exploitation of shallow mineral resources, deep mining has become an inevitable trend in mineral resource development. Considering that the rock surrounding deep wells is often eroded by groundwater, the mining process can be considered a loading and unloading process of the water-bearing rock mass [1]. Under loading and unloading, saturated rock produces plastic deformation and microfractures. Simultaneously, the stored energy is released in the form of an elastic wave, resulting in an acoustic emission (AE) phenomenon. Therefore, the deformation and fracture information of saturated rock can be dynamically monitored using AE technology, thereby providing the possibility for safety monitoring and early warning in deep rock engineering.

TABLE 1 | Mineral elements of the limestone according to XRF.

Element	Ca	S	Zn	Fe	Si	Mg
Content/%	60.194	2.704	0.274	0.818	0.222	0.212

TABLE 2 | Mineral composition of the limestone according to XRD.

Mineral	Calcite, dolomite compounds	Serpentinite	Pyrite	Talc	Zinc sulfide	Quartz
Content/%	94.4	1.4	2.2	1.0	0.8	0.2

In the process of mining, the stress of the surrounding rock is redistributed, and the advancing speed of the stope in the engineering site often changes because of the hydrogeological environment, which changes the time and speed of the stress redistribution of the surrounding rock. Therefore, the loading rate can affect the internal fracture of saturated rock, which can be characterized by AE well. Generally, at a higher loading rate, the hits are higher, and their relationship with time changes from linear to exponential [2]. The low-amplitude events gradually decrease, and high-amplitude events gradually appear [3]. The higher the unloading rate, the shorter the calm period after unloading, and the faster the change rate of AE in the entire test [4].

Different excavation strengths result in different loads on the surrounding rock, and the internal fracture and AE characteristics of saturated rock are different under different loading and unloading stresses. Generally, the maximum value of AE parameters of rock changes in accordance with the peak stress [5], which is active in loading, calm in unloading [6], and active again at the unloading point in the plastic stage, showing a change of "small-increase–decrease–sudden-increase–decrease." With an increase in the stress level, the felicity ratio decreases significantly. The AE event point source is produced intensively after the peak strength crosses 60% [7] and continuously expands along the joint surface. The AE parameters increase abruptly when the peak strength is approximately 85% [8] and exhibit fluctuations and calm. They then increase instantaneously when the rock approaches the peak strength [9] and decrease to 80% of the maximum value postpeak [10]. Meanwhile, the frequency decreases significantly before the peak strength. The crack develops from the top to the bottom before the peak and develops between the vertical planes after the peak. The above-mentioned research results demonstrate that the change law of AE parameters with the loading and unloading stress was obtained, but the development stage of the AE parameters was not considered comprehensively. The analysis of AE parameters in different stages under different stresses requires further study.

To understand the AE characteristics of saturated rock under different loading and unloading conditions further, saturated limestone was taken as the research object. The loading and unloading tests were carried out by varying the loading rates and initial cyclic peak stresses, and AE monitoring was simultaneously conducted. According to the test results, the evolution characteristics of AE characteristic parameters, steps, and development stages under different loading and unloading conditions can be summarized.

MATERIALS AND METHODS

Rock Samples

Limestone was selected as the rock sample. It was massive in structure and sampled from the Gaofeng tin mine, Guangxi, China, which is a deep mine that eroded by groundwater. The results of X-ray Fluorescence (XRF) and X-ray Diffraction (XRD) (see **Tables 1** and **2**) show that the rock was composed of argillaceous grains filled with calcite and cemented by serpentine, dolomite, pyrite, and a small amount of talc. According to the ISRM method, the limestone was processed into cylindrical samples with a size of 100 mm × *F* 50 mm [11]. After grouping, they were subjected to vacuum saturation treatment, and the average porosity of the limestone was 0.53%, as measured using a nuclear magnetic resonance testing system. Some rock samples were selected for the uniaxial compressive strength test, and the average compressive strength, σ_c, was 25.03 MPa as per the test result.

Experimental Procedure

The surrounding rock was gradually affected by the process of ore body mining [9], and the loading and unloading method of increasing the peak stress step by step, with an increased amplitude of $\sigma_{\triangle}$ = 5 MPa, was adopted in the test [12]. Because the surrounding rock of a roadway will not be disturbed by other stress environment before being disturbed by excavation, it can be considered as stable limit state, so the unloading mode of unloading to zero is selected [13]. The cyclic load path is shown in **Figure 1A**. Three loading rates of 0.15, 0.2, and 0.3 mm/min were set [14]. To study the AE characteristics at 10%, 30%, and 50% of the compressive strength, σ_c, three initial cyclic peak stresses, σ_0 (hereinafter referred to as the "initial stress") of 2.5, 7.5, and 12.5 MPa, respectively, were set at a loading rate of 0.2 mm/min. Besides, the unloading rate was fixed at 1 mm/min.

Pico sensor was used to collect AE signal, Micro-II Digital AE System was used to generate AE parameter data. AEwin^{TM} software was used to set AE test parameters, and record, analyze, process AE parameters and localization data, and it adopted the absolute location method to perform linear inversion, only considering the travel times irrespective of velocity model, that is, the isotropic velocity model was used in this test, in which AE signals are assumed to travel with same velocity in different directions [26, 27]. To ensure the integrity of the acquired waveform, the AE acquisition threshold value was set at 45 dB. To simplify the noise reduction process in the later stage, the minimum noise threshold was set as 18 dB in AEwin^{TM} software before the test.

In addition, the sensors were symmetrically arranged along the column at the level of 15 mm from the upper and lower ends of the sample and at the level of middle, as shown in **Figure 1B**. There were two sensors in each level, a total of six sensors were arranged. and the angle between adjacent levels is 90°. When

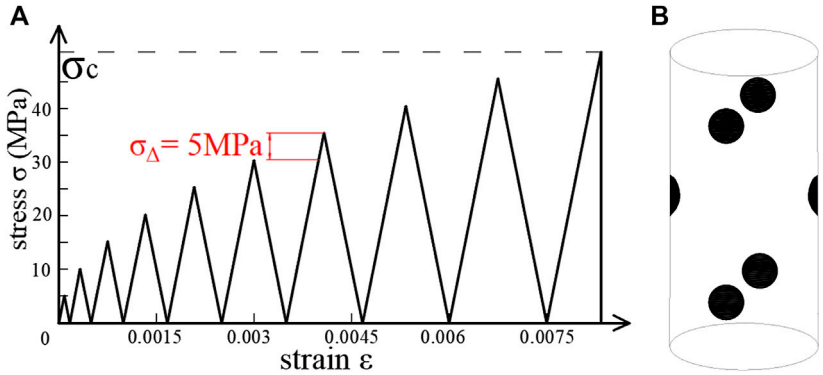

FIGURE 1 | Cyclic loading and unloading diagram. **(A)** v = 0.15 mm/min; **(B)** v = 0.2 mm/min path.

more than four sensors collect the hit signal, AE event will be generated, then AE system will generate the coordinate data of the event according to the distance data transmitted by the six sensors, finally complete the localization.

According to the procedure above, the loading and unloading tests were conducted, and AE monitoring was performed simultaneously. Finally, the stress, strain, and AE monitoring results were obtained.

ACOUSTIC EMISSION LOCALIZATION OF LIMESTONE DURING LOADING AND UNLOADING

AE location technology can accurately describe the distribution of AE event point sources and can be used to analyze the structural failure mode and the development of rock microcracks. Before the localization test, a certain sensor was taken as the transmitter to test the localization data of other sensors when the transmitter sent out the acoustic signal. The localization errors were obtained by comparing the localization data with the actual position of the transmitter. Finally, the errors of X direction, Y direction and absolute distance of each source point were obtained, which were all less than 2 mm, then the localization test was carried out. **Figure 2** shows the point source distribution and macroscopic failure structure of some typical rock samples. The lines in the point source diagram represent the density separation zone of the point source distribution, and the lines in the failure structure diagram represent the macroscopic failure surface. There is a good corresponding relationship that 1) the failure surface and the density separation zone of the point source are similar in each rock sample and 2) the fractures produced from the end of the dense point source gradually to the end of the sparse point source during the loading and unloading.

Figures 2A–C show that, under σ_0 = 2.5 MPa, the failure modes of the rock samples under different loading rates are clearly different. Considering the internal friction angle φ of the rock, $\varphi = 90^\circ - 2\theta$, where θ is the angle between the failure surface and the maximum principal stress [24]. Under the condition of v = 0.15 mm/min, the upper end of the rock sample is compacted rapidly in the early period of loading and unloading, resulting in a shear crack sprouting on the left side of the upper end. After the downward expansion of the crack, a spalling occurs in the middle corner of the left side, and then an obvious longitudinal through main crack is produced on the right side of the upper end owing to the Poisson effect, showing obvious tensile failure characteristics. The angle between the tensile crack and the maximum principal stress is approximately 6°. The rock fracture structure is relatively complete, and the fragmentation is large. Under the condition of v = 0.2 mm/min, a shear fracture develops from the upper and lower ends of the rock sample without coalescence, and the two fractures continue to extend to both sides, the right side of which developed a longitudinal crack. At this time, the rapid increase in lateral deformation limits the continuous development of the crack and, finally, continues to extend to the right side, resulting in parallel shear failure of the rock, with θ of approximately 11°. The small cracks are dense, and the rock is clearly broken at the lower part of the rock. Under the condition of v = 0.3 mm/min, the rock sample first forms a shear crack from the upper right to the lower left. Then, with the increase in the peak stress, the shear crack breaks and changes direction in the middle lower part of the rock and gradually produces another shear crack on the upper left side. Finally, lateral failure occurs under the shear force, with θ of approximately 21°. The width of the cracks is large, the damage degree of the rock is large, and the surface is uneven.

Figures 2B,D,E show that, under a loading rate of 0.2 mm/min, the typical parallel shear failure occurs at σ_0 = 2.5 MPa, with θ of approximately 11° and small cracks being densely distributed on the lower side of the rock. Under the condition of σ_0 = 7.5 MPa, a crack sprouts downward on both sides of the upper end of the rock sample, and an arc-shaped shear crack finally forms on the left side. After short-term local crushing on the right side, longitudinal tensile cracks are formed under tensile stress. Finally, the two cracks are connected, and the loading and unloading end with tension shear composite failure, with θ of approximately 10° and a rough rock surface and with fewer flakes but larger fragmentation. Under the condition of σ_0 = 12.5 MPa, there are left and right tension cracks, and most of the event point sources are concentrated in the middle of the rock sample. This is because the viscoplastic behavior of the rock under high initial stress is weak, and the lateral deformation produced is small. This increases the compression of the axial compressive stress on the

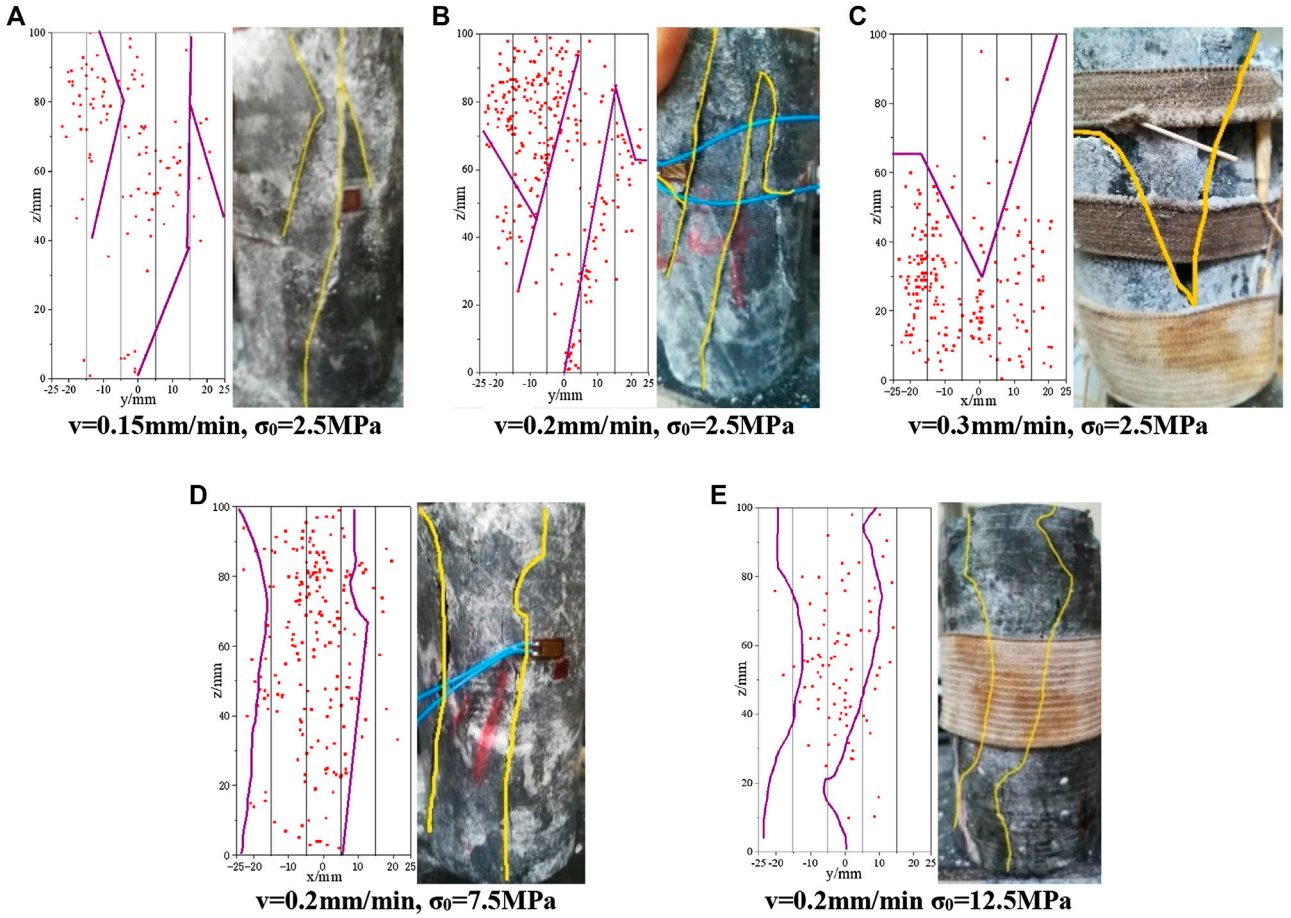

FIGURE 2 | AE event point source distribution and macroscopic failure structure of rock under different loading rates and initial stresses.

rock sample, which causes the rock to exhibit typical brittle and tensile failure, with θ of approximately 9°. Large blocks form that have the same height as the intact rock sample.

It can be observed from the above that, with the increase in loading rate and decrease in initial stress, the viscoplasticity of the rock sample strengthens, the damage increases, and the bonding effect between particles becomes worse. Moreover, the fragmentation caused by rock failure decreases, which causes the internal friction angle of the rock to decrease, that is to say, the sliding friction needed to overcome for sliding between rock particles reduced, which leads to a gradual change of the rock failure mode from tensile failure to shear failure.

ANALYSIS OF AE CHARACTERISTIC PARAMETERS UNDER DIFFERENT LOADING AND UNLOADING CONDITIONS

Variation Characteristics of Ringing Count, Cumulative Hits, and Cumulative Energy

Figures 3 and **4** show the changes in cumulative hits (hereinafter referred to as "hits"), cumulative energy (hereinafter referred to as "energy"), and ringing count under different loading rates and initial stresses. The hits and energy under each loading and unloading condition exhibit the step growth characteristic, in which the three steps that exhibit the largest increasing extent are screened out in the figure. Step I generally shows a rapid–slow change, and steps II and III mainly present a slow–rapid trend, which indicates that the generation of microfracture gradually slows down with loading and unloading.

The peak count is defined as the highest value of the ringing count under a certain peak stress. According to the change in peak count, the loading and unloading process can be divided into a slight increase period, attenuation period, intense growth period, and postpeak calm period (within the softening stage). **Figures 3** and **4** show that the ringing count increases sharply at the peak strength and then increases again suddenly at the end of the postpeak calm period. The highest ringing count in the entire test must appear in these two increases. In addition, the maximum increase in energy can only occur in the postpeak calm period, but the maximum increase in hits may also occur in the intense growth period. The peak count varies with the loading rate and initial stress.

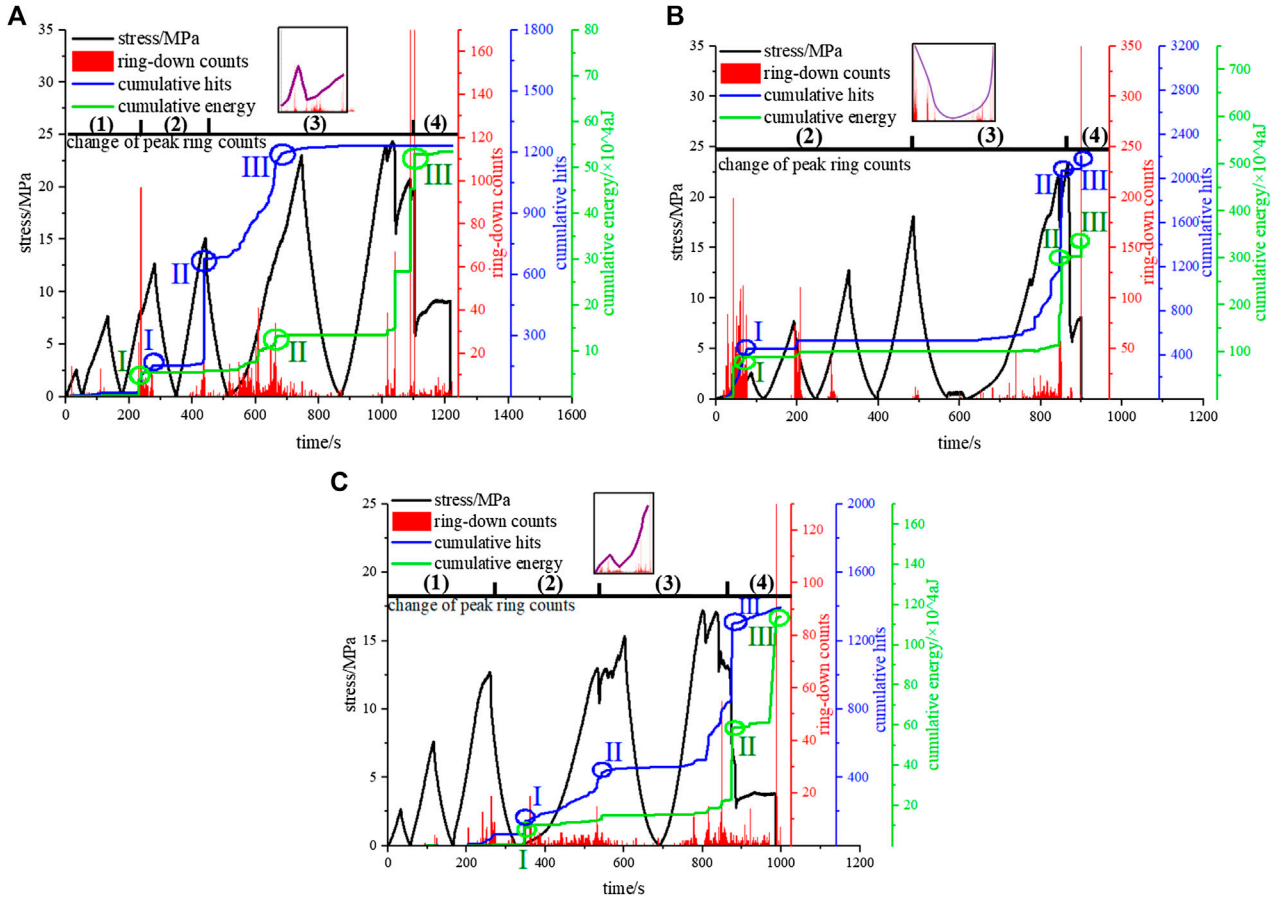

FIGURE 3 | AE test results under different loading rates. **(A)** v = 0.15 mm/min; **(B)** v = 0.2 mm/min; **(C)** v = 0.3 mm/min: 1) slight increase period; 2) attenuation period; 3) intense growth period; 4)the postpeak calm period.

Different Loading Rates

Taking the AE monitoring results with v = 0.15 mm/min as an example, as shown in **Figure 3A**, the changes in the ringing count, hits, and energy of each cycle are as follows.

(1) In the first two cycles, the hits and energy are close to zero, and the ringing count is not obvious. This is because the lower stress is not sufficient to provide energy for the formation of new microcracks. Only a small amount of AE information is produced by the closure and sliding of primary fractures and the occlusive failure of particles.

(2) At the end of the slight increase period, the ringing count is suddenly active, and the hits and energy appear in step Ⅰ. The change in the step curve is steep first and then tends to be flat, and the step occurs at the inflection point of the stress curve instead of the peak stress. This is because of the sudden loss of the bearing capacity of local rock particles, resulting in a large number of microfractures.

(3) When loading and unloading to the attenuation period, the energy and ringing count return to calm again, while the hits appear in another step, which indicates that the rock mainly stores energy and produces many small fractures. Therefore, the energy is rarely released.

(4) When the stress increases into the intense growth period, the microcracks begin to form, and the ringing count gradually becomes active. In the cycle of the peak stress of 22.5 MPa, the ringing count appear since the stress zero point, showing a strong Felicity effect. The hits and energy also exhibit a large step near the peak stress of 22.5 MPa. The step curve exhibits a slow–rapid–slow process. After this step, energy has not reached half of the entire process, but the hits have completed 89% of the entire process. It is considered that, under a lower loading rate, although the internal fracture of rock can continue to develop, the energy can only be released after long-term accumulation; hence, its growth is concentrated in the postpeak calm period, instead of this period.

(5) At the end of the intense growth period, microcracks polymerize and run through the sample, the rock skeleton structure is gradually destroyed, forming structural planes, and sliding occurs on both sides of the structural plane. With the increase in rock deformation, the fracture of the sliding block results in two fluctuations in the stress–strain curve at

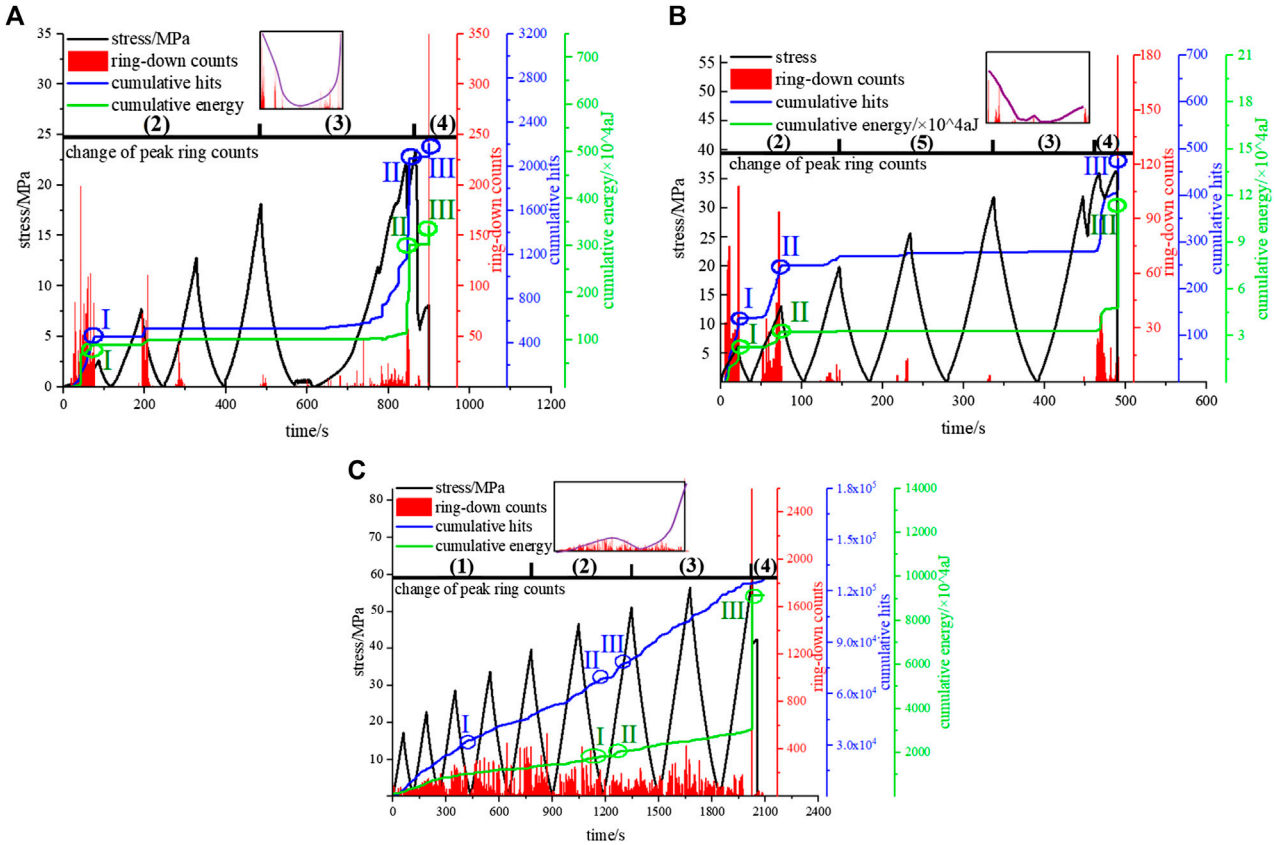

FIGURE 4 | AE test results under different initial stresses. **(A)** σ_0 = 2.5 MPa **(B)** σ_0 = 7.5 MPa; **(C)** σ_0 = 12.5 MPa: 1) slight increase period; 2) attenuation period; 3) intense growth period; 4) postpeak calm period; 5) transition period of increase and then decrease.

the end of the intense growth period. Each fluctuation is accompanied by a large number of ringing counts and a steep-step-type energy release, the increase of which is greater than that at the peak strength. However, the number of hits at the two fluctuations is extremely quiet because the current energy is not sufficient for the fracture to continue to expand, forcing the rock to release energy rapidly [16, 17].

(6) When the loading continues to the postpeak calm period, the hits still do not increase, indicating that the residual resistance process of rock at a lower rate does not produce fracture information.

With an increase in the loading rate to 0.2 mm/min, except that the cycle of σ = 22.5 MPa showed a long-term Felicity effect (same as v = 0.15 mm/min) and the cycle of σ = 12.5 MPa showed a instantaneous Felicity effect, the ringing counts only occur when the stress exceeds the peak stress of the upper cycle—that is, showed a Kaiser effect, and the development trend and step trend of hits and energy become relatively closer than v = 0.15 mm/min. Compared with the low loading rate, the AE behavior of the cycle of low peak stress is no longer active at v = 0.3 mm/min, the distribution of the ringing count is the sparsest during loading and unloading, and the ringing count is the lowest when rock failure occurs. This is because the pore water pressure replaces the effective force to resist the external force when the loading rate is too fast, resulting in significant plastic deformation and weakening microfracture behavior. Moreover, under v = 0.3 mm/min, the long-term Felicity effect of rock occur in the cycle of the peak stress of 15 MPa. Compared with the low loading rate, it can be seen that the condition of v = 0.3 mm/min can advance the long-term Felicity effect of rock.

In addition, the hit of rock near failure varies with loading rates. Under v = 0.15 mm/min, the hit appears no obvious change in the last cycle, and there is no increase at the peak strength and at in the peak stress of softening stage. It shows that the brittleness of saturated limestone is weak near the failure, the rupture scale is small, the fracture behavior is less and not enough to converge to form a large fracture can be collected by acoustic emission, with weak precursor information. Under v = 0.2 mm/min, the hit presents a increase of two to three steps in the last cycle (800 s), followed by a sudden increase at the peak strength and softening stage, and the increasing extent at the peak strength is much greater than that at the softening stage, which indicates that the fracture behavior of saturated limestone is much more sensitive to stress than to time. Compared with v = 0.2 mm/min, what the

difference which the hit appears under v = 0.3 mm/min is that there is no longer a sudden increase at peak stress, but a slow increase throughout the whole softening stage.

In **Figure 3**, the red part in the inset shows the development process of ringing count before softening stage, and the purple solid line shows the change trend of peak count, which is obtained by connecting the maximum ringing count values of each cycle. As can be seen from the insets, before the postpeak calm period, there are two types of change in peak count (including peak strength).

(1) When v = 0.2 mm/min, it is U-type, which means that the peak count was active in the early period, dropped to the lowest level after the attenuation period, and increased sharply at the end of the sudden rise.
(2) When v = 0.15 and 0.3 mm/min, it is N-type, which means that it increases slightly in the slight increase period, changes to a lower value in the attenuation period, and then increases sharply at the end of the intense growth period. Specifically, the peak count under v = 0.15 mm/min exhibits the former-N-type, which means that the final value of the intense growth period is higher than that of the slight increase period. The peak count under v = 0.3 mm/min is the latter-N-type.

With the increase in loading rate, before the postpeak calm period, the change of peak count gradually changes from the former-N-type to the U-type and the latter-N-type. Thus, the increase in the proportion of the intense growth period gradual.

Different Initial Stresses

Taking the AE monitoring results under σ_0 = 7.5 MPa as an example, it can be seen from **Figure 4B** that the AE behavior in each cycle has a good Kaiser effect—that is, no AE behavior occurs in each unloading section and loading section lower than the previous peak stress. There are two peaks in the ringing count of each cycle: one in the loading section, and the other at the peak stress. They are defined as the front peak count and the postpeak count, respectively. The postpeak count is higher than the front peak count. The times of steps for energy and hits are basically the same, but the energy does not increase significantly until the peak strength, and the hits exhibit a larger proportion in the early period. The changes in ringing count, hits, and energy of each cycle are as follows.

(1) In the first cycle of the attenuation period, the peak count reaches the maximum value before rock failure, owing to the instantaneous contact, extrusion, and closure of primary fractures and pores in the rock during the compaction stage. The front peak count occurs at 46.7% σ (σ is the stress peak of the current cycle). Step I of hits and energy appears at the peak stress of this cycle, and the step process presents a trend of "rapid–slow–rapid."
(2) In the second cycle of the attenuation period, the front peak count dropped sharply, which occurred at 47.8% σ, and then decreased slightly. The ringing count of this cycle was lower, but the duration was the longest among all cycles. Step II of hits and energy appeared in this cycle. Unlike in the past, this step exhibited a linear trend, and the increase in hits was larger than that of step I. This is because the pore water pressure in saturated rock drives the pore cavity to disappear instantaneously, which is not subjected to the external force. Therefore, rock microfracture occurs without energy consumption. The hits have reached 52.3% of the entire process, but the energy has only reached 28.6%. This shows that, under the higher initial stress, the microfracture behavior is more in the early period, and the release of elastic energy is mostly concentrated in the later period.
(3) At the beginning of the transition period of increase and then decrease, only a small number of ringing counts were produced. The occurrence time of the former peak count was 58.4% σ, and the hits and energy increased slightly.
(4) In the middle of the transition period of increase and then decrease, the ringing count increased, but the hits and energy were calm for the first time, indicating that the rock had entered the linear elastic stage. The uneven elastic deformation between grains was well coordinated in this linear elastic stage, resulting in no new elastic energy being produced. The synchronization and homogenization of elastic deformation also increased the signals crossing the threshold among the hits and further increased the ringing count. Moreover, the occurrence time of the front peak count in this cycle was 59.3% σ. Combined with the previous cycles, the occurrence time was delayed with an increase in the number of cycles.
(5) At the end of the transition period of increase and then decrease, the ringing count dropped to the lowest level, and the hits and energy remained unchanged. This indicates that the linear elastic stage was ending, and the rock stiffness would not continue to increase greatly. Because of this, the fracture cavity did not further expand.
(6) In the intense growth period, the local stress dropped at 73.1% σ_c and the peak strength σ_c. The ringing count appeared as a small signal at 73.1% σ_c but increased rapidly at σ_c for a long time. The hits and energy also exhibited step III at σ_c, but the increase in energy was small. This shows that the rock had entered the plastic stage, a large amount of uneven deformation had occurred between the grains, and the tensile force had formed on both sides of the fracture, resulting in a large number of microcracks connecting to form macrocracks. This increased the ringing count, hits, and energy. What the stored elastic energy was used for also changed from the initiation of new cracks to the destruction of the local structure of rock, and the elastic energy exhibited a short-term accumulation because suddenly there was no need for crack initiation; therefore, the increase in energy at the end of the intense growth period was extremely small.
(7) In the postpeak calm period, the stress increases automatically after decreasing, showing the characteristics of stress strengthening. The ringing count shows an abnormally sharp increase in rock failure, and the hits and energy also complete step III with the largest increase. This is because the dislocation and slip of macrocracks after the peak strength can still produce a large number of AE behaviors.

Figure 4 also shows that, with the increase in initial stress, the postpeak calm period (i.e., softening stage) becomes less obvious. The gap between the hits and the energy curve develops from a close fit to a larger difference, the increase in energy during rock failure tends to be more obvious than that of hits, and the peak count changes from U-type to W-type and N-type gradually. This indicates that the increase in initial stress tends to increases the AE behavior in the early period. When the initial stress increases from 2.5 to 7.5 MPa, the transition period of increase and then decrease occurs, in which the process of "increase" is caused by the fracture polymerization by the primary and secondary stress. When the initial stress increases to 12.5 MPa, most of the load acts on the rock in the form of microfracture, which results in the ringing count appearing throughout the loading and unloading process, showing a strong felicity effect. The hits and energy also show a trend of uniform growth with time and do not show step growth, as with the lower initial stress. Meanwhile, under σ_0 = 12.5 MPa, the distribution of the ringing count is the most dense, and the hits, energy, and ringing count are the largest during rock failure. This indicates that the rock has strong brittleness under a higher initial stress, which also leads to the tensile failure mode with large blocks, as in **Figure 2E**.

In addition, the hit of rock near failure varies with the initial stress. Under σ_0 = 2.5 MPa, the hit increases greatly and slightly at the peak strength and the peak stress of the softening stage respectively. Under σ_0 = 7.5 MPa, the rock does not increase suddenly near failure, showing a smooth growth from 460 s. It is considered via analysis that the increase of initial stress will accelerate the migration of water in saturated rock, thus buffer the increase of hit caused by rock fracture. Under σ_0 = 12.5 MPa, the change of hit near peak strength is the same as that in the earlier cycles, in both of which the hit all appears the tend of slow increase, moreover, the increase rate of hit in softening stage is even lower than the earlier cycles. The hit under σ_0 = 12.5 MPa verifies the rationality of the analysis on water migration.

Variation Characteristics of Different Periods

Table 3 shows the duration of ringing count evolution under different loading rates and initial stresses. With the increase in loading rate v, the durations of the slight increase period and attenuation period tend to get extended, whereas the durations of the intense growth period and postpeak calm period are gradually shortened. It is considered that the faster loading rate promotes free water seepage inside the saturated rock, increases the slip behavior of the primary microcracks, and aggravates the microfracture and occlusal failure of the rough surface, which requires a long time; therefore, the early period is longer. However, when loading to the intense growth period, the seepage of free water saturates, and an increase in the loading rate aggravates the compression of the main stress on macrocracks, thus shortening the later period. With the increase in initial stress σ_0, except for the slight increase period, the duration of each period decreases first and then increases, which can be interpreted as indicating the existence of a critical value of initial stress. When the initial stress is less than the critical value, the microfractures develop slowly, and the larger initial stress obviously shortens the development time of each period. When the initial stress is greater than the critical value, the pore water pressure replaces the rock skeleton to bear the compression of the external force. Therefore, a larger initial stress prolongs the process of each period.

Step Characteristics of the Acoustic Emission

Figures 3 and **4** show that there are some steps in the cumulative hits and energy. The three steps that exhibit the largest increasing amplitude and the slow-change period before each step (hereinafter referred to as the "slow-change period") are used to analyze the step characteristics. To describe the step characteristics conveniently, the duration proportion is defined as the proportion of the duration of a certain step (or slow-change period) to that of the entire test. The increase proportion is defined as the proportion of the increase in the hit (or energy) of a certain step (or slow-change period) to that of the entire test. The softening duration is defined as the calm duration of the hits (or energy) in the softening stage.

Table 4 shows the duration and increase proportion in each step and slow-change period under different loading rates v and initial stresses σ_0. From the transverse view, with the loading and unloading process, the increase proportion of hits and energy in the step and slow-change period gradually increase, and the increase proportion of energy in the step and slow-change period increases gradually. This indicates that there is a positive correlation between the damage of rock, the energy transformation behavior, and time at a lower loading rate. Under the condition of v = 0.2 mm/min, the increase proportion of hits and energy first increases and then decreases, and the value of step III is the smallest. It is considered that the expansion limit of pores is easier to reach at a higher loading rate, causing the coalescence of pores to become saturated at step II, leading to a decrease in the increase proportion of energy and hits in step III. Under the condition of v = 0.3 mm/min, the increase proportion in the slow-change period increases first and then decreases, whereas the increase proportion in the step increases gradually. This is because step III is close to failure, and the formation of the macrofailure surface destroys the bearing structure of the rock, resulting in a substantial increase in hits and energy. Under the condition of σ_0 = 7.5 and 12.5 MPa, the duration and increase proportion of energy in the step and slow-change period first decrease and then increase. Analysis shows that, under a larger initial stress, the rock at the linear elastic stage shows obvious elastic characteristics, and the plastic deformation is small. Furthermore, the high elasticity enables the storage of elastic energy to be completed earlier. Therefore, the duration and increase in the proportion of energy in step II and the second slow-change period occur through a trough.

From the longitudinal view, with the increase in loading rate, the duration and increase proportion of hits in steps I and II first increase and then decrease, and the it is same in step I of energy. With the increase in initial stress, the duration and increase

TABLE 3 | Duration of each period of ringing count evolution.

Loading rate and initial stress	Duration of each period			
	Slight increase period (s)	Attenuation period (s)	Intense growth period (s)	Postpeak calm period (s)
v = 0.15 mm/min, σ_0 = 2.5 MPa	280	161	888	277
v = 0.2 mm/min, σ_0 = 2.5 MPa	—	486	380	271
v = 0.3 mm/min, σ_0 = 2.5 MPa	475	751	257	145
v = 0.2 mm/min, σ_0 = 7.5 MPa	—	147	130	22
v = 0.2 mm/min, σ_0 = 12.5 MPa	868	476	681	38

TABLE 4 | Duration proportion and increase proportion in each step and slow-change period.

Loading rate and initial stress	AE parameters	Duration proportion in steps (%)			Increase proportion in steps (%)			Duration proportion in slow-change periods (%)			Increase proportion in slow-change periods (%)			Softening duration (s)	Average hits rate (hit/s)/ average energy rate (104 aJ/s)
		I	II	III	I	II	III	I	II	III	I	II	III		
v = 0.15 mm/min, σ_0 = 2.5 MPa	Hits	24	2	74	11	43	46	46	32	22	19	20	61	916	0.85
	Energy	10	40	50	10	11	79	18	29	53	4	46	50	204	342.03
v = 0.2 mm/min, σ_0 = 2.5 MPa	Hits	29	49	22	19	68	13	5	85	10	21	67	12	156	2.32
	Energy	43	47	10	25	57	18	5	85	10	11	83	6	156	3,260.43
v = 0.3 mm/min, σ_0 = 2.5 MPa	Hits	3	20	77	7	11	82	42	13	45	21	44	35	155	0.95
	Energy	6	93	1	9	37	54	35	57	8	4	80	16	31	710.64
v = 0.2 mm/min, σ_0 = 7.5 MPa	Hits	6	41	53	11	31	58	4	7	89	32	2	66	12	0.95
	Energy	50	24	26	10	5	85	10	4	86	41	16	43	12	229.13
v = 0.2 mm/min, σ_0 = 12.5 MPa	Hits	53	19	28	45	14	41	29	66	5	41	56	3	65	60.67
	Energy	67	16	17	4	3	93	57	3	40	61	1	38	65	43,808.54

proportion of hits in step I and the slow-change period first decrease and then increase. In addition, the average hits/energy rate at v = 0.15 mm/min is the minimum, and the maximum value is at σ_0 = 12.5 MPa, thereby indicating that a lower loading rate or initial stress slows the energy release under loading and unloading.

Frequency and Amplitude Characteristics Under Different Loading and Unloading Conditions

The amplitude and frequency of the AE signal vary with the loading rate and initial stress, which are affected by the fracture scale and structural evolution of the rock. To describe the variation characteristics of the maximum value of the amplitude signal better, the peak amplitude is defined as the signal with the highest amplitude in a certain cycle. **Figures 5** and **7** show the variation process of the amplitude and peak frequency of typical rock samples under different loading rates and initial stresses. The circular particles and the curve on **Figures 5** and **7** represent the amplitude signal and the variation of peak amplitude, respectively, and the triangular particles represent the peak frequency signal.

Figures 5 and **7** show that the peak amplitude generally appears at the peak stress, but it appears in advance at the plastic stage. In the softening stage, the high-amplitude signal gradually disappears. For the frequency, Su et al. took the frequency less than 120 kHz as low-frequency of rock [15], and Kong et al. took the frequency greater than 300 kHz as the high-frequency of rock [18]. Based on the division method above, combined with the density distribution of the frequency signals in this test, the frequency is divided into a low-frequency band (0–125 kHz), intermediate-frequency band (125–320 kHz), and high-frequency band (320–500 kHz) here, corresponding to the red, yellow, and blue areas, respectively, in **Figures 5** and **7**. In a certain cycle, the low-frequency signal is generated first, and its number is the highest, followed by the high-frequency signals and intermediate-frequency signals. Intermediate-frequency signals appear in the first one to two cycles and then become calm. They then become active in the plastic stage, while low- and high-frequency signals are more stable and continuous. With the increase in the number of cycles, the outer contour composed of signals in the three frequency bands gradually changes from rectangular to a concave triangle. It finally becomes a concave trapezoid in the plastic stage, as shown in **Figure 5A**.

With the increase in the number of cycles, the amplitude signals and frequency signals do not increase singly [19, 20], and the number changes of the two signals have good consistency. Before the plastic stage, the two signals are concentrated on the stress that exceeds the previous peak stress, showing a good

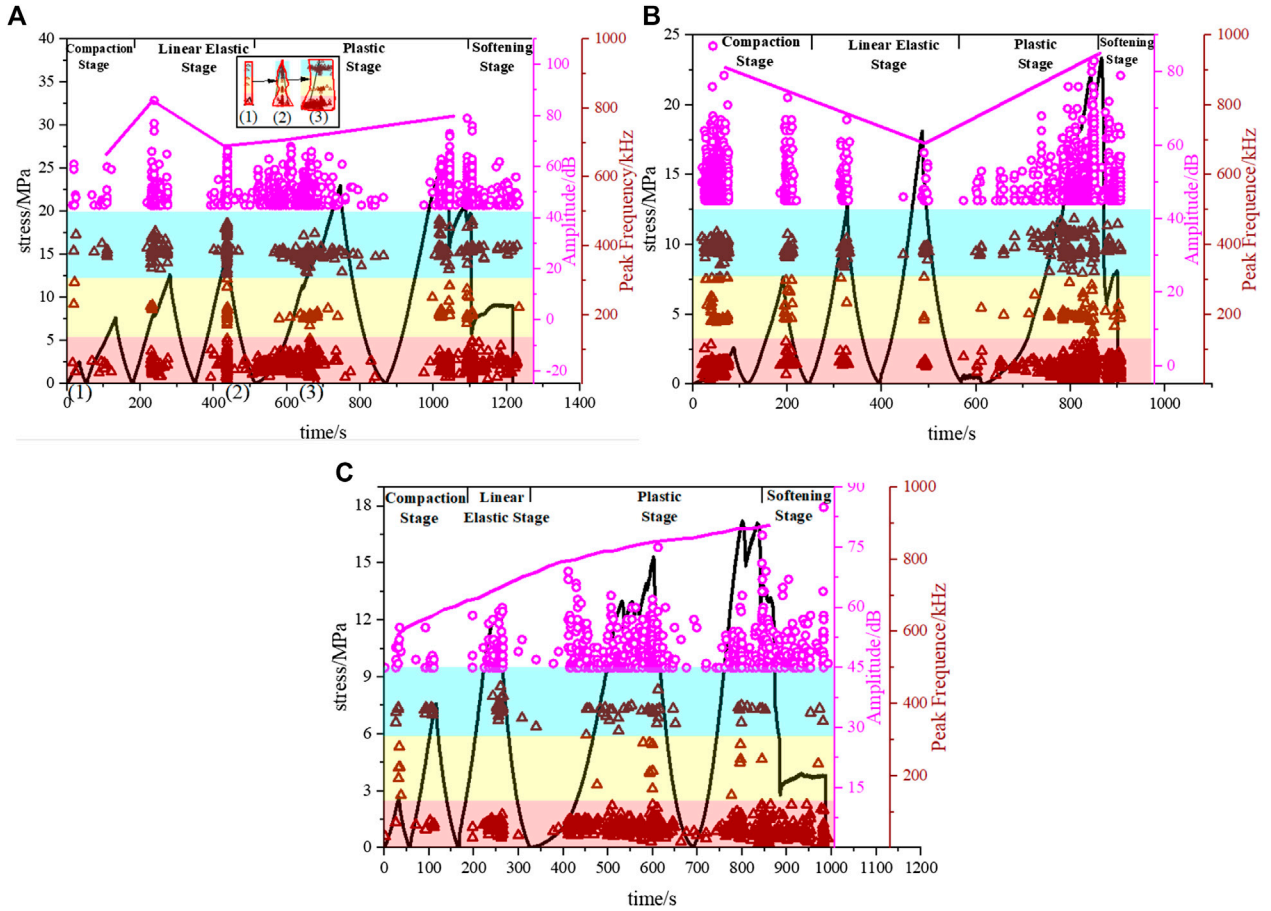

FIGURE 5 | Variation process of the amplitude and peak frequency signals under different loading rates. **(A)** v = 0.15 mm/min; **(B)** v = 0.2 mm/min; **(C)** v = 0.3 mm/min.

Kaiser effect, and become extremely dense in the plastic stage. This can be used as a precursor to determine the rock failure under loading and unloading [21, 22].

The amplitude and peak frequency show different laws under different loading rates and initial stresses.

Different Loading Rates

Taking the frequency and amplitude monitoring results with v = 0.15 mm/min as an example, **Figure 5A** shows that the variation characteristics of peak frequency and amplitude in each cycle are as follows.

(1) In the first cycle of the compaction stage, only a small number of amplitude signals is generated, with a peak amplitude of 60 dB. The peak frequency signals are distributed in all three frequency bands, exhibiting obvious band division characteristics, but there are few signals in each frequency band.

(2) In the second cycle of the compaction stage, the amplitude signal increases slightly. This is caused by the collision and friction of particles on both sides of the primary fracture, and the peak amplitude appears at the peak stress. The signal in the intermediate-frequency band disappears, while the signal in the low- and high-frequency bands increases, especially in the low-frequency band. This indicates that the signal source of the low-frequency band is the contact behavior of the particles.

(3) In the first cycle of the linear elastic stage, a large number of amplitude signals appeared. The amplitude signals were very dense between 45 and 60 dB, with a peak amplitude of 85 dB, reaching the highest value among all cycles. The peak amplitude did not appear at the peak stress but appeared at the stress fluctuation. It is considered that the microcracks began to expand in the linear elastic stage, and the local weak rock blocks could not bear the expansion tension of the fracture, leading to the generation of a high-amplitude signal and the redistribution of stress in the rock. The signal of the high-frequency band increased significantly and exceeded that of the low-frequency band, and the signal range and duration of both expanded by several times. However, the distribution range of the signal in the intermediate-frequency band was even smaller than that in the compaction stage. Therefore, the signal source of the high-frequency band is the expansion behavior of the fracture, and the signal source of

the intermediate-frequency band is the compression behavior of the fracture.

(4) In the second cycle of the linear elastic stage, the peak amplitude is 67 dB, which is lower than that of the previous cycle. This shows that the linear elastic stage is an important stage for storing elastic energy, and the released energy is very small. This is insufficient to make the crack continuously expand, and only a small amount of fracture is initiated. Moreover, the amplitude signal is continuous and symmetrical, the amplitude signal near the peak amplitude is continuous, and the signals on both sides of the peak amplitude decrease gradually. In terms of peak frequency, the frequency signal at the peak stress is continuous and dense, whereas the signal is sparse at other times, thereby indicating that the rock shows special characteristics before a large quantity of fracture propagation. The frequency range of each frequency band signal is double that in the previous cycle but exhibits a longer duration only at 400 kHz.

(5) In the first cycle of the plastic stage, the peak amplitude is 68 dB, which is higher than that of the previous cycles. The time of the peak amplitude is still at the stress fluctuation, and the amplitude signal decreases evenly from the peak amplitude to both sides, and the signal spreads throughout the entire cycle and is very dense. This indicates that the rock has begun to produce plastic damage. The frequency range of the intermediate- and high-frequency signals is shorter than that of the previous cycle, indicating that the contact behavior of particles in the early period of the plastic stage is the highest, followed by the expansion of cracks, and the fracture closure is the most rare.

(6) In the second cycle of the plastic stage, the peak amplitude is 80 dB, which is the highest among all cycles. The maximum amplitude increases from 970 to 1,100 s, in which only the stress fluctuation is broken. It is considered that the coalescence of a large number of cracks leads to a gradual increase in amplitude, while the macroscopic failure surface forms in this process. When the failure surface is not subjected to the compression suddenly, it stops rupturing, and only sliding friction occurs. As a result, the increase in the amplitude breaks at the stress fluctuation. After 970 s, the frequency signals in the intermediate- and high-frequency bands are only active at the peak strength and enhanced strength, while the low-frequency signals show continuous development characteristics. This indicates that the particles continuously produce sliding friction behavior, which is the same as the variation law of amplitude. In addition, the frequency range of the intermediate- and high-frequency signals is greatly increased, and the high-frequency signals have spread throughout the entire frequency band. However, the low-frequency signal is shortened. This indicates that the fracture is mainly expanded in the late period of the plastic stage, supplemented by being compacted, and the contact behavior of the particles is the least.

(7) In the softening stage, with the passage of time, the maximum amplitude of the amplitude signals gradually decreases, and it is densely distributed between 45 and 52 dB. It is sparse in the area of >52 dB. This is because the main failure crack of the rock has formed, and the amplitude signal can only be generated by the weak structural plane around the main crack. The number of intermediate-frequency signals decreases sharply, and the frequency range of intermediate- and high-frequency signals shortens several times. The low-frequency signals are dense and continuous. This shows that the contact behavior of particles only occurs in the process of residual resistance of rocks, and the expansion and compaction of fractures are limited.

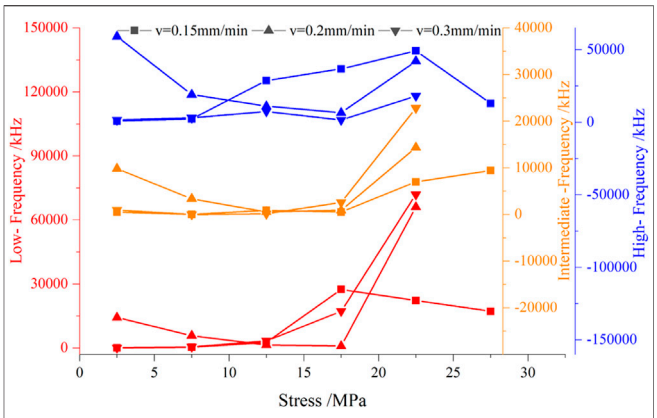

FIGURE 6 | Variation of frequency value with peak stress in each frequency band under different loading rates.

Figure 5 shows that, with the increase in loading rate, the change form of the peak amplitude before the peak strength gradually changes from N-type to V-type and linear-type. The increase in the loading rate conceals the early variation process of the peak amplitude. This is because a higher rate increases the compression frequency on pores and then reduces the chance of their recovery and prolongs the variation period of the rock structure. This causes the previous change of amplitude to disappear.

Figure 6 shows the change of frequency value with peak stress in each frequency band. It can be seen that in the low-frequency band, the frequency at v = 0.15 mm/min first increases and then decreases, with a change critical point of peak stress of 17.5 MPa, which indicates that the contact behavior of rock particles reduces relatively compared with the fracture propagation behavior under low loading rate; the frequency at v = 0.2 mm/min first decreases and then increases, and the change critical point is the same as that under v = 0.15 mm/min; the frequency at v = 0.3 mm/min increases exponentially. In the medium frequency band, the frequency at v = 0.2 mm/min also decreases and then increases, while the frequency at v = 0.15 mm/min and 0.3 mm/min presents a monotonic increasing trend, which indicates that both too low and too high loading rate will make the fracture compression process more uniform, but only too high loading rate can promote the fracture uniform expansion. In the high frequency band, the frequency change trend of v = 0.15 and 0.2 mm/min is the same as that of low frequency band, while the frequency at v = 0.3 mm/min shows a complex process of increase-decrease-increase, which indicates

TABLE 5 | Number of signals of the three frequency bands and amplitude attenuation value of the softening stage under different loading rates.

Loading rate v	Frequency and amplitude			
	Number of signals of the three frequency bands			Amplitude attenuation value of the softening stage
	High-frequency (%)	Intermediate-frequency (%)	Low-frequency (%)	
0.15 mm/min	33.0	13.0	54.0	35.0
0.2 mm/min	30.0	11.0	59.0	4.0
0.3 mm/min	5.2	0.1	94.7	-7.0

that the development of particle is similar to that of fracture at a low loading rate, but the fracture development is full of randomness at a high rate, which is easily affected by external factors, showing a reciprocating change.

In addition, the number of signals of the three frequency bands in **Figure 5** and the amplitude attenuation value of the softening stage were calculated. The results are shown in **Table 5**. With the increase in loading rate, the amplitude attenuation value of the softening stage gradually decreases. The rock is considered to exhibit obvious viscoplasticity in the softening stage, resulting in large deformation. A higher loading rate promotes more changes in rock structure; hence, the amplitude does not decrease excessively. In addition, the peak frequency is mainly distributed in the low-frequency band. With the increase in the loading rate, the intermediate- and high-frequency signals gradually decrease, and the low-frequency signals gradually increase, especially in the range of 0.2–0.3 mm/min.

Different Initial Stresses

Taking the frequency and amplitude monitoring results under σ_0 = 7.5 MPa as an example, as shown in **Figure 7B**, the variation characteristics of frequency and amplitude in each cycle are as follows.

(1) In the first cycle of the compaction stage, the amplitude and frequency signals are continuously generated in the loading section, and the peak amplitude is 67 dB. This is the highest value, except for the peak amplitude during rock failure.

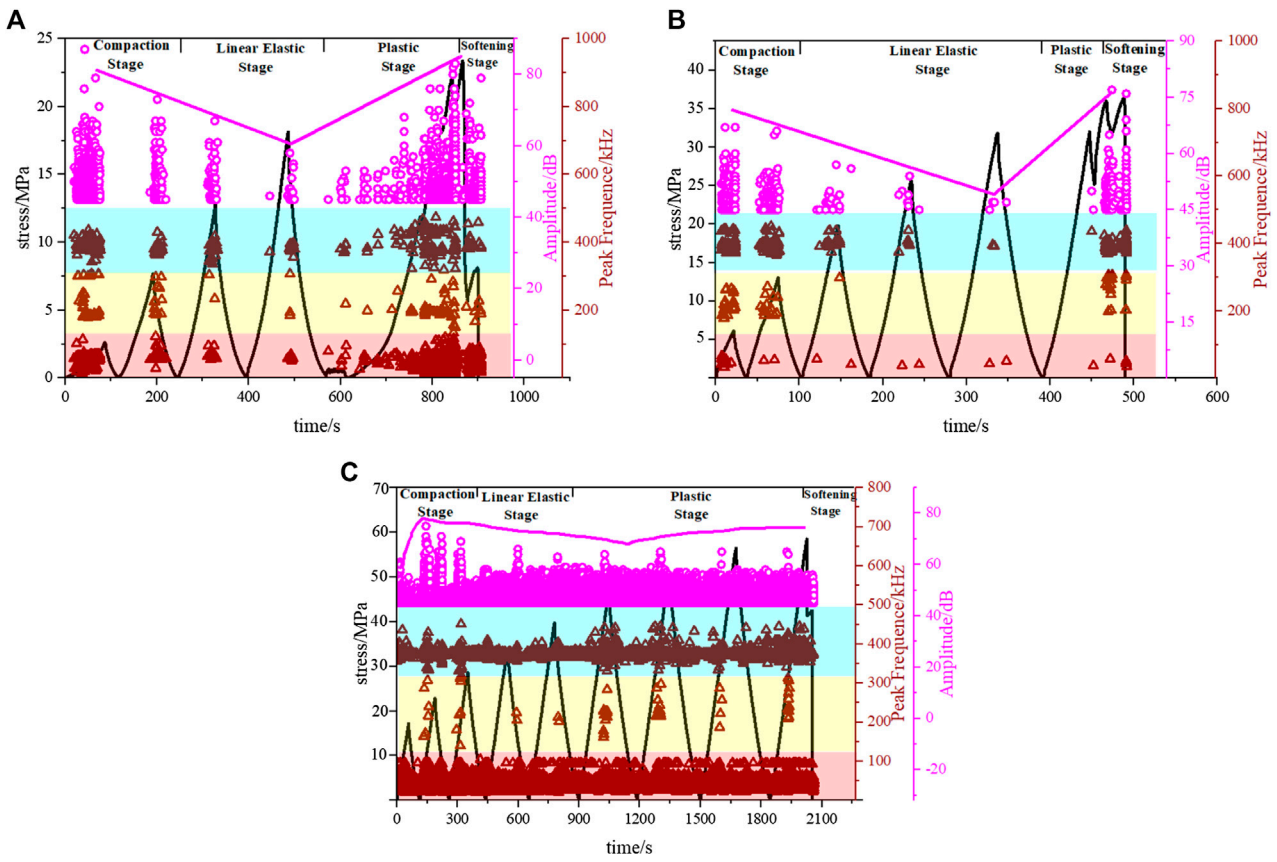

FIGURE 7 | Variation process of the amplitude and peak frequency signals under different initial stresses **(A)** σ_0 = 2.5 MPa, **(B)** σ_0 = 7.5 MPa; **(C)** σ_0 = 12.5 MPa.

The frequency signals of the three frequency bands are relatively concentrated, and their outer contours exhibit rectangular characteristics. The number of low-frequency signals reaches the maximum among all cycles, indicating that, under the higher initial stress, the effect of the load on the rock in the initial cycle is large, and the contact and chimerism behaviors of particles are relatively more in the compaction stage.

(2) In the second cycle of the compaction stage, the peak amplitude is 65 dB, which is lower than that of the previous cycles. This is because the effective bearing area of the rock block increases significantly after the pores are compacted for a period of time, which reduces the chance of fracture production. The outer contours of the frequency signals in the three frequency bands all exhibit triangular characteristics, and the number of high- and intermediate-frequency signals is the greatest among all cycles. The low-frequency signals significantly decrease and last until the rock failure, indicating that the chimerism of particles is easily saturated under high initial stress, causing the fracture to expand earlier.

(3) In the linear elastic stage, the amplitude signals and the peak amplitude continue to decrease gradually. Intermediate-frequency signals do not appear. Low-frequency signals continue to be calm, and the frequency range and duration of high-frequency signals gradually shorten. The results show that, under the higher initial stress, the compaction behavior of fracture no longer occurs in the linear elastic stage, and the contact behavior of the particles is low. With the increase in the number of cycles, local microcracks and small events are also increasingly fewer in the linear elastic stage.

(4) In the plastic stage, the stresses at 73% σ_c and σ_c show a stress-strengthening phenomenon of decrease first and then increase, and the amplitude signals also show a prominent characteristic at the stresses above. Compared with 73% σ_c, the duration at σ_c is longer, which indicates that the stress strengthening of rock can improve the stiffness of the rock block in a short time. This makes the rock produce microfractures in a more brittle form and causes the AE behavior to be easier to monitor. The number of high-frequency signals reaches the maximum among all cycles, and the frequency range of the intermediate-frequency signals also increases. This indicates that the damage accumulation in the rock is accelerated, and a large quantity of fracture expands rapidly. In the test process, the fractures coalesce to form macrocracks at 470 s.

(5) In the softening stage, the amplitude and high-frequency signals show a continuous change characteristic, and the peak amplitude decreases slightly. The intermediate- and low-frequency signals only appear at the peak strength and residual strength. This is because the stress in the rock is redistributed to reach the next equilibrium point, and the time provided for stress distribution in the softening stage is extremely short, resulting in few microfractures and causing a decrease in the peak strength and the sparsity of the intermediate- and low-frequency signals.

With the increase in initial stress, the variation form of the peak amplitude changes from V-type to N-type, and the distribution of the peak frequency is more concentrated. This is very dense in a certain small frequency range. It is considered that, in the loading section starting from zero stress, a higher initial stress reduces the occurrence of irregular plastic deformation, making the distribution range of the peak frequency more concentrated, so that it gathers the distribution of the peak frequency. In addition, the Kaiser effect of AE becomes weak when σ_0 = 12.5 MPa.

Figure 8 shows the change process of frequency value with peak stress in each frequency band. To better compare the frequency changes at each initial stress, the low-frequency and high-frequency values under σ_0 = 12.5 MPa in the figure were reduced by an order of magnitude. It can be seen from the figure that the variations of the three kinds of frequency at σ_0 = 2.5 MPa first decrease and then increase, with the change critical point of peak stress of 17.5 MPa, changing in a hook shape, which are consistent with the law under different loading rates. Under σ_0 = 7.5 MPa, the variations of the three kinds of frequency show a bowl shape change, which first decrease and then increase, in which the low-frequency changes not obviously because of its small value. Under σ_0 = 12.5 MPa, the changes of the three kinds of frequency become more complex, which are generally composed of two to three paraboloids, beginning with the decrease tend, ending with the decrease in the low-frequency and intermediate-frequency, ending with the increase in the high-frequency. This shows that the development process of particle and fracture in the earlier cycles reduce significantly, and the compression of fracture, the contact and extrusion of particles are restrained near the failure of rock, in which period the fracture expand vigorously.

The number of frequency signals in the three frequency bands in **Figure 7** and the amplitude attenuation value in the softening stage are recorded in **Table 6**. With the increase in initial stress, the amplitude attenuation value of the softening stage gradually decreases, and the intermediate-frequency signals also gradually decrease. This indicates that a higher initial stress inhibits the compaction behavior of fractures. Moreover, the high-frequency

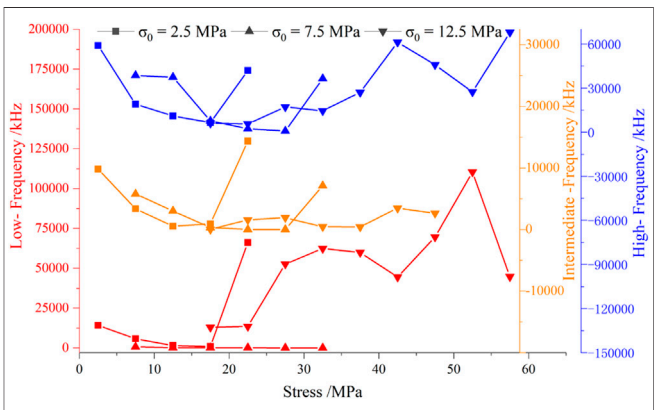

FIGURE 8 | Variation of frequency value with peak stress in each frequency band under different initial stresses.

TABLE 6 | Number of signals of the three frequency bands and amplitude attenuation value of the softening stage under different initial stresses.

Initial stresses σ_0	Frequency and amplitude			
	Number of signals of the three frequency bands			Amplitude attenuation value of the softening stage
	High-frequency (%)	Intermediate-frequency (%)	Low-frequency (%)	
2.5 MPa	30.0	11.0	59.0	4.0
7.5 MPa	71.0	4.0	25.0	2.0
12.5 MPa	6.9	0.1	93.0	0.0

signals increase first and then decrease, and the low-frequency signals decrease and then increase. It is considered that there is a critical value of initial stress σ_m = 7.5 MPa. When $\sigma_0 < \sigma_m$, the higher the initial stress, the more the extending behavior of fractures, and the less the extrusion behavior of particles. When $\sigma_0 > \sigma_m$, the opposite of the above occurs.

Distribution Characteristics of AE Event Amplitude and Energy

Different Loading Rates

Figure 9 shows the distribution of AE event amplitude and energy under different loading rates. It can be seen that under v = 0.15 mm/min, the distributions of amplitude and energy of rock were relatively dispersed, which mainly occurred in the three sections of 50–250, 500–700 and 1,000–1,180 s.

(1) In the first section (50–250 s), the energy was concentrated in a 10 s interval, and its value is very low, but the amplitude showed the law of dispersed change of decreasing first and then increasing, which shows that the internal lattice was moving back and forth, and when the movement accumulated to a certain extent, the energy was released concentratedly.
(2) In the second section (500–700 s), the energy also began to show a dispersed distribution, but the distribution of amplitude became dense, showing the law of increasing first and then decreasing, which is consistent with the stress change of loading first and then unloading, indicating that secondary fractures began to appear gradually in this section [23].
(3) In the third section (1,000–1,180 s), the energy and amplitude both increased first and then decreased. The maximum values were located at 1,080 s, which is the peak strength point of rock. Compared with other sections, the increase value of energy was far greater than the amplitude, which indicates that the large-scale fracture of saturated limestone was less when reaching the peak strength, only the sudden generation of many small-scale fractures leaded to the energy of rock was released concentratedly; the energy and amplitude decrease immediately after the peak strength point; at 1,180 s, the rock broke down, only the amplitude increased at that moment, but its value was lower than which at the peak strength point in terms of signal quantity and amplitude. The results also show that the energy increased suddenly from a very low value near 1,080 s, and the amplitude decreased first and then increased. Near 1,180 s, the rock was close to failure, and the energy showed a low value shortly after the peak strength (1,100 s), while the amplitude exhibited a trend of intermittent gradual decrease of 1,100 and 1,170 s.

Under v = 0.2 mm/min, the variation of amplitude and energy of rock can be divided into two types as following.

(1) The first type is 20–80 and 720–900 s. The characteristics of the change is that the amplitude and energy all showed continuous change, and generally increased first and then decreased. Near 850 s (the stress is close to the peak strength), the amplitude showed the law of sparsity first and then densification, decrease first and then increase, and the energy value was sporadic distribution and not obvious. Near rock-failure point, the amplitude also exhibited a trend of intermittent decrease, and the energy exhibited a low value between the peak strength and the rock-failure point.
(2) The second type is 200–300 and 500–600 s. The characteristic of the change is: the amplitude and energy first exhibited a trend of gradual increase, then the signal disappears after reaching the maximum value, and then the signal appears again in the next 100 s, the amplitude and energy of which are slightly less than the previous maximum value.

Under v = 0.3 mm/min, the amplitude of rock showed a continuous change, exhibiting a "increase decrease increase" trend, and the energy was distributed dispersedly at 350, 550, 875 and 1,000 s. At 875 s (the peak strength), the energy increased greatly, reaching the maximum value of the whole loading and unloading process, while the amplitude decreased. It is considered via analysis that when the rock is loaded to the peak strength, due to the high loading rate, there was almost no chance of forming large-scale fractures that can control the rock-failure, which made the rock develop macro cracks extensively in a short time, therefore, quantities of energy was released in the rock, but the amplitude of the signals was not high. Near 875 s (the stress is close to the peak strength), the amplitude exhibited a "decrease-increase" trend, in which the "increase" process made the amplitude show the maximum value of the whole loading and unloading process, and some sporadic energy signals appeared near 875 s. Near 1,000 s, the rock was close to failure at that moment, the amplitude exhibited a continuous downward trend, however, the energy increased slightly during the period of peak strength point to the rock-failure point.

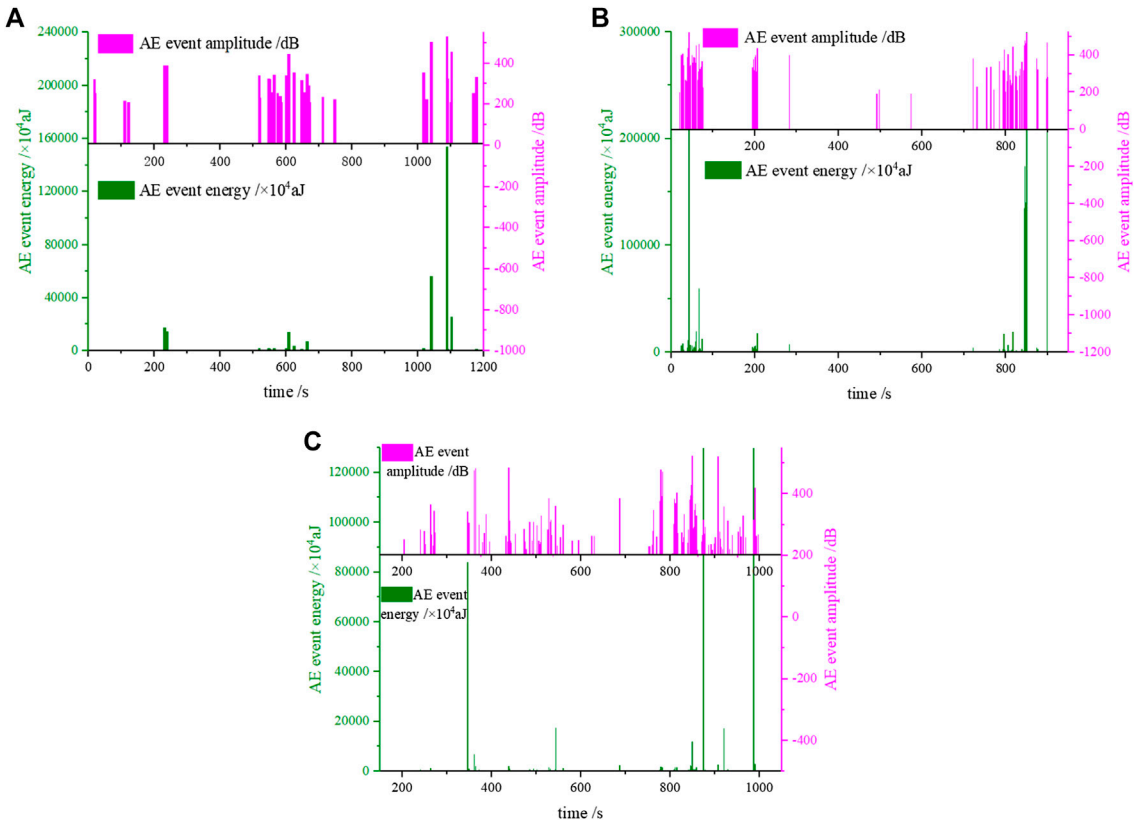

FIGURE 9 | The distribution of AE event amplitude and energy under different loading rates. **(A)** v = 0.15 mm/min; **(B)** v = 0.2 mm/min; **(C)** v = 0.3 mm/min.

Based on the data of the distribution of AE event amplitude and energy under different loading rates, it can be seen that the AE event energy of saturated limestone decreased first and then increased during loading and unloading. Except for the amplitude value under v = 0.3 mm/min, the maximum values of amplitude and energy in the whole test all occurred at the peak strength. Near the peak strength point, the amplitude decreased first and then increased, and the energy value exhibited less and low. Near rock-failure point, the amplitude exhibited a downward trend, and the energy value also exhibited less and low. The law above can be used as the precursor information of reaching the peak strength point and rock-failure point. With the increase of loading rate, the change form of amplitude in whole test was changed from disperse to continuity. Near rock-failure point, the change trend of amplitude changed from intermittent decrease to continuous decrease, during the period, the occurrence time of low energy value changed from peak strength point to the middle time between peak strength point and rock-failure point.

Different Initial Stresses

Figure 10 shows the distribution of AE event amplitude and energy under different initial stresses. It can be seen that under σ_0 = 2.5 MPa, 7.5 MPa, the amplitude and energy of rock exhibited a trend of decreasing first and then increasing, which was mainly composed of 4-6 sections, in which the amplitude was distributed in each section, however, the energy was only distributed in the first, second and last section. Near the peak strength point (850 s under σ_0 = 2.5 MPa, 470 s under σ_0 = 7.5 MPa), the amplitude of rock exhibited a trend of sparsity first and then densification, low first and then high, and the energy showed was not obvious. Near rock-failure point (900 s under σ_0 = 2.5 MPa, and 490 s at σ_0 = 7.5 MPa), the amplitude exhibited an intermittent decreasing trend, and the energy exhibited a very low value. Under σ_0 = 12.5 MPa, the distribution of amplitude and energy became dense and concentrated, which concentrated at 200–1,300 and 1.900–2,000 s. Before 1,960 s in the test, the energy varies slightly. Near 1,960 s (peak strength point), the amplitude and energy exhibited a change law of "low-high-low". Near 2,000 s, the rock is near rock-failure at that moment, but the amplitude and energy did not appear. It is considered via analysis that high initial stress made saturated limestone easier to show ductility, which made local rock block exhibit ductile failure at the peak strength point, triggering the adjustment of local stress, and further reduced the crack development near rock-failure [12].

According to the distribution data of AE event amplitude and energy under different initial stresses, it can be seen that the maximum value of amplitude of rock in the whole test all occurred at the peak strength point, and the maximum value of energy all occurred at the rock-failure point. Near peak strength point, with the increase of initial stress, the change trend of amplitude changed from "low-high" to "low-high-low" and the signal quantity is less and more concentrated,

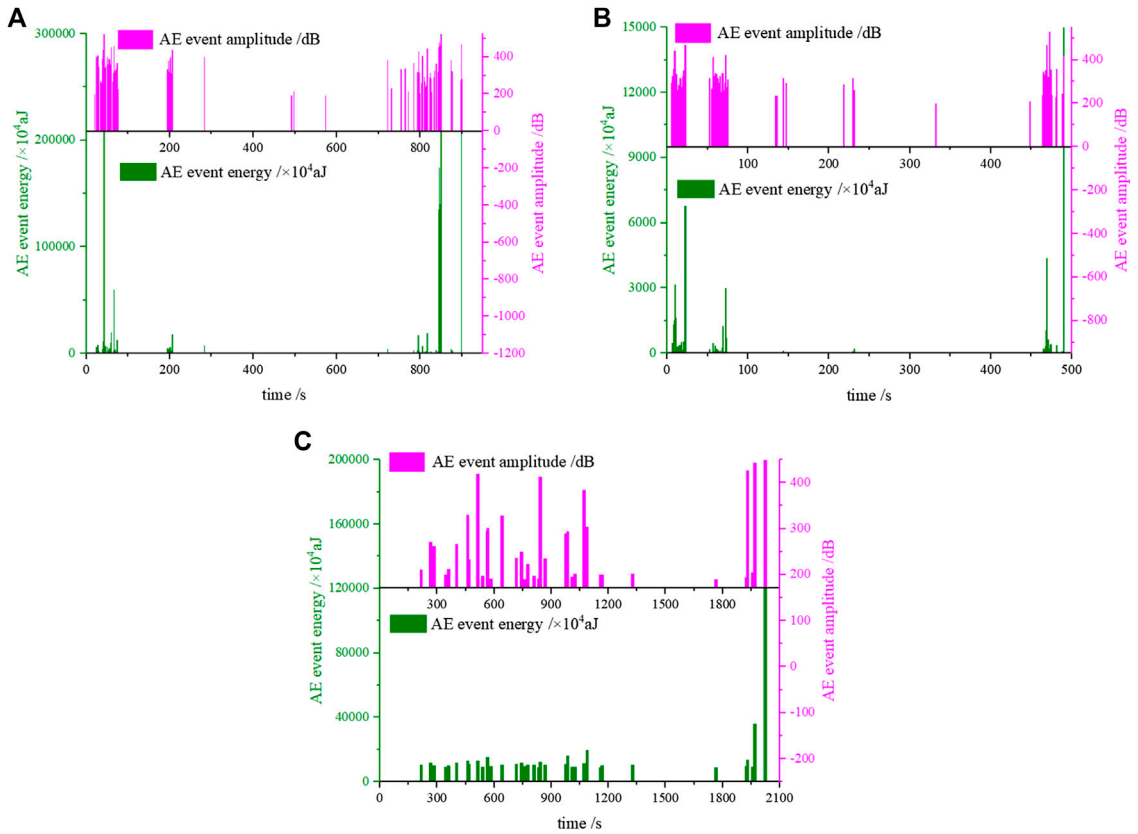

FIGURE 10 | The distribution of AE event amplitude and energy under different initial stresses. **(A)** σ_0 = 2.5 MPa; **(B)** σ_0 = 7.5 MPa; **(C)** σ_0 = 12.5 MPa.

which indicates that the energy distribution characteristic changed from dispersed under low initial stress to concentrated under high initial stress; however, the energy remained calm all the time, which indicates that the failure form of saturated limestone was gradual. On the other hand, near rock-failure point, with the increase of initial stress, the change trend of amplitude changed from "intermittent gradual decrease" to " not appear," which indicates that the rock-failure behavior and AE event evolution form changed from ductility to brittleness [25]. The phenomena above can be used as the precursory information of peak strength point and rock-failure point.

CONCLUSIONS

(1) With an increase in the loading rate and a decrease in the initial stress, the viscoplasticity of saturated limestone under loading and unloading is strengthened, the internal friction angle decreases, and the fragmentation during rock failure decreases. The failure mode changes from tensile failure to shear failure.

(2) During the loading and unloading, the intermediate-frequency signal shows a variation trend of sparse–dense–sparse and decreases with the increase in initial stress. However, the low-frequency signal is produced continuously and massively, and the amplitude attenuation value of the softening stage decreases with the increase in loading rate and initial stress.

(3) With an increase in the loading rate, the development trend of hits and energy becomes closer, and the maximum increase in hits is advanced. The variation form of ringing count changes from the former-N-type to U-type and latter-N-type, the slight increase period and attenuation period become longer, and the intense growth period and the postpeak calm period shorten. With the increase in initial stress, the felicity effect becomes better, and the variation of energy is more obvious near the failure than the hits. The variation form of the ringing count changes from U-type to W-type and N-type. Each period shortens first and then extends.

(4) With the process of loading and unloading, under a lower loading rate, the increase in hits and energy in the step and slow-change period increases continuously, and the duration of energy in the step and slow-change period increases gradually. With the increase in the loading rate, the variation trend of increase in the slow-change period tends to increase–decrease. In step, it tends to first increase–decrease and then gradually increase. With an increase in the initial stress, the variation trends of increase and duration of energy in the step and slow-change period all tend to decrease–increase.

(5) The increase and duration of hits in steps I and II exhibit the trend of increase–decrease with an increase in the loading rate, which exhibits a decreasing trend with an increase in the initial stress.
(6) The research results above bring the following enlightenment to the engineering site: for the deep surrounding rock which is eroded by groundwater for a long time, increasing the excavation speed and reducing the initial excavation footage, drilling strength can help to release the load in the form of deformation generally, and cause tension failure even burst not to occur easily and suddenly. With the progress of excavation, the compression behavior of surrounding rock fractures will appear a less-more-less change, so the support should be strengthened in the early and late period of excavation. With an increase in the excavation speed, the most period of rock fracture behavior will come in advance, and the synchronization of the change of rock fracture and its internal energy become better, but the duration of small fracture in the early stage become longer. Therefore, the roadway should be quickly excavated in the early stage, and slowly excavated after a certain period of time, so as to delay the most period of fracture behavior. In addition, if a roadway is already in excavating and the initial excavation footage is large, generally speaking, the changing extent of internal energy of surrounding rock is greater than that of fracture behavior, so the focus of safety monitoring should be transferred from crack inspection to rock deformation monitoring.

DATA AVAILABILITY STATEMENT

The raw data supporting the conclusions of this article will be made available by the authors, without undue reservation.

AUTHOR CONTRIBUTIONS

All authors listed have made a substantial, direct, and intellectual contribution to the work and approved it for publication.

FUNDING

This research was supported in part by Key Laboratory of Rock Mechanics and Geohazards of Zhejiang Province under Grant ZJRMG-2018-Z03; in part by the National Natural Science Foundation of China under Grant 51774323; and in part by the Fundamental Research Funds for the Central Universities of Central South University under Grant 2019zzts671.

REFERENCES

1. Wang H, Yang TH, Liu HL, Zhao YC. Deformation and acoustic emission characteristics of dry and saturated sand under cyclic loading and unloading process. *J North East Univ (Nat Sci)* (2016) 37:1161–5. doi:10.3969/j.jssn.1005-3026.2016.08.020.
2. Khandelwal M and Ranjith PG. Study of crack propagation in concrete under multiple loading rates by acoustic emission. *Geomech Geophy. Geo-energ Geo-resour* (2017) 3:393–404. doi:10.1007/s40948-017-0067-1.
3. Sagar RV and Rao MVMS. An experimental study on loading rate effect on acoustic emission based b-values related to reinforced concrete fracture. *Construct Build Mater* (2014) 7:460–72. doi:10.1016/j.conbuildmat.2014.07.076.
4. Cong Y, Wang ZQ, Zheng YR, and Zhang LM. Experimental study on acoustic emission features of marbles during unloading failure process. *J Southwest Jiao Tong Univ* (2014) 49:97–104.
5. Meng Q, Zhang M, Han L, Pu H, and Nie T. Effects of acoustic emission and energy evolution of rock specimens under the uniaxial cyclic loading and unloading compression. *Rock Mech Rock Eng* (2016) 49:1–14. doi:10.1007/s00603-016-1077-y.
6. Li HR, Yang CH, Liu YG, Chen F, and Ma HL. Experimental study of ultrasonic velocity and acoustic emission properties of salt rock under uniaxial compression load. *Chin J Rock Mech Eng* (2014) 33:2107–16.
7. Rodríguez P, Arab PB, and Celestino TB. Characterization of rock cracking patterns in diametral compression tests by acoustic emission and petrographic analysis. *Int J Rock Mech Min Sci* (2016) 83:73–85. doi:10.1016/j.ijrmms.2015.12.017.
8. He J, Pan JN, and Wang AH. Acoustic emission characteristics of coal specimen under triaxial cyclic loading and unloading. *J China Coal Soc* (2014) 39:84–90. doi:10.13225/j.cnki.jccs.2013.0159.
9. Song J, Li SC, Liu B, Yang L, Xu XJ, Nie LC, et al. Study on resistivity response law of limestone in processes of constant amplitude and tiered cyclic loading and unloading. *Chin J Rock Mech Eng* (2015) 34:3880–7. doi:10.13722/j.cnki.jrme.2014.1718.
10. Deng CF, Liu JF, Chen L, Li Y, and Xiang G. Mechanical behaviours and acoustic emission characteristics of fracture of granite under different moisture conditions. *Chin J Geotech Eng* (2017) 39:1538–44. doi:10.11779/cjge201708023.
11. International Society for Rock Mechanics. Basic geotechnical description of rock masses. *Int J Rock Mech Min Sci Geomech Abstr* (1981) 18:85–110. doi:10.1016/0148-9062(81)90277-1.
12. Yang DH, Zhao YX, Zhang C, Teng T, He X, Wang W, et al. Experimental study on the influence of cyclic loading on Kaiser effect of sedimentary rocks. *Chin J Rock Mech Eng* (2018) 37:2697–708. doi:10.13722/j.cnki.jrme.2018.0394.
13. AlShebani MM and Sinha SN. Deformation characteristics of brick masonry due to partial unloading. *Struct Eng Mech* (2001) 11:565–74. doi:10.12989/sem.2001.11.5.565.
14. Xiao XC, Ding X, Zhao X, Pan YS, Wang AW, and Wang L. Experimental study on acoustic emission and charge signals during coal failure process at different loading rates. *Rock Soil Mech* (2017) 38:3419–26. doi:10.5772/33834.
15. Su GS, Yan SZ, Yan ZF, Zhai SB, and Yan LB. Evolution characteristics of acoustic emission in rockburst process under true-triaxial loading conditions. *Rock Soil Mech* (2019) 40:1673–82.
16. Liu XS, Ning JG, Tan YL, and Gu QH. Damage constitutive model based on energy dissipation for intact rock subjected to cyclic loading. *Int J Rock Mech Min Sci* (2016) 85:27–32. doi:10.1016/j.ijrmms.2016.03.003.
17. Chen W, Konietaky H, Tan X, and Frühwirt T. Pre-failure damage analysis for brittle rocks under triaxial compression. *Comput Geotech* (2016) 74:45–55. doi:10.1016/j.compgeo.2015.11.018.
18. Kong B, Wang EY, Li ZH, Wang XR, Niu Y, and Kong XG. Acoustic emission signals frequency-amplitude characteristics of sandstone after thermal treated under uniaxial compression. *J Appl Geophys* (2017) 136:190–7. doi:10.1016/j.jappgeo.2016.11.008.
19. Ohnaka M and Mogi KJ. Frequency characteristics of acoustic emission in rocks under uniaxial compression and its relation to the fracturing process to failure. *Geophys. Res.* (1982) 87:3873–84. doi:10.1029/jb087ib05p03873.
20. Mavko G, Mukerji T, and Dvorkin J. *The rock physics handbook: tools for seismic analysis of porous media. Cambridge*, UK: Cambridge University Press (2003) p. 339.
21. Raymer LL. An improved sonic transit time-to-porosity transform. *Trans. Soc. Prof. Well Log Anal., Ann. Logging Symp.* (1980) 1–13.

22. Goodfellow SD, Tisato N, Ghofranitabari M, Nasseri MHB, and Young RP. Attenuation properties of fontainebleau sandstone during true-triaxial deformation using active and passive ultrasonics. *Rock Mech Rock Eng* (2015) 48:2551–66. doi:10.1007/s00603-015-0833-8.
23. Wang CY, Chang XK, Liu YL, and Chen SJ. Mechanistic characteristics of double dominant frequencies of acoustic emission signals in the entire fracture process of fine sandstone. *Energies* (2019) 12. doi:10.3390/en12203959.
24. Su ZD, Sun JZ, Xia J, and Wu CL. Research on effects of freeze-thaw cycles on acoustic emission characteristics of granite. *Chin J Rock Mech Eng* (2019) 38: 865–74. doi:10.13722/j.cnki.jrme.2018.0953.
25. Yang HM, Wen GC, Hu QT, Li YY, and Dai LC. Experimental investigation on influence factors of acoustic emission activity in coal failure process. *Energies* (2018) 11. doi:10.3390/en11061414.
26. Dong LJ, Hu QC, Tong XJ, Liu YF. Velocity-free MS/AE source location method for three-dimensional hole-containing structures. *Engineering* (2020) 6(7):827–834. https://doi.org/10.1016/j.eng.2019.12.016.
27. Dong LJ, Zou W, Li XB, Shu WW, Wang ZW. Collaborative localization method using analytical and iterative solutions for microseismic/acoustic emission sources in the rockmass structure for underground mining. *Eng Fract Mech* (2019) 210:95–112.

Conflict of Interest: The authors declare that the research was conducted in the absence of any commercial or financial relationships that could be construed as a potential conflict of interest.

frontiers in Physics

ORIGINAL RESEARCH
published: 15 January 2021
doi: 10.3389/fphy.2020.592483

Microscopic Failure Mechanism Analysis of Rock Under Dynamic Brazilian Test Based on Acoustic Emission and Moment Tensor Simulation

Zilong Zhou[1], *Jing Zhou*[1], *Yuan Zhao*[1]*, *Lianjun Chen*[2]* *and Chongjin Li*[1]

[1]School of Resources and Safety Engineering, Central South University, Changsha, China, [2]Key Laboratory of Mining Disaster Prevention and Control, Qingdao, China

The dynamic tensile failure of rock is a main failure mode in deep underground engineering projects. The microscopic failure mechanism analysis of this failure mode plays a key role in dynamic disaster warning. Moment tensor inversion is a very well-known method used to analyze failure mechanisms. However, an acoustic emission (AE) event cannot be accurately distinguished in rock dynamic experiments at the laboratory scale, because there are hundreds of AE events generated within a few hundred microseconds in one dynamic test. Therefore, moment tensor analysis is rarely applied in rock dynamic tests with laboratory scale. In this paper, AE and moment tensor simulations with the discrete element method (DEM) are introduced to analyze the microscopic failure mechanism of rock under a dynamic Brazilian test. Comparing the simulation results of AE and moment tensor analysis with the simulation results of micro-crack with DEM, the moment tensor discriminant method can obtain the mechanical mechanism and energy level of micro-cracks. Furthermore, R, which is the ratio of isotropic and deviatoric components of the moment tensor, is used to analyze the AE source mechanism. The implosion, shear, and tensile of the AE source mechanism can better explain the evolution process of main axial crack and the shear failure zones of the Brazilian disc specimen under dynamic tensile simulation. These findings contribute to a better understanding of the microscopic failure mechanism of rock under a dynamic tensile test than the statistical types of micro-cracks based on break bonds with DEM.

Keywords: moment tensor, rock dynamics, microscopic mechanism, discrete element method, acoustic emission

OPEN ACCESS

Edited by:
Guoyang Fu,
Monash University, Australia

Reviewed by:
Laurent Olivier Louis,
New England Research, United States
Shida Xu,
Northeastern University, China

***Correspondence:**
Yuan Zhao
zhaoyuan92@csu.edu.cn
Lianjun Chen
creejxk@163.com

Specialty section:
This article was submitted to Interdisciplinary Physics, a section of the journal Frontiers in Physics

Received: *07 August 2020*
Accepted: *30 November 2020*
Published: *15 January 2021*

Citation:
Zhou Z, Zhou J, Zhao Y, Chen L and Li C (2021) Microscopic Failure Mechanism Analysis of Rock Under Dynamic Brazilian Test Based on Acoustic Emission and Moment Tensor Simulation. Front. Phys. 8:592483. doi: 10.3389/fphy.2020.592483

INTRODUCTION

Dynamic tensile failure is a main mode of rock failure in deep underground engineering projects [1, 2]. The microscopic failure mechanism of this failure mode is vital for dynamic disaster warning. It is important and necessary to study the micromechanical mechanism of rock dynamic tensile failure [3]. Moment tensor inversion is a very well-known method used to analyze failure mechanisms [4, 5]. However, an acoustic emission (AE) event cannot be accurately distinguished in rock dynamic experiments at laboratory scale. The sampling rate of AE or micro-seismic monitoring equipment is about 10 MHz. The time of one rock dynamic experiment with SHPB is about 250 μs [6]. There are

hundreds of AE events generated in one rock dynamic test. Therefore, moment tensor analysis is rarely applied in rock dynamic tests with laboratory scale. DEM simulation is also widely used to study failure mechanisms [7, 8]. The bond between particles break and many broken bonds will lead to rock failure when the rock specimen is under force action in simulation, which is often used to analyze the meso-crack extension [9]. The type statistics of bond break is used to distinguish the rock dynamic failure type [10]. However, the rock dynamic experiment and simulation studies show that the micro-crack of rock materials is mainly of the tensile crack variety no matter what the macroscopic failure mode is [11]. Therefore, a wrong result may be found if the macroscopic failure pattern is directly judged by statistical micro-crack types [12].

Some scholars introduced AE simulation based on DEM. Then the theory of AE can be used to analyze the micromechanical steps of the rock failure process with simulation. Hazzard and Young defined the range of bond break interplay between each other according to the crack propagation speed, and recorded the kinetic energy release in the process of intergranular bond fracture. In a closely packed particle assembly, this kinetic energy manifests itself as a seismic wave that propagates out from the location of the bond breakage, similar to an AE in real rocks. This method was then used to simulate the AE source in the process of a granite compression experiment [13]. On the basis of these studies, Hazzard and Young proposed a method to simulate a moment tensor with DEM. Then it was used to simulate the AE and moment tensor analysis of the tunnel excavation process. Comparing with the actual monitoring results, it was found that the model generated many implosion events agreeing partially with the actual recorded seismicity [14]. Cai et al. established a coupled numerical method with the finite element method (FEM) and DEM to simulation AE at the Kannagawa underground powerhouse cavern in Japan [15]. Lisjak et al. used two-dimensional FEM–DEM coupling analysis to simulate the AE in brittle rocks [16]. Zhang and Zhang built a rock model with two prefabricated cracks by PFC. Then the moment tensor was simulated to analyze the compression failure process of this model. This study analyzed the crack generation mechanism by using the moment tensor solutions and the statistic of the types of bond break contained in an AE event. It was discovered that the main bond break model of an AE event is tensile, while the AE mechanism is compression [17]. Zhang and Zhang used the moment tensor to distinguish the nature of primary cracks and secondary cracks in a single flaw-contained specimen based on the bonded-particle model [12, 18].

Previous studies mentioned above show that AE source simulation and moment tensor analysis have great advantages in studying rock fracture mechanisms. In this paper, we introduce this method of AE and moment tensor simulation based on PFC to analyze the micromechanical mechanism of the rock dynamic tensile failure process. Firstly, the model of SHPB for dynamic Brazil splits is established. Then, we introduce the theory of AE definition and moment tensor. Finally, the microscopic mechanism of macroscopic tensile crack generated in the middle and the shear zone at both ends of the Brazilian disk during the dynamic tensile failure process are analyzed by using the simulation results of AE and moment tensor.

MODELING APPROACH

Brief Description of Discrete Element Method

DEM was first proposed by Cundall in the 1970s [19, 20]. After years of development, it is now widely used in different fields. As a mature commercial software of DEM, PFC is often used to study the micro-fracture process of rock mass in the field of rock mechanics.

In PFC, the numerical models are respectively composed of particles with a certain density bonded by the contact. The particles are disks with a certain thickness in PFC2D. And in PFC3D, the particles are small spheres. Each particle can be translated and rotated, and the interaction between particles is simulated through contact. Particles only interact with neighboring particles. The relative displacement between particles is the basic variable, and its motion follows the classical motion equation. When a particle is subjected to an external force or constraint, it will generate forces and torques acting on neighboring particles. The acceleration of related particles can be obtained from Newton's second law. The velocity and displacement of particles and other parameters can be obtained through the time integral. The physical quantities of acceleration, velocity, displacement, and rotation angle of all particles at any time can be obtained through the repeated iterative cycle of time step.

The Model of Split Hopkinson Pressure Bar for Dynamic Tension

The model of SHPB for the dynamic tension test, established in this paper, consists of two materials. One is the SHPB bar and the other is the rock specimen. There are two methods to simulate the bars of SHPB using PFC, one is generated by an extrusion exclusion method. Firstly, particles are generated randomly in the area of the bars according to the set porosity and particle radius. Then the repulsive force is generated between the particles through repeated cycle calculation, and the randomly generated overlapping particles enter a state of close contact with each other under the action of repulsive force [21]. Another method is the regular arrangement method, which can be realized by generating the particles with same radius, orderly distributed in the bar region. Studies have shown that the bars generated by the regular arrangement method can greatly improve the generation speed. The stress wave propagates in the bar constituted of regularly arranged particles without attenuation and dispersion [22]. Therefore, we use the regular arrangement method to generate the incident bar and transmission bar in our paper. The contact model of the particles in the bars is a linear contact bond. The incident and transmitted bars are 1,250 and 750 mm long, respectively, with a diameter of 50 mm.

The specimen in this model is generated by the extrusion exclusion method. The particles are randomly generated with

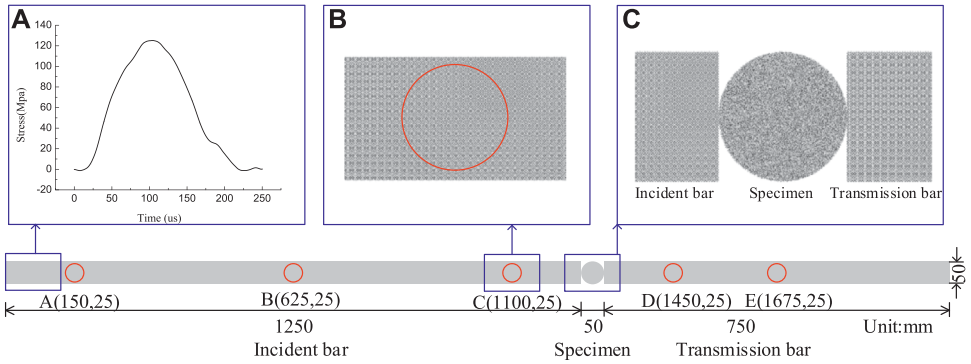

FIGURE 1 | The model of SHPB for dynamic tensile simulation. **(A)** The incident stress wave in simulation and experiment; **(B)** measure circles on the bars of this model; **(C)** the details of the specimen sandwiched between the incident and transmitted bars.

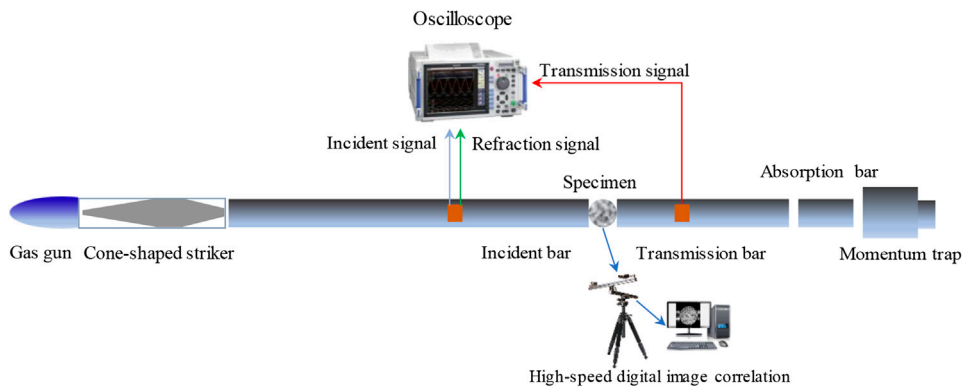

FIGURE 2 | SHPB, oscilloscope, and high-speed digital image correlation used in the rock dynamic tensile experiment.

specified porosity and radius in the specimen region. Then the repulsion force is generated between the originally overlapped particles through cyclic calculation, and finally the particle model with close contact is generated. The contact model of the particles in the specimen is a linear parallel bond. The model of SHPB for the dynamic tensile simulation is shown in **Figure 1**. The stress wave (**Figure 1A**) is loaded on the left end of the incident bar. Five measure circles (**Figure 1B**) are embedded in the incident and transmitted bars. **Figure 1C** contains the details of the specimen sandwiched between the incident and transmitted bars.

Microscopic Parameter Determined in the Simulation

To obtain microscopic parameters in the simulation, the dynamic tensile experiment of red sandstone is carried out using SHPB. SHPB, oscilloscope, and HS photography were used in this experiment as shown in **Figure 2**. The improved SHPB consists of a gas gun, a cone-shaped striker, an incident bar, a transmission bar, an absorption bar, and a momentum trap. All of the bars and the striker are made up of high strength 40 cr alloy with an elastic modulus of 233 GPa, a density of 7,670 kg/m^3, a P wave velocity of 5,462 m/s, and a yield strength of 800 MPa [23].

We use HS photography to obtain pictures during the failure process of the rock dynamic tensile test. The HS camera captured pictures in this experiment at a frequency of 79,161 frames/s with a resolution of 256 × 256 pixels. The HS camera uses an external trigger to start capturing images. When the voltage of strain gauge on the incident bar rises to −34 mv, the oscilloscope and HS camera are simultaneously triggered to ensure time consistency. The specimen used in this experiment is red sandstone with a radius of 50 mm and a height of 30 mm.

During the dynamic test, a longitudinal compressive wave (incident wave) is generated by the impact of a cone-shaped striker bar on the free end of the incident bar. Then this compressive wave (incident wave) propagates in the incident bar. When the compressive incident wave reaches the interfaces of bars and specimen, it is partly reflected (reflected wave), and the remainder passes through the rock specimen to the transmitted bar (transmitted wave). These three elastic stress pulses in the incident and transmitted bars are recorded with the strain gauges and denoted as the input strain pulse I(t), reflected strain pulse R(t), and transmitted strain pulse T(t), respectively

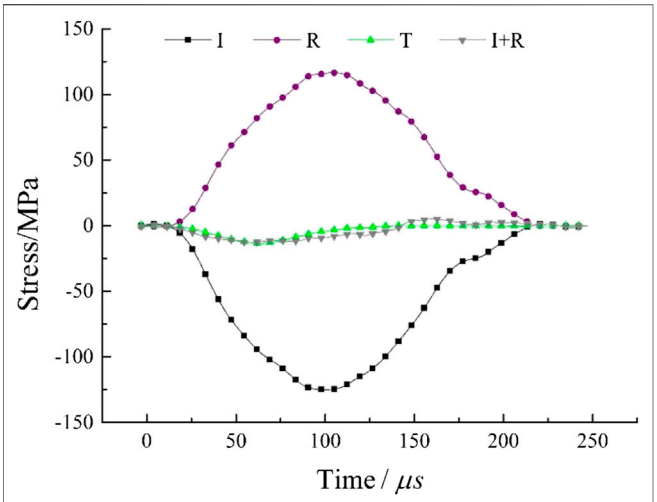

FIGURE 3 | Incident (I), reflected (R), transmitted (T), and incident + reflected (I + R) stress wave of the dynamic tensile experiment.

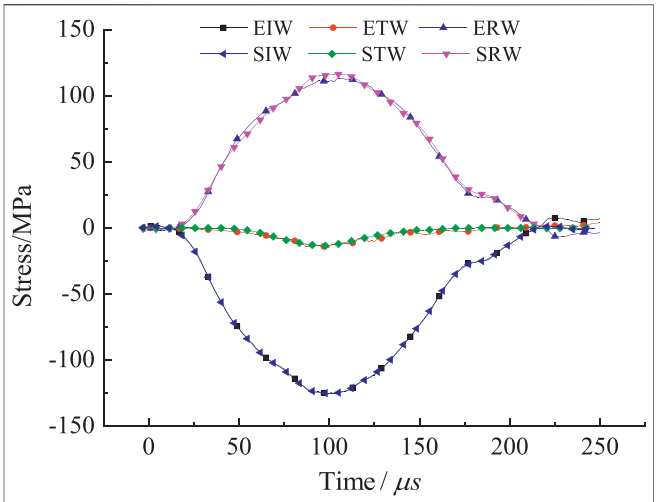

FIGURE 4 | The comparison of waveforms in experiment and simulation. The experimental incident wave (EIW) and the simulated incident wave (SIW) are identical. The experimental reflected wave (ERW) and the simulated reflected wave (SRW) as well as the experimental transmitted wave (ETW) and the simulated transmitted wave (STW) are also substantially similar.

[24]. The waveform data recorded by the oscilloscope are processed based on one dimensional stress wave theory [25, 26]. The results of incident stress wave, reflected stress wave, and transmitted stress wave are shown in **Figure 3**. The superposed waveform of the incident wave and the reflected wave is substantially the same as the transmitted wave near the peak, which verifies that this experiment satisfies the dynamic force balance.

We use the data of the incident wave in the dynamic test as the incident wave in the simulation. By adjusting the mesoscopic parameters in the simulation, the measured reflected wave and projected wave in the simulation are basically consistent with the experimental results, which ensures that the simulated dynamic tensile strength curve of red sandstone is basically consistent with the experimental results. The comparison results of the simulation and experimental waveforms are shown in **Figure 4**.

The microscopic and macroscopic parameters of the bars are shown in **Table 1**. The Young's modulus and density of the model corresponds to the experiment. The bond strength of the bar in this model is set extremely large to ensure that the bars will not deform during the impact process.

The specimen in this model is calibrated according to the dynamic tensile results of sandstone. The microscopic and macroscopic parameters of the specimen are shown in **Table 2**.

Acoustic Emission Definition in Dynamic Tensile Simulation

Studies have shown that, the bond break between contacted particles can simulate the micro-cracks in the simulation of rock with DEM [27]. Based on this, Young proposed that the break of a bond between particles can be used to simulate AE [8, 9]. When bonds break, energy is released and AE locations and magnitudes can be calculated. Therefore, bonded particle models provide a unique method to simulate AE [28]. Based on this, the AE definition in the dynamic tensile simulation will be introduced in this section.

When the incident wave propagates from the incident bar to the specimen, the bonds in the specimen begin to break under the action of the stress wave. This bond break is marked as the beginning of an AE. If each bond break is considered as an AE event, then the magnitudes of these AE events will be similar. This is not conformed to power-law distribution which is already a law of magnitude distribution recognized in seismology [29]. According to the characteristics of AE in rock mechanic experiments, bond breaks occurring close together in space and time are regarded as the same AE event in the simulation. This is similar with the actual AE monitoring, which distinguishes different AE events by setting peak definition time (PDT), hit definition time (HDT), and hit lockout time (HLT) of the AE signal. In the simulation, an AE event is determined by monitoring the bond break. The continuing AE event is determined by the number of calculating steps, which is 40 steps in this simulation. The restriction of an AE event calculating steps is verified by Hazzard and Damjanac [16]. The maximum area of an AE event is defined as 6 times the average particle radius. **Figure 5** is an AE event generation process in the dynamic tensile simulation. **Figure 5A** is the beginning state of this AE event. **Figure 5B** is the end state of this AE event.

The magnitude of AE is an important parameter for AE evaluation. In the PFC simulation, AE energy is calculated by the differences of strain energy before and after the AE event generation [30]. The strain energy can be expressed as:

TABLE 1 | The microscopic and macroscopic parameters of the bars.

Microscopic parameters		Macroscopic parameters	Steel	Model
Particle		Young's modulus (GPa)	233	233
Radius (mm)	0.5	Density (kg/m^3)	7,821	7,821
Density (kg/m^3)	9,963			
Bond				
Tensile strength (MPa)	1.05*10^5			
Shear strength (MPa)	1.05*10^5			

TABLE 2 | The microscopic and macroscopic parameters of the specimen.

Microscopic parameters		Macroscopic parameters	Red sandstone	Model
Particle		Density (kg/m^3)	2,337.5	2,350
Radius (mm)	0.25–0.5	Dynamic tensile strength	13.7	13.5
Density (kg/m^3)	2,350			
Young's modulus (GPa)	27			
Stiffness ratio kn/ks	2.0			
Friction coefficient	0.577			
Bond				
Radius multiplier	1			
Young's modulus (GPa)	27			
Stiffness ratio kn/ks	2.0			
Tensile strength (MPa)	18			
Frictional angle	40			

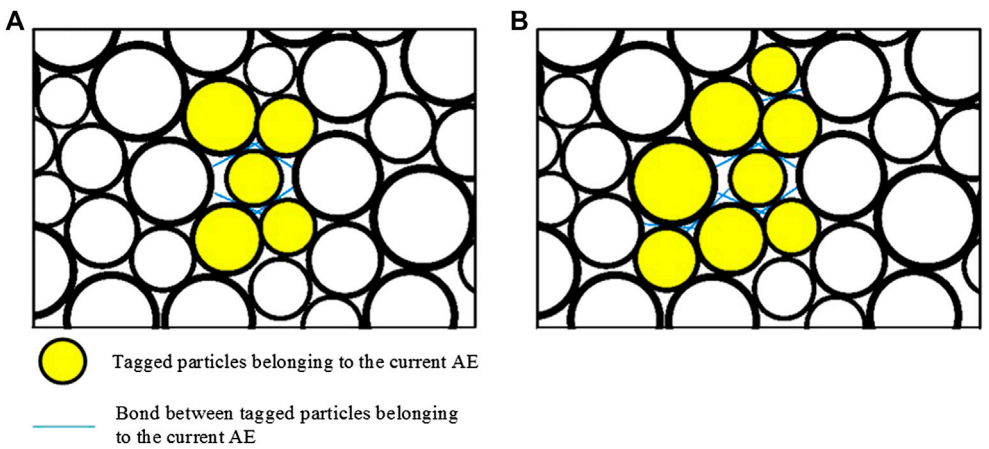

FIGURE 5 | An AE event generation process in this simulation. **(A)** is the start of an event and **(B)** is the finish state of this event.

$$E_c = \frac{1}{2}\left(\frac{|F^n|^2}{k^n} + \frac{|F^s|^2}{k^s}\right) \tag{1}$$

where F^n and F^s are normal and shear forces of contact; k_n and k_s are contact normal stiffness and contact shear stiffness.

For each calculation step, the strain energy of all particles in the AE region, E_k, is calculated, as:

$$E_k = \sum E_c^i \tag{2}$$

where E_c^i is the strain energy of the i contact in the AE region.

And the AE energy, ΔE_k, is equal to the final strain energy, E_k^f, minus the initial strain energy, E_k^0, in the AE region:

$$\Delta E_k = E_k^f - E_k^0 \tag{3}$$

then the magnitude can be expressed as [31]:

$$M_e = \frac{2}{3}\left(\log \Delta E_k^{\max} - 4.8\right) \tag{4}$$

Moment Tensor Calculation in the Dynamic Tensile Simulation

In seismology, a moment tensor is a mathematical representation of the movement on a fault during an earthquake, comprising

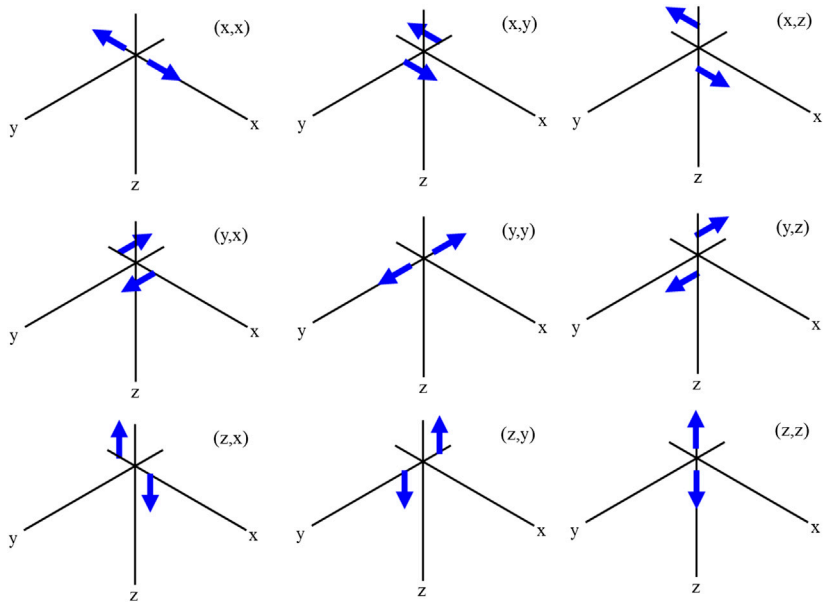

FIGURE 6 | The moment tensor comprising nine sets of two vectors.

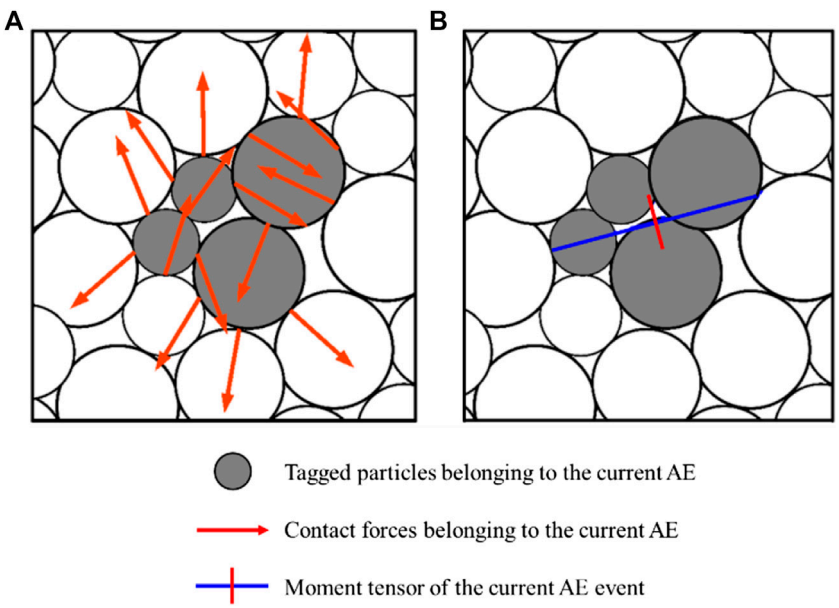

FIGURE 7 | The example of an AE event and its calculation moment tensor. **(A)** The contact force of all particles in an AE event. **(B)** The calculated moment tensor of this event. The length of these two lines represent the principal values of the moment tensor. The red line represents tensile and the blue line represents compression.

nine generalized couples, or nine sets of two vectors [32]. They are described in **Figure 6**. The tensor depends of the source strength and fault orientation.

In 2D, it can be expression as follows:

$$\mathrm{M} = \begin{bmatrix} M_{xx} & M_{xy} \\ M_{yx} & M_{yy} \end{bmatrix} \tag{5}$$

PFC simulation can directly obtain the force state and displacement of all particles under the external force of the model. In 2D, the contact force vector and the displacement vector between the contact point and the centroid of an AE event has components in two directions [14]. Then the moment tensor can be obtained based on the definition of AE in simulation. The detailed calculation process of a moment tensor is shown below:

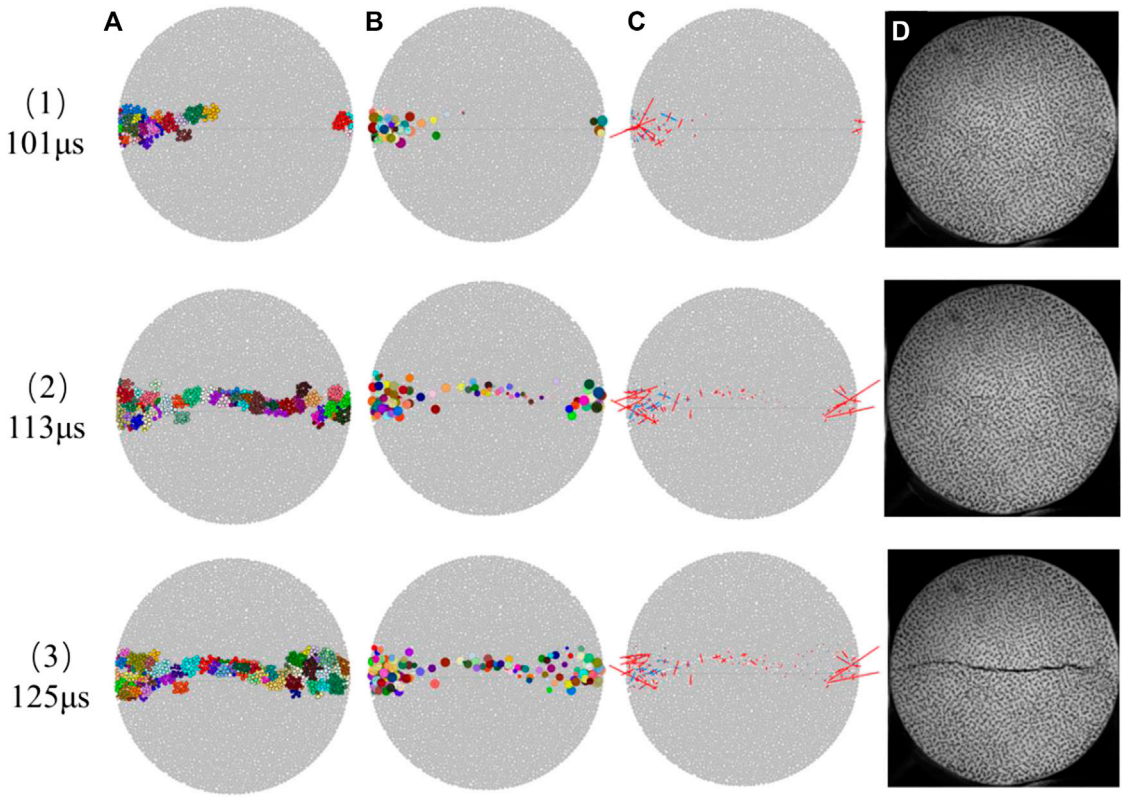

FIGURE 8 | The results of AE location, moment tensor in simulation, and HS photography before and after the axial macro-crack generated. **(A)** is the AE location at different moments; **(B)** is the AE normalization diagram with the initial generating position of each AE event as the center of the circle and the AE energy level value as the radius; **(C)** is the results of the moment tensor; **(D)** is the results of high speed photographs in the dynamic tensile experiment.

$$M_{ij} = \sum_{S} \Delta F_i R_j \tag{6}$$

where ΔF_i is the ith component of the contact force change in an AE event. R_j is the jth component of the distance between the contact point and the barycenter of the AE event. In 2D, there are two components of F and R, x and y. S is the number of contacts in the area of an AE event.

Figure 7 is the example of an AE event and its moment tensor. The contact forces of this AE event are shown in **Figure 7A**. The four Gy particles in the middle represent an AE event. The red arrows indicate the contact forces on the particles of this AE event. The value and action point of these contact forces can be directly obtained from the PFC simulation. Then the moment tensor can be calculated by **Eqs (5)** and **(6)**. The length of these two lines in **Figure 7B** represents the principle eigenvalues and eigenvectors of the matrix.

RESULTS OF ACOUSTIC EMISSION AND MOMENT TENSOR SIMULATION DURING THE DYNAMIC TENSION FAILURE OF ROCK

The rock dynamic tensile failure process is simulated by the SHPB model as established in the previous section. The AE and moment tensor of this failure process are calculated. The results of the moment tensor simulation and AE source mechanism are used to analyze the micro-mechanical mechanism of the rock dynamic tensile process. Studies show that the dynamic tensile process can be divided into two parts for analysis. One part analyzes the micro-mechanical mechanism of the main axial crack which is parallel to the impact direction and divides the specimen into two pieces. The other part analyzes the micro-mechanical mechanism of the shear failure zones that occur at the contact points of the Brazilian disk (BD) specimen [33]. These two parts will be analyzed separately in the following part.

Acoustic Emission and Moment Tensor of the Main Axial Crack Parallel to the Impact Direction

Figure 8 is the results of the AE and moment tensor before and after the axial macro-crack generated in the rock dynamic tensile simulation. **Figure 8A** shows the AE events as expressed by marked particles. **Figure 8B** is the normalized AE location of the left picture. Each AE event is expressed with a circle. The center of the circle is the barycenter of this AE event, and the radius is the value of the normalized AE event energy magnitude. Therefore, the middle picture can intuitively show the position and

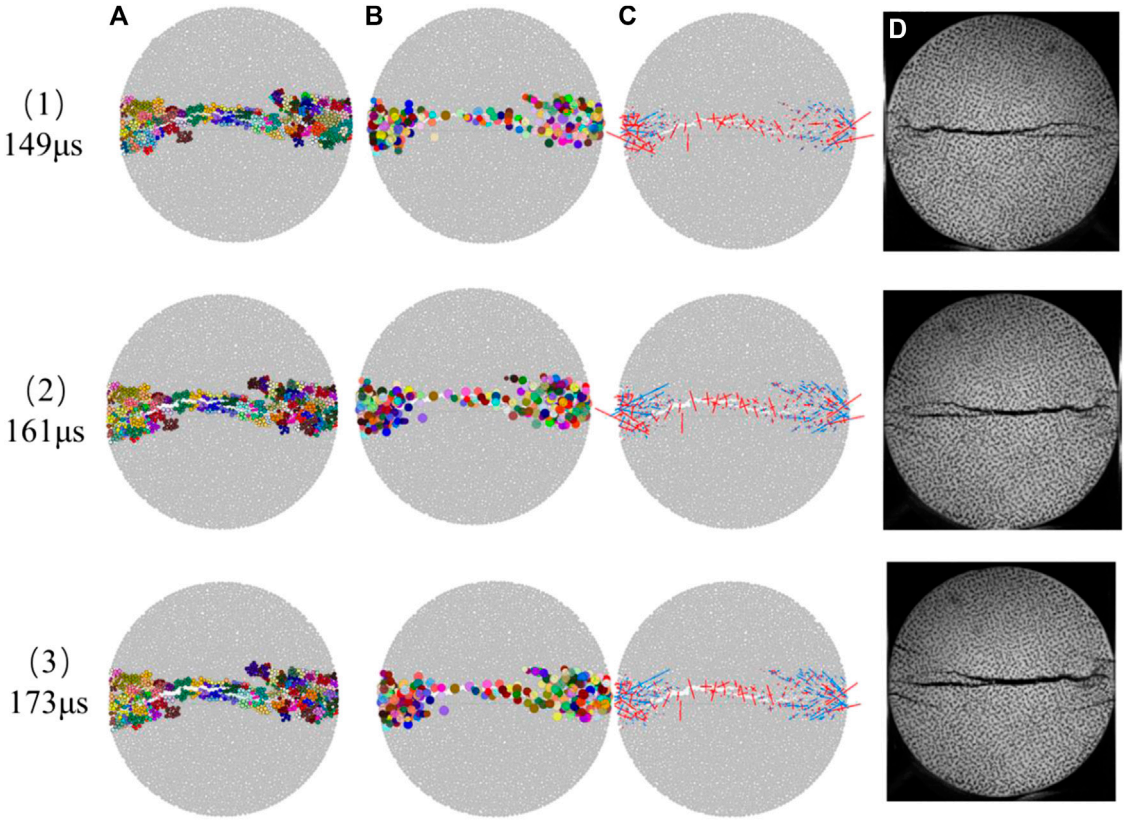

FIGURE 9 | The results of AE location, moment tensor in simulation, and HS photography before and after the shear failure zones. **(A)**–**(D)** of **Figure 9** correspond to the same figure values as **Figure 8**.

magnitude of each AE event. **Figure 8C** shows the results of the moment tensor simulation. The position of each moment tensor is the barycentric coordinates of an AE event. **Figure 8D** shows the results of HS photography.

Figures 8(1)–(3) are the results of the simulation and HS photography at 101 μs, 113 μs, and 125 μs, respectively. At 101 μs, the AE events distribute mainly in the two ends of the specimen, the cumulative number of these AE events is 76 with a magnitude range of −4.3 to −0.76. There is no macro-crack formation in the experiment from the results of the HS photographic image. **Figure 8**(2)B shows that most of these AE events are generated at middle of the specimen. The cumulative number of AE events is 116. The number of new AE events generated in this period is 40 with a magnitude range of −2.11 to −0.75. **Figure 8**(2)C shows the moment tensor of each AE event. **Figure 8**(2)D shows a macroscopic crack initiation at the middle of the specimen HS photographic image. At 125 μs, there are 41 new AE events generated with a magnitude range of −2.84 to −1.59. In the meantime, this initiation crack from the initiation position extends to the ends of the specimen in the experiment. From the results of the AE location and HS photography of these three stages, it can be found that macroscopic cracks occur only when the number of AE is enough or the AE magnitude reaches a certain value.

Acoustic Emission and Moment Tensor of the Shear Failure Zones

Studies show that there are shear failure zones that occur at the contact points of the BD specimen, which become more significant with an increase of loading rate, in the dynamic tensile experiment. The shear failure zone is a result of secondary fractures due to further compression between the bar and the cracked disc as demonstrated by the high-speed camera snapshots. In this section, the simulation results of the AE and moment tensor are used to analyze the generation process of the shear failure zones.

Figure 9 expresses the shear failure zones formation. **Figures 9**(1)–(3) show this new crack initiation, extension, and formation at 149 μs, 161 μs, and 173 μs, respectively. At 149, the new AE event generated at the ends of the specimen coincides with the results of the HS photographic image. There are 48 new AE events with a magnitude ranging from −3.25 to −1.08. At 161 μs, most of the new AE events continue to expand along the direction of the crack formed in the previous period. There are 23 new AE events with a magnitude of −2.6 to −1.27 in this period. The number of new AE events generated from 161 to 173 μs is 16 and the magnitude ranges from −2.14 to −0.89.

From the crack development process of the HS photography results and the corresponding AE simulation results in **Figures 8** and **9**, it can be concluded that the AE simulation in the rock dynamic tensile experiment is feasible. The simulation results of the AE location are consistent with the location of crack generation obtained by HS photography. The moment tensor simulation can explain the generation mechanism of the AE events. The microscopic failure mechanism of rock under a dynamic tensile test will be analyzed with the generation mechanism of AE events in the next section.

DISCUSSION

The results of AE and moment tensor simulation have shown that they can be used to analyze the dynamic tensile failure process. In this section, the AE source mechanism is calculated based on the simulation results of the AE location and moment tensor in order to analyze the micromechanical mechanism of the rock dynamic tensile failure process. Firstly, the calculation method of the AE source mechanism is described. Then, we compare the results of the discrete fracture network (DFN) obtained by the PFC to the results of the AE source mechanism.

The Calculation Method of the Acoustic Emission Source Mechanism

AE source mechanism analysis is an important method to study the rock crack propagation mechanism and rock failure mechanism [34, 35]. Based on the simulation results of the AE location and moment tensor, the AE source mechanism in the sandstone dynamic tensile simulation is analyzed in this section. According to the calculation method of the moment tensor in the rock dynamic tensile in Moment Tensor Calculation in the Dynamic Tensile Simulation, the moment tensor of the AE source at different moments is calculated and represented by a vector diagram.

The ratio R of the isotropic and deviatoric components of the moment tensor can be used to analyze the mechanical mechanism of each AE source, which was first proposed by Feignier and Young [32]. Zhang and Zhang [11] used this method to analyze the crack nature in the bridge region of two pre-existing flaws under compressive loading. In 2D, the ratio is expressed as follow:

$$R = \frac{tr(M) \times 100}{\left(\left| tr(M) \right| + \sum_{i=1}^{i} \left| m_i^* \right| \right)} \tag{7}$$

where tr(M) = (m_1+m_2), m_i and m_i^* (i = 1,2) are the eigenvalue and partial eigenvalues of matrix M, respectively.

$$m_i^* = m_i - tr(M)/2 \tag{8}$$

The value of R ranges from −100 to 100. The ratio R and corresponding AE source mechanism are shown in **Table 3**.

Microscopic Mechanism Analysis of the Rock Failure Process Under a Dynamic Brazilian Test

The value of R is calculated based on the moment tensor to analyze the AE source mechanism. AE source mechanisms can describe how the AE event is generated according to the position change of AE event formation relative to the initial position. Implosion is one of the AE source mechanisms, which means that this AE event is generated by extrusion. Therefore, the AE source mechanisms are used to analyze the microscopic mechanism.

Figure 10 is the microscopic mechanism of the generation process of main axial crack. **Figure 10A** is the results of DFN obtained by PFC. The blue lines are micro-shear cracks, and the red lines are micro-tensile cracks. In the user manual of PFC, the DFN is defined as a collection of fractures, which is often used to analyze failure type in rock mechanic simulations. A fracture will come out when a bond between two particles breaks. DFNs consist of two types: tensile fractures and shear fractures [36]. We use the results of DFN to obtain the micro-cracks. Then the statistics of micro-cracks are used to analyze mechanical mechanism of macro-crack. There are mainly micro-tensile cracks and a few micro-shear cracks in the generation process of main axial crack. **Figure 10B** is the AE source mechanism results of the main axial crack distinguished by the ratio R in the dynamic tensile simulation. The red box, blue triangle, and green circle show that the AE mechanism is tensile, implosion, and shear, respectively. The crack model in the center of the specimen is tensile in the process of the axial crack generation. At the ends of specimen, the crack model is mainly tensile in the initial stage. Then some shear cracks occurred. When the axial crack completely formed, the AE source mechanism models are mainly tensile, which is same with the results of the DFN fracture.

Figure 11 is the statistical results of **Figure 10**. **Figure 11A** is the number of different crack types increased from 100 to 126 μs obtained by PFC simulation. The tensile micro-cracks continued to increase, and no new shear micro-cracks appeared based on PFC simulation. **Figure 11B** is the number of different types of AE source mechanisms increased from 100 to 126 μs obtained by the value of R. The three types of AE source mechanisms all increase. The tensile fracture mechanism increases the most. Therefore, the fracture mechanism of axial crack in the middle of the specimen is tensile, which can be both obtained by the PFC simulation or AE source mechanisms.

Figure 12 is the microscopic mechanism of the shear zones generation in the ends of specimen. **Figure 12A** is the DFN fracture obtained by the PFC. The red lines represent the bond break mode between two particles, tensile crack. The blue lines represent the bond break mode, shear crack. **Figure 12B** is the results of the crack model obtained by the value R based on moment tensor simulation. The red box, blue triangle, and green circle show that the AE mechanism is tensile, implosion, and shear, respectively.

The results of the shear zone on both sides of the specimen in simulation are consistent in rock dynamic experiments of the existing research [37].

TABLE 3 | The ratio R and corresponding AE source mechanism.

Ratio R	−100	−100–−30	−30–30	30–100	100
AE mechanism	Pure implosion	Implosion	Shear	Tension	Pure tension

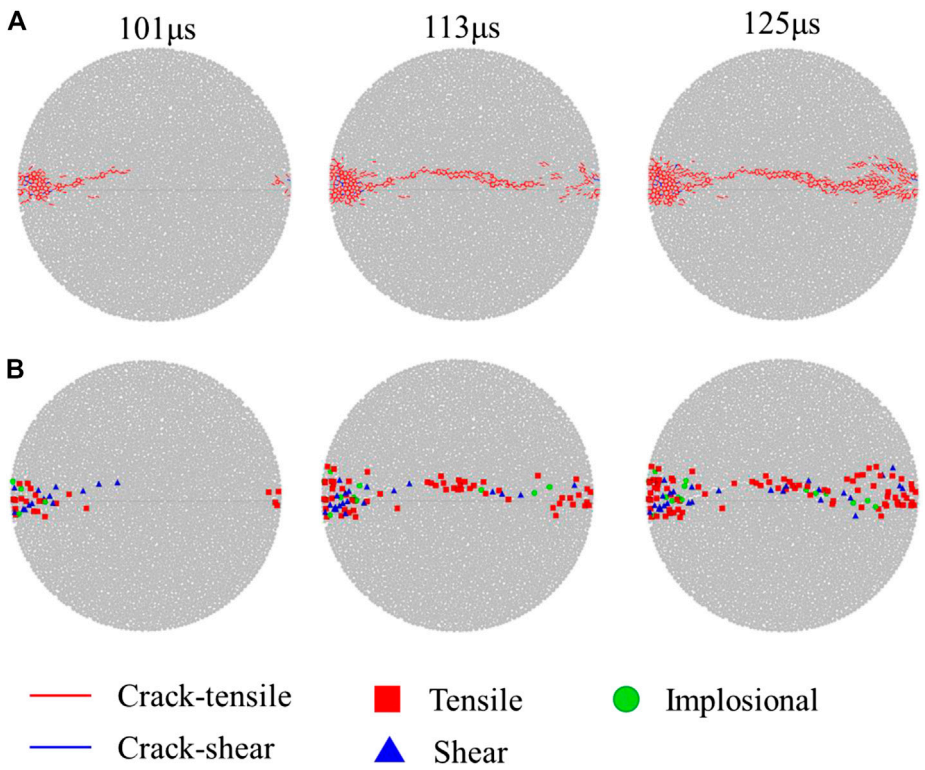

FIGURE 10 | Microscopic mechanism of the axial crack generation. **(A)** is the results of DFN obtained by PFC. **(B)** is the results of AE source mechanism obtained based on the moment tensor.

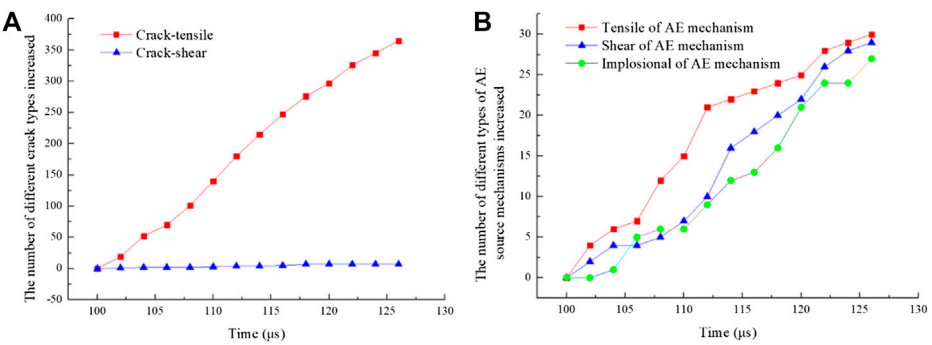

FIGURE 11 | The new increased micro-crack from 100 to 126 μs. **(A)** is the number of different crack types increased from 100 to 126 μs. **(B)** is the number of different types of AE source mechanisms increased from 100 to 126 μs.

Figure 13 is the statistical results of **Figure 12**. **Figure 13A** is the number of different crack types increased from 148 to 173 μs obtained by PFC simulation. The tensile micro-cracks continued to increase from 148 to 161 μs. Then it stays stable from 161 to 173 μs, between which time the shear zones are formed. This phenomenon coincides with the HS photograph in **Figure 7**. There are no new shear micro-cracks based on the PFC simulation. **Figure 13B** is the number of different types of AE

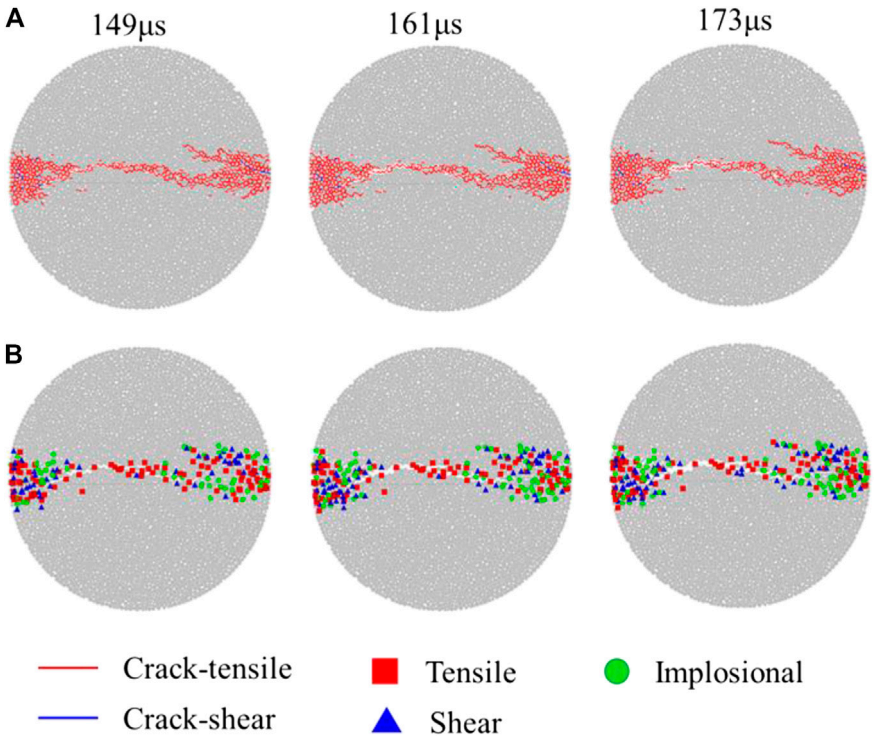

FIGURE 12 | Microscopic mechanism of the shear zones generation in the ends of specimen. **(A)** is the DFN fracture obtained by the PFC. **(B)** is the results of the AE source mechanism obtained based on the moment tensor.

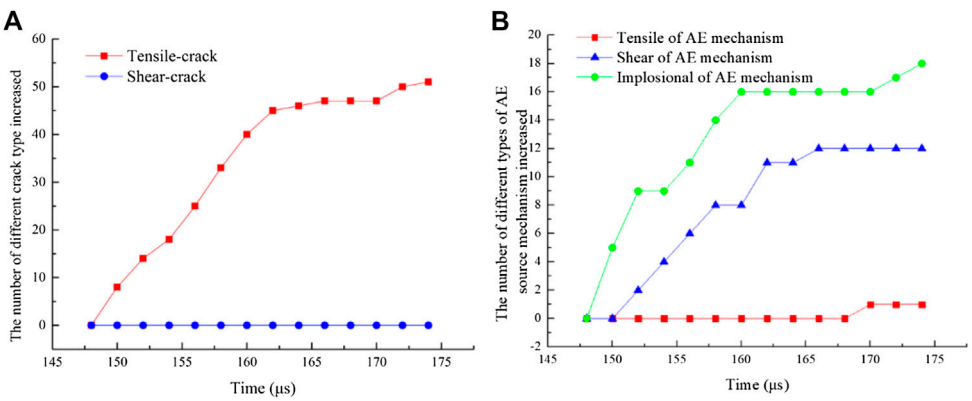

FIGURE 13 | The statistical results of different types of micro-crack. **(A)** is the number of different crack types increased from 148 to 173 μs obtained by PFC. **(B)** is the number of different types of AE source mechanisms increased from 148 to 173 μs.

source mechanisms increased from 148 to 173 μs obtained by the value of R. The implosion and shear of the AE source mechanisms both increase from 148 to 161 μs. The number of implosion fracture mechanisms is the highest, which can be explained by the fact that the shear zones at both ends of the dynamic Brazil split specimen are formed by secondary loading. Comparing **Figures 13A** and **Figure 13B**, the fracture mechanism of the shear zones at the ends of the specimen obtained by the PFC simulation or AE source mechanisms are different. The statistical result of different crack types obtained by PFC shows that the fracture mechanism is tensile, which does not coincide with the HS photograph in **Figure 8**.

Figure 14A is the cumulative counts of different crack types obtained by bond break with the PFC simulation. The results

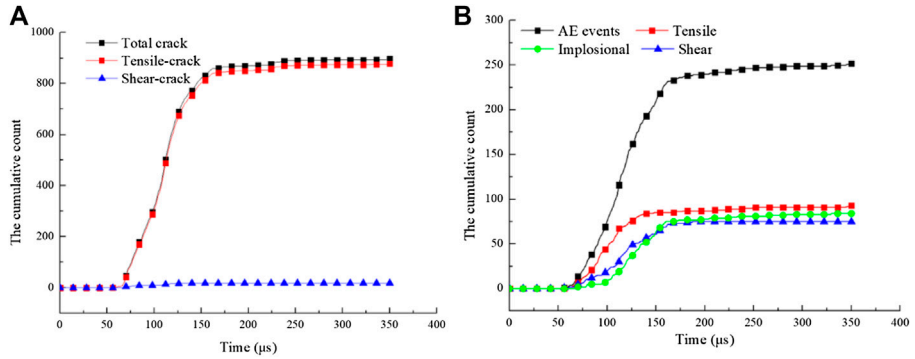

FIGURE 14 | The cumulative counts of different types of micro-crack. **(A)** is the cumulative counts of different crack types obtained by PFC. **(B)** is the cumulative counts of AE events and three kinds of AE source mechanism in the simulation.

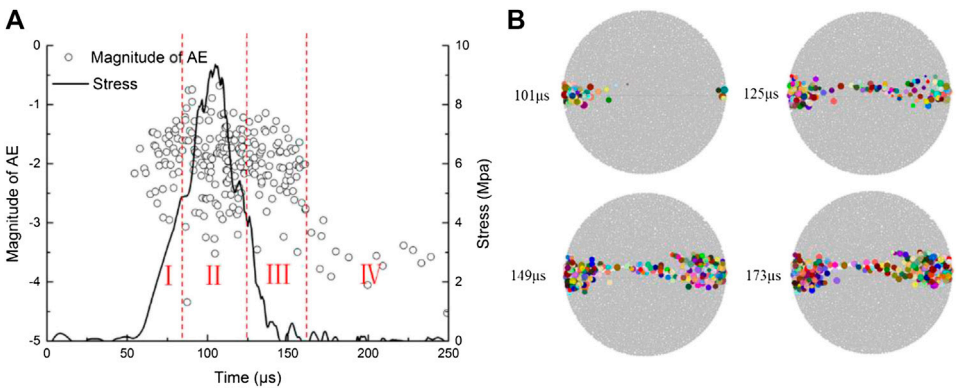

FIGURE 15 | (A) The magnitude of AE and stress on rock changing with time. **(B)** The AE location in this simulation.

show that the micro-mechanical mechanisms are tensile in all the failure processes. Therefore, we can confirm the macro-mechanical mechanisms of this dynamic test as tensile.

The number of AE events and three kinds of AE source mechanism (tensile, implosion, and shear) during the period from the initiation of micro-cracks to the formation of macroscopic cracks (no more new cracks generation) in the specimen are counted. These four cumulative counts are shown in **Figure 14B**. The cumulative counts of AE start to grow rapidly at 75 μs. and reach a stable value at about 175 μs. The cumulative counts of tension start to grow rapidly at 75 μs and reach a stable value at about 150 μs. The cumulative counts of implosion and shear start to grow rapidly at about 100 μs and reach a stable value at about 175 μs. The cumulative count of implosion and shear have an intersection point at about 150 μs. Before this point, the micro-mechanical mechanisms of the shear zones are mainly shear. After this point, the shear zone has been basically formed. The two ends of the specimen continue to be squeezed, the cumulative count of implosion becomes more than the shear.

Comparing with the results of the HS photograph in Acoustic Emission and Moment Tensor of the Main Axial Crack Parallel to the Impact Direction and Acoustic Emission and Moment Tensor of the Shear Failure Zones, the macro-mechanical mechanisms of the first macro-crack in the middle of the rock specimen is tensile. The macro-mechanical mechanisms of the other macro-crack in the two ends of the rock specimen are shear. The same results can be obtained by the simulation of the AE and moment tensor. However, the results of DFN with PFC can only explain the macro-mechanical mechanisms of the macro-crack generated in the middle of rock specimen in this dynamic test. Previous studies have also shown that the mechanical mechanisms of an AE event with moment tensor simulation are different with the result of DFN with PFC [14, 15].

Relationship Between AE Magnitude and Failure Process

Figure 15A shows that the failure process of rock under a dynamic Brazilian test can be divided into four stages according to magnitude and the stress on rock. **Figure 15B** shows the positions of these AE events. Before 101 μs, an AE event is mainly generated at the two ends of specimen. Magnitudes of these AE events are relatively small. There is

no macro-crack generated in this phase. AE events with high magnitude mainly occur in the second phase. The macro-crack in the center of the specimen is also generated in this phase. The magnitude of AE generated in the third stage is slightly lower than that in the previous stage, and the positions generated are at both ends of the specimen which is the same as the first phase. The superposition of AE events in these two phases led to macro-crack. Therefore, we can confirm that the number and energy magnitude of AE events both affect the prediction of macro-crack generation during the failure process of a dynamic Brazilian test. The macro-crack in the center of the rock specimen is accompanied by AE events with a larger energy magnitude, while the macro-crack in the shear areas at both ends is accompanied by the accumulation of more AE events.

CONCLUSIONS

In order to analyze the microscopic mechanism of rock under a dynamic Brazilian test, an AE source and AE source moment tensor are simulated with PFC in this paper. The dynamic indirect tensile experiment of red sandstone with SHPB is conducted. HS photography is used to obtain the macroscopic failure process of the rock specimen. The simulated AE counts, different kinds of AE sources mechanism solutions, and b values are counted and discussed. The simulation results of rock under a dynamic Brazilian test with PFC are also compared with the results of HS photography. The conclusions are as follows.

(1) The simulation of an AE source and AE moment tensor are feasible in analyzing the microscopic mechanism of dynamic tensile simulation in rock dynamics. The results of AE simulation can be used to analysis the micro-crack propagation process, which is consistent with macroscopic cracking shown by HS photography. The AE magnitude and moment magnitude can be used to distinguish key events in the rock failure process. The AE mechanism obtained by the value of R verifies that they can be used to analyze the generation mechanism of micro-crack and rock dynamic failure.

(2) The results of the AE mechanism can explain the micro-mechanical mechanism of the main axial crack, which is parallel to the impact direction and divides the specimen into two pieces, and the shear failure zones which occur at the contact points of the BD specimen. The micro-mechanical mechanisms of the main axial crack are tensile. The micro-mechanical mechanisms of the shear zones are mainly tensile before the macro-crack generated in the two ends of the specimen. When the macro-crack is generated in the two ends of the specimen, the cumulative count of implosion and shear have an intersection point. Before this point, the micro-mechanical mechanisms of the shear zones are mainly shear. After this point, the shear zone has been basically formed. The two ends of the specimen continue to be squeezed, the cumulative count of implosion becomes more than the shear.

DATA AVAILABILITY STATEMENT

The raw data supporting the conclusions of this article will be made available by the authors, without undue reservation.

AUTHOR CONTRIBUTIONS

JZ and YZ conceived the idea, performed the data analyses, and wrote the manuscript. ZZ and CL contributed significantly to analysis and manuscript preparation and helped to perform the analysis with constructive discussions. All authors contributed to the article and approved the submitted version.

FUNDING

The authors gratefully acknowledge financial support from the National Natural Science Foundation of China (41772313) and the Fundamental Research Funds for the Central Universities of Central South University (2019zzts308).

REFERENCES

1. Zhu WC, Niu LL, Li SH, Xu ZH. Dynamic Brazilian test of rock under intermediate strain rate: pendulum hammer-driven SHPB test and numerical simulation. *Rock Mech Rock Eng* (2015) 48(5):1867–81. doi:10.1007/s00603-014-0677-7
2. Ai D, Zhao Y, Xie B, Li C. Experimental study of fracture characterizations of rocks under dynamic tension test with image processing. *Shock Vib* (2019) 2019: 1–14. doi:10.1155/2019/6352609
3. Wu Z, Xu L, Liu Q. Numerical investigation of rock heterogeneity effect on rock dynamic strength and failure process using cohesive fracture model. *Eng Geol* (2015) 197:198–210. doi:10.1016/j.enggeo.2015.08.028
4. Zhao JS, Feng XT, Jiang Q, Zhou Y-Y. Microseismicity monitoring and failure mechanism analysis of rock masses with weak interlayer zone in underground intersecting chambers: a case study from the Baihetan Hydropower Station, China. *Eng Geol* (2018) 245:44–60. doi:10.1016/j.enggeo.2018.08.006
5. Chong Z, Li X, Hou P, Chen X, Wu Y. Moment tensor analysis of transversely isotropic shale based on the discrete element method. *Int J Min Sci Technol* (2017) 27(3):507–15. doi:10.1016/j.ijmst.2017.03.023
6. Cai X, Zhou ZL, Zang HZ, Song Z. Water saturation effects on dynamic behavior and microstructure damage of sandstone: phenomena and mechanisms. *Eng Geol* (2020) 276:105760. doi:10.1016/j.enggeo.2020.105760
7. Pei P, Dai F, Liu Y, Wei M. Dynamic tensile behavior of rocks under static pre-tension using the flattened Brazilian disc method. *Int J Rock Mech Min Sci* (2020) 126:104208. doi:10.1016/j.ijrmms.2019.104208
8. Imani M, Nejati HR, Goshtasbi K. Dynamic response and failure mechanism of Brazilian disk specimens at high strain rate. *Soil Dynam Earthq Eng* (2017) 100: 261–9. doi:10.1016/j.soildyn.2017.06.007
9. Wong LNY and Einstein HH. Crack coalescence in molded gypsum and carrara marble: Part 1. Macroscopic observations and interpretation. *Rock Mech Rock Eng* (2009) 42(3):475–511. doi:10.1007/s00603-008-0002-4
10. Zeng W, Yang SQ, Tian WL. Experimental and numerical investigation of brittle sandstone specimens containing different shapes of holes under uniaxial compression. *Eng Fract Mech* (2018) 200:430–50. doi:10.1016/j.engfracmech.2018.08.016

11. Wu BB, Xia KW, Chen R. "*Dynamic tensile failure of rocks subjected to simulated in situ stresses*", in *International Congress on rock mechanics* (2015).
12. Zhang Q and Zhang XP. The crack nature analysis of primary and secondary cracks: a numerical study based on moment tensors. *Eng Fract Mech* (2019) 210:70–83. doi:10.1016/j.engfracmech.2018.05.006
13. Hazzard JF and Young RP. Simulating acoustic emissions in bonded-particle models of rock. *Int J Rock Mech Min Sci* (2000) 37(5):867–72. doi:10.1016/S1365-1609(00)00017-4
14. Hazzard JF and Young RP. Moment tensors and micromechanical models. *Tectonophysics* (2002) 356(1):181–97. doi:10.1016/S1365-1609(00)00017-4
15. Cai M, Kaiser PK, Morioka H, Minami M, Maejima T, Tasaka Y, et al. FLAC/PFC coupled numerical simulation of AE in large-scale underground excavations. *Int J Rock Mech Min Sci* (2007) 44(4):550–64. doi:10.1016/j.ijrmms.2006.09.013
16. Lisjak A, Liu Q, Zhao Q, Mahabadi OK, Grasselli G. Numerical simulation of acoustic emission in brittle rocks by two-dimensional finite-discrete element analysis. *Geophys J Int* (2013) 195(1):423–43. doi:10.1093/gji/ggt221
17. Zhang XP and Zhang Q. Distinction of crack nature in brittle rock-like materials: a numerical study based on moment tensors. *Rock Mech Rock Eng* (2017) 50(10):1–9. doi:10.1007/s00603-017-1263-6
18. Ma J, Wu S, Zhang XP, Gan Y. Modeling acoustic emission in the Brazilian test using moment tensor inversion. *Comput Geotech* (2020) 123:103567. doi:10.1016/j.compgeo.2020.103567
19. Cundall PA. "*A computer model for simulating progressive, large-scale movement in blocky rock system*", in *Proceedings of the International Symposium on rock mechanics* (1971).
20. Cundall PA and Strack ODL. Discussion: a discrete numerical model for granular assemblies. *Geotechnique* (1980) 30(3):331–6.
21. Li XB, Zou Y, Zhou ZL. Numerical simulation of the rock SHPB test with a special shape striker based on the discrete element method. *Rock Mechanics and Rock Engineering* (2014) 47(5):1693–709. doi:10.1007/s00603-013-0484-6
22. Zhou ZL, Zhao Y, Jiang YH, Zou Y, Cai X, Li DY. Dynamic behavior of rock during its post failure stage in shpb tests. *Trans Nonferrous Metals Soc China* (2017) 27(1):184–96. doi:10.1016/S1003-6326(17)60021-9
23. Cai X, Zhou Z, Tan L, Song Z. Fracture behavior and damage mechanisms of sandstone subjected to wetting-drying cycles, *Eng Fract Mech* (2020) 234:107109. doi:10.1016/j.engfracmech.2020.107109
24. Dai F, Huang S, Xia KW, Tan Z. Some fundamental issues in dynamic compression and tension tests of rocks using split Hopkinson pressure bar. *Rock Mech Rock Eng* (2010) 43(6):657–66. doi:10.1007/s00603-010-0091-8
25. Ai DH, Zhao YC, Wang QF, Li CW. Experimental and numerical investigation of crack propagation and dynamic properties of rock in SHPB indirect tension test. *Int J Impact Eng* (2019) 126:135–46. doi:10.1016/j.ijimpeng.2019.01.001
26. Li DY, Han ZY, Sun XL, Zhou T, Li XB. Dynamic mechanical properties and fracturing behavior of marble specimens containing single and double flaws in SHPB tests. *Rock Mech Rock Eng* (2019) 52(6):1623–43. doi:10.1007/s00603-018-1652-5
27. Zhou ZL, Zhao Y, Cao WZ, Chen L, Zhou J. Dynamic response of pillar workings Induced by Sudden pillar recovery. *Rock Mechanics and Rock Engineering* (2018) 51(10):3075–3090. doi:10.1007/s00603-018-1505-2
28. Hazzard JF and Damjanac B. "*Further investigations of microseismicity in bonded particle models*", in *Proceedings of the 3rd International FLAC/DEM Symposium*. Minneapolis, MN: Itasca Consulting Group (2013), 22–4.
29. Gutenberg B and Richter CF. Frequency of earthquakes in California. *Bull Seismol Soc Am* (1944) 34(4):185–8. doi:10.1038/156371a0
30. Itasca Consulting Group Inc. *PFC2D (Particle flow Code in 2 dimensions)*. Minneapolis, Minnesota: ICG (1999).Version 2.0
31. Hanks TC and Kanamori H. A moment magnitude scale. *J Geophys Res* (1979) 84:2348–2350.
32. Feignier B and Young RP. Moment tensor inversion of induced microseisnmic events: evidence of non-shear failures in the− 4< M<− 2 moment magnitude range. *Geophys Res Lett* (1992) 19(14):1503–6.
33. Zhang QB and Zhao J. A review of dynamic experimental techniques and mechanical behaviour of rock materials. *Rock Mech Rock Eng* (2014) 47(4):1411–78. doi:10.1007/s00603-013-0463-y
34. Ren FQ, Zhu C, He MC. Moment tensor analysis of acoustic emissions for cracking mechanisms during schist strain burst. *Rock Mech Rock Eng* (2019) 53:1–18. doi:10.1007/s00603-019-01897-3
35. Yamamoto K, Naoi M, Chen YQ, Nishihara K, Yano S, Kawakata H, et al. Moment tensor analysis of acoustic emissions induced by laboratory-based hydraulic fracturing in granite. *Geophys J Int* (2018) 216(3):1507–16. doi:10.1093/gji/ggy493
36. Benedetto MF, Berrone S, Pieraccini S, Scialò S. The virtual element method for discrete fracture network simulations. *Comput Methods Appl Mech Eng* (2014) 280:135–56.
37. Zhang QB and Zhao J. Determination of mechanical properties and full-field strain measurements of rock material under dynamic loads. *Int J Rock Mech Min Sci* (2013) 60:423–39. doi:10.1016/j.ijrmms.2013.01.005

Conflict of Interest: The authors declare that the research was conducted in the absence of any commercial or financial relationships that could be construed as a potential conflict of interest.

frontiers in Physics

ORIGINAL RESEARCH
published: 04 February 2021
doi: 10.3389/fphy.2020.593701

Rock Burst Evaluation Using the CRITIC Algorithm-Based Cloud Model

Jiachuang Wang[1], *Mingjian Huang*[1,2] *and Jiang Guo*[1*†]

[1]School of Resources and Safety Engineering, Central South University, Changsha, China, [2]Hongda Blasting Engineering Group, Co., Ltd., Guangzhou, China

Under high-stress conditions, rock burst disasters can significantly impact underground civil engineering construction. For underground metal mines, rock burst evaluations and prevention during mining have become major research topics, and the prediction and prevention of rock burst must be based on the study of rocks and rock burst tendencies. To further prevent the risk of geological disasters and provide timely warnings, a finite-interval cloud model based on the CRITIC algorithm is proposed in this paper to address the uncertainty of rock burst evaluation, the complexity under multi-factor interactions, and the correlations between factors, and it then realizes a preliminary qualitative judgment of rock burst disasters. This paper selects the uniaxial compressive strength σ_c (I_1), ratio of the uniaxial compressive strength to the tensile strength σ_c/σ_t (brittleness coefficient, I_2), elastic deformation energy index W_{et} (I_3), ratio of the maximum tangential stress to the uniaxial compressive strength σ_θ/σ_c (stress coefficient, I_4) of the rock, depth of the roadway H (I_5), and integrity coefficient of the rock mass K_v (I_6) as indicators for rock burst propensity predictions. The CRITIC algorithm is used to consider the relationships between the evaluation indicators, and it is combined with an improved cloud model to verify 20 groups of learning samples. The calculation results obtained by the prediction method are basically consistent with the actual situation. The validity of the model is tested, and then the model is applied to the Dongguashan Copper Mine in Tongling, Anhui Province, China, for rock burst evaluation.

Keywords: cloud model, CRITIC algorithm, rock burst, uncertainty, prediction

OPEN ACCESS

Edited by:
Guoyang Fu,
Monash University, Australia

Reviewed by:
Wenzheng Yue,
China University of Petroleum, China
Abbas Taheri,
University of Adelaide, Australia

***Correspondence:**
Jiang Guo
guojiang@csu.edu.cn

[†]***ORCID:***
Jiang Guo
orcid.org/0000-0003-1418-2039

Specialty section:
This article was submitted to Interdisciplinary Physics, a section of the journal Frontiers in Physics

Received: *11 August 2020*
Accepted: *23 December 2020*
Published: *04 February 2021*

Citation:
Wang J, Huang M and Guo J (2021) Rock Burst Evaluation Using the CRITIC Algorithm-Based Cloud Model. Front. Phys. 8:593701. doi: 10.3389/fphy.2020.593701

INTRODUCTION

Rock burst is due to the impact of ground pressure on hard and brittle rock masses in high earth-stress states during the excavation of underground tunnels. Elastic strain energy is suddenly and rapidly released due to the stress concentration around the opening, and the dynamic instability of the energy leads to the sudden release of energy into the free space, thus destroying the equilibrium. This energy release is an earthquake induced by mining or tunnel excavation [1, 2]. As early as 1738, there were related reports of rock burst disasters [3]. Rock burst disasters are sudden and extremely destructive and will not only cause over-excavation, initiate support failure, and delay construction but may also cause earthquakes or destroy the entire tunnel or pit, thus causing casualties and serious economic losses. At the same time, rock burst disasters are often accompanied by the exfoliation and ejection of surrounding rock, the formation of a considerable amount of dust and the creation of air shock waves. Thus, these disasters can easily cause numerous casualties and determining a method of correctly predicting the risk of rock burst in underground engineering and geotechnical engineering practice has become a problem that must be solved.

Compared with other engineering fields, the occurrence of rock burst in underground metal mines is unique and mainly reflected in the following aspects: 1) Rock burst evaluation is an

important basis for determining the risk level and safety of mines; 2) In other metal mine production research fields, such as underground caverns, rock slopes and dam foundation stability, rock burst is a relatively important criterion; 3) Reasonable rock burst evaluations can provide effective theoretical criteria for process selection, disaster prevention and control during construction, which provides strong theoretical support for mining safety protection measures, such as safety support and safety shielding implementation; and 4) Underground engineering rock burst evaluations provide data for underground engineering surveys, designs and safe construction and represent an important research topic in rock mechanics and geotechnical engineering.

In recent decades, many scholars have performed a number of analyses and research based on the formation mechanism of rock burst and proposed many well-known theoretical criteria, such as the Russenes criterion, the Hoek criterion, the energy criterion, and the stress criterion. In recent years, rock burst criteria based on engineering experience have emerged. The above discrimination methods are based on the study of rock burst mechanisms and have been combined with qualitative or quantitative analysis methods to determine the rock burst tendency and hazard level. In general, current rock burst evaluation methods can be classified into three categories: theoretical analysis methods, field measurement methods and statistical evaluation methods. The specific contents and differences are as follows.

Theoretical Analysis

Theoretical analysis can be used in the process of rock burst evaluation. This method is inexpensive and can better simulate the influence of various on-site factors. The theoretical analysis method is based on different theories of rock burst mechanism, and the resulting criteria are used to form different prediction methods, including the following methods. 1) Rock burst tendency judgment method [4–6]: This method is mainly used in the engineering geological exploration stage after drilling rock samples on site and for conducting rock mechanics tests, and one indicator or a set of indicators (elastic deformation index, impact energy index, dynamic damage time, etc.) are used to analyze the possibility of rock burst. 2) Strength theory method [7, 8]: Strength theory suggests that rock burst may occur when the tensile stress or compressive strength of rock reaches a certain ratio, and the prediction criteria used in this method include the Norwegian Russenes criterion [9], elastic energy reserve criterion, brittleness coefficient criterion, and tangential stress criterion. 3) Energy release rate (ERR) index method [10–12]: The ERR value is the ratio of the energy release caused by the excavated ore to the volume of the mined rock, and it comprehensively reflects the influence of the geometry, depth, original rock stress field and rock mechanical properties of the excavation on rock burst. 4) Numerical prediction methods [13, 14]: These methods include the finite element method and finite difference method.

On-Site Measurement Method

The on-site measurement method uses the necessary instruments to determine whether a rock explosion occurs by investigating and analyzing the mining site or testing the rock mass [15]. This approach mainly includes the following methods. 1) Drill cutting method [16]: This method is mainly used for drilling and sampling analysis of surrounding rock through the collection of dynamic response information, such as popping sounds, friction sounds and stuck drilling phenomena and auxiliary judgements. 2) Acoustic emission method [17]: This method is the most direct monitoring method for rock burst detection and most direct forecasting method, and the occurrence of rock burst is determined according to the shape and frequency spectrum of the acoustic emission signals emitted at different stages of rock deformation. 3) Electromagnetic radiation method [18–20]: This method can predict the possibility and development of rock burst. 4) Microgravity method: this method can predict rock burst early and over a wider prediction range, although its costs are higher than those of other methods.

Statistical Forecasting Methods

Uncertainty is the main feature of most engineering problems, mainly the randomness and ambiguity discussed in probability theory and fuzzy mathematics. Because of the randomness and complexity of the rock mass structure of underground mines, the severity, timing, form, and location of rock burst are uncertain. To resolve the uncertainty of the rock burst problem, domestic and foreign scholars have performed many studies on rock burst tendency predictions and proposed a variety of rock burst grading prediction methods [21–27]. For example, Zhou et al. [28] selected seven data parameters and 132 rock burst databases and combined multiple data models to carry out rock burst tendency prediction work. Xu [29] considered the basic theory of the ideal point method and selected several factors for the evaluation prediction index to construct a coupled ideal point prediction analysis model. Lu et al. [30] used the basic principles of Analytic Hierarchy Process and the entropy weight method to select prediction indexes from three aspects, namely, lithology conditions, stress conditions and surrounding rock conditions, to calculate the critical rock burst risk and the closeness of actual mine data. Wen et al. [31] proposed a rock burst propensity prediction model based on a support vector machine (SVM) with mixed particle swarm optimization (PSO) based on combination weighting, constructed a combination weighting criterion and established a H-PSO-SVM rock burst tendency prediction model based on the concept of the harmonic mean. Zhang et al. [32] established the rock burst cloud model with the distance index and uncertainty metric. Faradonbeh and Taheri [33, 34] used data mining technology to study rock burst tendencies and innovatively proposed the use of field experiments and data analysis methods to conduct research on the predicting deep rock mass and explosion tendencies, and they verified the feasibility of the method. However, some uncertainty analysis methods still have shortcomings. For example, when the AHP method is used to analyze the index weight and usually only measures the relative importance of the index, and it also presents subjectivity; the extension model takes a long time to analyze large-scale training samples and is dependent on the selection of the kernel function; the coupled neural network algorithm is complicated to calculate, the obtained samples are not

representative, and the fitting speed is difficult to control; and the distance discrimination weighting model is strongly dependent on the sample data.

Due to the complexity of rock burst, the above methods also have some limitations: 1) Many risk evaluation factors are derived from subjective experience, which may not make sense in theory; 2) The evaluation criteria standard is generally vague, and traditional evaluation models cannot handle the problem of index classification near the threshold; 3) When different evaluation indicators belong to different grades, the method of defining the actual evaluation indicators of the sample is also somewhat ambiguous; 4) The measured value of the evaluation factors will have some errors, which will lead to the unreasonable classification of factor levels near the threshold; and 5) The traditional method of determining the importance of the risk level factors of the object relies too much on subjective experience. When the production system is complex and there are many influencing factors, many redundant factors will interfere, thereby reducing the reliability of the evaluation results. The entropy weight method [35] determines the variability of the evaluation index based on the sample data to calculate the amount of information included in the index, thereby assigning the weight according to the amount of information included in the index, although it does not consider the correlation between the indicators. Therefore, it is necessary to introduce a relatively perfect rock burst evaluation model.

In this paper, based on the uncertainty of rock burst evaluations, the complexity under multi-factor interactions, and the correlations between factors, a cloud model of finite intervals based on the CRITIC algorithm is proposed. When using the traditional normal cloud model to address the parameter distribution of the single interval boundary, the deviation between the actual situation and the model distribution will not be considered. The calculation result obtained in this case often differs from the actual engineering, and this difference affects the accuracy of the prediction result. When classifying rock burst grades, the determination of index weights is the key to object evaluation. Although the traditional method of objective weights is based on objective data, the results may be poorly interpreted. This paper uses the improved CRITIC method-normal cloud model for rock burst propensity prediction to determine the weight of the index. The model is applied to the rock burst examples of underground engineering worldwide, the validity of the model is tested, and the model is finally applied to the Dongguashan Copper Mine in Tongling, Anhui Province, for rock burst evaluation.

THEORETICAL BASIS

Identification Framework and BPA

For a fuzzy evaluation problem, the answers can be composed of a set, and the internal elements of the set are mutually exclusive. Under certain conditions, the answer to the question can be the only element in the set. For this reason, Shafer [36] refers to this mutually exclusive set Θ as the recognition framework according to the set theory:

$$\Theta = \{A_1, A_2 \ldots A_m\} \tag{1}$$

where Am indicates the evaluation level of the evaluation question and Θ indicates the evaluation standard in the evaluation question.

The evidence set is the basis for judging whether the identification framework of a problem Θ is a subset, which is equivalent to the index factor in the evaluation and is recorded as follows:

$$\Phi = \{E_1, E_2 \ldots E_k\} \tag{2}$$

where En represents the index factor in the evaluation question, which is usually used to express the sample and judge its subordinate level. In the recognition framework Θ, the basic probability distribution function f is a mapping of the set 2^{Θ} to [0, 1] and satisfies the following:

$$\sum_{A \in \Theta} f(A) = 1 \tag{3}$$

where A denotes any subset of the recognition frame Θ, which is denoted as $A \in \Theta$; and $f(A)$ is the basic probability distribution function of A, which indicates the degree of evidence support for A. In the evaluation question, $f(A)$ indicates the degree of membership, which is characterized by the fact that the measured values of the indicators of the evaluation factors belong to the degree of membership of different evaluation levels.

Definition of the Cloud Model

The essence of the membership function concept, which is the most basic of fuzzy mathematics, did not have good theoretical support before the cloud model was produced. In particular, it is basically impossible to use accurate membership functions to define fuzzy thinking activities. For this reason, Li Deyi et al. proposed the concept of a cloud model [37, 38]. From the perspective of membership degree, they analyzed the data randomness and ambiguity problems in engineering practice. Randomness means that there is a certain basic definition, although the events may not occur. The characteristic of this problem is randomness. In the evaluation model, the concept and distribution of each evaluation factor index are deterministic but for different evaluation subjects; however, the specific data distribution is uncertain. Therefore, the mine risk assessment problem shows randomness; moreover, the basic concept of ambiguity can be characterized as the uncertainty contained in the event that has occurred but is difficult to accurately define. The method has been applied in many fields [39–48] and achieved good evaluation results.

The "cloud" is a two-way cognitive model between a qualitative concept and its quantitative representation expressed by linguistic values to reflect the uncertainty of random and ambiguous concepts in natural language. The relevant definitions are as follows [39].

There is an exact numerical representation of the quantitative set $U = \{x\}$, where U is the domain (1D, 2D or multidimensional), the A_k inter-cell is the fuzzy interval in the domain U, K is the number of grade intervals in the domain segmentation, and C is the qualitative concept of A_k. An arbitrary element x is observed

in A_k, and each corresponding $x \in A_k$ has a stable random number in the mapping μ: $x \to \mu_A(x)$, which is randomly implemented in the qualitative concept $C\mu_A(x)$ is called the degree of certainty of x for concept C and can also be called the membership degree. The distribution of $\mu_A(x)$ on the domain U is called the cloud model, $\mu_A(x) \in (0, 1)$:

$$\mu: U \to \left(C_{\min}^{kl}, C_{\max}^{kr}\right), A_k \subseteq U, \forall x \in A_k, x \to \mu_A(x) \tag{4}$$

The distribution of $\mu_A(x)$ on each fuzzy set A_k is called a cloud, and each point $[x, \mu(x)]$ is called a cloud drop, where $C_{\min}^{kl}$ represents the smallest value in the smallest fuzzy level interval that is segmented, which is usually 0; and $C_{\max}^{kr}$ indicates the maximum corresponding maximum value of the segmented fuzzy level interval. For the one-sided interval $(C_{\min}^{kr}, +\infty)$, the expected value of the k-1 interval may be taken as E_x^{kr-1}, and then the expected value of the interval may be obtained. Alternatively, we can determine the default boundary parameters by considering the upper and lower limits of the data. When the rock burst risk is positively correlated with the evaluation index, kl and kr represent the minimum and maximum fuzzy level intervals, respectively; otherwise, they represent the maximum and minimum fuzzy level intervals, respectively. The traditional normal cloud model is shown in **Figure 1**, in which the abscissa X (x_1, x_2, ... x_n) represents the value corresponding to the qualitative concept in the domain at this time, the width of the domain represents the value of a certain fuzzy level interval A_k, while the ordinate represents the degree of certainty μ (x_i) (x_{1i}, x_{2i},...x_{ni}), which ranges from 0 to 1 and is a measure of the language value. Each point in the figure corresponds to one cloud drop, which is a specific implementation of the quantified language value.

Digital Characteristics of the Cloud

Usually, the support of the cloud model concept is mainly expressed by three numerical eigenvalues [49]: expectation E_x, entropy E_n, and super entropy H_e. The specific meaning of the expression is shown in **Figure 2**, where three lines are selected in the cloud drop graph and E_x is expected to represent the central value of the data parameter in the Universe. In the geometric sense, a random value corresponding to the highest point of the graph is selected. The location of the cloud drop distributions suggests that $E_{x3} > E_{x2} > E_{x1}$. Entropy E_n indicates the range of values of the cloud drop expressed in the qualitative domain of the Universe, thus reflecting the ambiguity and randomness of the basic concept, which also determines the cloud drop. The greater the confusion is, the greater the width of a cloud map, the larger the value range of the cloud droplet, the more blurred the qualitative concept, and the greater the dispersion of the cloud droplet; thus, $E_{n2} > E_{n1} = E_{n3}$. The super entropy H_e, which is the entropy of entropy and indicates the uncertainty of entropy, is the thickness of the cloud in the cloud drop diagram. The larger the super entropy is, the thicker the cloud, which is characterized as $H_{e1} = H_{e2} > H_{e3}$ in the cloud drop diagram.

In the cloud model, each cloud drop satisfies $x \sim N(E_x, E_n'^2)$, where $E_n' \sim N(E_n, H_e^2)$; then, the degree of certainty of x to C is as follows:

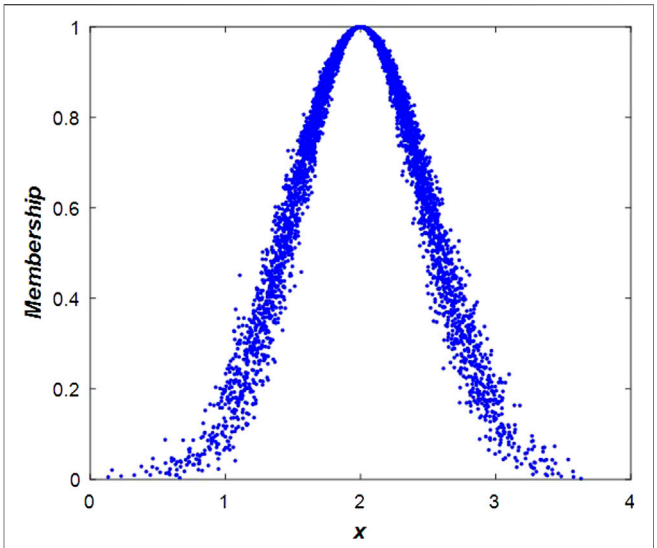

FIGURE 1 | Traditional normal cloud model.

$$\mu(x) = \exp\left[\frac{-(x - E_x)^2}{2 * E_n'^2}\right] \tag{5}$$

The boundary value C_k is a transition value of two levels, and the membership degrees belonging to the two fuzzy intervals are equal:

$$\exp\left[-\frac{\left(C_{\max}^k - C_{\min}^k\right)^2}{8E_n^2}\right] = 0.5 \tag{6}$$

For the rock burst hazard grading interval, there are fuzzy edge intervals of magnitude $A_{Kr} = (0, C_{\max}^{Kl})$ and $A_{Kl} = (C_{\min}^{Kr}, +\infty)$, and the index variables at this time no longer obey the traditional cloud model distribution. Therefore, $\mu_A(x)$ should be transformed into a uniform distribution with a degree of certainty of 1 on the edge blur intervals A_{kr} and A_{kl}, and it is usually described by a half-lift trapezoidal cloud and a half-fall trapezoidal cloud. The calculation equations of the cloud characteristic parameters are as follows:

$$\begin{aligned} E_x^k &= \frac{C_{\max}^k + C_{\min}^k}{2} \\ E_n^k &= \frac{C_{\max}^k - C_{\min}^k}{2.355} \\ H_e^k &= \lambda E_n^k \end{aligned} \tag{7}$$

where C^k is the half-length of the k-level; $C_{\max}^k$ and $C_{\min}^k$ are the upper and lower bounds of the level interval, respectively; and λ is the empirical value, which can be appropriately adjusted according to the fuzzy value of the index variable and is temporarily set to 0.01 in this article. It should be clear that the empirical value λ cannot affect the final result. A change of its value will only affect the value of He, and it does not affect the upper and lower thresholds of the fuzzy interval as shown in **Figure 2** and is mainly used to characterize the thickness of the "cloud."

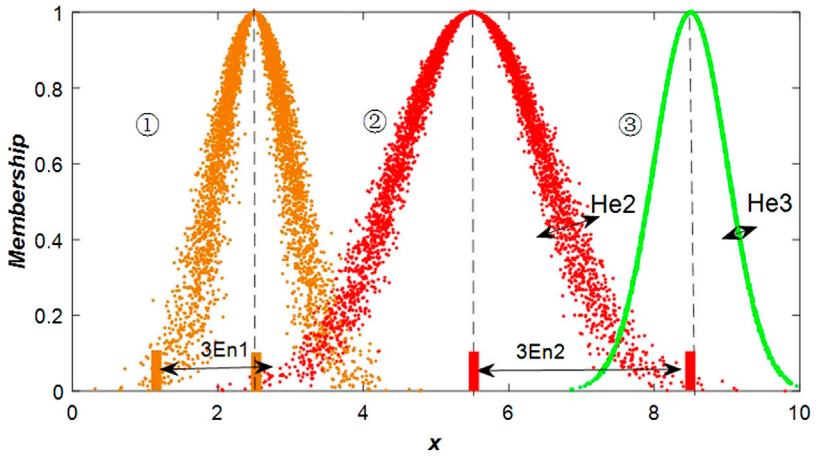

FIGURE 2 | Cloud model feature parameter representation.

Forward Cloud Generator

Cloud generators, including forward cloud generators and reverse cloud generators, are an important medium to transform qualitative concepts into quantitative data. This paper uses a forward cloud generator as a means of qualitative and quantitative conversion. According to the cloud characteristic parameter N (E_x, E_n, H_e), a cloud drop map is generated in the blur interval A_k by the forward cloud generator. For each cloud drop P [x_i, $\mu_A(x)$] (i = 1, 2,. . ., n), n is the number of cloud droplets to be generated in the fuzzy interval A_k and $N = n_1 + n_2 + n_k$ represents the total number of clouds generated in the entire Universe U (N = 5,000 in this paper). When the indicator is in the mean interval of the non-edge level cloud, the degree of certainty of x to C is $\mu(x) = \exp[-(x - E_x)^2/2E_{n,2}]$. When the indicator is in the edge level interval, x no longer has a normal distribution but has a uniform distribution with a degree of certainty of 1. Combining these two distributions, we have

$$\begin{cases} \mu_A(x) = 1 & x \in \left(0, E_x^{k1}\right) \cup \left(E_x^{kn}, C_{\max}^{kn}\right) \\ \mu_A(x) = \exp\left[\dfrac{-(x - Ex)^2}{2En'^2}\right] & x \in \text{otherrval} \end{cases} \tag{8}$$

The generated edge interval is a uniformly distributed cloud model as shown in **Figure 3**, where curve one and curve three represent a finite-interval cloud model and indicate hazard levels one and three, respectively, and the left and right edges of the two curves obey a uniform distribution with a degree of certainty of one.

The positive normal cloud model is applied to rock burst evaluation based on the following four reasons:

(1) Rock burst risk assessment is a problem of uncertainty, and the cloud model expresses and reflects the uncertainty of concepts in the process of human cognition through the three characteristic parameters of N (Ex, En, He);
(2) The cloud model with the edge obeys the normal distribution, and its main body still obeys the normal distribution, which has certain universality and extensiveness;
(3) In the natural sciences, the characteristic curves of many qualitative concepts approximately obey a normal distribution;
(4) The cloud model can convert qualitative concepts and quantitative values, and the rock burst risk assessment selected in this article is also a research process from qualitative to quantitative.

CLOUD MODEL BASED ON THE CRITIC ALGORITHM FOR ROCK BURST EVALUATION

To use the CRITIC algorithm-based cloud model for rock burst evaluation, the appropriate evaluation index system and its

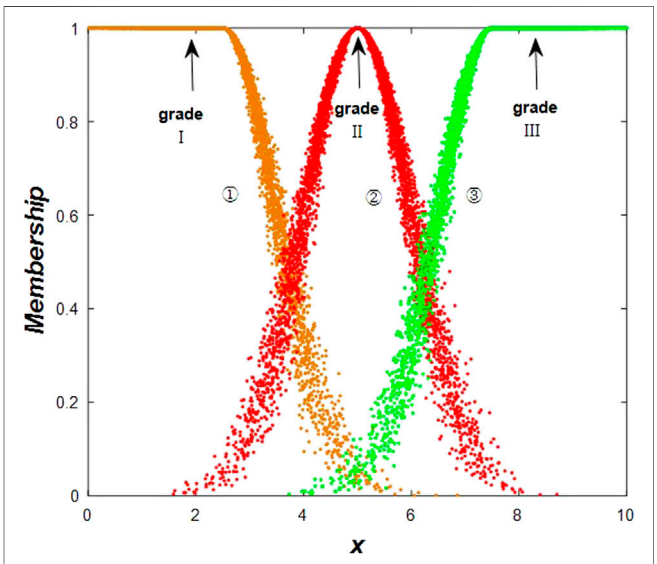

FIGURE 3 | Finite-interval cloud model cloud drop diagram.

corresponding evaluation criteria must be selected and the index weights are then calculated by the CRITIC algorithm; then, the corresponding evaluation index criteria are used to calculate the cloud characteristic parameters of each level. The cloud model is generated using the cloud generator, and the degree of certainty corresponding to each index is calculated according to the measured data of the sample. Finally, the comprehensive weight value is calculated, and the rock burst risk level is determined according to the principle of maximum membership degree. The evaluation flow chart is shown in **Figure 4**.

Selection of Rock Burst Evaluation Classification Indicators and Intensity Grading Standards

The mechanism of rock burst is complicated, and there are many influencing factors. The selection of indicators is a key step in the prediction process. The impact of rock burst is two-fold: internal and external. In a high-stress environment, excavation of a cavern will lead to stress redistribution and stress concentration in the surrounding rock mass. The environment in which the rock mass is located undergoes a certain change, which is the external factor of rock burst. The mechanical properties of the rock mass itself are internal factors, and hard rock and brittle rock are prone to rock burst. Therefore, it is necessary not only to carry out mechanical experiments on the rock but also to obtain the rock burst tendency index and consider external conditions in rock burst evaluation. Based on related research on rock burst [50, 51], the theory of rock burst tendency, and intrinsic rock burst conditions, lithological factors, energy factors and geological factors, this paper selects the uniaxial compressive strength σ_c (I_1), ratio of the uniaxial compressive strength to the tensile strength σ_c/σ_t (brittleness coefficient, I_2), elastic deformation energy index W_{et} (I_3), ratio of the maximum tangential stress to the uniaxial compressive strength σ_θ/σ_c (stress coefficient, I_4) of the rock, depth of the roadway H (I_5), and integrity coefficient of the rock mass K_v (I_6) as indicators for rock burst propensity prediction. According to the characteristics of rock burst occurrence during underground mining of metal mines, the selection of evaluation indicators should be scientific, independent and representative. The main factors should be included in the evaluation as much as possible. The stronger the independence of the indicators, the more accurate the prediction results will be.

According to the relevant research and classification criteria, the rock burst intensity can be divided into four grades. Grade I (no rock burst) is mainly manifested as a lack of rock wall tearing, rock fragmentation, sound emission phenomenon, etc., and there is no need to take any safety measures. Grade II (weak rock burst) is characterized by a loose rock wall surface and block spalling occurs, and safety and safety monitoring measures are required. Grade III (moderate rock burst) is characterized by block spalling of the rock in the diverticulum and roadway wall accompanied by occasional projectiles that often emit sharp ejecting sounds and may cause casualties and property losses; thus, it is necessary to implement

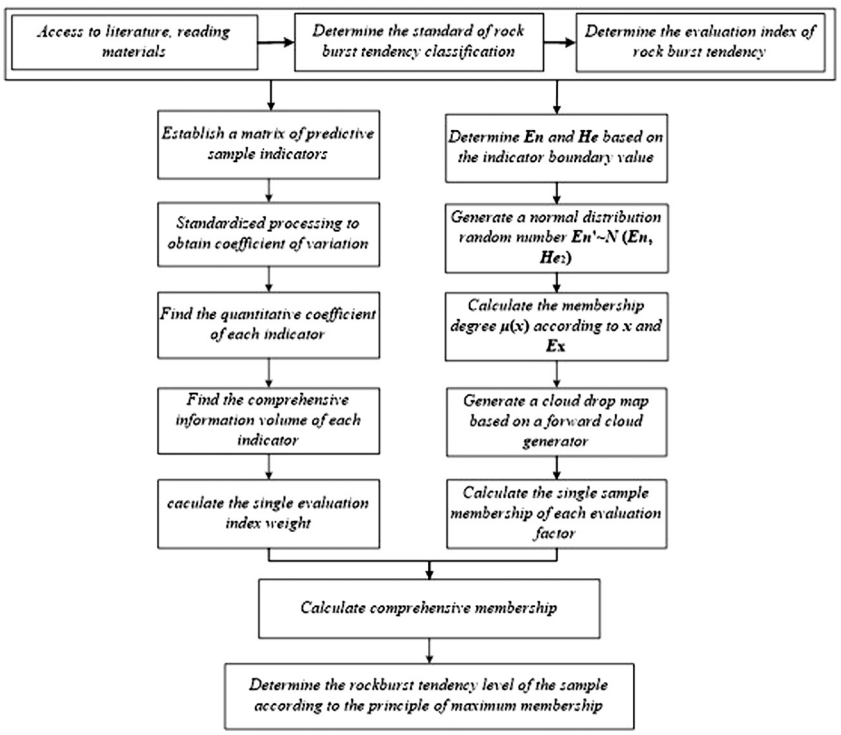

FIGURE 4 | Flow chart of rock burst tendency prediction and evaluation.

monitoring measures to perform isolation and protection work. Grade IV (violent rock burst) is characterized by large rock mass spalling, rapidly deformed surrounding rock, and a large number of blast pits; this type of rock burst is prone to causing numerous casualties and injuries, and relevant safety protection measures must be taken. The specific classification criteria are shown in **Table 1** [52–54]. Multiple studies at home and abroad indicate that the classification standards for rock burst tendencies are different. The classification standards selected in this article indicate a trend and only show the uncertainty of the rock burst problem.

Rock Burst Propensity Prediction CRITIC Algorithm

The so-called weight refers to the importance of the risk indicators that affect the problem in the evaluation process. The methods of determining weight mainly include subjective weighting methods and objective weighting methods. According to the engineering characteristics of the rock burst problem, this paper adopts the CRITIC objective weighting algorithm to determine the index weight. The CRITIC method was proposed by Diakoulaki et al. [55] in 1995, and it focuses on using the information and correlation of risk indicators to determine risk weights. The improved CRITIC algorithm is based on the original calculation steps, adding the concept of coefficient of variation (**Formula 12**), thereby reducing the shortcomings of using standard deviation to measure the variability of indicators [56], the main steps are as follows:

STEP 1: Using the initial data, establish a matrix of predicted sample indicator values:

$$X = \left(x_{ij}\right)_{m\times n} \tag{9}$$

where x_{ij} is the original value corresponding to the jth indicator of the ith evaluation object.

STEP 2: According to the Z-score method, standardize the index values in matrix X of the above formula:

$$x_{ij}^{*} = \frac{x_{ij} - \overline{x}_j}{s_j}\left(i = 1,\ 2, \ldots,\ m; j = 1,\ 2,\ \ldots, n\right) \tag{10}$$

According to the algorithm, the two parameters in the above formula are defined as follows:

$$\overline{x}_j = \frac{1}{m}\sum_{i=1}^{m} x_{ij},\quad s_j = \sqrt{\frac{1}{m-1}\sum_{i=1}^{m}\left(x_{ij} - \overline{x}_j\right)^2} \tag{11}$$

where $\overline{x_j}$ is the average of the jth indicator and s_j is the standard deviation of the jth indicator.

STEP 3: Find the coefficient of variation in the indicator:

$$v_j = \frac{s_j}{\overline{x}_j}\left(j = 1,\ 2,\ \ldots, n\right) \tag{12}$$

where v_j is the coefficient of variation in the jth indicator.

STEP 4: Use STEP 2 to obtain the normalized matrix X* and use the statistical concept to calculate the correlation coefficient:

$$r = \frac{\sum_{i=1}^{n}\left(x_i - \overline{x}\right)\left(y_i - \overline{y}\right)}{\sqrt{\sum_{i=1}^{n}\left(x_i - \overline{x}\right)^2 \cdot \sum_{i=1}^{n}\left(y_i - \overline{y}\right)^2}} \tag{13}$$

Obtain the Correlation Coefficient Matrix

$$R = \left(r_{kl}\right)_{n\times n}\left(k = 1, 2, \ldots, n\ ;\ l = 1,\ 2,\ \ldots\right) \tag{14}$$

where r_{kl} is the correlation coefficient between the kth indicator and the 1st indicator.

STEP 5: Identify the degree of independence—quantization coefficient—of each indicator:

$$\eta_j = \sum_{k=1}^{n}\left(1 - r_{kj}\right)\left(j = 1,\ 2, 3, \ldots n\right) \tag{15}$$

STEP 6: Calculate the total volume of information for each indicator:

$$D_j = v_j\sum_{k=1}^{n}\left(1 - r_{kj}\right), j = 1, 2, 3 \ldots n \tag{16}$$

STEP 7: Determine the weight of each evaluation index:

$$\omega_j = \frac{D_j}{\sum_{j=1}^{n} D_j}\left(j = 1, 2, 3, \ldots, n\right) \tag{17}$$

According to the cloud model theory and the improved CRITIC algorithm, the coupling process is as follows.

(1) With reference to the rock burst risk level classification standard and cloud model concept, determine the number and interval of the divided states.
(2) According to the numerical characteristics of the cloud model (**Eq. 7**) and the grading standard of the rock burst intensity level, the numerical eigenvalues of different hazard levels of different evaluation factors can be obtained. The specific values are shown in **Table 2**. When the edge interval is treated as (C_k, +∞), the expected value of the k-1 interval can be assumed, and then the expected value of the entire interval can be obtained.

TABLE 1 | Rock burst classification criteria.

Rock burst grade	$\sigma_{c/Mpa}$	σ_c/σ_t	W_{et}	σ_θ/σ_c	H/m	K_v
I (no rock burst)	(0, 80)	(40, +∞)	(0, 2)	(0, 0.3)	(0, 50)	(0, 0.55)
II (weak rock burst)	(80, 120)	(26.7, 40)	(2, 3.5)	(0.3, 0.5)	(50, 200)	(0.55, 0.65)
III (moderate rock burst)	(120, 180)	(14.5, 26.7)	(3.5, 5)	(0.5, 0.7)	(200, 700)	(0.65, 0.75)
IV (violent rock burst)	(180, +∞)	(0, 14.5)	(5, +∞)	(0.7, +∞)	(700, +∞)	(0.75, 1]

TABLE 2 | Characteristic parameters of the rock burst cloud model.

Rock burst grade	Model feature	Evaluation factor					
		I1	*I2*	*I3*	*I4*	*I5*	*I6*
I	*Ex*	40	46.65	1	0.15	25	0.275
	En	33.97	5.65	0.64	0.13	21.23	0.23
	He	0.34	0.057	0.0064	0.0013	0.21	0.0023
II	*Ex*	100	33.35	2.75	0.4	125	0.6
	En	16.98	5.65	0.64	0.085	63.69	0.042
	He	0.17	0.057	0.0064	0.00085	0.64	0.00042
III	*Ex*	150	20.6	4.25	0.6	450	0.7
	En	25.48	5.18	0.64	0.085	212.31	0.042
	He	0.25	0.052	0.0064	0.00085	2.12	0.00042
IV	*Ex*	210	7.25	5.75	0.8	950	0.875
	En	25.48	6.16	0.64	0.085	212.31	0.11
	He	0.25	0.062	0.0064	0.00085	2.12	0.0011

(3) Based on the evaluation criteria in this table and the characteristics of the cloud model, the MATLAB simulator is used to generate a cloud drop graph of each evaluation index by a forward cloud generator, and then the specific generation graph can be determined as shown in **Figure 5**. Let drop (x_{1i}, $x_{2i,}$. . .x_{ni}, μ_i) be a cloud drop, which is a specific implementation of the number of linguistic values represented by the cloud, where X (x_{1i}, $x_{2i,}$. . .x_{ni}) is the value of the qualitative concept in this field and $\mu(x_i)$ is the degree to which the x value (the measured value of the sample) belongs to different levels.

(4) Use the improved CRITIC weighting algorithm (**Eqs 9–17**) to calculate the importance of a single evaluation factor, i.e., the weight value.

(5) Combine the weights determined by the improved CRITIC algorithm with the cloud model feature parameters to obtain the final degree of certainty.

(6) After the expansion and calculation of the above steps, we can obtain the uncertainty in the different evaluation indicators x subordinate to a certain cloud μ (x) and then utilize the CRITIC algorithm to calculate the weight of different evaluation indicators. Then, the final comprehensive determination formula is as follows:

$$\mu_k = \sum_{i=1}^{m} \omega(E_i) \bullet \mu_{k,j} \tag{18}$$

where k is the degree of determination of the measured value of the jth indicator of the $\mu_{k,j}$ sample; and $\omega(E_j)$ represents the weight of the jth evaluation index of the sample.

(7) According to the final comprehensive determination and the principle of maximum membership, the membership level of the sample is determined:

$$L = \max(\mu_1, \mu_2, \ldots \mu_k) \tag{19}$$

ROCK BURST EVALUATION ANALYSIS OF LEARNING SAMPLES

To verify the rationality and effectiveness of the rock burst propensity prediction model used in this paper, referring to 20 sets of typical rockburst example data in literature [50]. The details of the measured index values and actual rock burst grades are listed in **Table 3**.

Indicator Weight Determination

In this paper, the CRITIC method is used to calculate the index weight and the information volume of the indicator and the correlation between the indicators are comprehensively considered. According to the steps outlined in **Formulas 10**

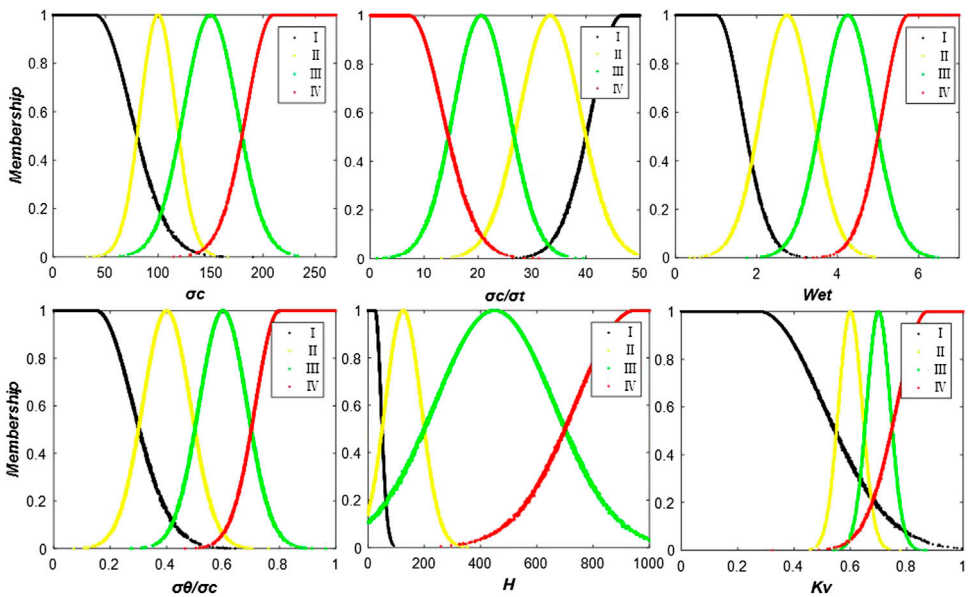

FIGURE 5 | Rock burst evaluation index cloud drop diagram.

TABLE 3 | Measured rock burst index values and actual rock burst grades.

Sample number	Evaluation factor						Actual rock burst grades
	I_1	I_2	I_3	I_4	I_5	I_6	
1	148.52	22.3	3.23	0.66	166	0.88	III
2	162.33	13.2	5.23	0.72	317	0.71	IV
3	116.78	29.73	3.52	0.37	177	0.68	II
4	109.33	32.77	2.97	0.42	148	0.71	II
5	98.56	42.73	2.17	0.28	171	0.49	I
6	156.73	20.13	3.82	0.49	289	0.91	III
7	100.32	28.77	3.02	0.38	182	0.70	II
8	142.20	27.52	4.30	0.72	308	0.73	III
9	160.32	16.55	5.72	0.69	265	0.90	IV
10	97.60	15.50	3.20	0.42	162	0.62	II
11	100.20	30.12	4.50	0.58	274	0.64	II
12	106.32	36.42	1.75	0.22	289	0.46	I
13	125.77	10.36	5.75	0.65	277	0.92	III
14	146.75	19.35	4.50	0.62	318	0.88	III
15	107.75	31.20	3.15	0.57	276	0.58	II
16	160.75	12.36	5.41	0.65	294	0.91	IV
17	146.72	18.75	4.20	0.59	342	0.84	III
18	162.70	29.70	3.82	0.73	278	0.70	III
19	95.50	42.30	2.75	0.37	215	0.36	I
20	105.70	37.35	3.08	0.37	155	0.66	II

and **11**, the Z-score method is used to standardize the index values in **Table 3** and then the mean and variance of each index are calculated. The coefficient of variation in each index is obtained by using **Eq. 12**. These results are shown in **Table 4**.

According to the basic concept of the Pearson correlation coefficient, the correlation coefficients of the standardized calculated indexes are obtained by referring to **Formula 13** as shown in **Table 5**.

The coefficient of independence of each index is obtained by using **Eq. 15**, and the coefficient of variation and the coefficient of independence of each index are multiplied by **Eq. 16**. Finally, using **Eq. 17**, we can obtain the weight values of each prediction index I_1 (σ_c), I_2 (σ_c/σ_t), I_3 (Wet), I_4 (σ_θ/σ_c), I_5 (H), and I_6 (K_v): 0.022, 0.142, 0.135, 0.340, 0.019, and 0.342, respectively.

Prediction Results and Analysis

According to the cloud model characteristic parameters obtained from the table, by substituting them into **Formula 8**, the degree of certainty of the selected test samples are calculated to categorize their hazard levels, and the corresponding weights are calculated according to **Formula 18**. According to the principle of maximum membership degree, the degrees of membership of the samples to be tested are shown in **Table 6**.

In order to further verify the accuracy of the calculation method proposed in this manuscript, we selected the calculation of F1 score for discussion and analysis. F1 Score is an indicator used in statistics to measure the accuracy of a binary classification model. It takes into account the accuracy and recall of the classification model. F1 score can be regarded as a weighted average of model accuracy and recall. Its maximum value is 1 and its minimum value is 0. The F1 score analysis includes the following four basic concepts, namely Tue Positive (*TP*: prediction is positive, actual is positive); False Positive (*FP*: prediction is positive, actual is negative); False Negative (*FN*: prediction is negative, actually positive); True Negative (*TN*: predicted negative, actual negative). The so-called positive means that the predicted result is correct; the negative concept means that the predicted result is wrong. Therefore, for the rockburst grading of level 1, the *TP* value is 3, and similarly corresponding to the 2, 3, and 4 levels, the *TP* values are 6, 6, and 3 respectively. In terms of *FP* value and *FN* value, the situation is shown in **Table 8**:

The calculation formula for the precision rate P and the recall rate R are:

$$Precision\ P = \frac{TP}{TP + FP} \tag{20}$$

$$Recall\ R = \frac{TP}{TP + FN} \tag{21}$$

The formula for calculating F1 score is:

$$F1 = 2 \bullet \frac{Precision \bullet Recall}{Precision + Recall} \tag{22}$$

The calculation shows that the p value, R value, and F1 score are all 0.9, which also verifies that the model is reasonable and feasible in the exploration of rockburst tendency classification.

The calculation results of the proposed rock burst cloud model based on the CRITIC algorithm are consistent with the actual data, indicating that the proposed model is reasonable and effective for rock burst grading. The generation of sample error is due to the gray features of the rock burst problem itself, causing its prediction to have some ambiguity, and the factors affecting the rock burst tendency are multi-faceted and include other external environmental factors, such as the installation of artificial support and the humidity of the internal environment, all of which complicate the accuracy of rock burst tendency.

In the CRITIC method, the correlation between the information volume and the indicator index is comprehensively considered and the reliability of the weight calculation result is improved. As a cognitive model that realizes the qualitative concept and the bidirectional transformation of quantitative data, the cloud model can transform the ambiguity and randomness of the rock burst evaluation process into quantitative data of certainty, which accurately reflects the uncertainty of rock burst grading. This approach is superior to other methods.

Since rock burst tendency is a qualitative concept, the classification of its hazard level will be affected and controlled by many uncertain factors. Although the application of the cloud model has certain predictability for the occurrence of rock burst, the finite-interval cloud model cannot completely eliminate the gray features of its existence by transforming its ambiguity and randomness into certainty. The current cloud model used for evaluation does not reflect the characteristics of rock burst affected by multiple factors and does not reflect the correlation of factors in the process. The form of the actual distribution of the rock burst tendency evaluation index will have an impact on the

TABLE 4 | Sample-normalized index values and CRITIC algorithm index parameters.

Sample number	Sample standardization					
1	1.857	−0.699	−0.295	0.186	−5.055	0.196
2	3.080	−2.489	0.731	0.269	4.589	−0.005
3	−0.953	0.762	−0.146	−0.214	−4.353	−0.040
4	−1.613	1.360	−0.428	−0.145	−6.205	−0.005
5	−2.566	3.319	−0.838	−0.338	−4.736	−0.265
6	2.584	−1.126	0.008	−0.048	2.801	0.232
7	−2.410	0.573	−0.402	−0.200	−4.033	−0.017
8	1.298	0.327	0.254	0.269	4.014	0.019
9	2.902	−1.830	0.982	0.228	1.268	0.220
10	−2.651	−2.037	−0.310	−0.145	−5.311	−0.111
11	−2.421	0.839	0.357	0.076	1.843	−0.088
12	−1.879	2.078	−1.053	−0.421	2.801	−0.301
13	−0.157	−3.047	0.997	0.173	2.034	0.244
14	1.701	−1.279	0.357	0.131	4.653	0.196
15	−1.753	1.051	−0.336	0.062	1.970	−0.159
16	2.940	−2.654	0.823	0.173	3.120	0.232
17	1.698	−1.397	0.203	0.090	6.186	0.149
18	3.113	0.756	0.008	0.283	2.098	−0.017
19	−2.837	3.234	−0.541	−0.214	−1.926	−0.419
20	−1.934	2.261	−0.371	−0.214	−5.758	−0.064
Mean value of the sample	127.54	25.86	3.80	0.53	245.15	0.71
Sample variance	11.29	5.08	1.95	0.72	15.66	0.84
Coefficient of variation	0.09	0.20	0.51	1.38	0.06	1.18

evaluation results. The cloud model generated by the combination of uniform and normal distributions reflects the actual situation more reasonably, the parameter method must be further improved to generate more accurate results. In addition, the selection of the evaluation index should also be performed according to the actual project conditions and cannot be rushed. Because of the location of the rock burst, the external environment and human factors will affect the occurrence of rock burst.

ENGINEERING APPLICATION

The Dongguashan copper deposit is located in the Shizishan orefield of Tongling City, Anhui Province, on the polymetallic metallogenic belt along the Yangtze River. The surface is a hilly area with a ground elevation of 15–182 m. The ore body is inclined to 35° and dips to the northwest and southeast with the surrounding rock. The inclination angle is generally approximately 20°, and the maximum inclination angle is 30–35°. The ore body is mainly composed of copper-bearing skarns, copper-bearing pyrite, copper-bearing pyrrhotite and copper-bearing serpentinite. The direct surrounding rock of the ore body is the Carboniferous Lower Gorilla Formation of quartz diorite, which is dominated by horny siltstone. Dongguashan Copper Mine is the main mine of Tongling Nonferrous Metals Group Holdings Co., Ltd. The deposit is a layer-controlled skarn-type deeply buried deposit, with a burial depth of more than 700 m. Therefore, the original rock stress and ore strength of the mining area are relatively high. In the process of mining, the prediction and prevention of rock burst has become a major issue and must be based on the study of rock burst tendency. Because the Dongguashan Copper Mine has a deep burial depth, a high initial rock stress, a favourable ore body structure and hard rock properties, rock burst is possible in this mine according to the experience of deep mine mining outside of China. Under the action of high stress, a destructive rock burst event with rock ejection as the main feature occurred during the construction of the tunnel during the construction and production of the Winter Melon Mountain Mine. Therefore, rock burst tendency predictions have become a focus of mine earthquake prevention and disaster reduction and important technical mean. In this paper, the physico-mechanical properties of the core of seven kinds of typical ore from the ore-bearing rock mass and the surrounding rock of the upper and lower layers are selected as the criterion for the 730 m middle section of the Dongguashan copper deposit (the geological map of this section is shown in

TABLE 5 | Normalized index Pearson correlation coefficients.

Forecast indicator	Pearson correlation coefficient					
	I1	*I2*	*I3*	*I4*	*I5*	*I6*
I1	1	−0.6473	0.6616	0.7770	0.5956	0.7381
I2	−0.6473	1	−0.8017	−0.6612	−0.4469	−0.8009
I3	0.6616	−0.8017	1	0.8066	0.5542	0.7315
I4	0.7770	−0.6612	0.8066	1	0.5719	0.6564
I5	0.5956	−0.4469	0.5542	0.5719	1	0.3291
I6	0.7381	−0.8009	0.7315	0.6564	0.3291	1

TABLE 6 | Rock burst propensity prediction results.

Sample number	Comprehensive certainty				Prediction results in this paper	Actual grade
	μ_1	μ_2	μ_3	μ_4		
1	0.011	0.134	0.442	0.414	III	III
2	0.049	0.010	0.442	0.499	IV	IV
3	0.126	0.469	0.347	0.058	II	II
4	0.084	0.508	0.321	0.087	II	II
5	0.647	0.339	0.013	0.001	I	I
6	0.018	0.230	0.418	0.334	III	III
7	0.109	0.479	0.336	0.076	II	II
8	0.043	0.084	0.545	0.329	III	III
9	0.008	0.004	0.335	0.652	IV	IV
10	0.126	0.628	0.181	0.065	II	II
11	0.088	0.335	0.521	0.056	IIIa	II
12	0.726	0.250	0.023	0.000	I	I
13	0.008	0.012	0.339	0.641	IV[a]	III
14	0.011	0.021	0.582	0.387	III	III
15	0.128	0.523	0.334	0.016	II	II
16	0.008	0.005	0.380	0.607	IV	IV
17	0.017	0.041	0.597	0.346	III	III
18	0.053	0.142	0.517	0.288	III	III
19	0.490	0.482	0.028	0.000	I~II	I
20	0.168	0.576	0.215	0.041	II	II

[a]*Indicates misjudgement.*

Figure 6). The core data of wells zk504 and zk504 are shown in **Table 8** [57].

In this paper, six rock burst propensity prediction indexes are selected: the uniaxial compressive strength σ_c (I_1), ratio of the uniaxial compressive strength to the tensile strength σ_c/σ_t (brittleness coefficient, I_2), elastic deformation energy index Wet (I_3), and ratio of the maximum tangential stress to the uniaxial compressive strength σ_θ/σ_c (stress coefficient, I_4) of the rock, depth of the roadway H (I_5), and integrity coefficient of the rock mass K_v (I_6). A comparison of σ_c/σ_t and Wet is easy to obtain, and σ_θ/σ_c is determined by the formula of the maximum shear stress around the circular roadway:

$$\sigma_\theta = \xi(3-\lambda)p_y \tag{23}$$

where ξ is the laneway shape correction coefficient and λ is the side stress coefficient, which is equal to the ratio of the horizontal stress p_x to the vertical stress p_y.

The rock mass integrity coefficient K_v is the square of the longitudinal wave velocity of the rock mass. The longitudinal wave velocity V_p of the rock is easy to determine (as shown in **Formula 23**). Therefore, the value of K_v is determined according to V_p. The higher the elastic wave velocity is, the better the rock integrity. The rock sample test data of the Dongguashan Copper Mine are shown in **Table 8** [58].

TABLE 7 | Analysis of prediction results (TP, FP, FN values of different rockburst prediction grades).

	I	II	III	IV	Total
TP	3	6	6	3	18
FP	0	0	1	1	2
FN	0	1	1	0	2

$$K_v = \left(\frac{V_{pm}}{V_{pr}}\right)^2 \tag{24}$$

where K_v is the rock mass integrity coefficient, and V_{pm} is the longitudinal wave velocity of rock mass, and V_{pr} is the longitudinal wave velocity of indoor rock (block).

For the roadway height, since the height span is not very large, this paper takes the average measured height; based on these data, the value of the prediction index can be calculated. The calculation results are shown in **Table 9**.

Referring to the calculation method of the learning sample, the calculation and analysis of the actual engineering data can be comprehensively determined. The prediction results shown in **Table 10** show that the rock burst tendencies of the diorite and siltstone are the strongest while those of the garnet skarn are the

TABLE 8 | Rock sample test data of seven typical ore rocks from Donggua Mountain.

Rock type	Sampling depth	Stress level (p_x, p_y)	σ_c	σ_t	V_p	W_{et}
Skarn	631–637	(30.0, 25.4)	132.2	16.4	6,430	3.97
Diorite	720–735	(32.9, 28.0)	304.2	20.9	6,108	10.57
Garnet skarn	761–764	(33.9, 29.0)	128.6	13	7,025	5.76
Qixia formation marble	792–798	(34.9, 29.9)	78.3	6.8	4,709	3.11
Siltstone	837–849	(36.4, 31.2)	171.3	22.6	5,804	7.27
Quartz sandstone	850–853	(36.6, 31.5)	237.2	17.66	5,735	6.38

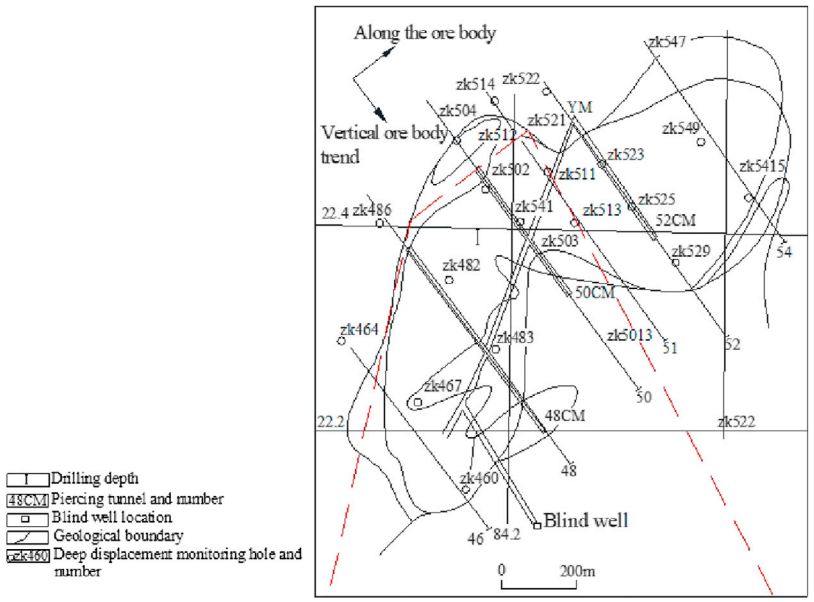

FIGURE 6 | Geological map of the 730 m middle section of the Dongguashan Copper Mine.

TABLE 9 | Rock burst tendency prediction value for the Dongguashan Copper Mine.

Rock type	Evaluation index					
	σ_c	σ_c/σ_t	W_{et}	σ_θ/σ_c	H	K_v
Skarn	132.2	8.06	3.97	0.55	634	0.75
Diorite	304.2	14.56	10.57	0.37	727.5	0.71
Garnet skarn	128.6	9.89	5.76	0.61	762.5	0.82
Qixia formation marble	78.3	11.51	3.11	0.82	795	0.55
Siltstone	171.3	7.58	7.27	0.53	843	0.68
Quartz sandstone	237.2	13.43	6.38	0.44	851.5	0.67

TABLE 10 | Rock burst tendency prediction results for the Dongguashan Copper Mine.

Rock type	Comprehensive certainty				Prediction results in this paper
	μ_1	μ_2	μ_3	μ_4	
Skarn	0.040	0.090	0.564	0.306	III
Diorite	0.128	0.306	0.178	0.389	IV
Garnet skarn	0.021	0.021	0.375	0.583	III~IV
Qixia formation marble	0.178	0.290	0.457	0.075	III
Siltstone	0.073	0.152	0.233	0.541	IV
Quartz sandstone	0.094	0.335	0.343	0.228	III

next strongest. The skarn grade is between III and IV, while the quartz sandstone and skarn are of grade III. The grade III predictions are the most certain, but the degree of membership for IV is not small. Finally, the Qixia Formation is predicted to be III (moderate rock burst).

Through the analysis of loading and unloading tests and the sum of the brittleness coefficient, impact energy index and elastic deformation energy index, the rock burst tendency of each rock sample type is ranked from the largest to the smallest: siltstone, quartz sandstone, garnet skarn, skarn, and Qixia group marble. The prediction results of this paper are basically consistent with this strong-to-weak ranking.

CONCLUSION

(1) To further evaluate the rock burst tendency and provide corresponding engineering technical guidance, this article selects the membership function cloud model that considers randomness and ambiguity and comprehensively accounts for the complexity of multi-factors and the correlation between factors in the rock burst evaluation problem. The CRITIC weighting algorithm is selected for the comprehensive evaluation, the rationality of the evaluation method is verified by selecting 20 groups of underground engineering rock burst example data, and the method is finally applied to the Dongguashan copper mine. The explosion tendency evaluation obtained good results.

(2) Although the edge of the cloud model with uniform distribution reduces the actual error to a certain extent, deviations may occur between the actual production situation and the analysis result, such as the calculation of some parameters for Dongguashan. Therefore, the risk assessment result can only be used as a reference and the actual situation needs to be analyzed in detail. Capturing the risk factors that affect the occurrence of the disaster by the theoretical analysis process is indeed difficult because regardless of the

influencing factor selected for modeling, analysis and calculation, other objective factors may be ignored.

DATA AVAILABILITY STATEMENT

The original contributions presented in the study are included in the article/Supplementary Material, further inquiries can be directed to the corresponding author.

AUTHOR CONTRIBUTIONS

The first author JW drafted the content of the manuscript, there are related contents about on-site practice in this manuscript, MH is a member of Hongda Blasting Engineering Group Co., Ltd had in China and he is a Doctor of Engineering in Central South University who made relevant contributions and, the corresponding author JG was responsible for the guidance of the manuscript and put forward relevant revision opinions.

REFERENCES

1. Wang Y-C, Hong-wen J, Zhang Q, Wei L, Zhi-min X. A normal cloud model-based study of grading prediction of rock burst intensity in deep underground engineering. *Rock Soil Mech* (2015) 4:1189–94. doi:10.16285/j.rsm.2015.04.037
2. Zhou C-J, Zhang Y, Xu H, Gao Y-D, Zhang R. Review of rock burst in underground engineering. *Adv Sci Technol Water Resour* (2013) 3:77–83+94.
3. Hui-lian Y. Rock burst characteristics, causes and influencing factors. *Coal Engineer* (1989) 2:37–42.
4. Mansurov VA. Prediction of rock bursts by analysis of induced seismicity data. *Int J Rock Mech Min Sci* (2001) 38:893–901. doi:10.1016/S1365-1609(01)00055-7
5. Tang L, Xia KA. Seismological method for prediction of areal rock bursts in deep mine with seismic source mechanism and unstable failure theory. *J Cent South Univ T* (2010) 17:947–53. doi:10.1007/s11771-010-0582-5
6. Fujii Y, Ishijima Y, Deguchi G. Prediction of coal face rock bursts and micro seismicity in deep longwall coal mining. *J Rock Mech Mining* (1997) 34:85–96. doi:10.1016/S1365-1609(97)80035-4
7. Sirit B, Wattimena RK, Widodo NP. Rock burst prediction of a cut and fill mine by using energy balance and induced stress. *Proc Earth Planet Sci* (2013) 6:426–34. doi:10.1016/j.proeps.2013.01.056
8. Cook NGW. The basic mechanics of rock bursts. *J South African Inst Mining Metallurgy* (1963) 64:71–81.
9. Russense BF. *Analysis of rock spalling for tunnels in steep valley sides (in Norwegian).* Trondheim, Norwegian: Norwegian Institute of Technology (1974).
10. Kornowski J, Kurzeja J. Prediction of rock burst probability given seismic energy and factors defined by the expert method of hazard evaluation (MRG). *Acta Geophys* (2012) 60:472–86. doi:10.2478/s11600-012-0002-3
11. Meng F, Zhou H, Wang Z, Zhang L, Kong L, Li S, et al. Experimental study on the prediction of rock burst hazards induced by dynamic structural plane shearing in deeply buried hard rock tunnels. *Int J Rock Mech Min Sci* (2016) 86:210–23. doi:10.1016/j.ijrmms.2016.04.013
12. Chen B, Feng X, Li Q, Luo R, Li S. Rock burst intensity classification based on the radiated energy with damage intensity at Jinping II hydropower station, China. *Rock Mech Rock Eng* (2015) 48:289–303. doi:10.1007/s00603-013-0524-2
13. Wang JA, Park HD. Comprehensive prediction of rock burst based on analysis of strain energy in rocks. *Tunn Undergr Space Technol* (2001) 16:49–57. doi:10.1016/S0886-7798(01)00030-X
14. Sharan SK. A finite element perturbation method for the prediction of rock burst. *Comput Struct* (2007) 85:1304–9. doi:10.1016/j.compstruc.2006.08.084
15. Hirata A, Kameoka Y, Hirano T. Safety management based on detection of possible rock bursts by AE monitoring during tunnel excavation. *Rock Mech Rock Eng* (2007) 40:563–76. doi:10.1007/s00603-006-0122-7
16. Bao-xin JIA, Chen H, Pan Y-s, Yang C. Rock burst evaluation technology of multi-parameters synthetic index. *J Disaster Prev Mitig Eng* (2019) 2:330–7. doi:10.13409/j.cnki.jdpme.2019.02.019
17. Zhang Z-Z, Tian Z-L, Lin B. Prediction research of rock burst tendency based on the acoustic emission test. *Metal Mine* (2011) 8:56–9.
18. Dou L, Chen T, Gong S, He H, Zhang S. Rock burst hazard determination by using computed tomography technology in deep workface. *Saf Sci* (2012) 50:736–40. doi:10.1016/j.ssci.2011.08.043
19. Li X, Wang E, Li Z, Liu Z, Song D, Qiu L. Rock burst monitoring by integrated microseismic and electromagnetic radiation methods. *Rock Mech Rock Eng* (2016) 49:4393–406. doi:10.1007/s00603-016-1037-6
20. Frid V. Rock burst hazard forecast by electromagnetic radiation excited by rock fracture. *Rock Mech Rock Eng* (1997) 30:229–36.
21. Sun J, Wang L-G, Zhang H-L, Shen Y-F. Application of fuzzy neural network in predicting the risk of rock burst. *Proc Earth Planet Sci* (2009) 1:536–43. doi:10.1016/j.proeps.2009.09.085
22. Li SH, Wang SY, Zhu J, Li B, Yang J, Wu LZ. Prediction of rock burst tendency based on weighted fusion and improved cloud model. *Chin J Geotech Eng* (2018) 6:1075–83. doi:10.11779/CJGE201806013
23. Guo J, Zhang W, Zhao Y. A multidimensional cloud model for Rock burst evaluation. *Chin J Rock Mech Eng* (2018) 37(5):1199–206. doi:10.13722/j.cnki.jrme.2017.1522
24. Zhang L-W, Zhang D-Y, Shu-cai L, Dao-hong Q. Application of RBF neural network to rock burst evaluation based on rough set theory. *Rock Soil Mech* (2012) 33:270–6. doi:10.16285/j.rsm.2012.s1.008
25. Gao W. Prediction of rock burst based on ant colony clustering algorithm. *Chin J Geotech Eng* (2010) 6:874–80.
26. Liu ZB, Shao JF, Xu WY, Meng YD. Prediction of rock burst classification using the technique of cloud models with attribution weight. *Nat Hazards* (2013) 68:549–68. doi:10.1007/s11069-013-0635-9
27. Zhou KP, Lin Y, Deng HW, Li J, Liu CJ. Prediction of rock burst classification using cloud model with entropy weight. *Trans Nonferrous Metals Soc China* (2016) 26:1995–2002. doi:10.1016/S1003-6326(16)64313-3
28. Zhou J, Li X, Shi X. Long-term prediction model of rockburst in underground openings using heuristic algorithms and support vector machines. *Saf Sci* (2012) 50:629–44. doi:10.1016/j.ssci.2011.08.065
29. Chen X, Xiao-li L, En-zhi W, Wang S-J. Rock burst evaluation and classification based on the ideal-point method of information theory. *Tunn Undergr Space Technol* (2018) 81:382–90. doi:10.1016/j.tust.2018.07.014
30. Lu F-R, Chen J-H. Rock burst evaluation method based on AHP and entropy weight TOPSIS model. *Gold Sci Technol* (2018) 3:365–71.
31. Ting-xin W, Xiao-yu C. Forecast research on the rock burst liability based on the comprehensive evaluation H-PSO-SVM Model. *J Saf Environ* (2018) 2:440–5. doi:10.13637/j.issn.1009-6094.2018.02.006
32. Zhang B, Dai X-G. A cloud model for predicting rock burst intensity grade based on index distance and uncertainty measure. *Rock Soil Mech* (2017) 38:257–65. doi:10.16285/j.rsm.2017.S2.036
33. Faradonbeh RS, Taheri A. Long-term prediction of rockburst hazard in deep underground openings using three robust data mining techniques. *Eng Comput* (2019) 2:659–75. doi:10.1007/s00366-018-0624-4
34. Faradonbeh RS, Taheri A, Sousa LRE, Karakus M. Rockburst assessment in deep geotechnical conditions using true-triaxial tests and data-driven approaches. *Int J Rock Mech Min Sci* (2020) 128:104279. doi:10.1016/j.ijrmms.2020.104279
35. Zou ZH, Yun Y, Sun JN. Entropy method for determination of weight of evaluating indicators in fuzzy synthetic evaluation for water quality assessment. *J Environ Sci (China)* (2006) 18:1020–3. doi:10.1016/s1001-0742(06)60032-6
36. Rissanen JJ. Fisher information and stochastic complexity. *IEEE Trans Inf Theory* (1996) 42(1):40–7. doi:10.1109/18.481776
37. De-yi LI, Meng H-J, Xue-mei SHI. Affiliated cloud and affiliated cloud generator. *Comput Res Develop* (1995) 32:15–20.
38. Li D, Chen H, Fan J, Shen C. A novel qualitative control method to inverted pendulum systems. *IFAC Proc Vol* (1999) 32:1495–500. doi:10.1016/S1474-6670(17)56253-9
39. Efremenko DS, Schüssler O, Doicu A, Loyola D. A stochastic cloud model for cloud and ozone retrievals from UV measurements. *J Quant Spectr Radiat Transf* (2016) 184:167–79. doi:10.1016/j.jqsrt.2016.07.008

40. Wang J, Guo J. Research on rock mass quality classification based on an improved rough set–cloud model. *IEEE Access* (2019) 7:123710–24. doi:10.1109/ACCESS.2019.2938567
41. Zhu M, Hahn A, Wen YQ. Identification-based controller design using cloud model for course-keeping of ships in waves. *Eng Appl Artif Intell* (2018) 75: 22–35. doi:10.1016/j.engappai.2018.07.011
42. Zang W, Ren L, Zhang W, Liu X. A cloud model-based DNA genetic algorithm for numerical optimization problems. *Future Generat Comput Syst* (2018) 81: 465–77. doi:10.1016/j.future.2017.07.036
43. Hongbo G, Guatao X, Hongzhe L, Xinyu Z, Deyi L. Lateral control of autonomous vehicles based on learning driver behavior *via* cloud model. *J China Univ Posts Telecommun* (2017) 24:10–7. doi:10.1016/S1005-8885(17)60194-8
44. Guo J, Wang J, Liu S. Application of an improved cloud model and distance discrimination to evaluate slope stability. *Math Probl Eng* (2019) 2019:1–18. doi:10.1155/2019/8315894
45. Mou R, Cai Q. Research on classification method of surrounding rock stability based on cloud model and rough set theory. *J Saf Environ* (2018) 18:1251–7. doi:10.13637/j.issn.1009-6094.2018.04.003
46. Khedim F, Labraoui N, Ari AAA. A cognitive chronometry strategy associated with a revised cloud model to deal with the dishonest recommendations attacks in wireless sensor networks. *J Netw Comput Appl* (2018) 123:42–56. doi:10.1016/j.jnca.2018.09.001
47. Bao Y, Lin L, Wu S, Deng KAW, Petropoulos GP. Surface soil moisture retrievals over partially vegetated areas from the synergy of Sentinel-1 and Landsat 8 data using a modified water-cloud model. *Int J Appl Earth Obs Geoinf* (2018) 72:76–85. doi:10.1016/j.jag.2018.05.026
48. Wang D, Zeng D, Singh VP, Xu P, Liu D, Wang Y, et al. A multidimension cloud model-based approach for water quality assessment. *Environ Res* (2016) 149:113–21. doi:10.1016/j.envres.2016.05.012
49. Li D, Du Y. *Artificial intelligence with uncertainty*. 2nd ed. Beijing, China: National Defense Industry Press (2017). p. 1–30.
50. Xue Y, Li Z, Li S, Qiu D, Tao Y, Wang L, et al. Prediction of rock burst in underground caverns based on rough set and extensible comprehensive evaluation. *Bull Eng Geol Environ* (2019) 78:417–29. doi:10.1007/s10064-017-1117-1
51. Lin Y, Zhou K, Li J. Application of cloud model in rock burst evaluation and performance comparison with three machine learning algorithms. *IEEE Access* (2018) 6:30958–68. doi:10.1109/ACCESS.2018.2839754
52. Wang Y-H, Wo-dong L, Qi-guang L, Xu Y, Tan G-H. Fuzzy comprehensive evaluation method pf Rock burst evaluation. *Chin J Rock Mech Eng* (1998) 5: 493–501.
53. Shang Y, Zhang J, Fu B. Analyses of three parameters for strain mode rock burst and expression of rock burst potential. *Chin J Rock Mech Eng* (2013) 8: 1520–7.
54. Wang Y-C, Hong-wen J, Xian-wei J, Mu T-A, Zhang C-L. Model for classification and prediction of rock burst intensity in a deep underground engineering with rough set and efficacy coefficient method. *J Centr South Univ (Sci Technol)* (2014) 6:1992–7.
55. Diakoulaki D, Mavrotas G, Papayannakis L. Determining objective weights in multiple criteria problems: the critic method. *Comput Oper Res* (1995) 7: 763–70. doi:10.1016/0305-0548(94)00059-H
56. Wang Y, Jiang X, Zhang L. Research on the evaluation of science and technological awards based on improved CRITIC method and cloud model. *J Hunan Univ (Nat Sci)* (2014) 04:118–24.
57. Guo J, Zhao Y, Zhang W, Dai X, Xie X. Stress analysis of mine wall in panel barrier pillar-stope under multi-directional loads. *J Central South Univ (Sci Technol)* (2018) 49(12):3020–8.
58. Dong-qing L. *Theory and technology of large-scale mining of deep well hard rocks—research and practice of mining of Dongguashan copper deposit*. 1st ed. Beijing, China: Metallurgical Industry Press (2009). p. 50–S78.

Conflict of Interest: Author MH was employed by company Hongda Blasting Engineering Group, Co., Ltd.

The remaining authors declare that the research was conducted in the absence of any commercial or financial relationships that could be construed as a potential conflict of interest.

frontiers in Physics

ORIGINAL RESEARCH
published: 11 March 2021
doi: 10.3389/fphy.2021.587477

An Analytical Method to Test Elastic Rock Mass Parameters Based on a Macro-Joint Model

Junting Dong[1], *Yuhua Fu*[2]* *and Guanshi Wang*[3]

[1]Fujian Makeng Mining Co., Ltd., Longyan, China, [2]College of Applied Science, Jiangxi University of Science and Technology, Ganzhou, China, [3]School of Architecture and Surveying and Mapping Engineering, Jiangxi University of Science and Technology, Ganzhou, China

The measurement of rock joint parameters is a hotly debated and difficult problem in rock mechanics. Joints have great influence on the propagation of stress waves in rock mass. Since the multiple reflections of stress waves propagating inside the joints is not considered accurately, the reflection wave shape cannot be obtained by using a discontinuous displacement model to describe the deformation characteristics of joints. A joint is regarded as a rock using the first analysis of the stress wave transmission in the course of a single joint and the propagation law of a reflection wave. For rocks orientated in the same direction with the same type of wave superposition, stress wave parameters can be established through the multiple reflection effect of a single-joint analysis model. Further to this, analysis using an extended single-joint model can estimate a stress wave under the condition of a vertical incidence group parallel strata analysis model. Taking a single macro-joint as an example, a measuring line is arranged in the normal direction of the joint, and two measuring points on both sides of the joint are arranged in a line to record the waveforms of the incident and transmitted waves. According to the established single-joint analysis model, the calculated waveform of the incident side measuring point is calculated by using the measured waveform of the transmission side measuring point, and the measured waveform of the incident side measuring point is compared with the measured waveform of the incident side measuring point, and the joint elastic parameters with the minimum error are obtained by using the principle of least square method. Six tests were carried out through joints with a thickness of 0.04 m. The results show that the primary wave (P-wave) and secondary vertical wave (SV wave) velocity of joints obtained from many tests have good consistency, which indicates that the joint analysis model has good stability, and the test solution of joint elastic parameters based on the model is reliable.

Keywords: stress wave, macro-joint, rock stratum model, vertical incidence, dynamic test

OPEN ACCESS

Edited by:
Guoyang Fu,
Monash University, Australia

Reviewed by:
Wenzheng Yue,
China University of Petroleum, China
Mohammad Fatehi Marji,
Yazd University, Iran

***Correspondence:**
Yuhua Fu
fyh1369@126.com

Specialty section:
This article was submitted to Interdisciplinary Physics, a section of the journal Frontiers in Physics

Received: *26 July 2020*
Accepted: *22 January 2021*
Published: *11 March 2021*

Citation:
Dong J, Fu Y and Wang G (2021) An Analytical Method to Test Elastic Rock Mass Parameters Based on a Macro-Joint Model. Front. Phys. 9:587477. doi: 10.3389/fphy.2021.587477

INTRODUCTION

Due to the stratification of rock, multiple transmission and reflection effects will occur when a stress wave passes through a rock formation. Some scholars have proposed a simplified calculation method for transmitted waves and reflected waves when stress waves pass through group parallel rock formations. Zhang [1]proposed that the multiple transmission and reflection times of stress waves

inside joints are related to the P wave velocity of the joint, the P wave velocity of rock, wavelength, and joint thickness. Li et al. [2] presented an equivalent wave resistance method for solving the propagation of stress waves in layered rocks, which can solve stress wave transmission and energy transfer effects under different waveforms and rock structures. Pyrak-Nolte et al. [3, 4] proposed a simplified method for calculating the transmission coefficients of multiple joints by multiplying the transmission coefficients of a single joint. Cai et al. [5, 6] calculated the numerical solution of a transmission wave in group parallel rock strata under a vertical incident of a P wave using the characteristic line method. On the basis of the virtual vibration source method, Li et al. [7, 8] proposed a time-domain recursive analysis method for grouped parallel joints, using the same mechanical parameters, under an oblique incidence of stress waves. The above methods were based on the assumption that the mechanical parameters of each rock stratum and joint are the same. In fact, the mechanical parameters of group rock strata are often different, and so it was necessary to put forward an improved analysis model and calculation method.

In addition, because the mechanical parameters of joints were smaller than those of the rocks on both sides, the joints will produce a larger deformation under external loads, which precedes the failure or instability of the rocks on both sides. Accurate testing of the mechanical parameters of joints is a precondition for geotechnical engineering design, stability analysis, and numerical simulation. At present, there are two methods to test joint parameters using a stress wave. The first is to test the longitudinal and transverse wave velocities by using the travel time variation of stress waves through a joint. The second method is to establish the relationship among the amplitude, frequency, and joint parameters according to the variation of the amplitude and frequency components of the wave when a stress wave passes through the joint. Because the change in the amplitude spectrum and phase spectrum produced by stress wave propagation in rock is reflected in the change of the waveform, the change in the waveform of the stress wave through joints is more obvious than that of the travel time; this has been confirmed through a large number of field tests [9–12, 17, 18]. Therefore, it is more practical to use the change in the waveform of the stress wave to test the mechanical parameters of joints.

To use the waveform change to test the mechanical parameters of joints, Wang, Guo, and Wang et al. [9, 10] established a joint analysis model based on the in-depth analysis of the stress wave propagation law in rock, and a method for testing the viscosity coefficient of the rock and joint elastic modulus by using the waveform change was proposed. Hu and Long [11, 12] equated joints to linear springs and described the deformation characteristics of joints with a displacement discontinuity model; they then established a testing method for rock joint stiffness based on the frequency spectrum variation law. The MF Marji [13] semi-analytical method is used to study the interaction between cracks and rock interface in heterogeneous rock materials under hydraulic action. M Behnia et al. [14] stated that the boundary displacement technique is used to predict the propagation path of the original crack and wing crack.

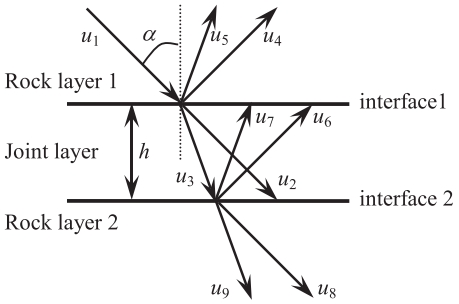

FIGURE 1 | Schematic diagram of multiple transmissions and reflections of a stress wave through joints.

However, without considering the multiple transmission and reflection effects of stress waves in joints, the displacement discontinuity model cannot accurately calculate the reflection wave through joints. Furthermore, for joints with greater thickness, the method has large errors.

In view of the limitation of the displacement discontinuity model, the joint is regarded as a rock stratum, and the multiple transmission and reflection effects in the joint are considered accurately. The analytical model of group parallel rock strata under single-joint and vertical incidence is established. On this basis, according to the principle of the least square method, the test method of joint elastic parameters is proposed, and the test method of joint elastic parameters is used. The elastic modulus and Poisson's ratio of *in situ* joints are calculated.

ANALYSIS MODEL OF A MACRO-JOINT

Single-Joint Model

The geotechnical model shown in **Figure 1** is a representative single-jointed rock mass model, assuming that the upper boundary of rock 1 is infinite, the lower boundary of rock layer 2 is infinite, the interface between the joint layer and rock layer 1 is interface 1, and the interface between the joint layer and rock layer 2 is interface 2. The interface between the joint layer and the rock layer is generally divided into two categories: one is the interface described by the displacement discontinuity model [15–25] and the other is the elastic interface of the tightly connected rocks [26]. When the stress wave passes through a single-jointed rock mass, multiple transmissions and reflections will occur at all interfaces (**Figure 1**). As shown by Snell's law, for stress waves in rock layer 1, the angles between all outgoing primary–secondary vertical waves (P–SV waves) and the normal line of interface 1 are the same. For stress waves in the joint layer, the angles between the inward P–SV wave and the normal line of interface 2 are the same, and the angle between the outward P–SV wave and the normal line of interface 1 is the same. For stress waves in rock layer 2, the angles between all inward P-SV waves and the normal line of interface 2 are the same.

According to the superposition principle, the relationship between the waveforms in a single-jointed rock mass can be obtained: The outgoing P wave $u4$ in rock layer 1 is equal to the

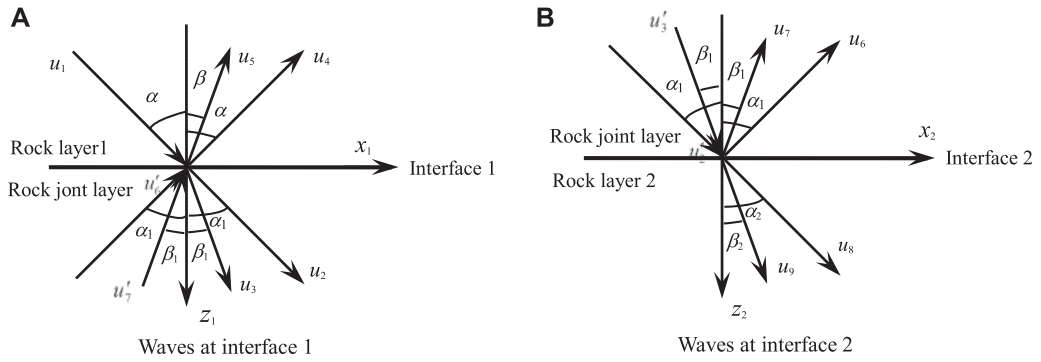

FIGURE 2 | Incidental, reflective, and transmitted stress waves at interfaces.

superposition of the reflected P wave component of incident P wave $u1$, the transmitted P wave component of outgoing P wave $u6$ in the joint layer, and the transmitted P wave component of outgoing SV wave $u7$ in the joint layer. The outgoing SV wave $u5$ in rock layer 1 is equal to the superposition of the reflected SV wave component of incident P wave $u1$, the transmitted SV wave component of outgoing P wave $u6$ in the joint layer, and the transmitted SV wave component of outgoing SV wave $u7$ in the joint layer. The inward P wave $u8$ in rock layer 2 is equal to the superposition of the transmitted P wave component of inward P wave $u2$ in the joint layer and the transmitted P wave component of inward SV wave $u3$. The inward SV wave $u9$ in rock layer 2 is equal to the superposition of the transmitted SV wave component of inward P wave $u2$ in the joint layer and the transmitted SV wave component of inward SV wave $u3$. The inward P wave $u2$ in the joint layer is equal to the superposition of the transmitted P wave component of incident P wave $u1$, the reflected P wave component of outgoing P wave $u6$ in the joint layer, and the reflected P wave component of outgoing SV wave $u7$ in the joint layer. The inward SV wave $u3$ in the joint layer is equal to the superposition of the transmitted SV wave component of incident P wave $u1$, the reflected SV wave component of outgoing P wave $u6$ in the joint layer, and the reflected SV wave component of outgoing SV wave $u7$ in the joint layer. The outgoing P wave $u6$ in the joint layer is equal to the superposition of the reflected P wave component of inward P wave $u2$ and the reflected P wave component of inward SV wave $u3$ in the joint layer. The outgoing SV wave $u7$ in the joint layer is equal to the superposition of the reflected SV wave component of inward P wave $u2$ and the reflected SV wave component of inward SV wave $u3$ in the joint layer.

Next, the stress wave systems on interfaces 1 and 2 are taken as research objects, and the coordinate systems are established (**Figure 2**). Assuming that waveforms on all sides are harmonic, the relationship between waveforms on interface 1 is shown in **Eqs. 1–4**:

$$u_2 = u_1 T_{\mathrm{PP1j}} + u_6' R_{\mathrm{PPj1}} + u_7' R_{\mathrm{SPj1}}, \tag{1}$$

$$u_3 = u_1 T_{\mathrm{PS1j}} + u_6' R_{\mathrm{PSj1}} + u_7' R_{\mathrm{SSj1}}, \tag{2}$$

$$u_4 = u_1 R_{\mathrm{PP1j}} + u_6' T_{\mathrm{PPj1}} + u_7' T_{\mathrm{SPj1}}, \tag{3}$$

$$u_5 = u_1 R_{\mathrm{PS1j}} + u_6' T_{\mathrm{PSj1}} + u_7' T_{\mathrm{SSj1}}, \tag{4}$$

where TPP1j represents the transmission coefficient of P wave transmitted from rock 1 through interface 1; TPS1j represents the transmission coefficient of SV wave transmitted by rock 1 through interface 1; RPP1j represents the reflection coefficient of P wave reflected by rock 1 through interface 1; RPS1j represents the reflection coefficient of SV wave reflected from rock 1 through interface 1.

TPPj1 represents the transmission coefficient of P wave transmitted by joint 1 through interface 1; TPSj1 represents the transmission coefficient of SV wave transmitted by joint 1 through interface 1; RPPj1 represents the reflection coefficient of P wave reflected by joint 1 through interface 1; RPSj1 represents the reflection coefficient of SV wave reflected by P wave passing through interface 1 from joint 1; TSPj1 represents the transmission coefficient of P wave transmitted by joint 1 through interface 1; TSSj1 represents the transmission coefficient of SV wave transmitted by joint 1 through interface 1; RSPj1 represents the reflection coefficient of P wave reflected by SV wave passing through interface 1 from joint 1; RSSj1 represents the reflection coefficient of SV wave reflected from joint 1 through interface 1.

The relationship between waveforms at interface 2 is shown in **Eqs. 5–8**:

$$u_6 = u_2' R_{\mathrm{PPj2}} + u_3' R_{\mathrm{SPj2}}, \tag{5}$$

$$u_7 = u_2' R_{\mathrm{PSj2}} + u_3' R_{\mathrm{SSj2}}, \tag{6}$$

$$u_8 = u_2' T_{\mathrm{PPj2}} + u_3' T_{\mathrm{SPj2}}, \tag{7}$$

$$u_9 = u_2' T_{\mathrm{PSj2}} + u_3' T_{\mathrm{SSj2}}, \tag{8}$$

where TPPj2 represents the transmission coefficient of P wave transmitted from joint 1 to interface 2; TPSj2 represents the transmission coefficient of SV wave transmitted by joint 1 through interface 2; RPPj2 represents the reflection coefficient of P wave reflected from joint 1 through interface 2; RPSj2 represents the reflection coefficient of SV wave reflected by P wave passing through interface 2 from joint 1; TSPj2 represents the transmission coefficient of P wave

transmitted from joint 1 to interface 2; TSSj2 represents the transmission coefficient of SV wave transmitted by joint 1 through interface 2; RSPj2 represents the reflection coefficient of P wave reflected by SV wave passing through interface 2 from joint 1; RSSj2 represents the reflection coefficient of SV wave reflected from joint 1 through interface 2.

u_2'-the waveform obtained by $u2$ propagating distance h/cosα1 at wave velocity cpj;

u_3'-the waveform obtained by u_3 propagating distance h/cosβ_1 at wave velocity c_{Sj}.

According to the propagation law of stress wave in elastic medium, the relationships between $u2$ and u_2', $u3$, and u_3' are [28]:

$$u_2 = u_2'\left(t + \frac{h}{c_{Pj}\cos\alpha_1}\right), \tag{9}$$

$$u_3 = u_3'\left(t + \frac{h}{c_{Sj}\cos\beta_1}\right), \tag{10}$$

where h is the thickness of the joint layer; c_pj and $c$sj are, respectively, the propagation velocities of the P wave and SV wave in the joint layer, α1 and β1 are, respectively, the angles between the P wave and SV wave in the joint layer and the interface normal.

u_6'-the waveform obtained by $u6$ propagating distance h/cosα1 at wave velocity cpj;

u_7'-the waveform obtained by u_7 propagating distance h/cosβ_1 at wave velocity c_{Sj}.

According to the propagation law of stress wave in elastic medium, the relationships between $u6$ and u' *6*, $u7$, and u' *7* are:

$$u_6 = u_6'\left(t + \frac{h}{c_{Pj}\cos\alpha_1}\right), \tag{11}$$

$$u_7 = u_7'\left(t + \frac{h}{c_{Sj}\cos\beta_1}\right). \tag{12}$$

The general expression of each wave is as follows [27]:

$$u_n = A_n \exp[i(\omega t - k_{xn}x - k_{zn}z)] \,(n = 1, 2, \ldots, 9), \tag{13}$$

where k_xn is the number of SV waves. When the component of the stress wave in the X-direction is in the same direction as the X-axis, k_xn = ωsinϕn/$c$sn. When the component of the stress wave in the X-direction is opposite to the X-axis direction, k_xn = -ωsinϕn/$c$sn. In a similar way, k_zn is the number of P waves. When the component of the stress wave in the Z-direction is in the same direction as the Z-axis, k_zn = ωcosϕn/$c$pn. When the component of the stress wave in the Z-direction is opposite to the Z-axis direction, k_zn = -ωcosϕn/$c$pn. ϕn is the angle between the stress wave and interface normal, $c$sn is the velocity of the SV wave, and $c$pn is the velocity of the SV wave.

The relationship between the amplitudes of each wave can be obtained from **Eqs. 1–13**:

$$\begin{bmatrix} 1 & 0 & 0 & 0 & -m_1R_{PPj1} & -m_2R_{SPj1} & 0 & 0 \\ 0 & 1 & 0 & 0 & -m_1R_{PSj1} & -m_2R_{SSj1} & 0 & 0 \\ 0 & 0 & 1 & 0 & -m_1T_{PPj1} & -m_2T_{SPj1} & 0 & 0 \\ 0 & 0 & 0 & 1 & -m_1T_{PSj1} & -m_2T_{SSj1} & 0 & 0 \\ -m_1R_{PPj2} & -m_2R_{SPj2} & 0 & 0 & 1 & 0 & 0 & 0 \\ -m_1R_{PSj2} & -m_2R_{SSj2} & 0 & 0 & 0 & 1 & 0 & 0 \\ -m_1T_{PPj2} & -m_2T_{SPj2} & 0 & 0 & 0 & 0 & 1 & 0 \\ -m_1T_{PSj2} & -m_2T_{SSj2} & 0 & 0 & 0 & 0 & 0 & 1 \end{bmatrix} \times \begin{bmatrix} M_2 \\ M_3 \\ R_{PP} \\ R_{PS} \\ M_6 \\ M_7 \\ T_{PP} \\ T_{PS} \end{bmatrix} = \begin{bmatrix} T_{PP1j} \\ T_{PS1j} \\ R_{PP1j} \\ R_{PS1j} \\ 0 \\ 0 \\ 0 \\ 0 \end{bmatrix}, \tag{14}$$

where $m1$ = exp [-iωh/($c$pjcosα1)], $m2$ = exp [-iωh/($c$sjcosβ1)], Rpp = $A4$/$A1$, Rps = $A5$/$A1$, Rpp and Rps are, respectively, the total reflection coefficients of the P and SV waves of the P wave reflected from rock layer 1 through the joint layer and back to rock layer 1, and ω is the circular frequency of the incident wave. Mk = Ak/A1 (k = 2,3,6,7) , Tpp = A8/A1, Tps = A9/A1, andTpp and Tps are, respectively, the total transmission coefficients of P and SV waves of the P wave transmitted from rock layer 1 through the joint layer and back to rock layer 2.

When the P wave is normally incident ($\alpha = 0^\circ$), the stress wave will not produce a converted wave, and then **Eq. 14** can be simplified to:

$$M_2 - m_1R_{PPj1}M_6 = T_{PP1j}, \tag{15}$$

$$R_{PP} - m_1T_{PPj1}M_6 = R_{PP1j}, \tag{16}$$

$$-m_1R_{PPj2}M_2 + M_6 = 0, \tag{17}$$

$$-m_1T_{PPj2}M_2 + T_{PP} = 0. \tag{18}$$

From equations (15) and (17):

$$M_2 = \frac{T_{PP1j}}{1 - m_1^2R_{PPj1}R_{PPj2}}, \tag{19}$$

$$M_6 = \frac{m_1R_{PPj2}T_{PP1j}}{1 - m_1^2R_{PPj1}R_{PPj2}}. \tag{20}$$

Substituting **Eqs. 20** and **(19)** into **Eqs. 16** and **(18)**, respectively:

$$R_{PP} = R_{PP1j} + \frac{m_1^2R_{PPj2}T_{PP1j}T_{PPj1}}{1 - m_1^2R_{PPj1}R_{PPj2}}, \tag{21}$$

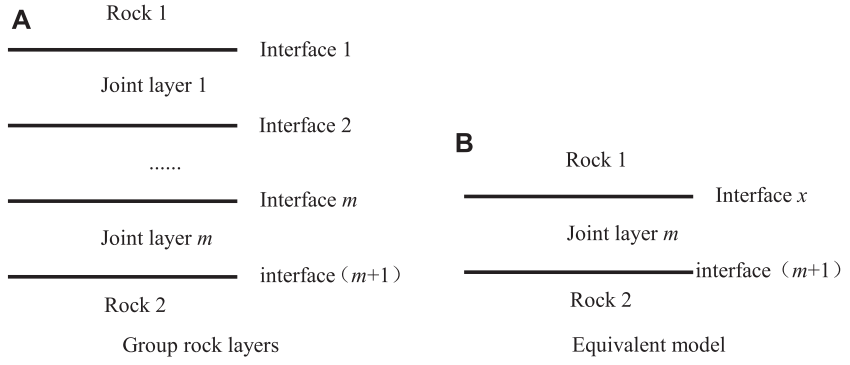

FIGURE 3 | Schematic diagram of group parallel joint model.

$$T_{\mathrm{PP}} = \frac{m_1^2 T_{\mathrm{PPj2}} T_{\mathrm{PP1j}}}{1 - m_1^2 R_{\mathrm{PPj1}} R_{\mathrm{PPj2}}}. \tag{22}$$

Group Parallel Joint Model

For the actual rock mass with multiple parallel joints, as shown in **Figure 3A**, the method of calculating the total transmission and reflection coefficients of a single-jointed rock mass when the P wave incident is vertical can still be generalized. First, the joint layers 1 to (*m*-1) are regarded as an interface *x* (**Figure 3B**). Then, the group parallel joint model can be equivalent to many single-joint models, so the recursive formula for the transmission and reflection coefficients with P wave vertical incidence can be deduced by **Eqs. (21)** and **(22)**.

In order to obtain the transmission and reflection coefficients of the joint layer *m* with P wave vertical incidence, it is necessary to know the transmission and reflection coefficients of the joint layer (*m*-1) with P wave vertical incidence. In order to obtain the transmission and reflection coefficients of the joint layer (*m*-1) with P wave vertical incidence, it is necessary to know the transmission and reflection coefficients of joint layer (*m*-2) with P wave vertical incidence. By analogy, in order to obtain the transmission and reflection coefficients of joint layer 2 with P wave vertical incidence, it is necessary to know the transmission and reflection coefficients of joint layer 1 with P wave vertical incidence. For the problem of P wave vertical incidence on the single-joint layer, the transmission and reflection coefficients of P wave vertical incidence on joint layer 1 can be obtained by using **Eqs. (21)** and **(22)**. By analogy, the transmission and reflection coefficients of joint layer *m* can be calculated when P waves incidents are vertical.

MECHANICAL PARAMETERS TEST OF A MACRO-JOINT

Test Principle of Macro-Joint Parameters

Suppose that there is a joint layer with thickness *h* in a rock mass, the two sides of the joint layer are complete rocks, and the joint is seamlessly connected with the rock. In order to test the elastic modulus and Poisson's ratio of the joint, measuring points for recording the stress waveform are arranged on both sides of the joint. The arrangement of vibration source points, measuring lines, and measuring points are shown in **Figure 4**. In the field test, the incident wave is generated by a geological hammer striking at the source point, and two three-directional acceleration sensors with frequencies ranging from 0.2 Hz to 5 kHz are arranged at measuring points 1 and 2 to record the vibration waveforms.

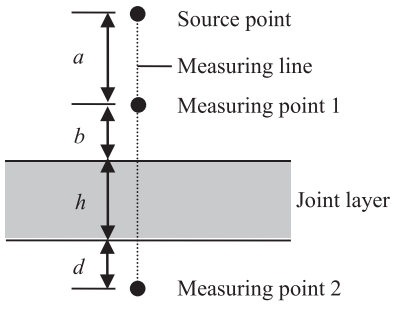

FIGURE 4 | Schematic diagram of measuring points.

A vibration load with small stress amplitude is generated at the source point, and both the rock layer and the joint layer are elastically deformed. According to the spherical diffusion effect of the stress wave excited by the point source in the rock mass and the spectrum of the transmitted wave at measuring point 2, the calculated spectrum of the incident and the reflected wave can be, respectively, obtained.

$$\tilde{u}_{I\mathrm{js}}(\omega) = \frac{k_1 \tilde{u}_2(\omega)}{T_{\mathrm{PP}}}, \tag{23}$$

$$\tilde{u}_{\mathrm{Rjs}}(\omega) = \frac{k_2 R_{\mathrm{PP}}}{T_{\mathrm{PP}}} \tilde{u}_2(\omega). \tag{24}$$

In the formula:

$$k_1 = D_{\mathrm{T}}/D_{\mathrm{I}} \exp(\mathrm{i}b\omega/c_{\mathrm{P1}} + \mathrm{i}d\omega/c_{\mathrm{P2}}),$$
$$k_2 = D_{\mathrm{T}}/D_{\mathrm{R}} \exp(\mathrm{i}d\omega/c_{\mathrm{P2}} - \mathrm{i}b\omega/c_{\mathrm{P1}}),$$

where $u2(\omega)$ is the measured P wave spectrum at point 2, *T*pp and *R*pp are, respectively, transmission and reflection coefficients of

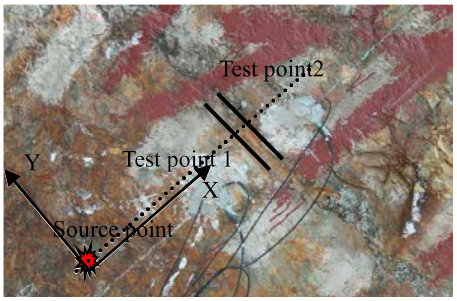

FIGURE 5 | The vibration source and measuring point locations of the field test.

the joint layer with P wave vertical incidence. $k1$ and $k2$ are the amplitude attenuation parameter caused by spherical diffusion of the point source and the waveform phase variation parameter caused by propagation distance, respectively, i is an imaginary number unit; DI, DR, and DT are the spherical diffusion compensation coefficients of incident, reflected, and transmitted waves, respectively [27]:

$$DI = a,$$

$$D_{\mathrm{R}} = (a + 2b)\left(c_{\mathrm{P1}}^2 + c_{\mathrm{Pj}}^2\right) \Big/ \left(2c_{\mathrm{P1}}^2\right),$$

$$D_{\mathrm{T}} = (a + b)\left(c_{\mathrm{P1}}^2 + c_{\mathrm{Pj}}^2\right) \Big/ \left(2c_{\mathrm{P1}}^2\right) + d\left(c_{\mathrm{Pj}}^2 + c_{\mathrm{P2}}^2\right) \Big/ \left(2c_{\mathrm{Pj}}c_{\mathrm{P2}}\right).$$

If the incident wave is a plane wave, the spherical compensation coefficient of each wave is 1, that is, DI = DR = DT = 1; cP1, cPj, and cP2 are the propagation velocities of P wave in rock, joint, and rock in point 2, respectively; TPP and RPP are calculated by equations [21, 22].

Since the measured waveform of measuring point 1 is a coherent waveform of the incident wave propagating to measuring point 1 and the reflected wave propagating to measuring point 1, the calculated spectrum of the measured waveform at measuring point 1 can be obtained by using the measured waveform spectrum at measuring point 2:

$$u_{1\mathrm{js}}(\omega) = \frac{k_1 u_2(\omega)}{T_{\mathrm{PP}}} - \frac{k_2 R_{\mathrm{PP}}}{T_{\mathrm{PP}}} u_2(\omega). \tag{25}$$

Inverse Fourier transformation on both sides of **Eq. 25** can be used to calculate the waveform u1js at measurement point 1. If the deformation characteristics of the joint conform to the single-joint model assumption, u1js is the same as the measured waveform u1. Due to the error of the model hypothesis and the interference factors in the field test, there is a deviation between u1js and u1. Using the principle of the least square method, taking P wave velocity $c$pj as an unknown variable and fitting u1js to the measured waveform u1 at point 1 (**Eq. 26**), finally, when the weighted average error is the smallest, the corresponding $c$pj is the calculated P wave velocity $c$pjjs in the joint.

$$\|\delta\|_2^2 = \min\left(\sum \left[u_{1\mathrm{js}} - u_1\right]^2\right). \tag{26}$$

TABLE 1 | P-SV wave velocity of the rock mass at point 1 (wave velocity method).

Test number	Velocity of the P wave (m/s)	Velocity of the SV wave (m/s)
Test 1	2751.11	1729.93
Test 2	2874.49	1852.22
Test 3	2582.73	1677.71
Test 4	3001.10	1798.70
Test 5	2603.69	1613.94
Average value	2753.46	1728.29

When the incident wave is the SV wave, the transmission and reflection coefficients are calculated by replacing the P wave velocity with the SV wave velocity of the rock on both joint sides, and the calculated SV wave velocity $c$sjjs can also be obtained by the least square method:

$$E_{\mathrm{jjs}} = 2\rho_{\mathrm{j}}\left(1 + \frac{c_{\mathrm{Pjjs}}^2 - 2c_{\mathrm{Sjjs}}^2}{2c_{\mathrm{Pjjs}}^2 - 2c_{\mathrm{Sjjs}}^2}\right)c_{\mathrm{Sjjs}}^2, \tag{27}$$

$$v_{\mathrm{jjs}} = \frac{c_{\mathrm{Pjjs}}^2 - 2c_{\mathrm{Sjjs}}^2}{2c_{\mathrm{Pjjs}}^2 - 2c_{\mathrm{Sjjs}}^2}, \tag{28}$$

where ρj is the joint density.

Field Test and Verification

We selected a typical macro-joint with a length of 5.60 m and a thickness of 0.04 m on a flat slope next to Luojiang Luquan Water Plant in Gangzhou China for the elastic parameter test [11, 12]. The measuring point and the vibration source are arranged as shown in **Figure 5**. Two three-directional acceleration sensors were closely attached to measuring points 1 and 2 using gypsum. The distance between the two measuring points and the joint was 0.10 m, and the distance between the source point and the joint was 0.60 m. The P-waveform is recorded in the x-direction of the sensor to test the P wave velocity of the joint, and the SV-waveform is recorded in the y-direction of the sensor to test the SV wave velocity of the joint.

In the method to test joint elastic parameters described above, it is necessary to know the P and SV wave velocities at measuring points 1 and 2, the rock density, and the joint density. We tested the velocities of the P and SV waves using the wave velocity method. First, a line parallel to the joint is arranged on the side of measuring point 1. Two measuring points are selected at a distance of 1.50 m from the measuring line. Then, a source point is selected on the extension line of the two measuring points, and a geological hammer is used to knock the source point five times. Finally, according to the time difference between the measured waveforms of the two measuring points and the distance between the two measuring points, the P and SV wave velocities at point 1 of the rock mass can be calculated (**Table 1**). Similarly, the P and SV wave velocities at point 2 can be measured. The joint and the rocks on both sides were sampled and physically processed into standard samples, and then, the mass and volume of the samples were measured to obtain a joint density of 2357 kg/m^3 and a rock density of 2645 kg/m^3.

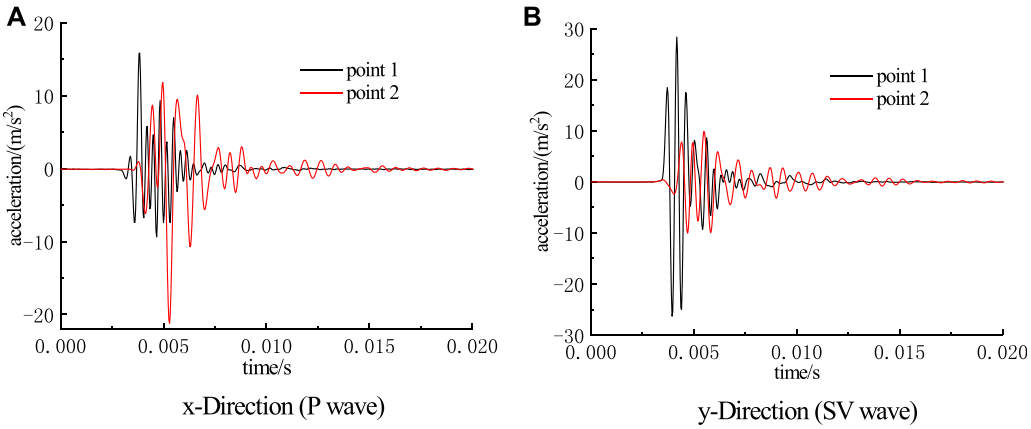

FIGURE 6 | Measured waveform of points 1 and 2.

TABLE 2 | P-SV wave velocity of the joint layer (waveform method).

Test number	Velocity of the P wave (m/s)	Velocity of the SV wave (m/s)
Test 1	1529.41	917.65
Test 2	1653.78	1076.47
Test 3	1628.57	1068.07
Test 4	1537.82	925.21
Test 5	1591.43	967.22
Test 6	1571.43	908.40
Average value	1585.41	977.17

The vibration source point shown in **Figure 5** is knocked, the P-SV waveforms of measurement points 1 and 2 are recorded as shown in **Figure 6**, and the P-SV waveforms of points 1 and 2 are recorded as up1, up2, us1, and us2, respectively. The Fourier transform of up2 and us2, respectively, can obtain frequency spectrums ũp2 and ũs2 of the measured waveform at point 2, and **Eqs. 23–26** can be used to calculate the velocities of the P and SV waves in the joint. Six tests were carried out on the site joints, and the wave velocities of P and SV were calculated by the above waveform method (**Table 2**). Finally, by substituting the average calculated wave velocity into **Eqs. 25** and **(26)**, the joint elastic modulus and Poisson's ratio are 6.03 GPa and 0.19, respectively.

CONCLUSION

According to the law of transmission and reflection of a stress wave through a single joint, the waves in the same direction and the same type are superposed in this article, and the analysis model of stress waves passing through single-joint rock is established. On this basis, the macro-joint model of stress waves passing through a group of parallel jointed rocks is proposed. Taking a vertical stress wave incident into a single macroscopic jointed rock stratum as an example, the calculation waveform of the incident wave is calculated according to the measured wave form of the transmission wave by using the above analysis model. The calculated wave form of the incident wave is compared with the measured wave form, and the node elastic parameter with the minimum error can be obtained by using the principle of the least square method. The results of six tests on joints with a thickness of 0.04 m show that the proposed method has good stability.

In this article, in order to simplify the analysis steps, it is assumed that the joint surface is straight and smooth, and the stress wave incident is vertical. In order to improve the applicability of the joint elastic parameter test method, more general joint model analyses and research will be developed in the future.

DATA AVAILABILITY STATEMENT

The original contributions presented in the study are included in the article/Supplementary Material; further inquiries can be directed to the corresponding author.

AUTHOR CONTRIBUTIONS

JD put forward the research ideas and designed the research scheme. YF and GW were responsible for the experiment. JD and YF were responsible for collecting, cleaning, and analyzing the data; JD, YF, and GW are responsible for drafting the paper. GW is responsible for the revision to the final version. In the end, all authors agreed to publish.

FUNDING

Financial support of the work by the National Natural Science Foundation of China (51464015, 41462009, and 51104069) and the Research Fund of Jiangxi University of Science and Technology (NSFJ2014-G06) is gratefully acknowledged.

REFERENCES

1. Zhang Q. The transfer process of stress waves at the joint. *Chin J Geotech Eng* (1986) 8(6):99–105. [in Chinese, with English summary].
2. Li XB, Chen SR. A new method for investigating the propagation of stress waves through layered rock mass. *J Cent South Univ (Sci Technol)* (1993) 24(6):738–42. [in Chinese, with English summary].
3. Pyrak-Nolte LJ, Myer LR, Cook NGW. Anisotropy in seismic velocities and amplitudes from multiple parallel fractures. *J Geophys Res* (1990) 95(B7): 11345–58. doi:10.1029/jb095ib07p11345
4. Pyrak-Nolte LJ, Myer LR, Cook NGW. Transmission of seismic waves across single natural fractures. *J Geophys Res* (1990) 95(B6):8617–38. doi:10.1029/jb095ib06p08617
5. Cai JG, Zhao J. Effects of multiple parallel fractures on apparent attenuation of stress waves in rock masses. *Int J Rock Mech Mining Sci* (2000) 37(4):661–82. doi:10.1016/s1365-1609(00)00013-7
6. Cai JG. *Effects of parallel fractures on wave attenuation in rock*. Singapore: Nanyang Technological University (2001).
7. Li JC, Li HB, Ma GW, Zhao J. A time-domain recursive method to analyse transient wave propagation across rock joints. *Geophys J Int* (2012) 188(2): 631–44. doi:10.1111/j.1365-246x.2011.05286.x
8. Li JC, Ma GW, Zhao J. An equivalent viscoelastic model for rock mass withparallel joints. *J Geophys Res* (2010) 115(B03305):1–10. doi:10.1029/2008jb006241
9. Wang GS, Guo Y, Hu SL. Measuring method for viscosity coefficient of rock. *Prog Geophys* (2014) 29(5):2411–5. [in Chinese, with English summary].
10. Wang G, Wang X, Hu S. A dynamic measurement method of elastic modulus of weak interlayer of rock mass. *Chin J Rock Mech Eng* (2015) 34(9):1828–35. [in Chinese, with English summary]. doi:10.13722/j.cnki.jrme.2014.0873
11. Hu SL. *Propagation rule and application of wavelet across the jointed rock mass*. Peiking: China University of Geosciences (2014) [in Chinese, with English summary].
12. Long P, Wang G, Hu S, Luo S. Measuring stiffness of jointed rock based on spectrum variation of stress wave. *Chin J Rock Mech Eng* (2015) 34(8):1677–83. [in Chinese, with English summary]. doi:10.13722/j.cnki.jrme.2015.0120
13. Gou Y, Shi X, Qiu X, Zhou J. Propagation characteristics of blast-induced vibration in parallel jointed rock mass. *Int J Geomechanics* (2019) 19(5):1–14. doi:10.1061/(asce)gm.1943-5622.0001393
14. Behnia M, Goshtasbi K, Marji MF, Golshani A Numerical simulation of crack propagation in layered formations. *Arab J Geosci* (2014) 7(7):2729–37. doi:10. 1007/s12517-013-0885-6
15. Marji MF. Numerical analysis of quasi-static crack branching in brittle solids by a modified displacement discontinuity method. *Int J Sol Structures* (2014) 51(9):1716–36. doi:10.1016/j.ijsolstr.2014.01.022
16. Chen E, Leung CKY, Tang S, Lu C. Displacement discontinuity method for cohesive crack propagation. *Eng Fracture Mech* (2018) 190:319–30. doi:10. 1016/j.engfracmech.2017.11.009
17. Wang GS, Xiong P, Hu SL, Meng SM. Application of displacement discontinuity model for calculating the viscoelastic stiffness of joints. *Rock Soil Mech* (2018) 39(6):2175–83. [in Chinese, with English summary]. doi:10. 16285/j.rsm.2016.2047
18. Wang GS, Liu SQ, Hu SL. Improved linear elastic model of discontinuous displacement and dynamic measurement of interface elastic modulus. *Chin J Rock Mech Eng* (2016) 35(10):2022–32. [in Chinese, with English summary].
19. Wang ZL, Chen Q, Zhang Y. A displacement discontinuity model for viscoelastic jointed rock mass. *Rock Soil Mech* (2015) 36(8):2177–83. [in Chinese, with English summary]. doi:10.16285/j.rsm.2015.08.007
20. Zhu JB, Zhao J. Obliquely incident wave propagation across rock joints with virtual wave source method. *J Appl Geophys* (2013) 88:23–30. doi:10.1016/j. jappgeo.2012.10.002
21. Gordeliy E, Detournay E. Displacement discontinuity method for modeling axisymmetric cracks in an elastic half-space. *Int J Sol Structures* (2011) 48(19): 2614–29. doi:10.1016/j.ijsolstr.2011.05.009
22. Li J, Ma G. Analysis of blast wave interaction with a rock joint. *Rock Mech Rock Eng* (2010) 43(6):777–87. doi:10.1007/s00603-009-0062-0
23. Schoenberg M. Elastic wave behavior across linear slip interfaces. *The J Acoust Soc Am* (1980) 68(5):1516–21. doi:10.1121/1.385077
24. Schoenberg M, Douma J. Elastic wave propagation in media with parallel fractures and aligned Cracks1. *Geophys Prospect* (1988) 36(6):571–90. doi:10. 1111/j.1365-2478.1988.tb02181.x
25. Pyrak-Nolte LJ. *Seismic visibility of fractures*. Berkeley: University of California (1988).
26. Ge G. *The basis of seismic wave dynamics[M]*. Peiking: Petroleum Industry Press (1980) [in Chinese, with English summary].
27. Wang LL. *Stress wave foundation*. Beijing: National Defense Industry Press (1985). p. 248. [in Chinese, with English summary].
28. Newman P. Divergence effects in a layered earth. *Geophysics* (1973) 38(3): 481–8. doi:10.1190/1.1440353

Conflict of Interest: JD was employed by the Fujian Makeng Mining Co., Ltd.

The remaining authors declare that the research was conducted in the absence of any commercial or financial relationships that could be construed as a potential conflict of interest.

frontiers in Physics

ORIGINAL RESEARCH
published: 25 March 2021
doi: 10.3389/fphy.2021.569453

A Method for Multihole Blasting Seismic Wave Prediction and Its Application in Pillar Recovery

Lianku Xie[1,2], *Daiyu Xiong*[1], *Tianhong Yang*[1], *Li He*[3] *and Qinglei Yu*[1]*

[1]School of Resources and Civil Engineering, Northeastern University, Shenyang, China, [2]BGRIMM Technology Group, Beijing, China, [3]College of Science, Wuhan University of Science and Technology, Wuhan, China

Long-hole blasting in mines is likely to cause strong vibration of surficial infrastructure, greatly damage the rock mass surrounding goaf near explosion center, and possibly induce blast vibration disasters. In this article, an improved method for multihole blasting seismic wave prediction is proposed to estimate far-field blast vibration. In this method, the fundamental vibration waveforms are firstly measured through the field blast with a single deck at an underground pilot area. The fundamental vibration waveforms are then used to simulate the vibration waveforms for a single-deck case in the production blast by considering the difference of the equivalent distances from the production blast site and the pilot area to the surface measuring point. The vibration waveforms for the single-deck case are linearly superposed to predict the possible vibration waveforms in production blast with multiple long holes and decks according to the designed delay time between decks. Based on these predicted waveforms, the blast vibration can be estimated and the blast design can be optimized to determine a rational delay time in accordance with the vibration limit. The proposed method was applied in pillar recovery of Hongling Polymetallic Mine to optimize the long-hole blast design to manage blast vibration. The rational delay time for the 716 production blast design was recommended as 26 ms. The practice showed that the blast vibration induced by the 716 production blast has been managed, and the predicted and the measured waveforms agree well. It provides an effective method for multihole blast design to control blast vibration.

Keywords: blast vibration, fundamental wave, seismic wave prediction, vibration velocity model, rational delay time interval

OPEN ACCESS

Edited by:
Longjun Dong,
Central South University, China

Reviewed by:
Yousef Azizi,
Institute for Advanced Studies in Basic Sciences (IASBS), Iran
Jian Zhou,
Central South University, China
Ju Ma,
Central South University, China

***Correspondence:**
Qinglei Yu
yuqinglei@mail.neu.edu.cn

Specialty section:
This article was submitted to Interdisciplinary Physics, a section of the journal Frontiers in Physics

Received: *04 June 2020*
Accepted: *28 January 2021*
Published: *25 March 2021*

Citation:
Xie L, Xiong D, Yang T, He L and Yu Q (2021) A Method for Multihole Blasting Seismic Wave Prediction and Its Application in Pillar Recovery. Front. Phys. 9:569453. doi: 10.3389/fphy.2021.569453

INTRODUCTION

Long-hole blasting has many advantages for mining engineering, such as a large blasting scale, a large volume of caved ore, and lower specific charge. However, if the long-hole blasting is not well controlled, it is likely to cause a strong vibration of surface constructions and greatly disturb the rock mass surrounding goaf. It may even cause issues between local residents and the enterprise, which seriously influences mining production. Therefore, increasing attention has been paid to the influence of blast vibration.

In recent years, many attempts have been made on blast vibration theories, analysis methods, and vibration control. A series of techniques and methodologies have been proposed to manage blast vibration. Yang et al. [1–4] developed a multiple-seed waveform (MSW) vibration model that

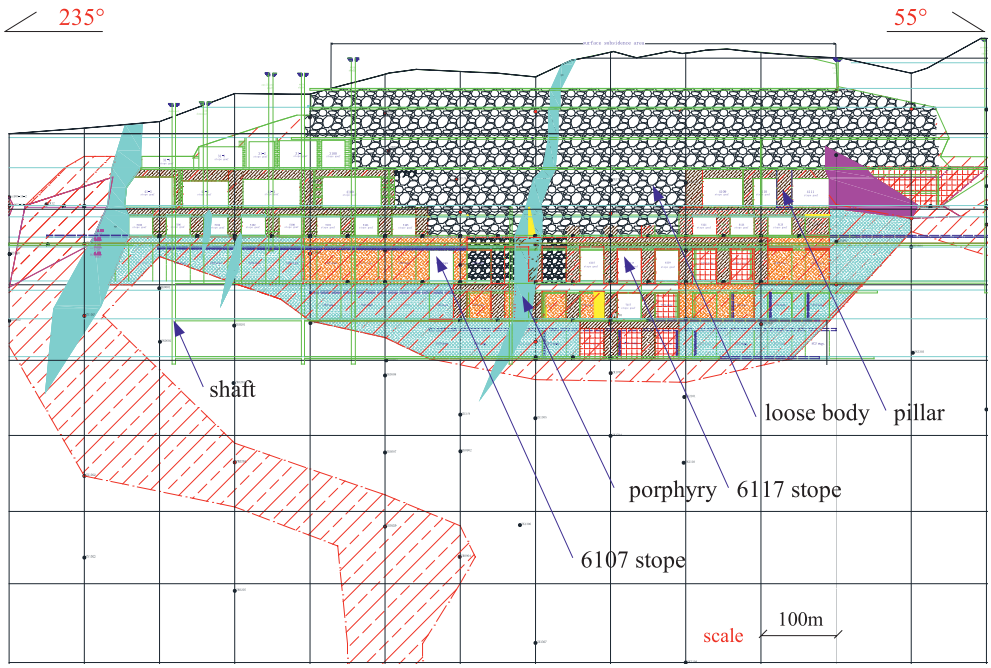

FIGURE 1 | Longitudinal projection map of the present mining situation.

considered the screening effect of an earlier firing hole on vibration from a later firing hole and the waveform change caused by the distance between the seed waves and the production blast. This model is suitable for near-field and far-field blast vibration simulations. Wu et al. [5] and Zhang et al. [6] systematically studied analytical prediction theory and control methodology of blast vibration. Li et al. [7] studied the influencing factors of blast vibration attenuation and the attenuation law of seismic wave energy. Ling et al. [8, 9] used the time-energy analysis method based on wavelet transforms to separate each deck wave from the measured delay blast vibration signals and obtained a rational millisecond delay time by waveform superposition of these single-deck waves with different delay time to control blast vibration disasters. Agrawal and Mishra et al. [10] proposed a new empirical approach of simplified signature hole analysis (SSHA) for the multihole blast design to predict production blast-induced ground vibrations, up to 15% more accuracy in the prediction of blast vibrations. Zhong et al. [11, 12] and Gao et al. [13] studied the impact of blast vibration duration and millisecond delay time on blast vibration disaster and proposed a vibration duration prediction formula with signal energy and an optimization method of millisecond delay time. Yang et al. [14], Zhao et al. [15], Chen et al. [16], and Qiu et al. [17] studied the time-frequency characteristics of blast vibration waves and the relationship between the energy distribution and frequency band based on linear superposition analysis of the single-deck blast vibration waves. Lou et al. [18], Duan et al. [19], and Zhang et al. [20] analyzed the theoretical hypothesis and technical status

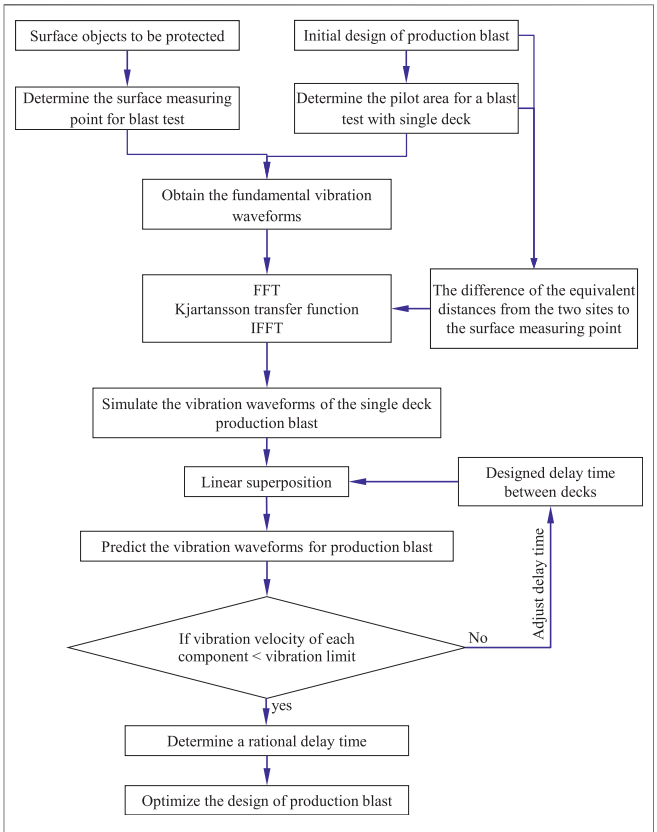

FIGURE 2 | Flowchart of seismic wave prediction for multihole blasting.

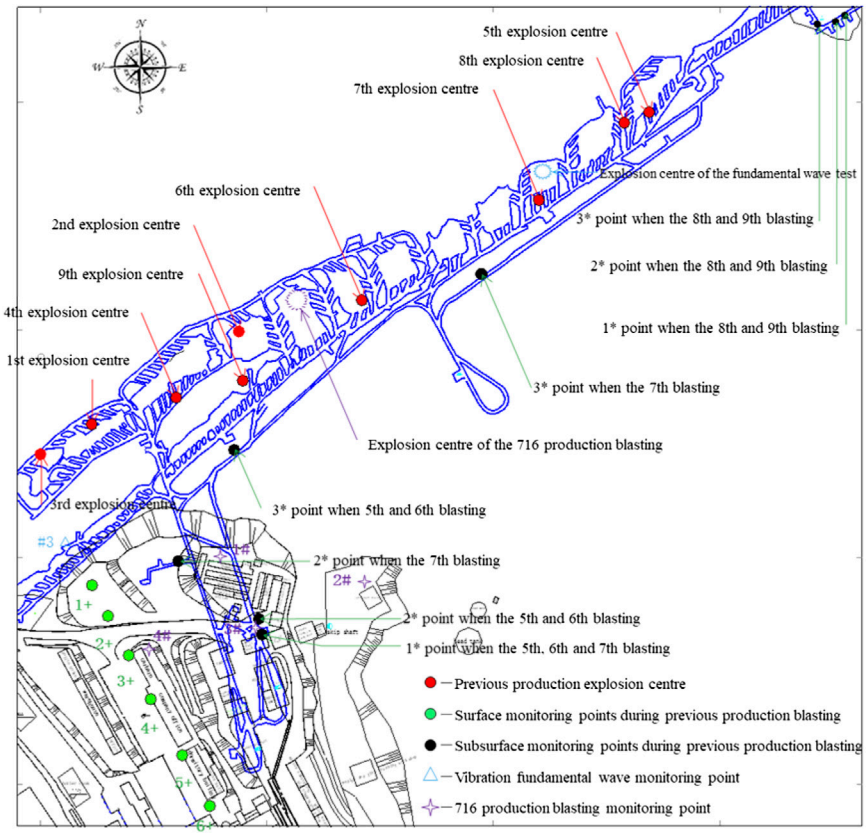

FIGURE 3 | Distribution of the monitoring points and explosion centers in the subsurface and on the surface.

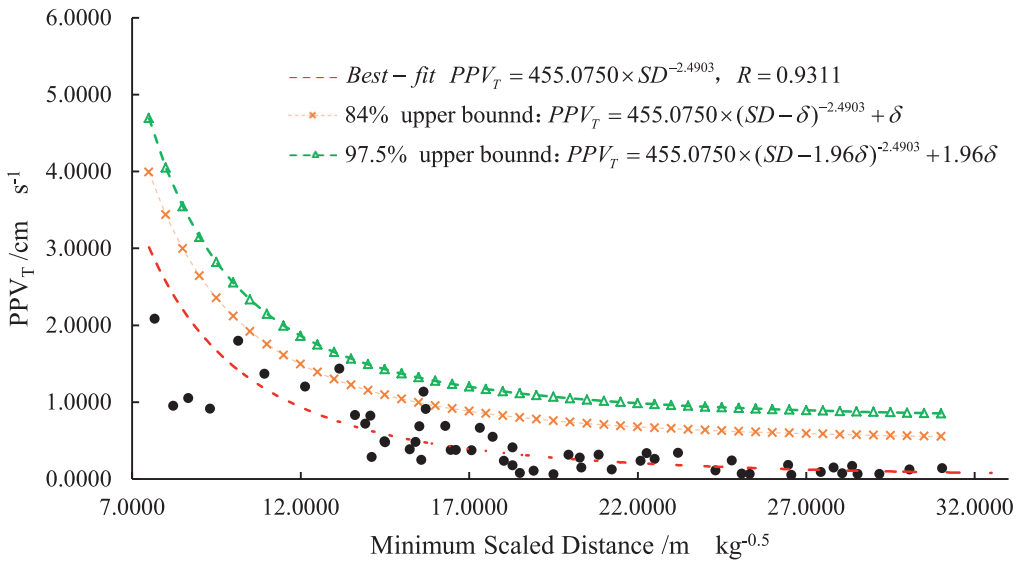

FIGURE 4 | The relationship between the transverse component of vibration velocity (PPV_T) and the scaled distance.

of delay blasting and proposed a rational millisecond delay time that should fully use the explosive energy after two-deck (or multideck) blasting. Monjezi et al. [21], Hajihassani et al. [22], Shang et al. [23], and Zhou et al. [24] used artificial neural networks or optimized neural networks to predict ground vibration induced by blasting. Azimi [25] used intelligence

TABLE 1 | Maximum single-deck charge weight recommended at different distances.

Number	Linear distance/m	Maximum single-deck charge weight/kg
1	250	220
2	300	320
3	350	430
4	400	570
5	450	720
6	500	890
7	550	1,080
8	600	1,290

committee machines (ICM) based on genetic algorithm to predict the seismic wave intensity generated by bench blasting in an open-pit mine, which is more accurate and reliable than those predicted previously by empirical formulas and neural network models. The above studies about blast vibration theories and vibration reduction provide useful references for controlling the blast vibration effect of underground long-hole blasting.

In mining practice, the underground mining environment and surrounding rock mass are very complex and the delay time is very short, usually tens of milliseconds, so it is difficult to determine a rational delay time for long-hole blasting to control blast vibration. For the above theory and methods, obtaining basic blasting parameters for applications is difficult. In this article, a method for multihole blasting seismic wave prediction was proposed to determine a rational delay time for multihole blasting, which is based on the fundamental vibration waveforms from a single-deck blast test. It was used to guide the blast design for pillar recovery in Hongling Polymetallic Mine to manage blast vibration.

UNDERGROUND MINING SITUATION OF HONGLING POLYMETALLIC MINE

Hongling Polymetallic Mine is a skarn-type deposit mainly composed of Fe and Zn. The stopes are firstly excavated using the open-stope method; then, the pillars are completely recovered using long-hole blasting. The blasted ore is mucked out under overburden. At present, the mine development levels are 755 and 705 m, the production levels are 805 m and above, and exploitation at the 905 m level and above has been finished. The rest of the ore is mainly in barrier pillars and crown pillars. The present mine layout is shown in **Figure 1**. After many years of mining, numerous mined-out stopes have been exposed for a long time. They become unstable due to stress disturbance and are prone to collapse with weak layers, fracture zones, or structural planes. The vibration of surface constructions is obvious when pillars are completely blasted with long holes. It is necessary to study the control measurements of blast vibration to solve the contradiction between overall blasting ore pillars and blast vibration limit to reduce the harmful effects, which is of great significance for resource recovery, the extension of mine life, and the protection of surface and subsurface constructions.

MULTIHOLE BLASTING SEISMIC WAVE PREDICTION METHOD

Simulation of the Vibration Waveforms for the Single-Deck Case

When using MSW vibration model [1] in practice, it is very difficult to obtain the basic blast parameters that the model needs and the test work for basic parameters is very much and relatively complicated. In fact, the screening effect of an earlier firing hole on vibration from a later firing hole is not obvious for far-field blast vibration modeling. On this basis, an improved method for multihole blasting seismic wave prediction is proposed based on the fundamental blast vibration waveforms, which contains advantages of the MSW vibration model and improves the shortcomings of the single-seed waveform model that waveforms are superimposed linearly without considering the waveform transformation factors. The fundamental blast vibration waveform data are collected from monitoring the single-deck blast at the underground pilot area. The measuring points are usually set on the ground surrounding surface constructions.

The fundamental vibration waveforms are then used to simulate the vibration waveforms for the single-deck case in the production blast. Firstly, the fundamental vibration waveforms as an input signal with the time domain are processed by fast Fourier transform (FFT) to determine the frequency domain $S(k)$. Secondly, the Kjartansson transfer function $B(k)$ [26] is used as a weight coefficient to determine the frequency domain of the output signal $W(k)$. The parameters of the Kjartansson transfer function $B(k)$ are obtained mainly considering the difference of the equivalent distance from the production blast site and the distance from the pilot area to the measuring point. Finally, the time-history curve of single-deck blast vibration is obtained by processing the output signal $W(k)$ according to the inverse fast Fourier transform (IFFT). The equations are as follows:

TABLE 2 | Single-deck charge weight and initiation time.

Blasthole number	Initiation time/ms	Single-deck charge/kg	Total charge/kg
1–18	0	515	1,163
19–31	3,000	306	
32–35, 39	5,975	166	
36–38, 41–42	6,000	176	

TABLE 3 | Vibration monitoring point arrangement.

Monitoring points	Horizontal distance/m	Vertical distance/m	Linear distance/m
#1, #2	240	240	339
#3, #4	290	240	376
#5	350	229	418

TABLE 4 | The blast vibration data.

Test points	Maximum vibration velocity with a 515 kg charge			Maximum vibration velocity with a 306 kg charge			Maximum vibration velocity with a 176 kg charge		
	Longitudinal/ $cm{\cdot}s^{-1}$	Transverse/ $cm{\cdot}s^{-1}$	Vertical/ $cm{\cdot}s^{-1}$	Longitudinal/ $cm{\cdot}s^{-1}$	Transverse/ $cm{\cdot}s^{-1}$	Vertical/ $cm{\cdot}s^{-1}$	Longitudinal/ $cm{\cdot}s^{-1}$	Transverse/ $cm{\cdot}s^{-1}$	Vertical/ $cm{\cdot}s^{-1}$
#1	0.1065	0.0040	0.0758	0.0364	0.0018	0.0505	0.0681	0.0017	0.0302
#2	0.1076	0.1820	0.0701	0.0308	0.0803	0.0508	0.0659	0.0675	0.0300
#3	0.1729	0.1344	0.0995	0.0672	0.0592	0.0419	0.0639	0.0391	0.0356
#4	0.1150	0.1849	0.0856	0.0420	0.0539	0.0370	0.0463	0.0560	0.0296
#5	0.1719	0.2093	0.0765	0.0708	0.0625	0.0423	0.0466	0.0684	0.0381

$$B(k) = \exp\left\{ -\frac{2\pi k_0 \delta_d}{c_0} \left|\frac{k}{k_0}\right|^{1-\gamma} \left[\tan\left(\frac{\pi\gamma}{2}\right) + i\,\mathrm{sign}(k)\right]\right\}, o \quad (1)$$

$$W(k) = S(k) \cdot B(k), \quad (2)$$

where k is the wave frequency, Hz; k_0 is the arbitrary specified frequency, Hz; δ_d is the difference of the equivalent distances from the production blast site and the test blast site to the surface measuring point, m; c_0 is the P-wave velocity of the propagation medium, m/s; $\gamma = 1/\pi \arctan(1/Q)$, where Q is the rock mass quality index; $\mathrm{sign}(k)$ is the sign function.

Seismic Wave Prediction in Production Blast with Multiple Holes and Decks

The vibration waveforms for the single-deck case are used by linear superposition to predict the vibration waveforms in production blast at a similar wave propagation path. Production blast vibration waves are considered to be superposed by a certain number of single-deck blast vibration waves, which are mutually interfering and superposed. The superposition process of blast vibration waveforms can be assumed to be represented by a linear system and expressed by the following formula:

$$V(t) = \sum_{i=1}^{n} v_i(t + \Delta t), \quad (3)$$

where $V(t)$ is the blast vibration velocity of multiholes predicted by linear superposition, cm/s; n is the total number of decks; $v_i(t)$ is the predicted vibration velocity of the single-deck blast, cm/s; i is the number of superposition decks, $i = 1, 2, 3, ..., n$; Δt is the delay time between seismic waves. The flowchart of the proposed method for multihole blasting seismic wave prediction is shown in **Figure 2**.

A program has been developed in MATLAB 7.0 to implement this calculation process automatically. Using this method, we can simulate the blast vibration of multihole blasting with different delay time to find a rational delay time to reduce the harmful effects of the blast. The advantage of this method is that the single-deck blast vibration waveforms used in this method imply the information of blasting conditions, explosive properties, and geological conditions, and using these waveforms to predict the vibration waveforms of multihole blasting does not need a large number of vibration tests.

CHARGE WEIGHT FOR LONG-HOLE BLASTING

Vibration Velocity Model of Long-Hole Blasting

The blast vibration velocity of a particle is mainly affected by the charge weight and the distance from the explosion center to the monitoring points. The peak particle vibration velocity (PPV) [27] can be expressed as follows:

$$PPV = K\left(D/\sqrt{\mathrm{Q}}\right)^{\alpha} = \mathrm{K}(\mathrm{SD})^{\alpha}, \quad (4)$$

$$SD = D\Big/\sqrt{Q}, \quad (5)$$

where Q is the maximum single-deck charge weight, kg; D is the distance from the explosion center to the point of interest, m; SD is the proportional distance, $m/kg^{0.5}$; K and α are site coefficients.

For complicated conditions, the coefficients in **Eq. 4** should be determined based on a large amount of data of blast vibration. Therefore, nine blast vibration monitoring tests were carried out using the Mini-Blast I. Six monitoring points were set on a straight line near the surface buildings according to the rule of "dense in the vicinity and sparse in the distance" and three more monitoring points were added underground near the substation and explosive magazine. The arrangement of the monitoring points and the blasting centers is shown in **Figure 3**.

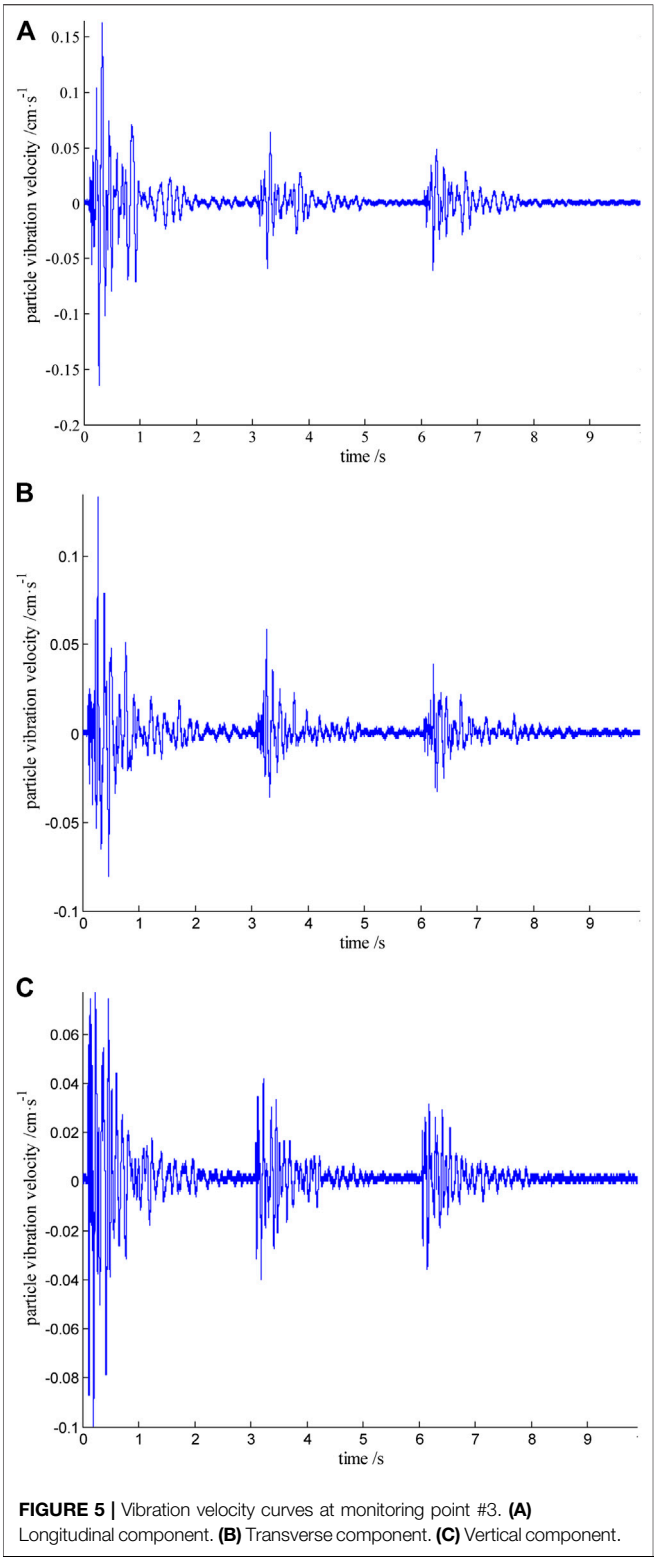

FIGURE 5 | Vibration velocity curves at monitoring point #3. **(A)** Longitudinal component. **(B)** Transverse component. **(C)** Vertical component.

Through monitoring, 93 groups of data were collected from nine surface blast vibration tests by a Mini-Blast I blast vibration tester. Using the monitoring data, we fitted the relationship between the scaled distance and the particle vibration velocity. Then, a vibration velocity model including three components (longitudinal L, transverse T, and vertical V) was established. The transverse vibration velocity is dominant and **Figure 4** shows the transverse vibration velocity model.

Maximum Charge Weight Determination

On the ground of Hongling Polymetallic Mine, there exist bunkhouses, office buildings, and skip shafts. According to the Safety Regulations for Blasting (GB6722-2014) (It was proposed and managed by the former State Administration of Work Safety and revised by the former China Society of Engineering Blasting. It is a mandatory standard and was implemented on July 1, 2015.), these buildings are considered general civil buildings. Besides, there are also some makeshift houses. Therefore, The main vibration frequency of the transverse component is allowed to range from 5 to 50 Hz, and the corresponding allowable vibration velocity is 0.45–0.90 cm/s. The upper limit of 0.90 cm/s is selected for the surface buildings of Hongling Polymetallic Mine. Using the transverse vibration velocity model with the upper confidence limit of 84% in **Figure 4**, we obtained the recommended maximum single-deck charge weight at different distances for the blast of pillar recovery in Hongling Polymetallic Mine, as shown in **Table 1**. Besides, the vibration limit may be adjusted according to the protection levels of buildings.

FUNDAMENTAL VIBRATION WAVEFORMS MEASUREMENT

The Pilot Area Selection and Blast Design

The pilot area for the fundamental blast vibration waveforms stands in a peach-shaped pillar (as shown in **Figures 1**, **3**) of stope No. 6117 at the 805 m level and stope No. 6117 and its neighbor stopes (stope No. 6115 and stope No. 6199) have been mined out. At the 855 m level, the stope No. 5117 and pillars above the pilot area have been exploited, and the overburden has fallen into the bottom of stope No. 5117. At the 755 m level, stope No. 7117 below the pilot area has also been mined out.

In the blast design for the fundamental vibration waveform, the No. 2 rock emulsion explosive is used, fan-shaped long holes are drilled upward, and the pillar is designed to be blasted row by row using the mined-out stope No. 6117 as free surface. The blastholes are set to be two rows and 42 blastholes in total, and the hole depth is about 7–19 m. The primary explosive is placed at the bottom of the holes for a reversed blasting. 42 XA digital electronic detonators are used, which can set the initiation time in the range of 0–6,000 ms. The charge weight of a single deck and the initiation time are shown in **Table 2**.

Five monitoring points surrounding the surface buildings were set to carry out blast vibration tests. The Mini-Blast I was used to record the time-history curves of seismic waves. An appropriate trigger level and acquisition time duration were set by estimating the maximum vibration velocity before the test to collect vibration data accurately. The vibration monitoring point arrangement is shown in **Table 3**.

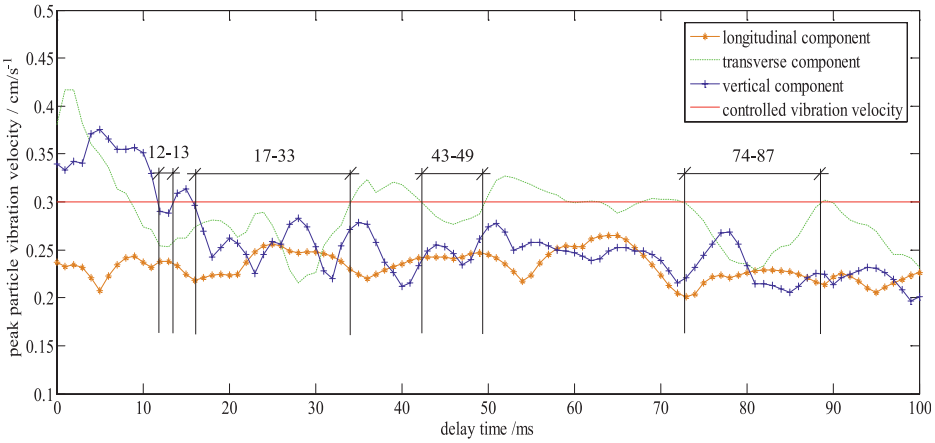

FIGURE 6 | The maximum particle vibration velocity of monitoring point #4 under different delay time.

Test Results Analysis

The test data of blast vibration are shown in **Table 4**. The time-history curves of the seismic wave at monitoring point #3 are shown in **Figure 5**. According to **Table 4** and **Figure 5**, the maximum vibration velocity occurred at the first wave peak when the single-deck charge weight is 515 kg and the delay time is 0 ms. The blast vibration waveforms of monitoring point #3 with the 3,084 ms duration were selected as the fundamental vibration waveforms because the monitoring point P3 is close to the main building in the mine area. These waveforms were input into the developed program in MATLAB 7.0 to predict vibration waveforms of multihole blast with different delay time.

APPLICATION IN PILLAR RECOVERY

General Conditions

The proposed method is applied in a production blast (716 production blast) for pillar recovery, which is located between the crown of stope No. 6107 and the barrier pillar between stope No. 6107 and stope No. 6109 at the 805 m level, as shown in **Figures 1**, **3**. The volume of the crown and barrier pillars is 45306 m^3. A blast pattern with long holes was designed to completely blast the pillars. The overall blasting can quickly deal with the mined-out stopes to eliminate the potential safety hazard and also obtain a large amount of ore volume for mucking out at the bottom structure.

The crown and the barrier pillars were uniformly charged and blasted. This fan-shaped blast design had 55 rows and 992 blastholes in total. The No. 2 rock emulsion explosive was charged with 218 decks in total. The total charge weight was 48396 kg, in which the maximum charge weight of a single deck was 498 kg, and 181746 t of ore would be exploited in this blast. XA digital electronic detonators were used for initiation and millisecond delay initiation was implemented for different decks in the same row. Monitoring point #1 at the bunkhouses is the closest point to the center of production blasting, with a straight line distance of 349 m. The maximum charge weight of a single deck was 425 kg, which is less than the permitted 430 kg in **Table 1**.

Delay Time Optimization

The fundamental blast vibration waveforms, determined in Test Results Analysis, were adopted to predict the blast vibration waveform of four monitoring points for the 716 production blast near the office building using the proposed method. **Figure 6** shows the maximum particle vibration velocity of monitoring point #4 predicted under different delay times. According to the category of protection objects and the corresponding allowable particle vibration velocity for safety, the safety factor is considered to be 1.5, so the controlled vibration velocity of monitoring point 4# at the office building is set to be 0.45/1.5 = 0.300 cm/s as the vibration limit (the red line in **Figure 6**). Based on the analysis of the predicted blast vibration waveforms of monitoring point #4, when the delay time was set to be 20–22, 25–27, 29–33, and 76–86 ms, the peak particle vibration velocity of the three components is less than 0.300 cm/s (see **Figure 6**). These delay times could be taken as the rational delay time for monitoring point #4. The rational delay time of another three monitoring points is shown in **Table 5**. Taking the intersection for the delay time of monitoring points #1, #2, #3, and #4, we determined the delay time to be 26 ~ 28 ms and 33 ms for the 716 production blast. The delay time should be as short as possible to improve the size of blasted ore pieces by making full use of the explosive energy [1]. Therefore, the recommended delay time for the 716 production blast was 26 ms.

Comparison Between Predictions and Measurements

Figure 7 shows the comparison o between the predicted and measured vibration waveforms for monitoring point #4. According to the blast vibration monitoring test, the duration of the blast vibration measured at monitoring point #4 in the office building is 7.658 s, and the measured values of the peak particle vibration velocity for the longitudinal, transverse, and

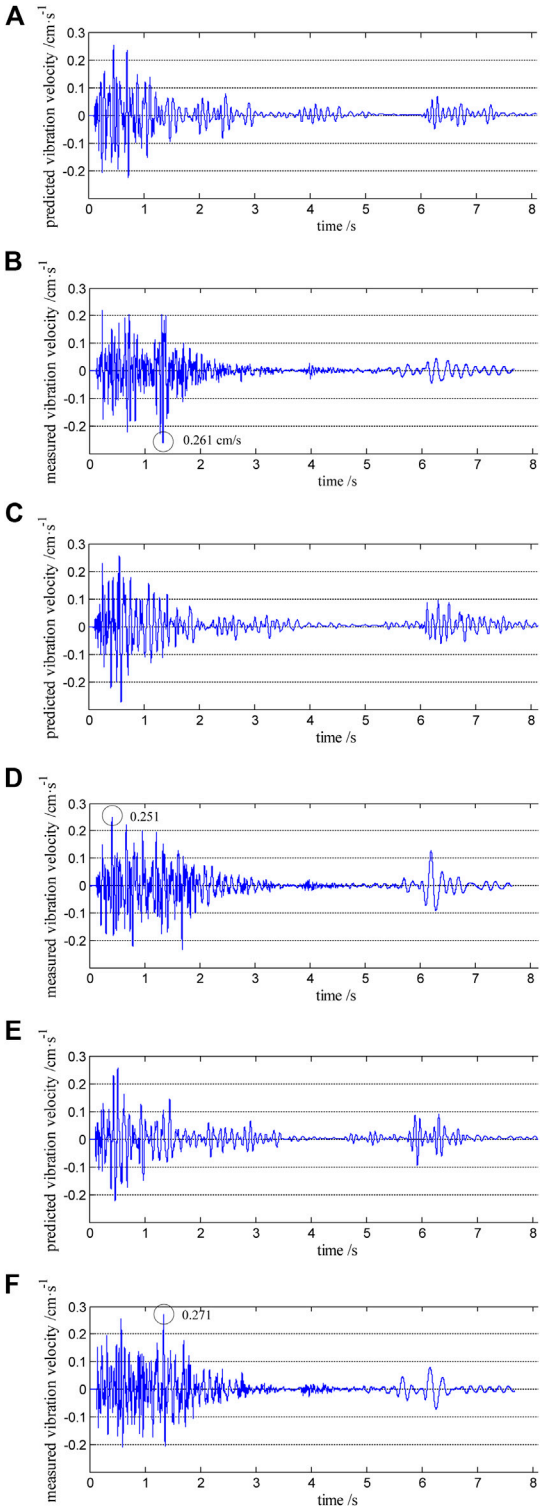

FIGURE 7 | Predicted and measured vibration waveforms of monitoring point #4. **(A)** Predicted longitudinal component. **(B)** Measured longitudinal component. **(C)** Predicted transverse component. **(D)** Measured transverse component. **(E)** Predicted vertical component. **(F)** Measured vertical component.

TABLE 5 | Rational delay time for the monitoring points.

Vibration monitoring point	Protected object	Distance from the explosion center/m	Rational delay time/ms
#1	Bunkhouse	348.54	0–3, 26–28, 33–41, 59–63
#2	Skip well winch room	353.58	14–38, 59–65
#3	Main shaft winch room	396.87	16, 21–100
#4	Mine office building	432.63	12–13, 17–33, 43–49, 74–86

vertical components are 0.261 cm/s, 0.251 cm/s, and 0.271 cm/s (**Figures 7B,D,F**), respectively. The predicted value is basically consistent with the measured value, and the predicted blast vibration waveforms are similar to the measured blast vibration waveforms (**Figure 7**). The peak particle vibration velocity of other monitoring points is also within the vibration limit (**Figure 8**). The management of blast vibration disasters is realized.

Figure 9 shows the comparison between the predicted and measured spectrum maps of monitoring point #4. The dominant frequencies of the predicted vibration wave are within 9–10 Hz, and the energy peaks are distributed in the range of 4–23 Hz (**Table 6**). The dominant frequencies of the measured vibration wave are within 8–10 Hz and energy peaks are distributed in the range of 4–30 Hz (**Table 6.**). The predicted and measured frequencies and energy peak agree well, as shown in the figure.

CONCLUSION

In this article, an improved method for long-hole blasting seismic wave prediction has been proposed to estimate the far-field blast vibration effect. It is based on the fundamental blast vibration waveforms from a single-deck blast test. The method was used to guide the blast design for pillar recovery of the Hongling Polymetallic Mine. The following conclusions are drawn:

(1) In the proposed method, the blast vibration waveform from a single-deck blast at the pilot area is used as fundamental vibration waveforms and the Kjartansson transfer function is adopted to consider the difference of the blast conditions between the pilot area and production blast area, which make it easy for engineering applications, comparing with the MSW model. This method can predict peak particle vibration velocity, rational delay time between decks, duration of blast vibration, and time-frequency domain information of multihole blasting.

(2) The proposed method was used to optimize the delay time of the blast design for pillar recovery of the Hongling Polymetallic Mine. It is found that the rational delay time has one or more

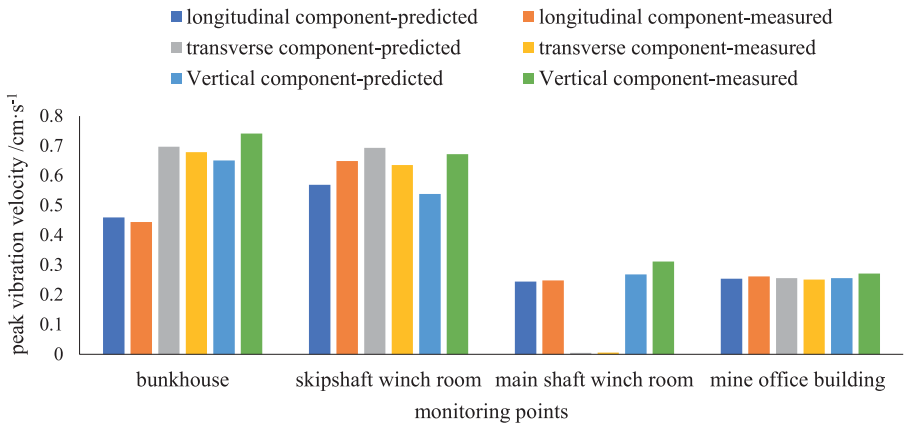

FIGURE 8 | Predicted and measured peak vibration velocity at the monitoring points.

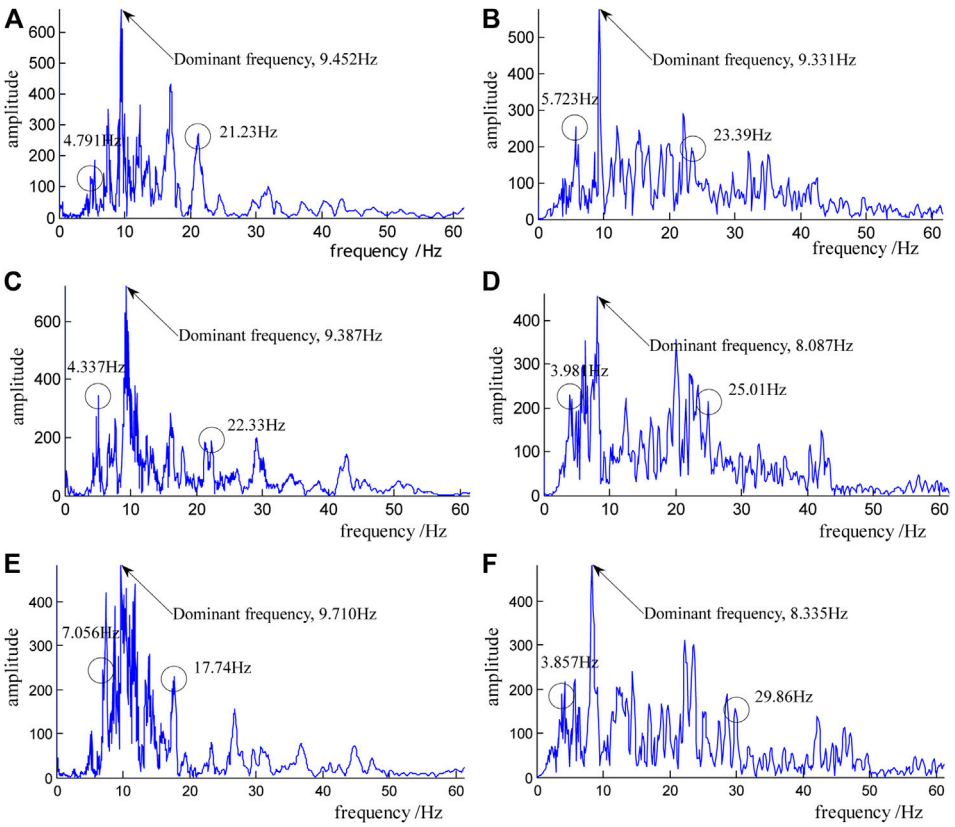

FIGURE 9 | Comparison between the predicted and measured spectrum maps of monitoring point #4. **(A)** Predicted longitudinal component. **(B)** Measured longitudinal component. **(C)** Predicted transverse component. **(D)** Measured transverse component. **(E)** Predicted vertical component. **(F)** Measured vertical component.

values, even a time range. A minimum value, 26 ms, is selected as the rational delay time for the 716 production blast.

(3) The monitoring data of the 716 production blast showed that the predicted value of the maximum particle vibration velocity is very close to the measured value, the predicted blast vibration waveforms are similar to the measured blast vibration waveforms, and the peak particle vibration velocity stays within the vibration limit. The

TABLE 6 | Comparison of between the predicted and measured amplitude and frequency of point #4.

Point #4	Range of energy peaks (Hz))		Dominant frequency (Hz)		Amplitude	
	Predicted	Measured	Predicted	Measured	Predicted	Measured
Longitudinal component	4.79–21.23	5.72–23.39	9.452	9.331	679.400	580.000
Transverse component	4.34–22.33	3.98–25.01	9.387	8.087	733.600	454.600
Vertical component	7.06–17.74	3.86–29.86	9.710	8.335	490.600	489.900

contradiction between the mass blasting for pillar recovery and the management of blast vibration is effectively solved. It also proved that the proposed method is feasible and reliable, easily applied in engineering practice.

DATA AVAILABILITY STATEMENT

The raw data supporting the conclusions of this article will be made available by the authors, without undue reservation.

AUTHOR CONTRIBUTION

All authors listed have made a substantial, direct, and intellectual contribution to the work and approved it for publication.

FUNDING

This work was partially supported by the National Natural Science Foundation of China-Joint Fund of Xinjiang (Grant No. U1903216), the National Key Research and Development Program of China (Grant No. 2016YFC0801602), and the National Natural Science Foundation of China (Grant Nos. 51904210 and 52074060).

ACKNOWLEDGMENTS

The authors also gratefully thank Cheng Wang of Shandong Gold Nonferrous Mining Group Co., Ltd., Wenbo Wang of Wuhan University of Science and Technology, and Zhuo Dong of Dalian University of Technology for their support and help in the process of mine blasting vibration tests and data analysis.

REFERENCES

1. Yang R, Wiseman T, Scovira DS. Multiple Seed Waveform (MSW) vibration model and some case studies. *Ijmme* (2011) 3(2):124–40. doi:10.1504/ijmme.2011.042427
2. Yang R, Scovira DS. "A model for near and far-field blast vibration based on multiple seed waveforms and transfer functions," in 36th Conference explosives and blasting technique, February, 2010, Orlando, Florida (2010).
3. Yang R, Lownds M. Modeling the effect of delay scatter on peak particle velocity of blast vibration using a multiple seed waveform vibration model. *Blasting and Fragmentation* (2011) 5(3):31–45. https://www.researchgate.net/publication/311923105
4. Yang R, Patterson N, Scovira DS. "An integrated approach of signature hole vibration monitoring and modeling for quarry vibration control. in: 9th international symposium on rock fragmentation by blasting; 2009 Aug; Granada, Spain (2009)–13:17.
5. Wu L, Rao YA, Huang CB. Synthetic study on the methods of blast vibration prediction and control. *Hydrogeology Eng Geology* (2004) (Suppl. 1):136–40. doi:10.16030/j.cnki.issn.1000-3665.2003.s1.030
6. Zhang ZY, Yang NH, Lu WB, Zhao G, Shi FQ. Progress of blast vibration control technology in China. *Blasting* (2013) 30(2):25–32. doi:10.3963/j.issn.1001-487X.2013.02.006
7. Li HT, Lu WB, Shu DQ, Yang XG, Yi CP. Study of energy attenuation law of blast-induced seismic wave. *Chin J Rock Mech Eng* (2010) 29 (Suppl. 1):3364–9. CNKI:SUN:YSLX.0.2010-S1-113
8. Ling TH, Li XB, Wang GY. A study on initiative control of blast vibration damages. *Rock Soil Mech* (2007) 28(7):1439–42. doi:10.16285/j.rsm.2007.07.029
9. Ling TH, Li XB. Time-energy analysis based on wavelet transform for identifying real delay time in millisecond blasting. *Chin J Rock Mech Eng* (2004) 23(13):2266–70. doi:10.3321/j.issn:1000-6915.2004.13.026
10. Agrawal H, Mishra AK. An innovative technique of simplified signature hole analysis for prediction of blast-induced ground vibration of multi-hole/production blast: an empirical analysis. *J Int Soc Prev Mitigation Nat Hazards* (2020) 100(8):111–32. doi:10.1007/s11069-019-03801-2
11. Zhong DW, He L, Cao P, Zhang K. Analysis of blast vibration duration and optimizing of delayed time for millisecond blasting. *Explos Shock Waves*(2016) 36(5):703–9. doi:10.11883/1001-1455(2016)05-0703-07
12. Zhong DW, He L, Cao P, Zhang K. Experimental study of reducing vibration intensity based on controlled blasting with precise time delay. *J China Coal Soc* (2015) 40.(Suppl. 1):107–12. doi:10.13225/j.cnki.jccs.2014.1447
13. Gao FQ, Hou AJ, Yang XL, Yang J. Analysis of blast vibration duration based on dimension theory. *Metal Mine* (2010) 411:143–5. CNKI:SUN:JSKS.0.2010-09-041
14. Yang NH, Zhang L. Blast vibration waveform prediction method based on superposition principle. *Explos Shock Waves* (2012) 32(1):84–90. doi:10.3969/j.issn.1001-1455.2012.01.015
15. Zhao MS, Liang KS, Yu DY, Ren SF. Effect of decks on time frequency characteristics of blast vibration signals. *J China Coal Soc* (2012) 37(1):55–61. doi:10.13225/j.cnki.jccs.2012.01.007
16. Chen SH, Yan YF, Qi GF, Zhang X.K, Zhang W. Analysis of influence factors of interference vibration reduction of millisecond blasting. *Rock Soil Mech* (2011) 32(10):3003–8. doi:10.16285/j.rsm.2011.10.035
17. Qiu XY, Shi XZ, Zhou J, Huang D, Chen X. On vibration reduction effect of short millisecond blasting by high-precision detonator based on HHT energy spectrum. *Explos Shock Waves* (2017) 37(1):107–13. doi:10.11883/1001-1455(2017)01-0107-07
18. Lou XM, Zhou WH. Selection of delayed time in millisecond blasting of open-pit mining. *Nonferrous Metals (Mining Section)* (2015) 67(4):82–8. doi:10.3969/j.issn.1671-4172.2015.04.019
19. Duan HF, Hou YB. Mechanism of millisecond blasting in open-pit mine and selection of millisecond time. *Nonferrous Metals (Mining Section)* (2003) 55(6):24–6. doi:10.3969/j.issn.1671-4172.2003.06.010
20. Zhang GX, Yang J, Lu HW. Research on seismic wave interference effect of millisecond blasting. *Eng Blasting* (2009) 15(3):17–21. doi:10.3969/j.issn.1006-7051.2009.03.004

21. Monjezi M, Hasanipanah M, Khandelwal M. Evaluation and prediction of blast-induced ground vibration at Shur River Dam, Iran, by artificial neural network. *Neural Comput Applic* (2013) 22:1637–43. doi:10.1007/s00521-012-0856-y
22. Hajihassani M, Jahed Armaghani D, Marto A, Tonnizam Mohamad E. Ground vibration prediction in quarry blasting through an articial neural network optimized by imperialist competitive algorithm. *Bull Eng Geol Environ* (2014) 74:873–86. doi:10.1007/s10064-014-0657-x
23. Shang YH, Nguyen H, Bui X-N, Tran Q-H, Moayedi H. A novel artificial intelligence approach to predict blast-induced ground vibration in open-pit mines based on the firefly algorithm and artificial neural network. *Nat Resour Res* (2019) 29:1–15. doi:10.1007/s11053-019-09503-7
24. Zhou J, Asteris PG, Armaghani DJ, Pham BT. Prediction of ground vibration induced by blasting operations through the use of the Bayesian Network and random forest models. *Soil Dyn Earthq Eng* (2020) 139, 106390. doi:10.1016/j.soildyn.2020.106390
25. Azimi Y. Prediction of seismic wave intensity generated by bench blasting using intelligence committee machines. *Int J Eng* (2019) 32(4):617–27. doi:10.5829/IJE.2019.32.04A.21
26. Kjartansson E. Constant Q-wave propagation and attenuation. *J Geophys Res* (1979) 84:4737–48. doi:10.1029/jb084ib09p04737
27. Rouse N, Schnell D, Worsey T. "Surface blast vibration regression model for underground mines," in: Tenth EFEE world conference on explosives and blasting; 2019 Sep; Helsinki, Finland (2019). pp. 16–8.

Conflict of Interest: The author LX was employed by BGRIMM Technology Group.

The remaining authors declare that the research was conducted in the absence of any commercial or financial relationships that could be construed as a potential conflict of interest.

frontiers in Physics

ORIGINAL RESEARCH
published: 24 May 2021
doi: 10.3389/fphy.2021.591651

Study on the Acoustic Emission Characteristics of Different Rock Types and Its Fracture Mechanism in Brazilian Splitting Test

Li Shengxiang[1,2], *Xie Qin*[1], *Liu Xiling*[1,2]*, *Li Xibing*[1], *Luo Yu*[1] *and Chen Daolong*[1]

[1] School of Resources and Safety Engineering, Central South University, Changsha, China, [2] State Key Laboratory of Coal Resources and Safe Mining, China University of Mining and Technology, Xuzhou, China

In order to investigate the relationship between rock microfracture mechanism and acoustic emission (AE) signal characteristic parameters under split loads, the MTS322 servo-controlled rock mechanical test system was employed to carry out the Brazilian split tests on granite, marble, sandstone, and limestone, while FEI Quanta-200 scanning electron microscope system was employed to carry out the analysis of fracture morphology. The results indicate that different scales of mineral particle, mineral composition, and discontinuity have influence on the fracture characteristics of rock, as well as the *b*-value. The peak frequency distribution of the AE signal has obvious zonal features, and these distinct peak frequencies of four types of rock fall mostly in ranges of 0–100 kHz, 100–300 kHz, and above 300 kHz. Due to the different rock properties and mineral compositions, the proportions of peak frequencies in these intervals are also different among the four rocks, which are also acting on the *b*-value. In addition, for granite, the peak frequencies of AE signals are mostly distributed above 300 kHz for granite, marble, and limestone, which mainly derive from the internal fracture of k-feldspar minerals; for marble, the AE signals with peak frequency are mostly distributed in over 300 kHz, which mainly derive from the internal fracture of dolomite minerals and calcite minerals; AE signals for sandstone are mostly distributed in the range of 0–100 kHz, which mainly derive from the internal fracture of quartz minerals; for limestone, the AE signals with peak frequency are mostly distributed in over 300 kHz, which mainly derive from the internal fracture of granular-calcite minerals. The relationship between acoustic emission signal frequency of rock fracture and the fracture scale is constructed through experiments, which is of great help for in-depth understanding of the scaling relationship of rock fracture.

Keywords: Brazilian split tests, *b*-value, AE frequency characteristic, scanning electron microscope, micro-fracture morphology

OPEN ACCESS

Edited by:
Guoyang Fu,
Monash University, Australia

Reviewed by:
Hai Pu,
China University of Mining and Technology, China
Stavros Kourkoulis,
National Technical University of Athens, Greece

***Correspondence:**
Liu Xiling
lxlenglish@163.com

Specialty section:
This article was submitted to Interdisciplinary Physics, a section of the journal Frontiers in Physics

Received: *05 August 2020*
Accepted: *26 March 2021*
Published: *24 May 2021*

Citation:
Shengxiang L, Qin X, Xiling L, Xibing L, Yu L and Daolong C (2021) Study on the Acoustic Emission Characteristics of Different Rock Types and Its Fracture Mechanism in Brazilian Splitting Test. Front. Phys. 9:591651. doi: 10.3389/fphy.2021.591651

INTRODUCTION

From a microscopic point of view, solids are made up of strong and rigid phases or crystalline grains, especially ceramic, rock, and concrete materials. Due to the diversity of chemical composition or crystal orientation, the different elastic moduli among crystalline grains could lead to local high stress under external stress, and microscopic processes would be activated by crack

tips under the stress and would eventually cause crack expansion and propagation, which could result in intergranular or transgranular cracks generated by cracks propagating along grains or grain boundaries [1]. From a macroscopic perspective, however, rocks are mostly polycrystalline and brittle, containing natural structural planes such as joints and weak intercalated layers; thus, the nucleation and propagation of cracks generated by rock failure emit energy outward as elastic waves when subjected to loading conditions. Such elastic waves are derived from microscopic dislocations; twinned crystals; crystal interfaces and the slip; and separation of macroscopic mineral grains, joints, and other weak planes; all of these are referred to as AE activity [2–6]. It is because of the complex composition of rock material that the cracks inside the rock sample, from microscopic to macroscopic level, will be in different scales and have different fracturing mechanisms under various loading conditions. These different cracking scales and fracturing mechanisms have close relationship with AE signal feature parameters [7, 8].

One of the critical AE parameters is signal frequency which could be used to infer the change of the internal stress state of a rock mass and reveal the rock fracture mechanism [6, 8, 9]. As a matter of fact, there is a natural correspondence between the rupture scale and the signal frequency; it is considered that the high frequency AE signals corresponded to the small scale crack, while the low frequency AE signals corresponded to the large scale crack [2, 5, 10–12]. Meanwhile, some researches based on laboratory AE experiments have shown that the AE signals of rock samples were characterized by a long duration time and a wide frequency spectrum when subjected to shear failure, whereas the results contrasted in tensile failure [11, 13, 14]. In field AE monitoring, it was also demonstrated that there were two typical signals, durative and attenuative, which were derived from the sliding and tensile failure or separation of faults, respectively [15, 16]. This derivation was mainly due to the larger part of energy transmitted in the form of shear waves, which were slower. Therefore, the maximum peak of the waveform delayed considerably compared with the onset of the initial longitudinal arrivals, and AE signals exhibited a higher frequency in tensile mode compared with a lower frequency in shear mode. For these frequency features given above, the AE signals at different stress stages and loading conditions have different dominant frequency characteristics because of various fracture modes generated [17, 18]. Therefore, the frequency spectrum of collected AE signal is determined by the loading condition, rock type, failure process, etc., and the development characteristics of signal frequency could provide a basis for the prediction of rock stability and localization of microseismic/acoustic emission sources [19]. Another characteristic parameter is the *b*-value. *b*-value is known to be an important scaling parameter in faulting evaluation, and the spatial and temporal variations of the *b*-value are always regarded as an essential clue for earthquake precursors. The variation of the *b*-value obtained in rock AE deformation tests has always been used to perform damage process and precursory analysis [3, 20–22].

As *b*-value is a rupture size scaling parameter, the structure composition, loading mode, and water content of the rock will affect the calculation result of *b*-value. Rocks with larger mineral particles and complex compositions will have more large-scale fractures with smaller *b*-value, while rocks with smaller mineral particles and simple compositions will have more small-scale fractures with larger *b*-value. Therefore, the *b*-value will reflect the composition of the rock sample to some extent.

Rock failure is a multi-scale and non-linear dynamic process. AE signals generated in an individual mineral particle are different from that on the boundaries of mineral particles. Some researchers found that the AE signals with high-energy and short pulse were produced by the failure process along particles while the signals with low energy and long pulse were generated by the slip of particle boundary and fracture surface under uniaxial compression tests. In addition, the microfracture mechanism depends on the number and distribution of weak mineral particles [23]. The internal structures of rock are composed of different mineral particles. Generally, the strength of a single intact crystal is the highest, followed by the coupling between crystals, and the strength of coupling between mineral grains and structural planes is the smallest. It is due to the complexity of the rock structure that the final macrofracture is often closely related to its internal microstructure and microcrack propagation after deformation, and the morphology characteristics of rupture surface of various structures are different [24, 25]. As mentioned above, the cracking of different structures in a rock sample will generate different types of AE signals; thus, the fracture morphology of various cracking can be related with AE parameters.

Scanning electron microscopes (SEM) has long been employed in metallurgy and material science. It has also been widely used to observe fracture surface morphology to reveal the microfracture mechanism of rocks, owing to its direct observation of sample surface and high magnification [26, 27]. Li et al. [28] found that different fracture modes have different morphological features: tensile fracture has 10 types of morphologies and shear fracture has eight. However, some morphologies, such as smoothly curving conchoidal appearance, are yet a specific feature of quartz; it was considered that river and step patterns belonged to transgranular failure while parallel slip line pattern belonged to intragranular failure [29–31]. The characteristics of fracture surface imply that the microscopic fracture mechanism is greatly influenced by loading conditions and the composition of the rock material, such as mineral components, grain bonding property, and joints. Under uniaxial compression, the microfracture mode of granite changes from intergranular fracture to transgranular fracture as the strain rate increases [32, 33]; under quasi-static loads, the intergranular fractures are in majority due to the toughness of grain boundary or due to the substantial weakness of the cement than that of the grain [34, 35]; whereas under dynamic loads, cleavage steps, multiple micro-conchoidal fracture, and transgranular fractures associated with smooth planar surfaces are frequently observed [33, 36, 37]. Kranz [33] and Alkan et al. [38] also explained that the proportion of transgranular cracks and intergranular cracks appeared to depend on mineral composition, rock types, stress state, etc. For polycrystalline rock materials, given that tensile fracture is the main fracture

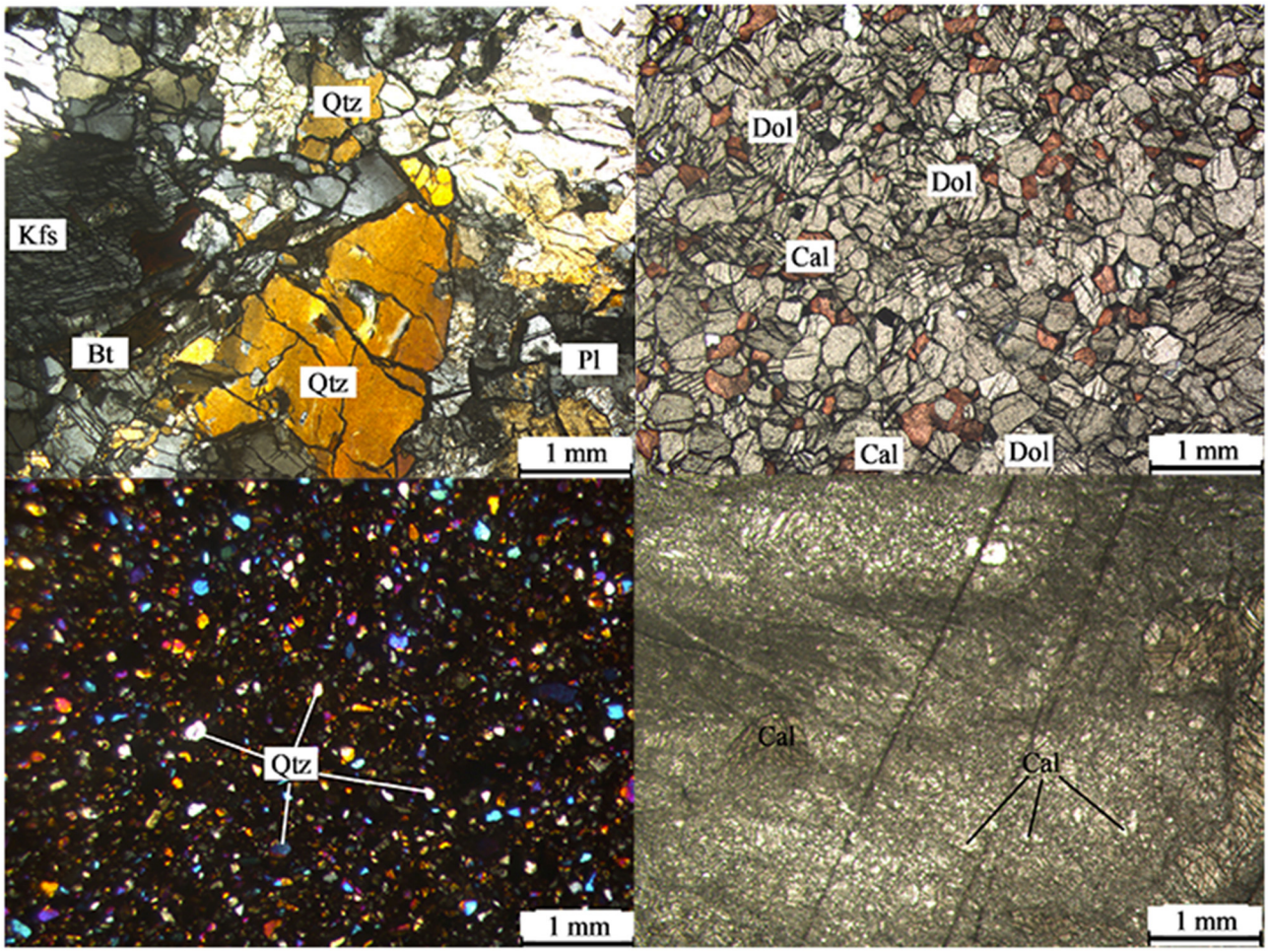

FIGURE 1 | The microstructure of rocks in transparent refractive index experiment, granite (top left), marble (top right), sandstone (bottom left), and limestone (bottom right) (Qtz, quartz; Kfs, k-feldspar; Bt, biotite; Pl, plagioclase; Dol, dolomite; Cal, calcite) [39].

mode in rock deformation tests, the tensile fracture would occur in different microstructures, which could release elastic wave signals with various characteristics. Therefore, the combination of SEM and AE technology will provide excellent insights into the microscopic fracture mechanism and the characteristics of corresponding AE signals.

For this purpose, four types of rock materials were used to perform Brazilian splitting tests for this study: granite, marble, sandstone, and limestone. By comparing the AE signals of four types of rocks and the SEM observations, we could explore more deeply the relationship of microfracture mechanisms and AE characteristic parameters from a microscopic perspective.

EXPERIMENTAL SETUPS

Granite, marble, sandstone, limestone were the four rock types selected as research objects of this experiment. They were all made into cylindrical samples with a diameter of 50 mm and length of 50 mm. Before the experiment, the mineral compositions of the four rock types were measured by transparent refractive index experiment (see **Figure 1**). The image indicates the preexisting microcracks and microcavities. The granite contains quartz, plagioclase, k-feldspar, and a small amount of biotite; the marble mainly consists of calcite and dolomite; and the main mineral component of the sandstone is quartz while that of the limestone is calcite.

The MTS322 servo-controlled rock mechanical test system is employed to carry out Brazilian split tests; its loading and sampling rates are set to 30 kN/min and 50 Hz, respectively. A PCI-2 system (Physical Acoustics Corporation, New Jersey, USA) is used for the collection of AE signals. The threshold, preamplifier gain, sampling length, and sampling rate are set at 45 dB, 40 dB, 5 K, and 10 MSPS, respectively. The PDT, HDT, and HLT are set at 50, 200, and 300 μs. Two ultra-mini sensor-NANO-30 with 140 kHz resonant frequency are glued onto the end face of the specimen, as shown in **Figure 2**.

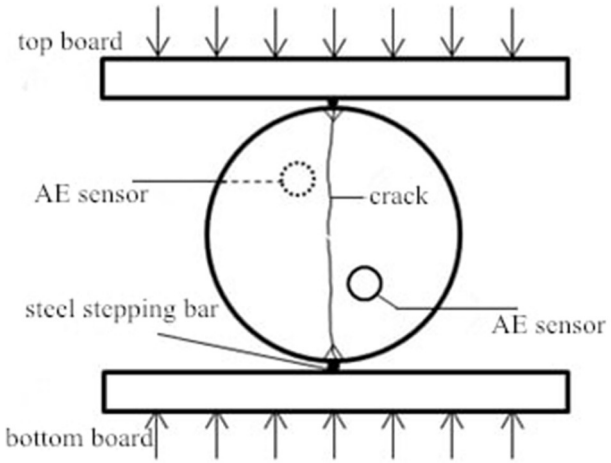

FIGURE 2 | The sketch of the Brazilian split test.

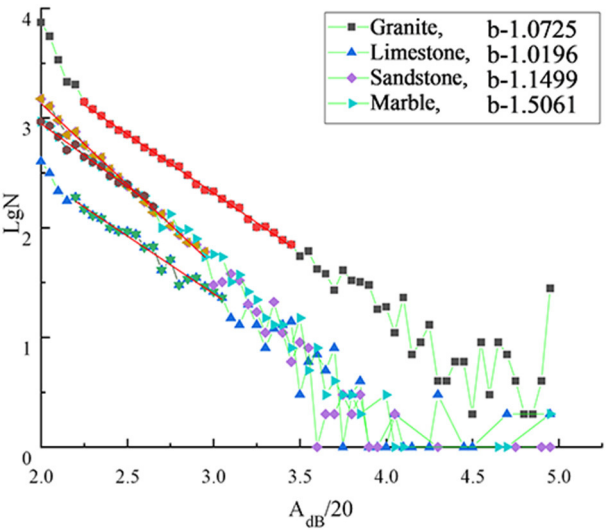

FIGURE 3 | *b*-Values of four kinds of rocks obtained by the FGS method.

RESULTS AND DISCUSSION

b-Value Analysis

The size distribution of earthquake commonly follows a relationship which is given as follows:

$$lgN = a - bM \tag{1}$$

where M is magnitude, N is the number of earthquakes with a magnitude $\geq M$, and a and b are the constants [40]. Here, the parameter b describes the size distribution scaling, which is often referred to as b-value, and the spatial and temporal variations of b-value are always regarded as an essential clue for earthquake precursor. In the calculation, magnitude in the G-R relation is replaced by amplitude [41]:

$$lgN = a - b(\frac{A_{dB}}{20}) \tag{2}$$

where a, b, and N refer to the same as Formula (1). A_{dB} is the maximum amplitude of an acoustic emission event expressed in decibels:

$$A_{dB} = 20lg\, A_{max} \tag{3}$$

where A_{max} is the maximum amplitude value of AE event expressed in microvolts.

The integral b-value of those rock samples were calculated by using FGS method proposed by Liu et al. [42]. As shown in **Figure 3**, the b-value of marble is the largest, followed by sandstone, granite, and limestone. As the heterogeneity and internal structure of the rock material plays an important role in b-value, different rock samples with various mineral particle size and uniformity will result in different calculated b-value. As shown in **Figure 1**, marble and sandstone are composed of fine-grained particles and seldom have large size discontinuities. With dolomite and calcite granules being closely related to mosaic crystal structures, the particles are small and uniform, a feature that accounts for a high proportion of small-scale ruptures in the loading process, so the b-value is high. Granite has various large-sized mineral grains and defects; more large-scale fractures will be generated during the whole loading process, so the b-value is low. Limestone contains a large number of joints during deposition and ruptures mainly along these joints, which would generate more large-scale ruptures, so the b-value of it is the lowest. Therefore, the b-value of the rock is inversely proportional to the size of its fracture scale.

Peak Frequency Distribution

Generally, earthquake signal frequency is below a few Hertz, and microseismic signal frequency ranges from a few Hertz to thousands of Hertz, while AE signal frequency is between several thousand Hertz and a number of megahertz [43]. In fact, many previous studies have shown that frequency is an important parameter to characterize the elastic wave [2–34]. For AE of rocks, different types of sources produce different scales of fracture, which release the AE signals with different frequencies. The signals generated by large-scale cracks contain significant low-frequency components, and the signals generated by small-scale cracks contain significant high-frequency components. In spectra analysis, peak frequency is an important parameter to analyze the spectral characteristics of signal, which is the frequency of the maximum energy spectrum, and can be approximately regarded as the main frequency of the signal, and the source type can be recognized by analyzing the value of peak frequency.

The peak frequencies of the four rock types mostly present the zonal distribution feature as shown in **Figure 4**. These signal peak frequencies mainly distribute in the range of 0–100, 100–300, and 300 kHz and above, and the proportion of each frequency band is listed in **Table 1**. Under splitting loads, the rock samples are dominated by tensile cracks, and

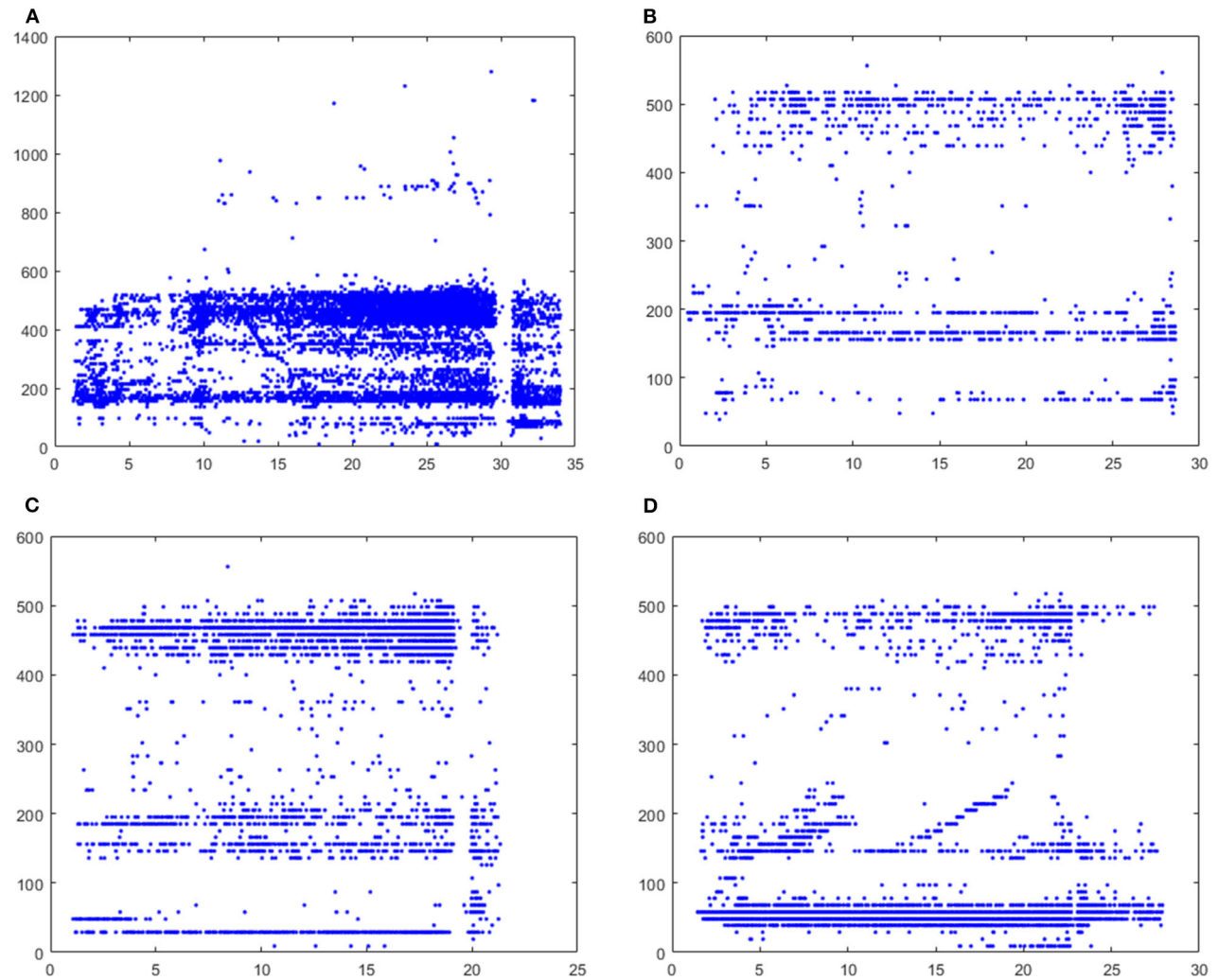

FIGURE 4 | Peak frequency distribution with loading time. **(A)** is the peak frequency distribution and corresponding density contours of granite; **(B)** is the peak frequency distribution and corresponding density contours of limestone; **(C)** is the peak frequency distribution and corresponding density contours of the peak frequency distribution with loading time of sandstone; **(D)** is the peak frequency distribution and corresponding density contours of the peak frequency distribution with loading time of marble.

tensile cracks are characterized by spectra with a rapid decay in high frequency, whereas shear sources are characterized by a broader spectra and a lower decay [11, 14, 44, 45]; this indicates the presence of more high-frequency content in the spectra of signals generated by tensile cracks. Besides, in the Brazilian split test, rock samples will split along axial center surface, which greatly reduces the probability of fracture along the internal discontinuous planes joints, in which the AE signals are mainly generated by the separation of mineral particles on the splitting surface. These smaller scale fractures usually release AE signals with high frequency. Therefore, for granite, marble, and limestone, the signal peak frequencies larger than 300 kHz are in the majority, whereas for sandstone, the high frequency component of AE signal will be greatly attenuated due to high porosity [46–49], thus resulting in relatively larger proportion of low frequency signals being collected.

Micromorphology of Split Surface

After the loading test, the FEI Quanta-200 was used to conduct fracture surface scanning. The rupture morphology of granite is mainly composed of three patterns, as shown in **Figures 5A–C**, according to the following energy spectrogram. The morphology of **Figure 5A** is derived from quartz mineral grains, showing smooth planar surfaces and shear sliding marks, while the morphology of **Figures 5B,C** is derived from k-feldspar mineral grains, showing noticeably rugged surfaces. It can be clearly seen in **Figure 1** (top lift) that there is a variety of coupling among mineral grains, as well as defects or voids within a single mineral particle, which determines the macroscopic physical properties of rocks. The integrity of quartz and plagioclase is better when k-feldspar has laminar fragmentized structure and its layer-to-layer is attracted by the coulomb force with relatively weak potassium ionic bond [1], all of which greatly reduces the strength of k-feldspar. For k-feldspar, the resulting fracture

TABLE 1 | Distribution percentage of AE peak frequency for four rock types under Brazilian split test.

Rock types	Sample codes	Peak frequency band (kHz)		
		<100	100–300	≥300
Granite	G1	4.00%	32.09%	77.95%
	G2	5.77%	36.18%	70.95%
	G3	8.50%	20.93%	69.98%
	Average	6.09%	29.72%	72.96%
Marble	M1	13.48%	19.34%	75.56%
	M2	10.49%	13.95%	75.03%
	M3	419.74%	8.02%	72.24%
	Average	10.52%	27.28%	74.28%
Sandstone	S1	79.19%	6.91%	13.93%
	S2	76.36%	12.41%	11.23%
	S3	69.63%	15.69%	14.65%
	Average	75.06%	11.67%	13.27%
Limestone	L1	18.17%	31.91%	50.66%
	L2	49.56%	23.84%	26.60%
	L3	8.36%	46.58%	45.06%
	Average	25.36%	34.11%	40.77%

surface morphology when the direction of stress is vertical to the laminar plates is shown in **Figure 5B**, namely, the laminar pattern, whereas the morphology of when the direction of stress is parallel to the plates is shown in **Figure 5C**, namely, flaky patterns. The microscopic fracture characteristics of the rock samples depend on the number and distribution of weak mineral particles under stress [23], and the fracture is more likely to occur in weak mineral particles. For granite in this experiment, k-feldspar belongs to the typical weak mineral grains and the internal microfracture within the samples subjected to splitting loads occurs more easily in k-feldspar mineral grains, which is also the reason why morphology in **Figures 5B,C** can be often observed. Compared with k-feldspar, there are also obvious discontinuity surfaces in quartz mineral grains; the cracks in quartz will propagate along its internal discontinuity surfaces or boundaries in a tensile failure manner. The smooth and flat surfaces, a special feature of quartz, are frequently observed and shown in **Figure 5A** [30, 34]. Meanwhile, the samples will be split along their center of loading direction under Brazilian split loads. The opportunity of the main cracks propagating through the quartz mineral grains is larger due to its main mineral components within granite, so the micromorphology of quartz is frequently observed as shown in **Figure 5A**.

Generally, marble has a typical granular crystalloblastic texture, as shown in **Figure 1** (top right), containing large amounts of dolomite mineral grains and a small amount of calcite mineral grains and with dolomite and calcite granules being closely related mosaic crystal structures. The microfracture morphologies, as shown in **Figures 6A,B**, are derived from dolomite and calcite particles, respectively. Because dolomite and calcite have similar crystal structures and the crystalline form belongs to the rhombohedral crystal system, gathering with massive and granular patterns, their morphologies are also similar, as shown in **Figures 6C,D**. Due to the closely related mosaic of dolomite and calcite after metamorphism, whether the cracks propagate between mineral grains or along the internal boundary, smooth crystal boundary surfaces are all frequently observed as shown in **Figures 6A,B**. Furthermore, there is also a common polysynthetic twinning in calcite as shown in **Figures 6B,D**.

Red sandstone is composed of numerous small-grained particles, so the bonding strength among grains is lower and its gap is larger. The internal microfracture of samples subjected to splitting loads occurs mainly in the cementation region of granules, and the rugged and rough surfaces will be formed by the separation of the cementations; therefore, the "candy shape" morphology is frequently observed in **Figures 7A,B**.

The limestone used in this experiment is bioclastic limestone and consists of small-grained calcium carbonate and bioclast. Its structure is dense and contains a small number of granular calcite veins and a large number of discontinuities during deposition, as shown in **Figure 1** (bottom right). The microfracture morphologies of the samples subjected to splitting loads are mostly observed as shown in **Figure 8A**, which are mainly the separation of the calcium carbonate cementite and also the apparent separation of the discontinuous surface of calcium carbonate cementite. and there is a secondary cracks (SC) on the fracture surface shown in **Figure 8B**. In addition, if the fracture surface occurs in granular calcite veins, it will have the morphology shown in **Figure 8C**, showing a typical rupture feature of calcite and there are smooth steps with streamline patterns on the fracture surface shown in **Figure 8D**.

Rock AE signal frequency has a close relationship with its internal crack scale, by constructing the relevant earthquake

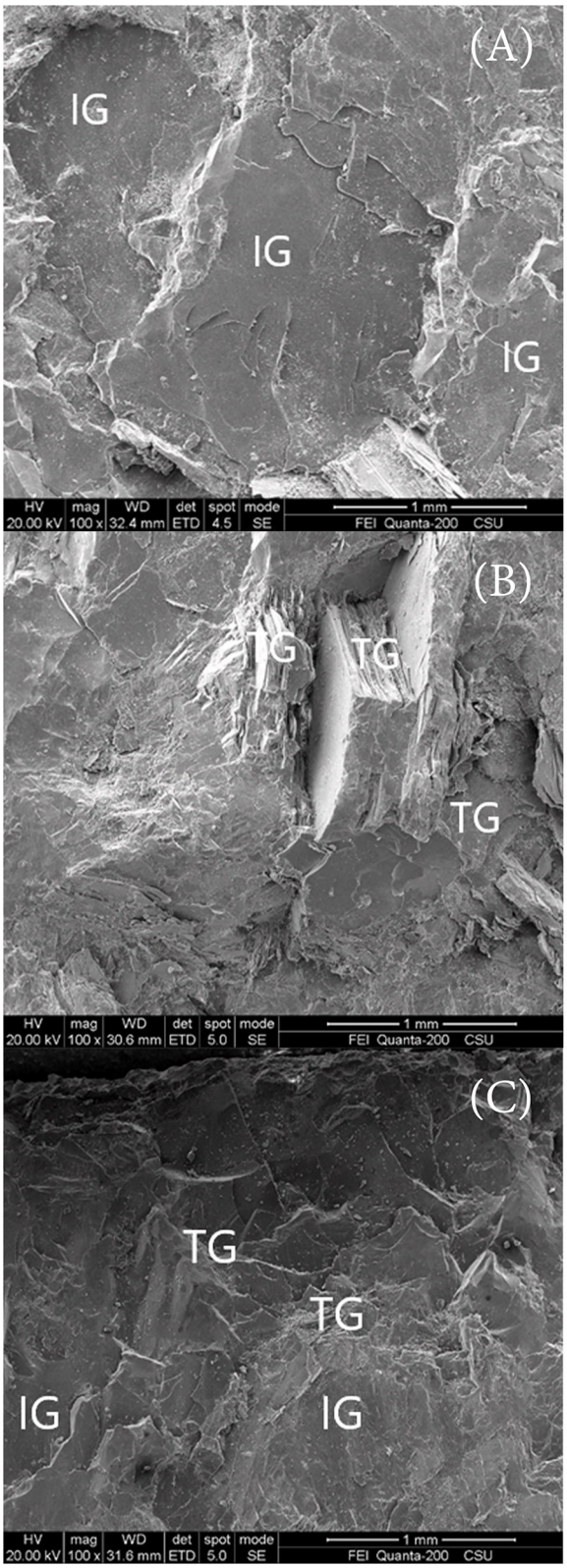

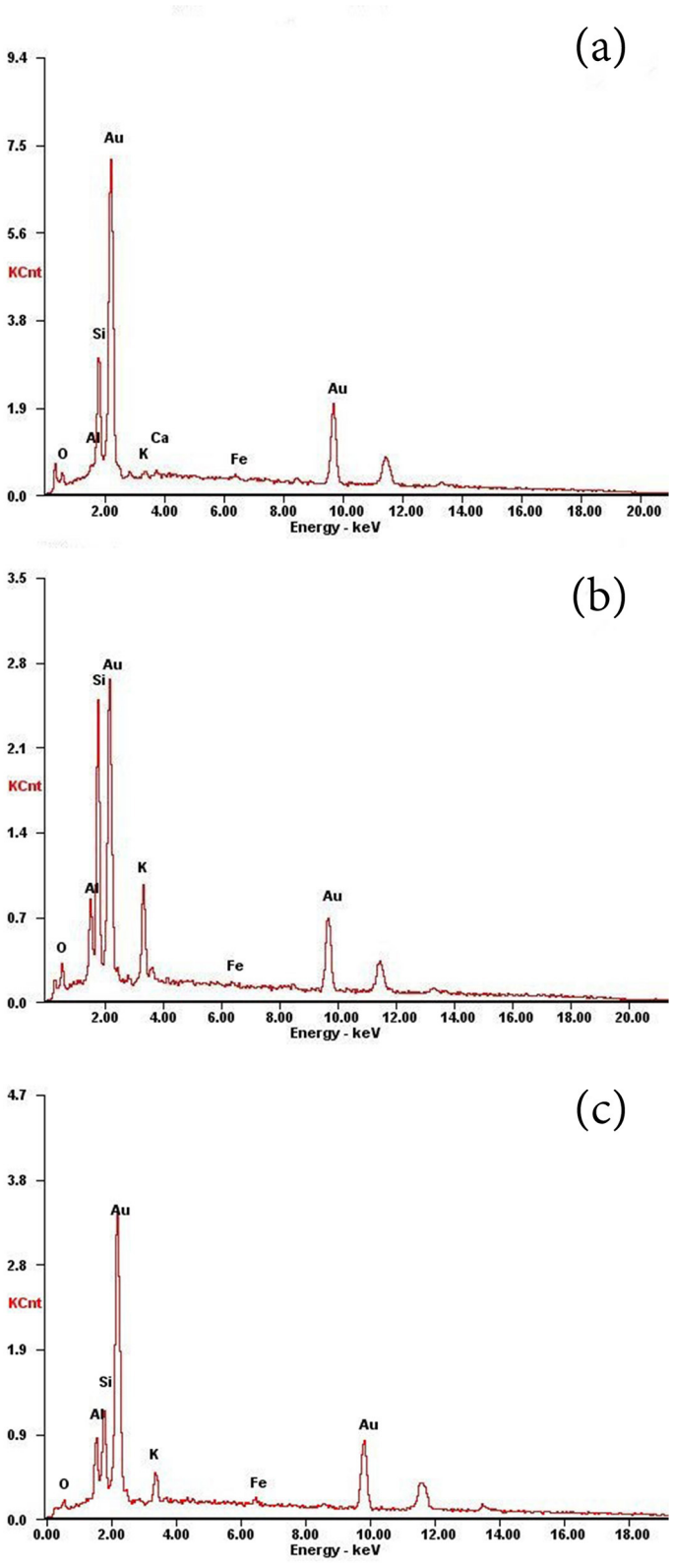

FIGURE 5 | Scanning electron miscroscope (SEM) photos of the fracture surfaces for granite under the Brazilian split test **(A)**, most of fracture surfaces have clear inter-granular cracks and shows "smooth planar" morphology of quartz, **(a)** energy spectrogram corresponding with **(A)**. **(B)** This is a typical transgranular crack surface and shows "sidestep" morphology of k-feldspar, **(b)** energy spectrogram corresponding with **(B)**. **(C)** There are intergranular and transgranular cracks and shows "stack-up" morphology of k-feldspar, **(c)** energy spectrogram corresponding with **(C)**.

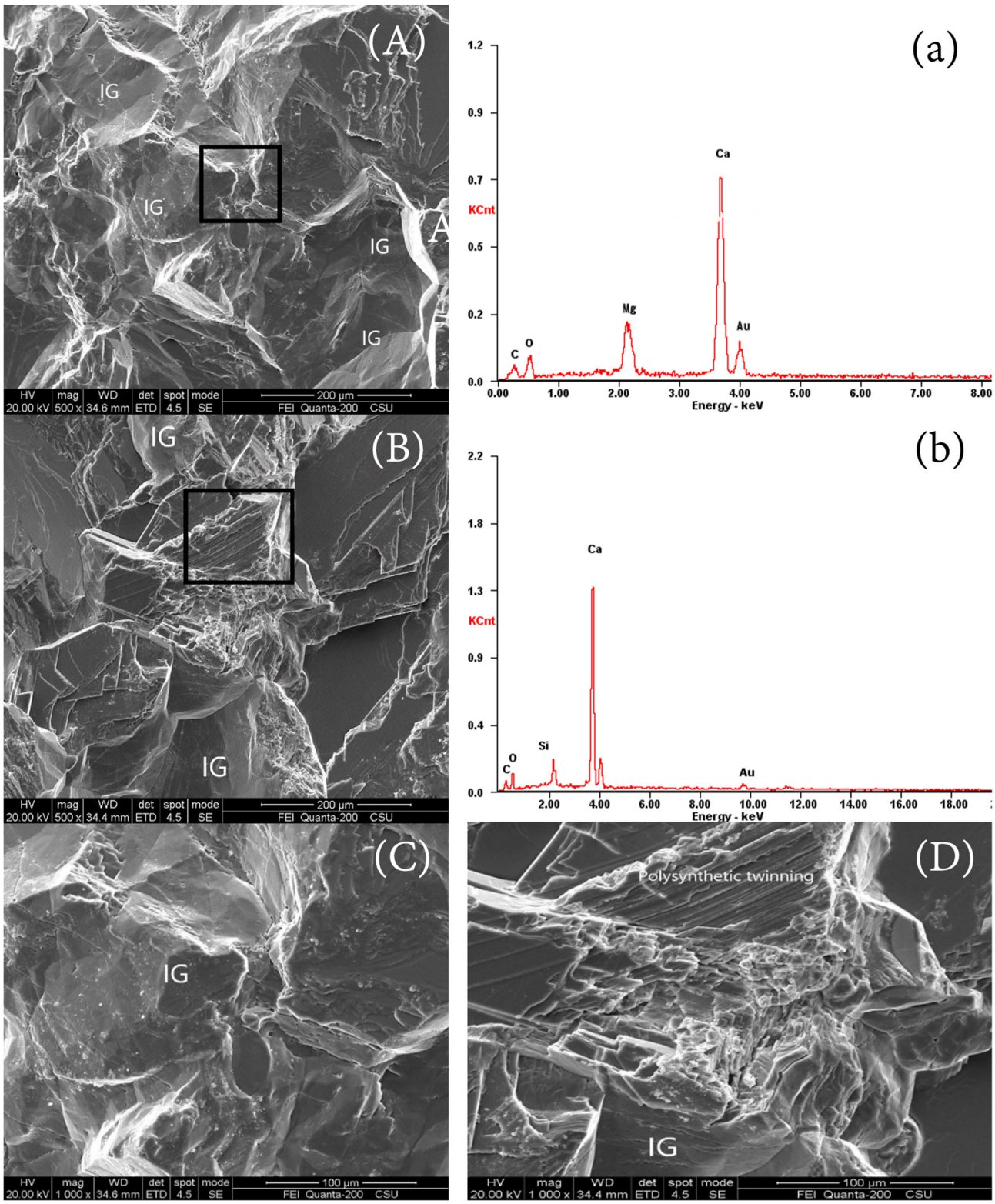

FIGURE 6 | SEM photos of the fracture surfaces for marble under the Brazilian split test. **(a,b)** The energy spectrogram corresponding with the black square in **(A,B)** and its mineral composition is dolomite and calcite, respectively; **(C,D)** represents the high magnification morphology of the black square in **(A,B)**, respectively.

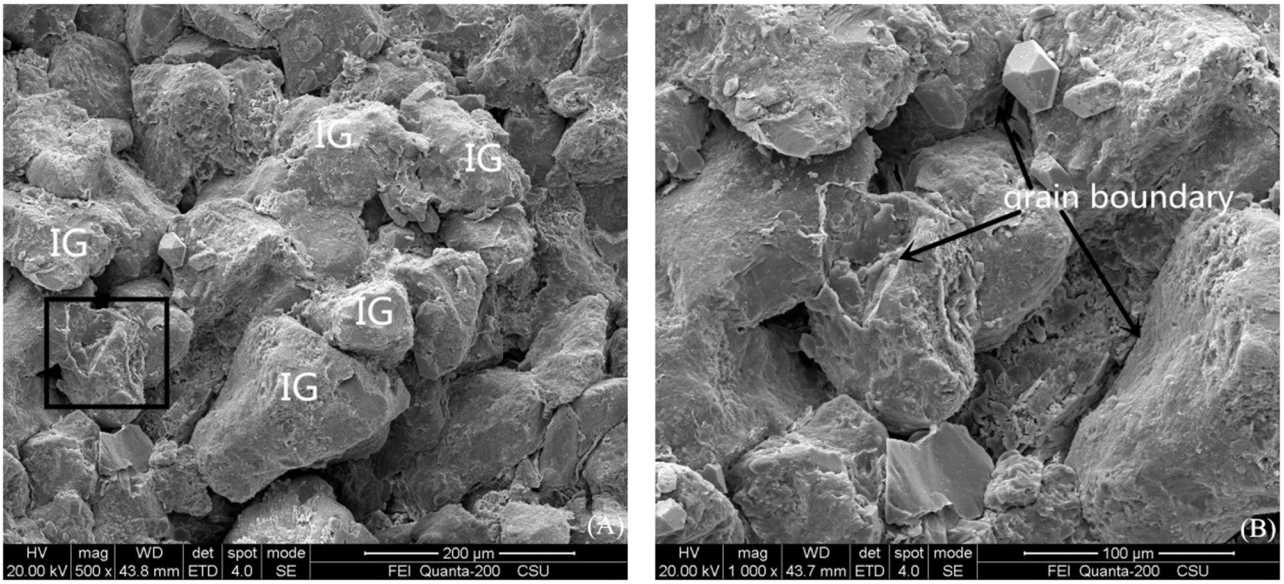

FIGURE 7 | SEM photos of the fracture surfaces for sandstone under the Brazilian split test. **(B)** is an inter-granular fracture surface which is amplified in black square for **(A)** and shows "candy" shape.

model and simulating the earthquake process in the laboratory. It is concluded that the rupture scale (or magnitude) M_0 is proportional to the -3 power of the frequency f. The scaling relation of size-frequency can be used to estimate the scale of the source of different frequency signals [12, 48, 49], and the relationship between source scale and frequency can be as follows [50]:

$$d_L \times f_L \approx d_V \times f_V \tag{4}$$

where d_L is the laboratory length, f_V is the laboratory frequency, d_V is the source dimensions, and f_V is the source dimensions.

The rock samples will be split along the center surface under Brazilian splitting loads, according to the above morphology. The cracks within rock samples mostly propagate along the grain boundaries or its internal discontinuous surfaces. On the one hand, the fracture scale is smaller due to its small-grained particles; on the other, it is accepted that AE signals exhibit a higher frequency in tensile mode compared with a lower frequency in shear mode [51–55], so the AE signals are dominated by high frequency signals under splitting loads. Moreover, the fixed rupture surface under Brazilian splitting loads reduces the opportunity of fracture along large-grained discontinuous surfaces, thus reducing the chance of producing low frequency signals. As mentioned above in the "Peak frequency distribution" section, the AE signals with peak frequencies of 100–300 kHz and over 300 kHz are in the majority, and the proportion of the signals with peak frequency of more than 300 kHz accounted for more than 50%. The signals with over 300 kHz are derived from the rupture of fracture dimension of $<$ 2.5 mm based on the above equation, so the high frequency signals are mainly from the fracture of grain boundaries or grains whether in granite, marble, sandstone, or limestone. Lower frequency signals are mainly generated by large scale discontinuous surfaces within rock samples. For sandstone, however, the high frequency signals are also from the fracture of small-scale mineral grains, but the attenuation of elastic wave becomes greater due to higher porosity of sandstone. The attenuation of high frequency signal becomes faster in the sandstone medium, so AE signal frequency is mostly $<$ 100 kHz. The micro-fracture characteristics of four type rocks under Brazilian split test are listed in **Table 2**.

CONCLUSIONS

The b-value of marble is the largest followed by sandstone, granite, and limestone, mainly determined by their compositions and internal structure. It was found in the microscopic morphology analysis that marble contains a large number of small mineral particles, and between dolomite and calcite granules are closely related mosaic crystal structures. Sandstone is composed of fine-grained particles and seldom has large size discontinuities, which account for a high proportion of small-scale ruptures. Granite has various large size mineral grains and defects or voids. Limestone contains a large number of joints during deposition, which would generate more large-scale ruptures. All of the above facts indicate that heterogeneity and internal structure of the rock material influence the G-R relationship.

Because the rock samples are subjected to tensile force of expansion under splitting loads, the cracks within samples always propagate along the weak surface. Due to gap or

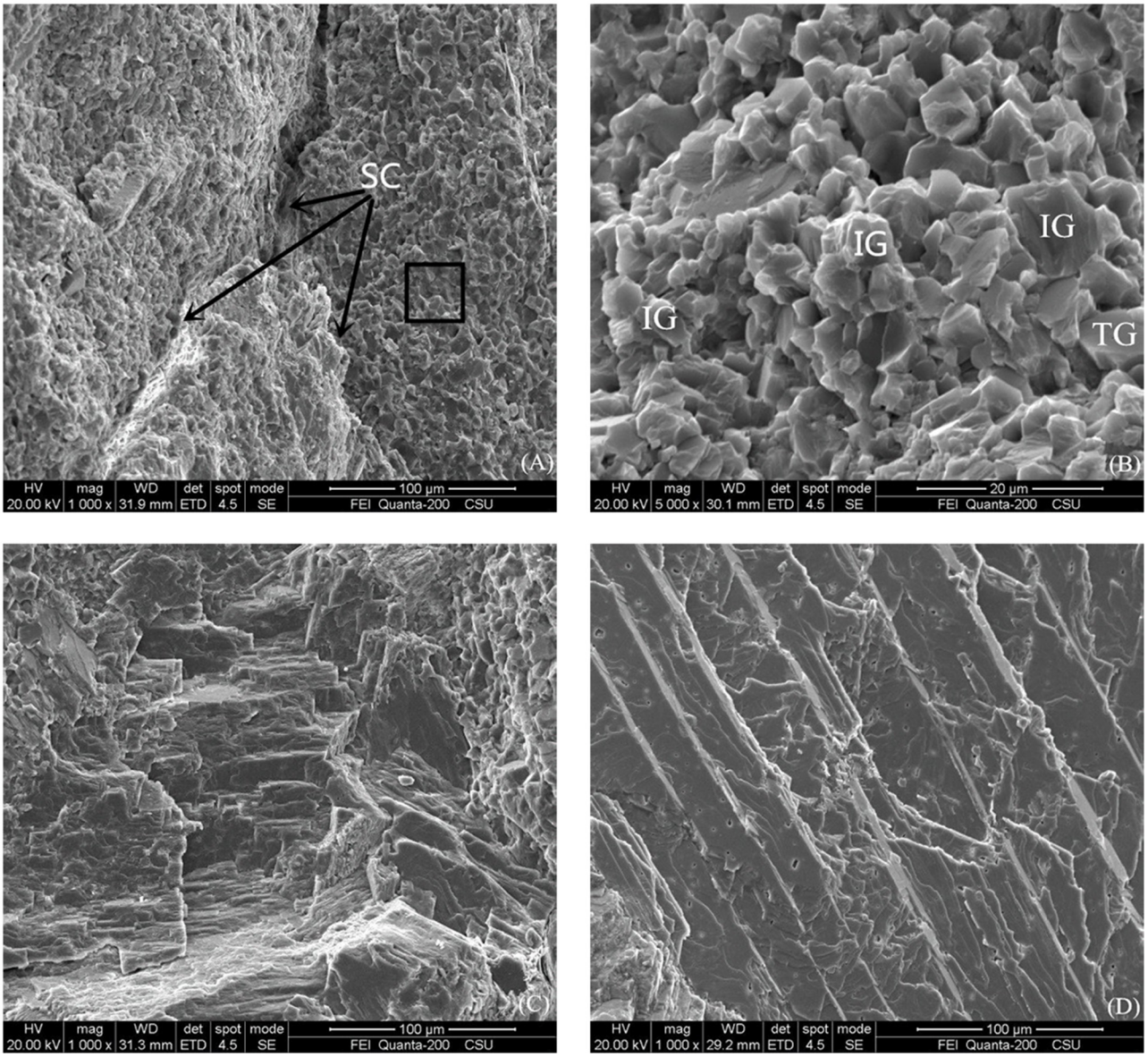

FIGURE 8 | SEM photos of the fracture surfaces for limestone under Brazilian split test. **(A)** Secondary Cracks (SC) on the fracture surface; **(B)** inter-granular and trans-granular cracks; **(C)** coarse sidesteps on fracture surface; **(D)** smooth steps with streamline patterns on the fracture surface.

filled impurities between grains and grain boundaries, the strength of discontinuous surfaces will be greatly weakened, and these small-scale discontinuities will first be separated under the tensile stress, which also determines the macro-mechanism of rocks. Whether the separation of mineral grain boundaries or internal discontinuous surfaces, these fractures are all extended along the grain boundary. Therefore, rock samples show more preference for intergranular cracking from microlevel under the tensile stress, which is also the reason why the smooth fracture surfaces occur commonly in the microscopic morphologies of this paper. Because the length of cracks along the grain boundaries are small, a large number of higher frequency signals are generated. In addition, the fixed rupture surface under splitting loads reduces the opportunity of fracture along large-grained discontinuous surfaces, thus reducing the chance of producing low frequency signals. Therefore, large amounts of small-scale fractures along the fixed rupturing surface in the rock split loading test led to the collected AE signals being dominated by high frequency waveforms. It is notable that, due to the high porosity of sandstone, the attenuation of elastic wave is greater and the signal with high frequency is difficult to be collected by AE sensors, thus resulting in a relatively small proportion of high frequency signals.

TABLE 2 | The micro-fracture characteristics of four type rocks under Brazilian split test.

Rock types	Mineral compositions	Morphology features	Predominant micro-mechanism	Peak frequency (kHz)
Granite	Quartz	Discontinuous surface smooth planar stack-up, sidestep	–	100–300
			IG	≥300
	K-feldspar			
Marble	Dolomite	Smooth plane	IG	≥300
	Calcite	Polysynthetic twinning		
Sandstone	Quartz	Candy shape	IG	≥300
Limestone	Granular-calcite	Ooid shape	IG	≥300
	Blocky-calcite	Discontinuities	–	100–300

DATA AVAILABILITY STATEMENT

The original contributions presented in the study are included in the article/supplementary material, further inquiries can be directed to the corresponding author/s.

AUTHOR CONTRIBUTIONS

LS and XQ are responsible for the implementation of the experiment and writing the main part of the paper. LY and CD are responsible for experiments and paper data processing and so on. LXil and LXib are responsible for the overall idea of the paper and the design of the experimental scheme. LXil was also responsible for writing part of the paper. All authors contributed to the article and approved the submitted version.

FUNDING

This study was funded by the Research Fund of The State Key Laboratory of Coal Resources and Safe Mining, CUMT (SKLCRSM21KF005).

REFERENCES

1. Derek H. *Fractography: Observing, Measuring, and Interpreting Fracture Surface Topography*. Cambridgeshire: Cambridge University Press (1999).
2. Mogi K. Study of the elastic shocks caused by the fracture of heterogeneous materials and its relation to earthquake phenomena. *Bull Earthq Res Inst.* (1962) 40:125–73.
3. Scholz CH. The frequency-magnitude relation of microfracturing in rock and its relation to earthquakes. *Bull Seismol Soc Am.* (1968) 58:399–415.
4. Scholz CH. Experimental study of the fracturing process in brittle rock. *J Geophys Res Atmosph.* (1968) 73:1447–54. doi: 10.1029/JB073i004p01447
5. Scholz CH. Microfracturing and inelastic deformation of rock in compression. *J. Geophys. Res.* (1968) 73:1417–32. doi: 10.1029/JB073i004p01417
6. Chugh YP, Hardy HR Jr, Stefanko R. *An Investigation of the Frequency Spectra of Microseismic Activity in Rock Under Tension, Proceedings Tenth Rock Mechanics Symposium*. New York, NY: AIME (1972). p. 73–113.
7. Shiotani T, Ohtsu M, Ikeda K. Detection and evaluation of AE waves due to rock deformation. *Construct Build Mater.* (2001) 15:235–46. doi: 10.1016/S0950-0618(00)00073-8
8. He MC, Miao JL, Feng JL. Rock burst process of limestone and its acoustic emission characteristics under true-triaxial unloading conditions. *Int J Rock Mech Mining Sci.* (2010) 47:286–98. doi: 10.1016/j.ijrmms.2009.09.003
9. Peng H, Feng G, Zhang Z, Yang Y, Teng T. Evaluation method of rock brittleness based on acoustic emission and energy evolution. *J China University Min Technol.* (2016) 45:702–8.
10. Cai M, Kaiser PK, Morioka H, Minami M, Maejima T, Tasaka Y, et al. Flac/pfc coupled numerical simulation of AE in large-scale underground excavations. *Int J Rock Mech Min Sci.* (2007) 44:550–64. doi: 10.1016/j.ijrmms.2006.09.013
11. Willxam RW, James NB. Spectra of seismic radiation from a tensile crack. *J Geophys Res.* (1993) 98:4449–59. doi: 10.1029/92JB02414
12. Aki K, Richards PG. *Quantitative Seismology*. Sausalito, CA: University Science Books (2002).
13. Bucheim WW. Geophysical methods for the study of rock pressure in coal and potash salt mining. In: *International Strata Control Congress*. Leipzig (1958). p. 222.
14. David WE, van der Baan M, Birkelo B, Tary J-B. Scaling relations and spectral characteristics of tensile microseisms: evidence for opening/closing cracks during hydraulic fracturing. *Geophys J Int.* (2014) 196:1844–57. doi: 10.1093/gji/ggt498
15. Vinagradov SD. *Acoustic Observations in Collieries of the Kizelsk Coal Basin*. Bulletin (Izvestiya), Academy of Sciences of the USSR, Geophysics Series (1957).
16. Vinagradov SD. *Experimental Study of the Distribution of Fractures in Respect to the Energy Liberated by the Destruction of Rocks*. Bulletin (Izvestiya), Academy of Sciences of the USSR, Geophysical Series (1962). p. 171–80.
17. Ohnaka M, Mogi K. Correction to 'frequency characteristics of acoustic emission in rocks under uniaxial compression and its relation to the fracturing process to failure' by Mitiyasu Ohnaka and Kiyoo Mogi. *J Geophys Res Atmospheres.* (1982) 87:6975. doi: 10.1029/JB087iB08p06975
18. Mogi K. *Magnitude-Frequency Relation for Elastic Shocks Accompanying Fractures of Various Materials and Some Related problems in Earthquakes (2nd Paper)*. Tokyo: Journal of university of Tokyo earthquake research institute (1962).
19. Dong LJ, Zou W, Li XB, Shu WW, Wang ZW. Collaborative localization method using analytical and iterative solutions for microseismic/acoustic emission sources in the rockmass structure for underground mining.

Eng Fracture Mech. (2019) 210:95–112. doi: 10.1016/j.engfracmech.2018.01.032
20. Lockner DA, Byerlee JD, Kuksenko V, Ponomarev A, Sidorin A. Quasi-static fault growth and shear fracture energy in granite. *Nature*. (1991) 350:39–42. doi: 10.1038/350039a0
21. Goebel THW, Schorlemmer D, Becker TW, Dresen G, Sammis CG. Acoustic emissions document stress changes over many seismic cycles in stick-slip experiments. *Geophys Res Lett.* (2013) 40:2049–54. doi: 10.1002/grl.50507
22. Dong LJ, Johan W, Yves P, Li XB. Discriminant models of blasts and seismic events in mine seismology. *Int J Rock Mech Min Sci.* (2016) 86:282–91. doi: 10.1016/j.ijrmms.2016.04.021
23. Zang A, Wagner CF, Dresen G. Acoustic emission, microstructure, and damage model of dry and wet sandstone stressed to failure. *J Geophys Res.* (1996) 101:17507–22. doi: 10.1029/96JB01189
24. Srivatsan TS. A review of: "fractography: observing, measuring, and interpreting fracture surface topography, D. Hull." *Mater Manufact Process.* (2009) 24:1229–30. doi: 10.1080/10426910902984033
25. Ravi-Chandar K, Knauss WG. An experimental investigation into dynamic fracture: II. Microstructural aspects. *Int J Fract*. (1984) 26:65–80. doi: 10.1007/BF01152313
26. Menendez B, David C, Darot M. A study of the crack network in thermally and mechanically cracked granite samples using confocal scanning laser microscopy. *Phys Chem Earth Part A: Solid Earth Geod.* (1999) 24:627–32. doi: 10.1016/S1464-1895(99)00091-5
27. Liu J, Li B, Tian W, Wu X, et al. Investigating and predicting permeability variation in thermally cracked dry rocks. *Int J Rock Mech Mining Sci.* (2018) 103:77–88. doi: 10.1016/j.ijrmms.2018.01.023
28. Li XW, Lan YR, Zou JX. A study of rock fractures. *J China University Min Technol.* (1983) 1983:18–24.
29. Xie HP, Chen ZD. Analysis of rock fracture micro-mechanism. *J China Coal Soc.* (1989) 1989:57–67.
30. Norton MG, Atkinson BK. Stress-dependent morphological features on fracture surfaces of quartz and glass. *Tectonophysics*. (1981) 77:283–95. doi: 10.1016/0040-1951(81)90267-5
31. Liu XM, Lee CF. Microfailure mechanism analysis and test study for rock failure surface. *Chin J Rock Mech Eng.* (1997) 16:509–13. doi: 10.13722/j.cnki.jrme.2014.0701
32. Liang CY, Wu SR, Li X. Reserch on micro-meso characteristics of granite fracture under uniaxial compression at low and intermedia strain rates. *Chin J Rock Mech Eng.* (2015) 2015:2977–86.
33. Kranz RL. Microcracks in rocks: a review. *Tectonophysics.* (1983) 100:449–80. doi: 10.1016/0040-1951(83)90198-1
34. Zhang QB, Zhao J. Effect of loading rate on fracture toughness and failure micromechanisms in marble. *Eng Fracture Mech.* (2013) 102:288–309. doi: 10.1016/j.engfracmech.2013.02.009
35. Zhang QB, Zhao J. Quasi-static and dynamic fracture behaviour of rock materials: Phenomena and mechanisms. *Int J Fracture.* (2014) 189:1–32. doi: 10.1007/s10704-014-9959-z
36. Mecholsky JJ, Mackin TJ. Fractal analysis of fracture in Ocala chert. *J Mater Sci Lett*. (1988) 7:1145–7. doi: 10.1007/BF00722319
37. Manthei G. Characterization of acoustic emission sources in a rock salt specimen under triaxial load. *Bull Seismol Soc America.* (2004) 95:1674–700. doi: 10.1785/0120040076
38. Alkan H, Cinar Y, Pusch G. Rock salt dilatancy boundary from combined acoustic emission and triaxial compression tests. *Int J Rock Mech Min Sci.* (2007) 44:108–19. doi: 10.1016/j.ijrmms.2006.05.003
39. Liu XL, Cui JH, Li XB, Liu Z. Study on attenuation characteristics of elastic wave in different types of rocks. *Chin J Rock Mech Eng.* (2018) 37:3223–30. doi: 10.13722/j.cnki.jrme.2017.0604
40. Gutenberg B, Richter CF. Frequency of earthquakes in California. *Bull Seismol Soc Am*. (1944) 34:185–8.
41. Qin SQ, Li ZD. Research on the fractal spatial distribution in space of rock acoustic emission events. *Appl Acoustics*. (1992) 11:19–21.
42. Liu X, Han M, He W, Li X, Chen D. A new b value estimation method in rock acoustic emission testing. *J Geophys Res Solid Earth*. (2020) 125:e2020JB019658. doi: 10.1029/2020JB019658
43. Grosse CU, Ohtsu M. *Acoustic Emission Testing: Basics for Research-Applications in Civil Engineering*. International Institute of Acoustics and Vibrations (2008). doi: 10.1007/978-3-540-69972-9
44. Majer EL, Doe TW. Studying hydrofractures by high frequency seismic monitoring. *Int J Rock Mech Min Sci Geomech Abstr*. (1986) 23:185–99. doi: 10.1016/0148-9062(86)90965-4
45. Madariaga R. Dynamics of an expanding circular fault. *Bull Seismol Soc Am.* (1976) 66:639–66.
46. Winkler KW. Frequency dependent ultrasonic properties of high-porosity sandstones. *J Geophys Res Solid Earth.* (1983) 88:9493–9. doi: 10.1029/JB088iB11p09493
47. Mashinskii EI. Nonlinear amplitude frequency characteristics of attenuation in rock under pressure. *J Geophys Eng.* (2006) 3:291. doi: 10.1088/1742-2132/3/4/001
48. Wanniarachchi WAM, Ranjith PG, Perera MSA, Rathnaweera TD, Lyu Q, Mahanta B. Assessment of dynamic material properties of intact rocks using seismic wave attenuation: an experimental study. *R Soc Open Sci.* (2017) 4:170896. doi: 10.1098/rsos.170896
49. Burlini L, Vinciguerra S, Toro GD, De Natale G, Meredith P, Burg JP. Seismicity preceding volcanic eruptions: new experimental insights. *Geology*. (2007) 35:183–6. doi: 10.1130/G23195A.1
50. Benson PM, Vinciguerra S, Meredith PG, Young RP. Laboratory simulation of volcano seismicity. *Science*. (2008) 322:249–52. doi: 10.1126/science.1161927
51. Aggelis DG, Mpalaskas AC, Ntalakas D, Matikas TE. Effect of wave distortion on acoustic emission characterization of cementitious materials. *Constr Build Mater*. (2012) 35:183–90. doi: 10.1016/j.conbuildmat.2012.03.013
52. Aggelis DG, Matikas TE. Effect of plate wave dispersion on the acoustic emission parameters in metals. *Comp Struct*. (2012) 98–99:17–22. doi: 10.1016/j.compstruc.2012.01.014
53. Aggelis DG, Mpalaskas AC, Matikas TE. Investigation of different fracture modes in cement-based materials by acoustic emission. *Cement Concrete Res.* (2013) 48:1–8. doi: 10.1016/j.cemconres.2013.02.002
54. Aggelis DG. Classification of cracking mode in concrete by acoustic emission parameters. *Mech Res Commun.* (2011) 38:153–7. doi: 10.1016/j.mechrescom.2011.03.007
55. Wang H, Liu D, Cui Z, Cheng C, Jian Z. Investigation of the fracture modes of red sandstone using XFEM and acoustic emissions. *Theor Appl Fracture Mech.* (2016) 85:283–93. doi: 10.1016/j.tafmec.2016.03.012

Conflict of Interest: The authors declare that the research was conducted in the absence of any commercial or financial relationships that could be construed as a potential conflict of interest.

frontiers in Physics

ORIGINAL RESEARCH
published: 09 August 2021
doi: 10.3389/fphy.2021.547991

Investigation on the Settlement of High Rockfill Embankment Using Centrifuge Tests

Hong Jun Jing[1]*, *Ming Jie Gou*[1], *Yan Qing Zhang*[1] and *Ki-IL Song*[2]

[1]School of Architecture and Civil Engineering, Xi'an University of Science and Technology, Xi'an, China, [2]Department of Civil Engineering, Inha University, Incheon, Korea

To study the deformation behavior of the high rockfill (HRF) embankment during construction and operation, based on more than a 50-m high rockfill embankment of the second-class road reconstruction project from Xunyang to Ankang of the national road 316 in Shaanxi, China, the centrifuge model test was performed to study the deformation laws of HRF embankment. The test results showed the following: (i) the HRF embankment was stable during construction and operation; (ii) during construction, the settlement occurred at the embankment top, and uplift occurred at the slope foot. Moreover, the deformation at the top was greater than that at the slope foot, and the deformations at both the top and the slope toe reached the maximum value at the end of construction; (iii) during operation, the settlement at the embankment top continued, and it changed rapidly at the start of operation. And then, the rate of the settlement slowed down and reached a steady state finally. The deformation of the slope foot was very small. This study can provide basis and reference for the design and construction of a similar project in mountain areas.

Keywords: road engineering, high rockfill embankment, centrifuge tests, settlement, long term deformation

OPEN ACCESS

Edited by:
Guoyang Fu,
Monash University, Australia

Reviewed by:
Anyuan Li,
Shaoxing University, China
M.H. Esmaeili,
University of Isfahan, Iran

***Correspondence:**
Hong Jun Jing
jinghongjun@xust.edu.cn

Specialty section:
This article was submitted to Interdisciplinary Physics, a section of the journal Frontiers in Physics

Received: *01 April 2020*
Accepted: *31 May 2021*
Published: *09 August 2021*

Citation:
Jing HJ, Gou MJ, Zhang YQ and Song K-IL (2021) Investigation on the Settlement of High Rockfill Embankment Using Centrifuge Tests. Front. Phys. 9:547991. doi: 10.3389/fphy.2021.547991

HIGHLIGHTS

A model of the HRF embankment was established based on the actual project.
A centrifuge test was performed to simulate the construction and operation of the HRF embankment.
The deformation laws of the HRF embankment during construction and operation were obtained.

INTRODUCTION

When building a road in mountainous areas, due to lack of adequate soil fillers, rock ballast generated by excavation of road cutting and tunnels becomes the main roadbed fillings [1]. High rockfill (HRF) embankment that makes full use of the excellent properties of wasted slag, reduces the damage of slags to the ecological environment, and resists the geological disasters to ensure the travel security has become a more common form of the roadbed for high-grade highways in mountainous areas. However, the uneven settlement of the rockfill embankment, in particular the HRF embankment, has been one of the subjects that road builders need to pay attention to.

Therefore, scholars at home and abroad have done a lot of research on the subgrade settlement. Some scholars have shown considerable interest in the laws of roadbed settlement and deformation by means of experiments. The deformation characteristics of high embankment were studied

through centrifuge tests with an airport in Southwest China as the engineering background [2]. The centrifuge test was used to study the settlement laws of loess high-filled under different boundary conditions (flexibility and rigidity) [3]. Jing et al. [4] took the 69-m high loess embankment of the Lanzhou–Haishiwan expressway in 109 National Highway as the background of the study, and used centrifuge tests to study the distribution laws of settlement along the height, the longitudinal, and the transverse of the high embankment. A set of centrifugal model tests were used to verify the suitability of the embankment with red-bed soft rock (the general name of Jurassic, Cretaceous purple-red, brown-red sandstone, mudstone, and shale interbedded strata with strength within the soft rock range). Meanwhile, a series of centrifuge tests were carried out on the soil-rock–filled roadbed with different water contents, different degrees of compaction, and different particle compositions to study the settlement and deformation behaviors of the soil-rock–filled roadbed [5]. The settlement deformation characteristics of the high fill embankment were developed under different designed dry densities and water contents through centrifuge tests [6,7]. Kohgo et al. [8] studied the influences of water level variation on the stability of rockfill embankment in reservoir areas by using a centrifugal model. But the results are affected by the rockfill parameters. A series of dynamic centrifugal model tests were conducted to explore the influences of water level, embankment height, slope height, compaction degree, and rockfill on the anti-seismic properties of embankment [9].

At the same time, the subgrade settlement laws had been predicted by some scholars using prediction models. Based on the combined prediction idea, a method of variable weight combination forecasting was proposed for various common prediction models, which can be used to predict the development of subgrade settlement with the limited settlement data [10]. Jing et al. [11] took advantage of the settlement data of the loess high embankment of the Lanzhou–Haishiwan expressway as the study sample, and adopted the GM(1,1) (gray theoretical prediction model) with modified nonuniform filling and unequal step settlement observation time to carry out the settlement prediction of the loess high embankment. Based on the gray theory, an equal-length gray differential equation was established for the settlement and used the optimization theory to predict the settlement of the HRF embankment [12]. With considerations to characteristics of soft soil and various geometric parameters of the embankment, a method was proposed to predict settlement deformation of embankment under loads by using the artificial neutral network system. This approach is highly applicable to soft soil foundation [13]. Miščević et al. [14] developed a calculation model to predict the additional settlement of the embankment caused by alteration of rock-fill and expanded the knowledge range on settlement deformation of the embankment for solving the additional settlement of the embankment caused by the worsening of soft rock-fill. Based on the hardening soil model, the elastic-plastic model of double-yield surfaces was improved and the settlement of the HRF embankment during the construction period was simulated [15].

Nevertheless, based on the existing theoretical and constitutive models, the subgrade settlement methods and laws have been studied more widely. Based on the stratified summation method, the settlement calculation of the subgrade and HRF embankment were analyzed separately [16], and with the help of the settlement observation data of the project, they proposed a calculation method for post-construction settlement of HRF embankment. The settlement laws, lateral displacement, and stability of HRF embankment during construction of the Mazhu Expressway were studied by numerical simulation [17]. A three-parameter constitutive model was proposed to describe the creep properties of rock-fills by regarding the fillers as a viscoelastic medium. On this basis, the genetic algorithm and finite element analysis was introduced, and an optimized inversion method was established to determine the parameters of the three-parameter constitutive model. The post-construction settlement analysis was carried out with an engineering example [18]. Based on the monitoring results of post-construction settlement of Lüliang Airport high fill foundation, Zhu et al. [19] analyzed the post-construction settlement components of the original foundation and building body and the causes of the uneven settlement and proposed a method of recursive analysis of the post-construction settlement based on the strain rate.

The settlement mechanism of the HRF embankment was developed based on the deformation characteristics of fillings [20]. A modified Duncan–Chang model was proposed that can consider both shear deformation and compression deformation to calculate subgrade settlement [21]. Zhang et al. [22] proposed a practical method to predict the subgrade settlement with long-term traffic loadings, based on the theory of the equivalent viscoelastic-plastic model.

As a result, it is clear that the current research findings of the subgrade settlement primarily focused on soil embankments using theoretical derivation, numerical simulation, and settlement prediction models. In order to analyze the stability of the HRF embankment during the construction and the long-term operation, and broaden the knowledge range of the HRF embankment, this study based on the section from K21 + 350 to K21 + 541.751 of the HRF embankment of the second-class road reconstruction project from Xunyang to Ankang of the national road 316 in Shaanxi, China, the centrifugal model test was carried out to explore the deformation behavior of the HRF embankment during the construction and operation. This study would provide reference for the construction and stability analysis of HRF embankment in the Qinba mountain district.

RESEARCH BACKGROUND

Engineering Background

There were two initial spoil grounds designed in the second-class highway reconstruction project from Xunyang to Ankang of national highway 316 in Hanbin District. The initial design capacity of waste slag was about 28.6 km^3, of which 91.837 km^3 was spoil and 188.728 km^3 was abandoned stone, which resulted in the need of ground of 47.69 acres to stack up the dregs temporarily. There are many house-intensive villages along

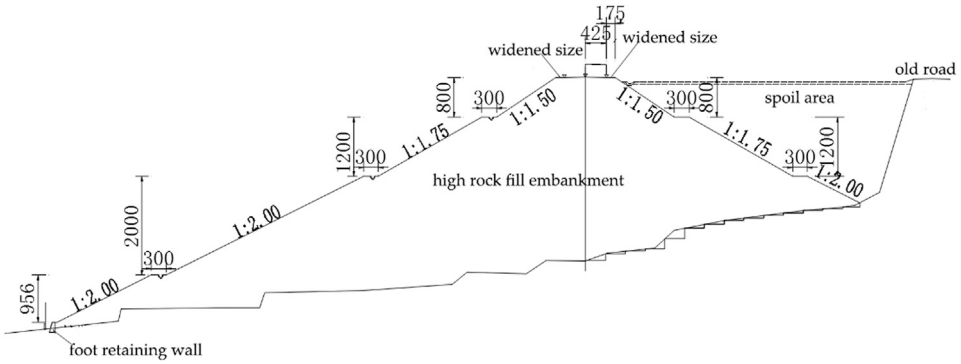

FIGURE 1 | Practical K21 + 460 sectional view (mm).

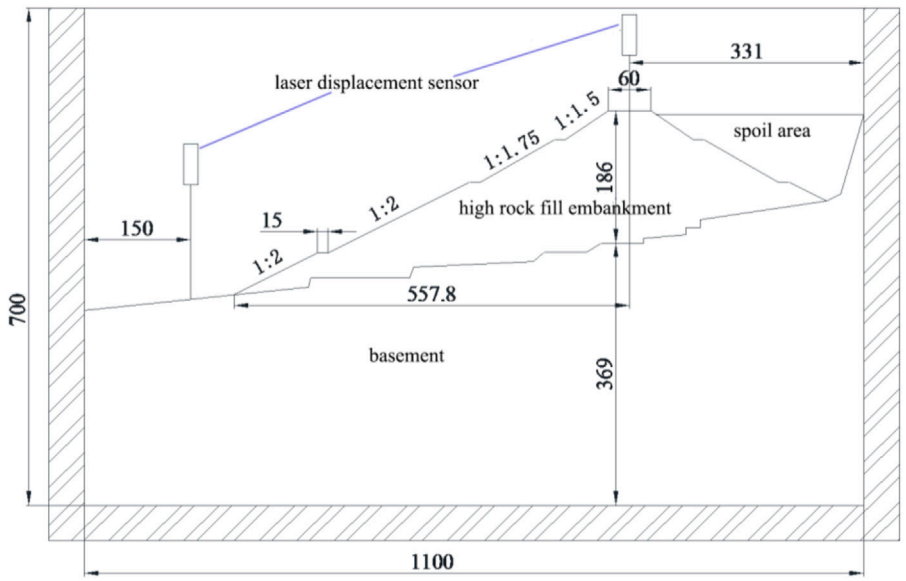

FIGURE 2 | Experimental model (mm).

the engineering. Meanwhile, there are mountains on the right and the Han Jiang River and the Xiangyu Railway on the left of the engineering, respectively.

However, the original construction drawings of spoil ground were narrow and steep, and the annual runoff and land occupied were large in the region. Therefore, the construction units proposed to turn the Zhoujiahe Bridge at K21 + 443 into the HRF embankment with lots of waste slags, which could make well use of the terrain to reduce the damage caused by slags. And including the following advantages (i) save land effectively, which reduce the difficulty of land acquisition, (ii) protect water quality of the Han River to ensure the safety of residents, and (iii) the potential risks in the railway operation to speed up progress of the project. It is worth noted that the roadbed width of the project from K21 + 350 to K21 + 541.751 designed HRF embankment is only 8.5 m in the original design. Given that the subgrade will be widened in the future, so the width of roadbed was being built up to 12 m by wide each side of the road about 1.75 m. Consequently, related parameters of the project from K21 + 350 to K21 + 541.751 are listed as the following: the maximum filling height of the subgrade center was 37.2 m, and the maximum height of the slope was 50.6 m. Three slopes were built with the slope rate 1:1.5, 1:1.75, and 1:2, respectively, at the height of 8, 12, and 20 m, respectively, and the width of all platforms was 3 m. The slope rate of the fourth slope was 1:2. Simultaneously, the lithologic nature of the foundation base from upper to lower is silty clay, strong weathered quartz schist, and middle weathered quartz schist, respectively, according to the geological survey. Based on the engineering background, settlement of the HRF embankment will be further studied in the following section.

Model Design

The actual profile of K21 + 460 as the objective in this study was shown in **Figure 1**. In view of the actual K24 + 460 profile is too

TABLE 1 | Physical quantity similarity ratio of the centrifuge model.

Physical quantity	Dimension	Similarity ratio
Length	L	1:200
Area	L^2	$1:200^2$
Volume	L^3	$1:200^3$
Water content	—	1:1
Density	ML^{-3}	1:1
Unit weight	$ML^{-2}T^{-2}$	200:1
Angle of internal friction		1:1
Deformation coefficient	$ML^{-1}T^{-2}$	1:1
Permeability coefficient	LT^{-1}	200:1
Quality	M	$1:200^3$
Displacement	L	1:200
Consolidation time	T	$1:200^2$

FIGURE 3 | Raw materials of rockfill embankment fillers.

complex for experimental research, some simplification was listed as the following: i) the small steps on the surface of the basement under the embankment were merged, ii) the boundary on the right of the model was extended to the shoulder of the old road, and iii) the footwall on the left of the embankment was removed. **Figure 2** shows the final experimental model.

According to "specification for geotechnical centrifuge model test techniques [23]," the geometric similarity scale of the model was determined to be 1/200 because the interface span is too large. Meanwhile, the NHRI-400 gt centrifuge centrifugal acceleration was determined to be the maximum centrifugal acceleration of 200 g. **Table 1** shows the similarity rates of other physical quantities.

MATERIALS AND METHODS

Raw Materials

The fillings of the HRF embankment consisted of sericite quartz schist and loess, which are introduced as follows. **Figure 3** shows the raw materials of rockfill embankment fillers.

TABLE 2 | Material mechanical parameters of sericite quartz schist.

Index	Parameters
Density (g/cm^3)	2.65
Mean value of uniaxial compressive strength (MPa)	23.8
Mean value uniaxial saturation compressive strength (MPa)	17.0
Softening coefficient	0.71

FIGURE 4 | Paving and compaction of the fillers.

Sericite Quartz Schist

The engineering was built along the natural slope of 15–60° on the left bank of the Han Jiang River, and the physiognomy belongs to the first terrace of the Han Jiang River. The overburden mainly consists of Quaternary alluvial deposits and residual slope deposits. And the underlying bedrock is sericite quartz schist, limestone, and siliceous slate of the Silurian Meiziya Formation. Therefore, the fillers of the project from K21 + 350 to K21 + 541.751 are sericite quartz schist with quality grade class of III and not easily softened. The space between the rocks was filled with loess. According to the report of engineering geological exploration, uniaxial saturation compressive strength of the rock meets the requirements of subgrade filling [24]. As a result, the rock can be used as roadbed fillings on the premise of crushing and rolling. **Table 2** presented detailed material mechanical parameters. Based on the sizes of the model box, the maximum size of the stone was 40 mm.

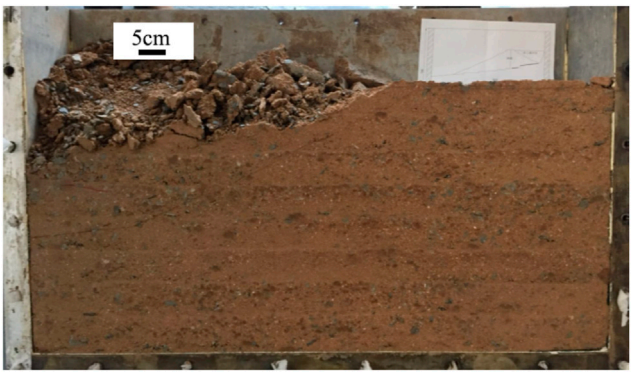

FIGURE 5 | Cutting of the model soil layer.

FIGURE 6 | Model of HRF embankment (before test).

Loess

The loess was taken from the construction site and was disposed by paving, drying, rolling, and sifting.

Water

Tap water was used as the mixing water.

Fillers Preparation

The raw materials of the embankment fillers were homogeneously mixed using a mixer (**Figure 3**). Based on the main purpose, contents of stone were identified as accounting for 30% of the total mass. Based on experience, the moisture content of 13.2% is the optimum moisture content for this soil, when water was added to the clay for mixing. Simultaneously, at this moisture content, the soil is most compacted. Finally, the filler was sealed for about 24 h.

According to the mass and volume of the model, the compaction density of the mixture was determined at about 2.32 g/cm^3. The moisture content was about 9.74% obtained by conversion of the proportion of soil to stone. The dry density was obtained by conversion of the compaction density and moisture content, which was about 2.11 g/cm^3.

FIGURE 7 | Model of HRF embankment (after test).

Experimental Process

(1) The fillings were spread evenly in the model box and compacted in layers; the layer between layers was treated with napping, and the thickness of the paving layer was not more than 50 mm (**Figure 4**).

(2) The model was hoisted into the centrifuge hanging basket platform, and the designed gravity acceleration of 200 g was applied to it for about 0.5 h to recover the self-weight stress field of the soil.

(3) According to the design data, the model was cut to form a model of the HRF embankment, and the deformation meshes were drawn in the model section (**Figures 5**, **6**). **Figure 5** shows, according to the design data, that the model was cut to form a model of the HRF embankment before the test. In order to prevent the surface of the soil from cracking due to water loss during a long-term test, a layer of silicone oil was brushed on the surface of the soil. Then, an organic glass and a laser displacement sensor were installed.

(4) After the silicone oil was completely dried, the model was weighed and hoisted into the centrifuge hanging basket platform; the laser displacement sensor was connected to the data acquisition system, and the centrifuge counterweight was adjusted.

(5) The centrifuge was turned on, and the centrifugal acceleration reached to 200 g in 396 s and continued to operate for about 3 h and 20 min. During the test, the laser displacement sensor was used to record the deformation of slope foot and pavement of the HRF embankment.

(6) The centrifuge was stopped and the coordinates of the deformed grid nodes were measured (**Figure 7**), and the test ended. The data acquisition system was working until the end of the test. The construction period of 6 months and the operation period of 15 years were simulated in this experiment.

Test Setup

As illustrated in **Figure 8**, a 400 gt geotechnical centrifuge of the Nanjing Hydraulic Research Institute (NHRI) was used to perform the centrifuge test. **Table 3** shows the main technical indexes of it. However, the geotechnical centrifuge setup also included a model box, a system of data acquisition, and sensors.

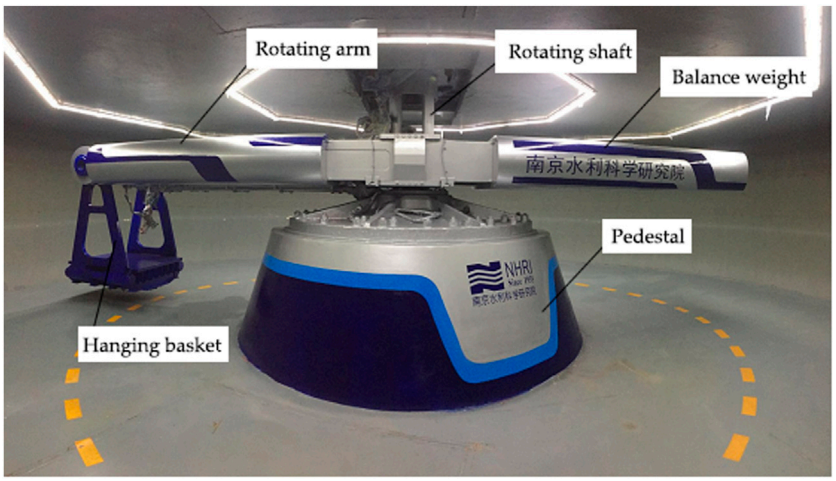

FIGURE 8 | NHRI-400 gt centrifuge.

TABLE 3 | Main technical indexes of the NHRI-400 gt centrifuge.

Key index	Performance
Load capacity	400 g-ton
Radius of the turning arm	5.50 m (from the hanging basket platform to the rotary center)
Maximum centrifugal acceleration	200 g
Internal sizes of the model box	1,100 mm (long) × 200 mm (wide) × 700 mm (high)

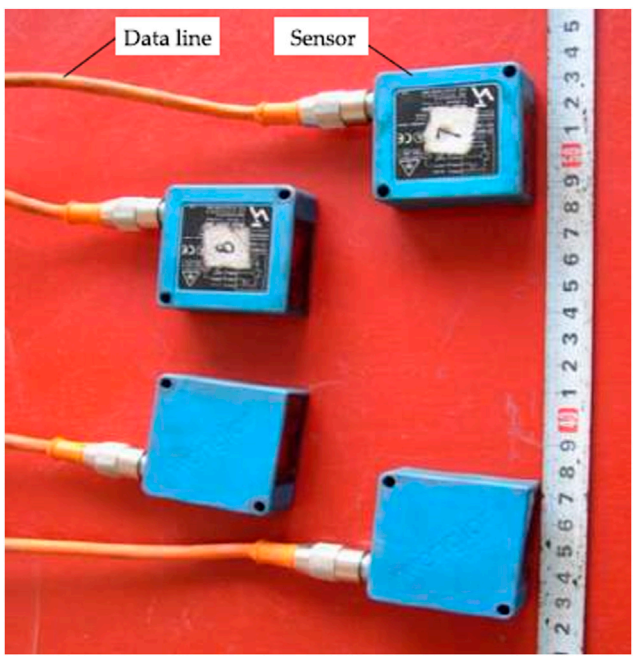

FIGURE 9 | High-precision laser displacement sensors used to measure the top of the embankment deformation.

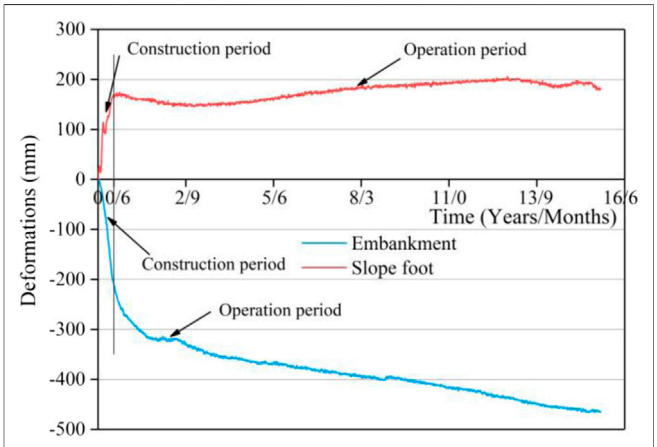

FIGURE 10 | Deformation curve of the toe and pavement during construction and operation.

The type of measuring instrument has a great influence on the results of the laboratory and field test [25]. The sensors that can be used to measure embankment displacement include strain gages and LVDTs, which are used in displacement measurement with high-precision requirements [26,27]. Considering the large running speed of the centrifuge, the sensor (**Figure 9**) used in the centrifuge model test is an ideal noncontact high-precision laser

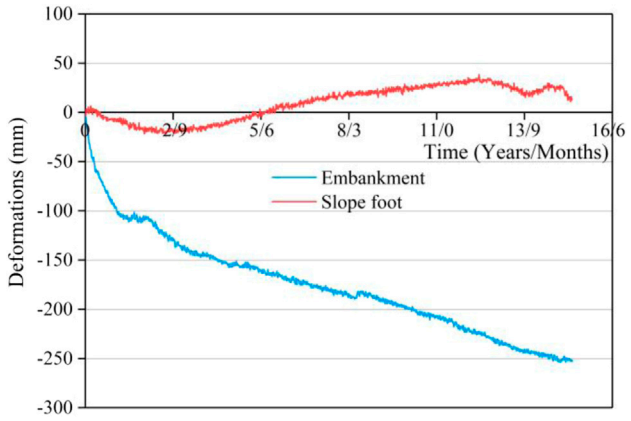

FIGURE 11 | Deformation curve of toe and embankment during long-term operation.

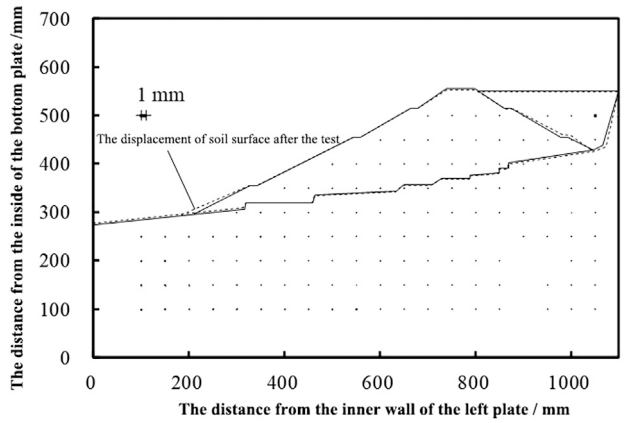

FIGURE 12 | Deformation vector field of the soil profile.

displacement sensor (Wenglor YP11MGVL80), with a range of 50 mm and an accuracy of 20 μm. Sadeghi and Esmaeili et al. [28–30] gave a detailed introduction to the specifications of more test measuring instruments.

RESULTS AND DISCUSSION

Results of Test

During construction and operation, the overall deformation of the slope foot and pavement of the HRF embankment was presented in **Figure 10**. During the operation period, the deformation of the slope foot and pavement was presented in **Figure 11**. Before and after the test, the coordinates of the deformation grid node in **Figures 8**, **9** were measured, and the deformation vector field of the soil was drawn, as shown in **Figure 12**.

Analysis of Results

It can be clearly seen from **Figure 10** that 1) for the HRF embankment, the settlement of top was not only considered in the construction period but also in the operation period; the deformation of the slope foot was mainly in the construction period, and the deformation of post-construction was small; 2) during the construction period, the settlement of the top occurred, at the same time, uplift of the slope foot occurred, and the settlement was greater than the uplift. At the end of the construction period, the deformation both at the top and at the slope foot has reached the maximum value, and 3) during the operation period, the settlement at the top continued, while the deformation of slope foot was small, but the law of deformation was complicated.

During the construction period (**Figure 10**), the settlement of the top was increasing with the increase in the filling height. When the progress of filling was completed, the settlement deformation at the top was about 212 mm, comparatively, the deformation law of the slope foot was a bit complicated, but it basically showed the law that increases with the settlement development of the top; at the end of filling, when the settlement of the top become the maximum, the uplift of the slope foot reached the maximum and was about 169 mm. The uplift at the slope foot of the embankment was less than the settlement at the top.

During the operation period (**Figure 11**), the law of the settlement at the top of the embankment was obvious: 1) in the initial period of operation, the variation of settlement was large and about 106 mm that occurred in two years; 2) from the second year to the fifth year, the settlement changed from about 108 mm to about 154 mm and increased by about 46 mm in 3 years, which should be seen as the rate of settlement had slowed down significantly; 3) from the fifth year to the fifteenth year, the rate of settlement with time was basically stable. The settlement changed from about 154 mm to about 253 mm and the average annual settlement was about 9.8 mm; 4) on the whole, after operation of fifteen years, the settlement at the top of the embankment was about 253 mm, of which about 42% occurred in the first two years, and the settlement in the first five years accounted for about 61% of the total, and in the following 10 years, the rate of settlement deformation tended to be stable. For the slope toe, the law of deformation was complicated. And from official operation to the fifth year and six months, the performance was settlement deformation and the maximum was about 21 mm; subsequently, the tendency of deformation showed as repeated uplift and settlement, but the overall trend was uplift and the maximum was about 34 mm. The data would indicate that the HRF embankment was stable during the long-term operation. Those findings in this study have a good agreement with [2, 4] in which the total settlement during the operation period increased with time, but the rate of change gradually decreased.

It should be noted that the simulation of filling progress in centrifuge tests is different from the construction of actual engineering. In centrifuge tests, the progress of embankment filling is simulated by increasing the centrifugal acceleration step by step, and at the end of construction, the settlement results in the elevation of the top of embankment lower than the design value. Therefore, the test results of the settlement of the top of embankment can be used as a basis to calculate the extra earthwork in the practical project, and accordingly, the results

of uplift of the slope foot can be used as a basis to calculate the extra excavated volume in practical engineering.

Through the deformation vector field of the model (**Figure 12**), we can see intuitively that for the deformation of the slope foot, the impact of construction and long-term operation of the HRF embankment, both from the value of deformation and the scope of deformation, was very limited, and it would not affect the stability of the slope foot and the adjacent railway and water area.

CONCLUSION

To analyze the stability of the HRF embankment during the construction and the long-term operation, and broaden the knowledge range of the HRF embankment, the centrifuge model test was carried out based on the actual project to explore the deformation behavior of the HRF embankment during the construction and operation. Although there is a similarity to a certain extent for centrifuge tests, it still plays an important role in guiding practical engineering. According to the above result analyses, the following conclusions can be drawn:

(1) For the HRF embankment, the settlement at the top of embankment had always existed both in the construction period and long-term operation period. While the deformation of the slope foot occurred mainly during the construction period, and the deformation of post-construction was small.

(2) During the construction period, the deformation of embankment was the settlement and the deformation of slope foot was uplift, and at the end of the construction, the settlement at the top of the embankment reached the maximum value, and the uplift of the slope toe reached the maximum value.

(3) During the long-term operation period, the settlement at the top of the embankment kept on increasing, and at the initial stage of operation the settlement changed faster. And then, the rate of settlement slowed down gradually and tended to stability. For the slope foot, the law of deformation was complicated, which showed the trend of settlement-uplift-settlement-uplift-settlement. However, the deformation of slope foot during operation was only in the range of about -21 mm (settlement)~34 mm (uplift), indicating that the operation of the engineering has a small impact on the stability of the slope foot.

DATA AVAILABILITY STATEMENT

The raw data supporting the conclusions of this article will be made available by the authors, without undue reservation.

AUTHOR CONTRIBUTIONS

M-jG and Y-qZ: writing—original draft preparation; H-jJ: methodology; and K-iS: validation. All authors have read and agreed to the published version of the manuscript.

FUNDING

The authors are grateful for the support provided by the National Natural Science Foundation of China (Grant No. 51378090) and School of Architecture and Civil Engineering, Xi'an University of Science and Technology.

REFERENCES

1. Zhang YQ, Jing HJ, Dai J, Li SF, and Zhang Z. Stability of High Rockfill Embankment Based on Orthogonal Test and Numerical Simulation. *Tehnički vjesnik* (2020) 27(1):191–9. doi:10.17559/tv-20191216092415
2. Liu H, Zhang ZY, and Han WX. Centrifugal Model Tests for Settlement of High Embankment. *J Southwest Jiao Tong Univ* (2003) 38(3):323–6.
3. Cao J, Zheng JG, and Zhang JW. Centrifuge Tests of Loess High-Filled Settlement under Different Boundary Conditions. *J China Water Resour Hydropower Res Inst* (2017) 15(4):256–61.
4. Jing HJ, Hu CS, and Wang BG. Study on Settlement and Deformation Laws of High Loess-Fill Embankment. *Chin J Rock Mech Eng* (2005) 24(S2): 5845–50.
5. Qing SH, Huang RQ, and Cao XW. Centrifugal Model Test of Red and Soft Rock-Filled Embankment. *J Railway Eng Soc* (2007)(2) 41–6.
6. Dong Y, Chai HJ, and Yan ZL. Centrifugal Model Test Study on the Settlement Character of the Rock-Soil Filled Roadbed. *J Highw Transportation Res Develop* (2007) 24(3):25–9.
7. Jiang Y, and Chai HJ. Study on Centrifugal Model Settlement experiment of High Filling Embankments. *Mod Transportation Techn* (2007) 4(6):5–8.
8. Kohgo Y, Takahashi A, and Suzuki T. Centrifuge Model Tests of a Rockfill Dam and Simulation Using Consolidation Analysis Method. *Soils and Foundations* (2010) 50(2):227–44. doi:10.3208/sandf.50.227
9. Enomoto T, and Sasaki T. Several Factors Affecting Seismic Behaviour of Embankments in Dynamic Centrifuge Model Tests. *Soils and Foundations* (2015) 55(4):813–28. doi:10.1016/j.sandf.2015.06.013
10. Zhao MH, Liu JB, and Yu Y. Study on Variable-Weight Combined Forecasting Method of the Settlement in High Rock-Filled Embankment. *J Hunan Univ Sci Techn (Natural Science)* (2005) 20(4):53–7.
11. Jing HJ, and Yu MH. Model Study for Prediction of Settlement of Loess-Fill High Embankments. *China Civil Eng J* (2006) 39(8):113–7.
12. Zhao MH, Zeng GX, and Xiang ZF. Gray Optimizing-Markov Predicating Model on Settlement of High-Enrockment Embankment. *J Highw Transportation Res Develop* (2006) 23(11):19–22.
13. Chik Z, and Aljanabi QA. Intelligent Prediction of Settlement Ratio for Soft clay with Stone Columns Using Embankment Improvement Techniques. *Neural Comput Applic* (2014) 25(1):73–82. doi:10.1007/s00521-013-1449-0
14. Miščević P, and Vlastelica G. Estimation of Embankment Settlement Caused by Deterioration of Soft Rock Grains. *Bull Eng Geology Environ* (2019) 78(3): 1843–53.
15. Sukkarak R, Pramthawee P, and Jongpradist P. A Modified Elasto-Plastic Model with Double Yield Surfaces and Considering Particle Breakage for the Settlement Analysis of High Rockfill Dams. *KSCE J Civ Eng* (2017) 21(3): 734–45. doi:10.1007/s12205-016-0867-9
16. Cao XR, Zhong SB, Yu YH, and Li L. Study on Settlement of High Fill Rock Embankment after Construction and its Engineering Algorithm. *J Hunan Univ (Natural Science)* (2002) 29(6):112–7.
17. Yang B, Wang B, Zhu JB, and Li C. Computational Analysis of Settlement and Stability of a High Rockfill Embankment in Construction Period of Ma-Zhu High Way. *Transportation Sci Techn* (2016)(1) 79–82.
18. Cao WG, Li P, and Cheng Y. Research of Creep FEM in Calculating Settlement of High Rock- Filled Embankment after Construction and its Back Analysis. *Rock Soil Mech* (2005) 26(S):175–8.

19. Zhu CH, Li N, Liu MZ, and Wei YF. Spatiotemporal Laws of Post-Construction Settlement of Loess-Filled Foundation of Lüliang Airport. *Chin J Geotechnical Eng* (2013) 35(2):293–301.
20. Xie YZ, Yang CZ, Xia XQ, Cheng YP, and Ren WB. Study on Settlement Mechanism of High Rockfill Embankment. *J Highw Transportation Res Develop (Applied Technology)* (2008)(3) 28–31.
21. Cao XR, Zhao ZY, and Zhao MH. Study on Settlement Calculation Method for Subgrade of High Rockfill Embankment. *J Highw Transportation Res Develop* (2005) 22(6):38–42.
22. Zhang XX, Zhang JM, and Wen YF. Practical Method to Predict Settlement of Subgrade Induced by Long-TermTraffic Loads. *Chin J Geotechnical Eng* (2015) 37(11):2067–72.
23. Specification for Geotechnical Centrifuge Model Test T. *echniques (DL/T 5102-2013)*. Beijing: China Electric Power Press (2014)5–16.
24. Wu YH. Highway Subgrade Design Code" JTG D30-2015 Phase I Evangelist Will Be Successfully Held in Guangzhou. *Standardization Eng Construction* (2015)(5) 70.
25. Zakeri J, Hassan Esmaeili M, Mazraeh A, and Shadfar M. Impact of Heavy Urban Rail Vehicles Running over Light Rail Turnouts. *Proc Inst Mech Eng F: J Rail Rapid Transit.* (2021) 235(3):300–12. doi:10.1177/0954409720924308
26. Sadeghi J, Liravi H, and Esmaeili MH. Experimental Investigation on Loading Pattern of Railway concrete Slabs. *Construction Building Mater* (2017) 153: 481–95. doi:10.1016/j.conbuildmat.2017.07.025
27. Sadeghi J, Esmaeili MH, and Akbari M. Reliability of FTA General Vibration Assessment Model in Prediction of Subway Induced Ground Borne Vibrations. *Soil Dyn Earthquake Eng* (2019) 117:300–11. doi:10.1016/j.soildyn.2018.11.002
28. Sadeghi J, Esmaeili MH, Shadfar M, and Ashari Ghomi A. Influences of Railway Track Geometry Parameters on Ground-Borne Vibration. *Int J Railway Res* (2014) 1(1):11–8.
29. Sadeghi J, and Esmaeili MH. Safe Distance of Cultural and Historical Buildings from Subway Lines. *Soil Dyn Earthquake Eng* (2017) 96:89–103. doi:10.1016/j.soildyn.2017.02.008
30. Sadeghi J, and Esmaeili MH. Effectiveness of Track Stiffness Reduction in Attenuation of Metro Induced Vibrations Received by Historical Buildings. *Lat Am J Solids Struct* (2018) 15(11):e142. doi:10.1590/1679-78255252

Conflict of Interest: The authors declare that the research was conducted in the absence of any commercial or financial relationships that could be construed as a potential conflict of interest.

Publisher's Note: All claims expressed in this article are solely those of the authors and do not necessarily represent those of their affiliated organizations, or those of the publisher, the editors and the reviewers. Any product that may be evaluated in this article, or claim that may be made by its manufacturer, is not guaranteed or endorsed by the publisher.

Advantages of publishing in Frontiers

OPEN ACCESS
Articles are free to read for greatest visibility and readership

FAST PUBLICATION
Around 90 days from submission to decision

HIGH QUALITY PEER-REVIEW
Rigorous, collaborative, and constructive peer-review

TRANSPARENT PEER-REVIEW
Editors and reviewers acknowledged by name on published articles

Frontiers
Avenue du Tribunal-Fédéral 34
1005 Lausanne | Switzerland

Visit us: www.frontiersin.org
Contact us: frontiersin.org/about/contact

REPRODUCIBILITY OF RESEARCH
Support open data and methods to enhance research reproducibility

DIGITAL PUBLISHING
Articles designed for optimal readership across devices

FOLLOW US
@frontiersin

IMPACT METRICS
Advanced article metrics track visibility across digital media

EXTENSIVE PROMOTION
Marketing and promotion of impactful research

LOOP RESEARCH NETWORK
Our network increases your article's readership